

nature

BLUE FOOD

Assessing the environmental performance of aquatic foods



Written in mRNA

The twisted path that led to some of the first COVID vaccines

Community service

Lessons from Brazil's project to improve reproducibility

Cellular history

Mutations reveal lineage and dynamics of human cells

Nature.2021.09.18

[Sat, 18 Sep 2021]

- [This Week](#)
- [News in Focus](#)
- [Books & Arts](#)
- [Opinion](#)
- [Work](#)
- [Research](#)

This Week

- **[Harness the world's aquatic 'blue' food systems to help end hunger](#)** [15 September 2021]
Editorial • Aquatic foods have been neglected by researchers and policymakers. It's time to recognize them.
- **[Politics will be poorer without Angela Merkel's scientific approach](#)** [15 September 2021]
Editorial • The departing German chancellor's support for science and rigour in policymaking has proved transformative — except on climate change.
- **[Biology must generate ideas as well as data](#)** [13 September 2021]
World View • Data should be a means to knowledge, not an end in themselves.
- **[An easily swallowed capsule injects drugs straight into the gut](#)** [08 September 2021]
Research Highlight • Exposure to digestive fluids triggers the deployment of a needle through which medication flows into the stomach tissue.
- **[A simulation exposes the secret spread of hospital infections](#)** [09 September 2021]
Research Highlight • Algorithm can pick out hospitalized people who are most likely to spread drug-resistant microbes.
- **[Quantum gas free-falls its way to a low-temperature record](#)** [08 September 2021]
Research Highlight • A cloud of rubidium atoms is said to have achieved the coldest temperature yet after being dropped from the top of a tower.
- **[Polar bears are inbreeding as their icy home disintegrates](#)** [07 September 2021]
Research Highlight • With climate change fracturing northern ice, the bears have begun to lose genetic diversity.
- **[Seismic sleuths unmask the 'earthquake' that wasn't](#)** [08 September 2021]
Research Highlight • People in one Indian state flooded into the streets and onto a seismology app after predictions of a quake that never happened.

- **Early Americans' huge earthworks show off their engineering might** [06 September 2021]

Research Highlight • Analysis of mysterious earth mounds reveals their rapid construction and sophisticated composition.

- **Flowing crystals for quick camouflage** [09 September 2021]

Research Highlight • A soft material can be guided to rapidly assume the same colour pattern as its background.

- EDITORIAL
- 15 September 2021

Harness the world's aquatic 'blue' food systems to help end hunger

Aquatic foods have been neglected by researchers and policymakers. It's time to recognize them.



Pelagic fish from the open ocean are richer in nutrients than are chicken, beef, lamb and pork.Credit: Aaron Bull/Getty

Next week, world leaders will gather for the United Nations Food Systems Summit. The event will be hosted by UN secretary-general António Guterres, with the aim of giving a much-needed boost to efforts to get the agency's flagship Sustainable Development Goals back on track.

One of these goals is to end hunger by 2030. Nearly 700 million people (almost 9% of the world's population) go hungry; of those, 250 million are potentially on the brink of starvation, according to the World Food Programme. Even before COVID-19, there had been limited progress towards ending hunger. Unless the summit's delegates take strong and coordinated action, 840 million will be going hungry by 2030.

Blue food collection

This week, journals in the Nature Portfolio shine a spotlight on how aquatic food systems — sometimes called blue foods — can help to end hunger and accelerate the creation of a truly sustainable global food system (see go.nature.com/3nw8qbf).

The research is part of the Blue Food Assessment, a collaboration involving more than 100 researchers. It is the first systematic assessment of how aquatic food contributes to food security, helping to build a fuller picture of the global food system, beyond food from agriculture.

Blue foods include fish and shellfish, but also encompass the diversity of animals, plants and algae harvested from rivers, seas and the ocean, which provide protein and other valuable nutrients for more 3.2 billion people.

To improve understanding of their nutritional value, Christopher Golden at the Harvard T.H. Chan School of Public Health in Boston, Massachusetts, and his colleagues compiled nutrient profiles of 3,753 types of aquatic food (including fish, crustaceans and cephalopods). They found¹ that several categories (including shellfish and fish from the open ocean) are, on average, richer than beef, lamb, chicken or pork in the seven nutrients assessed (omega-3 long-chain polyunsaturated fatty acids, vitamins A and B12, calcium, iodine, iron and zinc).

When blue is green

Globally, food production accounts for one-quarter of all greenhouse-gas emissions. However, Jessica Gephart at the American University in Washington DC and her colleagues² found that some forms of farmed

aquatic foods have lower emissions than do foods gathered or caught from the wild. For example, farmed bivalves (such as clams and oysters) and shrimp produce lower average emissions than their wild-caught counterparts.



A spotlight on seafood for global human nutrition

Globally, one billion people are fed by small-scale fisheries and aquaculture, which also support 100 million jobs for lone businesses and communities. Small-scale fisheries and aquaculture produce more than half of the world's fish catch, and two-thirds of aquatic foods that people eat.

But, as Rebecca Short at the Stockholm Resilience Centre and her colleagues report³, these communities have been neglected, both by science and in policymaking. As *Nature* has highlighted before, people who work alone or in small cooperatives tend to lack access to government and policy processes, and are under-studied by researchers. Short and colleagues have produced 70 case studies from around the world that demonstrate the many ways in which blue foods are produced at smaller scales — from fishing to feed individual households to small businesses joining in networks, perhaps as part of a cooperative.

Coastal communities are often among their countries' poorest, and most vulnerable — both to climate change and to changes in the global economy.

Michelle Tigchelaar at the Center for Ocean Solutions at Stanford University in California and her colleagues combined data on climate hazards, exposure and vulnerability for 219 countries and territories to show that the aquatic food systems most at risk from climate change are in Africa, south and southeast Asia and the Indo-Pacific⁴.

Blue food immersive feature

Rapidly increasing demand for fish is also adding to risks for coastal communities. Demand has doubled since the start of the twenty-first century and — as Rosamond Naylor, also at Stanford, and her colleagues report — there will be another near-doubling by the middle of the century⁵. That will benefit some, whose incomes will increase, but it could reduce the protein consumption of others if there is less locally harvested fish available to eat or buy.

At a World Food Summit 25 years ago, some 10,000 participants from nearly 200 nations pledged to end hunger, with an immediate goal of halving the numbers of undernourished people by 2015. That did not happen. Before that, the 1974 World Food Conference in Rome boldly proclaimed that people have an “inalienable right to be free from hunger and malnutrition”. These were stirring words, but not accompanied by meaningful action.

Delegates at next week’s summit have another valuable opportunity to act so that history is not repeated. And they must recognize blue foods for their potential in ending hunger and helping the world to transition to a sustainable food system.

Nature **597**, 303 (2021)

doi: <https://doi.org/10.1038/d41586-021-02476-9>

References

1. 1.

Golden, C. D. *et al. Nature* <https://doi.org/10.1038/s41586-021-03917-1> (2021).

2. 2.

Gephart, J. A. *et al.* *Nature* <https://doi.org/10.1038/s41586-021-03889-2> (2021).

3. 3.

Short, R. E. *et al.* *Nature Food* <https://doi.org/10.1038/s43016-021-00363-0> (2021).

4. 4.

Tigchelaar, M. *et al.* *Nature Food* <https://doi.org/10.1038/s43016-021-00368-9> (2021).

5. 5.

Naylor, R. L. *et al.* *Nature Commun.* <https://doi.org/10.1038/s41467-021-25516-4> (2021).

This article was downloaded by **calibre** from <https://www.nature.com/articles/d41586-021-02476-9>

| [Section menu](#) | [Main menu](#) |

- EDITORIAL
- 15 September 2021

Politics will be poorer without Angela Merkel's scientific approach

The departing German chancellor's support for science and rigour in policymaking has proved transformative — except on climate change.



Departing German Chancellor Angela Merkel has stood out among politicians for her commitment to science and evidence. Credit: Maciej Luczniewski/NurPhoto/Getty

German Chancellor Angela Merkel, a theoretical quantum chemist from the former East Germany, will stand down after federal elections on 26 September. This will mark the end of 16 years in the post and a 30-year political career.

Merkel leaves behind a powerful legacy for research and for evidence-based thinking. Over the years, her administration has strengthened and internationalized German science. Every government is imperfect when it comes to protecting peoples' rights, promoting security and well-being, and administering justice, but Merkel brought compassion and an insistence — unusual among politicians, even in the time of COVID-19 — that decision-making benefits from evidence. All of this will make her a hard act to follow.



The secret to Germany's scientific excellence

Merkel's passion for science is spurred, in part, by her grasp of the value scientific research and innovation holds for societies and economies. In interviews with *Nature*, Germany's researchers have talked about how, as chancellor, Merkel prioritized regular meetings with working scientists and research managers. Every few months, she presided over informal science soirees focused on different fields. She set the agenda for the sessions, with a particular interest in up-and-coming fields such as hydrogen technology, quantum computing and artificial intelligence.

Researchers were advised to prepare carefully for their presentations at these meetings, because Merkel would be ready with expert-level questions. These ‘innovation’ talks, as they became known, became the nucleus for initiatives such as a 2-billion (US\$2.4-billion) programme for quantum computing and related technologies.

But Merkel was just as committed to curiosity-driven research. In a speech to London’s Royal Society in 2010, she urged her audience to be sceptical of politicians who claim to be able to predict the course of scientific discovery.

It’s easy to forget that when Merkel became chancellor in 2005, reunified Germany was still only 15 years old. Two nations — and their science systems — were slowly re-learning how to function as one. Science in the communist east was organized in disciplinary research centres attached to the centralized Academy of Sciences of the German Democratic Republic. By contrast, West German science was organized through publicly funded research institutes as well as universities. It was also hierarchical and male-dominated — an area in which Germany still lags behind most European Union countries and must continue to improve.



[German science is thriving, but diversity remains an issue](#)

Science in Germany today is more collaborative, more cosmopolitan and comparatively less hierarchical. But according to data from Eurostat, in

2018, just 33% of Germany's researchers were women. This compares with the EU average of 42%. Around one-fifth of Germany's senior research leaders are women, which is more than double the proportion in 2005, and [approaching the EU average of 26%](#).

Merkel's government has increased budgets for research and universities by 3–5% every year since 2006. Annual federal science spending is now 24 billion, exceeding an EU target that member states should spend 3% of gross domestic product on research and development.

Merkel obtained a PhD in quantum chemistry in 1986 from the Academy of Sciences in Berlin–Adlershof in East Germany. She worked in the Prague laboratory of quantum chemist Rudolf Zahradník, studying the quantum mechanics of gas-particle collisions, and co-authored several papers (for example, [A. Merkel et al. J. Am. Chem. Soc. 110, 8355–8359 \(1988\)](#); [Z. Havlas et al. Chem. Phys. 127, 53–63; 1988](#)). “She was pushing the limits of accuracy using the data and computational tools available to researchers in the 1980s,” says Alán Aspuru-Guzik, a quantum chemist at the University of Toronto in Canada. “Merkel’s research was state of the art for its time.”



Angela Merkel, pictured in 1995, when she was Germany's Federal Minister for the Environment, Nature Conservation and Nuclear Safety. Credit: Ulrich Baumgarten/Getty

Although Merkel maintained close ties with the research world, there is one crucial policy area in which her decisions have not always been backed up by science. Germany is not a leader when it comes to phasing out fossil fuels. In the past, Merkel has even shown irritation at warnings of dangerous climate change from the Intergovernmental Panel on Climate Change. And she has stuck by the construction of Germany's controversial gas pipeline from Russia, Nord Stream 2, which was completed just last week.

Moreover, Merkel's decision, immediately after the 2011 Fukushima Daiichi nuclear disaster, to phase out nuclear power in Germany by 2022 has made decarbonization even harder to achieve. In April, Germany's Federal Constitutional Court ordered the government to explain how it will reach its climate targets of cutting emissions by 88% by 2040 and becoming greenhouse-gas neutral by 2045.

The pandemic brought more challenges in balancing science with politics. In March 2020, on the basis of expert advice, Merkel implemented lockdowns to bring the spread of COVID-19 under control. But Germany experienced further waves, in line with other countries. Merkel favoured an early return to tough restrictions — as advised by scientists — but the leaders of many of Germany's powerful state governments refused. As *Nature* went to press, Germany had recorded some 4 million infections and more than 93,000 people in the country had died.



How Germany retains one of the world's strongest research reputations

Germany will undoubtedly change after Merkel's departure. Many voters are concerned about climate change — especially after July's deadly floods in western Germany — and the government's slowness to embrace decarbonization. Opinion polls predict that the Green Party will do well enough in the elections to enter a coalition government.

Germany's electoral system makes it hard to predict front-runners for the chancellor's post, but the legacy of Germany's outgoing scientist leader is assured.

Nature **597**, 304 (2021)

doi: <https://doi.org/10.1038/d41586-021-02479-6>

This article was downloaded by **calibre** from <https://www.nature.com/articles/d41586-021-02479-6>

| [Section menu](#) | [Main menu](#) |

- WORLD VIEW
- 13 September 2021

Biology must generate ideas as well as data



Data should be a means to knowledge, not an end in themselves.

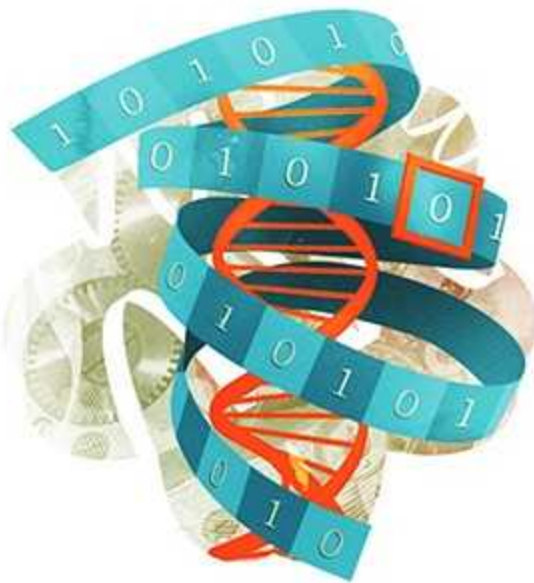
- [Paul Nurse](#) 0

Accepting a Nobel prize nearly two decades ago, my old friend Sydney Brenner had a warning for biology. “We are drowning in a sea of data and starving for knowledge,” he said. That admonishment, from one of the founders of molecular biology, who established the nematode worm *Caenorhabditis elegans* as a model organism, is even more relevant to biology today.

Rather often, I go to a research talk and feel drowned in data. Some speakers seem to think they must unleash a tsunami of data if they are to be taken seriously. The framing is neglected, along with why the data are being

collected; what hypotheses are being tested; what ideas are emerging. Researchers seem reluctant to come to biological conclusions or present new ideas. The same occurs in written publications. It is as if speculation about what the data might mean and the discussion of ideas are not quite ‘proper’.

I have a different view: description and data collection are necessary but insufficient. Ideas, even tentative ones, are also needed, along with the recognition that ideas will change as facts and arguments accumulate.



Life's code script

Why are researchers holding back on ideas? Perhaps they are worried about proposing an idea that turns out to be wrong, because that might damage their chances of getting promotion or funding. But as Charles Darwin put it: “False facts are highly injurious to the progress of science, for they often endure long; but false views, if supported by some evidence, do little harm, for everyone takes a salutary pleasure in proving their falseness; and when this is done, one path towards error is closed and the road to truth is often at the same time opened.” To wit, it’s important to get the facts right, but new ideas are useful, as long as they are based on reasonable evidence and are amenable to correction.

Don't get me wrong. We need data produced from new technologies to advance understanding. The importance of 'hypothesis-free research' is well established: the philosopher Francis Bacon proposed it as part of his 'empirical method' in 1620. In his book *Novum Organum*, he argued that the first step in establishing scientific truth should be the description of facts through systematic observations. But this is only the first step. For example, it would have been rather a pity if Darwin had stopped thinking after he had described the shapes and sizes of finch beaks, and had not gone on to propose the idea of evolution by natural selection.

The next step is to extract knowledge from the data. To refocus on that goal, we must improve our working processes, placing a greater emphasis on theory and shifting our research culture.



Better methods can't make up for mediocre theory

How? Embed engineers and experimentalists who are developing new technologies and methods deeply into the biological problems. It is through deep familiarity with the biology — not simply a drive to collect more and more data — that important questions will be asked. Such questions will sustain the investigators' passion to keep probing data until patterns and knowledge emerge, and will also influence the data that are gathered.

There are other necessary steps. Develop appropriate analytical tools, including programs for data mining and machine learning. Make certain that data are usable, properly annotated and openly shared. Model the molecular and cellular components involved in a biological phenomenon, to allow analysis of dynamic behaviours and interactions. Sometimes just writing down the equations without seeking solutions can be helpful, simply because it imposes greater rigour on model building.

More theory is needed. My exemplars for this include the evolutionary biologists Bill Hamilton and John Maynard Smith, and the geneticists Barbara McClintock and Francis Crick. Their papers are permeated with richly informed biological intuition, which makes them a delight to read. This sort of thinking will accelerate a shift from description to knowledge. Theorists can find fertile ground in considering the flow of information through living systems, which can help them to make better sense of the flood of biological data.

Seeking to be led by theory and knowledge will probably require shifts in research culture. Theorizing should be encouraged, and theories should be included in experimental papers to put data in context. Attempts to do this should not be dismissed by editorial and funding processes as idle speculation. As Darwin said, it allows ideas to be attacked and either dismissed or modified. A sort of ‘tyranny of the field’ sometimes inhibits the generation of explanations different from the current consensus, but this is a mistake. If the new ideas are not satisfactory, then they will soon be eliminated and progress will be made.

False facts should not be tolerated, but journals and research funders should be open to reasonable new ideas and interpretations, particularly if they differ from the current consensus. Evaluation committees should be tolerant when some of the ideas of people they are considering for promotion or funding are shown to be incorrect.

Such approaches will advance not only research, but also teaching. Students will be better motivated and will feel more inspired if they are taught that biology has ideas — and that they are worth talking about.

doi: <https://doi.org/10.1038/d41586-021-02480-z>

This article was downloaded by **calibre** from <https://www.nature.com/articles/d41586-021-02480-z>

| [Section menu](#) | [Main menu](#) |

- RESEARCH HIGHLIGHT
- 08 September 2021

An easily swallowed capsule injects drugs straight into the gut

Exposure to digestive fluids triggers the deployment of a needle through which medication flows into the stomach tissue.

 Sequential MicroCT images of egg-shaped capsule delivering contrast dye into tissue

A needle that pops out of the bottom of a pill taken by mouth can feed medications and other substances into the stomach tissue. Credit: A. Abramson *et al./Nature Biotechnol.*

A pill that pricks the stomach wall to administer drugs could be used to deliver medications to people squeamish about injections.

Access options

Subscribe to Journal

Get full journal access for 1 year

\$199.00

only \$3.90 per issue

[Subscribe](#)

All prices are NET prices.

VAT will be added later in the checkout.

Tax calculation will be finalised during checkout.

Rent or Buy article

Get time limited or full article access on ReadCube.

from \$8.99

[Rent or Buy](#)

All prices are NET prices.

Additional access options:

- [Log in](#)
- [Learn about institutional subscriptions](#)

Nature **597**, 306 (2021)

doi: <https://doi.org/10.1038/d41586-021-02443-4>

References

1. 1.

Abramson, A. *et al.* *Nature Biotechnol.*
<https://doi.org/10.1038/s41587-021-01024-0> (2021).

This article was downloaded by **calibre** from <https://www.nature.com/articles/d41586-021-02443-4>

- RESEARCH HIGHLIGHT
- 09 September 2021

A simulation exposes the secret spread of hospital infections

Algorithm can pick out hospitalized people who are most likely to spread drug-resistant microbes.

 Coloured scanning electron micrograph of *Staphylococcus aureus* bacteria on cultured human skin cells.

Staphylococcus aureus bacteria can become resistant to antimicrobial drugs, causing dangerous infections. Credit: Steve Gschmeissner/Science Photo Library

A modelling system could help to identify hospitalized people who are unknowingly carrying pathogens that are resistant to antimicrobial drugs.

Access options

Subscribe to Journal

Get full journal access for 1 year

\$199.00

only \$3.90 per issue

[Subscribe](#)

All prices are NET prices.

VAT will be added later in the checkout.

Tax calculation will be finalised during checkout.

Rent or Buy article

Get time limited or full article access on ReadCube.

from \$8.99

[Rent or Buy](#)

All prices are NET prices.

Additional access options:

- [Log in](#)
- [Learn about institutional subscriptions](#)

Nature **597**, 306 (2021)

doi: <https://doi.org/10.1038/d41586-021-02466-x>

References

1. 1.

Pei, S., Liljeros, F. & Shaman, J. *et al.* *Proc. Natl. Acad. Sci. USA* **118**, e2111190118 (2021).

This article was downloaded by **calibre** from <https://www.nature.com/articles/d41586-021-02466-x>

- RESEARCH HIGHLIGHT
- 08 September 2021

Quantum gas free-falls its way to a low-temperature record

A cloud of rubidium atoms is said to have achieved the coldest temperature yet after being dropped from the top of a tower.

 Computer simulation of vortices forming within a spinning Bose–Einstein condensate

Scientists have manipulated the strange form of matter called a Bose–Einstein condensate (computer simulation) to reach the coldest temperature achieved so far. Credit: National Institute of Standards and Technology/Science Photo Library

Physicists have achieved what they describe as the lowest temperature yet — 0.038 billionths of a degree above absolute zero — by cajoling a quantum gas to slow its expansion¹.

Access options

Subscribe to Journal

Get full journal access for 1 year

\$199.00

only \$3.90 per issue

[Subscribe](#)

All prices are NET prices.
VAT will be added later in the checkout.
Tax calculation will be finalised during checkout.

Rent or Buy article

Get time limited or full article access on ReadCube.

from \$8.99

[Rent or Buy](#)

All prices are NET prices.

Additional access options:

- [Log in](#)
- [Learn about institutional subscriptions](#)

Nature **597**, 306 (2021)

doi: <https://doi.org/10.1038/d41586-021-02437-2>

References

1. 1.

Deppner, C. *et al.* *Phys. Rev. Lett.* **127**, 100401 (2021).

This article was downloaded by **calibre** from <https://www.nature.com/articles/d41586-021-02437-2>

- RESEARCH HIGHLIGHT
- 07 September 2021

Polar bears are inbreeding as their icy home disintegrates

With climate change fracturing northern ice, the bears have begun to lose genetic diversity.



A polar bear and her yearling cub in Svalbard, Norway, where the knock-on effects of climate change are sapping the bears' genetic diversity. Credit: Andy Rouse/Nature Picture Library

Polar bears in Norway have undergone a staggering loss in genetic diversity in recent decades, as a result of the decline of Arctic sea ice.

Access options

Subscribe to Journal

Get full journal access for 1 year

\$199.00

only \$3.90 per issue

[Subscribe](#)

All prices are NET prices.

VAT will be added later in the checkout.

Tax calculation will be finalised during checkout.

Rent or Buy article

Get time limited or full article access on ReadCube.

from \$8.99

[Rent or Buy](#)

All prices are NET prices.

Additional access options:

- [Log in](#)
- [Learn about institutional subscriptions](#)

Nature **597**, 306 (2021)

doi: <https://doi.org/10.1038/d41586-021-02438-1>

References

1. 1.

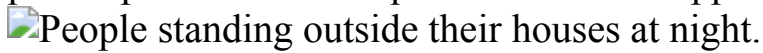
Maduna, S. N. *et al. Proc. R. Soc. B* **288**, 20211741 (2021).

This article was downloaded by **calibre** from <https://www.nature.com/articles/d41586-021-02438-1>

- RESEARCH HIGHLIGHT
- 08 September 2021

Seismic sleuths unmask the ‘earthquake’ that wasn’t

People in one Indian state flooded into the streets and onto a seismology app after predictions of a quake that never happened.



People stand outside their homes after northern India was struck by a verified earthquake in 2017. A rumoured quake in Punjab state the same year also sent people fleeing their houses. Credit: AFP/Getty

Rumours of an impending earthquake in northwestern India prompted people to sleep outdoors and temples to issue warnings — but sleuthing now confirms that no such quake occurred.

Access options

Subscribe to Journal

Get full journal access for 1 year

\$199.00

only \$3.90 per issue

[Subscribe](#)

All prices are NET prices.

VAT will be added later in the checkout.

Tax calculation will be finalised during checkout.

Rent or Buy article

Get time limited or full article access on ReadCube.

from \$8.99

[Rent or Buy](#)

All prices are NET prices.

Additional access options:

- [Log in](#)
- [Learn about institutional subscriptions](#)

Nature **597**, 307 (2021)

doi: <https://doi.org/10.1038/d41586-021-02442-5>

References

1. 1.

Martin, S. S. *et al.* *Seismol. Res. Lett.*
<https://doi.org/10.1785/0220210130> (2021).

This article was downloaded by **calibre** from <https://www.nature.com/articles/d41586-021-02442-5>

- RESEARCH HIGHLIGHT
- 06 September 2021

Early Americans' huge earthworks show off their engineering might

Analysis of mysterious earth mounds reveals their rapid construction and sophisticated composition.



Excavation of one of the mammoth ridges at the Poverty Point site in Louisiana revealed discrete layers of earth. Credit: T.R. Kidder

On the banks of a Louisiana bayou, the Native American earthwork complex called Poverty Point includes one of the largest earthen mounds in North America, and other enormous monuments: a feat of construction that was unrivalled for more than 2,000 years. Analysis of one structure now shows that it was built with speed, perhaps even in only a few weeks.

Access options

Subscribe to Journal

Get full journal access for 1 year

\$199.00

only \$3.90 per issue

[Subscribe](#)

All prices are NET prices.
VAT will be added later in the checkout.

Tax calculation will be finalised during checkout.

Rent or Buy article

Get time limited or full article access on ReadCube.

from \$8.99

[Rent or Buy](#)

All prices are NET prices.

Additional access options:

- [Log in](#)
- [Learn about institutional subscriptions](#)

Nature **597**, 307 (2021)

doi: <https://doi.org/10.1038/d41586-021-02439-0>

References

1. 1.

Kidder, T., Kai, S., Henry, E. R., Grooms, S. B. & Ervin, K. *Southeast. Archaeol.* <https://doi.org/10.1080/0734578X.2021.1958445> (2021).

This article was downloaded by **calibre** from <https://www.nature.com/articles/d41586-021-02439-0>

- RESEARCH HIGHLIGHT
- 09 September 2021

Flowing crystals for quick camouflage

A soft material can be guided to rapidly assume the same colour pattern as its background.



A flexible material changes colour when deformed, allowing it to match a spotty background. Credit: S.-U. Kim *et al./Nature Mater.*

A soft, stretchy film changes from transparent to red to blue as it bends, opening up opportunities for responsive 3D displays and robotics¹.

Access options

Subscribe to Journal

Get full journal access for 1 year

\$199.00

only \$3.90 per issue

[Subscribe](#)

All prices are NET prices.

VAT will be added later in the checkout.

Tax calculation will be finalised during checkout.

Rent or Buy article

Get time limited or full article access on ReadCube.

from \$8.99

[Rent or Buy](#)

All prices are NET prices.

Additional access options:

- [Log in](#)
- [Learn about institutional subscriptions](#)

Nature **597**, 307 (2021)

doi: <https://doi.org/10.1038/d41586-021-02458-x>

References

1. 1.

Kim, S.-U. *et al.* *Nature Mater.* <https://doi.org/10.1038/s41563-021-01075-3> (2021).

This article was downloaded by **calibre** from <https://www.nature.com/articles/d41586-021-02458-x>

News in Focus

- **[COVID research prizes, CRISPR-like enzymes and a face-mask trial](#)** [15 September 2021]
News Round-Up • The latest science news, in brief.
- **[China prepares to test thorium-fuelled nuclear reactor](#)** [09 September 2021]
News • If China's experimental reactor is a success it could lead to commercialization and help the nation meet its climate goals.
- **[Hurricane Ida forces Louisiana researchers to rethink their future](#)** [09 September 2021]
News • The category-4 storm is the latest in a line of tropical cyclones that have closed universities, caused scientists to evacuate and disrupted research projects.
- **[How COVID is derailing the fight against HIV, TB and malaria](#)** [10 September 2021]
News • The pandemic's effects on efforts to thwart other infectious diseases could exceed the direct impact of COVID-19.
- **[Pivotal climate summit dogged by COVID and equity concerns](#)** [10 September 2021]
News • Environmental network calls for delay to the November meeting, but many developing countries and the host nation vow to press on in face of climate threats.
- **[Most fossil-fuel reserves must remain untapped to hit 1.5 °C warming goal](#)** [08 September 2021]
News • Modelling suggests that many planned coal, oil and gas extraction projects will not be viable if the world hopes to achieve climate targets.
- **[Success! Mars rover finally collects its first rock core](#)** [07 September 2021]
News • NASA's Perseverance rover lives up to its name, drilling and storing Martian rock after a misstep in August.
- **[The tangled history of mRNA vaccines](#)** [14 September 2021]
News Feature • Hundreds of scientists had worked on mRNA vaccines for decades before the coronavirus pandemic brought a breakthrough.

| [Next section](#) | [Main menu](#) | [Previous section](#) |

- NEWS ROUND-UP
- 15 September 2021

COVID research prizes, CRISPR-like enzymes and a face-mask trial

The latest science news, in brief.



Biochemist Katalin Karikó helped to develop a way to deliver mRNA into cells without triggering an unwanted immune response. Credit: Hannah Yoon/Bloomberg/Getty

COVID advances win science's most lucrative awards

Techniques that have armed scientists in the battle against COVID-19 have scooped up two out of five [US\\$3-million Breakthrough prizes](#).

One award went to Katalin Karikó and Drew Weissman at the University of Pennsylvania in Philadelphia, who discovered how to smuggle mRNA into cells, leading to the development of a new class of vaccine. Another was won by three chemists who developed the sequencing technique that has been used to rapidly track SARS-CoV-2 variants: Shankar Balasubramanian and David Klenerman at the University of Cambridge, UK, and Pascal Mayer at the French research firm Alphanosos. A third life-sciences prize was awarded to Jeffery Kelly at Scripps Research in La Jolla, California, for work on amyloidosis — a disease that can affect various organs and cause neurodegeneration.

The fundamental physics prize went to Hidetoshi Katori at the University of Tokyo and Jun Ye at the US National Institute of Standards and Technology in Boulder, Colorado, for inventing the optical lattice clock, an extremely precise time-measuring device.

And Takuro Mochizuki at Kyoto University in Japan was awarded the maths prize for extending the understanding of algebraic structures called holonomic D-modules.

Trove of gene-cutting enzymes found in microbes

By exploring the evolutionary origins of an enzyme used in the CRISPR genome-editing system, researchers have unearthed [more than one million other potential editors lurking in microbial genomes](#).

They discovered the new editing enzymes among a family of proteins called IscB (H. Altae-Tran *et al. Science* <https://doi.org/gmq94w>; 2021). These proteins are thought to be the ancestors of the CRISPR enzyme Cas9. During genome editing, Cas9 teams up with a snippet of RNA that guides the enzyme to find and cut a specific DNA sequence. This allows

researchers to easily target Cas9 to the region of the genome they want to alter.

The researchers found that the DNA responsible for encoding IscB proteins is often located near the DNA for a class of RNA molecules that they dubbed ω RNAs. They discovered that some IscB proteins can cleave DNA at a site specified by the sequence of an ω RNA, much as Cas9 does with a guide RNA.

The team went on to investigate another family of proteins, called TnpB, which are thought to be the ancestors of another DNA-slicing CRISPR-associated enzyme, called Cas12. They found that some of these proteins could also cut DNA when guided by ω RNA. Database searches turned up more than one million genes that could carry the code for TnpB proteins, and some organisms contain more than 100 copies of these genes.

The discovery could yield further tools for genome editing, says lead author Feng Zhang, a molecular biologist at the Massachusetts Institute of Technology in Cambridge.



A rickshaw driver and passenger wear masks in Bangladesh. Credit: Maruf Rahman/Eyepix Group/Barcroft Media/Getty

Face masks for COVID pass largest test yet

A gold-standard clinical trial has concluded that [wearing masks reduces the spread of COVID-19](#), backing up the findings of hundreds of previous observational and laboratory studies.

Critics of mask mandates have cited the lack of relevant randomized clinical trials, which assign participants at random to either a control group or an intervention group. But the latest finding is based on a randomized trial involving nearly 350,000 people across rural Bangladesh. The study's authors found that surgical masks — but not cloth masks — reduced transmission of SARS-CoV-2 in villages where the research team distributed face masks and promoted their use (J. Abaluck *et al.* Innovations for Poverty Action Working Paper <https://go.nature.com/3hhfeki>; 2021).

“This really should be the end of the debate,” says study co-author Ashley Styczynski, an infectious-disease researcher at Stanford University in California.

Styczynski and her colleagues began by developing a strategy to promote mask wearing, with measures such as reminders from health workers in public places. This ultimately tripled mask usage, from only 13% in control villages to 42% in villages where it was encouraged. The researchers then compared numbers of COVID-19 cases in the control villages and the treatment communities.

The team found that the number of symptomatic cases was lower in treatment villages than in control villages. The decrease was a modest 9%, but the researchers suggest that the true risk reduction is probably much greater, in part because they did no SARS-CoV-2 testing of people who had no symptoms or whose symptoms did not meet the World Health Organization’s definition of the disease.

The study linked surgical masks with an 11% drop in risk, compared with a 5% drop for cloth masks. That finding was reinforced by laboratory experiments, which showed that even after 10 washes, surgical masks filter out 76% of small particles capable of airborne transmission of SARS-CoV-2. By contrast, the team found that 3-layered cloth masks had a filtration efficiency of only 37% before washing or use.

Nature **597**, 309 (2021)

doi: <https://doi.org/10.1038/d41586-021-02482-x>

This article was downloaded by **calibre** from <https://www.nature.com/articles/d41586-021-02482-x>

- NEWS
- 09 September 2021
- Correction [10 September 2021](#)

China prepares to test thorium-fuelled nuclear reactor

If China's experimental reactor is a success it could lead to commercialization and help the nation meet its climate goals.

- [Smriti Mallapaty](#)



China has more than 50 conventional nuclear power plants, such as this, but the experimental thorium reactor in Wuwei will be a first.Credit: Costfoto/Barcroft Media/Getty

Scientists are excited about an experimental nuclear reactor using thorium as fuel, which is about to begin tests in China. Although this radioactive element has been trialled in reactors before, experts say that China is the first to have a shot at commercializing the technology.

The reactor is unusual in that it has molten salts circulating inside it instead of water. It has the potential to produce nuclear energy that is relatively safe and cheap, while also generating a much smaller amount of very long-lived radioactive waste than conventional reactors.

Construction of the experimental thorium reactor in Wuwei, on the outskirts of the Gobi Desert, was due to be completed by the end of August — with trial runs scheduled for [this month](#), according to the government of Gansu province.

Thorium is a weakly radioactive, silvery metal found naturally in rocks, and currently has little industrial use. It is a waste product of the growing rare-earth mining industry in China, and is therefore an attractive alternative to imported uranium, say researchers.

Powerful potential

“Thorium is much more plentiful than uranium and so it would be a very useful technology to have in 50 or 100 years’ time,” when uranium reserves start to run low, says Lyndon Edwards, a nuclear engineer at the Australian Nuclear Science and Technology Organisation in Sydney. But the technology will take many decades to realize, so we need to start now, he adds.

China launched its molten-salt reactor programme in 2011, investing some 3 billion yuan (US\$500 million), according to Ritsuo Yoshioka, former president of the International Thorium Molten-Salt Forum in Oiso, Japan, who has worked closely with Chinese researchers.

Operated by the Shanghai Institute of Applied Physics (SINAP), the Wuwei reactor is designed to produce just 2 megawatts of thermal energy, which is only enough to power up to 1,000 homes. But if the experiments are a success, China hopes to build a 373-megawatt reactor by 2030, which could power hundreds of thousands of homes.

These reactors are among the “perfect technologies” for helping China to achieve its goal of zero carbon emissions by around 2050, says energy modeller Jiang Kejun at the Energy Research Institute of the National Development and Reform Commission in Beijing.

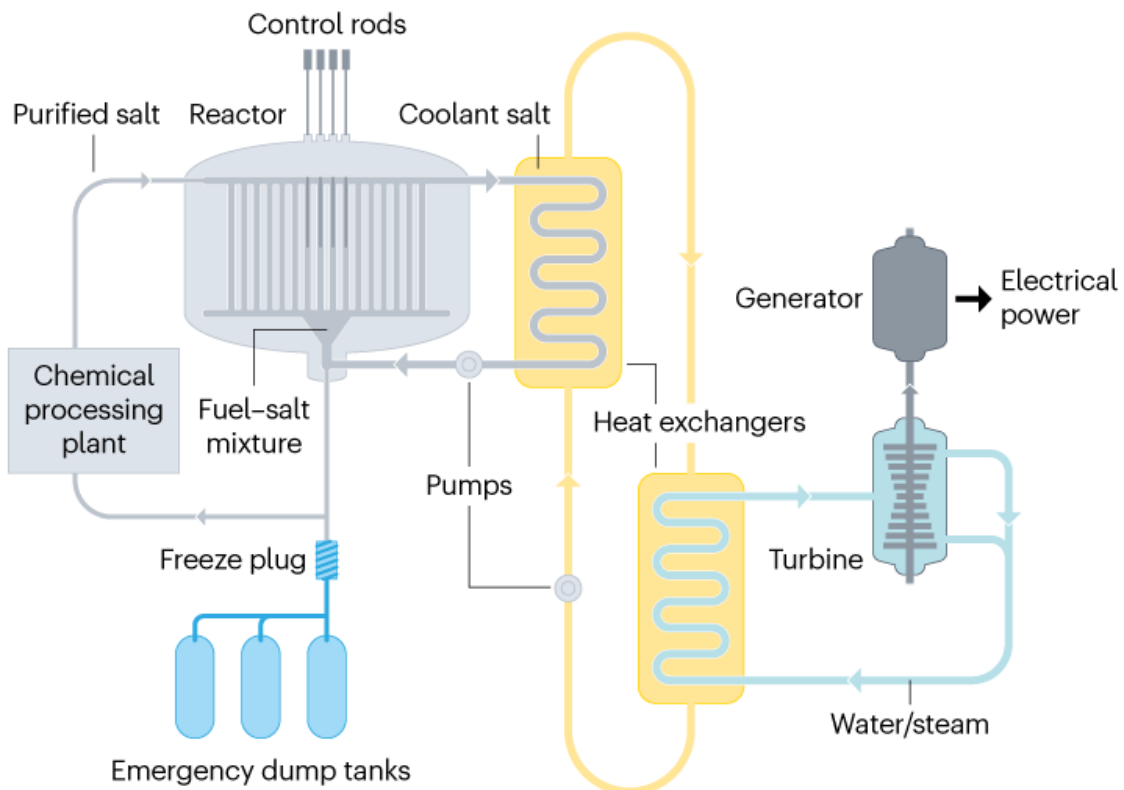
The naturally occurring isotope thorium-232 cannot undergo fission, but when irradiated in a reactor, it absorbs neutrons to form uranium-233, which is a fissile material that generates heat.

Thorium has been tested as a fuel in other types of nuclear reactor in countries including the United States, Germany and the United Kingdom, and is part of a nuclear programme in India. But it has so far not proved cost effective because it is more expensive to extract than uranium and, unlike some naturally occurring isotopes of uranium, needs to be converted into a fissile material.

Some researchers support thorium as a fuel because they say its waste products have less chance of being weaponized than do those of uranium, but others have argued that [risks still exist](#).

MOLTEN-SALT REACTOR

In a molten-salt nuclear reactor the fissile material is dissolved in liquid salt in the reactor core. Liquid salt also acts as a coolant in place of water. Fission occurs in the reactor core, generating heat, which is transmitted by the coolant salt and heat exchangers to water, producing steam. This drives a turbine to generate electricity. A frozen plug of salt melts if the reactor core overheats, allowing the fuel-salt mixture to drain into emergency dump tanks.



©nature

Source: US Department of Energy/International Atomic Energy Agency

Blast from the past

When China switches on its experimental reactor, it will be the first molten-salt reactor operating since 1969, when US researchers at the Oak Ridge National Laboratory in Tennessee shut theirs down. And it will be the first molten-salt reactor to be fuelled by thorium. Researchers who have collaborated with SINAP say the Chinese design copies that of Oak Ridge,

but improves on it by calling on decades of innovation in manufacturing, materials and instrumentation.

Researchers in China directly involved with the reactor did not respond to requests for confirmation of the reactor's design and when exactly tests will begin.

Compared with light-water reactors in conventional nuclear power stations, molten-salt reactors operate at significantly higher temperatures, which means they could generate electricity much more efficiently, says Charles Forsberg, a nuclear engineer at Massachusetts Institute of Technology in Cambridge.

China's reactor will use fluoride-based salts, which melt into a colourless, transparent liquid when heated to about 450 °C. The salt acts as a coolant to transport heat from the reactor core. In addition, rather than solid fuel rods, molten-salt reactors also use the liquid salt as a substrate for the fuel, such as thorium, to be directly dissolved into the core.

Molten-salt reactors are considered to be relatively safe because the fuel is already dissolved in liquid and they operate at lower pressures than do conventional nuclear reactors, which reduces the risk of explosive meltdowns.

Yoshioka says many countries are working on molten-salt reactors — to generate cheaper electricity from uranium or to use waste plutonium from light-water reactors as fuel — but China alone is attempting to use thorium fuel.



Thorium pellets at the Bhabha Atomic Research Centre in Mumbai, India. Credit: Pallava Bagla/Corbis/Getty

Next-generation reactors

China's reactor will be "a test bed to do a lot of learning", says Forsberg, from analysing corrosion to characterizing the radionucleotide composition of the mixture as it circulates.

"We are going to learn so much new science," agrees Simon Middleburgh, a nuclear materials scientist at Bangor University, UK. "If they would let me, I'd be on the first plane there."

It could take months for China's reactor to reach full operation. "If anything along the way goes wrong, you can't continue, and have to stop and start again," says Middleburgh. For example, the pumps might fail, pipes could

corrode or a blockage might occur. Nevertheless, scientists are hopeful of success.

Molten-salt reactors are just one of many advanced nuclear technologies China is investing in. In 2002, an intergovernmental forum identified six promising reactor technologies to fast-track by 2030, including reactors cooled by lead or sodium liquids. China has programmes for all of them.

Some of these reactor types could replace coal-fuelled power plants, says David Fishman, a project manager at the Lantau Group energy consultancy in Hong Kong. “As China cruises towards carbon neutrality, it could pull out [power plant] boilers and retrofit them with nuclear reactors.”

Nature **597**, 311-312 (2021)

doi: <https://doi.org/10.1038/d41586-021-02459-w>

Updates & Corrections

- **Correction 10 September 2021:** An earlier version of this story referred to reactors cooled by lead and sodium gases, while they are in fact liquids. It was also published with a different primary image, which was incorrectly captioned as a nuclear power plant. The story has been updated.

This article was downloaded by **calibre** from <https://www.nature.com/articles/d41586-021-02459-w>

- NEWS
- 09 September 2021

Hurricane Ida forces Louisiana researchers to rethink their future

The category-4 storm is the latest in a line of tropical cyclones that have closed universities, caused scientists to evacuate and disrupted research projects.

- [Max Kozlov](#)



Hurricane Ida destroyed almost 30,000 utility poles. Some Louisiana residents could be without power for up to a month.Credit: Nick Wagner/Xinhua/eyevine

When Hurricane Ida tore through New Orleans more than a week ago, researchers there were relieved that the category-4 storm didn't entirely flood the city. Its flood-regulating levee system, fortified after the devastation of Hurricane Katrina 16 years ago, seemed to hold. What took them by surprise was that Ida ravaged Louisiana's power grid, 30% of which has yet to be restored — leaving residents to bake in the heat, universities closed and researchers struggling to preserve samples and keep projects running.

Ida is the sixth tropical cyclone to make landfall in Louisiana since the start of 2020, and scientists are worried that the frequency of the storms, combined with a failure by state and local officials to adapt infrastructure to climate change, will imperil the millions of people who live along the Louisiana coast. Scientists also worry that the relentlessness of the storms could dissuade researchers from joining universities there and from conducting crucial investigations of the ecological impacts of climate change along the coast.

“You have to wonder, how much more can this area take and continue to spring back?” says Allyse Ferrara, a fish biologist at Nicholls State University in Thibodaux, Louisiana, who started a community-based coastal-restoration project after seeing the damage from Katrina. Thibodaux, which is southwest of New Orleans, was directly in Ida’s path and is unlikely to regain power for weeks. “I’m really scared to see what some of the sites we work at look like,” she says.

Freezer frenzy

Sunshine Van Bael, a microbial ecologist at Tulane University in New Orleans, describes the aftermath of Ida as an “inside out” version of the COVID-19 pandemic: last year, “we were in quarantine and trapped in our houses, and we couldn’t go to the lab”, she says. “And now with Hurricane Ida and its after-effects, it’s the opposite — it’s like we’re trapped away from our home. Everybody has evacuated to different places, and we still can’t get to our labs.”

With its 240-kilometre-per-hour winds, Ida damaged or destroyed more than 30,000 power-line poles and nearly 6,000 transformers across the region — more than the major Louisiana hurricanes Katrina, Zeta, Ike and Delta combined, according to Entergy Corporation, the New Orleans-based company that provides most of Louisiana's power. The firm is making progress in its repairs but says it might take until the end of the month to fully restore power to all Louisiana communities.



Hannah Frank at Tulane University in New Orleans packages frozen plant tissue for evacuation to Louisiana State University in Baton Rouge. Credit: Kathleen Gray Ferris

When Van Bael surveyed the damage the day after Ida rolled through, she was relieved it had spared her home and, for the most part, her neighbourhood. Her lab, by contrast, was in danger. A back-up generator at Tulane had failed, threatening to destroy freezer-stored seeds and genetic material — some of them the culmination of years of work. Despite spotty phone coverage after the storm, she and colleagues across the ecology and

evolutionary biology department frantically called and e-mailed collaborators to see whether they had freezer space to spare. Their pleas were answered, and Van Bael would go on to drive cooler-packed samples as far as 1,600 kilometres north, to Iowa State University in Ames.

Keith Clay, a microbial ecologist at Tulane, was also taken by surprise when Ida obliterated the New Orleans power grid. He had decided to stay in the city during the storm because he lives on high ground that didn't flood during Katrina. But afterwards, when "reality sunk in" that there would be no electricity for days or weeks, he says, he decided to evacuate.



Atlantic hurricanes' rapid growth spurts are intensifying

Apart from concerns about research disruptions, Clay and others worry that with each storm to hit Louisiana, universities will haemorrhage students and staff — impacts that could continue for the long term. In the face of the extended power cuts, Tulane announced on 30 August that it was closing its campus until mid-October, and evacuating students by bus to Houston, Texas. "I would not be surprised if some students don't come back, and faculty that might be nearing retirement may be deciding this is the straw that broke the camel's back," says Clay.

As this story was published, power had been restored to all of Tulane's buildings. And the university hopes to resume in-person classes and research

activities earlier than planned, says spokesperson Keith Brannon. But Clay still worries that Tulane's closure represents a "double hit" for the state's academic system — [universities were already struggling](#) because of COVID-19 restrictions and decreased student enrolment. "The long-term prognosis is grim," says Clay. "There may be some students that just say, 'I can't deal with this anymore.'"

Shocks to the system

Researchers, too, are contemplating how much more they can take. They say that climate change will become a factor in their decisions about what projects to take on, as hurricanes become stronger and intensify more quickly. "Instead of writing grants to work way out on the coast, which can get hammered over and over again, I might consider focusing more energy on wetlands that are closer to the city," says Van Bael, who studies how coastal plants and microbes interact. The cruel irony of the situation, she says, is that we "direly need" fieldwork out on the coast to understand the true ecological impacts of climate change. To keep such high-risk projects going, she adds, might require extra funding to incentivize researchers.

Lee Hamm, dean of Tulane's medical school, worries especially about the long-term effects of stronger storms on both the progress of junior researchers, who have already had their careers interrupted by COVID-19, and the recruitment of new faculty members. That's one of the reasons to hope for a "very quick" recovery from Ida, he says.



Puerto Rico struggles to assess hurricane's health effects

Louisiana's extended power cut underscores the urgent need to focus on climate adaptation in the area, experts say. Rather than just preparing for disasters over and over, says Jesse Keenan, a researcher in urban planning at Tulane, officials need to address the underlying issues that cause climate vulnerability. "We've framed climate change in very localized terms that are very episodic and are understood in terms of shocks," he says. Instead, he adds, local officials should be thinking about not just the short-term shocks to infrastructure, but also the long-term stresses on the system.

It is imperative that energy companies reinforce their existing infrastructure and even find ways to relocate parts of it to less-risky spots to prevent another power-grid collapse, says Keenan. "Are we going to continue making infrastructure investments that just perpetuate a cycle of recovery that we really can't afford anymore?"

Nature **597**, 313-314 (2021)

doi: <https://doi.org/10.1038/d41586-021-02456-z>

| [Section menu](#) | [Main menu](#) |

- NEWS
- 10 September 2021
- Correction [14 September 2021](#)

How COVID is derailing the fight against HIV, TB and malaria

The pandemic's effects on efforts to thwart other infectious diseases could exceed the direct impact of COVID-19.

- [Leslie Roberts](#)



Medical staff take blood samples for HIV testing in Nigeria. Credit: Emmanuel Osodi/Majority World/Universal Images Group/Getty

The COVID-19 pandemic has had a “devastating” impact on the fight against other deadly infectious diseases, according to a report that compares 2019 and 2020 data on HIV, tuberculosis (TB) and malaria in more than 100 low- and lower-middle-income countries.

The assessment was conducted by the Global Fund, an international organization that funds efforts to tackle these three health challenges.

“COVID-19 has been the most significant setback in the fight against HIV, TB and malaria, that we have encountered in the two decades since the Global Fund was established,” writes the organization’s executive director Peter Sands in an introduction to its [Results Report 2021](#).

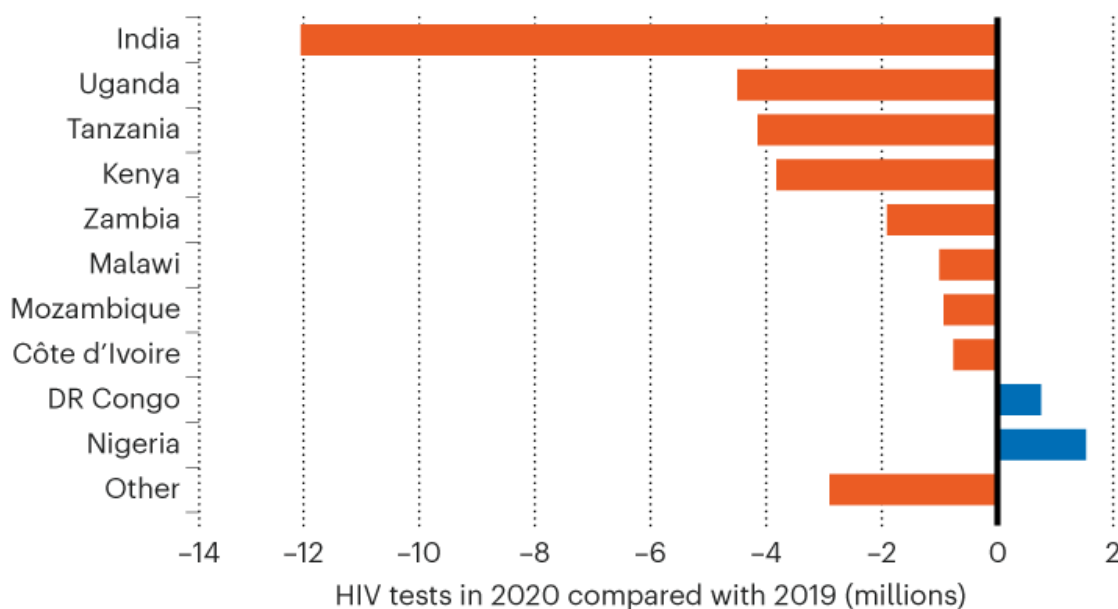
As countries went into lockdown and resources were diverted to combat the pandemic, prevention, testing and treatment services for all three dropped precipitously, although the impacts vary for each. In some countries, says Sands, “the knock-on effects on HIV, TB and malaria could exceed the direct impact of COVID-19”.

Treatment delays

For HIV, the number of people reached by prevention programmes that supply condoms or clean needles and syringes, for example, dropped by 11%. HIV testing fell by 22%, delaying treatment and contributing to ongoing transmission of the virus (see ‘Testing trouble’).

TESTING TROUBLE

Many countries where the Global Fund supports health care have seen a drop in HIV testing during the COVID-19 pandemic.



©nature

Source: The Global Fund Results Report 2021

Grace Ngulube, an HIV activist in Malawi, is particularly worried about adolescent girls and young women, who account for six out of seven new HIV infections among those aged 15 to 19 in sub-Saharan Africa, according to the report. In some places, the roll-out of COVID-19 vaccinations has also caused problems for HIV-related work. Because of misconceptions about their safety, many girls and young women are hesitant to seek any kind of medical care for fear they will be vaccinated, Ngulube says.

However, the number of people living with HIV who received antiretroviral drugs increased by 9%, in part because clinics in some countries began providing them with enough medicine to last several months, to reduce the need for frequent visits.



How COVID hurt the fight against other dangerous diseases

Efforts to combat TB, the second biggest cause of infectious-disease deaths globally after COVID-19, were dealt a more severe blow. TB is also caused by an airborne pathogen, so it lost out because resources such as isolation wards, diagnostic kits and medical specialists were diverted to the pandemic, says Jamie Tonsing, senior TB adviser at the Global Fund. In countries the Global Fund supports, the number of individuals tested and treated for TB fell by 18% — amounting to about one million people. For extensively drug-resistant TB, the fall was 37%, an especially severe impact. Untreated cases will lead to increased transmission and even more deaths from TB than the 1.4 million recorded in 2019.

Malaria ‘stable’

The outlook for malaria remains “somewhat stable” in countries the Global Fund supports, the report says, without significant setbacks or gains. Although campaigns to distribute insecticide-treated bed nets, currently the best tool for preventing malaria, were delayed early on in the pandemic, countries were quick to adapt, says Scott Filler, who heads the Global Fund’s malaria programme. When campaigns resumed, many countries switched from dispensing bed nets in public spaces to delivering them door-to-door, to avoid crowding. That contributed to a 17% rise in the number of

nets distributed. However, the number of people with suspected malaria who were tested fell by 4.3%. “A lot of kids did not get tested who should have been,” Filler says.

Even so, progress against malaria has stalled “at unacceptably high numbers”, says Pedro Alonso, who heads the Global Malaria Programme at the World Health Organization. There are still more than 400,000 deaths from malaria and 220 million cases a year.

Disease experts worry about the impact that waves of SARS-CoV-2 infections and the emergence of new variants will continue to have on efforts to combat these three diseases. “The crisis is far from over, especially with the Delta variant wreaking havoc,” says Sands. “We really won’t get back on track for HIV, TB and malaria until we get on top of COVID-19.”

Nature **597**, 314 (2021)

doi: <https://doi.org/10.1038/d41586-021-02469-8>

Updates & Corrections

- **Correction 14 September 2021:** An earlier version of this article stated that there are more than 220,000 million malaria cases per year. This has been corrected to 220 million.

This article was downloaded by **calibre** from <https://www.nature.com/articles/d41586-021-02469-8>

- NEWS
- 10 September 2021

Pivotal climate summit dogged by COVID and equity concerns

Environmental network calls for delay to the November meeting, but many developing countries and the host nation vow to press on in face of climate threats.

- [Jeff Tollefson](#)



Climate change ‘has not taken time off’, warns Alok Sharma, the designated president of November’s summit. Credit: Justin Tallis/AFP/Getty

An international climate-action coalition is calling for the postponement of a pivotal climate summit slated to take place this November in Glasgow, UK, because COVID-19 pandemic restrictions could prevent the world's poorest nations from fully participating. But many developing countries say that delaying the summit could have dangerous consequences for the planet and want to push forward.

The summit, the 26th United Nations Climate Change Conference of the Parties (COP26), is the most significant global climate meeting since countries gathered in Paris in 2015 to sign an accord to limit global warming to 1.5–2 °C above pre-industrial temperatures. The 196 governments participating in this year's summit are expected to [formalize a new round of commitments](#) to dial back greenhouse-gas emissions in an effort to limit the extreme weather currently pummelling countries around the globe.

COP26 organizers in the United Kingdom have responded to the call for postponement with concessions intended to enable broad participation. UK officials told *Nature* that COVID-19 vaccines are now being shipped out for delegations without access to them, and that the first jabs will begin within days. But some observers still fear the proceedings will not be equitable because of reduced participation from non-governmental organizations (NGOs), which often advise low-income countries and which are facing the most significant challenges in getting to Glasgow.

A risk of exclusion

Climate Action Network-International (CAN), which represents a global collection of more than 1,500 environmental groups, raised the alarm about COP26 on 7 September. The coalition says it had heard numerous complaints from delegates, including NGOs, in developing countries who worry that they will not be able to attend the negotiations in person because of a lack of vaccines and high travel costs associated with pandemic restrictions. NGOs are at particular risk of not being able to participate, and without them there could be “less pressure on polluters to act, less scrutiny on the outcomes, and potentially watered-down climate action, leading to more suffering for people around the world”, says Dharini Parthasarathy, a spokesperson for CAN in Bangalore, India.



Climate activists are concerned that representation across various nations at COP26 will not be equitable. Credit: Guy Smallman/Getty

Governments of developing nations have been working behind the scenes to address rising conference costs due to the pandemic, says Saleemul Huq, director of the International Centre for Climate Change and Development in Dhaka, Bangladesh, and an adviser to the Least Developed Countries coalition. Although some scientists and activists associated with NGOs might not be able to attend, Huq expects that officials charged with actually negotiating and setting climate targets will make it to the summit.

The conference has already been postponed by a year because of the COVID-19 pandemic, ratcheting up concerns over delayed climate action. Last month, the UN Intergovernmental Panel on Climate Change [issued its latest report](#), warning that drastic and immediate action is needed to avert severe impacts in the decades to come.



Where climate cash is flowing and why it's not enough

Island nations and low-income countries in the global south have been among the fiercest advocates for aggressive climate action so far, because they have contributed the least to global warming and are often more vulnerable to its impacts. Now they are struggling with low vaccination rates owing to [an inequitable global distribution of doses](#), making travel to COP26 more difficult — and more costly. The United Kingdom has loosened its quarantine rules for COP26 attendees, but still requires that unvaccinated delegates from some 60 high-risk countries isolate in hotel rooms for 10 days; even vaccinated individuals from those countries would need to quarantine for 5 days.

After CAN called for COP26's postponement, the UK government agreed to cover the cost of hotel quarantining for delegates from high-risk nations. In a statement, the United Kingdom's designated president of the summit, Alok Sharma, said the meeting must go ahead. "COP26 has already been postponed by one year, and we are all too aware climate change has not taken time off," he said. "Ensuring that the voices of those most affected by climate change are heard is a priority for the COP26 Presidency, and if we are to deliver for our planet, we need all countries and civil society to bring their ideas and ambition to Glasgow."

Although many countries have yet to weigh in, some have opposed delaying the summit: this week the Climate Vulnerable Forum, a coalition of countries in the global south that are at significant risk of impacts from global warming, released a statement saying that COP26 must take place as scheduled and in person.

And the Alliance of Small Island States said in a statement to *Nature* that its 39 members are ready to engage at the summit. “The only beneficiaries of the postponement are the fossil fuel industry and persons who gain financially from delay actions,” the statement said. “We hope to participate in a COP that is an inclusive and safe arena, particularly for the most vulnerable nations who must have a part to play in deciding our futures.”

Climate change presses on

Holding a global climate summit that attracts thousands of people from around the world presents significant logistical challenges, particularly in the middle of a pandemic. More than 26,700 people registered for the last meeting of this scale, in Madrid in 2019, and the UK says it is expecting around 25,000 in Glasgow.



[IPCC climate report: Earth is warmer than it's been in 125,000 years](#)

Even with hotel quarantine costs covered in the United Kingdom, travelling to and from Glasgow will still represent a challenge for many delegates, says Bill Hare, a physicist and one of the founders of Climate Analytics, a non-profit organization that advises many developing countries in the climate negotiations. “I know governments that we work with are concerned,” he says.

In addition, Hare says there are fears that countries that have been known to obstruct the negotiations — such as Saudi Arabia, whose economy depends on oil and gas — could use legitimate fears about representation among poor countries to argue that the COP26 process is tainted. “It could be explosive.”

During the pandemic, many high-level international climate meetings have moved online, but gatherings such as COP26 are fuelled by human interactions among activists, scientists and negotiators, says Durwood Zaelke, president of the Institute for Governance and Sustainable Development in Washington DC. Going virtual is a challenge, particularly for low-income countries where internet connections are less reliable, he says. “We need more than ever to have multilateral controls work much faster, yet we’re struggling to have our meetings,” says Zaelke. “COVID has put a lot of sand into the gears of this machinery of climate governance, and that has slowed things down.”

Nature **597**, 315 (2021)

doi: <https://doi.org/10.1038/d41586-021-02465-y>

This article was downloaded by **calibre** from <https://www.nature.com/articles/d41586-021-02465-y>.

- NEWS
- 08 September 2021

Most fossil-fuel reserves must remain untapped to hit 1.5 °C warming goal

Modelling suggests that many planned coal, oil and gas extraction projects will not be viable if the world hopes to achieve climate targets.

- [Bianca Nogrady](#) 0



A coal-fired power station in Tongling, China. Credit: Qilai Shen/Bloomberg/Getty

Nearly 90% of economically viable global coal reserves must be left in the ground to have even a 50% chance of hitting internationally agreed climate-change goals, according to an updated model of limits to fossil-fuel extraction, published today in *Nature*¹.

For a 50% chance of remaining below 1.5 °C of global warming — the more aspirational goal of the 2015 Paris agreement — the world must not emit more than 580 gigatonnes of carbon dioxide before 2100, report the authors. Under this scenario, researchers led by environmental and energy economist Dan Welsby at University College London calculate, 89% of coal reserves, 58% of oil reserves and 59% of gas reserves must remain unextracted (see ‘Resources off limits’).

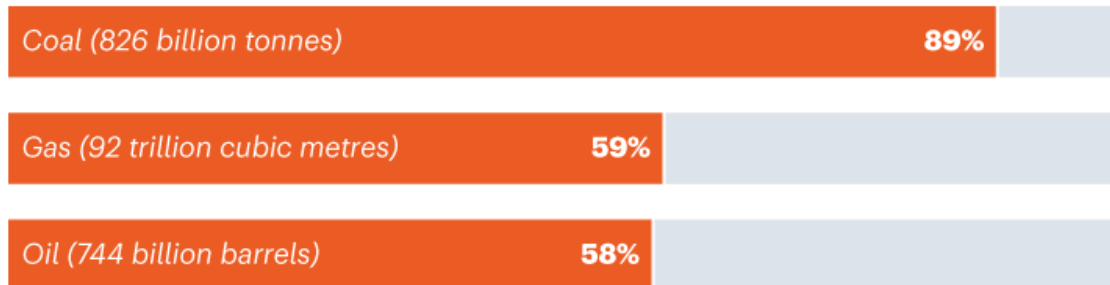
The authors stress that although the scenario already looks “bleak” for the global fossil-fuel industry, even tighter limits on extraction will be needed to improve the chances of constraining warming to 1.5 °C above pre-industrial levels.

The research “makes the fundamental point that the majority of known economic reserves will not be able to be used”, says Frank Jotzo, an environment and climate-change economist at the Australian National University in Canberra.

RESOURCES OFF LIMITS

A 2015 study found that, if the world is to stay below 2 °C of warming, then one-third of oil, half of gas and 80% of coal reserves must remain in the ground. Updated modelling to avoid dangerous warming above 1.5 °C now suggests that much higher proportions of fossil fuels must remain untapped.

■ Reserves that must remain in the ground



©nature

Source: Ref. 1

Never see the light of day

The study builds on a 2015 model² that examined how much fossil fuel must remain unused to limit global average temperature increases to no more than 2 °C compared with pre-industrial times. Updating the model was important because the entire debate has now moved beyond 2 °C being acceptable, says Welsby. “Actually, 2 °C is incredibly significant warming.”

The model captures key primary energy sources, such as fossil fuels, biomass, nuclear and renewables. It takes into account demand, economic factors and the geographical distribution of resources and emissions, and examines how these change over time. It also incorporates negative-emissions technologies, such as carbon dioxide removal.

Welsby and his co-authors calculate that oil and gas production must decline by 3% each year from now until 2050, which means fossil-fuel production must peak within the next decade — and that most existing and planned fossil-fuel projects would be unviable as a result.



IPCC climate report: Earth is warmer than it's been in 125,000 years

However, the study reveals significant regional differences in limits on fossil-fuel extraction, based on the carbon intensity and cost of exploiting different resources.

For example, the modelling suggests that 84% of Canada's oil sands must remain untapped, as well as all undeveloped oil and gas resources in the Arctic. Australia must leave 95% of its coal reserves in the ground, and both Russia and the United States will need to walk away from 97% of theirs.

Under the new model, only the mostly cheaply exploited fossil-fuel reserves will be viable, says Michael Jakob, an economist at the Mercator Research Institute on Global Commons and Climate Change in Berlin. "Others, like the Canadian tar sands, of course would be completely uncompetitive because you would never go in this area of expensive oil production."

The model also assumes substantial use of carbon dioxide removal and carbon capture and storage, because if they aren't included or are included at a smaller scale, "that target is unfeasible", Welsby says.

This mirrors the approach taken in [last month](#)'s Intergovernmental Panel on Climate Change (IPCC) report, which allowed a 40% increase in greenhouse-gas emissions while remaining below 1.5 °C by including

negative-emissions technologies, says Pep Canadell, chief research scientist at the CSIRO Climate Science Centre in Canberra, who has contributed to IPCC assessment reports.

Risky strategy

Canadell says the inclusion of carbon dioxide removal acknowledges the likely scenario that “we blow out our carbon budget”, but then remove enough carbon dioxide from the atmosphere to bring the temperature back down to, or even below, 1.5 °C above pre-industrial levels.



[Climate change made North America's deadly heatwave 150 times more likely](#)

However, this strategy is risky, says Nebojsa Nakicenovic, energy economist and former chief executive of the International Institute for Applied Systems Analysis in Vienna. Overshooting emissions targets and then removing the carbon from the atmosphere “means we are postponing the problem to the second half of this century”, and carbon dioxide removal technologies have a long way to go before they are scalable, he says.

It is clear, based on evidence such as the results of the new modelling, that achieving the deep fossil-fuel emissions reductions needed to keep warming

below 1.5 °C will be a “Herculean task” and we must start immediately, Nakicenovic says. “It’s not enough to have promises for 2050.”

Canadell says that it is an encouraging sign that coal use has been in free fall in the United States and Europe for more than a decade, but he has concerns about growing investment in natural gas, which is likely to leave some countries and investors heavily out of pocket if the limits of the model are adhered to. “You’re going to invest in a sector where there is no growth to come,” he says.

Nature **597**, 316-317 (2021)

doi: <https://doi.org/10.1038/d41586-021-02444-3>

References

1. 1.

Welsby, D., Price, J., Pye, S. & Ekins, P. *Nature*
<https://doi.org/10.1038/s41586-021-03821-8> (2021).

2. 2.

McGlade, C. & Ekins, P. *Nature* **517**, 187–190 (2015).

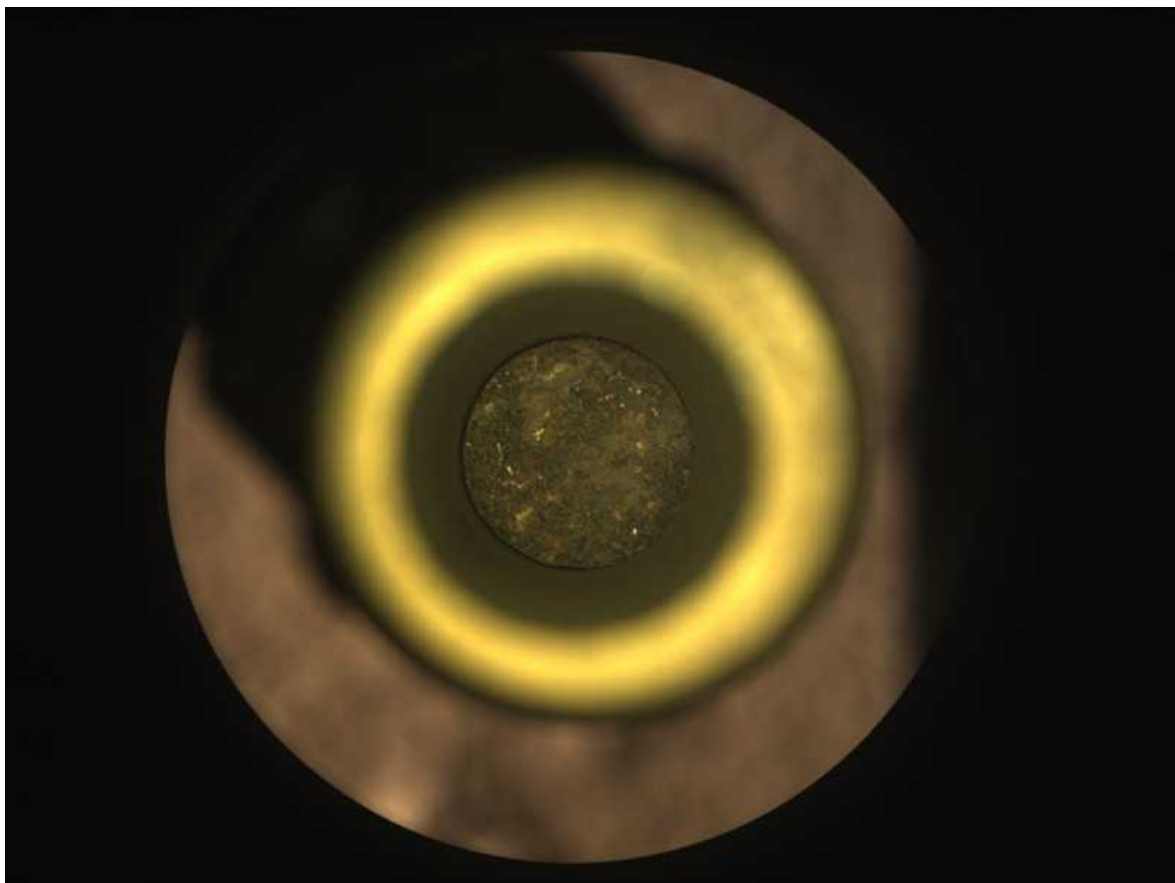
This article was downloaded by **calibre** from <https://www.nature.com/articles/d41586-021-02444-3>

- NEWS
- 07 September 2021

Success! Mars rover finally collects its first rock core

NASA's Perseverance rover lives up to its name, drilling and storing Martian rock after a misstep in August.

- [Alexandra Witze](#)



The Perseverance rover's first intact rock core was visible inside its sample tube, just before the tube was sealed on 6 September. Credit: NASA/JPL-

Caltech

After a [failed attempt last month](#), NASA's Perseverance rover has successfully drilled, extracted and stored a sample of Martian rock — the first ever Mars sample destined to be flown back to Earth for study.

"This is a momentous achievement," said NASA administrator Bill Nelson in a statement.

When the rover first attempted the manoeuvre, on 6 August, the rock it was trying to sample crumbled into powder before making it into a sample tube. The second attempt, on 1 September at a different location several hundred metres away, went smoothly: the drill bit pulled a slim cylinder out of a 70-centimetre-long rock named Rochette. Engineers then paused the process so that they could photograph the core in its sample tube, to ensure it was intact, before sealing the specimen inside days later, on 6 September.



The rover drilled into Rochette on 1 September.Credit: NASA/JPL-Caltech

The core from Rochette now rests in Perseverance's belly, hermetically sealed and ready to wait many years until future spacecraft can retrieve it and any other cores the rover manages to collect. The goal is to gather about 35 cores representing the geological history of Jezero Crater, Perseverance's landing site — which was home to a river delta billions of years ago and [might contain evidence of ancient Martian life.](#)

How Rochette fits into that history isn't yet clear. The rock comes from an area that mission scientists dubbed Citadelle, the French word for castle, because it stands high on a ridgeline like a citadel overlooking a valley. Some of the rocks along this ridgeline show layers that are geologically intriguing; such layers could have been deposited by wind, water, volcanic eruptions or other processes.

Early investigations by the rover suggest that Rochette is a rock type known as basalt, and might have been part of an ancient lava flow that makes up the ridge where Perseverance is parked, says Kenneth Farley, a geologist at the California Institute of Technology in Pasadena and the mission's project scientist. Rochette shows reddish patches and staining, as well as small cavities filled with salts, all of which suggest it interacted with water over some time — perhaps at the bottom of the ancient lake that once filled Jezero.

Planetary surprises

Rochette turned out to be a much better rock to drill than the one that the rover first attempted to sample — a rock named Roubion that lay elsewhere on the crater floor. Roubion, too, showed signs of interacting with water long ago, but in that case the water seems to have physically weakened the rock, because it turned to dust when Perseverance hammered in its drill bit. The rover might try drilling into another rock similar to Roubion later in its mission, says Farley, if it can find one that looks more robust.

If further studies confirm that Rochette is basalt, that would be scientifically exciting because once it is returned to Earth, researchers could use the decay of radioactive elements in the rock to precisely date its formation —

something never before possible because no rocks have ever been brought back from Mars.



A borehole was visible on the rock Rochette after drilling.Credit:
NASA/JPL-Caltech

NASA's previous Mars rover, Curiosity, which landed in a different crater in 2012, came across rocks that were, unexpectedly, too hard for it to drill — the opposite of Perseverance's initial problem. And a 2008 Mars lander, Phoenix, had trouble collecting grains of dirt until mission managers worked out that the dirt needed to be kept out of direct sunlight so that ice between the grains didn't melt, refreeze and cement them together. "Mars is a real planet, with surprises," says Raymond Arvidson, a planetary scientist at Washington University in St. Louis, Missouri, who has worked on a number of Mars rover missions, although not Perseverance.

Crunch time

Now the pressure is on for Perseverance to start collecting cores more efficiently. It [landed in Jezero in February](#), so it has taken more than six months to collect its first sample. It is supposed to collect its first suite of cores from the crater within one Mars year of landing (a little less than two Earth years). And because the rover landed slightly over 2 kilometres from its main sampling target, Jezero's ancient river delta, it probably won't even reach that formation until early next year.

But Arvidson says he's not concerned about the pace of the mission so far. The first three months were used, among other things, to [test and fly a miniature helicopter](#), which has made a dozen flights so far and is helping mission scientists to pick interesting directions for the rover to travel. The rover itself has driven 2.17 kilometres, south and then west from its landing site, surveying the terrain and doing experiments that don't involve drilling, such as using ground-penetrating radar to probe beneath the planet's surface.



[Why NASA's Mars rover failed to collect its first rock core](#)

Following its successful sample collection, Perseverance will drive northwest a few hundred metres into a region known as South Seítah, full of sand dunes, ridges and other rocks and boulders. Mission planners will soon have a brief break, from 2 October to 14 October, when it will not be possible to communicate with the rover because Mars will move behind the Sun relative to Earth.

NASA and the European Space Agency are planning a complex set of future robotic missions that would travel to Jezero, pick up the samples collected by Perseverance and fly them back to Earth for scientists to study. It will be at least 2031 by the time the samples arrive on Earth.

doi: <https://doi.org/10.1038/d41586-021-02394-w>

This article was downloaded by **calibre** from <https://www.nature.com/articles/d41586-021-02394-w>

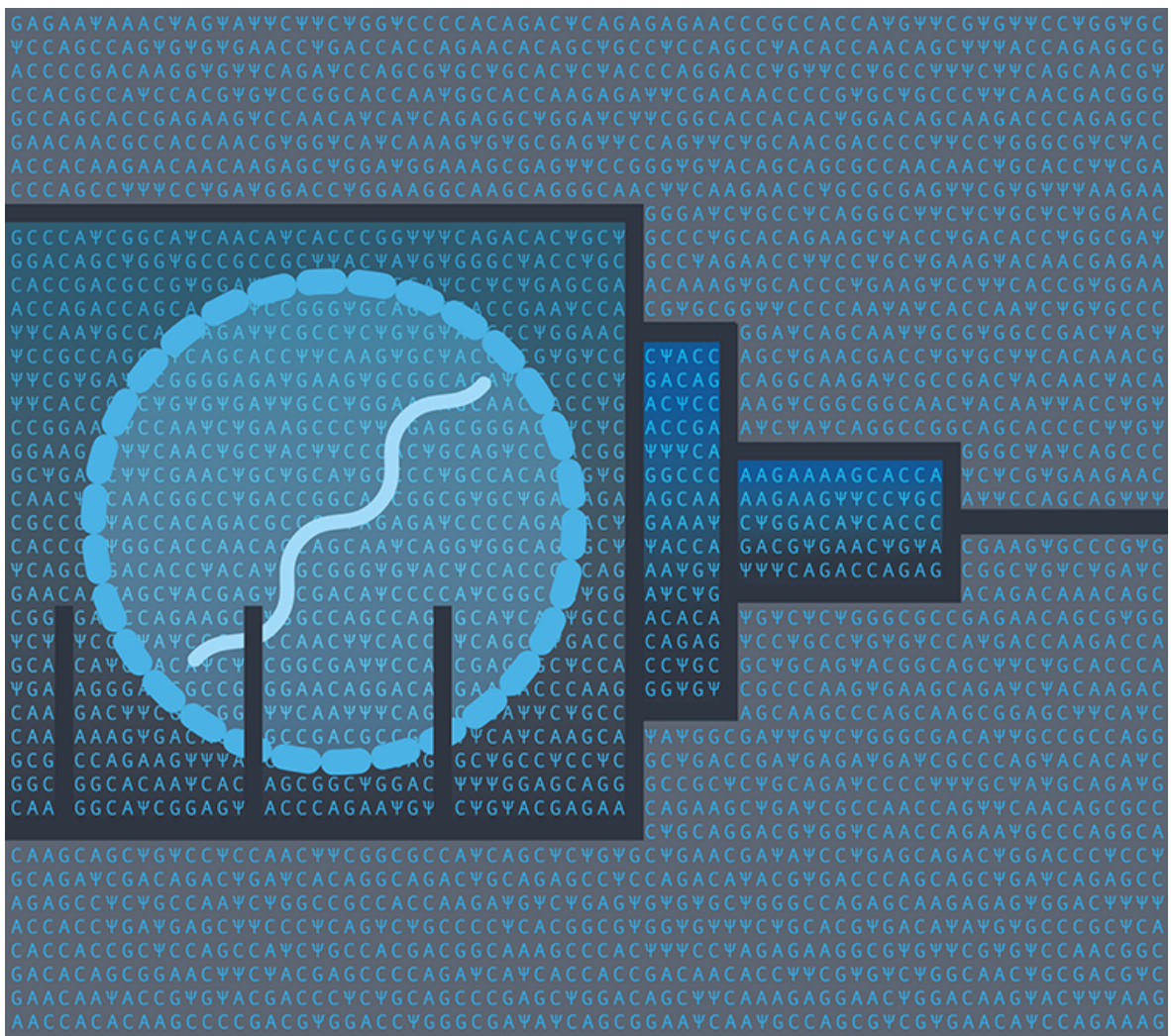
| [Section menu](#) | [Main menu](#) |

- NEWS FEATURE
- 14 September 2021

The tangled history of mRNA vaccines

Hundreds of scientists had worked on mRNA vaccines for decades before the coronavirus pandemic brought a breakthrough.

- [Elie Dolgin](#) 0



The RNA sequence used in the COVID-19 vaccine developed by Pfizer and BioNTech (Ψ is a modified form of the uridine nucleotide, U). Credit: Nik Spencer/*Nature*

In late 1987, Robert Malone performed a landmark experiment. He mixed strands of messenger RNA with droplets of fat, to create a kind of molecular stew. Human cells bathed in this genetic gumbo absorbed the mRNA, and began producing proteins from it¹.

Realizing that this discovery might have far-reaching potential in medicine, Malone, a graduate student at the Salk Institute for Biological Studies in La Jolla, California, later jotted down some notes, which he signed and dated. If cells could create proteins from mRNA delivered into them, he wrote on 11 January 1988, it might be possible to “treat RNA as a drug”. Another

member of the Salk lab signed the notes, too, for posterity. Later that year, Malone’s experiments showed that frog embryos absorbed such mRNA². It was the first time anyone had used fatty droplets to ease mRNA’s passage into a living organism.

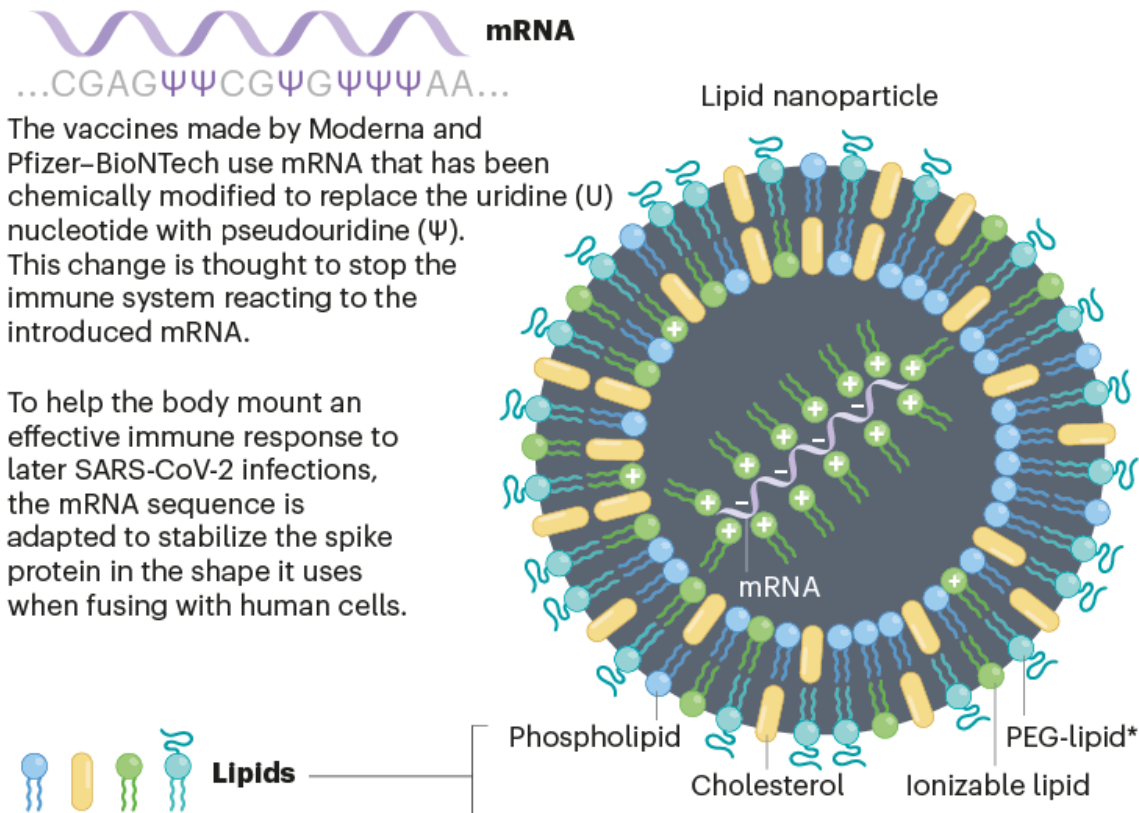
Those experiments were a stepping stone towards two of the most important and profitable vaccines in history: the mRNA-based COVID-19 vaccines [given to hundreds of millions of people around the world](#). Global sales of these are expected to top US\$50 billion in 2021 alone.

But the path to success was not direct. For many years after Malone’s experiments, which themselves had drawn on the work of other researchers, mRNA was seen as too unstable and expensive to be used as a drug or a vaccine. Dozens of academic labs and companies worked on the idea, struggling with finding the right formula of fats and nucleic acids — the building blocks of mRNA vaccines.

Today’s mRNA jabs have innovations that were invented years after Malone’s time in the lab, including chemically modified RNA and different types of fat bubble to ferry them into cells (see ‘Inside an mRNA COVID vaccine’). Still, Malone, who calls himself the “inventor of mRNA vaccines”, thinks his work hasn’t been given enough credit. “I’ve been written out of history,” he told *Nature*.

INSIDE AN mRNA COVID VACCINE

COVID-19 vaccines made from messenger RNA use lipid nanoparticles — bubbles of fats — to carry the molecules into cells. The mRNA contains the code for cells to produce the ‘spike’ protein that the coronavirus SARS-CoV-2 uses to enter cells. Here are key innovations in the design of these vaccines.



The fatty nanoparticle around the mRNA is made of four types of lipid molecule. One of these is ‘ionizable’: in the vaccine, many of these molecules have a positive charge and cling to negatively charged mRNA, but they lose that charge in the more alkaline conditions of the bloodstream, reducing toxicity in the body.

*Lipid attached to polyethylene glycol

©nature

Nik Spencer/*Nature*; Adapted from [M. D. Buschmann et al. *Vaccines* 9, 65 \(2021\)](#).

The debate over who deserves credit for pioneering the technology is heating up as awards start rolling out — and the speculation is getting more intense in advance of the Nobel prize announcements next month. But formal prizes restricted to only a few scientists will fail to recognize the

many contributors to mRNA's medical development. In reality, the path to mRNA vaccines drew on the work of hundreds of researchers over more than 30 years.

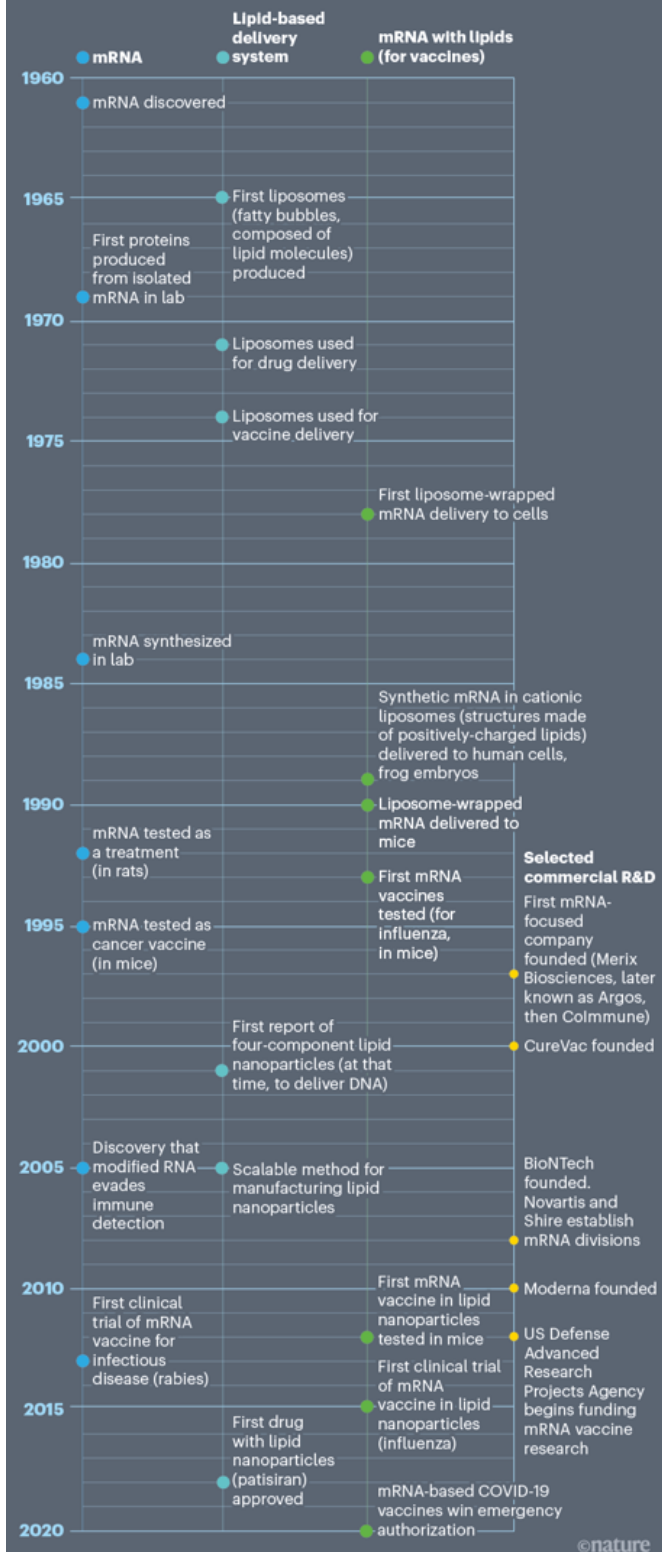
The story illuminates the way that many scientific discoveries become life-changing innovations: with decades of dead ends, rejections and battles over potential profits, but also generosity, curiosity and dogged persistence against scepticism and doubt. "It's a long series of steps," says Paul Krieg, a developmental biologist at the University of Arizona in Tucson, who made his own contribution in the mid-1980s, "and you never know what's going to be useful".

The beginnings of mRNA

Malone's experiments didn't come out of the blue. As far back as 1978, scientists had used fatty membrane structures called liposomes to transport mRNA into mouse³ and human⁴ cells to induce protein expression. The liposomes packaged and protected the mRNA and then fused with cell membranes to deliver the genetic material into cells. These experiments themselves built on years of work with liposomes and with mRNA; both were discovered in the 1960s (see 'The history of mRNA vaccines').

THE HISTORY OF mRNA VACCINES

A long chain of scientific advances led to the first messenger RNA (mRNA) vaccines, released last year to protect people against COVID-19. These vaccines, as well as mRNA drugs, make use of developments in the science of mRNA and in delivery systems, which are made of lipid molecules.

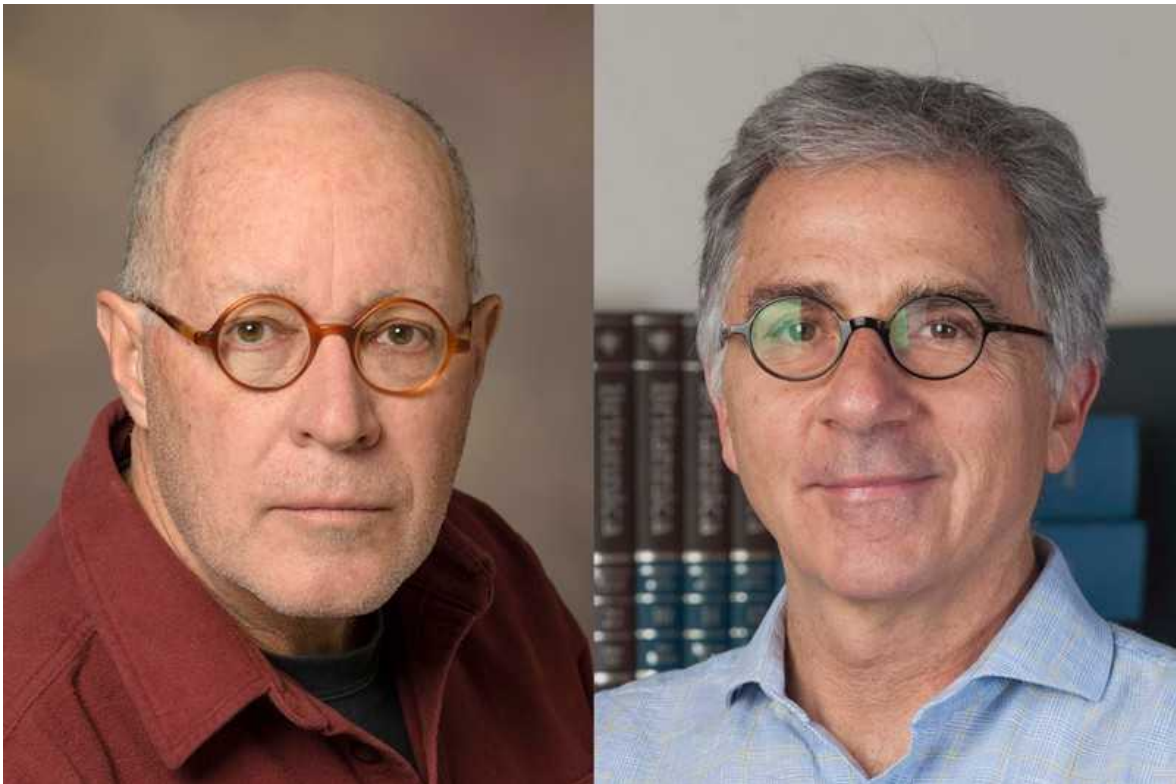


Nik Spencer/*Nature*; Adapted from [U. Şahin et al. *Nature Rev. Drug Discov.* 13, 759–780 \(2014\)](#) and X. Hou *et al. Nature Rev. Mater.* <https://doi.org/gmjsn5> (2021).

Back then, however, few researchers were thinking about mRNA as a medical product — not least because there was not yet a way to manufacture the genetic material in a laboratory. Instead, they hoped to use it to interrogate basic molecular processes. Most scientists repurposed mRNA from rabbit blood, cultured mouse cells or some other animal source.

That changed in 1984, when Krieg and other members of a team led by developmental biologist Douglas Melton and molecular biologists Tom Maniatis and Michael Green at Harvard University in Cambridge, Massachusetts, used an RNA-synthesis enzyme (taken from a virus) and other tools to produce biologically active mRNA in the lab⁵ — a method that, at its core, remains in use today. Krieg then injected the lab-made mRNA into frog eggs, and showed that it worked just like the real thing⁶.

Both Melton and Krieg say they saw synthetic mRNA mainly as a research tool for studying gene function and activity. In 1987, after Melton found that the mRNA could be used both to activate and to prevent protein production, he helped to form a company called Oligogen (later renamed Gilead Sciences in Foster City, California) to explore ways to use synthetic RNA to block the expression of target genes — with an eye to treating disease. Vaccines weren't on the mind of anyone in his lab, or their collaborators.



Paul Krieg (left) and Douglas Melton (right), who worked on ways to synthesize mRNA in the laboratory. Credit: University of Arizona; Kevin Wolf/AP Images for HHMI

“RNA in general had a reputation for unbelievable instability,” says Krieg. “Everything around RNA was cloaked in caution.” That might explain why Harvard’s technology-development office elected not to patent the group’s RNA-synthesis approach. Instead, the Harvard researchers simply gave their reagents to Promega Corporation, a lab-supplies company in Madison, Wisconsin, which made the RNA-synthesis tools available to researchers. They received modest royalties and a case of Veuve Clicquot Champagne in return.

Patent disputes

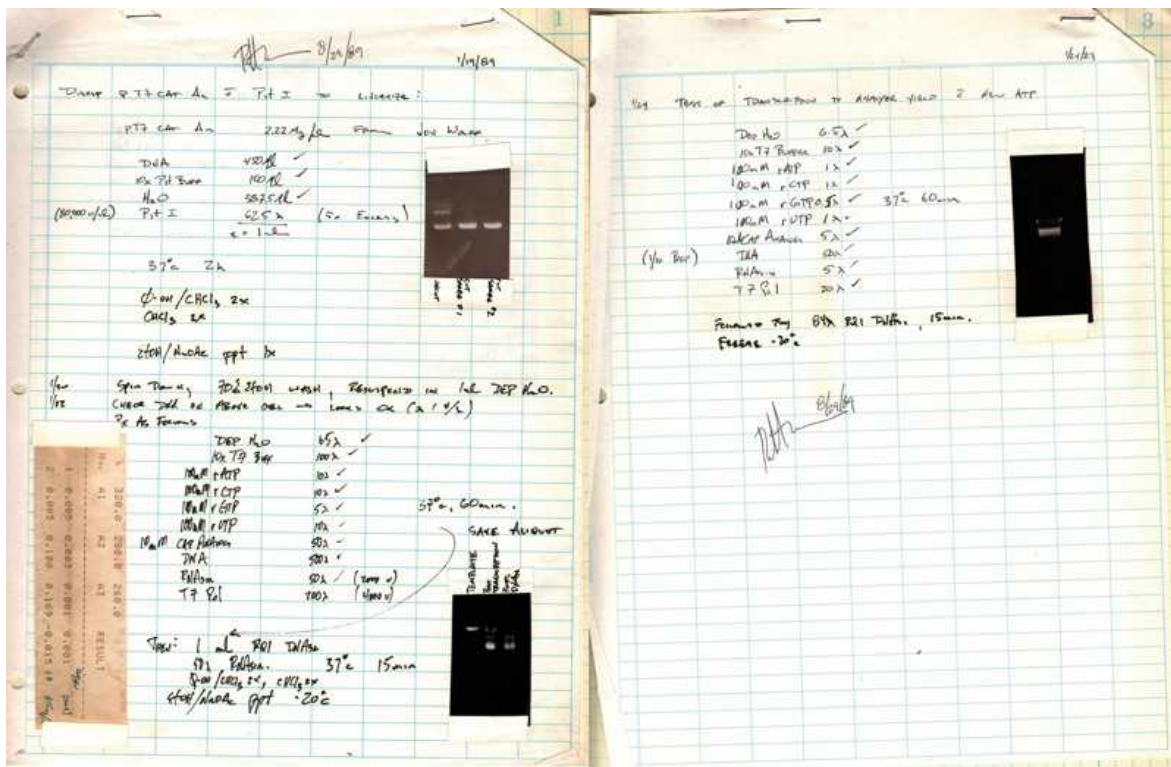
Years later, Malone followed the Harvard team’s tactics to synthesize mRNA for his experiments. But he added a new kind of liposome, one that carried a positive charge, which enhanced the material’s ability to engage with the negatively charged backbone of mRNA. These liposomes were developed

by Philip Felgner, a biochemist who now leads the Vaccine Research and Development Center at the University of California, Irvine.



Philip Felgner (left) and Robert Malone.Credit: Steve Zylius/UCI; Robert Malone

Despite his success using the liposomes to deliver mRNA into human cells and frog embryos, Malone never earned a PhD. He fell out with his supervisor, Salk gene-therapy researcher Inder Verma and, in 1989, left graduate studies early to work for Felgner at Vical, a recently formed start-up in San Diego, California. There, they and collaborators at the University of Wisconsin–Madison showed that the lipid–mRNA complexes could spur protein production in mice⁷.



An excerpt from Robert Malone's lab notebooks, describing the 1989 synthesis of mRNA for injection into mice. Credit: Robert Malone

Then things got messy. Both Vical (with the University of Wisconsin) and the Salk began filing for patents in March 1989. But the Salk soon abandoned its patent claim, and in 1990, Verma joined Vical's advisory board.

Malone contends that Verma and Vical struck a back-room deal so that the relevant intellectual property went to Vical. Malone was listed as one inventor among several, but he no longer stood to profit personally from subsequent licensing deals, as he would have from any Salk-issued patents. Malone's conclusion: "They got rich on the products of my mind."

Verma and Felgner categorically deny Malone's charges. "It's complete nonsense," Verma told *Nature*. The decision to drop the patent application rested with the Salk's technology-transfer office, he says. ([Verma resigned from the Salk in 2018](#), following allegations of sexual harassment, which he continues to deny.)

Malone left Vical in August 1989, citing disagreements with Felgner over “scientific judgment” and “credit for my intellectual contributions”. He completed medical school and did a year of clinical training before working in academia, where he tried to continue research on mRNA vaccines but struggled to secure funding. (In 1996, for example, he unsuccessfully applied to a California state research agency for money to develop a mRNA vaccine to combat seasonal coronavirus infections.) Malone focused on DNA vaccines and delivery technologies instead.

In 2001, he moved into commercial work and consulting. And in the past few months, he has started publicly attacking the safety of the mRNA vaccines that his research helped to enable. Malone says, for instance, that proteins produced by vaccines can damage the body’s cells and that the risks of vaccination outweigh the benefits for children and young adults — claims that other scientists and health officials have repeatedly refuted.

Manufacturing challenges

In 1991, Vical entered into a multimillion-dollar research collaboration and licensing pact with US firm Merck, one of the world’s largest vaccine developers. Merck scientists evaluated the mRNA technology in mice with the aim of creating an influenza vaccine, but then abandoned that approach. “The cost and feasibility of manufacturing just gave us pause,” says Jeffrey Ulmer, a former Merck scientist who now consults with companies on vaccine-research issues.

Researchers at a small biotech firm in Strasbourg, France, called Transgène, felt the same way. There, in 1993, a team led by Pierre Meulien, working with industrial and academic partners, was the first to show that an mRNA in a liposome could elicit a specific antiviral immune response in mice⁸. (Another exciting advance had come in 1992, when scientists at the Scripps Research Institute in La Jolla used mRNA to replace a deficient protein in rats, to treat a metabolic disorder⁹. But it would take almost two decades before independent labs reported similar success.)



Pierre Meulien.Credit: IMI Joint Undertaking

The Transgène researchers patented their invention, and continued to work on mRNA vaccines. But Meulien, who is now head of the Innovative Medicines Initiative, a public–private enterprise based in Brussels, estimated that he needed at least €100 million (US\$119 million) to optimize the platform — and he wasn't about to ask his bosses for that much for such a “tricky, high-risk” venture, he says. The patent lapsed after Transgène's parent firm decided to stop paying the fees needed to keep it active.

Meulien's group, like the Merck team, moved to focus instead on DNA vaccines and other vector-based delivery systems. The DNA platform ultimately yielded a few licensed vaccines for veterinary applications — helping, for example, to prevent infections in fish farms. And just last month, [regulators in India granted emergency approval to the world's first DNA vaccine for human use](#), to help ward off COVID-19. But for reasons that are not completely understood, DNA vaccines have been slow to find success in people.

Still, the industry's concerted push around DNA technology has had benefits for RNA vaccines, too, argues Ulmer. From manufacturing considerations and regulatory experience to sequence designs and molecular insights, “many of the things that we learned from DNA could be directly applied to RNA”, he says. “It provided the foundation for the success of RNA.”

Continuous struggle

In the 1990s and for most of the 2000s, nearly every vaccine company that considered working on mRNA opted to invest its resources elsewhere. The conventional wisdom held that mRNA was too prone to degradation, and its production too expensive. “It was a continuous struggle,” says Peter Liljeström, a virologist at the Karolinska Institute in Stockholm, who 30 years ago pioneered a type of ‘self-amplifying’ RNA vaccine.

“RNA was so hard to work with,” says Matt Winkler, who founded one of the first RNA-focused lab supplies companies, Ambion, in Austin, Texas, in 1989. “If you had asked me back [then] if you could inject RNA into somebody for a vaccine, I would have laughed in your face.”

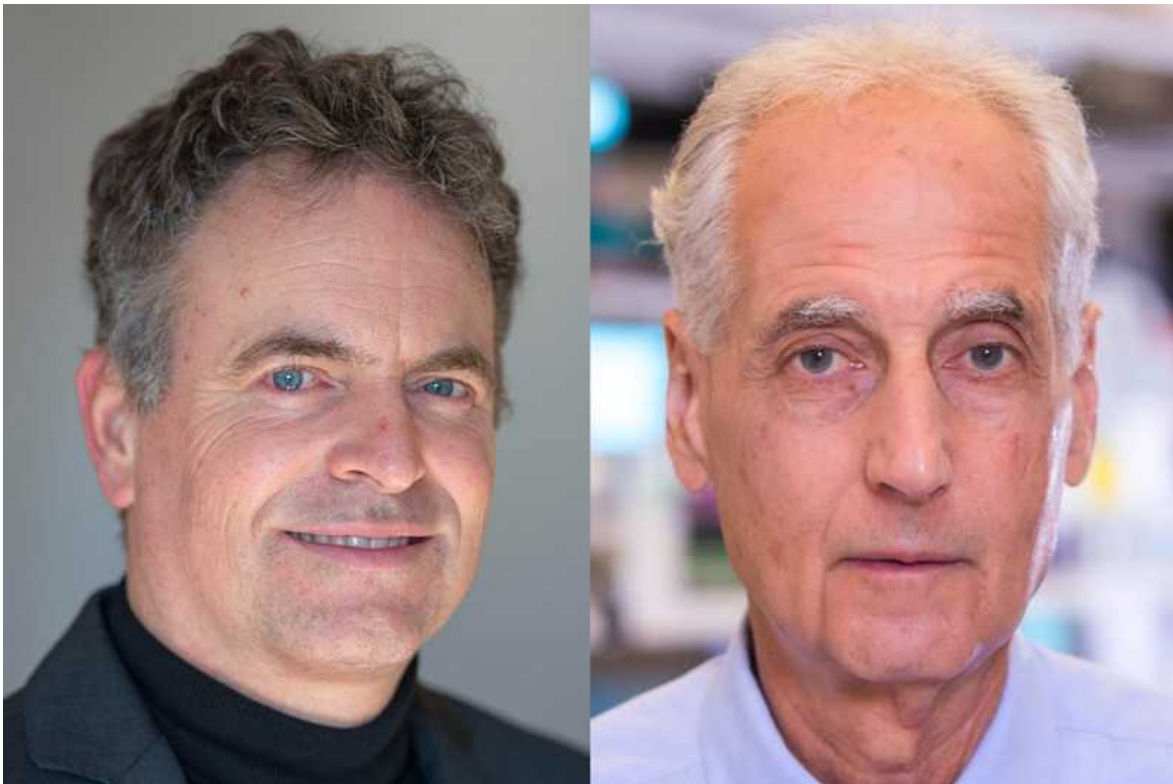
The mRNA vaccine idea had a more favourable reception in oncology circles, albeit as a therapeutic agent, rather than to prevent disease. Beginning with the work of gene therapist David Curiel, several academic scientists and start-up companies explored whether mRNA could be used to combat cancer. If mRNA encoded proteins expressed by cancer cells, the thinking went, then injecting it into the body might train the immune system to attack those cells.

Curiel, now at the Washington University School of Medicine in St Louis, Missouri, had some success in mice¹⁰. But when he approached Ambion about commercialization opportunities, he says, the firm told him: “We don’t see any economic potential in this technology.”

Another cancer immunologist had more success, which led to the founding of the first mRNA therapeutics company, in 1997. Eli Gilboa proposed taking immune cells from the blood, and coaxing them to take up synthetic mRNA that encoded tumour proteins. The cells would then be injected back into the body where they could marshal the immune system to attack lurking tumours.

Gilboa and his colleagues at Duke University Medical Center in Durham, North Carolina, demonstrated this in mice¹¹. By the late 1990s, academic collaborators had launched human trials, and Gilboa’s commercial spin-off, Merix Bioscience (later renamed to Argos Therapeutics and now called CoImmune), soon followed with clinical studies of its own. The approach was looking promising until a few years ago, when a late-stage candidate vaccine failed in a large trial; it has now largely fallen out of fashion.

But Gilboa’s work had an important consequence. It inspired the founders of the German firms CureVac and BioNTech — two of the largest mRNA companies in existence today — to begin work on mRNA. Both Ingmar Hoerr, at CureVac, and Uğur Şahin, at BioNTech, told *Nature* that, after learning of what Gilboa had done, they wanted to do the same, but by administering mRNA into the body directly.



Ingmar Hoerr (left) founded CureVac, and cancer immunologist Eli Gilboa (right) founded the first mRNA therapeutics firm. Credit: Sebastian Gollnow/dpa/Alamy; Eli Gilboa

“There was a snowball effect,” says Gilboa, now at the University of Miami Miller School of Medicine in Florida.

Start-up accelerator

Hoerr was the first to achieve success. While at the University of Tübingen in Germany, he reported in 2000 that direct injections could elicit an immune response in mice¹². He created CureVac (also based in Tübingen) that year. But few scientists or investors seemed interested. At one conference where Hoerr presented early mouse data, he says, “there was a Nobel prizewinner standing up in the first row saying, ‘This is completely shit what you’re telling us here — completely shit.’” (Hoerr declined to name the Nobel laureate.)

Eventually, money trickled in. And within a few years, human testing began. The company's chief scientific officer at the time, Steve Pascolo, was the first study subject: he injected himself¹³ with mRNA and still has match-head-sized white scars on his leg from where a dermatologist took punch biopsies for analysis. A more formal trial, involving tumour-specific mRNA for people with skin cancer, kicked off soon after.

Şahin and his immunologist wife, Özlem Türeci, also began studying mRNA in the late 1990s, but waited longer than Hoerr to start a company. They plugged away at the technology for many years, working at Johannes Gutenberg University Mainz in Germany, earning patents, papers and research grants, before pitching a commercial plan to billionaire investors in 2007. “If it works, it will be ground-breaking,” Şahin said. He got €150 million in seed money.



Özlem Türeci (left) and Uğur Şahin (right) co-founded the mRNA vaccine firm BioNTech.Credit: BioNTech SE 2021

The same year, a fledgling mRNA start-up called RNARx received a more modest sum: \$97,396 in small-business grant funding from the US

government. The company's founders, biochemist Katalin Karikó and immunologist Drew Weissman, both then at the University of Pennsylvania (UPenn) in Philadelphia, had made what some now say is a key finding: that altering part of the mRNA code helps synthetic mRNA to slip past the cell's innate immune defences.

Fundamental insights

Karikó had toiled in the lab throughout the 1990s with the goal of transforming mRNA into a drug platform, although grant agencies kept turning down her funding applications. In 1995, after repeated rejections, she was given the choice of leaving UPenn or accepting a demotion and pay cut. She opted to stay and continue her dogged pursuit, making improvements to Malone's protocols¹⁴, and managing to induce cells to produce a large and complex protein of therapeutic relevance¹⁵.



Katalin Karikó helped to show that chemical modifications to RNA can smuggle the molecule past the body's immune defences. Credit: Hannah Yoon/Bloomberg/Getty

In 1997, she began working with Weissman, who had just started a lab at UPenn. Together, they planned to develop an mRNA-based vaccine for HIV/AIDS. But Karikó's mRNAs set off massive inflammatory reactions when they were injected into mice.

She and Weissman soon worked out why: the synthetic mRNA was arousing¹⁶ a series of immune sensors known as Toll-like receptors, which act as first responders to danger signals from pathogens. In 2005, the pair reported that rearranging the chemical bonds on one of mRNA's nucleotides, uridine, to create an analogue called pseudouridine, seemed to stop the body identifying the mRNA as a foe¹⁷.



Drew Weissman worked with Karikó, and co-discovered the advantages of modified mRNA. Credit: Penn Medicine

Few scientists at the time recognized the therapeutic value of these modified nucleotides. But the scientific world soon awoke to their potential. In September 2010, a team led by Derrick Rossi, a stem-cell biologist then at Boston Children's Hospital in Massachusetts, described how modified mRNAs could be used to transform skin cells, first into embryonic-like stem cells and then into contracting muscle tissue¹⁸. The finding made a splash. Rossi was featured in *Time* magazine as one of 2010's 'people who mattered'. He co-founded a start-up, Moderna in Cambridge.

Moderna tried to license the patents for modified mRNA that UPenn had filed in 2006 for Karikó's and Weissman's invention. But it was too late. After failing to come to a licensing agreement with RNARx, UPenn had opted for a quick payout. In February 2010, it granted exclusive patent rights to a small lab-reagents supplier in Madison. Now called Cellscript, the company paid \$300,000 in the deal. It would go on to pull in hundreds of millions of dollars in sublicensing fees from Moderna and BioNTech, the originators of the first mRNA vaccines for COVID-19. Both products contain modified mRNA.

RNARx, meanwhile, used up another \$800,000 in small-business grant funding and ceased operations in 2013, around the time that Karikó joined BioNTech (retaining an adjunct appointment at UPenn).

The pseudouridine debate

Researchers still argue over whether Karikó and Weissman's discovery is essential for successful mRNA vaccines. Moderna has always used modified mRNA — its name is a portmanteau of those two words. But some others in the industry have not.

Researchers at the human-genetic-therapies division of the pharmaceutical firm Shire in Lexington, Massachusetts, reasoned that unmodified mRNA could yield a product that was just as effective if the right 'cap' structures were added and all impurities were removed. "It came down to the quality of

the RNA,” says Michael Heartlein, who led Shire’s research effort and continued to advance the technology at Translate Bio in Cambridge, to which Shire later sold its mRNA portfolio. (Shire is now part of the Japanese firm Takeda.)

Although Translate has some human data to suggest its mRNA does not provoke a concerning immune response, its platform remains to be proved clinically: its COVID-19 vaccine candidate is still in early human trials. But French drug giant Sanofi has been convinced of the technology’s promise: in August 2021, it announced plans to acquire Translate for \$3.2 billion. (Heartlein left last year to found another firm in Waltham, Massachusetts, called Maritime Therapeutics.)

CureVac, meanwhile, has its own immune-mitigation strategy, which involves altering the genetic sequence of the mRNA to minimize the amount of uridine in its vaccines. Twenty years of working on that approach seemed to be bearing fruit, with early trials of the company’s experimental vaccines for rabies¹⁹ and COVID-19²⁰ both proving a success. But in June, data from a later-stage trial showed that CureVac’s coronavirus vaccine candidate was [much less protective than Moderna’s or BioNTech’s](#).

In light of those results, some mRNA experts now consider pseudouridine an essential component of the technology — and so, they say, Karikó’s and Weissman’s discovery was one of the key enabling contributions that merits recognition and prizes. “The real winner here is modified RNA,” says Jake Becroft, co-founder and chief executive of Strand Therapeutics, a Cambridge-based synthetic-biology company working on mRNA-based therapeutics.

Not everyone is so certain. “There are multiple factors that may affect the safety and efficacy of an mRNA vaccine, chemical modification of mRNA is only one of them,” says Bo Ying, chief executive of Suzhou Abogen Biosciences, a Chinese company with an mRNA vaccine for COVID-19 now in late-stage clinical testing. (Known as ARCoV, the product uses unmodified mRNA.)

Fat breakthrough

As for linchpin technologies, many experts highlight another innovation that was crucial for mRNA vaccines — one that has nothing to do with the mRNA. It is the tiny fat bubbles known as lipid nanoparticles, or LNPs, that protect the mRNA and shuttle it into cells.

This technology comes from the laboratory of Pieter Cullis, a biochemist at the University of British Columbia in Vancouver, Canada, and several companies that he founded or led. Beginning in the late 1990s, they pioneered LNPs for delivering strands of nucleic acids that silence gene activity. One such treatment, patisiran, is now approved for a rare inherited disease.



Pieter Cullis.Credit: Paul Joseph for UBC

After that gene-silencing therapy began to show promise in clinical trials, in 2012, two of Cullis's companies pivoted to explore opportunities for the LNP delivery system in mRNA-based medicines. Acuitas Therapeutics in Vancouver, for example, led by chief executive Thomas Madden, forged partnerships with Weissman's group at UPenn and with several mRNA companies to test different mRNA–LNP formulations. One of these can now

be found in the COVID-19 vaccines from BioNTech and CureVac. Moderna's LNP concoction is not much different.

The nanoparticles have a mixture of four fatty molecules: three contribute to structure and stability; the fourth, called an ionizable lipid, is key to the LNP's success. This substance is positively charged under laboratory conditions, which offers similar advantages to the liposomes that Felgner developed and Malone tested in the late 1980s. But the ionizable lipids advanced by Cullis and his commercial partners convert to a neutral charge under physiological conditions such as those in the bloodstream, which limits the toxic effects on the body.

What's more, the four-lipid cocktail allows the product to be stored for longer on the pharmacy shelf and to maintain its stability inside the body, says Ian MacLachlan, a former executive at several Cullis-linked ventures. "It's the whole kit and caboodle that leads to the pharmacology we have now," he says.



Ian MacLachlan (left) and Thomas Madden (right). Credit: Ian MacLachlan; Acuitas Therapeutics

By the mid-2000s, a new way to mix and manufacture these nanoparticles had been devised. It involved using a ‘T-connector’ apparatus, which combines fats (dissolved in alcohol) with nucleic acids (dissolved in an acidic buffer). When streams of the two solutions merged, the components spontaneously formed densely packed LNPs²¹. It proved to be a more reliable technique than other ways of making mRNA-based medicines.

Once all the pieces came together, “it was like, holy smoke, finally we’ve got a process we can scale”, says Andrew Geall, now chief development officer at Replicate Bioscience in San Diego. Geall led the first team to combine LNPs with an RNA vaccine²², at Novartis’s US hub in Cambridge in 2012. Every mRNA company now uses some variation of this LNP delivery platform and manufacturing system — although who owns the relevant patents remains the subject of legal dispute. Moderna, for example, is locked in a battle with one Cullis-affiliated business — Arbutus Biopharma in Vancouver — over who holds the rights to the LNP technology found in Moderna’s COVID-19 jab.

An industry is born

By the late 2000s, several big pharmaceutical companies were entering the mRNA field. In 2008, for example, both Novartis and Shire established mRNA research units — the former (led by Geall) focused on vaccines, the latter (led by Heartlein) on therapeutics. BioNTech launched that year, and other start-ups soon entered the fray, bolstered by a 2012 decision by the US Defense Advanced Research Projects Agency to start funding industry researchers to study RNA vaccines and drugs. Moderna was one of the companies that built on this work and, by 2015, it had raised more than \$1 billion on the promise of harnessing mRNA to induce cells in the body to make their own medicines — thereby fixing diseases caused by missing or defective proteins. When that plan faltered, Moderna, led by chief executive Stéphane Bancel, chose to prioritize a less ambitious target: making vaccines.



Moderna's Derrick Rossi (left) and Stéphane Bancel (right). Credit: Derrick Rossi; Adam Glanzman/Bloomberg/Getty

That initially disappointed many investors and onlookers, because a vaccine platform seemed to be less transformative and lucrative. By the beginning of 2020, Moderna had advanced nine mRNA vaccine candidates for infectious diseases into people for testing. None was a slam-dunk success. Just one had progressed to a larger-phase trial.

But when COVID-19 struck, Moderna was quick off the mark, creating a prototype vaccine [within days of the virus's genome sequence becoming available online](#). The company then collaborated with the US National Institute of Allergy and Infectious Diseases (NIAID) to conduct mouse studies and launch human trials, all within less than ten weeks.

BioNTech, too, took an all-hands-on-deck approach. In March 2020, it partnered with New York-based drug company Pfizer, and clinical trials then moved at a record pace, going from first-in-human testing to emergency approval in less than eight months.

Both authorized vaccines use modified mRNA formulated in LNPs. Both also contain sequences that encode a form of the SARS-CoV-2 spike protein that adopts a shape more amenable to inducing protective immunity. Many experts say that the protein tweak, devised by NIAID vaccinologist Barney Graham and structural biologists Jason McLellan at the University of Texas at Austin and Andrew Ward at Scripps, is also a prize-worthy contribution, albeit one that is specific to coronavirus vaccines, not mRNA vaccination as a general platform.



[The lightning-fast quest for COVID vaccines — and what it means for other diseases](#)

Some of the furore in discussions of credit for mRNA discoveries relates to who holds lucrative patents. But much of the foundational intellectual property dates back to claims made in 1989 by Felgner, Malone and their colleagues at Vical (and in 1990 by Liljeström). These had only a 17-year term from the date of issue and so are now in the public domain.

Even the Karikó–Weissman patents, licensed to Cellscript and filed in 2006, will expire in the next five years. Industry insiders say this means that it will soon become very hard to patent broad claims about delivering mRNAs in lipid nanoparticles, although companies can reasonably patent particular sequences of mRNA — a form of the spike protein, say — or proprietary lipid formulations.

Firms are trying. Moderna, the dominant player in the mRNA vaccine field, which has experimental shots in clinical testing for influenza, cytomegalovirus and a [range of other infectious diseases](#), got two patents last year covering the broad use of mRNA to produce secreted proteins. But multiple industry insiders told *Nature* they think these could be challengeable.



[How COVID unlocked the power of RNA vaccines](#)

“We don’t feel there’s a lot that is patentable, and certainly not enforceable,” says Eric Marcussen, chief scientific officer of Providence Therapeutics, an mRNA vaccines company in Calgary, Canada.

Nobel debate

As for who deserves a Nobel, the names that come up most often in conversation are Karikó and Weissman. The two have already won several prizes, [including one of the Breakthrough Prizes](#) (at \$3 million, the most lucrative award in science) and Spain’s prestigious Princess of Asturias Award for Technical and Scientific Research. Also recognized in the Asturias prize were Felgner, Şahin, Türeci and Rossi, along with Sarah Gilbert, the vaccinologist behind the COVID-19 vaccine developed by the University of Oxford, UK, and the drug firm AstraZeneca, which uses a

viral vector instead of mRNA. (Cullis's only recent accolade was a \$5,000 founder's award from the Controlled Release Society, a professional organization of scientists who study time-release drugs.)

Some also argue that Karikó should be acknowledged as much for her contributions to the mRNA research community at large as for her discoveries in the lab. "She's not only an incredible scientist, she's just a force in the field," says Anna Blakney, an RNA bioengineer at the University of British Columbia. Blakney gives Karikó credit for offering her a speaking slot at a major conference two years ago, when she was still in a junior postdoc position (and before Blakney co-founded VaxEquity, a vaccine company in Cambridge, UK, focusing on self-amplifying-RNA technology). Karikó "is actively trying to lift other people up in a time when she's been so under-recognized her whole career".

Although some involved in mRNA's development, including Malone, think they deserve more recognition, others are more willing to share the limelight. "You really can't claim credit," says Cullis. When it comes to his lipid delivery system, for instance, "we're talking hundreds, probably thousands of people who have been working together to make these LNP systems so that they're actually ready for prime time."

"Everyone just incrementally added something — including me," says Karikó.

Looking back, many say they're just delighted that mRNA vaccines are making a difference to humanity, and that they might have made a valuable contribution along the road. "It's thrilling for me to see this," says Felgner. "All of the things that we were thinking would happen back then — it's happening now."

Nature **597**, 318-324 (2021)

doi: <https://doi.org/10.1038/d41586-021-02483-w>

References

1. 1.

Malone, R. W., Felgner, P. L. & Verma, I. M. *Proc. Natl Acad. Sci. USA* **86**, 6077–6081 (1989).

2. 2.

Malone, R. W. *Focus* **11**, 61–66 (1989).

3. 3.

Dimitriadis, G. J. *Nature* **274**, 923–924 (1978).

4. 4.

Ostro, M. J., Giacomoni, D., Lavelle, D., Paxton, W. & Dray, S. *Nature* **274**, 921–923 (1978).

5. 5.

Melton, D. A. *et al.* *Nucleic Acids Res.* **12**, 7035–7056 (1984).

6. 6.

Krieg, P. A. & Melton, D. A. *Nucleic Acids Res.* **12**, 7057–7070 (1984).

7. 7.

Wolff, J. A. *et al.* *Science* **247**, 1465–1468 (1990).

8. 8.

Martinon, F. *et al.* *Eur. J. Immunol.* **23**, 1719–1722 (1993).

9. 9.

Jirikowski, G. F., Sanna, P. P., Maciejewski-Lenoir, D. & Bloom, F. E. *Science* **255**, 996–998 (1992).

10. 10.

Conry, R. M. *et al.* *Cancer Res.* **55**, 1397–1400 (1995).

11. 11.

Boczkowski, D., Nair, S. K., Snyder, D. & Gilboa, E. *J. Exp. Med.* **184**, 465–472 (1996).

12. 12.

Hoerr, I., Obst, R., Rammensee, H. G. & Jung, G. *Eur. J. Immunol.* **30**, 1–7 (2000).

13. 13.

Probst, J. *et al.* *Gene Ther.* **14**, 1175–1180 (2007).

14. 14.

Karikó, K., Kuo, A., Barnathan, E. S. & Langer, D. J. *Biochim. Biophys. Acta* **1369**, 320–334 (1998).

15. 15.

Karikó, K., Kuo, A. & Barnathan, E. *Gene Ther.* **6**, 1092–1100 (1999).

16. 16.

Karikó, K., Ni, H., Capodici, J., Lamphier, M. & Weissman, D. *J. Biol. Chem.* **279**, 12542–12550 (2004).

17. 17.

Karikó, K., Buckstein, M., Ni, H. & Weissman, D. *Immunity* **23**, 165–175 (2005).

18. 18.

Warren, L. *et al.* *Cell Stem Cell* **7**, 618–630 (2010).

19. 19.

Aldrich, C. *et al.* *Vaccine* **39**, 1310–1318 (2021).

20. 20.

Kremsner, P. G. *et al.* *Wien. Klin. Wochenschr.*
<https://doi.org/10.1007/s00508-021-01922-y> (2021).

21. 21.

Jeffs, L. B. *et al.* *Pharm. Res.* **22**, 362–372 (2005).

22. 22.

Geall, A. J. *et al.* *Proc. Natl Acad. Sci. USA* **109**, 14604–14609 (2012)

This article was downloaded by **calibre** from <https://www.nature.com/articles/d41586-021-02483-w>

| [Section menu](#) | [Main menu](#) |

Books & Arts

- **Marauding elephants, menacing macaques and epicurean bears** [13 September 2021]

Book Review • As humans encroach on the habitat of wild animals, is it any surprise that they advance upon ours?

- BOOK REVIEW
- 13 September 2021

Marauding elephants, menacing macaques and epicurean bears

As humans encroach on the habitat of wild animals, is it any surprise that they advance upon ours?

- [Josie Glausiusz](#) ⁰



An adult male elephant wanders through the town of Siliguri, India, in February 2016. Credit: Diptendu Dutta/AFP/Getty

Fuzz: When Nature Breaks the Law Mary Roach (2021)

On 8 September 1488, the French fiefdom of Beaujeu issued an unusual order. Curates were charged with warning slugs three times “to cease from vexing the people by corroding and consuming the herbs of the fields and the vines, and to depart”. Mary Roach cites this episode in her introduction to *Fuzz: When Nature Breaks the Law* — eliciting the first laugh of many in a book in which she turns her deft wit on the destruction and death that results from human–wildlife conflict. It is a fitting sequel to her previous ‘science-ofs’: *Stiff* (about cadavers), *Spook* (the afterlife), *Bonk* (sex), *Gulp* (eating) and *Grunt* (combat).

Beyond medieval proceedings against slugs, caterpillars and weevils, Roach addresses more modern resolutions to our rivalry with species that “regularly commit acts that put them at odds with humans”. Travelling from the alleyways of Aspen, Colorado, where epicurean bears forage among restaurant dustbins, to “leopard-terrorized hamlets” in the Himalayas, she investigates how wild creatures from cougars to crows menace humans, their crops and their property.

Fundamentally, she asks: when we encroach on the habitat of wild creatures, is it any surprise that they advance on ours? Perhaps nowhere is this collision clearer than in the Indian region of North Bengal, where, each year, dozens of people die after elephant attacks. Elephants there forage at night and sleep by day in patches of teak and red sandalwood trees, the remnants of forests that once stretched from the state of Assam to the eastern border of Nepal. This elephant corridor was fractured by imperialist-era tea estates and more recently by military bases. As the population of elephants in the remaining pockets spikes, the animals are wandering into villages, eating crops and grain stores.



The long goodbye

A bull elephant in must — the periodic hormonal tumult signified by frequent erections and ogling eyeballs — is highly aggressive and can crush people. Roach accompanies researchers from the Wildlife Institute of India in Dehradun to visit “awareness camps”, where they teach villagers to stay calm and call the local Elephant Squad so that rangers can herd roving elephants back into the forest. Even better, conservationist Dipanjan Naha tells her, would be to install seismic sensors to warn of approaching elephant footfalls. But, as one officer notes: “We are disturbing them.”

In India, where in Hindu tradition elephants are the incarnation of the god Ganesha, it is customary to offer compensation to the families of those killed by elephants, and by leopards. In the United States, by contrast, the focus is not on compensation but on euthanizing the few bears who attack and kill humans. With bears, too, habitat fragmentation as well as climate change appear to play a major part in the conflict with humans. Major highways on the US–Canada border might restrict the movement of black bears. In California, drought is pushing bears into urban areas and, during a record-breaking heatwave earlier this year, into the waters of Lake Tahoe.



Pushed into urban areas by encroaching development, bears raid bins for food. Credit: Tomas Hulik ARTpoint/Shutterstock

Once upon a time, bears in the forests around Aspen, Colorado, dined well on acorns, chokecherries and “the outrageous fecundity of crabapple trees”. Roach watches them in the wee hours gorging instead on crab legs and cabbage leaves, tossed out by the city’s restaurants. Stewart Breck at the National Wildlife Research Center in Fort Collins, Colorado, argues that limiting the availability of human food can reduce the need to kill or ward off marauding bears. But replacing busted bear-resistant dumpsters, hiring staff to enforce bin-locking laws, and issuing tickets to restaurants and “alpha residents” who ignore local waste-disposal ordinances isn’t easy: “the county is home to about as many billionaires as bears,” Roach writes.

Complex trade-offs

Often, it's our meddling that created the threat in the first place, as when humans introduce animals that inflict unbridled harm upon native species. Case in point: carnivorous stoat (*Mustela erminea*), that were shipped from Europe to New Zealand in the late nineteenth century to control rabbits, themselves originally imported for food and sport. Stoats, which are agile climbers and swimmers, now prey upon New Zealand's birds, eating eggs and chicks of tree-trunk-nesting mohua (*Mohoua ochrocephala*), kākā (*Nestor meridionalis*) and yellow-crowned kākāriki (*Cyanoramphus auriceps*), as well as coastal-dwelling endangered hoiho (*Megadyptes antipodes*).



Conservation: Backyard jungles

New Zealand launched the Predator Free 2050 programme to protect native biodiversity by eradicating stoats and two other invasive predators, rats and brushtail possums (*Trichosurus vulpecula*). The effort relies on humane trapping as well as helicopter drops of a biodegradable toxin called 1080. The programme has led to some small predator-free havens such as Tiritiri Matangi island, but 1080 also kills deer and native kea birds (*Nestor notabilis*).

Such trade-offs are complex, and Roach does a fine job of weighing human needs against those of pests and predators. After all, it can be ruinous for Indian villagers to have their granaries looted by elephants and dangerous

for people in Delhi to be attacked by hordes of macaques. (Roach is at her most entertaining when she attempts to track down Ishwar Singh, chief wildlife warden for the Delhi government and an expert on macaque contraception. He finally answers her call with two words, “laparoscopic sterilization”, before slamming down the phone.)

But the biggest pest is clearly us. As a 2020 report by the conservation group WWF shows, populations of wild mammals, birds, fish, amphibians and reptiles have dropped by 68% on average since 1970, and one million wildlife species are in danger of extinction, because of burned forests, overfished seas, and the destruction of wild areas. There's no mirth in that.

Nature **597**, 325-326 (2021)

doi: <https://doi.org/10.1038/d41586-021-02484-9>

This article was downloaded by **calibre** from <https://www.nature.com/articles/d41586-021-02484-9>

| [Section menu](#) | [Main menu](#) |

Opinion

- **[Edmond Fischer \(1920–2021\)](#)** [13 September 2021]
Obituary • Nobel-winning biochemist who discovered a ubiquitous cell-regulatory mechanism.
- **[Reproducibility: expect less of the scientific paper](#)** [15 September 2021]
Comment • Make science more reliable by placing the burden of replicability on the community, not on individual laboratories.
- **[Africa: invest in local manufacturing of COVID-19 vaccines](#)** [14 September 2021]
Correspondence •
- **[Preventing spillover as a key strategy against pandemics](#)** [14 September 2021]
Correspondence •
- **[Anthropocene: event or epoch?](#)** [14 September 2021]
Correspondence •
- **[Afghanistan: conflict risks local and global health](#)** [14 September 2021]
Correspondence •

- OBITUARY
- 13 September 2021

Edmond Fischer (1920–2021)

Nobel-winning biochemist who discovered a ubiquitous cell-regulatory mechanism.

- [Philip Cohen](#) 0



Credit: Matt Todd/AP/Shutterstock

Edmond Fischer discovered the first example of reversible protein phosphorylation, a process that regulates most aspects of cell life. Two classes of enzymes, protein kinases and protein phosphatases, attach and remove phosphate to and from proteins. This simple modification alters their functions in many ways, switching their activities on or off, inducing them to interact with other proteins, or triggering their migration from one subcellular compartment to another. This fundamental discovery earned Fischer and his collaborator Edwin Krebs the Nobel Prize in Physiology or Medicine in 1992.

In the course of his long life, Fischer, who has died aged 101, witnessed his discovery being applied in ways that have saved millions of lives. Human cells contain more than 500 protein kinases and nearly 200 protein phosphatases, which act on thousands of proteins. The mutation or overproduction of kinases and phosphatases causes cancer and other diseases. Imatinib, the first drug developed by targeting a specific protein kinase, transformed chronic myeloid leukaemia from a rapidly fatal disease to a manageable condition soon after it entered clinical trials in 1998. Protein kinases have since become the pharmaceutical industry's most popular class of drug target. More than 70 kinase-inhibiting drugs have already been approved this century, transforming the clinical treatment of many cancers.

Fischer was born in Shanghai, China, in 1920. His French mother and Austrian father had taken Italian nationality for the family to help his father's business. At seven he was sent to be educated in Switzerland, where he and a school friend later resolved that one would become a doctor and the other a scientist, so that they "could cure all the ills of the world". Furious at the Italian leader Benito Mussolini's 1939 pact with Adolf Hitler, Fischer burnt his passport on the steps of the Italian consulate in Geneva and became a Swiss citizen. He studied chemistry and biology at the University of Geneva during the Second World War, receiving a PhD in 1947 for research on α -amylases, digestive enzymes that degrade glucose polymers such as starch and glycogen.



Biochemistry without boundaries

Moving to the United States in 1953 to begin postdoctoral research at the California Institute of Technology in Pasadena, he was unexpectedly offered an assistant professorship in biochemistry at the University of Washington, Seattle. The city reminded him of Switzerland, so he accepted, spending the rest of his life there. Within months of arriving, Fischer began to collaborate with Krebs, another young faculty member. Krebs had worked with Carl and Gerty Cori at Washington University in St. Louis, Missouri. The Coris had won the 1947 Nobel Prize in Physiology or Medicine for their discovery of the glycogen-metabolizing enzyme phosphorylase, which liberates glucose from stores in muscle and liver cells to fuel the body. They found that muscle phosphorylase existed in two forms, which they termed b and a. The b-form required the metabolite adenylic acid for activity, whereas the a-form, which could be converted to the b-form by enzyme activity present in cell extracts, did not. The source of this difference remained mysterious.

Fischer and Krebs decided to track it down and within 18 months had succeeded. They found that a previously unknown enzyme, phosphorylase kinase, converted phosphorylase b to a by transferring phosphate from the metabolite adenosine triphosphate (ATP) to phosphorylase. The cell-extract enzyme that converted phosphorylase a to b reversed this process, they found, by releasing phosphate, so they named it phosphate-releasing enzyme. Fischer and Krebs went on to discover that phosphorylase kinase

was switched on by calcium ions, which also initiate muscle contraction. This explains how glycogen is mobilized to provide glucose for energy when muscles are active.

It later emerged that cancers are frequently caused by mutations in protein kinases that attach phosphate to the amino acid tyrosine. Fischer studied enzymes that counter this process by releasing phosphate from tyrosine. During the mid- to late 1980s, his laboratory defined the first few members of an entirely new family of phosphatases. One is PTEN, encoded by a gene that others later discovered is often silenced in cancer cells. Alpelisib, a drug that switches off a kinase that opposes the action of PTEN, was approved for breast cancer in 2019.

Fischer was gifted in other ways. A talented pianist, as a schoolboy he began six years of training at the Geneva Conservatory of Music, and thought about becoming a professional musician. He continued to play the piano daily, and shortly before his death he played at the wedding of one of his grandsons. He had a great knowledge and love of history and art, and enjoyed painting, signing his works 'Tapernoux', his mother's unmarried name.

Eddy was informal and kind. It was important to him that science should always be fun. He treated his researchers as if they were his family, meeting new arrivals at the airport, and insisting that they stay at his house until they had found an apartment. In the winter, he'd take the entire lab skiing in the Cascade mountains, and in the summer they'd all go to his holiday home on Lopez Island in the San Juan Islands, off Washington State. He bought an aeroplane and learnt to fly at the age of 60, so that he could get to Lopez faster at weekends, and continued to fly until he was 80.

Engaged to the end, he held the distinction of being the oldest living Nobel prizewinner, and greatly enjoyed the virtual symposium that was held in October 2020 to celebrate his 100th birthday.

Nature **597**, 328 (2021)

doi: <https://doi.org/10.1038/d41586-021-02485-8>

This article was downloaded by **calibre** from <https://www.nature.com/articles/d41586-021-02485-8>

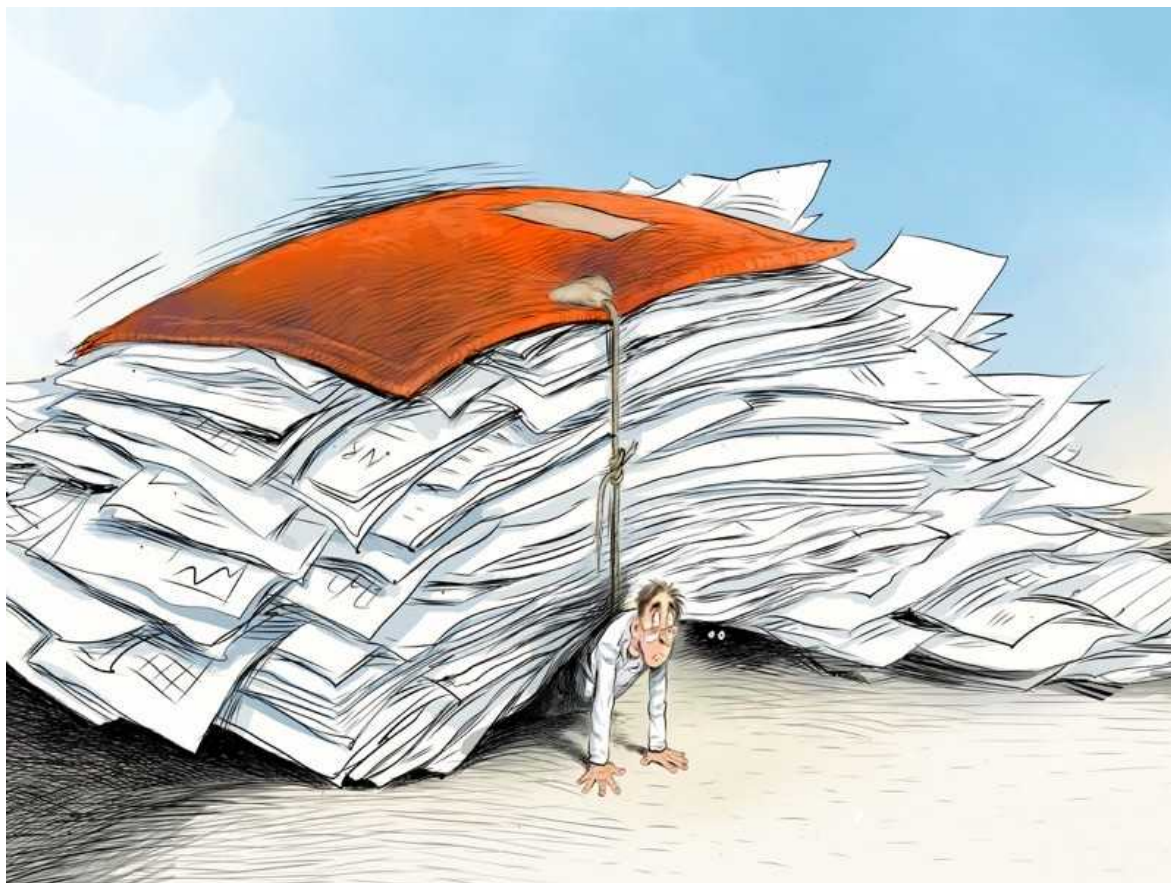
| [Section menu](#) | [Main menu](#) |

- COMMENT
- 15 September 2021

Reproducibility: expect less of the scientific paper

Make science more reliable by placing the burden of replicability on the community, not on individual laboratories.

- [Olavo B. Amaral](#) ⁰ &
- [Kleber Neves](#) ¹



Credit: David Parkins

In 2018, we embarked on a journey to assess the reproducibility of biomedical research papers from Brazil. Thus began a multicentre collaboration of more than 60 laboratories to replicate 60 experiments from 2 decades of Brazilian publications¹. We randomly selected experiments that used three common laboratory techniques: the MTT assay for cell viability, RT-PCR to measure specific messenger RNAs and the elevated plus maze to assess anxiety in rodents.

Each experiment will be repeated in three labs, and each lab has developed replication protocols based on the original article's written methods. The process of building, reviewing and preregistering these protocols has taken months of communication between the coordinating team and the labs performing replications. We had intense arguments around the meaning of positive and negative controls and the merits of different metrics to define replication success. We also spent many hours on mundane tasks, such as studying the nutritional content of different brands of bologna sausage to better emulate a cafeteria diet fed to rats in one experiment.

These are just some of the obstacles we have faced so far as coordinators of the Brazilian Reproducibility Initiative: there was also the massive shutdown of labs due to the COVID-19 pandemic and the sharp decline of Brazil's currency, the real. With all of this, experiments are starting slowly, and the project is now set to finish by the end of 2022.

That said, we have already reached conclusions that apply beyond Brazilian science. As a broad solution, more rigorous protocols and better descriptions of methods are important, but insufficient for reproducibility — and might not be feasible for every paper. Current requirements for wide-ranging experiments in a single article are part of the problem. To solve these issues, expectations placed on the scientific paper must change.

Reproducibility is costly

Research articles in the life sciences are more ambitious than ever. The amount of data in high-impact journals has doubled over 20 years², and basic-science papers are increasingly expected to include evidence of how

results will translate to clinical applications. An article in a journal such as *Nature* thus ends up representing many years of work by several people.

Still, that's no guarantee of replicability. The Reproducibility Project: Cancer Biology has so far managed to replicate the main findings in only 5 of 17 highly cited articles³, and a replication of 21 social-sciences articles in *Science* and *Nature* had a success rate of between 57 and 67%⁴.



No publication without confirmation

Many calls have been made to improve this scenario. Proposed measures include increasing sample sizes, preregistering protocols and using stricter statistical analyses. Another proposal is to introduce heterogeneity in methods and models to evaluate robustness — for instance, using more than one way to suppress gene expression across a variety of cell lines or rodent strains. In our work on the initiative, we have come to appreciate the amount of effort involved in following these proposals for a single experiment, let alone for an entire paper.

Even in a simple RT-PCR experiment, there are dozens of steps in which methods can vary, as well as a breadth of controls to assess the purity, integrity and specificity of materials. Specifying all of these steps in advance represents an exhaustive and sometimes futile process, because protocols inevitably have to be adapted along the way. Recording the entire method in

an auditable way generates spreadsheets with hundreds of rows for every experiment.

We do think that the effort will pay off in terms of reproducibility. But if every paper in discovery science is to adopt this mindset, a typical high-profile article might easily take an entire decade of work, as well as a huge budget. This got us thinking about other, more efficient ways to arrive at reliable science.

A stepwise process

There are typically three main expectations for a top-notch article in laboratory science: first, report original findings from exploratory research; second, confirm that they represent robust phenomena through further experiments using different methods; and, finally, suggest theoretical mechanisms to explain the results. However, these represent different aspects of the scientific process and do not have to be achieved all at once⁵.

In fact, trying to live up to all three expectations in a five-page paper can be a recipe for not fulfilling any of them well. Forcing exploratory and confirmatory research into a single publication can undermine both, either by stifling the former or corrupting the latter. Pressure to confirm an initial, exciting observation can bias subsequent data and analysis, particularly if certain results are required in further experiments to get the paper accepted. Rather than being sceptical of their original observation, many researchers will naturally distrust or dismiss further data that refute their hypothesis and jeopardize publication.

Moreover, requiring a large number of experiments in a single article can work against rigour: it shifts the workload towards many fragile experiments rather than a few robust ones. Studies have shown that neither statistical power⁶ nor quality of reporting of individual experiments⁷ improve as journal impact increases. And the amount and variety of data from many experiments can overwhelm reviewers' capacity to scrutinize evidence.



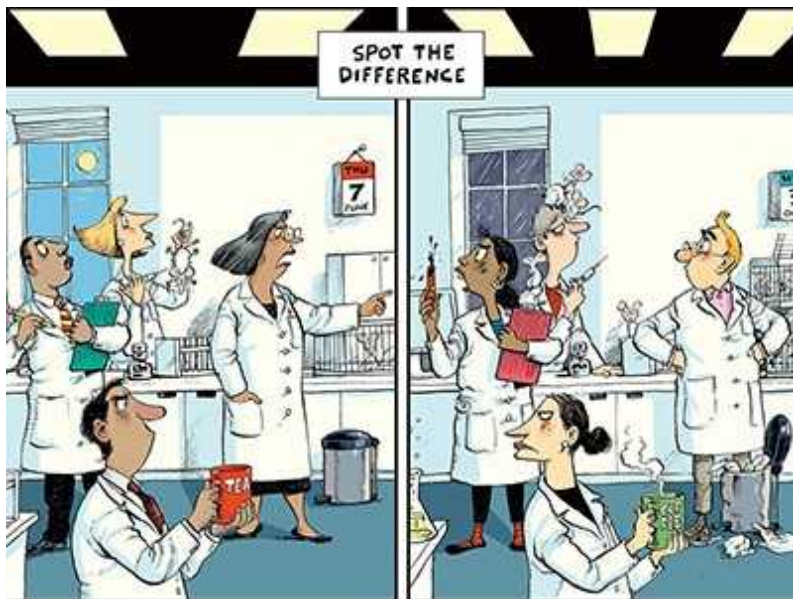
A researcher prepares samples for RT-PCR, which measures specific messenger RNAs.Credit: Amilcar Orfali/Getty

Finally, because a research group working on its own is inevitably limited in how much it can vary methods, models or conditions, most articles end up basing their conclusions on constrained data, without assessing generalizability⁸. In our work in the initiative, we were repeatedly surprised by the different ways researchers filled in the gaps in descriptions from original articles' protocols. Take experiments on macrophages obtained from the peritoneal cavity of mice, for example. Some labs used drugs to boost the number of these white blood cells, while others refrained out of concern that this would alter cellular responses. Most teams assessed the fraction of cultured cells that are viable macrophages — but there was little agreement on what fraction is high enough for experiments to proceed. Obtaining similar results under these different conditions can boost confidence that a phenomenon is robust; however, introducing such variability in methods is often beyond what a lab can do on its own.

Articles by individual research groups should thus be regarded as preliminary by default. If the expectation is that results of every publication hold true in other settings, models or populations, a reproducibility crisis seems inevitable. Instead of asking every author to conduct a decade's worth of confirmatory experiments, the scientific enterprise might be better served by other mechanisms to establish the validity of a claim — perhaps beyond the scope of a paper.

Paths to reproducible science

What other ways are there to assess whether findings are robust enough? One option is to synthesize the published literature, drawing on results from studies by different research groups. This already happens for most clinical guidelines, which are typically derived from a meta-analysis of existing evidence. This approach, however, is marred by publication bias and incomplete reporting in primary studies. Thus, assessing reliability by this method still requires widespread problems to be fixed.



[The best time to argue about what a replication means? Before you do it](#)

A potentially better approach is to organize confirmatory experiments that are specifically designed to assess robustness and generalizability. These will ideally incorporate multiple methods and experimental models (such as

mouse strains or cell types) in different laboratories. Coordination between groups can standardize data collection and guarantee access to results, thus facilitating synthesis and eliminating publication bias.

Diverse types of collaboration have been set up across various areas of science. The pharmaceutical industry has managed multicentre clinical trials for decades. Consortia working in genetic epidemiology pool samples from different populations to increase statistical power. Academic psychology labs have joined forces for community efforts such as the Reproducibility Project: Psychology, the Many Labs Projects and the Psychological Science Accelerator. And initiatives in neuroscience include the International Brain Laboratory, the Human Connectome Project and the ENIGMA consortium.

Such endeavours are intensive in terms of cost and labour, and cannot be conducted for every published finding. Still, they are a more efficient way to confirm key phenomena than waiting for data to accrue from uncoordinated efforts. Moreover, investing effort to increase rigour in selected confirmatory projects is probably more feasible than demanding that every biomedical publication be replicable, generalizable and clinically relevant.

Divide labour, foster collaboration

Other authors have argued that exploratory research that generates tentative findings should be more clearly separated from confirmatory projects that evaluate them, as a way of improving both ends of the process⁹.

Independence between exploratory and confirmatory work can allow greater freedom for scientists to explore hypotheses, while upholding rigour and preventing bias when they are put to the test. Moreover, each approach requires a different set of abilities and should be evaluated by distinct metrics.

Basic exploratory science would be helped if editorial policies reduced requests for new experiments and refrained from demanding evidence of clinical potential. Exploration can also benefit from forums that publish isolated findings of limited scope, as long as experiments and analyses are impartial. This can aid review, reduce bias and accelerate dissemination, while reducing incentives to dress up exploratory research as confirmatory

work by cutting corners — or descriptions of unsuccessful experiments — to tell a coherent story.



Publish houses of brick, not mansions of straw

Large-scale confirmatory science, by contrast, requires supportive infrastructure that is rarely available. There needs to be training, funding and rewards for researchers to focus on managing collaborations, participating in large experiments and synthesizing data — especially because this involves sacrificing academic freedom to some extent. If coordinated efforts to confirm published findings become routine, they can also stimulate the average scientist to be more rigorous in evaluating findings before publication, ultimately improving the quality of exploratory research.

All of this, however, requires reorganizing scientific labour, and one thing our initiative has taught us is that academic researchers are not used to being told what to do. Large-scale collaborations thus need to be centralized enough to guarantee rigour and adherence to guidelines, but should maintain some flexibility to accommodate each lab's own work routines.

Key to our strategy has been asking the right questions rather than being prescriptive. Requiring researchers to register how they will blind their study is more flexible than enforcing how they do it, but still serves to eliminate bias. Another key point has been to develop tools that enable best practices

— from automatically randomizing sample distribution on plates to standardizing spreadsheets for data collection.

Despite all this, we worry that grassroots efforts such as ours might not be scalable. Not only has the initiative kept the coordinating team absorbed for the past three years, but it has also frequently collided with other priorities in our collaborating labs.

A better mechanism might be to build formal systems to manage collaborative projects, driven by institutions or funders. Such collaborations already exist in specific areas, as exemplified by efforts from the US National Institute on Aging^{[10](#)}, the US Defense Advanced Research Projects Agency (DARPA)^{[11](#)} and the German Federal Ministry of Education and Research^{[12](#)}. Still, there is room for them to become much more widespread, and perhaps as much a part of biomedical science as grant applications or peer review.

Changing our expectations

Although there is scope to make the average paper more rigorous, an overemphasis on individual papers and their reproducibility should not detract us from other means of arriving at sound conclusions. Instead of expecting that every paper will establish reliable phenomena, it might be more feasible to improve systematic confirmation of preliminary findings.

For this to happen, the biomedical science community needs to be convinced that some resources should be diverted to larger projects investigating fewer ideas. Funders and institutions must be more proactive in coordinating the scientific workforce to select and address key research questions, rather than scattering resources between competing labs. This involves building incentive systems — in terms of funding, career advancement and credit — to encourage researchers to take on less autonomous roles in larger projects. Scientific societies and journals can also play a part in determining which findings in a given research field are considered crucial for replication — a tough decision that requires extensive input from the scientific community.

Moving the burden of reproducibility from individual researchers to organized communities can ultimately raise the bar of what is considered scientific fact, and could also have a salutary effect on the public communication of science. The ideal way to achieve all of this remains an open question. But we can at least agree that it is larger than what fits in a paper.

Nature **597**, 329-331 (2021)

doi: <https://doi.org/10.1038/d41586-021-02486-7>

References

1. 1.

Amaral, O. B., Neves, K., Wasilewska-Sampaio, A. P. & Carneiro, C. F. *eLife* **8**, e41602 (2019).

2. 2.

Cordero, R. J. B., de León-Rodriguez, C. M., Alvarado-Torres, J. K., Rodriguez, A. R. & Casadevall, A. *PLoS ONE* **11**, e0156983 (2016).

3. 3.

Errington, T. M. *et al.* *eLife* **3**, e04333 (2014).

4. 4.

Camerer, C. F. *et al.* *Nature Hum. Behav.* **2**, 637–644 (2018).

5. 5.

Haig, B. Preprint at PsyArXiv <https://doi.org/10.31234/osf.io/v784s> (2020).

6. 6.

Brembs, B., Button, K. & Munafò, M. *Front. Hum. Neurosci.* **7**, 291 (2013).

7. 7.

Carneiro, C. F. D. *et al. Res. Integr. Peer Rev.* **5**, 16 (2020).

8. 8.

Yarkoni, T. *Behav. Brain Sci.*
<https://doi.org/10.1017/s0140525x20001685> (2020).

9. 9.

Kimmelman, J., Mogil, J. S. & Dirnagl, U. *PLoS Biol.* **12**, e1001863 (2014).

10. 10.

Lithgow, G. J., Driscoll, M. & Phillips, P. *Nature* **548**, 387–388 (2017).

11. 11.

Raphael, M. P., Sheehan, P. E. & Vora, G. J. *Nature* **579**, 190–192 (2020).

12. 12.

Drude, N. I., Gamboa, L. M., Danziger, M., Dirnagl, U. & Toelch, U. *eLife* **10**, e62101 (2021).

This article was downloaded by **calibre** from <https://www.nature.com/articles/d41586-021-02486-7>

- CORRESPONDENCE
- 14 September 2021

Africa: invest in local manufacturing of COVID-19 vaccines

- [James Ayodele](#)⁰ &
- [Sylvain Boko](#)¹

High-income countries' limited COVID-19 vaccine donations to Africa are prolonging the pandemic and worsening its social and economic impact here. African governments need to allocate more resources to making their own vaccines ([J. N. Nkengasong *Nature* 567, 147; 2019](#)), forming alliances with wealthy Africans and African businesses to build local manufacturing capacity ([Nature 592, 487–488; 2021](#)).

With some 200,000 deaths reported so far in a population of 1.3 billion, Africa accounts for 4% of COVID-related deaths worldwide. Just 2.8% of Africans were fully vaccinated against COVID-19 by the end of August (see [go.nature.com/2vp7gmw](#)). The situation could deteriorate further as high-income countries embark on booster jabs for their citizens.

Foreign aid to Africa provides treatment and care for prevalent diseases and conditions, such as tuberculosis and AIDS. The continent's health systems, already badly affected, must not be further crippled by any diversion of this aid into COVID-19 vaccination. In addition to mobilizing its own resources, Africa must seek more donated doses, patent waivers and technology transfer.

Nature 597, 332 (2021)

doi: <https://doi.org/10.1038/d41586-021-02425-6>

This article was downloaded by **calibre** from <https://www.nature.com/articles/d41586-021-02425-6>

| [Section menu](#) | [Main menu](#) |

- CORRESPONDENCE
- 14 September 2021

Preventing spillover as a key strategy against pandemics

- [Neil M. Vora](#) [ORCID: http://orcid.org/0000-0002-4989-3108](#)⁰,
- [Nigel Sizer](#)¹ &
- [Aaron Bernstein](#)²

Most new infectious diseases result from the spillover of pathogens from animals, particularly wildlife, to people. Spillover prevention should not be dismissed in discussions on how best to address pandemics (see [Nature 596, 332–335; 2021](#)).

The belief that we are powerless to prevent spillover is, unfortunately, endorsed by many in public health and government. Improved management of farmed animals, regulations on wildlife trade and conservation of tropical forests have all helped to prevent spillover and subsequent outbreaks, as well as boosting greenhouse-gas mitigation and wildlife conservation (see [go.nature.com/2uqwx1u](#)). Moreover, preventing spillover is cheap compared with the costs of a single pandemic ([A. P. Dobson et al. Science 369, 379–381; 2020](#)).

Outbreak containment measures will always be necessary, especially for the most vulnerable people in resource-limited settings, because spillover can never be completely eliminated. But if prioritized alongside post-spillover initiatives, outcomes will be more cost-effective, scientifically informed and equitable.

Nature **597**, 332 (2021)

doi: <https://doi.org/10.1038/d41586-021-02427-4>

This article was downloaded by **calibre** from <https://www.nature.com/articles/d41586-021-02427-4>

| [Section menu](#) | [Main menu](#) |

- CORRESPONDENCE
- 14 September 2021

Anthropocene: event or epoch?

- [Andrew M. Bauer](#) ORCID: <http://orcid.org/0000-0002-6668-8587>⁰
- [Matthew Edgeworth](#) ORCID: <http://orcid.org/0000-0002-9375-0753>¹
- [Lucy E. Edwards](#) ORCID: <http://orcid.org/0000-0003-4075-3317>²,
- [Erle C. Ellis](#) ORCID: <http://orcid.org/0000-0002-2006-3362>³,
- [Philip Gibbard](#) ORCID: <http://orcid.org/0000-0001-9757-7292>⁴ &
- [Dorothy J. Merritts](#) ORCID: <http://orcid.org/0000-0003-3663-8172>⁵

The concept of the Anthropocene has inspired more than two decades of constructive scholarship and public discussion. Yet much of this work seems to us incompatible with the proposal to define the Anthropocene as an epoch or series in the geological timescale, with a precise start date and stratigraphic boundary in the mid-twentieth century. As geologists, archaeologists, environmental scientists and geographers, we have another approach to suggest: recognize the Anthropocene as an ongoing geological event.

Access options

Subscribe to Journal

Get full journal access for 1 year

\$199.00

only \$3.90 per issue

Subscribe

All prices are NET prices.
VAT will be added later in the checkout.
Tax calculation will be finalised during checkout.

Rent or Buy article

Get time limited or full article access on ReadCube.

from \$8.99

Rent or Buy

All prices are NET prices.

Additional access options:

- [Log in](#)
- [Learn about institutional subscriptions](#)

Nature **597**, 332 (2021)

doi: <https://doi.org/10.1038/d41586-021-02448-z>

This article was downloaded by **calibre** from <https://www.nature.com/articles/d41586-021-02448-z>

- CORRESPONDENCE
- 14 September 2021

Afghanistan: conflict risks local and global health

- [Muhammad Jawad Noon](#) ORCID: <http://orcid.org/0000-0003-3639-0242> 0

Deteriorating health care for children, women and older people in Afghanistan, resulting from the country's armed conflict, requires urgent attention. Given that Afghanistan (along with neighbouring Pakistan) is polio's last redoubt, the situation could lead to grave global health problems.

Access options

Subscribe to Journal

Get full journal access for 1 year

\$199.00

only \$3.90 per issue

[Subscribe](#)

All prices are NET prices.

VAT will be added later in the checkout.

Tax calculation will be finalised during checkout.

Rent or Buy article

Get time limited or full article access on ReadCube.

from \$8.99

[Rent or Buy](#)

All prices are NET prices.

Additional access options:

- [Log in](#)
- [Learn about institutional subscriptions](#)

Nature **597**, 332 (2021)

doi: <https://doi.org/10.1038/d41586-021-02468-9>

This article was downloaded by **calibre** from <https://www.nature.com/articles/d41586-021-02468-9>

| [Section menu](#) | [Main menu](#) |

Work

- **[Springboard to science: the institutions that shaped Black researchers' careers](#)** [13 September 2021]
Career Feature • Historically Black colleges and universities offer personal and professional support that predominantly white US institutions do not.
- **[Breeding the sweetest biofuels in the business](#)** [13 September 2021]
Where I Work • Morexa Martin-Gardiner relishes the seasonal shifts of her work on a sugar-cane research station in Barbados.

- CAREER FEATURE
- 13 September 2021

Springboard to science: the institutions that shaped Black researchers' careers

Historically Black colleges and universities offer personal and professional support that predominantly white US institutions do not.

- [Virginia Gewin](#) &
- [David Payne](#)

[Find a new job](#)



Students at the historically Black Hampton University in Virginia cheer their graduation after an address by former US president Barack Obama. Credit: Jahi Chikwendiu/The Washington Post/Getty

More than 100 historically Black colleges and universities (HBCUs) operate across the United States, most dating to the late 1800s, when they were founded in the wake of the US Civil War.

Nearly 20% of the nation's Black population who hold an undergraduate degree in science, technology, engineering and mathematics (STEM) earned it at an HBCU institution, as did one-third of US Black people with a PhD.

Although HBCUs excel at creating a nurturing environment for Black students, many have struggled to secure the same financial resources — including endowments and federal and state funding — as predominantly white institutions (PWIs). Many also find it difficult to recruit and retain Black faculty members in STEM disciplines.

US federal and employment data suggest that Black and Hispanic adults are less likely to earn degrees in STEM subjects than in other fields. And the proportion holding STEM bachelor's degrees continues to be lower than for the US adult population as a whole, the data indicate (see go.nature.com/3tmuf7).

Federal agencies and other organizations have tried to address some of the disparities. The US National Science Foundation awarded US\$9 million in 2020 to investigate HBCUs' record in promoting student well-being and conferring degrees on Black students, including those in STEM PhD programmes. Some HBCUs have secured funding in 2021 to bolster their STEM offerings.

As HBCUs experience a record surge in enrolment for the 2021 academic year, *Nature* spoke to five scholars who work at or attended an HBCU about why the institutions are key to increasing the Black STEM workforce.

TAYLOR HARRIS: Instil pride and confidence

PhD student specializing in bacterial pathogenesis in cotton at Washington University in St. Louis, Missouri.



Taylor Harris hopes her experience will help her to build up the Black STEM workforce. Credit: Ron Klein

I decided to attend Fisk University, a private HBCU in Nashville, Tennessee, at 16 years old. I wanted my skin colour to be the last thing to provide any hurdles for me in college. Fisk lived up to my expectations. I think HBCUs typically have smaller classes than other universities, and this helped me to build a community and flourish. Professors and mentors are akin to aunts and uncles, invested in student success enough to ask about well-being after absences. They were able to reach me in a way that I don't think I'd have experienced elsewhere. They could identify with students and communicate in a way that I was receptive to, which helped a lot. Feeling comfortable with my professors also helped me not feel afraid to make mistakes. I was always calling out wrong answers in chemistry class because I was never afraid to be wrong.

Even though students at Fisk couldn't major in plant biology, I got interested in plants when my freshman biology course focused on the topic for a few weeks. Every summer, I did research internships at different institutions to get experience in all aspects of plant molecular biology. My first internship was at the Chicago Botanic Garden in Glencoe, Illinois. In the next one, I studied the effects of plant extracts on cancer at Vanderbilt University Medical Center in Nashville. My final internship was at the Plant Gene Expression Center, affiliated with the University of California, Berkeley, where I studied resistance to a bacterial pathogen in wild tomatoes.



The hashtags that brought Black scientists together

This last period sparked my interest in plant–microbe interactions. During all my internships, I was also learning for myself that Black people are not represented well in science. I was never the only person of colour, but I was definitely in the minority. As a result, during my first two years in a PhD programme at Washington University in St. Louis, Missouri, I developed anxiety. I had never had problems with anxiety or confidence before then. Coming to a PWI has been a culture shock. I've been blatantly ignored when speaking. And people have said inappropriate things that they think are funny. These might seem like small things, but they eat away at you, a little bit at a time.

Still, I've learnt how to navigate this space. Washington University has a programme for doctoral students in biomedical sciences, the Initiative for Maximizing Student Development, which is designed to support students like myself from under-represented backgrounds. It's helped me to create a network and is an example of what PWIs can do to support Black students. You can get support and find cultural resources at PWIs, but you have to seek them out. At an HBCU, that support is more universal. We all come from different backgrounds, but we still have a sense of understanding of each other.

The allocation of more resources to HBCUs is needed now more than ever, to eliminate the gap in Black STEM representation. HBCUs do a good job of training their students to feel confident enough to succeed in STEM spaces. Let's put the money where it's working well. My ultimate career goal is to return to an HBCU and contribute to cultivating the Black STEM workforce. There's a great sense of pride after graduating from an HBCU, and doing that offers an instant connection with people who have gone to one.

JALAAL HAYES: Create a nurturing, familial environment

Assistant professor of chemistry at Lincoln University near Oxford, Pennsylvania.

I graduated from high school at 15 before starting my bachelor's degree in chemistry at Lincoln University, near Oxford, Pennsylvania, the first degree-granting HBCU in the United States. In 2008, when I was attending, the majority of my professors were Black, although now there is more diversity. I had never seen Black scientists in my life until then. Their presence motivated me to stay in chemistry throughout my three years at Lincoln. I graduated from high school in two years, college in three and graduate school in four.

After gaining my degree from Lincoln, I did an internship at Howard University in Washington DC that focused on atmospheric chemistry. I went on to train for a PhD, studying renewable energy and climate change at Delaware State University in Dover, the only HBCU in that state. It's quite

small — with roughly 5,000 undergraduate and master's students — but it's like a family. Everyone looks out for one another. During the second semester of my first year, I worked with Andrew Goudy, director of the university's Hydrogen Storage Research Center, to produce an innovative hydrogen-storage system. We published a paper on it ([T. Durojaiye et al. *J. Phys. Chem. C* 117, 6554–6560; 2013](#)) and filed a US patent in 2013.



[Science diversified: Black researchers' perspectives](#)

After that, I was invited to a Gordon Research Conference — a series of international, off-the-record conferences to discuss frontier, unpublished research — in Barga, Italy, to speak on the technology. That was cool — I was 20 years old, it was my first international science conference and I met researchers from places like Africa, Australia and Denmark. Just four people at that conference were Black.

In June 2015, I became the youngest PhD student in applied chemistry at Delaware to finish my doctorate. To help expand the Black STEM workforce, I was hired there in 2017, before returning to Lincoln University in 2019, where I'm working to get more black STEM graduates engaged in chemistry — particularly in the clean-energy area, a predominantly white field. The Black STEM workforce training has always taken place at HBCUs; now people are becoming more aware of these universities' successes in this area.

If an institution wants to recruit and retain Black talent, it has to be culturally inclusive and not treat Black students as a check mark. Being

culturally inclusive is one thing that HBCUs have always done well. When a Black person — be they African American, Caribbean or from other parts of the diaspora — steps into a HBCU campus, it feels like home identity-wise. We know that we share many of the same struggles, and that makes us a family no matter our backgrounds. However, at a PWI, Black students have to navigate how to fit into the culture. When a Black student hears the word ‘homecoming’ at an HBCU, they know it’s going to be a big family barbecue; at a PWI, a homecoming usually centres on a football game.

With prospective graduate students, I don’t target schools but programmes, especially for STEM. I encourage my students to focus not on Harvard or Yale universities but on who is doing great work in a specific scientific field. I want them to go where they will excel in a particular field without their mental health taking a beating because they don’t feel like they belong. My undergraduate and graduate students increasingly want to go to HBCUs — an interest that has grown in the wake of the George Floyd murder last year and the 400th anniversary of the first captured slaves being brought to this country in 1619.

ANDREA TYLER: Focus on identity and socialization

Director of graduate student services and POTUS fellowship at Tennessee State University in Nashville, and author of Seeing The HiddEn Minority: Increasing the Talent Pool through Identity, Socialization, and Mentoring Constructs.



Andrea Tyler (standing) at an orientation lecture.Credit: Roneisha Simpson

I earned a mechanical engineering degree in 1989 from North Carolina Agricultural and Technical State University, an HBCU in Greensboro. I put theory to practice when I accepted a job in 1990 at NASA in New Orleans, Louisiana, in design and product engineering. That was my first experience with a non-inclusive, non-diverse environment: I was the first Black female in my department. Adversarial moments came in different ways, from being excluded from meetings to being socially isolated. At that time, diversity, equity and inclusion were not buzzwords.

I was laid off as part of a downsizing in 1995, and ultimately got a PhD in engineering education. My research today focuses on how to further enhance representation of Black people, particularly women, in STEM. I always tell people that my research is who I am; that's why I do it so well.

After a few years at two different PWIs, I came to Tennessee State University (TSU) in Nashville in 2011, with the hope that there would be more STEM students from minority groups, but that was not the case. PWIs not only have more money to offer graduate students — they are also better

able to expose students of colour to STEM topics. HBCUs typically don't have the same financial resources, equipment or facilities in STEM programmes as PWIs do. So, in 2014, I got a grant from the US Department of Education to launch a fellowship programme called Preparing Our Tomorrow Uniquely in STEM (POTUS).



What Black scientists want from colleagues and their institutions

The fellowship pays a stipend as well as covering tuition, research supplies, books and travel, and it offers mentoring and seminars on such issues as career pathways or how to socially engage as a member of a minority group in a majority setting. All the things I felt I lacked during my graduate career, I built into this programme. I don't want my students to worry about anything other than breathing and going to classes. I want to take away all the other stressors so they can focus on doing good work.

When I started the POTUS programme, not many students applied because it wasn't well known and there was too much competition from other STEM programmes. I would try to recruit, but I couldn't compete with PWIs that were better funded and resourced.

The fellowship programme started taking off, however, around 2018, when we were at a full capacity of 21 graduate students; by 2020, we had a waiting list. Now, students from all over the country apply. Still, the TSU

doesn't have the financial wherewithal to institutionalize this programme at the scale it has now reached. On average, the grant pays around US\$75,000 per student per year. If the TSU were able to take it on, it would be at a much smaller scale.

Celebrity validation — from singer Beyoncé promoting HBCUs in recent concerts to US vice-president Kamala Harris being a graduate of Howard University — has helped to instil pride and raise interest within the Black community in attending HBCUs. Although these institutions excel at creating a sense of family or community, they still struggle to recruit Black STEM professors. When I attended an HBCU, I had one Black American STEM professor; at the TSU right now, I estimate that less than 10% of professors in the engineering and computer-science departments are Black.

Despite the funding challenges, those of us who work at HBCUs do so because we love to be at these institutions. At HBCUs, we often have to be resourceful — writing grant applications or partnering with a university to get access to STEM equipment. I care so much about these students that I write applications, seek out employers, network with companies to help students find jobs. That's why I came back to an HBCU — to give back.

ANTENTOR HINTON: Rethink rankings and funding

Assistant professor of molecular physiology and biophysics at Vanderbilt University in Nashville, Tennessee.

I was quite under-confident when I started my bachelors's degree in 2006 at Winston-Salem State University in North Carolina. I did nursing and biology initially, but ended up majoring in biology with a minor in chemistry.

The class I took in botany changed my life. I loved it. I didn't know about cell or plant biology, or that plants have individual cells with molecules moving around. I loved the variety of teaching styles at Winston-Salem. Maths isn't my forte and I didn't like calculus, but one professor taught it in a way that suited me and made me want to do more of it.

Another professor there, Morris J. Clarke, who studies biochemistry and pharmacology, taught me never to settle for anything other than excellence. He believed in me even when I didn't myself. There was a mandatory course on African American culture that straddled history, literature, art, music and dance. It looked at historical and cultural roots in Africa, slavery in the United States, and the post-slavery period up to contemporary times. All these different experiences made the university feel like a complete brotherhood. In its cafeteria, you could talk to anyone about anything. Everyone went there.



The time tax put on scientists of colour

In 2008, I took part in one of the 10-week Summer Research Opportunity Programs run each year by Duke University in Durham, North Carolina. These give undergraduates experience in graduate-level biomedical research, but I also picked up some good life lessons there: how to interact with individuals, how to repair relationships when networking didn't go well, how to be collaborative. I also found life-long mentors there. At an event run by Duke's Bouchet Society (an all-Black graduate and postdoc community named after the first Black person to earn a PhD at a US university), I met a Black graduate physicist who talked about time travel. He was in the Alpha Phi Alpha fraternity, the nation's first intercollegiate historically Black fraternity.

For HBCUs, fraternities and sororities have historical relevance to what a Black person can achieve. Until I met this graduate, I had not known Black people were physicists. I thought, “If they could get into a top graduate school and do well, then so could I.” I plan to join Alpha Phi Alpha once I settle down here.

I now work with Winston-Salem’s chancellor, provost and dean’s office, and with its biology department, on grant-writing, career development and mentoring programmes, and I do some bioinformatics teaching. HBCUs are still very much needed alongside PWIs, but the partnerships between them need to be more equitable, with PWIs reinvesting in HBCUs when they take time and talent from them.

Rankings also need a rethink. The [US News & World Report rankings](#), for example, treat HBCUs separately from PWIs. But at the undergraduate level, HBCUs are serving different populations from those served by PWIs. They also have less funding and resources, which needs to be recognized.

I’d like to see a higher investment in HBCUs from the US National Institutes of Health (NIH). The R01 grant, its original funding programme for individual scientists or multi-investigator teams, offers supplements to fund such applicants as graduate students or postdocs. But the NIH doesn’t have ‘Phase 2’, follow-on, supplemental funds for HBCU faculty members to apply for research support. This would give them a second line of funding besides the conventional mechanisms.

Philanthropy is another issue. HBCUs don’t need a one-off donation from a billionaire. It’s better to have continuous investment so that they can do exploratory research into topics such as health disparities that are less covered and that affect their local communities.

Vanderbilt University, where I started my laboratory in January, has three HBCUs nearby (East Tennessee State University in Johnson City, and Fisk University and Meharry Medical College, in Nashville). We take their students. It’s important to hold your hand back out when you reach a position where you can help others. If you have the luxury of helping lots of people, then do it.

RONALD SMITH: Be culturally inclusive

*Director of the Karsh STEM Scholars Program at Howard University,
Washington DC.*



Ronald Smith runs mentoring programmes. Credit: Howard University Communications

I am not a STEM professional, but I attended Morgan State University, an HBCU in Baltimore, Maryland, to conduct doctoral research in urban-education leadership. I spent more than 20 years in administration, both at the University of Maryland, Baltimore County (UMBC), the top non-HBCU in producing Black undergraduates who complete PhDs across the natural sciences and engineering, and at Baltimore City Community College. An old friend at Howard University hired me in 2016 to replicate UMBC's Meyerhoff Scholars Program, a successful initiative mentoring students from minority groups that are under-represented in the sciences. Our version is called the Karsh STEM programme, after receiving a US\$10-million endowment from the Karsh Family Foundation in 2020.

Meyerhoff is a wonderful template, but it's in a PWI setting. We had to change some things to optimize it, because we're the only replication of the Meyerhoff programme in an HBCU setting. The design didn't change, but the way in which we interact with students did. For example, all the students in our programme come from a wide range of under-represented groups. Often, students who are from minority groups have experienced trauma from racism or social exclusion in the communities they come from. By the time they get to us, those issues are largely unaddressed and the students can reach a breaking point. We help them to deal with those traumas, first through mentoring, particularly if we can align them with an individual — a student or professor — who has faced similar challenges. We also offer counselling services to help students deal with sometimes dark issues.

In our six-week summer bridge programme, students take two academic classes — in maths and in African American studies — and attend three seminars, one of them on chemistry. There is also a college-success seminar focused on emotional wellness and resilience. Overall, the programme aims to fortify the students and address some of the emotional factors that they need to overcome to achieve success. We talk about things such as developing grit, and understanding how to choose a growth mindset versus a victim mindset. We teach students how to become creators who are able to take responsibility for their own self-management and personal development.

It's not unusual for students who experience housing or food insecurity during semester breaks to be taken to an administrator's home and given care and support. Not all institutions are going to provide that kind of support — especially if they don't know that students need it. If a student doesn't feel welcome and supported, their sense of belonging becomes fragile. Fewer students who belong to under-represented groups will make it to the end of the journey without that support.

I think programmes such as ours, particularly at HBCUs, prepare students for what to expect, and show them how to survive and how to build their own safety nets and support groups. We encourage them to reach back out to us for support when and if they are not getting it — but not to give up on the journey. The 30 students in our inaugural cohort are now graduating; 100% will graduate by spring 2022. They are going to some of the most respected universities in the country — such as Johns Hopkins, in Baltimore, Maryland; Stanford, in California; Columbia, in New York City; and Yale, in New Haven, Connecticut — with a commitment to pursue a PhD or MD–PhD.

I remind white colleagues that they have a huge responsibility to challenge any racist or demeaning things that are said. It's not enough to be an ally; somebody's got to be a disruptor. We can have all the diversity, equity and inclusion officers that an institution wants, but if we can't get the cultural environment to change, we are not going to make progress.

Nature **597**, 435–438 (2021)

doi: <https://doi.org/10.1038/d41586-021-02487-6>

These interviews have been edited for length and clarity.

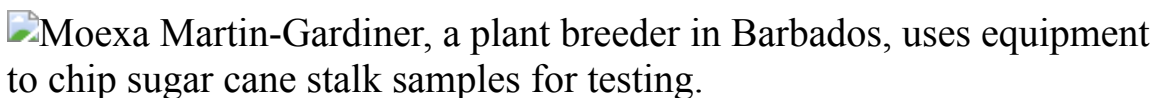
This article was downloaded by **calibre** from <https://www.nature.com/articles/d41586-021-02487-6>

- WHERE I WORK
- 13 September 2021

Breeding the sweetest biofuels in the business

Morexa Martin-Gardiner relishes the seasonal shifts of her work on a sugar-cane research station in Barbados.

- [James Mitchell Crow](#) ⁰



Morexa Martin-Gardiner is principal plant breeder for the West Indies Central Sugar Cane Breeding Station in Sweet Vale, Barbados. Credit: Micah B. Rubin for *Nature*

Sugar-cane research in Barbados goes back to colonial times. The breeding programme of the West Indies Central Sugar Cane Breeding Station, where I work, began in 1888.

The operation is owned by its members, including countries across the West Indies and three Florida sugar companies. I was fascinated by this network as an undergraduate student on Trinidad, where the sugar-cane selection protocol was part of my training. After I earned a master's degree in plant science in 1999, I learnt that the station had a vacancy. Today, I select the varieties to cross-breed each year to produce seed for our members' cane crop.

In the 1950s and 1960s, staff travelled to New Guinea, home to one of the original sugar-cane species, to establish a genetically diverse, disease-resistant population by incorporating wild genes. The resulting plants are

also more fibrous, which appeals to growers interested in biofuel production.

We assess the sugar content of our output by measuring its Brix level, the percentage of dissolved sugar in the cane juice, by mass. A Brix value of 20 was once the industry standard, and breeders thought that it couldn't be increased. But we realized that we could breed to accumulate genes for sugar production, and now routinely produce commercial clones with a Brix level of 27.

Measurements of our cane's fibre levels, sugar content and moisture guide our breeding selections. We used to analyse about 50 samples a day. With our SpectraCane — the customized infrared spectrometer into which I am feeding the cane in the photograph — we now analyse up to 600 a day. The feed chute is a modified meat grinder.

If I had a conventional laboratory job, I would be doing much the same thing year round. Here, what I do changes continually with the seasons. I like the fact that I get to do science while working outdoors. Each day is different, and I enjoy the adventure in that.

Nature **597**, 440 (2021)

doi: <https://doi.org/10.1038/d41586-021-02488-5>

This article was downloaded by **calibre** from <https://www.nature.com/articles/d41586-021-02488-5>

Research

- **[Triple-decker layered perovskite materials](#)** [15 September 2021]
News & Views • Layered perovskites are useful materials that contain sheets of a perovskite semiconductor enclosed by organic molecules. Crystals of layered perovskites that include sheets of a second inorganic lattice can now be grown from solution.
- **[Mutation fingerprints encode cellular histories](#)** [25 August 2021]
News & Views • Cells continually acquire mutations and pass them on to their progeny. The mutation profiles of human cells shine a light on the cells' developmental history and their dynamics in adult tissue.
- **[Text-message nudges encourage COVID vaccination](#)** [02 August 2021]
News & Views • A field trial shows that text-message 'nudges' encourage people to get vaccinated against COVID-19. To be effective, nudge approaches such as this must combine three aspects: they must prompt, enable and motivate behaviour.
- **[From the archive](#)** [14 September 2021]
News & Views • Nature's pages feature a look at psychology in industrial workplaces, and a mystery surrounding fish in a Swiss lake.
- **[Traces of a series of human dispersals through Arabia](#)** [01 September 2021]
News & Views • The Arabian Peninsula was a key migratory crossroads when humans and our hominin relatives began to leave Africa. Archaeological evidence and climate reconstructions reveal episodes when early humans inhabited Arabia.
- **[The diffuse γ-ray background is dominated by star-forming galaxies](#)** [15 September 2021]
Article • The diffuse, isotropic background of gamma rays comes mainly from star-forming galaxies, according to a physical model of gamma-ray emission.
- **[Quantum criticality in twisted transition metal dichalcogenides](#)** [15 September 2021]
Article • Metal-to-insulator transitions are characterized in twisted WSe_x, revealing strange metal behaviour and quantum criticality at low temperatures.
- **[Continuous Mott transition in semiconductor moiré superlattices](#)** [15 September 2021]

Article • The interaction strength in moiré superlattices is tuned to drive a continuous metal-to-insulator transition at a fixed electron density.

- **Directed assembly of layered perovskite heterostructures as single crystals** [15 September 2021]

Article • Using organic molecules as directing groups, a wide range of perovskite heterostructures are shown to self-assemble in solution to yield single crystals.

- **Environmental performance of blue foods** [15 September 2021]

Article • A range of environmental stressors are estimated for farmed and wild capture blue foods, including bivalves, seaweed, crustaceans and finfish, with the potential to inform more sustainable diets.

- **Vast CO₂ release from Australian fires in 2019–2020 constrained by satellite** [15 September 2021]

Article • The amount of carbon dioxide released by the Australian wildfires of 2019–2020 is uncertain, but is estimated here using satellite observations of carbon monoxide to be more than twice the amount suggested by fire inventories.

- **Widespread phytoplankton blooms triggered by 2019–2020 Australian wildfires** [15 September 2021]

Article • Oceanic deposition of wildfire aerosols can enhance marine productivity, as supported here by satellite and in situ profiling floats data showing that emissions from the 2019–2020 Australian wildfires fuelled phytoplankton blooms in the Southern Ocean.

- **Multiple hominin dispersals into Southwest Asia over the past 400,000 years** [01 September 2021]

Article • Dated palaeolake sequences show that there were at least five Pleistocene hominin expansions into the Arabian interior, coinciding with windows of reduced aridity between 400 and 55 thousand years ago.

- **The mutational landscape of human somatic and germline cells** [25 August 2021]

Article • The authors report the mutational landscape of 29 cell types from microdissected biopsies from 19 organs and explore the mechanisms underlying mutation rates in normal tissues.

- **Extensive phylogenies of human development inferred from somatic mutations** [25 August 2021]

Article • Somatic mutations obtained from laser microdissected biopsies of human tissues are used to reconstruct the developmental phylogenies of these tissues back to the zygote.

- **Clonal dynamics in early human embryogenesis inferred from somatic mutation** [25 August 2021]

Article • Adult human tissues from diverse sites around the body are used to reconstruct cellular phylogenies from early development, using somatic mutations as an internal barcode.

- **A body map of somatic mutagenesis in morphologically normal human tissues** [25 August 2021]

Article • Laser-capture microdissection and mini-bulk exome sequencing are combined to analyse somatic mutations in morphologically normal tissues from nine organs from five donors, revealing variation in mutation burdens, mutational signatures and clonal expansions.

- **Behavioural nudges increase COVID-19 vaccinations** [02 August 2021]

Article • Two randomized controlled trials demonstrate the ability of text-based behavioural ‘nudges’ to improve the uptake of COVID-19 vaccines, especially when designed to make participants feel ownership over their vaccine dose.

- **Neuro-mesenchymal units control ILC2 and obesity via a brain–adipose circuit** [18 August 2021]

Article • Signals from the sympathetic nervous system act via mesenchymal stromal cells to regulate the function of group 2 innate lymphoid cells and control adipocyte metabolism.

- **AIM2 forms a complex with pyrin and ZBP1 to drive PANoptosis and host defence** [01 September 2021]

Article • AIM2 responds to infection with herpes simplex virus 1 or Francisella novicida by driving assembly of a large multi-protein complex containing multiple inflammasome sensors and cell death regulators.

- **The polar oxy-metabolome reveals the 4-hydroxymandelate CoQ10 synthesis pathway** [01 September 2021]

Article • ¹⁸O₂ labelling is used to identify metabolites in human cells that incorporate gaseous oxygen, including 4-hydroxymandelate, an intermediate in the synthesis of the coenzyme Q10 head group.

- **RecA finds homologous DNA by reduced dimensionality search** [01 September 2021]

Article • Observations of rapid repair of double-stranded DNA breaks in sister chromatids in *Escherichia coli* are consistent with a reduced-dimensionality-search model of RecA-mediated repair.

- **Structure of Geobacter pili reveals secretory rather than nanowire behaviour** [01 September 2021]

Article • Structural, functional and localization studies reveal that *Geobacter sulfurreducens* pili cannot behave as microbial nanowires, instead functioning in a similar way to secretion pseudopili to export cytochrome nanowires that are essential for extracellular electron transfer.

| [Main menu](#) | [Previous section](#) |

- NEWS AND VIEWS
- 15 September 2021

Triple-decker layered perovskite materials

Layered perovskites are useful materials that contain sheets of a perovskite semiconductor enclosed by organic molecules. Crystals of layered perovskites that include sheets of a second inorganic lattice can now be grown from solution.

- [Roman Krahne](#) ⁰ &
- [Milena P. Arciniegas](#) ¹

Materials consisting of atomically thin layers of semiconductors or metals are at the heart of a revolution in energy and information technologies, and constitute an inspiring platform for basic research into physical phenomena¹. The co-assembly of different types of these 2D materials can produce systems that have new functionalities. To ensure predictable and reproducible physical properties of such systems, the atomic order at the interfaces between the co-assembled materials must be well defined². However, current assembly approaches are time-consuming and technically demanding. [Writing in Nature](#), Aubrey *et al.*³ propose a different strategy based on solution chemistry, in which organic molecules promote the crystallization of further atomically thin inorganic sublattices between the organic and inorganic layers of materials known as layered perovskites. The authors' method provides a highly versatile approach to engineering single crystals containing multiple heterostructures — in this context, referring to the interfaces between different 2D materials — with unusual and potentially useful properties.

Access options

[Subscribe to Journal](#)

Get full journal access for 1 year

\$199.00

only \$3.90 per issue

[Subscribe](#)

All prices are NET prices.

VAT will be added later in the checkout.

Tax calculation will be finalised during checkout.

Rent or Buy article

Get time limited or full article access on ReadCube.

from \$8.99

[Rent or Buy](#)

All prices are NET prices.

Additional access options:

- [Log in](#)
- [Learn about institutional subscriptions](#)

Nature **597**, 333-334 (2021)

doi: <https://doi.org/10.1038/d41586-021-02433-6>

References

1. 1.

Liu, Y., Huang, Y. & Duan, X. *Nature* **567**, 323–333 (2019).

2. 2.

Novoselov, K. S., Mishchenko, A., Carvalho, A. & Castro Neto, A. H. *Science* **353**, aac9439 (2016).

3. 3.

Aubrey, M. L. *et al. Nature* **597**, 355–359 (2021).

4. 4.

Tartakovskii, A. *Nature Rev. Phys.* **2**, 8–9 (2020).

5. 5.

Wang, Z. *et al. Nature Energy* **2**, 17135 (2017).

6. 6.

Li, X., Hoffman, J. M. & Kanatzidis, M. G. *Chem. Rev.* **121**, 2230–2291 (2021).

7. 7.

Dhanabalan, B. *et al. Adv. Mater.* **33**, 2008004 (2021).

8. 8.

Passarelli, J. V. *et al. J. Am. Chem. Soc.* **140**, 7313–7323 (2018).

9. 9.

Long, G. *et al. Nature Rev. Mater.* **5**, 423–439 (2020).

10. 10.

Roy, C. R. *et al. J. Am. Chem. Soc.* **143**, 5212–5221 (2021).

| [Section menu](#) | [Main menu](#) |

- NEWS AND VIEWS
- 25 August 2021

Mutation fingerprints encode cellular histories

Cells continually acquire mutations and pass them on to their progeny. The mutation profiles of human cells shine a light on the cells' developmental history and their dynamics in adult tissue.

- [Kamila Naxerova](#) 0

The human body consists of trillions of cells that perform innumerable tasks as members of different organ systems. They are all descendants of the fertilized egg, which divides again and again to generate large numbers of progeny during embryonic development. Later in life, cells continue dividing to compensate for cell death and to ensure consistent tissue function. The ancestral relationships between the body's cells can inform us about their division and migration histories. Writing in *Nature*, [Park et al.¹](#), [Coorens et al.²](#), [Li et al.³](#) and [Moore et al.⁴](#) provide insights into human embryonic development and tissue maintenance by uncovering the lineage relationships between cells that reside in different parts of the body.

Access options

Subscribe to Journal

Get full journal access for 1 year

\$199.00

only \$3.90 per issue

Subscribe

All prices are NET prices.
VAT will be added later in the checkout.
Tax calculation will be finalised during checkout.

Rent or Buy article

Get time limited or full article access on ReadCube.

from \$8.99

Rent or Buy

All prices are NET prices.

Additional access options:

- [Log in](#)
- [Learn about institutional subscriptions](#)

Nature **597**, 334–336 (2021)

doi: <https://doi.org/10.1038/d41586-021-02269-0>

References

1. 1.

Park, S. *et al.* *Nature* **597**, 393–397 (2021).

2. 2.

Coorens, T H. H. *et al.* *Nature* **597**, 387–392 (2021).

3. 3.

Li, R. *et al.* *Nature* **597**, 398–403 (2021).

4. 4.

Moore, L. *et al.* *Nature* **597**, 381–386 (2021).

5. 5.

Bizzotto, S. *et al.* *Science* **371**, 1249–1253 (2021).

6. 6.

Ju, Y. S. *et al.* *Nature* **543**, 714–718 (2017).

7. 7.

Spencer Chapman, M. *et al.* *Nature* **595**, 85–90 (2021).

8. 8.

Martincorena, I. *et al.* *Science* **348**, 880–886 (2015).

9. 9.

Zhu, M., Lu, T., Yopp, A. C., Wang, T. & Zhu, H. *Cell* **177**, 608–621 (2019).

10. 10.

Colom, B. *et al.* Preprint at bioRxiv
<https://doi.org/10.1101/2021.06.25.449880> (2021).

11. 11.

Yoshida, K. *et al.* *Nature* **578**, 266–272 (2020).

12. 12.

Campbell, P. J. *et al.* *Nature* **578**, 82–93 (2020).

| [Section menu](#) | [Main menu](#) |

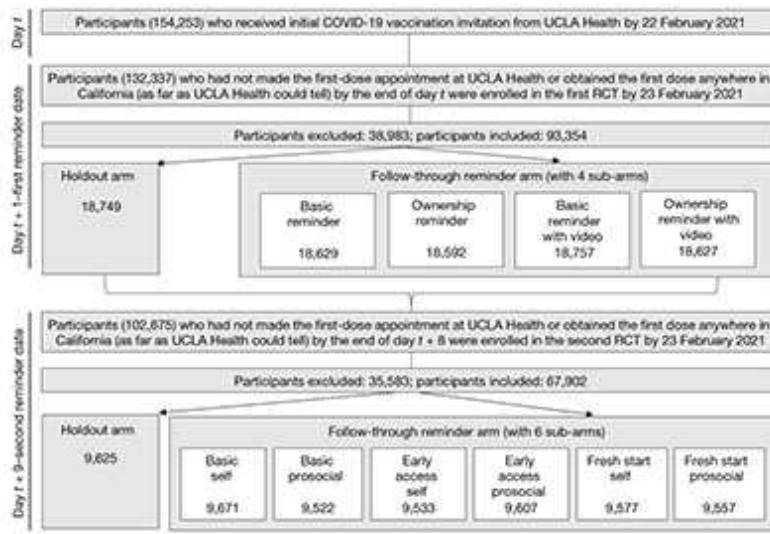
- NEWS AND VIEWS
- 02 August 2021

Text-message nudges encourage COVID vaccination

A field trial shows that text-message ‘nudges’ encourage people to get vaccinated against COVID-19. To be effective, nudge approaches such as this must combine three aspects: they must prompt, enable and motivate behaviour.

- [Mitesh S. Patel](#) [ORCID: http://orcid.org/0000-0002-5997-9984](http://orcid.org/0000-0002-5997-9984) ⁰

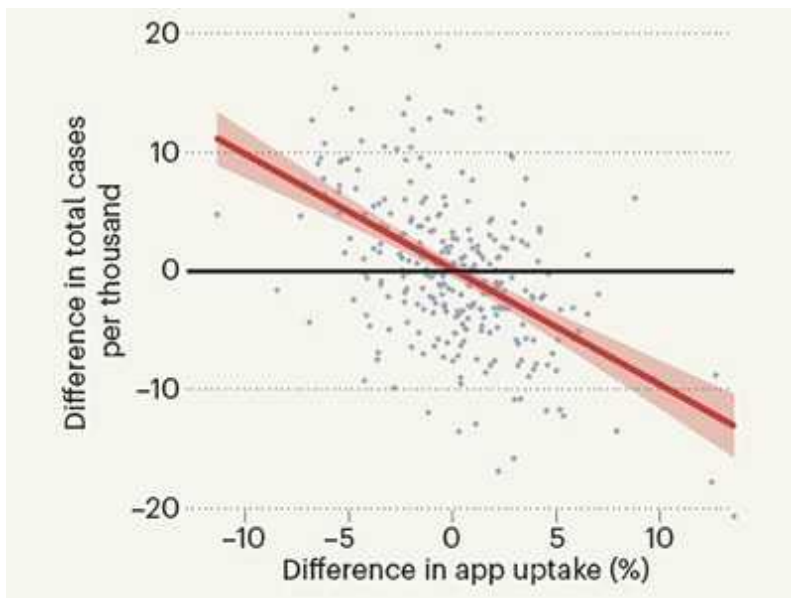
Nudges are subtle changes to the way in which choices are offered or information is framed that can have an outsize impact on behaviour. As the supply of COVID-19 vaccines increases around the world, many nations are faced with the challenge of how best to encourage people to get vaccinated. Although various campaigns to do this have been implemented, little is known about which types of approach work and which do not. [Writing in Nature](#), Dai *et al.*¹ present findings from a large field experiment that reveal new insights into the three key elements that must be combined in strategies aimed at increasing the likelihood that people will get their vaccination against COVID-19.



Read the paper: Behavioural nudges increase COVID-19 vaccinations

Dai and colleagues set out to determine whether a single text message from a person's health-care provider could change COVID-19 vaccination rates. In addition, they tested whether vaccination rates differed when recipients were told the vaccine was already theirs — that is, when they had psychological ownership of the vaccine. These text messages included phrases such as the vaccine has “just been made available to you”, and encouraged recipients to “claim your dose”. Such an approach has been used successfully to nudge influenza vaccination², but has not previously been tested for vaccination against COVID-19.

In the main clinical trial, more than 93,000 individuals in a large health-care system who had not organized an appointment by the first weekday after an initial invitation were randomly placed in a control group or a test group and then followed for 4 weeks. These individuals were among the first wave of people eligible for vaccinations (owing to age or pre-existing medical conditions). Of the control-group individuals who did not receive any text-message reminders, 13.9% got vaccinated. Among individuals who received a simple text-message reminder with a link to a website where they could schedule a COVID-19 vaccine appointment, the vaccination rate increased to 17.1%. Adding language to induce psychological ownership further increased vaccination rates to 18.2%.



Contact-tracing app curbed the spread of COVID in England and Wales

Before this clinical trial, the investigators conducted an online experiment with individuals participating as hypothetical patients. They found that asking individuals to watch a two-minute educational video on the vaccine led to slightly higher stated intentions to get vaccinated than were seen for individuals who had not watched the video. However, unexpectedly, when the authors added a link to this video in the text-messaging experiment, it led to slightly lower vaccination rates than did sending text messages alone.

These conflicting results might be explained by some key differences between the two studies. For example, the online group of hypothetical patients had a mean age of 37 years, and 100% were required to watch the video, whereas individuals in the clinical trial had a mean age of 73 years and only 21% watched the video. Although the precise reasons for the inconsistent effect of the video are unclear, these findings demonstrate the value of conducting rigorous testing of approaches in real-world groups of individuals, rather than hypothetical ones³.

So, how can we apply these findings to future vaccination efforts?

According to the Fogg Behavior Model (see behaviormodel.org), three key aspects need to be combined to successfully nudge behaviour: ability to act, motivation and a prompt. Moreover, the best nudging approaches to use will vary depending on individuals' attitudes towards the COVID-19 vaccine

(Fig. 1). For example, individuals who are hesitant about the vaccination often have a strong emotional response to the risks and benefits of the vaccine, whereas those who are apathetic about it have weakly held attitudes and often have not invested much effort in considering vaccination⁴. Appropriately tailoring interventions to the population of interest is likely to lead to higher success than is a one-size-fits-all approach.

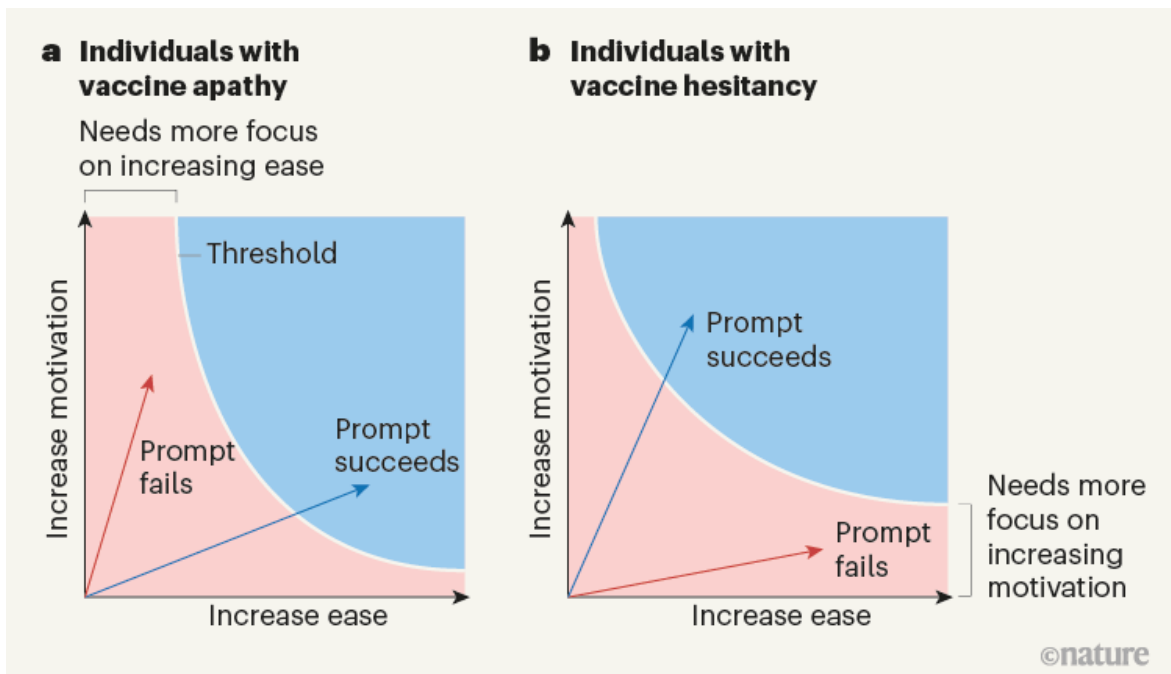
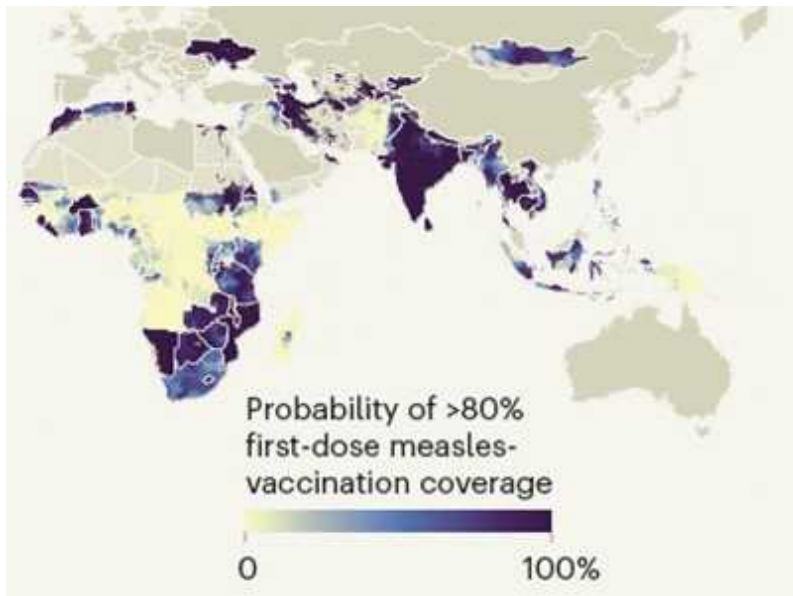


Figure 1 | Nudges to encourage vaccination uptake will depend on individuals' attitudes. Nudges are ways in which information is presented or choices offered that drive behavioural change. Dai *et al.*¹ report the effects of sending individuals text-message reminders to encourage them to book an appointment to receive their vaccine against COVID-19. According to the Fogg Behavior Model, nudges should combine three aspects for success: they should prompt an action, increase motivation and make action easier. But nudges need to be tailored to individuals with different attitudes. **a**, If individuals are apathetic about getting a vaccine, prompting nudges will need to focus more on making it easier to arrange an appointment. Dai *et al.* achieved this by including a link to the booking website in the text messages. **b**, If individuals are more hesitant about getting vaccinated, such nudges will need to focus on increasing motivation.

First, interventions should aim to make the intended behaviour easier. In this case, the text messages provided a link to schedule an appointment. This made setting up vaccination quick and convenient. This aspect of the intervention boosted vaccination rates the most and probably addressed barriers among people with vaccine apathy who were unlikely to go out of their way to look up scheduling information (Fig. 1a).



Precise mapping reveals gaps in global measles vaccination coverage

Second, interventions should focus on increasing an individual's motivation for the intended behaviour. The text-message reminders that invoked psychological ownership probably boosted vaccination by increasing motivation. However, compared with the simple text-with-link intervention, the increase in vaccine uptake following this intervention was relatively small (about 1 percentage point). The investigators also tried sending a second text-message reminder after another eight days to those who had still not scheduled an appointment. Individuals in this group were probably more hesitant than were those who had already set up their vaccine appointment, and that second reminder did not change overall vaccination rates compared with the control group. Individuals with vaccine hesitancy thus might often require further approaches to increase motivation (Fig. 1b), either through other types of nudge or different approaches, such as incentives^{5,6}.

Third, interventions should prompt action. Sending a text message to consider vaccination forces a person to think about the decision ‘now’, rather than relying on them to remember to think about it on their own. The best channel for sending the notification will probably vary for different groups of people. For example, someone who is not tech-savvy might respond better to a phone call.

Although even the best text-messaging approach in the clinical trial increased vaccination by only a few percentage points, one must keep in mind that these approaches were very low cost and, if applied on a broader scale, could lead to millions of extra vaccinations that might otherwise have been delayed or not occurred at all. Nudges can be an effective tool for changing an individual’s behaviour, but they must be carefully designed. As health systems, public-health agencies and other stakeholders look for methods to increase COVID-19 vaccination rates, they should consider ways to implement nudges that make getting a vaccine easier, that increase motivation and that prompt action.

Nature **597**, 336–337 (2021)

doi: <https://doi.org/10.1038/d41586-021-02043-2>

References

1. 1.

Dai, H. *et al. Nature* **597**, 404–409 (2021).

2. 2.

Milkman, K. L. *et al. Proc. Natl Acad. Sci. USA* **118**, e2101165118 (2021).

3. 3.

Patel, M. *Nature* **590**, 185 (2021).

4. 4.

Wood, S. & Schulman, K. *JAMA* **325**, 2435–2436 (2021).

5. 5.

Patel, M. S. *Nature Hum. Behav.* **2**, 720–721 (2018).

6. 6.

Volpp, K. G. & Cannuscio, C. C. *N. Engl. J. Med.* **385**, e1 (2021).

This article was downloaded by **calibre** from <https://www.nature.com/articles/d41586-021-02043-2>

| [Section menu](#) | [Main menu](#) |

- NEWS AND VIEWS
- 14 September 2021

From the archive

Nature's pages feature a look at psychology in industrial workplaces, and a mystery surrounding fish in a Swiss lake.

100 years ago

Access options

Subscribe to Journal

Get full journal access for 1 year

\$199.00

only \$3.90 per issue

[Subscribe](#)

All prices are NET prices.

VAT will be added later in the checkout.

Tax calculation will be finalised during checkout.

Rent or Buy article

Get time limited or full article access on ReadCube.

from \$8.99

[Rent or Buy](#)

All prices are NET prices.

Additional access options:

- [Log in](#)
- [Learn about institutional subscriptions](#)

Nature **597**, 337 (2021)

doi: <https://doi.org/10.1038/d41586-021-02434-5>

This article was downloaded by **calibre** from <https://www.nature.com/articles/d41586-021-02434-5>

| [Section menu](#) | [Main menu](#) |

- NEWS AND VIEWS
- 01 September 2021

Traces of a series of human dispersals through Arabia

The Arabian Peninsula was a key migratory crossroads when humans and our hominin relatives began to leave Africa. Archaeological evidence and climate reconstructions reveal episodes when early humans inhabited Arabia.

- [Robin Dennell](#) ⁰

Ten years ago, no dated archaeological sites more than 10,000 years old had been recorded in the three million square kilometres of the Arabian Peninsula. [Writing in Nature](#), Groucutt *et al.*¹ show just how much our knowledge about the presence of early humans in the region has improved after a decade of sustained, multidisciplinary archaeological and geological field research by multiple teams.

Access options

Subscribe to Journal

Get full journal access for 1 year

\$199.00

only \$3.90 per issue

[Subscribe](#)

All prices are NET prices.
VAT will be added later in the checkout.
Tax calculation will be finalised during checkout.

Rent or Buy article

Get time limited or full article access on ReadCube.

from \$8.99

[Rent or Buy](#)

All prices are NET prices.

Additional access options:

- [Log in](#)
- [Learn about institutional subscriptions](#)

Nature **597**, 338–339 (2021)

doi: <https://doi.org/10.1038/d41586-021-02321-z>

References

1. 1.

Groucutt, H. S. *et al.* *Nature* **597**, 376–380 (2021).

2. 2.

Groucutt, H. S. *et al.* *Nature Ecol. Evol.* **2**, 800–809 (2018).

3. 3.

Stewart, M. *et al.* *Sci. Adv.* **6**, eaba8940 (2020).

4. 4.

Hublin, J.-J. *et al.* *Nature* **546**, 289–292 (2017).

5. 5.

Hershkovitz, I. *et al.* *Science* **359**, 456–459 (2018).

6. 6.

Shea, J. J. *J. World Prehist.* **17**, 313–394 (2003).

7. 7.

Boivin, N., Fuller, D. Q., Dennell, R., Allaby, R. & Petraglia, M. D. *Quat. Int.* **300**, 32–47 (2013).

8. 8.

Green, R. E. *et al.* *Science* **328**, 710–722 (2010).

9. 9.

Dennell, R. *From Arabia to the Pacific: How Our Species Colonised Asia* (Routledge, 2020).

10. 10.

O'Connell, J. F. *et al.* *Proc. Natl Acad. Sci. USA* **115**, 8482–8490 (2018).

11. 11.

Clarkson, C. *et al.* *Nature* **547**, 306–310 (2017).

12. 12.

Akhilesh, K. *et al.* *Nature* **554**, 97–101 (2018).

13. 13.

Clarkson, C., Jones, S. & Harris, C. *Quat. Int.* **258**, 165–179 (2012).

14. 14.

Liu, W. *et al.* *Nature* **526**, 696–699 (2015).

15. 15.

Westaway, K. E. *et al.* *Nature* **548**, 322–325 (2017).

This article was downloaded by **calibre** from <https://www.nature.com/articles/d41586-021-02321-z>

| [Section menu](#) | [Main menu](#) |

- Article
- [Published: 15 September 2021](#)

The diffuse γ -ray background is dominated by star-forming galaxies

- [Matt A. Roth](#) ORCID: [orcid.org/0000-0002-4204-5026¹](https://orcid.org/0000-0002-4204-5026),
- [Mark R. Krumholz](#) ORCID: [orcid.org/0000-0003-3893-854X^{1,2}](https://orcid.org/0000-0003-3893-854X),
- [Roland M. Crocker](#) ORCID: [orcid.org/0000-0002-2036-2426¹](https://orcid.org/0000-0002-2036-2426) &
- [Silvia Celli](#) ORCID: [orcid.org/0000-0002-7592-0851³](https://orcid.org/0000-0002-7592-0851)

[Nature](#) volume 597, pages 341–344 (2021)

- 671 Accesses
- 89 Altmetric
- [Metrics details](#)

Subjects

- [Galaxies and clusters](#)
- [High-energy astrophysics](#)
- [Particle astrophysics](#)

Abstract

The Fermi Gamma-ray Space Telescope has revealed a diffuse γ -ray background at energies from 0.1 gigaelectronvolt to 1 teraelectronvolt, which can be separated into emission from our Galaxy and an isotropic, extragalactic component¹. Previous efforts to understand the latter have been hampered by the lack of physical models capable of predicting the γ -

ray emission produced by the many candidate sources, primarily active galactic nuclei^{2,3,4,5} and star-forming galaxies^{6,7,8,9,10}, leaving their contributions poorly constrained. Here we present a calculation of the contribution of star-forming galaxies to the γ -ray background that does not rely on empirical scalings and is instead based on a physical model for the γ -ray emission produced when cosmic rays accelerated in supernova remnants interact with the interstellar medium¹¹. After validating the model against local observations, we apply it to the observed cosmological star-forming galaxy population and recover an excellent match to both the total intensity and the spectral slope of the γ -ray background, demonstrating that star-forming galaxies alone can explain the full diffuse, isotropic γ -ray background.

Access options

Subscribe to Journal

Get full journal access for 1 year

\$199.00

only \$3.90 per issue

[Subscribe](#)

All prices are NET prices.

VAT will be added later in the checkout.

Tax calculation will be finalised during checkout.

Rent or Buy article

Get time limited or full article access on ReadCube.

from \$8.99

[Rent or Buy](#)

All prices are NET prices.

Additional access options:

- [Log in](#)
- [Access through your institution](#)
- [Learn about institutional subscriptions](#)

Fig. 1: The γ -ray spectra of nearby SFGs.



Fig. 2: The FIR– γ correlation.

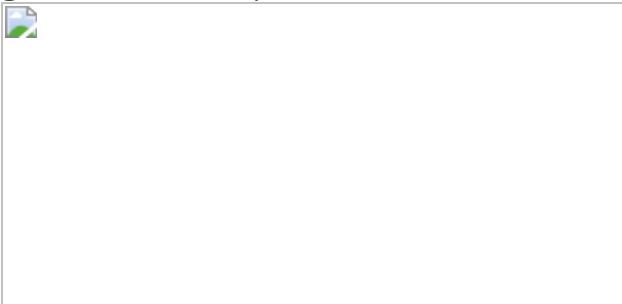


Fig. 3: The γ -ray source count distribution.

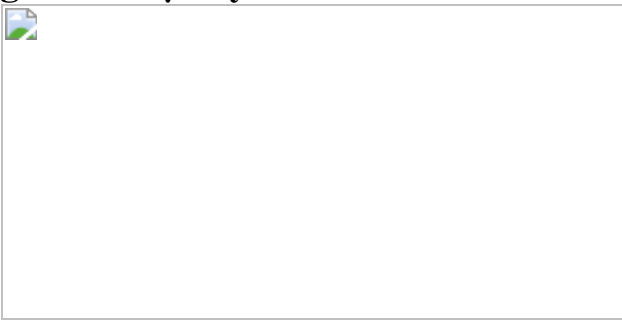
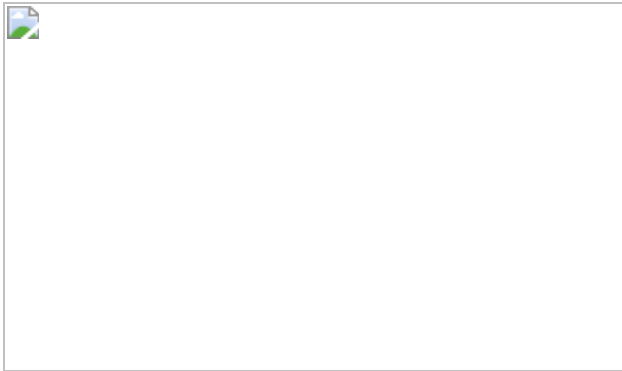


Fig. 4: The diffuse isotropic γ -ray background.



Data availability

The data that were used to produce the figures and that support the findings of this study are available in Zenodo with the identifier <https://doi.org/10.5281/zenodo.4764111>. [Source data](#) are provided with this paper.

Code availability

The code used to derive the key findings of this study is available in Zenodo with the identifier <https://doi.org/10.5281/zenodo.4609628>.

References

1. 1.

Ackermann, M. et al. The spectrum of isotropic diffuse gamma-ray emission between 100 MeV and 820 GeV. *Astrophys. J.* **799**, 86 (2015).

2. 2.

Cuoco, A., Komatsu, E. & Siegal-Gaskins, J. M. Joint anisotropy and source count constraints on the contribution of blazars to the diffuse gamma-ray background. *Phys. Rev. D* **86**, 063004 (2012).

3. 3.

Di Mauro, M., Calore, F., Donato, F., Ajello, M. & Latronico, L. Diffuse γ -ray emission from misaligned active galactic nuclei. *Astrophys. J.* **780**, 161 (2014).

4. 4.

Fornasa, M. & Sánchez-Conde, M. A. The nature of the diffuse gamma-ray background. *Phys. Rep.* **598**, 1–58 (2015).

5. 5.

Qu, Y., Zeng, H. & Yan, D. Gamma-ray luminosity function of BL Lac objects and contribution to the extragalactic gamma-ray background. *Mon. Not. R. Astron. Soc.* **490**, 758–765 (2019).

6. 6.

Fields, B. D., Pavlidou, V. & Prodanović, T. Cosmic gamma-ray background from star-forming galaxies. *Astrophys. J.* **722**, L199–L203 (2010).

7. 7.

Ackermann, M. et al. GeV observations of star-forming galaxies with the Fermi Large Area Telescope. *Astrophys. J.* **755**, 164 (2012).

8. 8.

Xia, J.-Q., Cuoco, A., Branchini, E. & Viel, M. Tomography of the Fermi-LAT γ -ray diffuse extragalactic signal via cross correlations with galaxy catalogs. *Astrophys. J. Suppl.* **217**, 15 (2015).

9. 9.

Linden, T. Star-forming galaxies significantly contribute to the isotropic gamma-ray background. *Phys. Rev. D* **96**, 083001 (2017).

10. 10.

Ajello, M., Di Mauro, M., Paliya, V. S. & Garrappa, S. The γ -ray emission of star-forming galaxies. *Astrophys. J.* **894**, 88 (2020).

11. 11.

Krumholz, M. R. et al. Cosmic ray transport in starburst galaxies. *Mon. Not. R. Astron. Soc.* **493**, 2817–2833 (2020).

12. 12.

Ajello, M. et al. The origin of the extragalactic gamma-ray background and implications for dark matter annihilation. *Astrophys. J.* **800**, L27 (2015).

13. 13.

Bell, A. R. Cosmic ray acceleration. *Astropart. Phys.* **43**, 56–70 (2013).

14. 14.

Woosley, S. E. & Weaver, T. A. The evolution and explosion of massive Stars II: explosive hydrodynamics and nucleosynthesis. *Astrophys. J. Suppl.* **101**, 181–235 (1995).

15. 15.

Dermer, C. D. & Powale, G. Gamma rays from cosmic rays in supernova remnants. *Astron. Astrophys.* **553**, A34 (2013).

16. 16.

Lacki, B. C., Thompson, T. A. & Quataert, E. The physics of the far-infrared-radio correlation. I. Calorimetry, conspiracy, and implications. *Astrophys. J.* **717**, 1–28 (2010).

17. 17.

Bell, A. R. The acceleration of cosmic rays in shock fronts—I. *Mon. Not. R. Astron. Soc.* **182**, 147–156 (1978).

18. 18.

Blandford, R. & Eichler, D. Particle acceleration at astrophysical shocks: a theory of cosmic ray origin. *Phys. Rep.* **154**, 1–75 (1987).

19. 19.

Caprioli, D. Understanding hadronic gamma-ray emission from supernova remnants. *J. Cosmol. Astropart. Phys.* **2011**, 026 (2011).

20. 20.

Caprioli, D. Cosmic-ray acceleration in supernova remnants: non-linear theory revised. *J. Cosmol. Astropart. Phys.* **2012**, 038 (2012).

21. 21.

Grogin, N. A. et al. CANDELS: The Cosmic Assembly Near-infrared Deep Extragalactic Legacy Survey. *Astrophys. J. Suppl.* **197**, 35 (2011).

22. 22.

van der Wel, A. et al. Structural parameters of galaxies in CANDELS. *Astrophys. J. Suppl.* **203**, 24 (2012).

23. 23.

Ballet, J., Burnett, T. H., Digel, S. W. & Lott, B. Fermi Large Area Telescope Fourth Source Catalog Data Release 2. Preprint at <https://arxiv.org/abs/2005.11208> (2020).

24. 24.

Peng, F.-K., Wang, X.-Y., Liu, R.-Y., Tang, Q.-W. & Wang, J.-F. First detection of GeV emission from an ultraluminous infrared galaxy: Arp

220 as seen with the Fermi Large Area Telescope. *Astrophys. J.* **821**, L20 (2016).

25. 25.

Kornecki, P. et al. The γ -ray/infrared luminosity correlation of star-forming galaxies. *Astron. Astrophys.* **641**, A147 (2020).

26. 26.

Ando, S., Fornasa, M., Fornengo, N., Regis, M. & Zechlin, H.-S. Astrophysical interpretation of the anisotropies in the unresolved gamma-ray background. *Phys. Rev. D* **95**, 123006 (2017).

27. 27.

Manconi, S. et al. Testing gamma-ray models of blazars in the extragalactic sky. *Phys. Rev. D* **101**, 103026 (2020).

28. 28.

Komis, I., Pavlidou, V. & Zezas, A. Extragalactic gamma-ray background from star-forming galaxies: will empirical scalings suffice? *Mon. Not. R. Astron. Soc.* **483**, 4020–4030 (2019).

29. 29.

Cherenkov Telescope Array Consortium et al. *Science with the Cherenkov Telescope Array* (World Scientific, 2019).

30. 30.

Di Sciascio, G. & Lhaaso Collaboration. The LHAASO experiment: from gamma-ray astronomy to cosmic rays. *Nucl. Part. Phys. Proc.* **279–281**, 166–173 (2016).

31. 31.

Kafexhiu, E., Aharonian, F., Taylor, A. M. & Vila, G. S. Parametrization of gamma-ray production cross sections for pp interactions in a broad proton energy range from the kinematic threshold to PeV energies. *Phys. Rev. D* **90**, 123014 (2014).

32. 32.

Chabrier, G. Galactic stellar and substellar initial mass function. *Publ. Astron. Soc. Pacif.* **115**, 763–795 (2003).

33. 33.

Heger, A., Fryer, C. L., Woosley, S. E., Langer, N. & Hartmann, D. H. How massive single stars end their life. *Astrophys. J.* **591**, 288–300 (2003).

34. 34.

Crocker, R. M., Krumholz, M. R. & Thompson, T. A. Cosmic rays across the star-forming galaxy sequence—I. Cosmic ray pressures and calorimetry. *Mon. Not. R. Astron. Soc.* **502**, 1312–1333 (2021).

35. 35.

Peretti, E., Blasi, P., Aharonian, F. & Morlino, G. Cosmic ray transport and radiative processes in nuclei of starburst galaxies. *Mon. Not. R. Astron. Soc.* **487**, 168–180 (2019).

36. 36.

Kelner, S. R., Aharonian, F. A. & Bugayov, V. V. Energy spectra of gamma rays, electrons, and neutrinos produced at proton–proton interactions in the very high energy regime. *Phys. Rev. D* **74**, 034018 (2006).

37. 37.

Kelner, S. R., Aharonian, F. A. & Bugayov, V. V. Erratum: Energy spectra of gamma rays, electrons, and neutrinos produced at proton–

proton interactions in the very high energy regime. *Phys. Rev. D* **79**, 039901 (2009).

38. 38.

Magnelli, B. et al. The evolution of the dust temperatures of galaxies in the SFR– M_* plane up to $z \sim 2$. *Astron. Astrophys.* **561**, A86 (2014).

39. 39.

Persic, M., Rephaeli, Y. & Arieli, Y. Very-high-energy emission from M 82. *Astron. Astrophys.* **486**, 143–149 (2008).

40. 40.

Thompson, T. A. Gravitational instability in radiation pressure-dominated backgrounds. *Astrophys. J.* **684**, 212–225 (2008).

41. 41.

Schlickeiser, R. *Cosmic Ray Astrophysics* (Springer, 2002).

42. 42.

Ghisellini, G. *Radiative Processes in High Energy Astrophysics* (Springer, 2013).

43. 43.

Fang, K., Bi, X.-J., Lin, S.-J. & Yuan, Q. Klein–Nishina effect and the cosmic ray electron spectrum. Preprint at <https://arxiv.org/abs/2007.15601> (2020).

44. 44.

Bethe, H. & Heitler, W. On the stopping of fast particles and on the creation of positive electrons. *Proc. R. Soc. Lond. A* **146**, 83–112 (1934).

45. 45.

Gould, R. J. High-energy bremsstrahlung in collisions of electrons with one- and two-electron atoms. *Phys. Rev.* **185**, 72–79 (1969).

46. 46.

Blumenthal, G. R. & Gould, R. J. Bremsstrahlung, synchrotron radiation, and Compton scattering of high-energy electrons traversing dilute gases. *Rev. Mod. Phys.* **42**, 237–270 (1970).

47. 47.

Razzaque, S., Mészáros, P. & Zhang, B. GeV and higher energy photon interactions in gamma-ray burst fireballs and surroundings. *Astrophys. J.* **613**, 1072–1078 (2004).

48. 48.

Franceschini, A. & Rodighiero, G. The extragalactic background light revisited and the cosmic photon–photon opacity. *Astron. Astrophys.* **603**, A34 (2017).

49. 49.

Berezinsky, V. & Kalashev, O. High-energy electromagnetic cascades in extragalactic space: physics and features. *Phys. Rev. D* **94**, 023007 (2016).

50. 50.

van der Wel, A. et al. 3D-HST+CANDELS: The evolution of the galaxy size-mass distribution since $z = 3$. *Astrophys. J.* **788**, 28 (2014).

51. 51.

Shi, Y. et al. Extended Schmidt law: role of existing stars in current star formation. *Astrophys. J.* **733**, 87 (2011).

52. 52.

Yu, X. et al. What drives the velocity dispersion of ionized gas in star-forming galaxies? *Mon. Not. R. Astron. Soc.* **486**, 4463–4472 (2019).

53. 53.

Forbes, J., Krumholz, M. & Burkert, A. Evolving gravitationally unstable disks over cosmic time: implications for thick disk formation. *Astrophys. J.* **754**, 48 (2012).

54. 54.

Madau, P. & Dickinson, M. Cosmic star-formation history. *Annu. Rev. Astron. Astrophys.* **52**, 415–486 (2014).

55. 55.

Kennicutt, R. C. Jr The global Schmidt law in star-forming galaxies. *Astrophys. J.* **498**, 541–552 (1998).

56. 56.

Crain, R. A., McCarthy, I. G., Frenk, C. S., Theuns, T. & Schaye, J. X-ray coronae in simulations of disc galaxy formation. *Mon. Not. R. Astron. Soc.* **407**, 1403–1422 (2010).

57. 57.

Bothwell, M. S. et al. The star formation rate distribution function of the local Universe. *Mon. Not. R. Astron. Soc.* **415**, 1815–1826 (2011).

58. 58.

Bothwell, M. S. et al. Erratum: The star formation rate distribution function of the local Universe. *Mon. Not. R. Astron. Soc.* **438**, 3608 (2014).

59. 59.

Rodríguez Zaurín, J., Tadhunter, C. N. & González Delgado, R. M. Optical spectroscopy of Arp220: the star formation history of the closest ULIRG. *Mon. Not. R. Astron. Soc.* **384**, 875–885 (2008).

60. 60.

Wright, G. S., James, P. A., Joseph, R. D., McLean, I. S. & Doyon, R. Infrared images of merging galaxies. In *NASA Conference Publication* (eds Sulentic, J. W. et al.) 3098, 321–326 (1990).

61. 61.

Parkash, V., Brown, M. J. I., Jarrett, T. H. & Bonne, N. J. Relationships between HI gas mass, stellar mass, and the star formation rate of HICAT+WISE (H I-WISE) galaxies. *Astrophys. J.* **864**, 40 (2018).

62. 62.

IRSA. NASA/IPAC Infrared Science Archive,
<https://irsa.ipac.caltech.edu>.

63. 63.

Sakamoto, K. et al. Molecular superbubbles in the Starburst Galaxy NGC 253. *Astrophys. J.* **636**, 685–697 (2006).

64. 64.

Bendo, G. J. et al. ALMA observations of 99 GHz free-free and H40 α line emission from star formation in the centre of NGC 253. *Mon. Not. R. Astron. Soc.* **450**, L80–L84 (2015).

65. 65.

Rahmani, S., Lianou, S. & Barmby, P. Star formation laws in the Andromeda galaxy: gas, stars, metals and the surface density of star formation. *Mon. Not. R. Astron. Soc.* **456**, 4128–4144 (2016).

66. 66.

Iijima, T., Ito, K., Matsumoto, T. & Uyama, K. Near-infrared profile of M31. *Pub. Astron. Soc. Japan* **28**, 27–34 (1976).

67. 67.

Braun, R. & Walterbos, R. A. M. Physical properties of neutral gas in M31 and the galaxy. *Astrophys. J.* **386**, 120 (1992).

68. 68.

Caldú-Primo, A. & Schruba, A. Molecular gas velocity dispersions in the Andromeda galaxy. *Astron. J.* **151**, 34 (2016).

69. 69.

Davis, B. L., Graham, A. W. & Cameron, E. Black hole mass scaling relations for spiral galaxies. II. $M_{\text{BH-M}\star,\text{tot}}$ and $M_{\text{BH-M}\star,\text{disk}}$. *Astrophys. J.* **869**, 113 (2018).

70. 70.

de Vaucouleurs, G. Southern galaxies. V. Isophotometry of the large barred spiral NGC 4945. *Astrophys. J.* **139**, 899 (1964).

71. 71.

Bendo, G. J. et al. Free-free and H42 α emission from the dusty starburst within NGC 4945 as observed by ALMA. *Mon. Not. R. Astron. Soc.* **463**, 252–269 (2016).

72. 72.

Ott, M., Whiteoak, J. B., Henkel, C. & Wielebinski, R. Atomic and molecular gas in the starburst galaxy NGC 4945. *Astron. Astrophys.* **372**, 463–476 (2001).

73. 73.

Stettner, J. Measurement of the diffuse astrophysical muon-neutrino spectrum with ten years of IceCube data. In *36th International Cosmic Ray Conference (ICRC2019) 36*, 1017 (2019).

Acknowledgements

This research has made use of the NASA/IPAC Infrared Science Archive, which is funded by the National Aeronautics and Space Administration and operated by the California Institute of Technology. Funding for this work was provided by the Australian Government through the Australian Research Council, awards FT180100375 (M.R.K.) and DP190101258 (R.M.C. and M.R.K.), and the Australian National University through a research scholarship (M.A.R.). R.M.C. thanks O. Macias and S. Ando for conversations while a Kavli IPMU-funded guest of the GRAPPA Institute at the University of Amsterdam.

Author information

Affiliations

1. Research School of Astronomy and Astrophysics, The Australian National University, Canberra, Australian Capital Territory, Australia

Matt A. Roth, Mark R. Krumholz & Roland M. Crocker

2. ARC Centre of Excellence for All-Sky Astrophysics in Three Dimensions (ASTRO-3D), Canberra, Australian Capital Territory, Australia

Mark R. Krumholz

3. Dipartimento di Fisica dell'Università La Sapienza and INFN, Rome, Italy

Silvia Celli

Contributions

All authors were involved in the design of the study and the interpretation of the results. M.A.R. performed the modelling and data analysis with input from M.R.K., R.M.C. and S.C. The manuscript was written by M.A.R., M.R.K. and R.M.C., and reviewed by all authors.

Corresponding author

Correspondence to Matt A. Roth.

Ethics declarations

Competing interests

The authors declare no competing interests.

Additional information

Peer review information *Nature* thanks Paula Kornecki and the other, anonymous, reviewer(s) for their contribution to the peer review of this work.

Publisher's note Springer Nature remains neutral with regard to jurisdictional claims in published maps and institutional affiliations.

Extended data figures and tables

[Extended Data Fig. 1 The effect of varying model parameters.](#)

The plots presented here show the result of our calculations when varying the model parameters as discussed in the [Supplementary Information](#). Our fiducial choice is plotted as a solid blue line, with the dashed and dash-dotted lines showing the spectrum for the upper and lower limits respectively of the varied parameter. The black points correspond to the

Fermi data as in Fig. 4. Plot **a** shows M_A plotted for reasonable values of 1.6 and 2.3, and extremal values of 1.1 and 3.0; **b** the ionization fraction χ for values of 10^{-2} and 10^{-6} ; **c** the injection index q for values 2.1 and 2.3; and finally **d** the conversion fraction of supernova energy to CR electrons for values of 1% and 3%, which is equivalent to 10% and 30% of the total energy injected in all cosmic ray species. Note that varying the total CR energy budget results in a trivial scaling of the result by the same fraction, and thus is not shown

[Source data.](#)

[Extended Data Fig. 2 The contribution of SFGs in the \$\(\dot{M}_\ast - z\)\$ plane.](#)

The contribution of SFGs to the total γ -ray spectrum at selected energies in the star-formation rate (\dot{M}_\ast) , redshift (z) plane. Coloured pixels show the fractional contribution (as indicated in the colourbar) from galaxies in each bin of (\dot{M}_\ast) and z to the diffuse isotropic γ -ray background at the indicated energy; a fractional contribution of unity corresponds to that pixel producing all of the background, with no contribution from galaxies outside the pixel. Grey points show individual CANDELS galaxies in regions of (\dot{M}_\ast) and z that contribute $<10^{-3}$ of the total. Flanking histograms show the fractional contribution binned in one dimension – (\dot{M}_\ast) (right) and z (top). We see that the background at lower energies is dominated by emission from galaxies on the high side of the star forming main sequence at $z \sim 1-2$, while at high energies it is dominated by the brightest systems at low redshift.

[Extended Data Fig. 3 The diffuse isotropic \$\gamma\$ -ray and neutrino backgrounds.](#)

The blue line and black points show the model-predicted and observed γ -ray background, and are identical to those shown in Fig. 4. The red lines show our model prediction for the neutrino background (single flavour) with $E_{\text{cut}} = 100$ PeV (solid line) and $E_{\text{cut}} = 1$ PeV (dashed line), computed

as described in the [Supplementary Information](#). We assume a neutrino flavour ratio at the detector of $(\nu_e:\nu_\mu:\nu_\tau) = (1:1:1)$. The red filled band shows a power-law fit^{[73](#)} to the single flavour astrophysical neutrino background with the 90% likelihood limit, as measured by IceCube, which is also shown as grey points, where the horizontal bars show the energy bin and the vertical bars the 1σ uncertainty limit

[Source data](#).

[Extended Data Fig. 4 Cosmic ray calorimetry in the \$E - \Sigma_g\$ plane.](#)

Mean calorimetry fraction $f_{\text{cal}}(E)$ in the surface gas density Σ_g , cosmic ray energy E plane, binned in redshift intervals. This figure is constructed by deriving the gas surface density and energy dependent calorimetry fraction for each galaxy in the CANDELS sample using our model. The colour of each pixel gives the mean calorimetry fraction of all the galaxies within that particular range of Σ_g , E , and redshift. The horizontal white stripes correspond to ranges of Σ_g into which no CANDELS galaxies fall for the corresponding redshift range. Several physical processes contribute to the behaviour visible in the plot. At low Σ_g , galaxies have low f_{cal} at all energies E because there are few targets for hadronic collisions with CRs. As Σ_g increases, the increased ISM density results in efficient calorimetry and conversion of CR energy into γ -rays for low CR energies; however, at higher energies the CR number density is low, yielding a high CR streaming velocity and rapid escape, resulting in low f_{cal} . As Σ_g increases further, the increasing density results in the streaming instability being suppressed efficiently by ion-neutral damping towards lower energies, reducing the calorimetry fraction further. Finally, at the highest Σ_g , the streaming instability is suppressed completely by ion-neutral damping, but streaming is still limited to the speed of light. Consequently, increasing Σ_g further only results in increased collisions, and thus a higher calorimetry fraction.

Extended Data Fig. 5 Cosmic ray calorimetry in the z - Σ_g plane.

Mean calorimetry fraction in the surface gas density (Σ_g), redshift (z) plane at CR energies $E = 1$ GeV, 10 GeV, 1 TeV and 10 TeV. To construct this figure, for each CANDELS sample galaxy, we apply our model to compute Σ_g and $f_{\text{cal}}(E)$ at the indicated energies. The colour indicates the average $f_{\text{cal}}(E)$ value computed over bins of (z, Σ_g) , while contours indicate the density of the CANDELS sample in this plane. Note that the non-monotonic behaviour of $f_{\text{cal}}(E)$ with Σ_g that is most prominently visible in the 1 TeV panel is expected, for the reasons explained in the caption of Extended Data Fig. 4.

Extended Data Fig. 6 Contributions to the diffuse isotropic γ -ray background.

The blue line and black points show the model-predicted and observed γ -ray background, and are identical to those shown in Fig. 4. The green line shows the contribution from π^0 decay, the olive lines the contribution from bremsstrahlung emission, and the cyan lines the contribution from the inverse Compton emission. In both cases, dashed lines show the spectrum produced by primary CR electrons and the dash-dotted lines the spectrum from secondary electrons and positrons. The red line shows the contributions from the EBL cascade

[Source data](#).

Extended Data Table 1 Local galaxy data

Supplementary information

Supplementary Information

This file contains the following supplementary sections: Confidence intervals for source count distributions; Sensitivity of the result to model

parameters; Comparison to earlier work; Neutrinos. Supplementary equations 1 – 10 are included within these sections.

[**Peer Review File**](#)

Source data

[**Source Data Fig. 1**](#)

[**Source Data Fig. 3**](#)

[**Source Data Fig. 4**](#)

[**Source Data Extended Data Fig. 1**](#)

[**Source Data Extended Data Fig. 3**](#)

[**Source Data Extended Data Fig. 6**](#)

Rights and permissions

[**Reprints and Permissions**](#)

About this article

Cite this article

Roth, M.A., Krumholz, M.R., Crocker, R.M. *et al.* The diffuse γ -ray background is dominated by star-forming galaxies. *Nature* **597**, 341–344 (2021). <https://doi.org/10.1038/s41586-021-03802-x>

- Received: 11 November 2020
- Accepted: 06 July 2021

- Published: 15 September 2021
- Issue Date: 16 September 2021
- DOI: <https://doi.org/10.1038/s41586-021-03802-x>

Share this article

Anyone you share the following link with will be able to read this content:

[Get shareable link](#)

Sorry, a shareable link is not currently available for this article.

[Copy to clipboard](#)

Provided by the Springer Nature SharedIt content-sharing initiative

This article was downloaded by **calibre** from <https://www.nature.com/articles/s41586-021-03802-x>

| [Section menu](#) | [Main menu](#) |

- Article
- [Published: 15 September 2021](#)

Quantum criticality in twisted transition metal dichalcogenides

- [Augusto Ghiotto](#) [ORCID: orcid.org/0000-0003-0860-9817](#)¹,
- [En-Min Shih](#) [ORCID: orcid.org/0000-0001-8423-1428](#)¹,
- [Giancarlo S. S. G. Pereira](#)¹,
- [Daniel A. Rhodes](#)²,
- [Bumho Kim](#)²,
- [Jiawei Zang](#) [ORCID: orcid.org/0000-0002-3671-9282](#)¹,
- [Andrew J. Millis](#)^{1,3},
- [Kenji Watanabe](#) [ORCID: orcid.org/0000-0003-3701-8119](#)⁴,
- [Takashi Taniguchi](#) [ORCID: orcid.org/0000-0002-1467-3105](#)⁴,
- [James C. Hone](#) [ORCID: orcid.org/0000-0002-8084-3301](#)²,
- [Lei Wang](#) ^{1 nAff5},
- [Cory R. Dean](#) [ORCID: orcid.org/0000-0003-2967-5960](#)¹ &
- [Abhay N. Pasupathy](#) [ORCID: orcid.org/0000-0002-2744-0634](#)^{1 nAff6}

[Nature](#) volume **597**, pages 345–349 (2021)

- 2412 Accesses
- 33 Altmetric
- [Metrics details](#)

Subjects

- [Phase transitions and critical phenomena](#)

- [Quantum fluids and solids](#)

Abstract

Near the boundary between ordered and disordered quantum phases, several experiments have demonstrated metallic behaviour that defies the Landau Fermi paradigm^{1,2,3,4,5}. In moiré heterostructures, gate-tunable insulating phases driven by electronic correlations have been recently discovered^{6,7,8,9,10,11,12,13,14,15,16,17,18,19,20,21,22,23}. Here, we use transport measurements to characterize metal–insulator transitions (MITs) in twisted WSe₂ near half filling of the first moiré subband. We find that the MIT as a function of both density and displacement field is continuous. At the metal–insulator boundary, the resistivity displays strange metal behaviour at low temperatures, with dissipation comparable to that at the Planckian limit. Further into the metallic phase, Fermi liquid behaviour is recovered at low temperature, and this evolves into a quantum critical fan at intermediate temperatures, before eventually reaching an anomalous saturated regime near room temperature. An analysis of the residual resistivity indicates the presence of strong quantum fluctuations in the insulating phase. These results establish twisted WSe₂ as a new platform to study doping and bandwidth-controlled metal–insulator quantum phase transitions on the triangular lattice.

Access options

Subscribe to Journal

Get full journal access for 1 year

\$199.00

only \$3.90 per issue

[Subscribe](#)

All prices are NET prices.
VAT will be added later in the checkout.
Tax calculation will be finalised during checkout.

Rent or Buy article

Get time limited or full article access on ReadCube.

from \$8.99

[Rent or Buy](#)

All prices are NET prices.

Additional access options:

- [Log in](#)
- [Access through your institution](#)
- [Learn about institutional subscriptions](#)

Fig. 1: Continuous metal–insulator transition in twisted WSe₂.

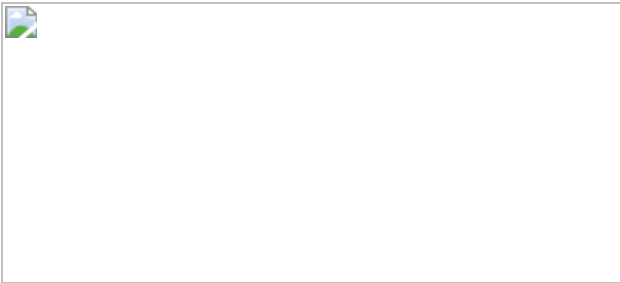


Fig. 2: Doping-driven metal–insulator transition in twisted WSe₂.

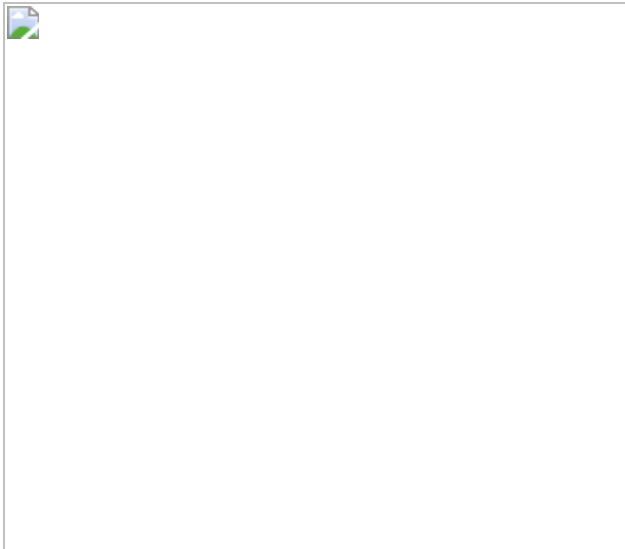


Fig. 3: Quantum critical fan in twisted WSe₂.

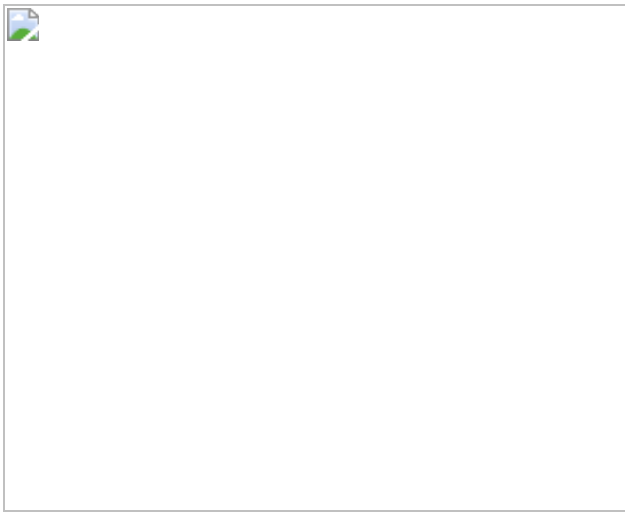


Fig. 4: Anomalous magnetotransport.

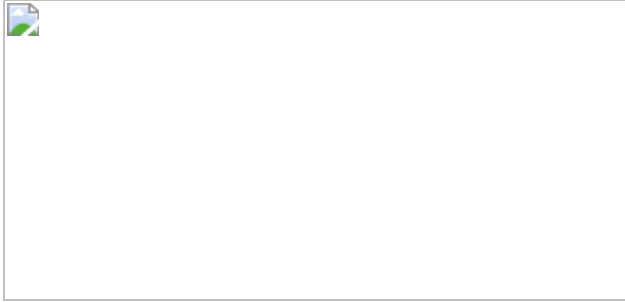
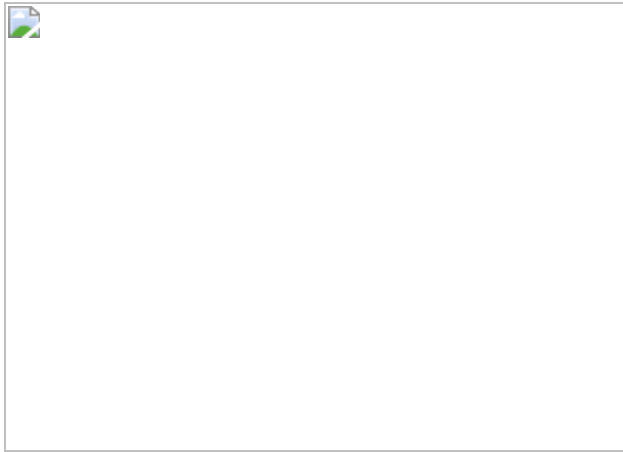


Fig. 5: Bandwidth-driven quantum criticality.



Data availability

The data that support the findings of this study are available from the corresponding authors upon request.

References

1. 1.

Varma, C. M. Colloquium: linear in temperature resistivity and associated mysteries including high temperature superconductivity. *Rev. Mod. Phys.* **92**, 031001 (2020).

2. 2.

Paschen, S. & Si, Q. Quantum phases driven by strong correlations. *Nat. Rev. Phys.* **3**, 9–26 (2020).

3. 3.

Zaanen, J. Why the temperature is high. *Nature* **430**, 512-513 (2004).

4. 4.

Imada, M., Fujimori, A. & Tokura, Y. Metal-insulator transitions. *Rev. Mod. Phys.* **70**, 1039–1263 (1998).

5. 5.

Taillefer, L. Scattering and pairing in cuprate superconductors. *Annu. Rev. Condens. Matter Phys.* **1**, 51–70 (2010).

6. 6.

Cao, Y. et al. Correlated insulator behaviour at half-filling in magic-angle graphene superlattices. *Nature* **556**, 80–84 (2018).

7. 7.

Cao, Y. et al. Unconventional superconductivity in magic-angle graphene superlattices. *Nature* **556**, 43–50 (2018).

8. 8.

Yankowitz, M. et al. Tuning superconductivity in twisted bilayer graphene. *Science* **363**, 1059–1064 (2019).

9. 9.

Burg, G. W. et al. Correlated insulating states in twisted double bilayer graphene. *Phys. Rev. Lett.* **123**, 197702 (2019).

10. 10.

Liu, X. Tunable spin-polarized correlated states in twisted double bilayer graphene. *Nature* **583**, 221–225 (2020).

11. 11.

Shen, C. et al. Correlated states in twisted double bilayer graphene. *Nat. Phys.* **16**, 520–525 (2020).

12. 12.

Cao, Y. Tunable correlated states and spin-polarized phases in twisted bilayer–bilayer graphene. *Nature* **583**, 215–220 (2020).

13. 13.

Wang L., et al Correlated electronic phases in twisted bilayer transition metal dichalcogenides. *Nat. Mater.* **19**, 861–866 (2020).

14. 14.

Regan, E. C. et al. Mott and generalized Wigner crystal states in WSe₂/WS₂ moiré superlattices. *Nature* **579**, 359–363 (2020).

15. 15.

Tang, Y. et al. Simulation of Hubbard model physics in WSe₂/WS₂ moiré superlattices. *Nature* **579**, 353 (2020).

16. 16.

Chen, S. et al. Electrically tunable correlated and topological states in twisted monolayer–bilayer graphene. *Nat. Phys.* **17**, 374–380 (2021).

17. 17.

Xu, S. et al. Tunable van Hove singularities and correlated states in twisted monolayer–bilayer graphene. *Nat. Phys.* **17**, 619–626 (2021).

18. 18.

Chen, G. et al. Evidence of a gate-tunable Mott insulator in a trilayer graphene moiré superlattice. *Nat. Phys.* **15**, 237 (2019).

19. 19.

Hao, Z. et al. Electric field–tunable superconductivity in alternating-twist magic-angle trilayer graphene. *Science* **371**, 1133–1138 (2021).

20. 20.

Park, J. M. et al. Tunable strongly coupled superconductivity in magic-angle twisted trilayer graphene. *Nature* **590**, 249–255 (2021).

21. 21.

Kerelsky, A. et al. Maximized electron interactions at the magic angle in twisted bilayer graphene, *Nature* **572**, 95–100 (2019).

22. 22.

Cao, Y. et al. Nematicity and competing orders in superconducting magic-angle graphene. *Science* **372**, 264–271 (2020)

23. 23.

Rubio-Verdú, C. et al. Universal moiré nematic phase in twisted graphitic systems. Preprint at <http://arxiv.org/abs/2009.11645> (2020).

24. 24.

Pan, H., Wu, F. & Das Sarma, S. Band topology, Hubbard model, Heisenberg model, and Dzyaloshinskii-Moriya interaction in twisted bilayer WSe₂. *Phys. Rev. Res.* **2**, 033087 (2020).

25. 25.

Zhang, Z. et al. Flat bands in twisted bilayer transition metal dichalcogenides. *Nat. Phys.* **16**, 1093–1096 (2020).

26. 26.

Cao, Y. et al. Strange metal in magic-angle graphene with near Planckian dissipation *Phys. Rev. Lett.* **124**, 076801 (2020).

27. 27.

Kormányos, A. et al. k.p theory for two-dimensional transition metal dichalcogenide semiconductors. *2D Mater.* **2**, 022001 (2015).

28. 28.

Bruin, J. A. N., Sakai, H., Perry, R. S. & Mackenzie, A. P. Similarity of scattering rates in metals showing T-linear resistivity. *Science* **339**, 804–807 (2013).

29. 29.

Giraldo-Gallo, P. et al. Scale-invariant magnetoresistance in a cuprate superconductor. *Science* **361**, 479–481 (2018).

30. 30.

Hayes, I. M. et al. Scaling between magnetic field and temperature in the high-temperature superconductor $\text{BaFe}_2(\text{As}_{1-x}\text{P}_x)_2$. *Nat. Phys.* **12**, 916–919 (2016).

31. 31.

Movva, H. C. P. et al. Density-dependent quantum Hall states and Zeeman splitting in monolayer and bilayer WSe₂. *Phys. Rev. Lett.* **118**, 247701 (2017).

32. 32.

Motrunich, O. I. Variational study of triangular lattice spin-1/2 model with ring exchanges and spin liquid state in $\kappa-(\text{ET})_2\text{Cu}_2(\text{CN})_3$. *Phys. Rev. B* **72**, 045105 (2005).

33. 33.

Sahébsara, P. & Sénéchal, D. Hubbard model on the triangular lattice: spiral order and spin liquid. *Phys. Rev. Lett.* **100**, 136402 (2008).

34. 34.

Szász, A., Motruk, J., Zaletel, M. P. & Moore, J. E. Chiral spin liquid phase of the triangular lattice Hubbard model: a density matrix renormalization group study. *Phys. Rev. X* **10**, 021042 (2020).

35. 35.

Polshyn, H. et al. Large linear-in-temperature resistivity in twisted bilayer graphene. *Nat. Phys.* **15**, 1011–1016 (2019).

36. 36.

Wu, F., Hwang, E. & Das Sarma, S. Phonon-induced giant linear-in-T resistivity in magic angle twisted bilayer graphene: ordinary strangeness and exotic superconductivity. *Phys. Rev. B* **99**, 165112 (2019).

37. 37.

Sharma, G. et al. Carrier transport theory for twisted bilayer graphene in the metallic regime. Preprint at: <http://arxiv.org/abs/2003.00018> (2020).

38. 38.

Senthil, T. Theory of a continuous Mott transition in two dimensions. *Phys. Rev. B* **78**, 045109 (2008).

39. 39.

Pan, H. & Das Sarma, S. Interaction-driven filling-induced metal-insulator transitions in 2D moiré lattices. *Phys. Rev. Lett.* **127**, 096802 (2021).

40. 40.

Wang, L. et al. One-dimensional electrical contact to a two-dimensional material. *Science* **342**, 614–617 (2013).

41. 41.

Kim, K. van der Waals heterostructures with high accuracy rotational alignment. *Nano Lett.* **16**, 1989–1995 (2016).

42. 42.

Movva, H. C. P. et al. High-mobility holes in dual-gated WSe₂ field-effect transistors. *ACS Nano* **9**, 10402–10410 (2015).

Acknowledgements

We thank J. Cano, A. Georges, C. Varma, T. Uemura, T. Senthil, I. Bozovic, M. Yankowitz, S. Das Sarma, Q. Si, A. Tsvelik, A. Wietek and J. Wang for fruitful discussions. Studies of the quantum critical behaviour of twisted bilayer WSe₂ were supported as part of Programmable Quantum Materials, an Energy Frontier Research Center funded by the US Department of Energy, Office of Science, Basic Energy Sciences, under award DE-SC0019443. The synthesis of the WSe₂ crystals was supported by the National Science Foundation Materials Research Science and Engineering Centers programme through Columbia University in the Center for Precision-Assembled Quantum Materials (DMR-2011738). Support for cryogenic measurements was provided by the Air Force Office of Scientific Research through grant FA9550- 16-1-0601. The Flatiron Institute is a division of the Simons Foundation.

Author information

Author notes

1. Lei Wang

Present address: National Laboratory of Solid-State Microstructures, School of Physics, Nanjing University, Nanjing, China

2. Abhay N. Pasupathy

Present address: Condensed Matter Physics and Materials Science Division, Brookhaven National Laboratory, Upton, NY, USA

Affiliations

1. Department of Physics, Columbia University, New York, NY, USA

Augusto Ghiotto, En-Min Shih, Giancarlo S. S. G. Pereira, Jiawei Zang, Andrew J. Millis, Lei Wang, Cory R. Dean & Abhay N. Pasupathy

2. Department of Mechanical Engineering, Columbia University, New York, NY, USA

Daniel A. Rhodes, Bumho Kim & James C. Hone

3. Center for Computational Quantum Physics, Flatiron Institute, New York, NY, USA

Andrew J. Millis

4. National Institute for Materials Science, Tsukuba, Japan

Kenji Watanabe & Takashi Taniguchi

Contributions

A.G., L.W., E.-M.S. and D.A.R. fabricated the samples. A.G., L.W. and E.-M.S. performed the transport measurements. A.G. and G.S.S.G.P. analysed the data. D.A.R., B.K. and J.H. grew the WSe₂ crystals. K.W. and T.T. grew the hBN crystals. J.Z. and A.J.M. supervised the theoretical aspects of this work. A.G., A.N.P., C.R.D. and A.J.M wrote the manuscript with input from all the authors.

Corresponding authors

Correspondence to Lei Wang or Cory R. Dean or Abhay N. Pasupathy.

Ethics declarations

Competing interests

The authors declare no competing interests.

Additional information

Peer review information *Nature* thanks You Zhou and the other, anonymous, reviewer(s) for their contribution to the peer review of this work.

Publisher's note Springer Nature remains neutral with regard to jurisdictional claims in published maps and institutional affiliations.

Extended data figures and tables

[Extended Data Fig. 1 Quantum critical transport at a twist angle of 4.5 °.](#)

a, color plot of resistivity as a function of temperature and doping. **b**, line cuts showing the regimes of T^2 , T-linear and insulating behaviour as a function of doping.

[Extended Data Fig. 2 Arrhenius fits to resistance.](#)

When our samples show insulating behaviour, they display metal-insulator transition region that is 1-5 K wide. Below the metal-insulator transition, the temperature-dependent resistance displays activated behaviour over 1-2 decades in resistance. Arrhenius fits to extract gap magnitudes are made in this range of temperature. At the lowest temperature, the temperature dependence is often not exponential, likely due to disorder. Shown here is an example of a typical curve that has the insulating temperature dependence described above. The linear fit is defined over a region chosen such that r^2 is maximized (always greater than 0.9).

[Extended Data Fig. 3 Planckian parameter C.](#)

Planckian parameter C defined from fits to T-linear resistivity on a device with twist angle 4.2° and top gate voltage $TG = -6.75V$ and plotted against nominal density v as defined in the text. The insulating regime extends from $v \approx -1.15$ to $v \approx -0.95$.

Extended Data Fig. 4 Anomalous magnetotransport for 4.2° twist sample.

a, Longitudinal and **c**, Hall magnetoresistance as a function of doping density in the metallic regime, approaching the quantum critical point. **b**, Temperature dependence for the same doping range. **d**, Fit coefficient β from $\rho(B) \propto (\sqrt{\gamma + \beta B^2})$ shows a marked increase on approaching the quantum critical point near $v = -1$.

Extended Data Fig. 5 Magnetotransport beyond full filling.

B-quadratic behaviour of **a**, longitudinal resistivity near full-filling. **b**, The Hall effect shows a sign change as is expected when going across bands.

Extended Data Fig. 6 Collapse of the Fermi temperature in the D-driven transition.

Quadratic coefficient versus displacement field at half-filling for the 4.2° sample. The rise of α_Q as one approaches the displacement field-driven metal-insulator transition indicates the collapse of the Fermi temperature similarly to what is observed in the doping-driven transition.

Extended Data Fig. 7 Hartree-Fock calculations at half-filling.

Our Hartree-Fock calculations are based on an effective single-band Hubbard model with on-site interactions with a bandwidth chosen to match DFT calculations of the electronic structure. At zero displacement field, the system goes from paramagnetic metal to 120° antiferromagnetic metal with a first order transition at non-zero U_{c1} , then quickly becomes an insulator at a slightly larger U_{c2} . As the displacement field is applied, the critical U_{c1} to

turn on magnetism decreases first and then increases continuously. The U_{c2} of the metal-insulator transition and the size of the energy gap change in the same manner. Shown here are the energy gap sizes versus displacement field at a twist angle of 5.09° .

Extended Data Fig. 8 Non-magnetism in the insulating gap.

Correlated gap versus B field for different displacement fields for the 4.2° sample. The correlated gap is non-magnetic and eventually closes at higher magnetic fields. When a perpendicular magnetic field is applied, we would expect the insulating gap to increase if the insulator is a ferromagnet, while we would expect it to decrease if it is an antiferromagnetic state or a spin liquid.

Extended Data Fig. 9 Ohmic contacts and twist angle homogeneity.

a, Optical microscope image of the 4.2° sample. **b**, Representative I-V at 200mK for the 4.2° sample indicating good contact quality. Curves are offset for clarity. Dashed lines indicate $V_{xx} = 0$. We find our contact resistances to be between 2 to $10\text{k}\Omega$ for all contacts for the data shown in main figures and that value is fairly temperature independent. We perform a four-probe measurement to minimize the effects of contact resistance. We also monitor the lock-in phase of our low frequency ($\sim 17.7\text{Hz}$) AC measurements to ensure that it is close to zero at all times. **c**, Resistivity curves at 1.6K from two different pairs of leads, they correspond to slightly different twist angles for the two pairs of contacts (4.1° and 4.2°). Crossed out leads indicated high contact resistance. Hall bar channel is $3\mu\text{m}$ wide and $7\mu\text{m}$ long.

Extended Data Fig. 10 Crossover from T-quadratic to T-linear at $v = -0.84$ for 4.2° sample.

An example of our fitting procedures described in our method section is shown here for the doping of $v = -0.84$ (also in the main text figure 3c). We find that the resistivity is fit well ($r^2 = 0.997$) by a T^2 form up to a

temperature of 16.5K, and is fit well ($r^2 = 0.993$) by T– linear form between 16.5 and 47 K. We note that a linear fit between 1.6 and 6 K yields a r^2 of 0.92, clearly worse than the quadratic fit.

Supplementary information

Peer Review File

Rights and permissions

Reprints and Permissions

About this article

Cite this article

Ghiotto, A., Shih, EM., Pereira, G.S.S.G. *et al.* Quantum criticality in twisted transition metal dichalcogenides. *Nature* **597**, 345–349 (2021). <https://doi.org/10.1038/s41586-021-03815-6>

- Received: 17 March 2021
- Accepted: 06 July 2021
- Published: 15 September 2021
- Issue Date: 16 September 2021
- DOI: <https://doi.org/10.1038/s41586-021-03815-6>

Share this article

Anyone you share the following link with will be able to read this content:

[Get shareable link](#)

Sorry, a shareable link is not currently available for this article.

[Copy to clipboard](#)

Provided by the Springer Nature SharedIt content-sharing initiative

This article was downloaded by **calibre** from <https://www.nature.com/articles/s41586-021-03815-6>

| [Section menu](#) | [Main menu](#) |

- Article
- [Published: 15 September 2021](#)

Continuous Mott transition in semiconductor moiré superlattices

- [Tingxin Li¹ na1](#),
- [Shengwei Jiang](#) [ORCID: orcid.org/0000-0001-5213-0139²](#) na1,
- [Lizhong Li¹ na1](#),
- [Yang Zhang](#) [ORCID: orcid.org/0000-0003-4630-5056³](#),
- [Kaifei Kang¹](#),
- [Jiacheng Zhu¹](#),
- [Kenji Watanabe](#) [ORCID: orcid.org/0000-0003-3701-8119⁴](#),
- [Takashi Taniguchi](#) [ORCID: orcid.org/0000-0002-1467-3105⁴](#),
- [Debanjan Chowdhury](#) [ORCID: orcid.org/0000-0003-0758-0282²](#),
- [Liang Fu³](#),
- [Jie Shan](#) [ORCID: orcid.org/0000-0003-1270-9386^{1,2,5}](#) &
- [Kin Fai Mak](#) [ORCID: orcid.org/0000-0002-5768-199X^{1,2,5}](#)

[Nature](#) volume **597**, pages 350–354 (2021)

- 1739 Accesses
- 31 Altmetric
- [Metrics details](#)

Subjects

- [Phase transitions and critical phenomena](#)
- [Quantum simulation](#)
- [Two-dimensional materials](#)

Abstract

The evolution of a Landau Fermi liquid into a non-magnetic Mott insulator with increasing electronic interactions is one of the most puzzling quantum phase transitions in physics^{1,2,3,4,5,6}. The vicinity of the transition is believed to host exotic states of matter such as quantum spin liquids^{4,5,6,7}, exciton condensates⁸ and unconventional superconductivity¹. Semiconductor moiré materials realize a highly controllable Hubbard model simulator on a triangular lattice^{9,10,11,12,13,14,15,16,17,18,19,20,21,22}, providing a unique opportunity to drive a metal–insulator transition (MIT) via continuous tuning of the electronic interactions. Here, by electrically tuning the effective interaction strength in MoTe₂/WSe₂ moiré superlattices, we observe a continuous MIT at a fixed filling of one electron per unit cell. The existence of quantum criticality is supported by the scaling collapse of the resistance, a continuously vanishing charge gap as the critical point is approached from the insulating side, and a diverging quasiparticle effective mass from the metallic side. We also observe a smooth evolution of the magnetic susceptibility across the MIT and no evidence of long-range magnetic order down to ~5% of the Curie–Weiss temperature. This signals an abundance of low-energy spinful excitations on the insulating side that is further corroborated by the Pomeranchuk effect observed on the metallic side. Our results are consistent with the universal critical theory of a continuous Mott transition in two dimensions^{4,23}.

Access options

Subscribe to Journal

Get full journal access for 1 year

\$199.00

only \$3.90 per issue

[Subscribe](#)

All prices are NET prices.
VAT will be added later in the checkout.
Tax calculation will be finalised during checkout.

Rent or Buy article

Get time limited or full article access on ReadCube.

from \$8.99

[Rent or Buy](#)

All prices are NET prices.

Additional access options:

- [Log in](#)
- [Access through your institution](#)
- [Learn about institutional subscriptions](#)

Fig. 1: Bandwidth-tuned metal-insulator transition.



Fig. 2: Continuous Mott transition.



Fig. 3: Quantum critical scaling.



Fig. 4: Magnetic properties near the Mott transition.

Data availability

The source data that support the findings of this study are available with the paper. [Source data](#) are provided with this paper.

References

1. 1.

Imada, M., Fujimori, A. & Tokura, Y. Metal-insulator transitions. *Rev. Mod. Phys.* **70**, 1039–1263 (1998).

2. 2.

Georges, A., Kotliar, G., Krauth, W. & Rozenberg, A. J. Dynamical mean-field theory of strongly correlated fermion system and the limit of infinite dimensions. *Rev. Mod. Phys.* **68**, 13–125 (1996).

3. 3.

Dobrosavljević, V., Trivedi, N. & Valles, J. M. Jr *Conductor-Insulator Quantum Phase Transitions* (Oxford Univ. Press, 2012).

4. 4.

Senthil, T. Theory of a continuous Mott transition in two dimensions. *Phys. Rev. B* **78**, 045109 (2008).

5. 5.

Balents, L. Spin liquids in frustrated magnets. *Nature* **464**, 199–208 (2010).

6. 6.

Mishmash, R. V., González, I., Melko, R. G., Motrunich, O. I. & Fisher, M. P. A. Continuous Mott transition between a metal and a quantum spin liquid. *Phys. Rev. B* **91**, 235140 (2015).

7. 7.

Szasz, A., Motruk, J., Zaletel, M. P. & Moore, J. E. Chiral spin liquid phase of the triangular lattice hubbard model: a density matrix renormalization group study. *Phys. Rev. X* **10**, 021042 (2020).

8. 8.

Qi, Y. & Sachdev, S. Insulator-metal transition on the triangular lattice. *Phys. Rev. B* **77**, 165112 (2008).

9. 9.

Wu, F., Lovorn, T. Tutuc, E. & MacDonald, A. H. Hubbard Model physics in transition metal dichalcogenide moiré bands. *Phys. Rev. Lett.* **121**, 026402 (2018).

10. 10.

Regan, E. C. et al. Mott and generalized Wigner crystal states in WSe₂/WS₂ moiré superlattices. *Nature* **579**, 359–363 (2020).

11. 11.

Tang, Y. et al. Simulation of Hubbard model physics in WSe₂/WS₂ moiré superlattices. *Nature* **579**, 353–358 (2020).

12. 12.

Shimazaki, Y. et al. Strong correlated electrons and hybrid excitons in a moiré heterostructure. *Nature* **580**, 472–477 (2020).

13. 13.

Wang, L. et al. Correlated electronic phases in twisted bilayer transition metal dichalcogenides. *Nat. Mater.* **19**, 861–866 (2020).

14. 14.

Xu, Y. et al. Correlated insulating states at fractional fillings of moiré superlattices. *Nature* **587**, 214–218 (2020).

15. 15.

Jin, C. et al. Stripe phases in WSe₂/WS₂ moiré superlattices. *Nat. Mater.* **20**, 940–944 (2021).

16. 16.

Huang, X. et al. Correlated insulating states at fractional fillings of the WS₂/WSe₂ moiré lattice. *Nat. Phys.* **17**, 715–719 (2021).

17. 17.

Balents, L., Dean, C. R., Efetov, D. K. & Young, A. F. Superconductivity and strong correlations in moiré flat bands. *Nat. Phys.* **16**, 725–733 (2020).

18. 18.

Andrei, E. Y. & MacDonald, A. H. Graphene bilayers with a twist. *Nat. Mater.* **19**, 1265–1275 (2020).

19. 19.

Zhang, Y., Yuan, N. F. Q. & Fu, L. Moiré quantum chemistry: charge transfer in transition metal dichalcogenide superlattices. *Phys. Rev. B* **102**, 201115(R) (2020).

20. 20.

Pan, H., Wu, F. & Das Sarma, S. Quantum phase diagram of a moiré-Hubbard model. *Phys. Rev. B* **102**, 201104(R) (2020).

21. 21.

Morales-Durán, N., Potasz, P. & MacDonald, A. H. Metal-insulator transition in transition metal dichalcogenide heterobilayer moiré superlattices. *Phys. Rev. B* **103**, L241110 (2021).

22. 22.

Pan, H. & Das Sarma, S. Interaction-driven filling-induced metal-insulator transition in 2D moiré lattices. *Phys. Rev. Lett.* **127**, 096802 (2021).

23. 23.

Wietek, A. et al. Mott insulating states with competing orders in the triangular lattice Hubbard model. Preprint at <https://arxiv.org/abs/2102.12904> (2021).

24. 24.

Brinkman, W. F. & Rice, T. M. Application of Gutzwiller's variational method to the metal-insulator transition. *Phys. Rev. B* **2**, 4302–4304 (1970).

25. 25.

Florens, S. & Georges, A. Slave-rotor mean-field theories of strongly correlated systems and the Mott transition in finite dimensions. *Phys. Rev. B* **70**, 035114 (2004).

26. 26.

Yang, H. Y., Läuchli, A. M., Mila, F. & Schmidt, K. P. Effective spin model for the spin-liquid phase of the Hubbard model on the triangular lattice. *Phys. Rev. Lett* **105**, 267204 (2010).

27. 27.

Terletska, H., Vučičević, J., Tanasković, D. & Dobrosavljević, V. Quantum critical transport near the Mott transition. *Phys. Rev. Lett* **107**, 026401 (2011).

28. 28.

Spivak, B., Kravchenko, S. V., Kivelson, S. A. & Gao, X. P. A. *Colloquium: Transport in strongly correlated two dimensional electron fluids.* *Rev. Mod. Phys.* **82**, 1743–1766 (2010).

29. 29.

Vučićević, J., Terletska, H., Tanasković, D. & Dobrosavljević, V. Finite-temperature crossover and the quantum Widom line near the Mott transition. *Phys. Rev. B* **88**, 075143 (2013).

30. 30.

Furukawa, T., Miyagawa, K., Taniguchi, H., Kato, R. & Kanoda, K. Quantum criticality of Mott transition in organic materials. *Nat. Phys.* **11**, 221–242 (2015).

31. 31.

Pustogow, A. et al. Quantum spin liquids unveil the genuine Mott state. *Nat. Mater.* **17**, 773–777 (2018).

32. 32.

Kadowaki, K. & Woods, S. B. Universal relationship of the resistivity and specific heat in heavy-Fermion compounds. *Solid State Comm.* **58**, 507–509 (1986).

33. 33.

Emery, V. J. & Kivelson, S. A. Superconductivity in bad metals. *Phys. Rev. Lett.* **74**, 3253–3256 (1995).

34. 34.

Xiao, D., Liu, G. B., Feng, W., Xu, X. & Yao, W. Coupled spin and valley physics in monolayers of MoS₂ and other group-VI dichalcogenides. *Phys. Rev. Lett.* **108**, 196802 (2012).

35. 35.

Werner, F., Parcollet, O., Georges, A. & Hassan S. R. Interaction-induced adiabatic cooling and antiferromagnetism of cold fermions in optical lattices. *Phys. Rev. Lett.* **95**, 056401 (2005).

36. 36.

MacNeill, D. et al. Breaking of valley degeneracy by magnetic field in monolayer MoSe₂. *Phys. Rev. Lett.* **114**, 037401 (2015).

37. 37.

Abrahams, E., Kravchenko, S. V. & Sarachik, M. P. Metallic behavior and related phenomena in two dimensions. *Rev. Mod. Phys.* **73**, 251–266 (2001).

38. 38.

Wang, Z., Shan, J. & Mak, K. F. Valley- and spin-polarized Landau levels in monolayer WSe₂. *Nat. Nanotechnol.* **12**, 144–149 (2017).

39. 39.

Wang, L. et al. One-dimensional electrical contact to a two-dimensional material. *Science* **342**, 614–617 (2013).

40. 40.

Perdew, J. P., Burke, K. & Ernzerhof, M. Generalized gradient approximation made simple. *Phys. Rev. Lett.* **77**, 3865–3868 (1996).

41. 41.

Grimme, S., Antony, J., Ehrlich, S. & Krieg, H. A consistent and accurate ab initio parametrization of density functional dispersion correction (DFT-D) for the 94 elements H-Pu. *J. Chem.* **132**, 154104 (2010).

42. 42.

Kresse, G. & Furthmüller, J. Efficiency of ab-initio total energy calculations for metals and semiconductors using a plane-wave basis set. *Comp. Mat. Sci.* **6**, 15–50 (1996).

43. 43.

Shabani, S. et al. Deep moiré potentials in twisted transition metal dichalcogenide bilayers. *Nat. Phys.* **17**, 720–725 (2021).

44. 44.

Li, H. et al. Imaging moiré flat bands in three-dimensional reconstructed WSe₂/WS₂ superlattices. *Nat. Mater.* **20**, 945–950 (2021).

45. 45.

Li, T. et al. Charge-order-enhanced capacitance in semiconductor moiré superlattices. *Nature Nanotechnol.* <https://doi.org/10.1038/s41565-021-00955-8> (2021).

46. 46.

Zhang, F. C. & Rice, T. M. Effective Hamiltonian for the superconducting Cu oxides. *Phys. Rev. B* **37**, 3759(R) (1988).

47. 47.

Lee, P. A., Nagaosa, N. & Wen, X. G. Doping a Mott insulator: physics of high-temperature superconductivity. *Rev. Mod. Phys.* **78**, 17–85 (2006).

48. 48.

Yin, J. et al. Dimensional reduction, quantum Hall effect and layer parity in graphite films. *Nat. Phys.* **15**, 437–442 (2019).

49. 49.

Skinner, B. & Shklovskii, B. I. Anomalously large capacitance of a plane capacitor with a two-dimensional electron gas. *Phys. Rev. B* **82**, 155111 (2010).

50. 50.

Xu, Y. et al. Creation of moiré bands in a monolayer semiconductor by spatially periodic dielectric screening. *Nat. Mater.* **20**, 645–649 (2021).

Acknowledgements

We thank V. Dobrosavljevic, E.-A. Kim, A. H. MacDonald, L. Rademaker and S. Todadri for fruitful discussions. Research was primarily supported by the US Department of Energy (DOE), Office of Science, Basic Energy Sciences (BES), under award no. DE-SC0019481 (electrical measurements) and award no. DE-SC0018945 (band structure calculations). The study was partially supported by the National Science Foundation (NSF) under DMR-1807810 (magneto-optical measurements) and the US Army Research Office under grant number W911NF-17-1-0605 (device fabrication).

Growth of the hBN crystals was supported by the Elemental Strategy Initiative of MEXT, Japan and CREST (JPMJCR15F3), JST. This work made use of the Cornell Center for Materials Research Shared Facilities, which are supported through the NSF MRSEC program (DMR-1719875) and the Cornell NanoScale Facility, an NNCI member supported by NSF Grant NNCI-1542081. D.C. acknowledges support from faculty startup grants at Cornell University; K.F.M. acknowledges support from the David and Lucille Packard Fellowship.

Author information

Author notes

1. These authors contributed equally: Tingxin Li, Shengwei Jiang and Lizhong Li

Affiliations

1. School of Applied and Engineering Physics, Cornell University, Ithaca, NY, USA

Tingxin Li, Lihong Li, Kaifei Kang, Jiacheng Zhu, Jie Shan & Kin Fai Mak

2. Laboratory of Atomic and Solid State Physics, Cornell University,
Ithaca, NY, USA

Shengwei Jiang, Debanjan Chowdhury, Jie Shan & Kin Fai Mak

3. Department of Physics, Massachusetts Institute of Technology,
Cambridge, MA, USA

Yang Zhang & Liang Fu

4. National Institute for Materials Science, Tsukuba, Japan

Kenji Watanabe & Takashi Taniguchi

5. Kavli Institute at Cornell for Nanoscale Science, Ithaca, NY, USA

Jie Shan & Kin Fai Mak

Contributions

T.L., S.J. and L.L. fabricated the devices, performed the measurements and analysed the data. K.K. and J.Z. provided assistance in the device fabrication. Y.Z. and L.F. performed the DFT calculations and theoretical analysis. D.C. helped with the theoretical analysis. K.W. and T.T. grew the bulk hBN crystals. T.L., S.J., J.S. and K.F.M. designed the scientific objectives and oversaw the project. All authors discussed the results and commented on the manuscript.

Corresponding authors

Correspondence to Jie Shan or Kin Fai Mak.

Ethics declarations

Competing interests

The authors declare no competing interests.

Additional information

Peer review information *Nature* thanks Lede Xian, You Zhou and the other, anonymous, reviewer(s) for their contribution to the peer review of this work. Peer reviewer reports are available.

Publisher's note Springer Nature remains neutral with regard to jurisdictional claims in published maps and institutional affiliations.

Extended data figures and tables

[Extended Data Fig. 1 Square resistance versus electric field and filling factor.](#)

2D map of the square resistance (in log scale) as a function of electric field and filling factor at 300 mK, converted from the data in Fig. 1c. Electric-field-induced MITs are observed at both filling factor $f=1$ and $f=2$.

[Source data](#)

[Extended Data Fig. 2 Metal-insulator transition at \$f=2\$.](#)

a, Temperature dependence of square resistance at varying electric fields at $f=2$. MIT is observed near 0.49 V nm^{-1} . Compared to the MIT at $f=1$, strong effective mass divergence and the Pomeranchuk effect on the metallic side are not observed. **b**, Magnetoresistance at varying electric fields at 300 mK. Compared to the MIT at $f=1$, magnetic-field-induced metal–insulator transition is not observed.

[Source data](#)

Extended Data Fig. 3 Extraction of activation gap at $f=1$ and Landau Fermi liquid behaviour at low temperatures.

a, Temperature dependence of the square resistance (symbols) at varying electric fields in an Arrhenius plot. Thermal activation behaviour (dashed lines) is observed at high temperatures, from which the activation gaps are extracted. **b**, Square resistance (symbols) as a function of temperature squared at varying electric fields. The dashed lines are fits at low temperatures to $\langle\langle R \rangle\rangle_{\rm square} = R_0 + A T^2$ with fitting parameter R_0 denoting the residual resistance and slope $A \propto (m^*)^2$. The slope increases substantially near the critical electric field. The deviation from the Landau Fermi liquid behaviour at low temperatures very close to the critical point $|E - E_c| < 1$ mV nm⁻¹ is likely to be caused by sample disorders. Typical error bars for the applied electric field are ± 0.2 mV nm⁻¹.

[Source data](#)

Extended Data Fig. 4 Resistance scaling at $f=1$ near the critical point.

a, Temperature dependence of square resistance at varying electric fields in a log–log plot. A power-law dependence $\propto T^{-1.2}$ (dashed line) is observed at the critical electric field. **b**, Electric-field dependence of $\langle\langle \log \rangle\rangle \langle\langle R \rangle\rangle_{\rm square}$ at different temperatures. The inflection points are marked by the colour symbols. The inset shows the temperature dependence of the electric field at the inflection point. The data shows that the Widom line is nearly a vertical line in Fig. 3c

[Source data](#)

Extended Data Fig. 5 Absence of in-plane magnetic field dependence.

Square resistance as a function of bottom gate voltage at varying in-plane magnetic fields. The bottom gate voltage primarily changes the filling

factor $\langle f \rangle$. The electric field is fixed at 3.5 mV nm^{-1} (from $\langle E \rangle_{\langle \rm c \rangle}$) near $f=1$. No in-plane magnetic field dependence is observed due to the strong Ising spin–orbit coupling in monolayer TMDs

[Source data](#).

Extended Data Fig. 6 Pomeranchuk effect at $f=1$.

a, Temperature dependence of square resistance at $f=1$ and near 3.5 mV nm^{-1} above the critical field. **b**, Temperature dependence of the inverse magnetic susceptibility under the same condition as **a**. The susceptibility saturates at low temperatures; it follows the Curie–Weiss dependence (dashed lines) above the crossover from a Fermi liquid to an incoherent metal (denoted by the arrow). **c**, Square resistance as a function of temperature and bottom gate voltage at a fixed top gate voltage. The bottom gate voltage mainly changes the filling factor. The electric field is fixed at 3.5 mV nm^{-1} near the $f=1$ resistance peak (with deviations $< 0.2 \text{ mV nm}^{-1}$, the typical uncertainty in applied electric fields). The $f=1$ resistance peak is absent below $\sim 7 \text{ K}$ (horizontal dashed line), where the $\langle R \rangle_{\langle \rm square \rangle} - T$ dependence at $f=1$ shows Fermi liquid behaviour (**a**). Above $\sim 7 \text{ K}$ but below $\langle T \rangle^{\langle \ast \rangle} \approx 16 \text{ K}$, the $f=1$ resistance peak emerges and the $\langle R \rangle_{\langle \rm square \rangle} - T$ dependence deviates from the Fermi liquid behaviour (but still metallic $\langle \frac{\partial R}{\partial T} \rangle > 0$). The emergence of the resistance peak and the deviation from the Fermi liquid behaviour are correlated with the emergence of local moments (**b**), demonstrating the Pomeranchuk effect. Above $\langle T \rangle^{\langle \ast \rangle} \approx 16 \text{ K}$, the $f=1$ resistance peak remains but the system displays insulating-like behaviour ($\langle \frac{\partial R}{\partial T} \rangle < 0$). The result is fully consistent with the results presented in the main text, where the filling factor is kept constant at $f=1$

[Source data](#).

Extended Data Fig. 7 Spatial homogeneity of device 1.

Two-point current as a function of bottom gate voltage at fixed top gate voltage. The excitation bias voltage is 2 mV. The insulating states at $f=1$ and $f=2$ are seen at different source–drain pairs corresponding to the optical image in Fig. 1b. The slight shift of the insulating states in gate voltage manifests sample inhomogeneity. The two-point resistance also varies from pair to pair, reflecting the variation in contact/sample resistance

[Source data](#).

Extended Data Fig. 8 Major results for device 2.

a, Temperature dependence of the longitudinal resistance at $f=1$ under varying electric fields. The critical electric field is near $\langle\{E\}_{\rm C}\rangle = 0.63 \text{ V nm}^{-1}$. A MIT similar to that in device 1 is observed. **b**, Longitudinal resistance at 1.6 K in logarithmic scale as a function of top and bottom gate voltages. The gate voltages relate to the hole filling factor f and the applied electric field E . Electric-field-induced MIT is observed at $f=1$ and 2. Compared to device 1, there is a higher degree of spatial inhomogeneity in device 2, which prevents reliable scaling analysis near the critical point

[Source data](#).

Extended Data Fig. 9 MCD spectrum under a perpendicular magnetic field of 3 T.

a, Electric-field dependence of the MCD spectrum near the WSe₂ exciton resonance. Resonance enhancement is observed near 1.66 eV. The vertical dashed line marks the photon energy of the probe laser beam used for the MCD measurements in Fig. 4 and the horizontal dashed line marks the critical point for the MIT. **b**, MCD spectra at selected electric fields illustrating the resonance enhancement near the exciton peak

[Source data](#).

Extended Data Fig. 10 Quantum oscillations in the insulating states.

a, Square resistance as a function of bottom gate voltage at 300 mK. The $f = 2$ insulating state is labeled. **b**, Magnetoresistance under a perpendicular magnetic field at selected bottom gate voltages marked by the arrows in **a**. Quantum oscillations due to the nearby graphite gate are observed near the insulating state. The oscillations disappear away from the $f = 2$ insulating state. **c**, Two-terminal magnetoresistance at the $f = 2$ insulating state with a graphite gate about 5 nm separated from the sample. **d**, The same as in **c** except the graphite gate is replaced by a few-layer metallic TaSe₂ gate that is ~3 nm away from the sample. No quantum oscillations are developed in both the TaSe₂ gate and in the sample under magnetic fields up to 9 T. The results verify that the quantum oscillations are originated from the high mobility graphite gate.

[Source data](#)

Supplementary information

Supplementary Information

Supplementary Figs. 1–12 and discussion.

[Peer Review File](#)

Source data

[Source Data Fig. 1](#)

[Source Data Fig. 2](#)

[Source Data Fig. 3](#)

[Source Data Fig. 4](#)

[**Source Data Extended Data Fig. 1**](#)

[**Source Data Extended Data Fig. 2**](#)

[**Source Data Extended Data Fig. 3**](#)

[**Source Data Extended Data Fig. 4**](#)

[**Source Data Extended Data Fig. 5**](#)

[**Source Data Extended Data Fig. 6**](#)

[**Source Data Extended Data Fig. 7**](#)

[**Source Data Extended Data Fig. 8**](#)

[**Source Data Extended Data Fig. 9**](#)

[**Source Data Extended Data Fig. 10**](#)

Rights and permissions

[Reprints and Permissions](#)

About this article

Cite this article

Li, T., Jiang, S., Li, L. *et al.* Continuous Mott transition in semiconductor moiré superlattices. *Nature* **597**, 350–354 (2021).
<https://doi.org/10.1038/s41586-021-03853-0>

- Received: 03 March 2021
- Accepted: 22 July 2021

- Published: 15 September 2021
- Issue Date: 16 September 2021
- DOI: <https://doi.org/10.1038/s41586-021-03853-0>

Share this article

Anyone you share the following link with will be able to read this content:

[Get shareable link](#)

Sorry, a shareable link is not currently available for this article.

[Copy to clipboard](#)

Provided by the Springer Nature SharedIt content-sharing initiative

This article was downloaded by **calibre** from <https://www.nature.com/articles/s41586-021-03853-0>

| [Section menu](#) | [Main menu](#) |

- Article
- [Published: 15 September 2021](#)

Directed assembly of layered perovskite heterostructures as single crystals

- [Michael L. Aubrey^{1 na1}](#),
- [Abraham Saldivar Valdes^{1 na1}](#),
- [Marina R. Filip^{2,3,4}](#),
- [Bridget A. Connor¹](#),
- [Kurt P. Lindquist ORCID: orcid.org/0000-0002-2107-2455¹](#),
- [Jeffrey B. Neaton^{3,4,5}](#) &
- [Hemamala I. Karunadasa ORCID: orcid.org/0000-0003-4949-8068^{1,6}](#)

Nature volume 597, pages 355–359 (2021)

- 2432 Accesses
- 81 Altmetric
- [Metrics details](#)

Subjects

- [Coordination chemistry](#)
- [Materials chemistry](#)
- [Solid-state chemistry](#)

Abstract

The precise stacking of different two-dimensional (2D) structures such as graphene and MoS₂ has reinvigorated the field of 2D materials, revealing exotic phenomena at their interfaces^{1,2}. These unique interfaces are typically constructed using mechanical or deposition-based methods to build a heterostructure one monolayer at a time^{2,3}. By contrast, self-assembly is a scalable technique, where complex materials can selectively form in solution^{4,5,6}. Here we show a synthetic strategy for the self-assembly of layered perovskite–non-perovskite heterostructures into large single crystals in aqueous solution. Using bifunctional organic molecules as directing groups, we have isolated six layered heterostructures that form as an interleaving of perovskite slabs with a different inorganic lattice, previously unknown to crystallize with perovskites. In many cases, these intergrown lattices are 2D congeners of canonical inorganic structure types. To our knowledge, these compounds are the first layered perovskite heterostructures formed using organic templates and characterized by single-crystal X-ray diffraction. Notably, this interleaving of inorganic structures can markedly transform the band structure. Optical data and first principles calculations show that substantive coupling between perovskite and intergrowth layers leads to new electronic transitions distributed across both sublattices. Given the technological promise of halide perovskites⁴, this intuitive synthetic route sets a foundation for the directed synthesis of richly structured complex semiconductors that self-assemble in water.

Access options

Subscribe to Journal

Get full journal access for 1 year

\$199.00

only \$3.90 per issue

[Subscribe](#)

All prices are NET prices.
VAT will be added later in the checkout.

Tax calculation will be finalised during checkout.

Rent or Buy article

Get time limited or full article access on ReadCube.

from \$8.99

[Rent or Buy](#)

All prices are NET prices.

Additional access options:

- [Log in](#)
- [Access through your institution](#)
- [Learn about institutional subscriptions](#)

Fig. 1: Reaction design scheme for targeting templated perovskite intergrowths.

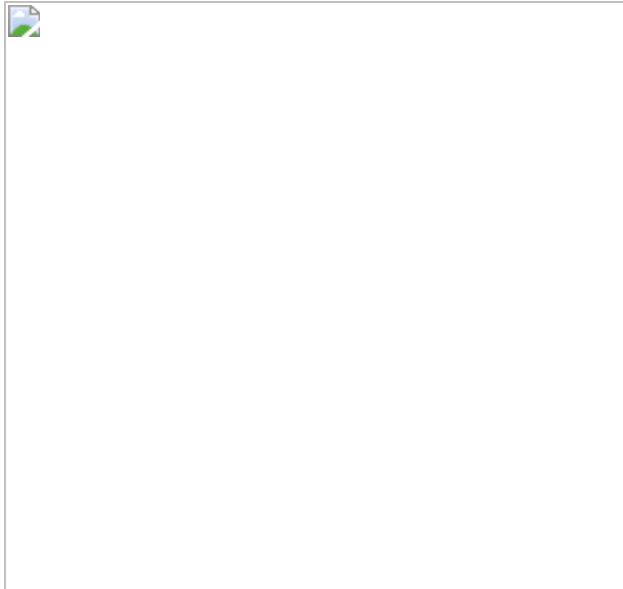


Fig. 2: Oxyacids in the organic layers of perovskites and the exchange of H_3O^+ with Li^+ .

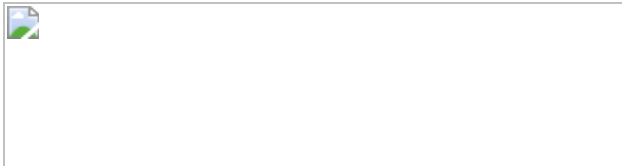


Fig. 3: Conceptualized dimensional reduction of 3D parent structures to afford the layered heterostructures.

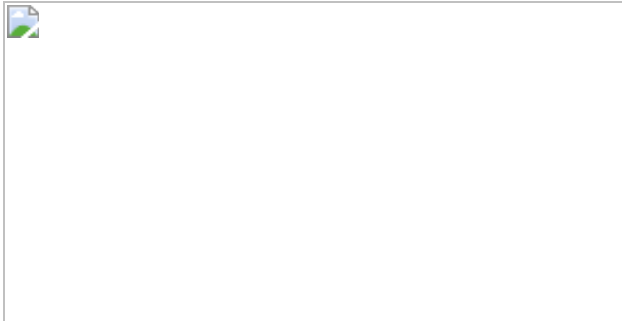
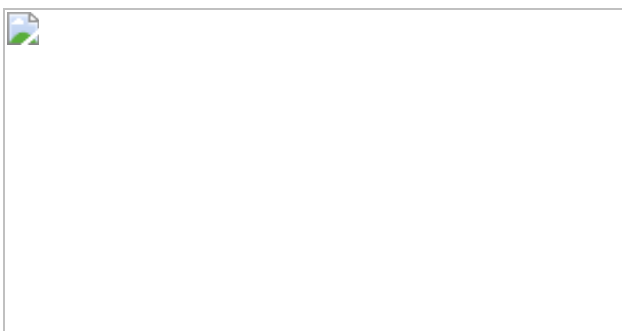


Fig. 4: Comparison of the perovskite-PbX₂ (X = Cl, Br) heterostructures.



Data availability

Additional crystallographic information, powder X-ray diffraction data, optical data, and animated structural relationships between intergrowths and parent structures are available in the [Supplementary Information](#).

Crystallographic information files (CIFs) for the new structures are available from the Cambridge Crystallographic Data Center under reference numbers 1994577–1994579 and 1995031–1995037.

References

1. 1.

Hwang, H. Y. et al. Emergent phenomena at oxide interfaces. *Nat. Mater.* **11**, 103–113 (2012).

2. 2.

Novoselov, K. S., Mishchenko, A., Carvalho, A. & Neto, A. H. C. 2D materials and van der Waals heterostructures. *Science* **353**, aac9439 (2016).

3. 3.

Wong, F. J. & Ramanathan, S. Nonisostructural complex oxide heteroepitaxy. *J. Vac. Sci. Technol. A* **32**, 040801–040817 (2014).

4. 4.

Saparov, B. & Mitzi, D. B. Organic–inorganic perovskites: structural versatility for functional materials design. *Chem. Rev.* **116**, 4558–4596 (2016).

5. 5.

Li, J., Chen, Z., Wang, R.-J. & Proserpio, D. M. Low temperature route towards new materials: solvothermal synthesis of metal chalcogenides in ethylenediamine. *Coord. Chem. Rev.* **190**, 707–735 (1999).

6. 6.

Lobo, R. F., Zones, S. I. & Davis, M. E. Structure-direction in zeolite synthesis. *J. Incl. Phenom. Mol. Recognit. Chem.* **21**, 47–78 (1995).

7. 7.

Rao, C. N. R. & Thomas, J. M. Intergrowth structures: the chemistry of solid-solid interfaces. *Acc. Chem. Res.* **18**, 113–119 (2002).

8. 8.

Schaak, R. E. & Mallouk, T. E. Perovskites by design: a toolbox of solid-state reactions. *Chem. Mater.* **14**, 1455–1471 (2002).

9. 9.

Viciu, L., Koenig, J., Spinu, L., Zhou, W. L. & Wiley, J. B. Insertion of a two-dimensional iron-chloride network between perovskite blocks. Synthesis and characterization of the layered oxyhalide, $(\text{FeCl})\text{LaNb}_2\text{O}_7$. *Chem. Mater.* **15**, 1480–1485 (2003).

10. 10.

Tulsky, E. G. & Long, J. R. Dimensional reduction: a practical formalism for manipulating solid structures. *Chem. Mater.* **13**, 1149–1166 (2001).

11. 11.

Shi, E. et al. Two-dimensional halide perovskite lateral epitaxial heterostructures. *Nature* **580**, 614–620 (2020).

12. 12.

Mercier, N. & Riou, A. An organic–inorganic hybrid perovskite containing copper paddle-wheel clusters linking perovskite layers: $[\text{Cu}(\text{O}_2\text{C}-(\text{CH}_2)_3-\text{NH}_3)_2]\text{PbBr}_4$. *Chem. Commun.* **123**, 844–845 (2004).

13. 13.

AlShammari, M. B. et al. Phase transitions, optical and electronic properties of the layered perovskite hybrid $[\text{NH}_3(\text{CH}_2)_2\text{COOH}]_2\text{CdCl}_4$ of γ -aminobutyric acid (GABA). *Chem. Phys. Lett.* **702**, 8–15 (2018).

14. 14.

Spencer, J. B. & Lundgren, J.-O. Hydrogen bond studies. LXXIII.* The crystal structure of trifluoromethanesulphonic acid monohydrate,

$\text{H}_3\text{O}^+\text{CF}_3\text{SO}_3^-$, at 298 and 83°K. *Acta Crystallogr. B* **29**, 1923–1928 (1973).

15. 15.

King, E. J. The ionization constants of taurine and its activity coefficient in hydrochloric acid solutions from electromotive force measurements. *J. Am. Chem. Soc.* **75**, 2204–2209 (1953).

16. 16.

Pietraszko, A. & Lukaszewicz, K. Crystal structure of α - LiNH_4SO_4 in the basic polytypic modification. *Pol. J. Chem.* **66**, 2057–2061 (1992).

17. 17.

Nord, A. G. Crystal structure of β - Li_2SO_4 . *Acta Crystallogr. B* **32**, 982–983 (1976).

18. 18.

Doudin, B. & Chapuis, G. Structure analysis of the high-temperature phases of $[\text{NH}_3(\text{C}_3\text{H}_7)]_2\text{CuCl}_4$. I. The commensurate phases. *Acta Crystallogr. B* **46**, 175–180 (1990).

19. 19.

Komornicka, D., Wołcyrz, M. & Pietraszko, A. Polymorphism and polytypism of α - LiNH_4SO_4 crystals. Monte Carlo modeling based on X-ray diffuse scattering. *Cryst. Growth Des.* **14**, 5784–5793 (2014).

20. 20.

Macíček, J., Gradišarov, S., Bontchev, R. & Balarew, C. A short dynamically symmetrical hydrogen bond in the structure of $\text{K}[\text{Mg}(\text{H}_{0.5}\text{SO}_4)_2(\text{H}_2\text{O})_2]$. *Acta Crystallogr. C* **50**, 1185–1188 (1994).

21. 21.

Rentzepelis, P. J. & Soldatos, C. T. The crystal structure of the anhydrous magnesium sulphate. *Acta Crystallogr.* **11**, 686–688 (1958).

22. 22.

Wolf, N. R., Connor, B. A., Slavney, A. H. & Karunadasa, H. Doubling the stakes: the promise of halide double perovskites. *Angew. Chem. Int. Ed.* **60**, 16264–16278 (2021).

23. 23.

Subramanian, L. & Hoffmann, R. Bonding in halocuprates. *Inorg. Chem.* **31**, 1021–1029 (1992).

24. 24.

Plasseraud, L., Cattey, H. & Richard, P. Isolation and X-ray characterization of $\{[\text{phthalazinium}](\text{CuCl}_2)\}_{\infty}$: a new example of a dichlorocuprate(I) presenting a rare staircase chain structure. *Z. Naturforschung B* **65**, 317–322 (2010).

25. 25.

Lumbreras, M. Structure and ionic conductivity of mixed lead halides $\text{PbCl}_{2x}\text{Br}_{2(1-x)}$. II. *Solid State Ion.* **20**, 295–304 (1986).

26. 26.

Meresse, A. & Daoud, A. Bis(*n*-propylammonium) tetrachloroplumbate. *Acta Crystallogr. C* **45**, 194–196 (1989).

27. 27.

Kamminga, M. E. et al. Confinement effects in low-dimensional lead iodide perovskite hybrids. *Chem. Mater.* **28**, 4554–4562 (2016).

28. 28.

Smith, M. D., Connor, B. A. & Karunadasa, H. I. Tuning the luminescence of layered halide perovskites. *Chem. Rev.* **119**, 3104–3139 (2019).

29. 29.

Hybertsen, M. S. & Louie, S. G. Electron correlation in semiconductors and insulators: band gaps and quasiparticle energies. *Phys. Rev. B* **34**, 5390–5413 (1986).

30. 30.

Rohlfing, M. & Louie, S. G. Electron-hole excitations in semiconductors and insulators. *Phys. Rev. Lett.* **81**, 2312–2315 (1998).

31. 31.

Rohlfing, M. & Louie, S. G. Electron-hole excitations and optical spectra from first principles. *Phys. Rev. B* **62**, 4927–4944 (2000).

32. 32.

Strinati, G. Application of the Green's functions method to the study of the optical properties of semiconductors. *Riv. Nuovo Cimento* **11**, 1–86 (1988).

33. 33.

Rivera, P. et al. Interlayer valley excitons in heterobilayers of transition metal dichalcogenides. *Nat. Nanotechnol.* **13**, 1004–1015 (2018).

34. 34.

Stokes, H. T., Hatch, D. M. & Campbell, B. J. ISODISTORT, ISOTROPY software suite, <https://iso.byu.edu> (2020).

35. 35.

Campbell, B. J., Stokes, H. T., Tanner, D. E. & Hatch, D. M. ISODISPLACE: a web-based tool for exploring structural distortions. *J. Appl. Crystallogr.* **39**, 607–614 (2006).

36. 36.

Brese, N. E. & O’Keeffe, M. Bond-valence parameters for solids. *Acta Crystallogr. B* **47**, 192–197 (1991).

37. 37.

Slater, J. C. Atomic radii in crystals. *J. Chem. Phys.* **41**, 3199–3204 (1964).

38. 38.

Earnshaw, A. & Greenwood, N. N. *Chemistry of the Elements* 367–405 (Elsevier, 1997).

39. 39.

SAINT and SADABS 8.38A (Bruker AXS, 2017).

40. 40.

Sheldrick, G. M. SHELXT – integrated space-group and crystal-structure determination. *Acta Crystallogr. A* **71**, 3–8 (2015).

41. 41.

Sheldrick, G. M. Crystal structure refinement with SHELXL. *Acta Crystallogr. C* **71**, 3–8 (2015).

42. 42.

Dolomanov, O. V., Bourhis, L. J., Gildea, R. J., Howard, J. A. K. & Puschmann, H. OLEX2: a complete structure solution, refinement and analysis program. *J. Appl. Crystallogr.* **42**, 339–341 (2009).

43. 43.

Toby, B. H. & Von Dreele, R. B. GSAS-II: the genesis of a modern open-source all purpose crystallography software package. *J. Appl. Crystallogr.* **46**, 544–549 (2013).

44. 44.

Momma, K. & Izumi, F. VESTA 3 for three-dimensional visualization of crystal, volumetric and morphology data. *J. Appl. Crystallogr.* **44**, 1272–1276 (2011).

45. 45.

Hohenberg, P. & Kohn, W. Inhomogeneous electron gas. *Phys. Rev.* **136**, B864–B871 (1964).

46. 46.

Perdew, J. P., Burke, K. & Ernzerhof, M. Generalized gradient approximation made simple. *Phys. Rev. Lett.* **77**, 3865–3868 (1996).

47. 47.

Giannozzi, P. et al. QUANTUM ESPRESSO: a modular and open-source software project for quantum simulations of materials. *J. Phys. Condens. Matter* **21**, 395502 (2009).

48. 48.

Giannozzi, P. et al. Advanced capabilities for materials modelling with quantum ESPRESSO. *J. Phys. Condens. Matter* **29**, 465901 (2017).

49. 49.

van Setten, M. J. et al. The PseudoDojo: Training and grading a 85 element optimized norm-conserving pseudopotential table. *Comput. Phys. Commun.* **226**, 39–54 (2018).

50. 50.

Deslippe, J. et al. BerkeleyGW: A massively parallel computer package for the calculation of the quasiparticle and optical properties of materials and nanostructures. *Comput. Phys. Commun.* **183**, 1269–1289 (2012).

51. 51.

Del Ben, M. et al. Large-scale GW calculations on pre-exascale HPC systems. *Comput. Phys. Commun.* **235**, 187–195 (2019).

52. 52.

Del Ben, M. D. et al. Accelerating large-scale excited-state GW calculations on leadership HPC systems. In *SC20 Int. Conf. High Performance Computing, Networking, Storage and Analysis*, <https://doi.org/10.1109/SC41405.2020.00008> (IEEE, 2020).

53. 53.

Connor, B. A. et al. Alloying a single and a double perovskite: a Cu⁺²⁺ mixed-valence layered halide perovskite with strong optical absorption. *Chem. Sci.* **12**, 8689–8697 (2021).

54. 54.

Depmeier, V. W. Die Kristallstruktur von Athylammoniumtetrachloromanganat(II) bei Raumtemperatur. *Acta Crystallogr. B* **32**, 303–305 (1976).

55. 55.

Dou, L. et al. Atomically thin two-dimensional organic-inorganic hybrid perovskites. *Science* **349**, 1518–1521 (2015).

Acknowledgements

This work was funded by the US Department of Energy (DOE), Office of Basic Energy Sciences, Division of Materials Sciences and Engineering, under contract DE-AC02-76SF00515. M.L.A. is supported by an EERE (Office of Energy Efficiency and Renewable Energy) postdoctoral fellowship and B.A.C. is supported by a National Science Foundation (NSF) graduate fellowship (DGE-114747) and the McBain award from Stanford Chemistry. K.P.L. thanks the Center for Molecular Analysis and Design at Stanford University for a graduate fellowship and Stanford Chemistry for the William S. Johnson award. SC-XRD studies were performed either at the Advanced Light Source (beamline 11.3.1) at the Lawrence Berkeley National Laboratory (LBNL) or at Stanford Nano Shared Facilities, supported by the NSF (award ECCS-1542152). We thank S. Teat for helpful discussion and M. Smith and E. Crace for experimental assistance. DFT calculations were supported by the US DOE, Office of Basic Energy Sciences, Division of Materials Sciences and Engineering (Theory FWP), under contract no. DE-AC02-05CH11231. We acknowledge computational resources at the Molecular Foundry, supported by the Office of Science, Office of Basic Energy Sciences, of the US DOE under contract DE-AC02-5CH11231, at the National Energy Research Scientific Computing Center (NERSC; Cori), at the Oak Ridge Leadership Computing Facility (Summit) accessed through the INCITE program (a DOE Office of Science User Facility; grant number DE-AC05-00OR22725), and the Texas Advanced Computing Center (TACC; Stampede 2) through an XSEDE Award (DMR190070) supported by the NSF grant number ACI-1548562.

Author information

Author notes

1. These authors contributed equally: Michael L. Aubrey and Abraham Saldivar Valdes

Affiliations

1. Department of Chemistry, Stanford University, Stanford, CA, USA

Michael L. Aubrey, Abraham Saldivar Valdes, Bridget A. Connor, Kurt P. Lindquist & Hemamala I. Karunadasa

2. Department of Physics, University of Oxford, Oxford, UK

Marina R. Filip

3. Department of Physics, University of California Berkeley, Berkeley, CA, USA

Marina R. Filip & Jeffrey B. Neaton

4. Materials Sciences Division, Lawrence Berkeley National Laboratory, Berkeley, CA, USA

Marina R. Filip & Jeffrey B. Neaton

5. Kavli Energy NanoSciences Institute at Berkeley, Berkeley, CA, USA

Jeffrey B. Neaton

6. Stanford Institute for Materials and Energy Sciences, SLAC National Accelerator Laboratory, Menlo Park, CA, USA

Hemamala I. Karunadasa

Contributions

The authors M.L.A., A.S.V. and B.A.C. synthesized and structurally characterized the materials. M.L.A. and K.P.L. performed the optical measurements. H.I.K. defined and guided the project direction. M.R.F. and J.B.N. conducted the electronic structure calculations and theoretical analyses. All authors helped write the manuscript.

Corresponding author

Correspondence to Hemamala I. Karunadasa.

Ethics declarations

Competing interests

Stanford University has submitted a provisional patent application on this work with H.I.K., M.L.A. and A.S.V. as co-inventors.

Additional information

Peer review information *Nature* thanks the anonymous reviewers for their contribution to the peer review of this work.

Publisher's note Springer Nature remains neutral with regard to jurisdictional claims in published maps and institutional affiliations.

Extended data figures and tables

[Extended Data Fig. 1 The crystal structure of \$\text{RPO\(OH\)}_2\text{CuCl}_4\$ viewed along the *c*-axis highlighting the hydrogen bond network in the organic bilayer.](#)

Carbon bonded hydrogens are not shown for clarity. Each phosphonic acid donates two hydrogen bonds and accepts two hydrogen bonds at the unprotonated oxygen atom. Each phosphonic acid hydrogen bonds only to phosphonic acid groups on the opposing face of the organic bilayer to form the checkerboard pattern illustrated. The elements P, C, H, N and O are coloured pink, grey, white, blue and red, respectively.

[Extended Data Fig. 2 Schematic illustrating the templating of a hydronium sulfonate between layers of a \$\text{CuCl}_4^{2-}\$ -perovskite sublattice.](#)

a, The archetypal parent 3D perovskite with the relevant slice highlighted. The parent structure RbCuCl_3 is unknown though RbCuF_3 is known. **b**, The

dimensionally reduced product of a copper chloride perovskite as isolated in the single-crystal structure of (propylammonium)₂CuCl₄ and the previously reported layered crystal structure of hydronium triflate. Structure directing functional groups are highlighted in blue (ammonium) and red (sulfonate). **c**, The same interactions from **b** are shown in the compound (H₃O)₂(taurine)₂CuCl₄. The elements Cu, Cl, C, H, N, S, O and F are coloured dark-green, green, grey, white, blue, yellow, red and lime-green, respectively.

Extended Data Fig. 3 Structural comparison between intergrowths and layered reference structures.

a, b, The slab for the magnesium intergrowth in (Mg(H₂O)₂) (taurine)₂CuCl₄ (**a**) and the reference structure KMg(H_{0.5}SO₄)₂•2(H₂O) (**b**). **c, d**, The slab for the lithium intergrowth in Li₂(taurine)₂CuCl₄ (**c**) and the reference structure α -Li(NH₄)SO₄ (**d**). Mg, Li, S, O and H atoms are shown as green, light blue, yellow, red and white spheres, respectively.

Extended Data Fig. 4 Schematic illustrating the templating of a heterostructure with CuInCl₈ double perovskite layers and anionic chains of CuCl₂¹⁻.

a, The parent layered structure (PEA)₄CuInCl₈ and 1D chain structure (phthalazinium)CuCl₂ crystallize with structure directing hydrogen bonds between the organic molecules and the inorganic sublattices highlighted in blue and yellow, respectively. **b**, The corresponding interactions are highlighted in the templated layered heterostructure (CuCl₂)₄(HIS)₄CuInCl₈. Cu, In, Cl, C and N atoms are coloured gold, light-grey, lime-green, grey and blue, respectively. Some H atoms are omitted for clarity.

Extended Data Fig. 5 Schematic illustrating the templating of heterostructures containing layered lead-halide perovskites and

layers derived from (001) slices of the PbX₂ (X = Cl, Br) structure-type.

a, b, The parent 3D inorganic structures with relevant slices highlighted (**a**) and their dimensionally reduced progeny (**b**). Note dimensionally reduced (001) slices of PbX₂ have not been isolated outside of the layered heterostructures reported here. Structure directing alkylammonium groups are highlighted in blue and substitution sites for the coordinating ether and sulfide groups in the heterostructures are highlighted in yellow. **c,** The location of these same templating groups and substitution sites are highlighted in the templated layered heterostructures (PbBr₂)₂(AMTP)₂PbBr₄ and (Pb₂Cl₂)(CYS)₂PbCl₄. Pb, Cl, Br, C, N, O and S atoms are coloured light-blue, green, orange, grey, blue, red and yellow, respectively. H atoms are omitted for clarity.

Extended Data Fig. 6 Structural comparison between lead-halide intergrowths and slices of the 3D reference structure.

a–c, Face-on comparisons of the (001) slab of PbCl₂ (**a**)—which is isostructural to that of PbBr₂—to the intergrowth sublattices in (Pb₂Cl₂)(CYS)₂PbCl₄ (**b**) and (PbBr₂)₂(AMTP)₂PbBr₄ (**c**). The atoms Pb, Cl, S, Br and O atoms are shown as light-blue, green, yellow, orange and red spheres, respectively.

Extended Data Fig. 7 Comparison between the crystal structure and the structural model used in electronic structure calculations.

a, The crystal structure of (Pb₂Cl₂)(CYS)₂PbCl₄. **b,** The structural model used for calculation of absorption spectra and electron–hole interactions with half the unit-cell volume. Disordered atoms in **a** are resolved and hydrogen atoms in **b** are removed for clarity. Both structures are viewed along the *c* axis. Unit-cell borders are shown in red. The atoms Pb, Cl, C, N and S are coloured light-blue, green, grey, blue and yellow, respectively.

Extended Data Table 1 Summary of lattice strains estimated for the intergrowth slabs relative to non-intergrowth parent structures

Extended Data Table 2 Summary of lattice strains estimated for perovskite slabs relative to non-intergrowth parent structures

Extended Data Table 3 Relative strain tensors for the perovskite slabs

Extended Data Table 4 Relative strain tensors for the intergrowth slabs

Supplementary information

Supplementary Information

Powder diffraction, crystallographic tables, and supplementary spectra.

Supplementary Data

CIF (Crystallographic information file) for the compounds (3-(ammoniopropyl)-phosphonic acid)₂CuCl₄, (4-(ammoniomethyl)-benzoic acid)₂CuCl₄, (phenethylammonium)₂CuInCl₈, (PbBr₂)₂(AMTP)₂PbBr₄, (Pb₂Cl₂)(CYS)₂PbCl₄, (Mg(H₂O)₂)(taurine)₂CuCl₄, Li₂(taurine)₂MnCl₄, Li₂(taurine)₂CuCl₄, (H₃O)₂(taurine)₂CuCl₄, (CuCl₂)₄(HIS)₄CuInCl₈.

Supplementary Video 1

Animation illustrating relative atom displacements to relate the intergrowth sublattice in (H₃O)₂(taurine)₂CuCl₄ to the non-intergrowth parent structure in Extended Data Table 1.

Supplementary Video 2

Animation illustrating relative atom displacements to relate the intergrowth sublattice in Li₂(taurine)₂CuCl₄ to the non-intergrowth parent structure in Extended Data Table 1.

Supplementary Video 3

Animation illustrating relative atom displacements to relate the intergrowth sublattice in $\text{Li}_2(\text{taurine})_2\text{MnCl}_4$ to the non-intergrowth parent structure in Extended Data Table 1.

Supplementary Video 4

Animation illustrating relative atom displacements to relate the intergrowth sublattice in $(\text{Mg}(\text{H}_2\text{O})_2)(\text{taurine})_2\text{CuCl}_4$ to the non-intergrowth parent structure in Extended Data Table 1.

Supplementary Video 5

Animation illustrating relative atom displacements to relate the intergrowth sublattice in $(\text{CuCl}_2)_4(\text{HIS})_4\text{CuInCl}_8$ to the non-intergrowth parent structure in Extended Data Table 1.

Supplementary Video 6

Animation illustrating relative atom displacements to relate the intergrowth sublattice in $(\text{Pb}_2\text{Cl}_2)(\text{CYS})_2\text{PbCl}_4$ to the non-intergrowth parent structure in Extended Data Table 1. This is the same animation as in Supplementary Video 7 viewed along [001].

Supplementary Video 7

Animation illustrating relative atom displacements to relate the intergrowth sublattice in $(\text{Pb}_2\text{Cl}_2)(\text{CYS})_2\text{PbCl}_4$ to the non-intergrowth parent structure in Extended Data Table 1. This is the same animation as in Supplementary Video 6 viewed along [100].

Supplementary Video 8

Animation illustrating relative atom displacements to relate the intergrowth sublattice in $(\text{PbBr}_2)_2(\text{AMTP})_2\text{PbBr}_4$ to the non-intergrowth parent

structure in Extended Data Table 1. This is the same animation as in Supplementary Video 9 viewed along [001].

Supplementary Video 9

Animation illustrating relative atom displacements to relate the intergrowth sublattice in $(\text{PbBr}_2)_2(\text{AMTP})_2\text{PbBr}_4$ to the non-intergrowth parent structure in Extended Data Table 1. This is the same animation as in Supplementary Video 8 viewed along [100].

Rights and permissions

Reprints and Permissions

About this article

Cite this article

Aubrey, M.L., Saldivar Valdes, A., Filip, M.R. *et al.* Directed assembly of layered perovskite heterostructures as single crystals. *Nature* **597**, 355–359 (2021). <https://doi.org/10.1038/s41586-021-03810-x>

- Received: 22 April 2020
- Accepted: 07 July 2021
- Published: 15 September 2021
- Issue Date: 16 September 2021
- DOI: <https://doi.org/10.1038/s41586-021-03810-x>

Share this article

Anyone you share the following link with will be able to read this content:

[Get shareable link](#)

Sorry, a shareable link is not currently available for this article.

[Copy to clipboard](#)

Provided by the Springer Nature SharedIt content-sharing initiative

Triple-decker layered perovskite materials

- Roman Krahne
- Milena P. Arciniegas

News & Views 15 Sept 2021

This article was downloaded by **calibre** from <https://www.nature.com/articles/s41586-021-03810-x>

| [Section menu](#) | [Main menu](#) |

- Article
- [Published: 15 September 2021](#)

Environmental performance of blue foods

- [Jessica A. Gephart](#) [ORCID: orcid.org/0000-0001-6836-9291](#)¹ nal,
- [Patrik J. G. Henriksson](#) [ORCID: orcid.org/0000-0002-3439-623X](#)^{2,3,4} nal,
- [Robert W. R. Parker](#)^{5,6} nal,
- [Alon Shepon](#)^{7,8,9} nal,
- [Kelvin D. Gorospe](#)¹,
- [Kristina Bergman](#) [ORCID: orcid.org/0000-0001-5888-4943](#)¹⁰,
- [Gidon Eshel](#) [ORCID: orcid.org/0000-0001-5422-9968](#)¹¹,
- [Christopher D. Golden](#) [ORCID: orcid.org/0000-0002-2258-7493](#)^{9,12,13},
- [Benjamin S. Halpern](#) [ORCID: orcid.org/0000-0001-8844-2302](#)^{14,15},
- [Sara Hornborg](#) [ORCID: orcid.org/0000-0003-0814-5258](#)¹⁰,
- [Malin Jonell](#) [ORCID: orcid.org/0000-0002-1813-7684](#)^{2,4,16},
- [Marc Metian](#)¹⁷,
- [Kathleen Mifflin](#)⁵,
- [Richard Newton](#)¹⁸,
- [Peter Tyedmers](#) [ORCID: orcid.org/0000-0002-5150-0756](#)⁵,
- [Wenbo Zhang](#) [ORCID: orcid.org/0000-0003-3765-3980](#)¹⁹,
- [Friederike Ziegler](#)¹⁰ &
- [Max Troell](#) [ORCID: orcid.org/0000-0002-7509-8140](#)^{2,4}

[Nature](#) volume 597, pages 360–365 (2021)

- 4589 Accesses
- 152 Altmetric
- [Metrics details](#)

Subjects

- [Environmental impact](#)
- [Sustainability](#)

Abstract

Fish and other aquatic foods (blue foods) present an opportunity for more sustainable diets^{1,2}. Yet comprehensive comparison has been limited due to sparse inclusion of blue foods in environmental impact studies^{3,4} relative to the vast diversity of production⁵. Here we provide standardized estimates of greenhouse gas, nitrogen, phosphorus, freshwater and land stressors for species groups covering nearly three quarters of global production. We find that across all blue foods, farmed bivalves and seaweeds generate the lowest stressors. Capture fisheries predominantly generate greenhouse gas emissions, with small pelagic fishes generating lower emissions than all fed aquaculture, but flatfish and crustaceans generating the highest. Among farmed finfish and crustaceans, silver and bighead carps have the lowest greenhouse gas, nitrogen and phosphorus emissions, but highest water use, while farmed salmon and trout use the least land and water. Finally, we model intervention scenarios and find improving feed conversion ratios reduces stressors across all fed groups, increasing fish yield reduces land and water use by up to half, and optimizing gears reduces capture fishery emissions by more than half for some groups. Collectively, our analysis identifies high-performing blue foods, highlights opportunities to improve environmental performance, advances data-poor environmental assessments, and informs sustainable diets.

Main

The food system is a major driver of environmental change, emitting a quarter of all greenhouse gas (GHG) emissions, occupying half of all ice-free land, and responsible for three quarters of global consumptive water use and eutrophication^{3,6}. Yet, it still fails to meet global nutrition needs⁷, with 820 million people lacking sufficient food⁸ and with one in three people globally overweight or obese⁹. As a critical source of nutrition^{8,10} generating relatively low average environmental pressures^{1,2,11,12}, blue foods present an opportunity to improve nutrition with lower environmental burdens, in line with the Sustainable Development Goals to improve nutrition (Goal 2), ensure sustainable consumption and production (Goal 12), and sustainably use marine resources (Goal 14).

Blue foods, however, are underrepresented in food system environmental assessments¹³ and the stressors considered are limited⁴ such that we have some understanding of GHG emissions^{14,15}, but less of others such as land or freshwater use¹⁶. Where blue foods are included, they are typically represented by only one or a few broad categories (see, for example, refs. ^{3,17,18}), masking the vast diversity within blue food production. Finally, estimates combining results of published life cycle

assessments undertaken for different purposes, and consequently using incompatible methodologies^{19,20}, cannot be compared reliably. It is therefore critical to examine the environmental performance across the diversity of blue foods in a robust, methodologically consistent manner to serve as a benchmark within the rapidly evolving sector as blue food demand increases²¹, production shifts toward aquaculture and production technologies advance.

Here, we provide standardized estimates of GHG emissions, consumptive freshwater use (water use), terrestrial land occupation (land use), and nitrogen (N) and phosphorus (P) emissions for blue foods, reported per tonne of edible weight. We identify a set of key life cycle inventory data (that is, material and energy input, and farm-level performance data) from published studies and datasets to which a harmonized methodology is applied. We draw on studies that collectively report data from over 1,690 farms and 1,000 unique fishery records around the world. The 23 species groups represented in our results cover over 70% of global blue food production. We then discuss environmental impacts not covered by the standard stressors, most notably biodiversity loss. Finally, we leverage our model to identify and quantify improvement opportunities and discuss public and private policy options to realize these improvements. In doing so, these results help to identify current and future opportunities for blue foods within sustainable diets.

Blue food environmental stressors

Reducing food system GHG emissions is central to meeting global emission targets⁸. Fed aquaculture emissions result primarily from feeds²², while fuel use drives capture fisheries emissions¹¹. Across assessed blue foods, farmed seaweeds and bivalves generate the lowest emissions, followed by small pelagic capture fisheries, while flatfish and crustacean fisheries produce the highest (Fig. 1). For fed aquaculture, feed production is responsible for more than 70% of emissions for most groups (Supplementary Fig. 6). Farmed bivalves and shrimp produce lower average emissions than their capture counterparts (bivalves, 1,414 versus 11,400 kgCO₂e t⁻¹ (kilograms of CO₂ equivalent per tonne); shrimps, 9,428 versus 11,956 kgCO₂e t⁻¹), while salmon/trout are similar whether farmed or fished (5,101–5,410 versus 6,881 kgCO₂e t⁻¹).

Fig. 1: Stressor posterior distributions.

 **figure1**

a, Aquaculture GHG emissions ($\text{kgCO}_2\text{e t}^{-1}$). **b**, Aquaculture N (kgNe t^{-1}). **c**, Aquaculture P (kgPe t^{-1}). **d**, Capture GHG emissions ($\text{kgCO}_2\text{e t}^{-1}$) **e**, Aquaculture Water use ($\text{m}^3 \text{t}^{-1}$). **f**, Aquaculture land use ($\text{m}^2\text{a t}^{-1}$). Values represent tonnes of edible weight and use mass allocation. Dot indicates the median, coloured regions show credible intervals (that is, range of values that have a 95% (light), 80% and 50% (dark) probability of containing the true parameter value). Beige bands represent estimated chicken minimum to maximum range. See Supplementary Fig 10 for estimates expressed in terms of live weight [Source data](#).

Land use, especially conversion of natural areas, results in a range of context-dependent biodiversity impacts and GHG emissions²³ and creates potential trade-offs with alternate uses, including production of other foods. On-farm land use is low (<1,000 m^2 annual terrestrial land occupation per tonne, $\text{m}^2\text{a t}^{-1}$; <10%) for most systems and highest (3,737–8,689 $\text{m}^2\text{a t}^{-1}$) for extensive ponds (for example, milkfish, shrimp and silver and bighead carp). Generally, most land use is associated with feed production for fed systems and explains the overall rankings (Fig. 1), though milkfish uses the highest amount of on- and off-farm land.

Freshwater increasingly constrains agriculture production but capture fisheries and unfed mariculture require little to no freshwater²⁴. Although blue foods are produced in water, consumptive freshwater use is largely limited to feed production and on-farm evaporative losses for freshwater production¹⁶, with feeds accounting for essentially all water use for marine species, but on-farm evaporative losses accounting for over 60% of water use for freshwater species. (Supplementary Fig. 6). High evaporative losses cause silver and bighead carps to have the highest total water use, 2.6 times the water use of other carps and 4.4 times the water use of catfish, while milkfish and miscellaneous marine and diadromous fishes have the highest feed-associated water use. Among fed aquaculture, trout and salmon have the lowest water use, in part

attributable to lower crop utilization, highlighting a trade-off with fishmeal and fish oil.

Nitrogen and phosphorus emissions are responsible for marine and freshwater eutrophication and are highly correlated due to natural biomass N:P ratios (Supplementary Table 4). For fed systems, the majority of N (>87%) and P (>94%) emissions occur on-farm. The highest total N and P emissions result from miscellaneous farmed marine and diadromous fishes, milkfish and fed carp. Non-fed groups such as seaweeds and bivalves, as well as unfed and unfertilized finfish systems (for example, some silver and bighead carp), represent extractive systems that remove more N and P than is emitted during production, resulting in negative emissions (Fig. 1).

Across all blue foods, farmed seaweeds and bivalves generate the lowest stressors. However, these groups also highlight several assumptions and nuances. First, bivalve estimates change by nearly five-fold when expressed in terms of edible portion (Fig. 1) compared to live weight (Supplementary Fig. 10) due to the shell weight. Second, some processes falling outside our system boundaries represent a potentially large fraction of life cycle emissions for these groups, even if still small in absolute value in some cases. For seaweeds, a large proportion of GHG emissions can occur at the drying stage²⁵ while for bivalves, CO₂ emissions during shell formation²⁶ and high emissions associated with live product from transport²⁷ can be important. Third, impacts on biogeochemical cycling and habitats are highly context dependent. For example, the systems represented here extract nitrogen and phosphorus, which could be problematic in nutrient-poor environments. Additionally, ozone effects from volatile short-lived substances depend on the location and varies widely across species^{28,29}. Fourth, sustainable diet recommendations based on these or similar results must account for differences in nutrition content and bioavailability, a particularly important consideration for seaweeds³⁰. Finally, these systems are underrepresented in the literature, particularly for edible seaweeds (Supplementary Fig. 3). As recommendations point towards the potential of these groups, it is important to increase data on these systems, deepen understanding of the above nuances, and be mindful of the total impacts associated with large-scale production on coastal habitats.

Capture fisheries, with negligible land, water, N and P values, also compare favourably, though groups fall at both the bottom and top of GHG rankings. Among farmed finfish and crustaceans, silver and bighead carps result in the lowest GHG, N and P emissions, while salmon and trout use the least land and water. To compare with terrestrial foods, we estimated stressors for industrial chicken produced in the USA and Europe and find it falls in the middle of farmed blue foods, with similar stressors as tilapia (Fig. 1, Supplementary Fig. 14). Because chicken typically has lower

stressors than other livestock³, it follows that many blue food groups compare favourably to other animal-sourced foods. Notably, groups generating among the lowest stressors (for example, bivalves and small pelagic fishes) also provide the greatest nutritional quality across all forms of aquatic foods^{2,10}.

Our results represent the most comprehensive and standardized blue food stressor estimates to date. Overall, data availability is correlated with global aquaculture production across these taxa groups, but there are still notable taxonomic and geographic gaps (Supplementary Figs. 3, 4). Critically, there are substantial data gaps for silver and bighead carp and seaweeds given their level of production (Supplementary Fig. 3). Furthermore, our capture fishery data primarily represents commercial marine fisheries³¹. However, subsistence marine and inland catches often utilize non-motorized or no vessels, which probably generate few emissions, but there is insufficient data on fuel use across the diversity of small-scale fishing methods to reliably estimate emissions. These systems should be prioritized for additional research. Our estimates represent a snapshot of the knowledge of current production, but future work on emerging production technologies, feed innovations and growing sub-sectors is important for tracking changes against these benchmarks.

From stressors to ecosystem impacts

Emission and resource-use stressors are valuable for comparing environmental performance across foods but cannot fully capture final ecosystem and biodiversity consequences (that is, impacts). Estimating impacts stemming from blue food production requires considering additional stressors and accounting for local context.

While GHG, N, P, land and water are important stressors commonly used to compare foods, other less studied stressors can be critical drivers of ecosystem impacts (Fig. 2). Both aquaculture and fisheries may impose other stressors through toxic substance applications (for example, antifouling and pesticides in agriculture) and physical disturbance (for example, bottom trawling and on-bottom culture). Additional stressors include genetic pollution, invasive species introductions³², application of antibiotics³³, and disease spread³⁴. While capture fisheries have negligible N, P, water and land stressors, other stressors can markedly alter ecosystems. Fisheries often shift size structure and abundance of targeted species (see, for example, refs. 35,36), alter the structure of food webs (see, for example, ref. 37) and impact non-targeted fauna through bycatch³⁸.

Fig. 2: Major stressors stemming from aquaculture and capture fisheries.

 **figure2**

Icons with magenta border are quantified in this study while the others are discussed qualitatively.

Local context, such as ecosystem function, carrying/assimilating capacity, and species composition influence how stressors translate into environmental impacts^{[39,40](#)}.

Notably, land use impacts on biodiversity depend on the land use history and ecological context^{[41](#)}. While all land used for food cultivation represents habitats converted at one point, avoiding additional agricultural expansion is important for preventing further habitat loss^{[42](#)}. This is also true for on-farm land use by aquaculture, where conversion of ecologically valuable ecosystems, such as mangrove forests^{[23](#)} that serve as critical carbon sinks^{[43](#)} and nursery habitats, can generate severe impacts.

Local species composition and management contexts are also important, including risks associated with marine mammal bycatch (Box 1). Individual stressors may also have nonlinear relationships with impacts or act interactively^{[44,45](#)}, such as climate change impacts compounding land use patterns that limit climate refuges or migration options^{[46](#)}, or resulting in more frequent disease outbreaks, that increase antibiotic use and risk of antibiotic resistance.

Fig. 3: GHG emissions compared to marine mammal risk.

 **figure3**

Data represent fisheries in Europe (NE Atl) and Central America (C Am SSF) by gear type. Dot indicates the median estimate of the mean $\text{kgCO}_2\text{e t}^{-1}$ and intervals show 95% (light), 80% and 50% (dark) credible intervals. Risk index is the sum of the number of marine mammals at risk times 3, 2 or 1 for high, medium or low risk, respectively [Source data](#).

Capturing the full suite of environmental impacts will require more systematic data collection and methodological advancements. This is crucial for informing policy decisions and realizing the potential contributions of blue foods to sustainable diets while avoiding undesirable trade-offs. Combining local ecological risk and stressor estimates can reveal these important trade-offs, as well as potential synergies (Box 1). While there are no impact-free foods, highlighting synergies simplifies sustainability messaging and helps identify priority interventions.

Box 1 Emissions and biodiversity risk

Stressors from life cycle assessments quantify fishery emissions but fail to capture local ecological risks. Combining stressors and impact assessments can illuminate potential sustainability trade-offs. Ecological risk assessments have been developed for capture fisheries to promote holistic assessment of local ecological risks. Integrating GHG emissions with marine mammal risk assessments reveals that some low-GHG emission gears are associated with higher marine mammal risks (for example, gillnets and entangling nets; Fig. 3), while bottom trawls show the opposite.

Acknowledging ecological context is critical because risk from similar gears varies across regions. For example, traps and lift nets generally pose low risk to marine mammals (Fig. 3). However, North Atlantic right whales (*Eubalaena glacialis*) in the northwest Atlantic are at high risk from entanglements in American lobster (*Homarus americanus*) traps⁷⁰.

Levers for reducing environmental impacts

Variance in stressors indicates diversity across fishing/farming systems (Supplementary Figs. 7–9) as well as potential ‘performance gaps’. High variability in milkfish and miscellaneous marine and diadromous fish stressors points to large potential performance gains per unit. This is promising given the interest in marine finfish expansion⁴⁷. Meanwhile, smaller performance gains per unit for high production groups such as carps are likely to generate larger total gains. While some variability within a taxa group is due to differences in on-farm practices, production technology is an important factor across stressors⁴⁸ as variability in stressors for a given species reared in different farming systems can be considerable (see, for example, ref. 49).

We find feed conversion ratios (FCRs) represent the strongest lever, wherein a 10% reduction results in a 1–24% decrease in all stressors (Fig. 4a). To evaluate potential shifts under current technology, we estimate the effect of moving each species to the 20th percentile FCR and find the largest reductions for silver and bighead carps (Fig. 4b). However, lower FCRs generally come at the cost of larger pond area³³, suggesting a potential trade-off with land and water use.

Fig. 4: Aquaculture stressor intervention opportunities.

 figure4

a, Change (%) in each stressor associate with a 10% reduction in the parameter value (black cell indicates stressor change >20%). **b**, Change (%) in each stressor under four scenarios (defined in Supplementary Table 8) relative to the current estimate. Arrows indicate changes greater than 50%. Additional aquaculture scenario results displayed

in Supplementary Fig. 15 and capture scenario results in Supplementary Fig. 16 [Source data](#).

Holding all else constant, a 10% fish production yield improvement ($t \text{ ha}^{-1}$) reduces land and water use for freshwater pond systems by 1–10% (Fig. 4a). Increasing yields to the 80th percentile reduces land and water use by up to 50% (Fig. 4b). Intensifying production, however, can require more energy for aeration and water pumping as well as increased disease risks with higher animal densities.

Feed composition represents another potential lever. Overall, shifting relative proportions of crop- and fish-derived inputs to feeds results in negligible changes in stressors (Fig. 4a). Comparing changes in feed sourcing, we found switching to deforestation-free soy and crops reduced GHG emissions by 5–50% (Fig. 4b). This could create a co-benefit of also reducing biodiversity impacts. However, as part of integrated global commodity markets, reductions by aquaculture producers will only help to meet emissions targets if broader food sector commitments are made.

Replacing fish meal and fish oil with fishery by-products has a relatively small effect (Fig. 4b), but increased by-product utilization can improve system-wide performance when it directs potential wastes toward more favourable applications⁵⁰. Finally, novel aquaculture feeds, including algal, microorganism and insect meals, are increasingly available but currently account for a small fraction of feeds. While they are likely to hold potential to improve feed quality and reduce forage fish demand⁵¹, their impacts at scale remain uncertain⁵² and therefore could not be modelled here.

For capture fisheries, reducing fuel use represents the primary stressor improvement opportunity. Increasing stock biomass could reduce fuel use per tonne of fish landed^{12,53}, where a 13% catch increase with 56% of the effort⁵⁴ corresponds to a 50% reduction in GHG emissions. Alternatively, we find that prioritizing low-fuel gears within each fishery can reduce GHG emissions by 4–61%, depending on the species (Supplementary Fig. 16). In some cases, this could create co-benefits for biodiversity impacts (Box 1). Another strategy is to transition fishing fleets to low-emission technologies⁸. While some fleets have transitioned to electric, hydrogen fuel and sail-assisted vessels, general adoption necessitates transformations beyond traditional fishery management.

Realizing blue food's environmental potential

Blue foods already have great potential for reducing food system environmental stressors. Unfed aquaculture results in negligible values for most considered stressors, and many fed aquaculture groups outperform industrial chicken, the most efficient major terrestrial animal-source food. Capture fisheries vary widely in their GHG emissions but are low impact with respect to the other stressors considered. This

underscores the value of sustainably managing wild fisheries to avoid the environmental replacement cost that would be incurred under fish catch declines²⁴.

Our standardized estimates enhance the resolution of the potential role of blue foods within sustainable diets, highlighting opportunities to shift demand from relatively high- to low-stressor blue foods and from terrestrial animal-source foods to comparatively low-stressor blue foods. Shifting to non-animal alternatives remains an efficient lever but low-stressor blue foods may represent an appealing alternative for some consumers. Furthermore, blue foods provide the highest nutrient richness across multiple micronutrients (for example, iron and zinc), vitamins (for example, B12), and long-chain polyunsaturated fatty acids (for example, EPA and DHA) relative to terrestrial animal-source foods¹⁰, which may provide greater incentive to shift demand as consumers generally prioritize seafood freshness, food safety, health and taste over sustainability⁵⁵.

Major challenges remain for shifting demand, as well as meeting increased demand. While improved management offers potential opportunities for expanding some production from low-stressor capture fisheries, uncertainty remains around the extent and feasibility of rebuilding many fisheries⁴⁷. Additional research is needed to understand the total environmental impacts of large-scale expansion of low per unit stressor foods, especially for system-specific impacts (Box 1). Increasing production also requires creating appropriate incentives and reducing barriers for producers. Historical food system transitions required public investment technologies that could be scaled up by the private sector and public policy leadership⁵⁶. Overly strict regulations or lack of capital can prevent expansion of low-stressor blue foods such as offshore mussel farms (see, for example, ref. ⁵⁷). Facilitating low-stressor blue food expansion and novel production methods may require new and more adaptive policies and distribution of grants or other forms of start-up capital. Finally, policies can steer production and consumption through taxes and subsidies⁵⁸ as well as softer policies, such as dietary advice that considers environmental impacts⁵⁹.

Within the diversity of blue food production there are numerous opportunities to reduce environmental stressors. As a young and rapidly growing sector, there are many promising technological innovations in aquaculture (for example, recirculating aquaculture systems, offshore farming and novel feeds). However, less charismatic interventions may represent greater potential for rapid and substantial impact reductions. These include policy or technological interventions that improve husbandry measures (especially reducing disease and mortality) and lower FCRs. Improved management in salmon aquaculture demonstrated considerable sustainability benefits through disease and area management plans⁶⁰ and improved stock management with precision aquaculture and automation⁶¹. Furthermore, selective breeding, genetic improvements and high-quality feeds can all reduce FCRs

(Supplementary Table 8). While we looked at individual interventions, improvements are likely to occur through a suite of interventions and the synergistic or antagonistic interactions of interventions represents an important area for future work.

Unfortunately, many innovations are often beyond the reach of smallholder producers of low-value species. This highlights a need for public research and development as well as technology transfer to enable all farmers to adopt practices that reduce environmental stressors. For capture fisheries, continued management reforms together with incentives to use low-fuel gears could substantially improve the performance of capture fisheries^{11,47}. A range of actors will be important for stimulating a shift to more sustainable production methods and, for instance, nation states, civil society and the private sector all have important roles. Private sector pre-competitive collaborations; for example, SeaBOS⁶² and the Global Salmon Initiative can help to stimulate production improvements at scale. Likewise, government-led initiatives helping small-holders improve their farming practices through, for example, access to high quality feeds, seed and broodstock, are crucial for closing the aquaculture performance gap^{63,64,65}. Certification and improvement projects can help to reduce ecosystem impacts⁶⁶, but have been criticized for passive exclusion of small-scale producers. Moving towards best practices such as state-led, national certification schemes and area-based approaches will therefore be key⁶⁷. Finally, the finance sector can help to steer the sector towards sustainability through strategic investments⁶⁸.

The above findings do not suggest unlimited blue food growth is possible nor that expansion comes without environmental trade-offs. Furthermore, without careful consideration for local contexts and inclusion of relevant stakeholders, environmentally focused interventions can generate social and economic trade-offs that undermine broader sustainability goals. Nevertheless, farmed blue food is among the fastest growing food sectors and the global community now faces a unique window of opportunity to steer expansion towards sustainability⁶⁹. Our model and results provide blue food stressor benchmarks and enable data-poor environmental stressor assessments. This serves as a critical foundation for understanding blue food environmental performance and to ensuring sustainable and healthy blue foods are available now and into the future.

Data availability

All data used to produce the results of our analysis are available in the [Supplementary Information](#) and on GitHub (<https://github.com/jagephart/FishPrint>), with the published version archived (<https://doi.org/10.5281/zenodo.5338614>). [Source data](#) are provided with this paper.

Code availability

All code used to produce the results of our analysis are available in the [Supplementary Information](#) and on GitHub (<https://github.com/jagephart/FishPrint>), with the published version archived (<https://doi.org/10.5281/zenodo.5338614>). [Source data](#) are provided with this paper.

References

1. 1.

Gephart, J. A. et al. The environmental cost of subsistence: optimizing diets to minimize footprints. *Sci. Total Environ.* **553**, 120–127 (2016).

2. 2.

Hallström, E. et al. Combined climate and nutritional performance of seafoods. *J. Clean. Prod.* **230**, 402–411 (2019).

3. 3.

Poore, J. & Nemecek, T. Reducing food's environmental impacts through producers and consumers. *Science* **360**, 987–992 (2018).

4. 4.

Halpern, B. S. et al. Opinion: Putting all foods on the same table: achieving sustainable food systems requires full accounting. *Proc. Natl Acad. Sci. USA* **116**, 18152–18156 (2019).

5. 5.

The State of World Fisheries and Aquaculture (SOFIA) (FAO, 2020).

6. 6.

The State of the World's Land and Water Resources for Food and Agriculture (SOLAW): Managing Systems at Risk (FAO, 2011).

7. 7.

Food Security and Nutrition: Building a Global Narrative Towards 2030 (HLPE, 2020).

8. 8.

Willett, W. et al. Food in the Anthropocene: the EAT–Lancet Commission on healthy diets from sustainable food systems. *Lancet* **393**, 447–492 (2019).

9. 9.

Micha, R. et al. *2020 Global Nutrition Report: Action on Equity to End Malnutrition* (Global Nutrition Report, 2020).

10. 10.

Golden, C. D. Aquatic foods to nourish nations. *Nature* (in the press).

11. 11.

Parker, R. W. R. et al. Fuel use and greenhouse gas emissions of world fisheries. *Nat. Clim. Change* **8**, 333–337 (2018).

12. 12.

Hoegh-Guldberg, O. et al. *The Ocean as a Solution to Climate Change: Five Opportunities for Action* (Ocean Panel, 2019).

13. 13.

Farmacy, A. K., Gardner, C., Jennings, S., Green, B. S. & Watson, R. A. Assessing the inclusion of seafood in the sustainable diet literature. *Fish Fish.* **18**, 607–618 (2017).

14. 14.

MacLeod, M. J., Hasan, M. R., Robb, D. H. F. & Mamun-Ur-Rashid, M. Quantifying greenhouse gas emissions from global aquaculture. *Sci. Rep.* **10**, 11679 (2020).

15. 15.

Hilborn, R., Banobi, J., Hall, S. J., Pucylowski, T. & Walsworth, T. E. The environmental cost of animal source foods. *Front. Ecol. Environ.* **16**, 329–335 (2018).

16. 16.

Gephart, J. A. et al. The ‘seafood gap’ in the food-water nexus literature—issues surrounding freshwater use in seafood production chains. *Adv. Water Resour.* **110**, 505–514 (2017).

17. 17.

Tilman, D. & Clark, M. Global diets link environmental sustainability and human health. *Nature* **515**, 518–522 (2014).

18. 18.

Springmann, M. et al. Options for keeping the food system within environmental limits. *Nature* **562**, 519–525 (2018).

19. 19.

Reap, J., Roman, F., Duncan, S. & Bras, B. A survey of unresolved problems in life cycle assessment: Part 2: impact assessment and interpretation. *Int. J. Life Cycle Assess.* **13**, 374–388 (2008).

20. 20.

Henriksson, P. J. G. et al. A rapid review of meta-analyses and systematic reviews of environmental footprints of food commodities and diets. *Glob. Food Secur.* **28**, 100508 (2021).

21. 21.

Naylor, R. L. et al. Blue food demand across geographic and temporal scales. *Nature* (in the press).

22. 22.

Henriksson, P. J. G., Pelletier, N. L., Troell, M. & Tyedmers, P. Life cycle assessment and its application to aquaculture production systems. In *Encyclopedia of Sustainability Science and Technology* (ed. Meyers, R.) (Springer, 2012).

23. 23.

Richards, D. R., Thompson, B. S. & Wijedasa, L. Quantifying net loss of global mangrove carbon stocks from 20 years of land cover change. *Nat. Commun.* **11**, 4260 (2020).

24. 24.

Gephart, J. A., Pace, M. L. & D'Odorico, P. Freshwater savings from marine protein consumption. *Environ. Res. Lett.* **9**, 014005 (2014).

25. 25.

van Oirschot, R. et al. Explorative environmental life cycle assessment for system design of seaweed cultivation and drying. *Algal Res.* **27**, 43–54 (2017).

26. 26.

Ray, N. E., O'Meara, T., Williamson, T., Izursa, J.-L. & Kangas, P. C. Consideration of carbon dioxide release during shell production in LCA of bivalves. *Int. J. Life Cycle Assess.* **23**, 1042–1048 (2018).

27. 27.

Iribarren, D., Moreira, M. T. & Feijoo, G. Revisiting the life cycle assessment of mussels from a sectorial perspective. *J. Clean. Prod.* **18**, 101–111 (2010).

28. 28.

Tegtmeier, S. et al. Emission and transport of bromocarbons: from the West Pacific ocean into the stratosphere. *Atmospheric Chem. Phys.* **12**, 10633–10648 (2012).

29. 29.

King, G. M. Aspects of carbon monoxide production and oxidation by marine macroalgae. *Mar. Ecol. Prog. Ser.* **224**, 69–75 (2001).

30. 30.

Flores, S. R. L., Dobbs, J. & Dunn, M. A. Mineral nutrient content and iron bioavailability in common and Hawaiian seaweeds assessed by an in vitro digestion/Caco-2 cell model. *J. Food Compos. Anal.* **43**, 185–193 (2015).

31. 31.

Parker, R. W. R. & Tyedmers, P. H. Fuel consumption of global fishing fleets: current understanding and knowledge gaps. *Fish Fish.* **16**, 684–696 (2015).

32. 32.

Molnar, J. L., Gamboa, R. L., Revenga, C. & Spalding, M. D. Assessing the global threat of invasive species to marine biodiversity. *Front. Ecol. Environ.* **6**, 485–492 (2008).

33. 33.

Henriksson, P. J. G. et al. Unpacking factors influencing antimicrobial use in global aquaculture and their implication for management: a review from a systems perspective. *Sustain. Sci.* **13**, 1105–1120 (2018).

34. 34.

Murray, A. G. Epidemiology of the spread of viral diseases under aquaculture. *Curr. Opin. Virol.* **3**, 74–78 (2013).

35. 35.

Myers, R. A. & Worm, B. Rapid worldwide depletion of predatory fish communities. *Nature* **423**, 280–283 (2003).

36. 36.

Svedäng, H. & Hornborg, S. Selective fishing induces density-dependent growth. *Nat. Commun.* **5**, 4152 (2014).

37. 37.

Howarth, L. M., Roberts, C. M., Thurstan, R. H. & Stewart, B. D. The unintended consequences of simplifying the sea: making the case for complexity. *Fish Fish.* **15**, 690–711 (2014).

38. 38.

Roda, M. A. P. et al. *A Third Assessment of Global Marine Fisheries Discards* (FAO, 2019).

39. 39.

Halpern, B. S., Selkoe, K. A., Micheli, F. & Kappel, C. V. Evaluating and ranking the vulnerability of global marine ecosystems to anthropogenic threats. *Conserv. Biol.* **21**, 1301–1315 (2007).

40. 40.

Weitzman, J. & Filgueira, R. The evolution and application of carrying capacity in aquaculture: towards a research agenda. *Rev. Aquac.* **12**, 1297–1322 (2019).

41. 41.

Martin, D. A. et al. Land-use history determines ecosystem services and conservation value in tropical agroforestry. *Conserv. Lett.* **13**, e12740 (2020).

42. 42.

Williams, D. R. et al. Proactive conservation to prevent habitat losses to agricultural expansion. *Nat. Sustain.* **4**, 314–322 (2021).

43. 43.

Mcleod, E. et al. A blueprint for blue carbon: toward an improved understanding of the role of vegetated coastal habitats in sequestering CO₂. *Front. Ecol. Environ.* **9**, 552–560 (2011).

44. 44.

Selkoe, K. A. et al. Principles for managing marine ecosystems prone to tipping points. *Ecosyst. Health Sustain.* **1**, 1–18 (2015).

45. 45.

Crain, C. M., Kroeker, K. & Halpern, B. S. Interactive and cumulative effects of multiple human stressors in marine systems. *Ecol. Lett.* **11**, 1304–1315 (2008).

46. 46.

Guo, F., Lenoir, J. & Bonebrake, T. C. Land-use change interacts with climate to determine elevational species redistribution. *Nat. Commun.* **9**, 1315 (2018).

47. 47.

Costello, C., Cao, L. & Gelcich, S. *The Future of Food from the Sea* (Ocean Panel, 2019).

48. 48.

Bohnes, F. A., Hauschild, M. Z., Schlundt, J. & Laurent, A. Life cycle assessments of aquaculture systems: a critical review of reported findings with

recommendations for policy and system development. *Rev. Aquac.* **11**, 1061–1079 (2019).

49. 49.

Bergman, K. et al. Recirculating aquaculture is possible without major energy tradeoff: life cycle assessment of warmwater fish farming in Sweden. *Environ. Sci. Technol.* **54**, 16062–16070 (2020).

50. 50.

Stevens, J. R., Newton, R. W., Tlusty, M. & Little, D. C. The rise of aquaculture by-products: increasing food production, value, and sustainability through strategic utilisation. *Mar. Policy* **90**, 115–124 (2018).

51. 51.

Cottrell, R. S., Blanchard, J. L., Halpern, B. S., Metian, M. & Froehlich, H. E. Global adoption of novel aquaculture feeds could substantially reduce forage fish demand by 2030. *Nat. Food* **1**, 301–308 (2020).

52. 52.

Pelletier, N., Klinger, D. H., Sims, N. A., Yoshioka, J.-R. & Kittinger, J. N. Nutritional attributes, substitutability, scalability, and environmental intensity of an illustrative subset of current and future protein sources for aquaculture feeds: joint consideration of potential synergies and trade-offs. *Environ. Sci. Technol.* **52**, 5532–5544 (2018).

53. 53.

Hornborg, S. & Smith, A. D. M. Fisheries for the future: greenhouse gas emission consequences of different fishery reference points. *ICES J. Mar. Sci.* **77**, 1666–1671 (2020).

54. 54.

The Sunken Billions Revisited: Progress and Challenges in Global Marine Fisheries. (World Bank, 2017).

55. 55.

Understanding seafood consumers. MSC <https://www.msc.org/understanding-seafood-consumers> (2021).

56. 56.

Moberg, E. et al. Combined innovations in public policy, the private sector and culture can drive sustainability transitions in food systems. *Nat. Food* **2**, 282–290 (2021).

57. 57.

Fairbanks, L. Moving mussels offshore? Perceptions of offshore aquaculture policy and expansion in New England. *Ocean Coast. Manag.* **130**, 1–12 (2016).

58. 58.

Säll, S. & Gren, I.-M. Effects of an environmental tax on meat and dairy consumption in Sweden. *Food Pol.* **55**, 41–53 (2015).

59. 59.

Fischer, C. G. & Garnett, T. *Plates, Pyramids, Planet: Developments in National Healthy and Sustainable Dietary Guidelines: A State of Play Assessment* (FAO, 2016).

60. 60.

Jones, S., Bruno, D., Madsen, L. & Peeler, E. Disease management mitigates risk of pathogen transmission from maricultured salmonids. *Aquac. Environ. Interact.* **6**, 119–134 (2015).

61. 61.

Antonucci, F. & Costa, C. Precision aquaculture: a short review on engineering innovations. *Aquac. Int.* **28**, 41–57 (2020).

62. 62.

Österblom, H., Jouffray, J.-B., Folke, C. & Rockström, J. Emergence of a global science–business initiative for ocean stewardship. *Proc. Natl Acad. Sci. USA* **114**, 9038–9043 (2017).

63. 63.

Watson, J. R., Armerin, F., Klinger, D. H. & Belton, B. Resilience through risk management: cooperative insurance in small-holder aquaculture systems. *Heliyon* **4**, e00799 (2018).

64. 64. Hasan, M. R. *On-farm Feeding and Feed Management in Aquaculture* (FAO, 2010).
65. 65. Bondad-Reantaso, M. G. *Assessment of Freshwater Fish Seed Resources for Sustainable Aquaculture* (FAO, 2007).
66. 66. Gutiérrez, N. L. et al. Eco-label conveys reliable information on fish stock health to seafood consumers. *PLoS ONE* **7**, e43765 (2012).
67. 67. Bush, S. R. et al. Inclusive environmental performance through ‘beyond-farm’ aquaculture governance. *Curr. Opin. Environ. Sustain.* **41**, 49–55 (2019).
68. 68. Jouffray, J.-B., Crona, B., Wassénius, E., Bebbington, J. & Scholtens, B. Leverage points in the financial sector for seafood sustainability. *Sci. Adv.* **5**, eaax3324 (2019).
69. 69. Gephart, J. A. et al. Scenarios for global aquaculture and its role in human nutrition. *Rev. Fish. Sci. Aquac.* **29**, 122–138 (2021).
70. 70. Myers, H. J. & Moore, M. J. Reducing effort in the U.S. American lobster (*Homarus americanus*) fishery to prevent North Atlantic right whale (*Eubalaena glacialis*) entanglements may support higher profits and long-term sustainability. *Mar. Policy* **118**, 104017 (2020).

Acknowledgements

This paper is part of the Blue Food Assessment (<https://www.bluefood.earth/>), a comprehensive examination of the role of aquatic foods in building healthy, sustainable and equitable food systems. The assessment was supported by the Builders

Initiative, the MAVA Foundation, the Oak Foundation, and the Walton Family Foundation, and has benefitted from the intellectual input of the wider group of scientists leading other components of the Blue Food Assessment work. J.A.G., K.D.G. and C.D.G. were supported by funding under NSF 1826668. A.S. was supported by a grant from the Nature Conservancy. P.H. undertook this work as part of the CGIAR Research Programs on Fish Agri-Food Systems (FISH) led by WorldFish and on Climate Change, Agriculture and Food Security (CCAFS) led by CIAT. P.H. and A.S. were partially supported by FORMAS Inequality and the Biosphere project (2020-00454). Funding for participation of S.H., K.B.; M.T., P.H. and F.Z. came from Swedish Research Council Formas (grants 2016-00227 and 2017-00842). This work was financially supported, in part, by the Harvard Data Science Initiative. We thank Fernando Cagua for his review of the model code.

Author information

Author notes

1. These authors contributed equally: Jessica A. Gephart, Patrik J. G. Henriksson, Robert W. R. Parker, Alon Shepon

Affiliations

1. Department of Environmental Science, American University, Washington, DC, USA

Jessica A. Gephart & Kelvin D. Gorospe

2. Stockholm Resilience Centre, Stockholm, Sweden

Patrik J. G. Henriksson, Malin Jonell & Max Troell

3. WorldFish, Penang, Malaysia

Patrik J. G. Henriksson

4. Beijer Institute of Ecological Economics, The Royal Swedish Academy of Sciences, Stockholm, Sweden

Patrik J. G. Henriksson, Malin Jonell & Max Troell

5. School for Resource and Environmental Studies, Dalhousie University, Halifax, Nova Scotia, Canada

Robert W. R. Parker, Kathleen Mifflin & Peter Tyedmers

6. Aquaculture Stewardship Council, Utrecht, the Netherlands

Robert W. R. Parker

7. Department of Environmental Studies, The Porter School of the Environment and Earth Sciences, Tel Aviv University, Tel Aviv, Israel

Alon Shepon

8. The Steinhardt Museum of Natural History, Tel Aviv University, Tel Aviv, Israel

Alon Shepon

9. Department of Nutrition, Harvard T. H. Chan School of Public Health, Boston, MA, USA

Alon Shepon & Christopher D. Golden

10. Department of Agriculture and Food, RISE Research Institutes of Sweden, Göteborg, Sweden

Kristina Bergman, Sara Hornborg & Friederike Ziegler

11. Department of Environmental Science, Bard College, Annandale-on-Hudson, NY, USA

Gidon Eshel

12. Department of Environmental Health, Harvard T. H. Chan School of Public Health, Boston, MA, USA

Christopher D. Golden

13. Department of Global Health and Population, Harvard T. H. Chan School of Public Health, Boston, MA, USA

Christopher D. Golden

14. National Center for Ecological Analysis and Synthesis, University of California, Santa Barbara, CA, USA

Benjamin S. Halpern

15. Bren School of Environmental Science and Management, University of California, Santa Barbara, CA, USA

Benjamin S. Halpern

16. Global Economic Dynamics and the Biosphere, The Royal Swedish Academy of Sciences, Stockholm, Sweden

Malin Jonell

17. International Atomic Energy Agency–Environment Laboratories (IAEA-EL), Radioecology Laboratory, Principality of Monaco, Monaco

Marc Metian

18. Institute of Aquaculture, University of Stirling, Stirling, UK

Richard Newton

19. College of Fisheries and Life Science, Shanghai Ocean University, Shanghai, China

Wenbo Zhang

Contributions

J.A.G., P.J.G.H., R.P. and A.S. contributed equally to the study. J.A.G. and C.G. organized the initial workshop. J.A.G., P.J.G.H., R.P., A.S., G.E., C.D.G., P.T. and M.T. conceived the idea and designed the overall study. J.A.G., P.J.G.H., R.P., A.S., K.D.G., S.H., K.M., M.M., R.N., W.Z. and F.Z. compiled the data. J.A.G. and K.D.G. developed the model and analysed the data. All authors reviewed the results and contributed to and approved the final manuscript.

Corresponding author

Correspondence to Jessica A. Gephart.

Ethics declarations

Competing interests

The authors declare the following competing interests: R.W.R.P. became employed by the Aquaculture Stewardship Council while this manuscript was under consideration.

Additional information

Peer review information *Nature* thanks Michael Clark, Alexis Laurent and the other, anonymous, reviewer(s) for their contribution to the peer review of this work. Peer reviewer reports are available.

Publisher's note Springer Nature remains neutral with regard to jurisdictional claims in published maps and institutional affiliations.

Supplementary information

Supplementary Information

This Supplementary Information file contains the following sections: 1) Methods overview – including a methods flow chart and description of the goal and scope of the study; 2) Data characterization – description of the data; 3) Model – description of the stressor models; 4) Stressor estimates – additional stressor estimate figures, including figures with alternative allocation methods and functional unit; 5) Analysis of levers – description of lever scenarios and figures with additional scenarios and alternative allocation methods.

Peer Review File

Supplementary Table 9

This file contains details of all studies reviewed for this study.

Supplementary Table 10

This file contains life cycle inventory data compiled in this study.

Supplementary Table 11

This file contains stressor estimates for each taxa group for each functional unit and allocation method.

Source data

Source Data Fig. 1

Source Data Fig. 3

Source Data Fig. 4

Rights and permissions

Reprints and Permissions

About this article

Cite this article

Gephart, J.A., Henriksson, P.J.G., Parker, R.W.R. *et al.* Environmental performance of blue foods. *Nature* **597**, 360–365 (2021). <https://doi.org/10.1038/s41586-021-03889-2>

- Received: 20 January 2021
- Accepted: 09 August 2021
- Published: 15 September 2021
- Issue Date: 16 September 2021
- DOI: <https://doi.org/10.1038/s41586-021-03889-2>

Share this article

Anyone you share the following link with will be able to read this content:

[Get shareable link](#)

Sorry, a shareable link is not currently available for this article.

[Copy to clipboard](#)

Provided by the Springer Nature SharedIt content-sharing initiative

This article was downloaded by **calibre** from <https://www.nature.com/articles/s41586-021-03889-2>

- Article
- [Published: 15 September 2021](#)

Vast CO₂ release from Australian fires in 2019–2020 constrained by satellite

- [Ivar R. van der Velde](#) [ORCID: orcid.org/0000-0003-3223-295X](#)^{1,2},
- [Guido R. van der Werf](#)²,
- [Sander Houweling](#)^{1,2},
- [Joannes D. Maasakkers](#)¹,
- [Tobias Borsdorff](#) [ORCID: orcid.org/0000-0002-4421-0187](#)¹,
- [Jochen Landgraf](#)¹,
- [Paul Tol](#)¹,
- [Tim A. van Kempen](#) [ORCID: orcid.org/0000-0001-8178-5054](#)¹,
- [Richard van Hees](#) [ORCID: orcid.org/0000-0002-3846-0753](#)¹,
- [Ruud Hoogeveen](#)¹,
- [J. Pepijn Veefkind](#)^{3,4} &
- [Ilse Aben](#)^{1,5}

Nature volume **597**, pages 366–369 (2021)

- 1423 Accesses
- 287 Altmetric
- [Metrics details](#)

Subjects

- [Atmospheric chemistry](#)

- [Climate-change mitigation](#)
- [Environmental impact](#)
- [Natural hazards](#)

Abstract

Southeast Australia experienced intensive and geographically extensive wildfires during the 2019–2020 summer season^{1,2}. The fires released substantial amounts of carbon dioxide into the atmosphere³. However, existing emission estimates based on fire inventories are uncertain⁴, and vary by up to a factor of four for this event. Here we constrain emission estimates with the help of satellite observations of carbon monoxide⁵, an analytical Bayesian inversion⁶ and observed ratios between emitted carbon dioxide and carbon monoxide⁷. We estimate emissions of carbon dioxide to be 715 teragrams (range 517–867) from November 2019 to January 2020. This is more than twice the estimate derived by five different fire inventories^{8,9,10,11,12}, and broadly consistent with estimates based on a bottom-up bootstrap analysis of this fire episode¹³. Although fires occur regularly in the savannas in northern Australia, the recent episodes were extremely large in scale and intensity, burning unusually large areas of eucalyptus forest in the southeast¹³. The fires were driven partly by climate change^{14,15}, making better-constrained emission estimates particularly important. This is because the build-up of atmospheric carbon dioxide may become increasingly dependent on fire-driven climate–carbon feedbacks, as highlighted by this event¹⁶.

Access options

Subscribe to Journal

Get full journal access for 1 year

\$199.00

only \$3.90 per issue

Subscribe

All prices are NET prices.

VAT will be added later in the checkout.

Tax calculation will be finalised during checkout.

Rent or Buy article

Get time limited or full article access on ReadCube.

from \$8.99

Rent or Buy

All prices are NET prices.

Additional access options:

- [Log in](#)
- [Access through your institution](#)
- [Learn about institutional subscriptions](#)

Fig. 1: Comparison of fire emission estimates for Southeast Australia.

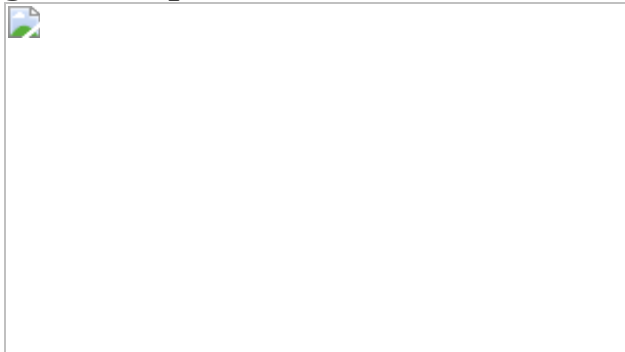


Fig. 2: Comparison of simulated and observed CO column mixing ratios.

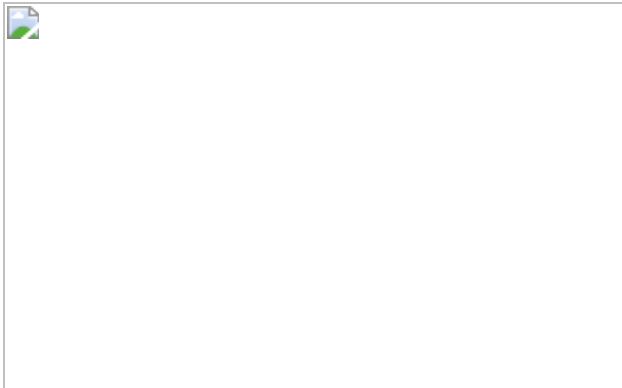


Fig. 3: CO emissions from inventories and satellite constraints.

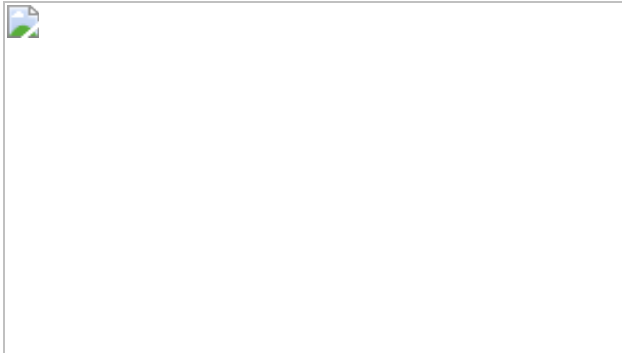
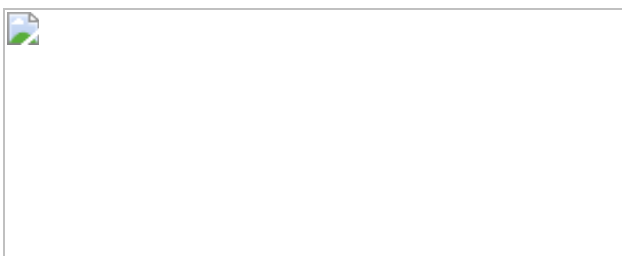


Fig. 4: CO₂ emissions from inventories and satellite constraints.



Data availability

TROPOMI measurements of CO can be downloaded from <https://s5phub.copernicus.eu>. GFED4s-based fire emissions can be downloaded from <https://www.geo.vu.nl/~gwerf/GFED/GFED4/>. GFAS-based fire emissions can be downloaded from <https://apps.ecmwf.int/datasets/data/cams-gfas/>. QFED-based fire emissions can be downloaded from <https://portal.nccs.nasa.gov/datashare/iesa/aerosol/emissions/QFED/v2.5r1/0.1/QFED/>. FEER-based fire emissions can be downloaded from <https://feer.gsfc.nasa.gov/data/emissions/>. FINN-based fire emissions can be downloaded from <https://www.acom.ucar.edu/Data/fire/>. Prior and posterior

emissions and CO concentrations can be downloaded from
<https://doi.org/10.5281/zenodo.4692417>.

Code availability

The Weather Research and Forecasting with Chemistry (WRF-CHEM) atmospheric transport model version 4.0 can be downloaded from https://www2.mmm.ucar.edu/wrf/users/download/get_source.html. Inversion and emission preparation codes are available at <https://doi.org/10.5281/zenodo.4692678>. Python notebooks used to create the figures and tables are at <https://doi.org/10.5281/zenodo.5060184>.

References

1. 1.
Bowman, D. M. et al. Wildfires: Australia needs national monitoring agency. *Nature* **584**, 188–191 (2020).
2. 2.
Australian Government Annual Climate Statement 2019.
<http://www.bom.gov.au/climate/current/annual/aus/2019/> (last accessed 23 July 2021) (2019).
3. 3.
Australian Government Technical Update 2020. Estimating greenhouse gas emissions from bushfires in Australia's temperate forests: focus on 2019–20.
<https://www.industry.gov.au/sites/default/files/2020-04/estimating-greenhouse-gas-emissions-from-bushfires-in-australias-temperate-forests-focus-on-2019-20.pdf> (last accessed 23 July 2021) (2020).
4. 4.

Pan, X. et al. Six global biomass burning emission datasets: intercomparison and application in one global aerosol model. *Atmos. Chem. Phys.* **20**, 969–994 (2020).

5. 5.

Veefkind, J. P. et al. TROPOMI on the ESA Sentinel-5 precursor: a GMES mission for global observations of the atmospheric composition for climate, air quality and ozone layer applications. *Remote Sens. Environ.* **120**, 70–83 (2012).

6. 6.

Tarantola, A. *Inverse Problem Theory and Methods for Model Parameter Estimation* (Soc. Indust. Appl. Math., Philadelphia, PA, 2005).

7. 7.

Guérette, E.-A. et al. Emissions of trace gases from Australian temperate forest fires: emission factors and dependence on modified combustion efficiency. *Atmos. Chem. Phys.* **18**, 3717–3735 (2018).

8. 8.

Van der Werf, G. R. et al. Global fire emissions estimates during 1997–2016. *Earth Syst. Sci. Data* **9**, 697–720 (2017).

9. 9.

Wiedinmyer, C. et al. The Fire Inventory from NCAR (FINN): a high resolution global model to estimate the emissions from open burning. *Geosci. Model Dev.* **4**, 625–641 (2011).

10. 10.

Kaiser, J. W. et al. Biomass burning emissions estimated with a global fire assimilation system based on observed fire radiative power. *Biogeosciences* **9**, 527–554 (2012).

11. 11.

Darmenov, A. & da Silva, A. The quick fire emissions dataset (QFED): documentation of versions 2.1, 2.2 and 2.4. *NASA Global Modeling and Assimilation Office* <https://gmao.gsfc.nasa.gov/pubs/docs/Darmenov796.pdf> (last accessed 23 July 2021) (2015).

12. 12.

Ichoku, C. & Ellison, L. Global top-down smoke-aerosol emissions estimation using satellite fire radiative power measurements. *Atmos. Chem. Phys.* **14**, 6643–6667 (2014).

13. 13.

Bowman, D. M. J. S., et al. Australian forests, megafires and the risk of dwindling carbon stocks. *Plant Cell Environ.* **44**, 347–355 (2021).

14. 14.

Van Oldenborgh, G. J. et al. Attribution of the Australian bushfire risk to anthropogenic climate change. *Nat. Hazards Earth Syst. Sci.* **21**, 941–960 (2021).

15. 15.

Abram, N. J. et al. Connections of climate change and variability to large and extreme forest fires in southeast Australia. *Commun. Earth Environ.* **2**, 8 (2021).

16. 16.

Shukla, P. R. et al. (eds). in *Climate Change and Land: an IPCC Special Report on Climate Change, Desertification, Land Degradation, Sustainable Land Management, Food Security, and Greenhouse Gas Fluxes in Terrestrial Ecosystems* (eds Shukla, P. R. et al.) (in the press).

17. 17.

Andreae, M. O. & Merlet, P. Emission of trace gases and aerosols from biomass burning. *Glob. Biogeochem. Cycles* **15**, 955–966 (2001).

18. 18.

Van Leeuwen, T. T. et al. Biomass burning fuel consumption rates: a field measurement database. *Biogeosciences* **11**, 7305–7329 (2014).

19. 19.

Seiler, W. & Crutzen, P. J. Estimates of gross and net fluxes of carbon between the biosphere and the atmosphere from biomass burning. *Clim. Change* **2**, 207–247 (1980).

20. 20.

Wooster, M. J. et al. Fire radiative energy for quantitative study of biomass burning: derivation from the BIRD experimental satellite and comparison to MODIS fire products. *Remote Sens. Environ.* **86**, 83–107 (2003).

21. 21.

Global Fire Emissions Database, version 4.1 (GFED4s): monthly and daily 1997–present.

<https://www.geo.vu.nl/~gwerf/GFED/GFED4/Readme.pdf> (last accessed 23 July 2021)

22. 22.

Yin, Y. et al. Variability of fire carbon emissions in equatorial Asia and its nonlinear sensitivity to El Niño. *Geophys. Res. Lett.* **43**, 10472–10479 (2016).

23. 23.

Huijnen, V. et al. Fire carbon emissions over maritime Southeast Asia in 2015 largest since 1997. *Sci. Rep.* **6**, 26886 (2016).

24. 24.

Heymann, M. et al. CO₂ emission of Indonesian fires in 2015 estimated from satellite-derived atmospheric CO₂ concentrations. *Geophys. Res. Lett.* **44**, 1537–1544 (2017).

25. 25.

Lohberger, S. et al. Spatial evaluation of Indonesia's 2015 fire-affected area and estimated carbon emissions using Sentinel-1. *Glob. Change Biol.* **24**, 644–654 (2018).

26. 26.

Nechita-Banda, N. et al. Monitoring emissions from the 2015 Indonesian fires using CO satellite data. *Phil. Trans. R. Soc. Lond. B* **373**, 20170307 (2018).

27. 27.

Schneising, O. et al. Severe Californian wildfires in November 2018 observed from space: the carbon monoxide perspective. *Atmos. Chem. Phys.* **20**, 3317–3332 (2020).

28. 28.

Van der Velde, I. R. et al. Biomass burning combustion efficiency observed from space using measurements of CO and NO₂ by the TROPOspheric Monitoring Instrument (TROPOMI). *Atmos. Chem. Phys.* **21**, 597–616 (2021).

29. 29.

Taylor, K. E. Summarizing multiple aspects of model performance in a single diagram. *J. Geophys. Res.* **106**, 7183–7192 (2001).

30. 30. Wain, A. et al. Managing smoke from wildfires and prescribed burning in southern Australia. *Dev. Env. Sci.* **8**, 535–550 (2008).
31. 31. Akagi, S. K. et al. Emission factors for open and domestic biomass burning for use in atmospheric models. *Atmos. Chem. Phys.* **11**, 4039–4072 (2011).
32. 32. Yokelson, R. J. et al. Emissions of formaldehyde, acetic acid, methanol, and other trace gases from biomass fires in North Carolina measured by airborne Fourier transform infrared spectroscopy. *J. Geophys. Res.* **104** (D23), 30109–30125 (1999).
33. 33. Houghton, R. A. & Nassikas, A. A. Global and regional fluxes of carbon from land use and land cover change 1850–2015. *Glob. Biogeochem. Cycles* **31**, 456–472 (2017).
34. 34. Lucas, C. et al. *Bushfire weather in Southeast Australia: recent trends and projected climate change impacts*. Technical Report (Bushfire CRC and CSIRO Marine and Atmospheric Research, Melbourne, Australia, 2007).
35. 35. Clarke, H. et al. Regional signatures of future fire weather over eastern Australia from global climate models. *Int. J. Wildland Fire* **20**, 550–562 (2011).
36. 36.

Matthews, S. et al. Climate change, fuel and fire behaviour in a eucalypt forest. *Glob. Change Biol.* **18**, 3212–3223 (2012).

37. 37.

Muntean, M. et al. *Fossil CO₂ Emissions of All World Countries: 2018 Report*. (European Commission JRC Science for Policy Report, 2018).

38. 38.

Hurst, D. F. et al. *Trace-Gas Emissions from Biomass Burning in Australia, in: Biomass Burning and Global Change*. (ed. Levine, J. S.) (MIT Press, 1996).

39. 39.

Lawson, S. J. et al. Biomass burning emissions of trace gases and particles in marine air at Cape Grim, Tasmania. *Atmos. Chem. Phys.* **15**, 13393–13411 (2015).

40. 40.

Paton-Walsh, C. et al. New emission factors for Australian vegetation fires measured using open-path Fourier transform infrared spectroscopy. Part 1. Methods and Australian temperate forest fires. *Atmos. Chem. Phys.* **14**, 11313–11333 (2014).

41. 41.

Rea, G. et al. Impact of the New South Wales fires during October 2013 on regional air quality in eastern Australia. *Atmos. Environ.* **131**, 150–163 (2016).

42. 42.

Reisen, F. et al. Ground-based field measurements of PM2.5 emission factors from flaming and smoldering combustion in eucalypt forests. *J. Geophys. Res.* **123**, 8301–8314 (2018).

Acknowledgements

We thank the team that realized the TROPOMI instrument, comprising a partnership between Airbus Defence and Space Netherlands, the Royal Netherlands Meteorological Institute (KNMI), the SRON Netherlands Institute for Space Research and the Netherlands Organisation for Applied Scientific Research (TNO), commissioned by the Netherlands Space Office (NSO) and the European Space Agency (ESA). The Sentinel-5 Precursor is part of the European Union (EU) Copernicus programme, and Copernicus Sentinel data from 2019 and 2020 have been used here. The WRF model computations were carried out on the Dutch national e-infrastructure with the support of the SURF Cooperative. We also thank the large team of scientists and technicians who worked on the fire emission data sets available online. G.R.v.d.W. and I.R.v.d.V. are partly supported by the Netherlands Organization for Scientific Research (NWO; VICI research programme 016.160.324).

Author information

Affiliations

1. SRON Netherlands Institute for Space Research, Utrecht, The Netherlands

Ivar R. van der Velde, Sander Houweling, Joannes D. Maasakkers, Tobias Borsdorff, Jochen Landgraf, Paul Tol, Tim A. van Kempen, Richard van Hees, Ruud Hoogeveen & Ilse Aben

2. Department of Earth Sciences, Vrije Universiteit, Amsterdam, The Netherlands

Ivar R. van der Velde, Guido R. van der Werf & Sander Houweling

3. Royal Netherlands Meteorological Institute (KNMI), De Bilt, The Netherlands

J. Pepijn Veefkind

4. Department of Geoscience and Remote Sensing, Delft University of Technology, Delft, The Netherlands

J. Pepijn Veefkind

5. Department of Physics and Astronomy, Vrije Universiteit, Amsterdam, The Netherlands

Ilse Aben

Contributions

I.R.v.d.V. analysed data, designed and ran the model simulations and wrote the paper. G.R.v.d.W., S.H. and I.A. provided scientific advice and detailed comments on the manuscript. J.D.M., T.B., T.A.v.K. and P.T. provided additional comments on the manuscript and TROPOMI products. J.L. and T.B. developed the TROPOMI CO product. R.v.H., T.A.v.K., P.T. and R.H. contributed to the TROPOMI shortwave-infrared (SWIR) calibration. J.P.V. is the principal investigator for the TROPOMI instrument.

Corresponding author

Correspondence to Ivar R. van der Velde.

Ethics declarations

Competing interests

The authors declare no competing interests.

Additional information

Peer review information *Nature* thanks Johannes Kaiser and the other, anonymous, reviewer(s) for their contribution to the peer review of this work.

Publisher's note Springer Nature remains neutral with regard to jurisdictional claims in published maps and institutional affiliations.

Extended data figures and tables

Extended Data Table 1 Comparison of prior and posterior emissions of CO from fire for Southeast Australia

Extended Data Table 2 Comparison of prior and posterior emissions of CO₂ from fire for Southeast Australia

Extended Data Table 3 Comparison of published CO₂ and CO emission factors and their ratios

Extended Data Table 4 Overview of CO and CO₂ emission estimates for different experiments

Supplementary information

Supplementary Information

This file contains Supplementary Methodology and additional information, including Supplementary Figures 1-6, and additional references.

Supplementary Video 1

Video of daily simulated and observed CO column mixing ratios. The video shows on the first row the daily prior (using GFAS emissions), posterior and TROPOMI CO column mixing ratios [ppb]. The second row shows prior minus TROPOMI and posterior minus TROPOMI, and the third panel shows the average wind direction in the planetary boundary layer from WRF-CHEM.

Rights and permissions

Reprints and Permissions

About this article

Cite this article

van der Velde, I.R., van der Werf, G.R., Houweling, S. *et al.* Vast CO₂ release from Australian fires in 2019–2020 constrained by satellite. *Nature* **597**, 366–369 (2021). <https://doi.org/10.1038/s41586-021-03712-y>

- Received: 18 January 2021
- Accepted: 07 June 2021
- Published: 15 September 2021
- Issue Date: 16 September 2021
- DOI: <https://doi.org/10.1038/s41586-021-03712-y>

Share this article

Anyone you share the following link with will be able to read this content:

[Get shareable link](#)

Sorry, a shareable link is not currently available for this article.

[Copy to clipboard](#)

Provided by the Springer Nature SharedIt content-sharing initiative

This article was downloaded by **calibre** from <https://www.nature.com/articles/s41586-021-03712-y>.

- Article
- [Published: 15 September 2021](#)

Widespread phytoplankton blooms triggered by 2019–2020 Australian wildfires

- [Weiyi Tang¹ na1 nAff11](#),
- [Joan Llort](#) [ORCID: orcid.org/0000-0003-1490-4521^{2,3} na1](#),
- [Jakob Weis](#) [ORCID: orcid.org/0000-0002-9493-4888^{2,4}](#),
- [Morgane M. G. Perron²](#),
- [Sara Basart](#) [ORCID: orcid.org/0000-0002-9821-8504³](#),
- [Zuchuan Li^{1,5}](#),
- [Shubha Sathyendranath](#) [ORCID: orcid.org/0000-0003-3586-192X⁶](#),
- [Thomas Jackson⁶](#),
- [Estrella Sanz Rodriguez⁷](#),
- [Bernadette C. Proemse²](#),
- [Andrew R. Bowie](#) [ORCID: orcid.org/0000-0002-5144-7799^{2,8}](#),
- [Christina Schallenberg^{2,8}](#),
- [Peter G. Strutton^{2,4}](#),
- [Richard Matear](#) [ORCID: orcid.org/0000-0002-3225-0800⁹](#) &
- [Nicolas Cassar](#) [ORCID: orcid.org/0000-0003-0100-3783^{1,10}](#)

[Nature](#) volume **597**, pages 370–375 (2021)

- 2977 Accesses
- 1053 Altmetric
- [Metrics details](#)

Subjects

- [Atmospheric chemistry](#)
- [Carbon cycle](#)
- [Fire ecology](#)
- [Marine chemistry](#)

Abstract

Droughts and climate-change-driven warming are leading to more frequent and intense wildfires^{1,2,3}, arguably contributing to the severe 2019–2020 Australian wildfires⁴. The environmental and ecological impacts of the fires include loss of habitats and the emission of substantial amounts of atmospheric aerosols^{5,6,7}. Aerosol emissions from wildfires can lead to the atmospheric transport of macronutrients and bio-essential trace metals such as nitrogen and iron, respectively^{8,9,10}. It has been suggested that the oceanic deposition of wildfire aerosols can relieve nutrient limitations and, consequently, enhance marine productivity^{11,12}, but direct observations are lacking. Here we use satellite and autonomous biogeochemical Argo float data to evaluate the effect of 2019–2020 Australian wildfire aerosol deposition on phytoplankton productivity. We find anomalously widespread phytoplankton blooms from December 2019 to March 2020 in the Southern Ocean downwind of Australia. Aerosol samples originating from the Australian wildfires contained a high iron content and atmospheric trajectories show that these aerosols were likely to be transported to the bloom regions, suggesting that the blooms resulted from the fertilization of the iron-limited waters of the Southern Ocean. Climate models project more frequent and severe wildfires in many regions^{1,2,3}. A greater appreciation of the links between wildfires, pyrogenic aerosols¹³, nutrient cycling and marine photosynthesis could improve our understanding of the contemporary and glacial–interglacial cycling of atmospheric CO₂ and the global climate system.

Access options

[Subscribe to Journal](#)

Get full journal access for 1 year

\$199.00

only \$3.90 per issue

[Subscribe](#)

All prices are NET prices.

VAT will be added later in the checkout.

Tax calculation will be finalised during checkout.

Rent or Buy article

Get time limited or full article access on ReadCube.

from \$8.99

[Rent or Buy](#)

All prices are NET prices.

Additional access options:

- [Log in](#)
- [Access through your institution](#)
- [Learn about institutional subscriptions](#)

Fig. 1: Maps of black carbon AOD and [Chla] anomalies and their historical records.

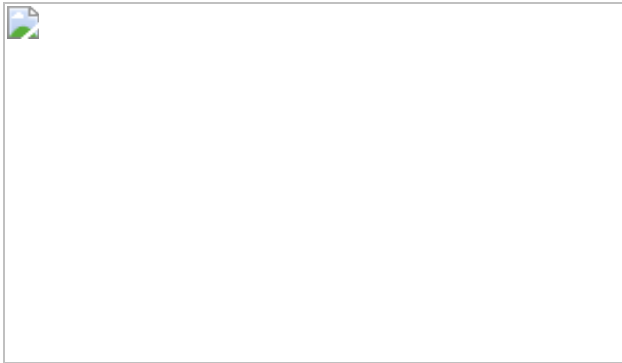


Fig. 2: Temporal patterns of black carbon AOD and satellite [Chla] in two regions denoted in Fig. 1 during the 2019–2020 Australian wildfire season.

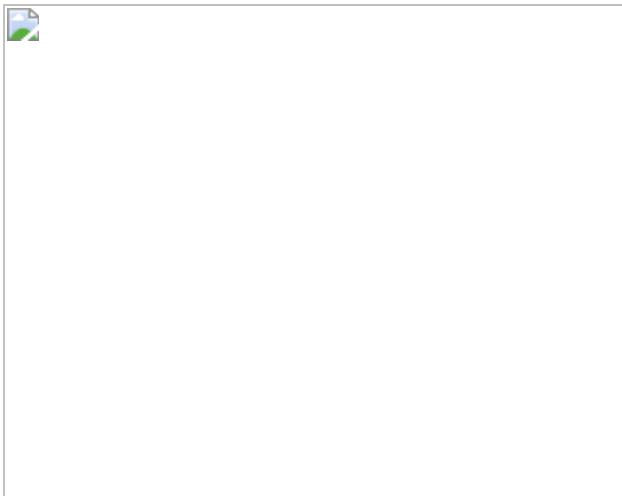


Fig. 3: Plankton blooms observed by in situ measurements from BGC-Argo floats and satellites.

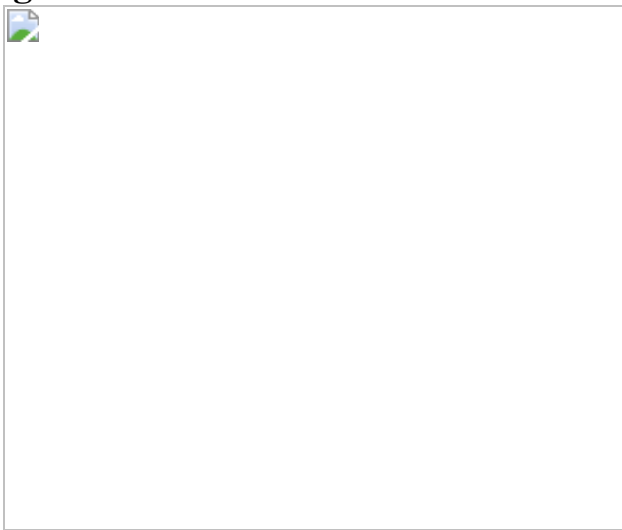
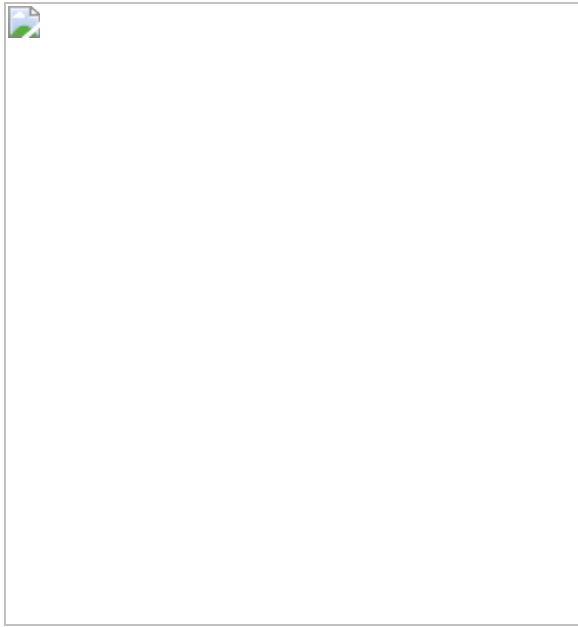


Fig. 4: Enhancement in marine phytoplankton productivity during the 2019–2020 Australian wildfires.



Data availability

The ESA's chlorophyll-a products can be accessed at <http://www.esa-oceancolour-cci.org/>. Satellite aerosol data are available from the Giovanni online data system (<https://giovanni.gsfc.nasa.gov/giovanni/>). The Copernicus Atmosphere Monitoring Service (CAMS) aerosol reanalysis datasets can be downloaded from the CAMS Atmosphere Data Store (ADS; <https://ads.atmosphere.copernicus.eu/cdsapp#!/dataset/cams-global-reanalysis-eac4?tab=overview>). The Argo float data are openly available on the Ifremer ftp-server (<ftp://ftp.ifremer.fr/ifremer/argo/dac/>). The net primary production estimates are available from the Ocean Productivity website (http://sites.science.oregonstate.edu/ocean_productivity/index.php). Access to datasets analysed in this study is also provided in the Methods section. Datasets generated in this study are provided as Source data and at <https://doi.org/10.5281/zenodo.4895657>. [Source data](#) are provided with this paper.

References

1. 1.

Bowman, D. M. J. S. et al. Vegetation fires in the Anthropocene. *Nat. Rev. Earth Environ.* **1**, 500–515 (2020).

2. 2.

Abatzoglou, J. T., Williams, A. P. & Barbero, R. Global emergence of anthropogenic climate change in fire weather indices. *Geophys. Res. Lett.* **46**, 326–336 (2019).

3. 3.

Huang, Y., Wu, S. & Kaplan, J. O. Sensitivity of global wildfire occurrences to various factors in the context of global change. *Atmos. Environ.* **121**, 86–92 (2015).

4. 4.

van Oldenborgh, G. J. et al. Attribution of the Australian bushfire risk to anthropogenic climate change. *Nat. Hazards Earth Syst. Sci.* **21**, 941–960 (2021).

5. 5.

Ward, M. et al. Impact of 2019–2020 mega-fires on Australian fauna habitat. *Nat. Ecol. Evol.* **4**, 1321–1326 (2020).

6. 6.

Kablick III, G. P., Allen, D. R., Fromm, M. D. & Nedoluha, G. E. Australian PyroCb smoke generates synoptic-scale stratospheric anticyclones. *Geophys. Res. Lett.* **47**, e2020GL088101 (2020).

7. 7.

Hirsch, E. & Koren, I. Record-breaking aerosol levels explained by smoke injection into the stratosphere. *Science* **371**, 1269–1274 (2021).

8. 8.

Schlosser, J. S. et al. Analysis of aerosol composition data for western United States wildfires between 2005 and 2015: Dust emissions, chloride depletion, and most enhanced aerosol constituents. *J. Geophys. Res. Atmos.* **122**, 8951–8966 (2017).

9. 9.

Barkley, A. E. et al. African biomass burning is a substantial source of phosphorus deposition to the Amazon, Tropical Atlantic Ocean, and Southern Ocean. *Proc. Natl Acad. Sci. USA* **116**, 16216–16221 (2019).

10. 10.

Guieu, C., Bonnet, S., Wagener, T. & Loÿe-Pilot, M.-D. Biomass burning as a source of dissolved iron to the open ocean? *Geophys. Res. Lett.* **32**, L19608 (2005).

11. 11.

Ito, A. Mega fire emissions in Siberia: potential supply of bioavailable iron from forests to the ocean. *Biogeosciences* **8**, 1679–1697 (2011).

12. 12.

Abram, N. J., Gagan, M. K., McCulloch, M. T., Chappell, J. & Hantoro, W. S. Coral reef death during the 1997 Indian Ocean Dipole linked to Indonesian wildfires. *Science* **301**, 952–955 (2003).

13. 13.

Ito, A. et al. Pyrogenic iron: the missing link to high iron solubility in aerosols. *Sci. Adv.* **5**, eaau7671 (2019).

14. 14.

Jia, G. et al. in *Climate Change and Land: an IPCC Special Report on Climate Change, Desertification, Land Degradation, Sustainable Land Management, Food Security, and Greenhouse Gas Fluxes in Terrestrial Ecosystems* Ch. 2 (IPCC, in the press).

15. 15.

Jiang, Y. et al. Impacts of wildfire aerosols on global energy budget and climate: the role of climate feedbacks. *J. Clim.* **33**, 3351–3366 (2020).

16. 16.

Bowman, D. et al. Wildfires: Australia needs national monitoring agency. *Nature* **584**, 188–191 (2020).

17. 17.

New WWF report: 3 billion animals impacted by Australia's bushfire crisis. *WWF* <https://www.wwf.org.au/news/news/2020/3-billion-animals-impacted-by-australia-bushfire-crisis#gs.ebzve2> (2020).

18. 18.

van der Velde, I. R. et al. Vast CO₂ release from Australian fires in 2019–2020 constrained by satellite. *Nature* <https://doi.org/10.1038/s41586-021-03712-y> (2021).

19. 19.

National Greenhouse Gas Inventory Report: 2018 (Australian Government, 2020); <https://www.industry.gov.au/data-and-publications/national-greenhouse-gas-inventory-report-2018>.

20. 20.

Mahowald, N. M. et al. Aerosol impacts on climate and biogeochemistry. *Annu. Rev. Environ. Res.* **36**, 45–74 (2011).

21. 21.

Boyd, P. W. et al. Mesoscale iron enrichment experiments 1993–2005: synthesis and future directions. *Science* **315**, 612–617 (2007).

22. 22.

Jickells, T. et al. Global iron connections between desert dust, ocean biogeochemistry, and climate. *Science* **308**, 67–71 (2005).

23. 23.

Martin, J. H. Glacial-interglacial CO₂ change: the iron hypothesis. *Paleoceanography* **5**, 1–13 (1990).

24. 24.

Tagliabue, A. et al. Surface-water iron supplies in the Southern Ocean sustained by deep winter mixing. *Nat. Geosci.* **7**, 314–320 (2014).

25. 25.

Cassar, N. et al. The Southern Ocean biological response to aeolian iron deposition. *Science* **317**, 1067–1070 (2007).

26. 26.

Gabric, A. J., Cropp, R., Ayers, G. P., McTainsh, G. & Braddock, R. Coupling between cycles of phytoplankton biomass and aerosol optical depth as derived from SeaWiFS time series in the Subantarctic Southern Ocean. *Geophys. Res. Lett.* **29**, 16-11–16-14 (2002).

27. 27.

Ardyna, M. et al. Hydrothermal vents trigger massive phytoplankton blooms in the Southern Ocean. *Nat. Commun.* **10**, 2451 (2019).

28. 28.

Duprat, L. P. A. M., Bigg, G. R. & Wilton, D. J. Enhanced Southern Ocean marine productivity due to fertilization by giant icebergs. *Nat. Geosci.* **9**, 219–221 (2016).

29. 29.

Bixby, R. J. et al. Fire effects on aquatic ecosystems: an assessment of the current state of the science. *Freshwater Sci.* **34**, 1340–1350 (2015).

30. 30.

Inness, A. et al. The CAMS reanalysis of atmospheric composition. *Atmos. Chem. Phys.* **19**, 3515–3556 (2019).

31. 31.

Shafeeque, M., Sathyendranath, S., George, G., Balchand, A. N. & Platt, T. Comparison of seasonal cycles of phytoplankton chlorophyll, aerosols, winds and sea-surface temperature off Somalia. *Front. Marine Sci.* **4**, 384 (2017).

32. 32.

Cassar, N. et al. The influence of iron and light on net community production in the Subantarctic and Polar Frontal zones. *Biogeosciences* **8**, 227–237 (2011).

33. 33.

Mitchell, B. G. & Holm-Hansen, O. Observations of modeling of the Antarctic phytoplankton crop in relation to mixing depth. *Deep Sea Res. Part A* **38**, 981–1007 (1991).

34. 34.

Longo, A. F. et al. Influence of atmospheric processes on the solubility and composition of iron in Saharan dust. *Environ. Sci. Technol.* **50**, 6912–6920 (2016).

35. 35.

Meskhidze, N., Nenes, A., Chameides, W. L., Luo, C. & Mahowald, N. Atlantic Southern Ocean productivity: fertilization from above or below? *Global Biogeochem. Cycles* **21**, GB2006 (2007).

36. 36.

Sarmiento, J. L., Slater, R. D., Dunne, J., Gnanadesikan, A. & Hiscock, M. R. Efficiency of small scale carbon mitigation by patch iron fertilization. *Biogeosciences* **7**, 3593–3624 (2010).

37. 37.

Brzezinski, M. A., Jones, J. L. & Demarest, M. S. Control of silica production by iron and silicic acid during the Southern Ocean Iron Experiment (SOFeX). *Limnol. Oceanogr.* **50**, 810–824 (2005).

38. 38.

Lovenduski, N. S. & Gruber, N. Impact of the Southern Annular Mode on Southern Ocean circulation and biology. *Geophys. Res. Lett.* **32**, L11603 (2005).

39. 39.

Cai, W., Cowan, T. & Raupach, M. Positive Indian Ocean Dipole events precondition southeast Australia bushfires. *Geophys. Res. Lett.* **36**, L19710 (2009).

40. 40.

Chen, Y. et al. A pan-tropical cascade of fire driven by El Niño/Southern Oscillation. *Nat. Climate Change* **7**, 906–911 (2017).

41. 41.

Lim, E.-P. et al. Australian hot and dry extremes induced by weakenings of the stratospheric polar vortex. *Nat. Geosci.* **12**, 896–901 (2019).

42. 42.

Cai, W. et al. Increased frequency of extreme Indian Ocean Dipole events due to greenhouse warming. *Nature* **510**, 254–258 (2014).

43. 43.

Cropp, R. A. et al. The likelihood of observing dust-stimulated phytoplankton growth in waters proximal to the Australian continent. *J. Mar. Syst.* **117–118**, 43–52 (2013).

44. 44.

Hamilton, D. S. et al. Impact of changes to the atmospheric soluble iron deposition flux on ocean biogeochemical cycles in the anthropocene. *Global Biogeochem. Cycles* **34**, e2019GB006448 (2020).

45. 45.

Duce, R. et al. Impacts of atmospheric anthropogenic nitrogen on the open ocean. *Science* **320**, 893–897 (2008).

46. 46.

Han, Y. et al. Asian inland wildfires driven by glacial-interglacial climate change. *Proc. Natl Acad. Sci. USA* **117**, 5184–5189 (2020).

47. 47.

van der Werf, G. R. et al. Global fire emissions estimates during 1997–2016. *Earth Sys. Sci. Data* **9**, 697–720 (2017).

48. 48.

Orsi, A. H., Whitworth, T. & Nowlin, W. D. On the meridional extent and fronts of the Antarctic Circumpolar Current. *Deep Sea Res. Part I* **42**, 641–673 (1995).

49. 49.

Sathyendranath, S. et al. An ocean-colour time series for use in climate studies: the experience of the Ocean-Colour Climate Change Initiative (OC-CCI). *Sensors* **19**, 4285 (2019).

50. 50.

Morcrette, J.-J. et al. Aerosol analysis and forecast in the European Centre for Medium-Range Weather Forecasts Integrated Forecast System: forward modeling. *J. Geophys. Res. Atmospheres* **114**, D06206 (2009).

51. 51.

Levy, R. C. et al. Exploring systematic offsets between aerosol products from the two MODIS sensors. *Atmos. Meas. Tech.* **11**, 4073–4092 (2018).

52. 52.

Benedetti, A. et al. Aerosol analysis and forecast in the European Centre for Medium-Range Weather Forecasts Integrated Forecast System: 2. Data assimilation. *J. Geophys. Res.* **114**, D13 (2009).

53. 53.

Kaiser, J. W. et al. Biomass burning emissions estimated with a global fire assimilation system based on observed fire radiative power. *Biogeosciences* **9**, 527–554 (2012).

54. 54.

Y. Bennouna et al. *Validation Report of the CAMS Global Reanalysis of Aerosols and Reactive Gases, Years 2003–2019* (Copernicus Atmosphere Monitoring Service, 2020).

55. 55.

Ito, A. et al. Evaluation of aerosol iron solubility over Australian coastal regions based on inverse modeling: implications of bushfires on bioaccessible iron concentrations in the Southern Hemisphere. *Prog. Earth Planet. Sci.* **7**, 42 (2020).

56. 56.

Khaykin, S. et al. The 2019/20 Australian wildfires generated a persistent smoke-charged vortex rising up to 35 km altitude. *Commun. Earth Environ.* **1**, 22 (2020).

57. 57.

Haëntjens, N., Boss, E. & Talley, L. D. Revisiting Ocean Color algorithms for chlorophyll a and particulate organic carbon in the Southern Ocean using biogeochemical floats. *J. Geophys. Res. Oceans* **122**, 6583–6593 (2017).

58. 58.

Boss, E. et al. The characteristics of particulate absorption, scattering and attenuation coefficients in the surface ocean; contribution of the Tara Oceans expedition. *Methods Oceanogr.* **7**, 52–62 (2013).

59. 59.

de Boyer Montégut, C., Madec, G., Fischer, A. S., Lazar, A. & Iudicone, D. Mixed layer depth over the global ocean: an examination of profile data and a profile-based climatology. *J. Geophys. Res. Oceans* **109**, C12003 (2004).

60. 60.

Dong, S., Sprintall, J., Gille, S. T. & Talley, L. Southern Ocean mixed-layer depth from Argo float profiles. *J. Geophys. Res. Oceans* **113**, C06013 (2008).

61. 61.

Cutter, G. A. et al. Sampling and Sample-handling Protocols for GEOTRACES Cruises, version 3.0 (2017).

62. 62.

Morton, P. L. et al. Methods for the sampling and analysis of marine aerosols: results from the 2008 GEOTRACES aerosol intercalibration

experiment. *Limnol. Oceanogr. Methods* **11**, 62–78 (2013).

63. 63.

Perron, M. M. G. et al. Assessment of leaching protocols to determine the solubility of trace metals in aerosols. *Talanta* **208**, 120377 (2020).

64. 64.

Shelley, R. U., Landing, W. M., Ussher, S. J., Planquette, H. & Sarthou, G. Regional trends in the fractional solubility of Fe and other metals from North Atlantic aerosols (GEOTRACES cruises GA01 and GA03) following a two-stage leach. *Biogeosciences* **15**, 2271–2288 (2018).

65. 65.

Sanz Rodriguez, E. et al. Analysis of levoglucosan and its isomers in atmospheric samples by ion chromatography with electrospray lithium cationisation—triple quadrupole tandem mass spectrometry. *J. Chromatogr. A* **1610**, 460557 (2020).

66. 66.

McLennan, S. M. Relationships between the trace element composition of sedimentary rocks and upper continental crust. *Geochim. Geophys. Geosyst.* **2**, 1201 (2001).

67. 67.

Shelley, R. U. et al. Quantification of trace element atmospheric deposition fluxes to the Atlantic Ocean (>40°N; GEOVIDE, GEOTRACES GA01) during spring 2014. *Deep Sea Res. Part I* **119**, 34–49 (2017).

68. 68.

Sholkovitz, E. R., Sedwick, P. N., Church, T. M., Baker, A. R. & Powell, C. F. Fractional solubility of aerosol iron: synthesis of a

global-scale data set. *Geochim. Cosmochim. Acta* **89**, 173–189 (2012).

69. 69.

Stein, A. F. et al. NOAA's HYSPLIT atmospheric transport and dispersion modeling system. *Bull. Am. Meteorol. Soc.* **96**, 2059–2077 (2016).

70. 70.

Kalnay, E. et al. The NCEP/NCAR 40-year reanalysis project. *Bull. Am. Meteorol. Soc.* **77**, 437–471 (1996).

71. 71.

Tatlhego, M., Bhattachan, A., Okin, G. S. & D'Odorico, P. Mapping areas of the Southern Ocean where productivity likely depends on dust-delivered Iron. *J. Geophys. Res. Atmospheres* **125**, e2019JD030926 (2020).

72. 72.

Stein, A. F., Rolph, G. D., Draxler, R. R., Stunder, B. & Ruminski, M. Verification of the NOAA smoke forecasting system: model sensitivity to the injection height. *Weather Forecast.* **24**, 379–394 (2009).

73. 73.

Behrenfeld, M. J. & Falkowski, P. G. Photosynthetic rates derived from satellite-based chlorophyll concentration. *Limnol. Oceanogr.* **42**, 1–20 (1997).

74. 74.

Behrenfeld, M. J., Boss, E., Siegel, D. A. & Shea, D. M. Carbon-based ocean productivity and phytoplankton physiology from space. *Global Biogeochem. Cycles* **19**, GB1006 (2005).

75. 75.

Westberry, T., Behrenfeld, M. J., Siegel, D. A. & Boss, E. Carbon-based primary productivity modeling with vertically resolved photoacclimation. *Global Biogeochem. Cycles* **22**, GB2024 (2008).

76. 76.

Silsbe, G. M., Behrenfeld, M. J., Halsey, K. H., Milligan, A. J. & Westberry, T. K. The CAFE model: a net production model for global ocean phytoplankton. *Global Biogeochem. Cycles* **30**, 1756–1777 (2016).

77. 77.

Laws, E. A., D'Sa, E. & Naik, P. Simple equations to estimate ratios of new or export production to total production from satellite-derived estimates of sea surface temperature and primary production. *Limnol. Oceanogr. Methods* **9**, 593–601 (2011).

78. 78.

Dunne, J. P., Armstrong, R. A., Gnanadesikan, A. & Sarmiento, J. L. Empirical and mechanistic models for the particle export ratio. *Global Biogeochem. Cycles* **19**, GB4026 (2005).

79. 79.

Li, Z. & Cassar, N. Satellite estimates of net community production based on O₂/Ar observations and comparison to other estimates. *Global Biogeochem. Cycles* **30**, 735–752 (2016).

80. 80.

Siegel, D. A. et al. Global assessment of ocean carbon export by combining satellite observations and food-web models. *Global Biogeochem. Cycles* **28**, 181–196 (2014).

81. 81.

Marshall, G. J. Trends in the Southern Annular Mode from observations and reanalyses. *J. Climate* **16**, 4134–4143 (2003).

82. 82.

Saji, N. H. & Yamagata, T. Possible impacts of Indian Ocean Dipole mode events on global climate. *Climate Res.* **25**, 151–169 (2003).

Acknowledgements

Analyses of satellite aerosol observations used in this study were produced with the Giovanni online data system, developed and maintained by the NASA GES DISC. We thank SeaWiFS and MODIS mission scientists and associated NASA personnel for the production of the data used in this research effort. The BGC-Argo data were collected and made freely available by the International Argo Program and the national programs that contribute to it (<http://www.argo.ucsd.edu>, <http://argo.jcommops.org>). The Argo Program is part of the Global Ocean Observing System (<https://doi.org/10.17882/42182>). W.T. is supported by the Harry H. Hess Postdoctoral Fellowship from Princeton University. N.C. is supported by the “Laboratoire d’Excellence” LabexMER (ANR-10-LABX-19) and co-funded by a grant from the French government under the program “Investissements d’Avenir”. S.B. acknowledges the AXA Research Fund for the support of the long-term research line on Sand and Dust Storms at the Barcelona Supercomputing Center (BSC) and CAMS Global Validation (CAMS-84). P.G.S., J.L., M.M.G.P. and A.R.B. are supported by the Australian Research Council Discovery Projects scheme (DP190103504). P.G.S. and J.W. are supported by the Australian Research Council Centre of Excellence for Climate Extremes (CLEX: CE170100023). J.L. is supported by the European Union’s Horizon 2020 research and innovation programme under the Marie Skłodowska-Curie grant agreement no. 754433. A.R.B. is supported by the Australian Research Council Future Fellowship scheme (FT130100037). R.M. is supported by the CSIRO Decadal Climate Forecasting Project. We thank M. Strzelec, M. East, T. Holmes, M. Corkill, S. Meyerink and the Wellington Park Management Trust for help with installation and sampling the Tasmanian aerosol time-series station; A. Townsend for iron aerosol analyses by ICPMS at the University of

Tasmania; and A. Benedetti and S. Remy for providing insights on the validation of aerosol reanalysis.

Author information

Author notes

1. Weiyi Tang

Present address: Department of Geosciences, Princeton University, Princeton, NJ, USA

2. These authors contributed equally: Weiyi Tang, Joan Llort

Affiliations

1. Division of Earth and Climate Sciences, Nicholas School of the Environment, Duke University, Durham, NC, USA

Weiyi Tang, Zuchuan Li & Nicolas Cassar

2. Institute for Marine and Antarctic Studies, University of Tasmania, Hobart, Tasmania, Australia

Joan Llort, Jakob Weis, Morgane M. G. Perron, Bernadette C. Proemse, Andrew R. Bowie, Christina Schallenberg & Peter G. Strutton

3. Barcelona Supercomputing Centre, Barcelona, Spain

Joan Llort & Sara Basart

4. Australian Research Council Centre of Excellence for Climate Extremes, University of Tasmania, Hobart, Tasmania, Australia

Jakob Weis & Peter G. Strutton

5. Applied Ocean Physics and Engineering, Woods Hole Oceanographic Institution, Woods Hole, MA, USA

Zuchuan Li

6. Plymouth Marine Laboratory, Plymouth, UK

Shubha Sathyendranath & Thomas Jackson

7. Australian Centre for Research on Separation Science (ACROSS), School of Natural Sciences, University of Tasmania, Hobart, Tasmania, Australia

Estrella Sanz Rodriguez

8. Australian Antarctic Program Partnership, University of Tasmania, Hobart, Tasmania, Australia

Andrew R. Bowie & Christina Schallenberg

9. CSIRO Oceans and Atmosphere, Hobart, Tasmania, Australia

Richard Matear

10. CNRS, Univ Brest, IRD, Ifremer, LEMAR, Plouzané, France

Nicolas Cassar

Contributions

This study was conceived by N.C., J.L. and R.M. W.T. and N.C. wrote the manuscript with contribution from co-authors. J.L. and W.T. analysed the spatial distribution and time-series of AOD, aerosol deposition and [Chla], and coordinated the interdisciplinary approach. J.W., C.S. and P.G.S. conducted the analysis of BGC-Argo float observations. S.B. and J.L. conducted the AOD decomposition reanalysis. Z.L. calculated MLD from Argo floats and estimated marine production with W.T. S.S. and T.J. provided and helped with interpretation of satellite observations of [Chla].

M.M.G.P., B.C.P. and A.R.B. collected the aerosol samples and analysed the aerosol Fe content and solubility. E.S.R. analysed levoglucosan in the aerosol samples. All authors contributed to the interpretation of the results.

Corresponding authors

Correspondence to Richard Matear or Nicolas Cassar.

Ethics declarations

Competing interests

The authors declare no competing interests.

Additional information

Peer review information *Nature* thanks the anonymous reviewers for their contribution to the peer review of this work.

Publisher's note Springer Nature remains neutral with regard to jurisdictional claims in published maps and institutional affiliations.

Extended data figures and tables

[Extended Data Fig. 1 Emission and deposition of aerosols and response of phytoplankton.](#)

a, Monthly aerosol optical depth (AOD) at 550 nm observed by MODIS satellite during the 2019–2020 Australian wildfires from November 2019 to February 2020. **b**, Monthly chlorophyll-a absolute anomaly. **c**, Monthly cumulative black carbon aerosol deposition. Contour lines indicate the monthly maximum black carbon AOD (black = 0.05, grey = 0.1, light-grey = 0.15). All: Subtropical, Subantarctic and Polar Fronts are indicated with a dotted, a dashed and a solid black line, respectively⁴⁸.

Extended Data Fig. 2 Forward trajectories tracking the emission and transport of aerosols from major fire events during the 2019–2020 Australian wildfires.

a, Seven-day trajectories (grey lines) launched every 6 h and originated from wildfires during the period of 26 October to 4 November 2019 and black carbon AOD from the same period shown as the background map. The trajectory origins are depicted by black circles. The distribution of trajectories generally follows the black AOD pattern. **b**, Seven-day trajectories (grey lines) originated from wildfires during the period of 26 November to 5 December 2019. **c**, The spatial distribution of 7-day trajectory endpoints frequencies in 2° by 2° grid over the period of November 2019 to January 2020. The trajectory origins are depicted by black circles to represent the major fires' locations. The 7-day air parcel forward trajectories were launched daily. The red contours depict regions where [Chla] more than doubled during the same period compared with their climatologies. The large [Chla] anomalies generally occurred in regions over which the trajectories passed.

Extended Data Fig. 3 Identification of regions of interest with potential aerosol fertilization.

a, Austral summer (DJF) 2019–2020 averaged chlorophyll-a relative anomaly map with cyan contour lines indicating where the anomaly is equal to 100%. **b**, Austral summer (DJF) 2019–2020 cumulative deposition of dust and black-carbon with black contour line indicating where deposition is equal to 150 mg m^{-2} . **c**, Pixels where both [Chla] relative anomaly exceeds 100% and cumulative deposition exceeds 150 mg m^{-2} are marked in green. Black boxes indicate the South of Australia and Pacific Southern Ocean regions defined in this study. All: Subtropical, Subantarctic and Polar Fronts are indicated with a dotted, a dashed and a solid black line, respectively.

Extended Data Fig. 4 Large chlorophyll-a ([Chla]) anomaly in a big box region of the South Pacific and Southern Ocean during 2019–2020 Australian wildfires.

a, [Chla] anomaly map from December 2019 to February 2020 in comparison to their climatologies. A large portion of the ocean basin (solid black box) was selected to calculate [Chla] time-series. STF, Subtropical Front; SAF, Subantarctic Front. **b**, Time-series of average [Chla] in the selected box region. Monthly climatological values shown in solid black line. Red and blue areas denote monthly data higher or lower than climatological values, respectively. **c**, Monthly average [Chla] in individual years in the selected box region. Grey lines, historical years; solid black line, monthly climatologies; dashed black line, 2002 Australian wildfire season; red line, 2019–2020 Australian wildfire season.

[Extended Data Fig. 5 Large chlorophyll-a \(\[Chla\]\) anomaly in numerous small box regions during 2019–2020 Australian wildfires.](#)

a, [Chla] time-series was calculated in 4,681 of 10° by 10° boxes from 1997 to 2020 in the broad South Pacific and Southern Ocean (20° S– 60° S; 120° E– 80° W). Yellow circles and yellow dashed boxes are examples to show the center and coverage of each box region. Box moves by 1° eastward and southward sequentially illustrated by the black arrows. Box position 1, 151, 4,531 and 4,681 denoting the edge of the study region are shown as examples on the map of annual [Chla] climatology. The ratio of monthly [Chla] to its monthly climatology is calculated for each 10° by 10° box starting from October 1997 to May 2020. Black circles: centre locations of 10° by 10° boxes where $\frac{\text{monthly}}{\text{climatology}} > 2.5$ before the 2019–2020 wildfires (from October 1997 to August 2019); red circles: centre locations of 10° by 10° boxes where $\frac{\text{monthly}}{\text{climatology}} > 2.5$ during or after the 2019–2020 wildfires (from September 2019 to May 2020). Historically, regions with a large anomaly (black circles) are mostly located in coastal waters (for example, east coast of Australia). In contrast, during the 2019–2020 Australian wildfires (red circles), large areas of the open ocean show a high [Chla] anomaly (for example, south of Australia and Pacific sector of the Southern Ocean).

Oceanic [Chla] anomalies of this magnitude are unprecedented in the historical record. Some of the black and red circles are on land because a fraction of the 10° by 10° box around these circles covers the ocean. **b**, Ratio of monthly [Chla] to its corresponding monthly climatologies for each box region from 1997 to 2020. **c**, Frequency distributions of the monthly [Chla] to monthly climatology ratios over the historical and 2019–2020 austral summers.

Extended Data Fig. 6 Maps of b_{bp} anomalies and comparison between calibrated and uncalibrated BGC Argo in situ b_{bp} measurements.

a, Satellite backscatter b_{bp} relative anomaly for the 2019–2020 austral summer. Bloom region and BGC-Argo float trajectories superimposed on the map. Float positions from September 2019 through March 2020 highlighted. The southern float (red) was in a biologically more active region of the bloom than the two northern floats (blue and yellow). This corroborates the stronger bloom signal shown by the southern float. Dotted, dot-dashed, and solid lines in **a** represent the climatological positions of the Subtropical Front, Subantarctic Front and Polar Front, respectively⁴⁸. **b**, Satellite b_{bp} averaged over two sub-regions encompassing the float paths. The solid lines are 2019–2020 observations and the dotted lines with coloured standard deviation envelopes are the climatology. This analysis corroborates the stronger bloom signal shown by the southern float compared with the two northern floats. **c**, Comparison between uncalibrated (dashed lines) and calibrated (solid lines) in situ b_{bp} measured by the three BGC-Argo floats. Surface b_{bp} estimates were calculated as the median b_{bp} between 0 and 20 m depth and then calibrated using a linear regression (see [Methods](#) for details). The calibration was applied to allow for comparison between float b_{bp} and the satellite-based climatology. The general trend of the float signal is not altered by the calibration.

Extended Data Fig. 7 Iron (Fe) concentration and origin of aerosols collected at an aerosol time-series sampling station in Tasmania during the 2019–2020 Australian wildfires.

a, Total Fe concentration (blue line) during the 2019–2020 Australian wildfire season is compared with the historical median value from 2016–2019 (dashed black line). High levoglucosan concentration (green bar) indicates wildfire-derived aerosols. Grey shaded areas represent samples influenced by anthropogenic sources. See [Methods](#) for the use of tracers to track the sources of aerosols. **b**, Labile Fe concentration (blue line) during the 2019–2020 Australian wildfire season is compared with the historical median value from 2016–2019 (dashed black line). The aerosols with high Fe content collected around 15 January 2020 are likely to have originated from wildfires, indicated by the high concentration of levoglucosan concentrations and low concentration of anthropogenic tracers.

Extended Data Fig. 8 Tracking the origins of aerosols with high iron content collected at an aerosol time-series sampling station in Tasmania during 15–17 January 2020.

a, High black carbon AOD plume passing the sampling station (cyan star). **b**, Five-day backward trajectories were launched every 6 h from the sampling station (cyan star) during 15–17 January 2020. Both the distribution of trajectories and the frequency of trajectories' endpoints confirm that the majority of the aerosols came from southeastern Australia where wildfires were raging.

Extended Data Fig. 9 Anomalies in marine phytoplankton productivity during 2019–2020 Australian wildfires.

a, b, Net primary production (NPP) (**a**) and export production (EP) (**b**) anomalies in 2019–2020 austral summer relative to their climatologies. Black boxes denote the basin-scale regions (20° S– 55° S, 120° E– 90° W) used to estimate changes in marine production during the 2019–2020 Australian wildfires.

Extended Data Fig. 10 Relations of large-scale climate patterns to the occurrence of wildfires and to chlorophyll a distribution.

a–c, Time-series of climate indices Indian Ocean Dipole (IOD) (**a**), Southern Annular Mode (SAM) (**b**) and Oceanic Niño Index (**c**). Historical Australian mega-wildfire periods shaded in orange (>1 million hectares of land burned). **d**, [Chla] anomaly predicted by IOD index during the 2019–2020 Australian wildfires. **e**, [Chla] anomaly predicted by SAM index during the 2019–2020 Australian wildfires. The [Chla] anomaly potentially induced by the climate patterns are substantially smaller than the observed [Chla] anomaly (Fig. [1d](#)).

Supplementary information

[Supplementary Information](#)

This file contains Supplementary Discussion, Tables 1–3, Figs. 1–9, and additional references.

[Supplementary Video 1](#)

Animation of daily black carbon aerosol optical depth (BC AOD) derived from CAMS reanalysis during the 2019–2020 Australian wildfires.

Source data

[Source Data Fig. 1](#)

[Source Data Fig. 2](#)

[Source Data Fig. 3](#)

[Source Data Fig. 4](#)

Rights and permissions

[Reprints and Permissions](#)

About this article

Cite this article

Tang, W., Llort, J., Weis, J. *et al.* Widespread phytoplankton blooms triggered by 2019–2020 Australian wildfires. *Nature* **597**, 370–375 (2021). <https://doi.org/10.1038/s41586-021-03805-8>

- Received: 25 August 2020
- Accepted: 05 July 2021
- Published: 15 September 2021
- Issue Date: 16 September 2021
- DOI: <https://doi.org/10.1038/s41586-021-03805-8>

Share this article

Anyone you share the following link with will be able to read this content:

[Get shareable link](#)

Sorry, a shareable link is not currently available for this article.

[Copy to clipboard](#)

Provided by the Springer Nature SharedIt content-sharing initiative

This article was downloaded by **calibre** from <https://www.nature.com/articles/s41586-021-03805-8>

- Article
- Open Access
- [Published: 01 September 2021](#)

Multiple hominin dispersals into Southwest Asia over the past 400,000 years

- [Huw S. Groucutt](#) [ORCID: orcid.org/0000-0002-9111-1720](#)^{1,2,3},
- [Tom S. White](#) [ORCID: orcid.org/0000-0001-9056-7286](#)⁴,
- [Eleanor M. L. Scerri](#) [ORCID: orcid.org/0000-0002-7468-9977](#)^{5,6,3},
- [Eric Andrieux](#) [ORCID: orcid.org/0000-0003-1688-0543](#)^{7,8},
- [Richard Clark-Wilson](#)^{8,9},
- [Paul S. Breeze](#) [ORCID: orcid.org/0000-0003-2575-8021](#)¹⁰,
- [Simon J. Armitage](#) [ORCID: orcid.org/0000-0003-1480-9188](#)^{8,11},
- [Mathew Stewart](#) [ORCID: orcid.org/0000-0002-0413-8133](#)¹,
- [Nick Drake](#)^{10,2},
- [Julien Louys](#) [ORCID: orcid.org/0000-0001-7539-0689](#)^{12,13},
- [Gilbert J. Price](#) [ORCID: orcid.org/0000-0001-8406-4594](#)¹⁴,
- [Mathieu Duval](#) [ORCID: orcid.org/0000-0003-3181-7753](#)^{12,15},
- [Ash Parton](#)^{16,17},
- [Ian Candy](#)⁸,
- [W. Christopher Carleton](#) [ORCID: orcid.org/0000-0001-7463-8638](#)¹,
- [Ceri Shipton](#)^{18,19},
- [Richard P. Jennings](#) [ORCID: orcid.org/0000-0001-9996-7518](#)²⁰,
- [Muhammad Zahir](#) [ORCID: orcid.org/0000-0002-1765-6319](#)^{2,21},
- [James Blinkhorn](#)^{5,8},
- [Simon Blockley](#)⁸,
- [Abdulaziz Al-Omari](#)²²,
- [Abdullah M. Alsharekh](#) [ORCID: orcid.org/0000-0002-2666-3262](#)²³ &
- [Michael D. Petraglia](#) [ORCID: orcid.org/0000-0003-2522-5727](#)^{2,12,24,25}

Nature volume 597, pages 376–380 (2021)

- 22k Accesses

- 1769 Altmetric
- [Metrics details](#)

Subjects

- [Archaeology](#)

Abstract

Pleistocene hominin dispersals out of, and back into, Africa necessarily involved traversing the diverse and often challenging environments of Southwest Asia^{1,2,3,4}. Archaeological and palaeontological records from the Levantine woodland zone document major biological and cultural shifts, such as alternating occupations by *Homo sapiens* and Neanderthals. However, Late Quaternary cultural, biological and environmental records from the vast arid zone that constitutes most of Southwest Asia remain scarce, limiting regional-scale insights into changes in hominin demography and behaviour^{1,2,5}. Here we report a series of dated palaeolake sequences, associated with stone tool assemblages and vertebrate fossils, from the Khall Amayshan 4 and Jubbah basins in the Nefud Desert. These findings, including the oldest dated hominin occupations in Arabia, reveal at least five hominin expansions into the Arabian interior, coinciding with brief ‘green’ windows of reduced aridity approximately 400, 300, 200, 130–75 and 55 thousand years ago. Each occupation phase is characterized by a distinct form of material culture, indicating colonization by diverse hominin groups, and a lack of long-term Southwest Asian population continuity. Within a general pattern of African and Eurasian hominin groups being separated by Pleistocene Saharo-Arabian aridity, our findings reveal the tempo and character of climatically modulated windows for dispersal and admixture.

[Download PDF](#)

Main

As the only land bridge between Africa and Eurasia, Southwest Asia occupies a unique position for understanding key stages of human evolution and the peopling of the planet. Changing environmental and ecological conditions at the shifting interface between the Saharo-Arabian and Palaearctic biomes strongly influenced patterns of human demography through the isolation, diversification and subsequent mixing of populations^{4,6,7,8,9,10,11} (Supplementary Information, section 1). A prominent example concerns the geographical context of Neanderthal–*sapiens* admixture. Although it has been suggested that this occurred in Southwest Asia owing to the ubiquity of

Neanderthal ancestry in humans outside Africa⁶, ‘on-the-ground’ evidence for admixture, or even spatial and temporal contemporaneity with *H. sapiens*, has remained elusive in the region. One reason for this is the severely fragmented nature of Southwest Asian palaeontological, palaeoenvironmental and archaeological records. This has in turn limited our ability to overcome problematic generalizations regarding the palaeoanthropological record of Southwest Asia and address key questions about the extent to which hominin occupations of the region were continuous, the role of hominin dispersals into and within the region, and how these dispersals and interactions between hominin populations related to changes in biogeography, environment and ecology.

Research in Southwest Asia has traditionally focussed on deeply stratified cave sequences in the Levantine winter-rainfall woodland zone^{11,12,13,14,15} (Fig. 1, Supplementary Information, section 1). This has led to a detailed record for the woodlands, a southern extension of the Palaearctic biome^{4,16}. However, in the past decade, research in the Arabian Peninsula has begun to document hominin occupations of the arid Saharo-Arabian biome during episodically wetter periods characterized by grasslands, lakes and rivers^{5,10,17,18,19,20,21,22,23,24,25,26,27,28,29}. Emerging patterns of spatially divergent cultural-evolutionary developments in Southwest Asia include a young (less than 200 thousand years ago (ka)) Acheulean in central Arabia²⁴, a technology typically associated with earlier hominins such as *Homo erectus*. There are also repeated manifestations of distinctive local characteristics, commonly interpreted as autochthonous developments, in ‘refugial’ areas in southern Arabia^{22,23}.

Fig. 1: Palaeoanthropological sites in Southwest Asia dating to between 50 and 500 ka.

 figure1

a, Sites plotted on a map of modern biomes. **b**, Sites plotted on map of modern precipitation. **c**, Sites plotted on model of MIS 5e precipitation³⁴, as an illustration of the changes that occurred during humid periods.

Despite these advances, the few reported sites in interior and northern Arabia^{20,24,25,26,27,28,29} (Supplementary Information, section 1) have small sample sizes of artefacts, and are often raw material procurement and workshop sites, with a very different character to the cave and rockshelter ‘living sites’ that dominate the Levantine woodland record. The absence of permanent fluvial systems and deeply stratified cave sequences in Arabia has hampered the construction of long-timescale archaeological and hydroclimatic sequences. This has limited efforts to recognize important patterns in archaeological and palaeontological records associated with changes in hominin distribution, demography and behaviour.

Here we report multiple palaeolake sedimentary sequences with associated lithic (stone tool) assemblages and fossil fauna in the Nefud Desert of northern Arabia, representing the first detailed long-timescale record of hominin occupations in Arabia (Figs. 1–3). Khall Amayshan 4 (KAM 4) consists of a series of superimposed lake sequences within a single interdunal basin (Extended Data Figs. 1, 2, Supplementary Information, sections 2, 3). This site, currently unique in Arabia, has preserved a record analogous to the detailed fluvial archives preserved in regions such as northwest Europe. Additionally, we present further evidence for multiple hominin occupations from excavated sites dating to Marine Isotope Stage (MIS) 7 and MIS 5 from the nearby Jubbah palaeolake basin. Together the KAM 4 and Jubbah assemblages show that there were multiple hominin dispersals into Arabia over the last 400,000 years, in association with a unique hydroclimate record.

Fig. 2: The chronology and environmental context of hominin occupations in northern Arabia.

 **figure2**

a, Al Marrat 3²⁷. **b**, Jebel-Qattar 1²⁸. **c**, Al Wusta²⁰. **d**, JSM 1 (present study). **e**, Central (C), Northeast (NE), Northwest (NW), Southwest (SW), Southeast (SE) and South (S) lakes at KAM 4. US, an age for sands underlying the lake (that is, a maximum age for overlying phase of lake formation); IL, in lake (direct date on sediments within lake-related deposits). Black arrows pointing to the left (Southeast and South Lakes) reflect that the luminescence ages provide maximum ages, and the overlying lakes are younger. Filled symbols show quartz ages and open symbols show feldspar ages. **f**, East Mediterranean sapropel record³⁵, insolation³⁶ (grey), monsoon index³⁷ (black) and oxygen isotope record³⁸ (blue). Southern Arabian humid periods are defined by speleothems in green²¹. Luminescence ages are presented with 1σ uncertainties and the single U-series age is presented with a 2σ uncertainty.

Fig. 3: Stone tools from KAM 4 and Jebel Umm Sanman 1 (JSM 1).

 **figure3**

From left to right: assemblage A, KAM 4 (approximately 400 ka), assemblage B, KAM 4 (approximately 300 ka), assemblage C, KAM 4 (approximately 200 ka), JSM 1 (approximately 75 ka), assemblage E, KAM 4 (approximately 55 ka?). Scale bar, 1 cm.

Each KAM 4 palaeolake deposit is stratigraphically similar, being predominantly composed of massive or finely-laminated carbonate rich marls overlying sands (Extended Data Figure 3, Supplementary Information, section 3). The similarity of these marls, each formed by a discrete lake phase, implies that the palaeoenvironment of KAM 4 was broadly similar during successive humid phases. The sediments are comparable to other palaeolake deposits from the western Nefud Desert^{18,20}, but are notable for their stratigraphically distinct and superimposed character, and abundance of associated lithics and fossils. The sediments at the site are fine-grained (sands, silts and marls), reflecting deposition under low-energy or still-water conditions. Larger clasts (gravels) are absent, emphasizing the lack of higher-energy current flow processes feeding the basin during sediment accumulation. Reworking of lithics and fossils from the surrounding landscape into these lake bodies is therefore highly unlikely. Consequently, we argue that the assemblages of lithics and the fossils found in association with these deposits are *in situ*, which was confirmed by excavations in the case of the Northwest Lake.

The unique KAM 4 record has survived owing to migrating sand dunes that moved in a conveyor-belt-like fashion across the basin, protecting older parts of the sequence from erosion and preventing the mixing of the distinct archaeological and palaeontological assemblages associated with each lake phase. KAM 4 provides the first long-term composite sequence for the later Middle Pleistocene and Late Pleistocene in Arabia, with each phase of hominin occupation associated with a broadly similar environment and lithic raw material availability.

The oldest deposit at KAM 4, the Central Lake, is dated by luminescence to 412 ± 87 ka (Fig. 2, Extended Data Figs. 2, 3, Supplementary Information, section 5). The Central Lake deposits are also heavily iron-stained compared with other deposits at the site, attesting to their greater antiquity within the basin. The Central Lake is stratigraphically overlain by the southernmost edge of the Northeast Lake, which yielded luminescence ages of 337 ± 39 ka and 306 ± 47 ka. Although the age estimates for both the Central and Northeast Lakes have large uncertainties, we emphasize evidence for regional aridity in the millennia either side of both MIS 11 and 9 (Fig. 2), making attribution of Central Lake to MIS 11 and Northeast Lake to MIS 9 parsimonious. The Northwest Lake, which partly overlies the Northeast Lake, is dated by a suite of luminescence estimates on carbonate-rich sands bracketed between two phases of marl deposits to between 192 ± 20 ka and 210 ± 16 ka. A direct U-series age estimate of a bovid fossil from the same layer produced a consistent date of 205 ± 2 ka (2σ) (Supplementary Information, section 6). The Northwest Lake can therefore be correlated with MIS 7, the final humid phase of the Middle Pleistocene. The Southwest Lake has a luminescence estimate of 143 ± 10 ka, and therefore dates either to late MIS 6 or, less probably, to the transition to MIS 5. Sands underlying the Southeast Lake, which overlies the Central and Northeast Lakes, yielded luminescence estimates of 159 ± 11 ka to 149 ± 9 ka, similar to the South Lake at $168 \text{ ka} \pm 12$ ka to 142 ± 13 ka. These maximum age estimates derived from underlying sand indicate that the Southeast and South Lakes date to either the final millennia of the Middle Pleistocene or, more probably, to the subsequent Late Pleistocene. As discussed below, we hypothesize on archaeological grounds that the South Lake dates to MIS 5 and the Southeast Lake to early MIS 3.

The Jubbah record, consisting of excavated stratified lithics, enables us to further extend the occupation sequence of the region. Substantially enlarged excavations at Jebel Qattar 1 (JQ 1) increased the sample size of lithics dating to 211 ± 16 ka reported by ref. 28 by 250%. At Jebel Umm Sanman 1 (JSM 1), four new trenches were placed immediately west of earlier test excavations²⁸. The JSM 1 trenches revealed deep (more than 1.5–2.5 m) stratigraphic sequences, comprising a series of silty sands with variable frequencies of local gravel clasts. Luminescence dating indicates that the lower part of the JSM 1 sequence dates to 130 ± 10 ka, whereas the upper part, in which lithics were found, dates to approximately 75 ka (77 ± 7 ka, 72 ± 6.4 ka) (Supplementary Information, section 5).

Each phase of lake formation (apart from the Southwest Lake) at KAM 4 is associated with a distinct lithic assemblage (Fig. 3, Extended Data Figs. 4–8, Supplementary Information, section 7). Assemblage A (Central Lake, approximately 400 ka) consists of handaxes and associateddebitage (Extended Data Fig. 4) and is the oldest dated Acheulean assemblage in Arabia. It shows the production of small and refined handaxes produced by shaping (*façonnage*) of angular slabs of quartzite. Assemblage

B (Northeast Lake, approximately 300 ka) is also characterized by the production of small handaxes (Extended Data Figs. 5, 6). These handaxes are rather homogeneous in their technology and morphology, being small and pointed. Core reduction technology to produce flakes is also present in low frequencies in assemblage B, mostly characterized by preferential Levallois reduction. The subsequent assemblage C (Northwest Lake, approximately 200 ka) shows a Middle Palaeolithic technology. Lithics recovered from the surface and from excavations show a complete absence of handaxe manufacture, and a focus on Levallois technology, often centripetal in character (Extended Data Fig. 7), but somewhat diverse (Supplementary Information, section 7). Assemblage D (Southeast Lake, approximately 125–75 ka) and assemblage E (South Lake, approximately 55 ka) are both of Middle Palaeolithic character— assemblage D has a focus on centripetal Levallois technology and assemblage E has a somewhat diverse technology, but with a strong component of unidirectional-convergent preparation to produce convergent Levallois flakes.

With the enlarged excavations at JQ 1, the assemblage dating to approximately 210 ka has a clearly Middle Palaeolithic character; Levallois flakes are present, and bifacial technology is absent (Supplementary Information, section 8). The JSM 1 assemblage from approximately 75 ka is the largest excavated and dated Palaeolithic assemblage from northern Arabia, and shows a clear focus on centripetal Levallois reduction, with 83% of Levallois flakes having centripetal scar patterns (Extended Data Fig. 9).

This unique record of hydroclimate and associated hominin occupations demonstrates that Acheulean Lower Palaeolithic technology was present during late Middle Pleistocene wet phases, with Levallois technology being present in the final stage of the Acheulean. Assemblages showing similarities to the Acheulo-Yabrudian of the Levantine woodlands have not been identified in Arabia, highlighting distinct trajectories within Southwest Asia. From MIS 7, Arabian Middle Palaeolithic assemblages appear with each phase of increased precipitation, showing varying technological foci in terms of the reduction methods used, from varied Levallois in MIS 7, to centripetal Levallois in MIS 5^{3,20}, and unidirectional-convergent in MIS 3^{23,27}.

KAM 4 assemblage C has technological characteristics—such as frequent centripetal Levallois flaking—that are more similar to those of the East African Middle Stone Age (MSA) than to the contemporaneous Levantine early Middle Palaeolithic (Supplementary Information, sections 7, 8). Principal components analysis (PCA) of late Middle Pleistocene Levallois flakes shows that KAM 4 assemblage C falls between Omo Kibish-AHS in East Africa³⁰ and Misliya in the Levant³¹. For the Late Pleistocene, PCA distinguished between *H. sapiens*-associated assemblages such as Omo Kibish-BNS³⁰ and Al Wusta in Arabia²⁰, and the Neanderthal-associated Levantine assemblages from Kebara¹⁵ and Tor Faraj³². KAM 4 assemblage D and

JSM 1 orientate to the MIS 5 *H. sapiens* assemblages, whereas the negative score on the second principal component for KAM 4 assemblage E orientates it to MIS 4–3 Levantine Neanderthal assemblages.

Animal fossils (primarily vertebrates) from KAM 4 allow us to reconstruct the palaeoenvironmental and biogeographical context of hominin occupations.

Hippopotamus fossils had previously been reported in Arabia from MIS 5 contexts (for example, in refs. ^{20,33}). KAM 4 shows that hippopotamuses were also present during MIS 7 and, provisionally, MIS 9 (Supplementary Information, section 10). We also identified hippopotamus in the surface scatter of fossils at the nearby site of Ti's al Ghadah. The repeated presence of hippopotamuses, which are obligate semi-aquatic mammals that require permanent water bodies several metres deep, provides powerful evidence for the extent of environmental amelioration during repeated ‘green Arabia’ pluvial phases. In addition, the KAM 4 palaeontological assemblages contribute to a growing corpus of evidence indicating that Arabian mammal fauna had stronger affinity with Africa in the Middle and Late Pleistocene than with the Levantine woodland zone^{4,33}. The presence of African bovid taxa such as *Synclerus* and *Hippotragus* in northern Arabia indicates the repeated establishment of contiguous regions of grasslands across North Africa and Arabia with abundant freshwater, providing dispersal routes for a variety of species, including hominins. Arabia, however, also features Eurasian and endemic taxa (Supplementary Information 10), indicating that it was a key biogeographical nexus between Africa and the rest of Eurasia that may have also comprised an important interaction zone for hominins.

The northern Arabian late Middle Pleistocene lithic assemblages likewise show greater similarities to African assemblages than to those of Levantine woodland zone sites. The continued production of large handaxes and cleavers in central Arabia at the time the Middle Palaeolithic had appeared in northern Arabia²⁴ indicates high levels of population structure at this time, perhaps to the extent of different hominin species occupying the region. In MIS 5, it seems that much of Northeast Africa and Southwest Asia shared similar material culture, consistent with widespread dispersals of *H. sapiens*²⁰. Subsequently the cooling and aridification of the last glacial cycle led to the fracturing and decline of populations. Renewed dispersals, perhaps including Neanderthals from the north, occurred during the partial amelioration of early MIS 3 (around 59–50 ka). Comparatively stable environmental and ecological conditions in areas such as the Levantine woodland fostered the development of distinctive localized material culture phases¹¹. By contrast, the record of interior northern Arabia indicates pulses of occupation during episodic phases of increased environmental humidity, seemingly followed by repeated regional depopulation under increasing aridity.

We have identified at least five pulses of human dispersal into northern Arabia, each associated with a phase of decreased aridity. The differences in material culture between these phases—with two phases of Acheulean technology and then three distinct forms of Middle Palaeolithic—suggests that diverse hominin populations, and probably even species, were expanding into the region at different times (we discuss the implications of our findings further in Supplementary Information, section 11). The emerging palaeoanthropological record of Arabia highlights the dynamism and regional distinctiveness of Middle and Late Pleistocene hominin demography and behaviour in different parts of Southwest Asia. These processes were intimately connected to regional climatic changes. The available record emphasizes pulsed, long-ranging terrestrial dispersals followed by local variation, and finally population contraction. Given the temporal overlap of radically different technologies within Arabia, and the biogeographical evidence for faunal mixture, it is possible that some of the hominin admixture processes identified by genetic analyses occurred in this region. Arabia, and Southwest Asia more generally, is therefore a key region for unravelling not only the increasingly complex history of how our species spread beyond Africa, but more broadly, how our species' recent success relates to a longer history of hominin dispersals, regional developments and admixture, which occurred in a context of marked environmental oscillation.

Methods

Site identification and survey

KAM 4 was initially identified through remote sensing analysis²⁶ (Supplementary Information, section 2). Two main seasons of research were conducted at the site (2014 and 2017) as part of the Palaeodeserts/Green Arabia Project. The site was systematically surveyed with pedestrian transects. Using a total station and Trimble XRS Pro Differential Global Positioning System, the topography of the site was recorded in detail, and all points of interest (stone tools, fossils and sedimentary features) were recorded and entered into a geographic information system. JSM 1 and JQ 1 were first identified in 2011²⁸. We carried out renewed excavation of the sites in 2013. With JQ 1, the stratigraphic sequence was already understood, so the aim was simply to increase the sample size of lithics. At JSM 1, the original excavations had rapidly hit bedrock, so renewed excavations were conducted slightly further west in the hope of identifying deeper stratigraphic sequences.

Stratigraphy and sedimentology

Sections for sedimentary analysis and luminescence sampling were excavated for each of the palaeolake phases at KAM 4 (Supplementary Information, section 3). The

Northwest Lake was identified as having the best potential to recover buried material, as fossils and lithics appeared to be emerging from sediments, so four trenches (1–4) were dug here. These trenches and the excavations at JSM 1 and JQ 1 (Supplementary Information, section 4) were conducted using single-context excavation methods. All sediments were dry sieved through 5-mm mesh. The focus of this paper is on the archaeological assemblages, and not detailed palaeoenvironmental analysis so our sedimentary description consists of field observations from logging sections. Fossils from KAM 4 have previously been reported^{[33](#)}.

Chronometric dating methods

We used luminescence (OSL on quartz and pIRIR on feldspar) methods to date the sedimentary deposits at KAM 4 and at JSM 1 (Supplementary Information, section 5). These measure the time since sediments were last exposed to sunlight. Opaque metal tubes were hammered into cleaned sections, transported to the UK and analysed as described in Supplementary Information, section 5. Environmental dose rates were calculated using location and overburden density (cosmic rays), field gamma spectrometry (gamma), and thick-source beta counting (beta). A bovid tooth (KAM16/85) was recovered from unit 3 of the Northwest Lake at KAM 4. A direct age was obtained using the U-series dating method, which dates the moment uranium is incorporated into the fossil. Powdered samples of both enamel and dentine tissues were drilled from the tooth at Griffith University, and U-series analyses were subsequently carried out at the University of Queensland. While it was initially planned to combine with electron spin resonance analyses, the U-series results obtained showed that the tooth was not suitable for that purpose (Supplementary Information, section 6).

Lithic analysis

Lithics (stone tools) from the excavations at all sites and from the systematic transect survey at KAM 4 were studied using the methodology described previously in refs. ^{[9,20](#)} and in Supplementary Information, sections 7, 8. Our initial focus was on describing the basic typo-technological features of the assemblages. We selected illustrative examples for photography, 3D scanning, and illustration. For the Middle Palaeolithic samples, we carried out a full metric and attribute analysis following the above references and references therein. As well as allowing the description of the assemblages in quantitative terms, we focussed on the characteristics of Levallois flakes from these assemblages as a way to compare assemblages. We did this both in terms of univariate features (such as dorsal scar patterns), and using PCA to compare the morphology of Levallois flakes between the assemblages (Supplementary Information, section 8).

Reporting summary

Further information on research design is available in the [Nature Research Reporting Summary](#) linked to this paper.

Data and code availability

Data for the PCA analysis are archived at <https://doi.org/10.5281/zenodo.5082293>. All other relevant data are included in the paper and Supplementary Information.

Code availability

Code for the PCA analysis are archived at <https://doi.org/10.5281/zenodo.5082293>.

References

1. 1.
Dennell, R. *The Palaeolithic Settlement of Asia* (CUP, 2008).
2. 2.
Dennell, R. *From Arabia to the Pacific: How our species colonised Asia* (Routledge, 2020).
3. 3.
Groucutt, H. S. et al. Rethinking the dispersal of *Homo sapiens* out of Africa. *Evol. Anthropol.* **24**, 149–164 (2015).
4. 4.
Stewart, M. et al. Middle and Late Pleistocene mammal fossil records of Arabia and surrounding regions: Implications for biogeography and hominin dispersals. *Quatern. Int.* **515**, 12–29 (2019).
5. 5.
Petraglia, M. D., Groucutt, H. S., Parton, A. & Alsharekh, A. Green Arabia: human prehistory at the cross-roads of continents. *Quatern. Int.* **382**, 1–7 (2015).
6. 6.

Green, R. E. et al. A draft sequence of the Neanderthal genome. *Science* **328**, 710–722 (2010).

7. 7.

Drake, N. A., Blench, R. M., Armitage, S. J., Bristow, C. S., White, K. H. Ancient watercourses and biogeography of the Sahara explain the peopling of the desert. *Proc. Natl Acad. Sci. USA* **108**, 458–462 (2011).

8. 8.

Blome, M. W., Cohen, A. S., Tryon, C. A., Brooks, A. S. & Russell, J. The environmental context for the origins of modern human diversity: a synthesis of regional variability in African climate 150,000–30,000 years ago. *J. Hum. Evol.* **62**, 563–592 (2012).

9. 9.

Scerri, E. M. L., Drake, N. A., Jennings, R. & Groucutt, H. S. Earliest evidence for the structure of *Homo sapiens* populations in Africa. *Quatern. Sci. Rev.* **101**, 207–2016 (2014).

10. 10.

Breeze, P. S. et al. Palaeohydrological corridors for hominin dispersals in the Middle East ~250–70,000 years ago. *Quatern. Sci. Rev.* **11**, 155–185 (2016).

11. 11.

Malinsky-Buller, A. & Hovers, E. One size does not fit all: group size and the late middle Pleistocene prehistoric archive. *J. Hum. Evol.* **127**, 118–132 (2019).

12. 12.

Shea, J. J. The Middle Paleolithic of the East Mediterranean Levant. *J. World Prehist.* **17**, 313–394 (2003).

13. 13.

Hovers, E. *The Lithic Assemblages of Qafzeh Cave* (Oxford Univ. Press, 2009).

14. 14.

Hovers, E. & Belfer-Cohen, A. On variability and complexity: lessons from the Levantine Middle Paleolithic record. *Curr. Anthropol.* **54**, S337–S357 (2013).

15. 15.

Meignen, L. & Bar-Yosef, O. *Kebara Cave, Mt. Carmel, Israel, Part II: The Middle and Upper Palaeolithic Archaeology* (Peabody Museum Press, 2020).

16. 16.

Holt, B. G. et al. An update of Wallace's zoogeographic regions of the world. *Science* **339**, 74–78 (2012).

17. 17.

Groucutt, H. S. & Petraglia, M. D. The prehistory of Arabia: deserts, dispersals and demography. *Evol. Anthropol.* **21**, 113–125 (2012).

18. 18.

Rosenberg, T. M. et al. Middle and Late Pleistocene humid periods recorded in palaeolake deposits of the Nafud desert, Saudi Arabia. *Quatern. Sci. Rev.* **70**, 109–123 (2013).

19. 19.

Parton, A. et al. Middle-Late Quaternary palaeoclimate variability from lacustrine deposits in the Nefud Desert, Northern Arabia. *Quatern. Sci. Rev.* **202**, 78–97 (2018).

20. 20.

Groucutt, H. S. et al. *Homo sapiens* in Arabia by 85,000 years ago. *Nature Eco. Evo.* **2**, 800–809 (2018).

21. 21.

Nicholson, S. et al. Pluvial periods in southern Arabia over the last 1.1 million-years. *Quatern. Sci. Rev.* **229**, 106112 (2020).

22. 22.

Armitage, S. J. et al. The southern route “Out of Africa”: evidence for an early expansion of modern humans into Arabia. *Science* **331**, 453–456 (2011).

23. 23.
Delagnes, A. et al. Inland human settlement in southern Arabia 55,000 years ago. New evidence from the Wadi Surdud Middle Paleolithic site complex, western Yemen. *J. Hum. Evol.* **63**, 452–474 (2012).
24. 24.
Scerri, E. M. L. et al. The expansion of later Acheulean hominins into the Arabian Peninsula. *Sci. Rep.* **8**, 17165 (2018).
25. 25.
Scerri, E. M. L. et al. Middle to Late Pleistocene human habitation in the western Nefud Desert. *Quatern. Int.* **382**, 200–214 (2015).
26. 26.
Breeze, P. S. et al. Prehistory and palaeoenvironments of the Western Nefud, Saudi Arabia. *Arch. Res. Asia* **10**, 1–16 (2017).
27. 27.
Jennings, R. P. et al. Human occupation of the northern Arabia interior during early Marine Isotope State 3. *J. Quat. Sci.* **31**, 953–966 (2016).
28. 28.
Petruglia, M. D. et al. Hominin dispersal into the Nefud Desert and Middle Palaeolithic settlement along the Jubbah palaeolake, Northern Arabia. *PLoS ONE* **7**, e49840 (2012).
29. 29.
Scerri, E. M. L., et al. The expansion of Acheulean hominins into the Nefud Desert of Arabia. *Sci. Rep.* **11**, 10111 (2021).
30. 30.
Shea, J. J. The Middle Stone Age archaeology of the Lower Omo Valley Kibish formation: excavations, lithic assemblages, and inferred patterns of early *Homo sapiens* behaviour. *J. Hum. Evol.* **55**, 448–485 (2008).
31. 31.

Zaidner, Y. & Weinstein-Evron, M. The emergence of the Levallois technology in the Levant: a view from the early Middle Palaeolithic site of Misliya Cave, Israel. *J. Hum. Evol.* **144**, 102785 (2020).

32. 32.

Henry, D. O. *Neanderthals in the Levant. Behavioral Organization and the Beginning of Human Modernity* (Continuum, 2003).

33. 33.

Stewart, M. et al. A taxonomic and taphonomic study of Pleistocene fossil deposits from the western Nefud Desert, Saudi Arabia. *Quatern. Res.* **95**, 1–22 (2020).

34. 34.

Otto-Bliesner, B. L. et al. Simulating Arctic climate warmth and icefield retreat in the Last Interglaciation. *Science* **311**, 1751–1753 (2006).

35. 35.

Zhao, Y. et al. Variations of the Nile suspended discharges during the last 1.75 Myr. *Palaeogeog. Palaeoclim. Palaeoecol.* **311**, 230–241 (2011).

36. 36.

Berger, A. & Loutre, M. F. Insolation values for the climate of the last 10 million years. *Quatern. Sci. Rev.* **10**, 297–317 (1991).

37. 37.

Grant, K. M. et al. A 3 million year index for North African humidity/aridity and the implication of potential pan-African humid periods. *Quatern. Sci. Rev.* **171**, 100–118 (2017).

38. 38.

Lisiecki, L. E. & Raymo, M. E. A Pliocene–Pleistocene stack of 57 globally distributed benthic $\delta^{18}\text{O}$ records. *Paleoceanography* **20**, 1–17 (2005).

Acknowledgements

We thank the Heritage Commission, Ministry of Culture, Saudi Arabia for fieldwork support and permission to conduct this research. The research was funded by the Max Planck Society, the European Research Council (295719 to M.D.P.), the British Academy (H.S.G.), the Leverhulme Trust (ECF-2019-538 to S.B., ECF-2019-538 to P.S.B. and PG-2017-087 to S.B., E.A., S.J.A. and M.D.P.), the Research Council of Norway, through its Centres of Excellence funding scheme, SFF Centre for Early Sapiens Behaviour (SapienCE), project number 262618 (S.J.A.), the Natural Environmental Research Council (NERC) through its London DTP studentship funding (R.C.-W.), The Nature and Science Researchers Supporting Project (NSRSP-2021-5), DSFP, King Saud University, Riyadh, Saudi Arabia (A.M.A.), the Leakey Foundation (M.S.) the Australian Research Council (FT160100450 to J.L. and FT150100215 to M.D.), and the Spanish Ramón y Cajal Fellowship (RYC2018-025221-I to M.D.). We thank L. Clark-Balzan for assistance with the luminescence dating, I. Cartwright for lithic photography and M. O'Reilly for assistance with figures. We thank the museums listed in the Supplementary Information for access to comparative collections.

Funding

Open access funding provided by Max Planck Society.

Author information

Affiliations

1. Extreme Events Research Group, Max Planck Institutes for Chemical Ecology, the Science of Human History, and Biogeochemistry, Jena, Germany

Huw S. Groucutt, Mathew Stewart & W. Christopher Carleton

2. Department of Archaeology, Max Planck Institute for the Science of Human History, Jena, Germany

Huw S. Groucutt, Nick Drake, Muhammad Zahir & Michael D. Petraglia

3. Institute of Prehistoric Archaeology, University of Cologne, Cologne, Germany

Huw S. Groucutt & Eleanor M. L. Scerri

4. Department of Life Sciences, Natural History Museum, London, UK

Tom S. White

5. Pan-African Evolution Research Group, Max Planck Institute for the Science of Human History, Jena, Germany

Eleanor M. L. Scerri & James Blinkhorn

6. Department of Classics and Archaeology, University of Malta, Msida, Malta

Eleanor M. L. Scerri

7. Department of Archaeology, Durham University, Durham, UK

Eric Andrieux

8. Centre for Quaternary Research, Department of Geography, Royal Holloway University of London, Egham, UK

Eric Andrieux, Richard Clark-Wilson, Simon J. Armitage, Ian Candy, James Blinkhorn & Simon Blockley

9. Department of Geography and Environmental Science, University of Reading, Reading, UK

Richard Clark-Wilson

10. Department of Geography, King's College London, London, UK

Paul S. Breeze & Nick Drake

11. SFF Centre for Early Sapiens Behaviour (SapienCE), University of Bergen, Bergen, Norway

Simon J. Armitage

12. Australian Research Centre for Human Evolution, Griffith University, Brisbane, Queensland, Australia

Julien Louys, Mathieu Duval & Michael D. Petraglia

13. College of Asia and the Pacific, The Australian National University, Canberra, Australia Capital Territory, Australia

Julien Louys

14. School of Earth and Environmental Sciences, University of Queensland, Brisbane, Australia Capital Territory, Australia

Gilbert J. Price

15. Geochronology and Geology, Centro Nacional de Investigación sobre la Evolución Humana, Paseo de Atapuerca, Burgos, Spain

Mathieu Duval

16. Human Origins and Palaeoenvironments Research Group, School of Social Sciences, Oxford Brookes University, Oxford, UK

Ash Parton

17. Mansfield College, University of Oxford, Oxford, UK

Ash Parton

18. Institute of Archaeology, University College London, London, UK

Ceri Shipton

19. Centre of Excellence for Australian Biodiversity and Heritage, Australian National University, Canberra, Australia Capital Territory, Australia

Ceri Shipton

20. School of Biological and Environmental Sciences, Liverpool John Moores University, Liverpool, UK

Richard P. Jennings

21. Department of Archaeology, Hazara University, Mansehra, Pakistan

Muhammad Zahir

22. Heritage Commission, Ministry of Culture, Riyadh, Saudi Arabia

Abdulaziz Al-Omari

23. Department of Archaeology, College of Tourism and Archaeology, King Saud University, Riyadh, Saudi Arabia

Abdullah M. Alsharekh

24. Human Origins Program, National Museum of Natural History, Smithsonian Institution, Washington, USA

Michael D. Petraglia

25. School of Social Science, University of Queensland, St Lucia, Queensland, Australia

Michael D. Petraglia

Contributions

Conceptualization: H.S.G., A.M.A. and M.D.P. Data collection: all authors.

Luminescence dating: E.A. and S.J.A. U-series dating: G.J.P. and M.D.

Palaeoenvironmental analysis: T.S.W., E.A., R.C.-W., P.S.B., S.J.A., N.D., J.L., A.P. and I.C. Lithic analysis: H.S.G., E.M.L.S. and J.B. PCA: W.C.C. Writing: all authors.

Corresponding authors

Correspondence to Huw S. Groucutt or Michael D. Petraglia.

Ethics declarations

Competing interests

The authors declare no competing interests.

Additional information

Peer review information *Nature* thanks Robin Dennell, Peter deMenocal and the other, anonymous, reviewer(s) for their contribution to the peer review of this work.

Publisher's note Springer Nature remains neutral with regard to jurisdictional claims in published maps and institutional affiliations.

Extended data figures and tables

[**Extended Data Fig. 1 KAM 4 looking south, team members are visible on the Northwest Lake**](#)

[Extended Data Fig. 2 Plan of Khall-Amayshan-4, showing multiple phases of lake formation, associated with lithic and fossil assemblages](#)

[Extended Data Fig. 3 Stratigraphic logs and chronometric dates for KAM 4, JSM 1 and JQ 1](#)

[Extended Data Fig. 4 Assemblage A handaxes from Central Lake \(MIS 11\), KAM 4.](#)

Scale: 1 cm.

[Extended Data Fig. 5 Assemblage B handaxes from Northeast Lake \(MIS 9\), KAM 4.](#)

Scale: 1 cm.

[Extended Data Fig. 6 3D scans of assemblage B \(MIS 9\) handaxes from KAM 4](#)

[Extended Data Fig. 7 Middle Palaeolithic artefacts from KAM 4 and JSM 1.](#)

Top left: KAM 4 assemblage C (MIS 7) Levallois flake, top right: JSM 1 Levallois flake (MIS 5), bottom row: Levallois points from assemblage E (MIS 3?), KAM 4.

Scale: 1 cm.

[Extended Data Fig. 8 Levallois flakes from assemblage C, KAM 4 \(MIS 7\).](#)

Scale: 1 cm.

[Extended Data Fig. 9 Levallois flakes from JSM 1 \(MIS 5, ca. 75 ka\).](#)

Scale: 1 cm.

Supplementary information

Supplementary Information

This file contains Supplementary Methods, Discussion, Tables 1–26, Figs. 1–39 and references

Reporting Summary

Peer Review File

Rights and permissions

Open Access This article is licensed under a Creative Commons Attribution 4.0 International License, which permits use, sharing, adaptation, distribution and reproduction in any medium or format, as long as you give appropriate credit to the original author(s) and the source, provide a link to the Creative Commons license, and indicate if changes were made. The images or other third party material in this article are included in the article's Creative Commons license, unless indicated otherwise in a credit line to the material. If material is not included in the article's Creative Commons license and your intended use is not permitted by statutory regulation or exceeds the permitted use, you will need to obtain permission directly from the copyright holder. To view a copy of this license, visit <http://creativecommons.org/licenses/by/4.0/>.

Reprints and Permissions

About this article

Cite this article

Groucutt, H.S., White, T.S., Scerri, E.M.L. *et al.* Multiple hominin dispersals into Southwest Asia over the past 400,000 years. *Nature* **597**, 376–380 (2021).
<https://doi.org/10.1038/s41586-021-03863-y>

- Received: 12 February 2021
- Accepted: 29 July 2021
- Published: 01 September 2021
- Issue Date: 16 September 2021

- DOI: <https://doi.org/10.1038/s41586-021-03863-y>

Share this article

Anyone you share the following link with will be able to read this content:

[Get shareable link](#)

Sorry, a shareable link is not currently available for this article.

[Copy to clipboard](#)

Provided by the Springer Nature SharedIt content-sharing initiative

[**Traces of a series of human dispersals through Arabia**](#)

- Robin Dennell

News & Views 01 Sept 2021

This article was downloaded by **calibre** from <https://www.nature.com/articles/s41586-021-03863-y>.

| [Section menu](#) | [Main menu](#) |

- Article
- [Published: 25 August 2021](#)

The mutational landscape of human somatic and germline cells

- [Luiza Moore](#) ORCID: [orcid.org/0000-0001-5315-516X^{1,2 nA1}](https://orcid.org/0000-0001-5315-516X),
- [Alex Cagan](#) ORCID: [orcid.org/0000-0002-7857-4771^{1 nA1}](https://orcid.org/0000-0002-7857-4771),
- [Tim H. H. Coorens](#) ORCID: [orcid.org/0000-0002-5826-3554^{1 nA1}](https://orcid.org/0000-0002-5826-3554),
- [Matthew D. C. Neville](#) ORCID: [orcid.org/0000-0001-5816-7936¹](https://orcid.org/0000-0001-5816-7936),
- [Rashesh Sanghvi](#) ORCID: [orcid.org/0000-0002-7703-9216¹](https://orcid.org/0000-0002-7703-9216),
- [Mathijs A. Sanders](#)^{1,3},
- [Thomas R. W. Oliver](#) ORCID: [orcid.org/0000-0003-4306-0102^{1,2}](https://orcid.org/0000-0003-4306-0102),
- [Daniel Leongamornlert](#) ORCID: [orcid.org/0000-0002-3486-3168¹](https://orcid.org/0000-0002-3486-3168),
- [Peter Ellis](#)^{1 nAff12},
- [Ayesha Noorani](#)¹,
- [Thomas J. Mitchell](#) ORCID: [orcid.org/0000-0003-0761-9503^{1,4}](https://orcid.org/0000-0003-0761-9503),
- [Timothy M. Butler](#) ORCID: [orcid.org/0000-0001-5803-1035¹](https://orcid.org/0000-0001-5803-1035),
- [Yvette Hooks](#)¹,
- [Anne Y. Warren](#)²,
- [Mette Jorgensen](#)⁵,
- [Kevin J. Dawson](#)¹,
- [Andrew Menzies](#)¹,
- [Laura O'Neill](#)¹,
- [Calli Latimer](#)¹,
- [Mabel Teng](#)¹,
- [Ruben van Boxtel](#) ORCID: [orcid.org/0000-0003-1285-2836⁶](https://orcid.org/0000-0003-1285-2836),
- [Christine A. Iacobuzio-Donahue](#) ORCID: [orcid.org/0000-0002-4672-3023^{7,8}](https://orcid.org/0000-0002-4672-3023),
- [Inigo Martincorena](#) ORCID: [orcid.org/0000-0003-1122-4416¹](https://orcid.org/0000-0003-1122-4416),
- [Rakesh Heer](#)^{9,10},

- [Peter J. Campbell](#) ORCID: [orcid.org/0000-0002-3921-0510¹](https://orcid.org/0000-0002-3921-0510),
- [Rebecca C. Fitzgerald](#) ORCID: [orcid.org/0000-0002-3434-3568¹¹](https://orcid.org/0000-0002-3434-3568),
- [Michael R. Stratton](#) ORCID: [orcid.org/0000-0001-6035-153X¹](https://orcid.org/0000-0001-6035-153X) &
- [Raheleh Rahbari](#) ORCID: [orcid.org/0000-0002-1839-7785¹](https://orcid.org/0000-0002-1839-7785)

Nature volume **597**, pages 381–386 (2021)

- 14k Accesses
- 4 Citations
- 396 Altmetric
- [Metrics details](#)

Subjects

- [Cancer genomics](#)
- [Genetic variation](#)
- [Mutation](#)
- [Phylogenetics](#)

Abstract

Over the course of an individual's lifetime, normal human cells accumulate mutations¹. Here we compare the mutational landscape in 29 cell types from the soma and germline using multiple samples from the same individuals. Two ubiquitous mutational signatures, SBS1 and SBS5/40, accounted for the majority of acquired mutations in most cell types, but their absolute and relative contributions varied substantially. SBS18, which potentially reflects oxidative damage², and several additional signatures attributed to exogenous and endogenous exposures contributed mutations to subsets of cell types. The rate of mutation was lowest in spermatogonia, the stem cells from which sperm are generated and from which most genetic variation in the human population is thought to originate. This was due to low rates of ubiquitous mutational processes and may be partially attributable to a low rate of cell division in basal spermatogonia. These

results highlight similarities and differences in the maintenance of the germline and soma.

Access options

Subscribe to Journal

Get full journal access for 1 year

\$199.00

only \$3.90 per issue

[Subscribe](#)

All prices are NET prices.

VAT will be added later in the checkout.

Tax calculation will be finalised during checkout.

Rent or Buy article

Get time limited or full article access on ReadCube.

from \$8.99

[Rent or Buy](#)

All prices are NET prices.

Additional access options:

- [Log in](#)
- [Access through your institution](#)
- [Learn about institutional subscriptions](#)

Fig. 1: Summary of the experimental design and clonal structures across tissues.

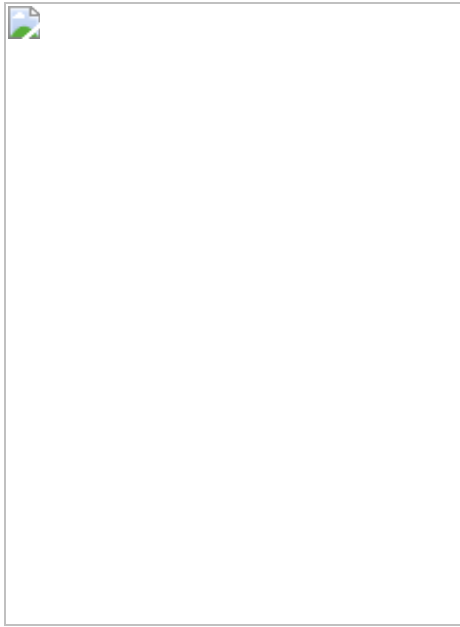


Fig. 2: Mechanisms underlying the low rate of germline mutations.

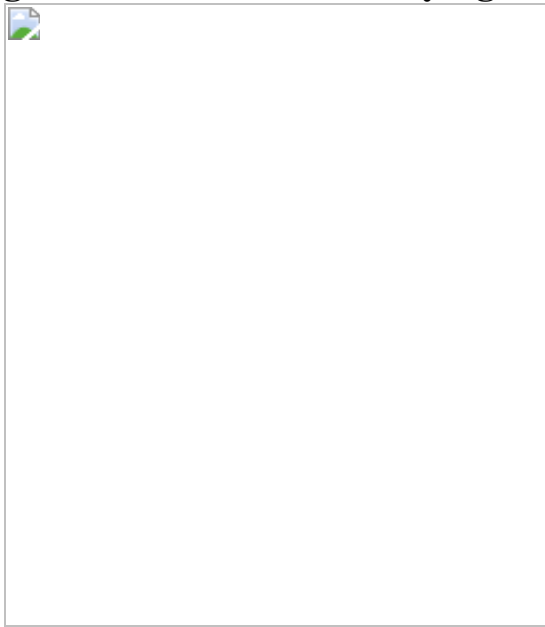


Fig. 3: Mutational signatures in normal tissues.

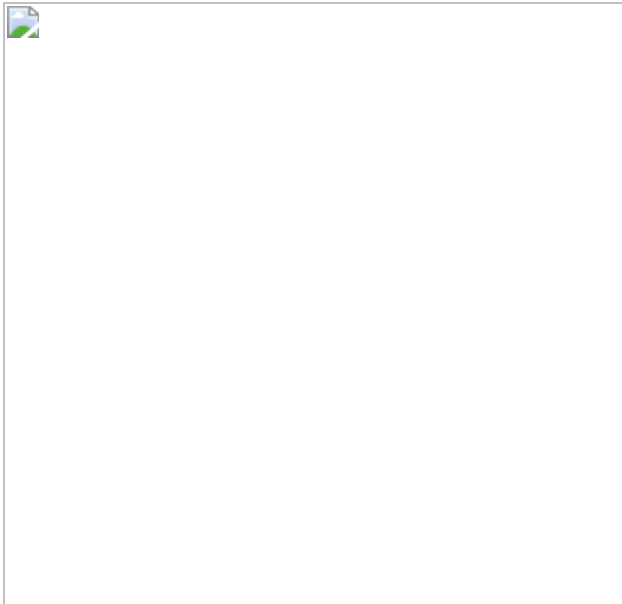


Fig. 4: Comparison of mutational biases between the germline and the soma.



Data availability

Information on data availability for all samples is available in Supplementary Table 4. Sequencing data have been deposited in the European Genome-Phenome Archive under the dataset accession number [EGAD00001006641](#) and are available for general research purposes. Substitutions, indels and SVs are available in Supplementary Tables 3–6.

Code availability

Pipelines to call SBSs, indels, SVs, CNVs, mutation burden analysis, signature extraction with HDP and SigProfiler, and mutation burden for different genomic contexts are available from
https://github.com/Rashesh7/PanBody_manuscript_analyses.

References

1. 1.
Martincorena, I. & Campbell, P. J. Somatic mutation in cancer and normal cells. *Science* **349**, 1483–1489 (2015).
2. 2.
Rouhani, F. J. et al. Mutational history of a human cell lineage from somatic to induced pluripotent stem cells. *PLoS Genet.* **12**, e1005932 (2016).
3. 3.
Coorens, T. H. H. et al. Extensive phylogenies of human development reveal variable embryonic patterns. Preprint at *bioRxiv* <https://doi.org/10.1101/2020.11.25.397828> (2020).
4. 4.
Blokzijl, F. et al. Tissue-specific mutation accumulation in human adult stem cells during life. *Nature* **538**, 260–264 (2016).
5. 5.
Bae, T. et al. Different mutational rates and mechanisms in human cells at pregastrulation and neurogenesis. *Science* **359**, 550–555 (2018).

6. 6.

Osorio, F. G. et al. Somatic mutations reveal lineage relationships and age-related mutagenesis in human hematopoiesis. *Cell Rep.* **25**, 2308–2316.e4 (2018).

7. 7.

Martincorena, I. et al. Somatic mutant clones colonize the human esophagus with age. *Science* **362**, 911–917 (2018).

8. 8.

Lee-Six, H. et al. The landscape of somatic mutation in normal colorectal epithelial cells. *Nature* **574**, 532–537 (2019).

9. 9.

Moore, L. et al. The mutational landscape of normal human endometrial epithelium. *Nature* **580**, 640–646 (2020).

10. 10.

Zhu, M. et al. Somatic mutations increase hepatic clonal fitness and regeneration in chronic liver disease. *Cell* **177**, 608–621.e12 (2019).

11. 11.

Schmitt, M. W. et al. Detection of ultra-rare mutations by next-generation sequencing. *Proc. Natl Acad. Sci. USA* **109**, 14508–14513 (2012).

12. 12.

Abascal, F. et al. Somatic mutation landscapes at single-molecule resolution. *Nature* **593**, 405–410 (2021).

13. 13.

Rahbari, R. et al. Timing, rates and spectra of human germline mutation. *Nat. Genet.* **48**, 126–133 (2016).

14. 14.

Goldmann, J. M. et al. Parent-of-origin-specific signatures of de novo mutations. *Nat. Genet.* **48**, 935–939 (2016).

15. 15.

Kong, A. et al. Rate of de novo mutations and the importance of father's age to disease risk. *Nature* **488**, 471–475 (2012).

16. 16.

Lynch, M. Rate, molecular spectrum, and consequences of human mutation. *Proc. Natl Acad. Sci. USA* **107**, 961–968 (2010).

17. 17.

Milholland, B. et al. Differences between germline and somatic mutation rates in humans and mice. *Nat. Commun.* **8**, 15183 (2017).

18. 18.

Visvader, J. E. & Clevers, H. Tissue-specific designs of stem cell hierarchies. *Nat. Cell Biol.* **18**, 349–355 (2016).

19. 19.

Jónsson, H. et al. Parental influence on human germline de novo mutations in 1,548 trios from Iceland. *Nature* **549**, 519–522 (2017).

20. 20.

Ozturk, S. Telomerase activity and telomere length in male germ cells. *Biol. Reprod.* **92**, 53 (2015).

21. 21.

Demanelis, K. et al. Determinants of telomere length across human tissues. *Science* **369**, eaaz6876 (2020).

22. 22.

Fryxell, K. J. & Zuckerkandl, E. Cytosine deamination plays a primary role in the evolution of mammalian isochores. *Mol. Biol. Evol.* **17**, 1371–1383 (2000).

23. 23.

Alexandrov, L. B. et al. Clock-like mutational processes in human somatic cells. *Nat. Genet.* **47**, 1402–1407 (2015).

24. 24.

Alexandrov, L. B. et al. The repertoire of mutational signatures in human cancer. *Nature* **578**, 94–101 (2020).

25. 25.

Boot, A. et al. In-depth characterization of the cisplatin mutational signature in human cell lines and in esophageal and liver tumors. *Genome Res.* **28**, 654–665 (2018).

26. 26.

Forbes, S. A. et al. COSMIC: somatic cancer genetics at high-resolution. *Nucleic Acids Res.* **45**, D777–D783 (2017).

27. 27.

Pleguezuelos-Manzano, C. et al. Mutational signature in colorectal cancer caused by genotoxic pks⁺ *E. coli*. *Nature* **580**, 269–273 (2020).

28. 28.

Li, X. C. et al. A mutational signature associated with alcohol consumption and prognostically significantly mutated driver genes in

esophageal squamous cell carcinoma. *Ann. Oncol.* **29**, 938–944 (2018).

29. 29.

Nik-Zainal, S. et al. Mutational processes molding the genomes of 21 breast cancers. *Cell* **149**, 979–993 (2012).

30. 30.

Alexandrov, L. B. et al. Mutational signatures associated with tobacco smoking in human cancer. *Science* **354**, 618–622 (2016).

31. 31.

Di Persio, S. et al. Spermatogonial kinetics in humans. *Development* **144**, 3430–3439 (2017).

32. 32.

Scally, A. Mutation rates and the evolution of germline structure. *Phil. Trans. R. Soc. B* **371**, 20150137 (2016).

33. 33.

Frigola, J. et al. Reduced mutation rate in exons due to differential mismatch repair. *Nat. Genet.* **49**, 1684–1692 (2017).

34. 34.

Rodríguez-Galindo, M., Casillas, S., Weghorn, D. & Barbadilla, A. Germline de novo mutation rates on exons versus introns in humans. *Nat. Commun.* **11**, 3304 (2020).

35. 35.

GTEX Consortium. The GTEX Consortium atlas of genetic regulatory effects across human tissues. *Science* **369**, 1318–1330 (2020).

36. 36.

Karczewski, K. J. et al. The mutational constraint spectrum quantified from variation in 141,456 humans. *Nature* **581**, 434–443 (2020).

37. 37.

Xia, B. et al. Widespread transcriptional scanning in the testis modulates gene evolution rates. *Cell* **180**, 248–262.e21 (2020).

38. 38.

Koren, A. et al. Differential relationship of DNA replication timing to different forms of human mutation and variation. *Am. J. Hum. Genet.* **91**, 1033–1040 (2012).

39. 39.

Francioli, L. C. et al. Genome-wide patterns and properties of de novo mutations in humans. *Nat. Genet.* **47**, 822–826 (2015).

40. 40.

Chen, C., Qi, H., Shen, Y., Pickrell, J. & Przeworski, M. Contrasting determinants of mutation rates in germline and soma. *Genetics* **207**, 255–267 (2017).

41. 41.

.Walsh, C. et al. Somatic mutations in single human cardiomyocytes demonstrate accelerated age-related DNA damage and cell fusion. Preprint at *Research Square* <https://doi.org/10.21203/rs.3.rs-84503/v1> (2020).

42. 42.

Kirkwood, T. B. Evolution of ageing. *Nature* **270**, 301–304 (1977).

43. 43.

Sakkas, D., Ramalingam, M., Garrido, N. & Barratt, C. L. R. Sperm selection in natural conception: what can we learn from Mother Nature to improve assisted reproduction outcomes? *Hum. Reprod. Update* **21**, 711–726 (2015).

44. 44.

Brunner, S. F. et al. Somatic mutations and clonal dynamics in healthy and cirrhotic human liver. *Nature* **574**, 538–542 (2019).

45. 45.

Lawson, A. R. J. et al. Extensive heterogeneity in somatic mutation and selection in the human bladder. *Science* **370**, 75–82 (2020).

46. 46.

Olafsson, S. et al. Somatic evolution in non-neoplastic IBD-affected colon. *Cell* **182**, 672–684.e11 (2020).

47. 47.

Ellis, P. et al. Reliable detection of somatic mutations in solid tissues by laser-capture microdissection and low-input DNA sequencing. *Nat. Protoc.* **16**, 841–871 (2021).

48. 48.

Li, H. Aligning sequence reads, clone sequences and assembly contigs with BWA-MEM. Preprint at *arXiv* <https://arxiv.org/abs/1303.3997v2> (2013).

49. 49.

Tischler, G. & Leonard, S. biobambam: tools for read pair collation based algorithms on BAM files. *Source Code Biol. Med.* **9**, 13 (2014).

50. 50.

Jones, D. et al. cgpCaVEManWrapper: simple execution of CaVEMan in order to detect somatic single nucleotide variants in NGS data. *Curr. Protoc. Bioinformatics* **56**, 15.10.1–15.10.18 (2016).

51. 51.

Coorens, T. H. H. et al. Lineage-independent tumors in bilateral neuroblastoma. *N. Engl. J. Med.* **383**, 1860–1865 (2020).

52. 52.

Yoshida, K. et al. Tobacco smoking and somatic mutations in human bronchial epithelium. *Nature* **578**, 266–272 (2020).

53. 53.

Raine, K. M. et al. cgPindel: identifying somatically acquired insertion and deletion events from paired end sequencing. *Curr. Protoc. Bioinformatics* **52**, 15.7.1–15.7.12 (2015).

54. 54.

Slater, G. S. C. & Birney, E. Automated generation of heuristics for biological sequence comparison. *BMC Bioinformatics* **6**, 31 (2005).

55. 55.

Suzuki, M. et al. Late-replicating heterochromatin is characterized by decreased cytosine methylation in the human genome. *Genome Res.* **21**, 1833–1840 (2011).

56. 56.

Coorens, T. H. H. et al. Embryonal precursors of Wilms tumor. *Science* **366**, 1247–1251 (2019).

57. 57.

Blokzijl, F., Janssen, R., van Boxtel, R. & Cuppen, E. MutationalPatterns: comprehensive genome-wide analysis of mutational processes. *Genome Med.* **10**, 33 (2018).

58. 58.

Stamatoyannopoulos, J. A. et al. Human mutation rate associated with DNA replication timing. *Nat. Genet.* **41**, 393–395 (2009).

59. 59.

Potten, C. S., Kellett, M., Rew, D. A. & Roberts, S. A. Proliferation in human gastrointestinal epithelium using bromodeoxyuridine in vivo: data for different sites, proximity to a tumour, and polyposis coli. *Gut* **33**, 524–529 (1992).

60. 60.

Heller, C. G. & Clermont, Y. Spermatogenesis in man: an estimate of its duration. *Science* **140**, 184–186 (1963).

61. 61.

Farmacy, J. H. R., Smith, M. L., NIHR BioResource - Rare Diseases & Lynch, A. G. Telomerecat: a ploidy-agnostic method for estimating telomere length from whole genome sequencing data. *Sci. Rep.* **8**, 1300 (2018).

62. 62.

Martincorena, I. et al. Universal patterns of selection in cancer and somatic tissues. *Cell* **171**, 1029–1041.e21 (2017).

Acknowledgements

We thank the staff of WTSI Sample Logistics, Genotyping, Pulldown, Sequencing and Informatics facilities for their contribution; K. Roberts and the cgp-lab for their assistance; P. Robinson, M. Goddard, P. S. Tarpey and

P. Scott for their assistance with sample collection and the LCM pipeline; and M. Hurles, A. Scally and Y. S. Ju for providing useful feedback. This research is supported by core funding from the Wellcome Trust. R.R. is funded by Cancer Research UK (CRUK; C66259/A27114). L.M. is a recipient of a CRUK Clinical PhD fellowship (C20/A20917) and the Jean Shank/Pathological Society of Great Britain and Ireland Intermediate Research Fellowship (grant reference no. 1175). T.J.M. is supported by CRUK and the Royal College of Surgeons (C63474/A27176). The laboratory of R.C.F. is funded by a Core Programme Grant from the Medical Research Council (RG84369). Funding for sample collection was through the ICGC and was funded by a programme grant from CRUK (RG81771/84119). R.H. is a recipient of a PCF Challenge Research Award (ID #18CHAL11). I.M. is funded by CRUK (C57387/A21777) and the Wellcome Trust. P.J.C. is a Wellcome Trust Senior Clinical Fellow.

Author information

Author notes

1. Peter Ellis

Present address: Inivata, Cambridge, UK

2. These authors contributed equally: Luiza Moore, Alex Cagan, Tim H. H. Coorens

Affiliations

1. Cancer, Ageing and Somatic Mutation (CASM), Wellcome Sanger Institute, Hinxton, UK

Luiza Moore, Alex Cagan, Tim H. H. Coorens, Matthew D. C. Neville, Rashesh Sanghvi, Mathijs A. Sanders, Thomas R. W. Oliver, Daniel Leongamornlert, Peter Ellis, Ayesha Noorani, Thomas J. Mitchell, Timothy M. Butler, Yvette Hooks, Kevin J. Dawson, Andrew Menzies, Laura O'Neill, Calli Latimer, Mabel Teng, Inigo

Martincorena, Peter J. Campbell, Michael R. Stratton & Raheleh Rahbari

2. Department of Pathology, Cambridge University Hospitals NHS Foundation Trust, Cambridge, UK

Luiza Moore, Thomas R. W. Oliver & Anne Y. Warren

3. Department of Hematology, Erasmus University Medical Center, Rotterdam, Netherlands

Mathijs A. Sanders

4. Department of Surgery, University of Cambridge, Cambridge, UK

Thomas J. Mitchell

5. Great Ormond Street Hospital for Children NHS Foundation Trust, London, UK

Mette Jorgensen

6. Princess Máxima Center for Pediatric Oncology and Oncoode Institute, Utrecht, Netherlands

Ruben van Boxtel

7. Department of Pathology, Sol Goldman Pancreatic Cancer Research Center, Johns Hopkins University School of Medicine, Baltimore, MD, USA

Christine A. Iacobuzio-Donahue

8. Department of Oncology, Sidney Kimmel Comprehensive Cancer Center, Johns Hopkins University School of Medicine, Baltimore, MD, USA

Christine A. Iacobuzio-Donahue

9. Translational and Clinical Research Institute, Faculty of Medical Sciences, Newcastle University, Newcastle upon Tyne, UK

Rakesh Heer

10. Newcastle Urology, Freeman Hospital, Newcastle upon Tyne Hospitals NHS Foundation Trust, Newcastle upon Tyne, UK

Rakesh Heer

11. MRC Cancer Unit, University of Cambridge, Cambridge, UK

Rebecca C. Fitzgerald

Contributions

M.R.S., R.R. and L.M. conceived the project. R.R. and M.R.S. supervised the project. A.C., L.M., M.R.S. and R.R. wrote the manuscript. All authors reviewed and edited the manuscript. L.M., A.C. and T.H.H.C. led the analysis of the data with help from M.D.C.N., R.S., M.A.S., T.R.W.O., D.L., T.M.B., A.M., K.J.D. and R.R. L.M., A.C. and T.R.W.O. performed LCM. L.M. performed the rapid autopsy with help from T.J.M. and M.T. P.E., Y.H., L.O. and C.L. processed samples. L.M., A.N., R.v.B., C.A.I.-D., R.H. and R.C.F. collected samples. L.M., T.R.W.O., M.J. and A.Y.W. reviewed the histological images and clinical reports. I.M., P.J.C., M.R.S. and R.R. helped with data interpretation and statistical analysis.

Corresponding authors

Correspondence to Michael R. Stratton or Raheleh Rahbari.

Ethics declarations

Competing interests

The authors declare no competing interests.

Additional information

Peer review information *Nature* thanks Ziyue Gao, Nuria Lopez-Bigas and the other, anonymous, reviewer(s) for their contribution to the peer review of this work. Peer reviewer reports are available.

Publisher's note Springer Nature remains neutral with regard to jurisdictional claims in published maps and institutional affiliations.

Extended data figures and tables

[Extended Data Fig. 1 Number of somatic mutations per genome.](#)

The number of somatic mutations per genome for the 47-year-old man (PD43851), a 54-year-old woman (PD43850) and a 78-year-old man (PD28690) is shown by each tissue type. **a**, Median VAF per sample. **b**, SBS burden. **c**, Indel burden.

[Extended Data Fig. 2 Mutation burden across tissues.](#)

Mutation burden was estimated on a subset of tissues that passed all filtering criteria. Minor clone mutations were identified and removed using a truncated binomial algorithm. Cell types with a minimum of three samples from more than one individual were included for mutation burden analysis. **a**, Proportion of SBS mutations that were assigned to the major clone by the truncated binomial method. **b**, Peak VAF of SBSs belonging to the major clone. **c**, Clonal SBS burden.

[Extended Data Fig. 3 Summary of indel burden for all 13 individuals.](#)

a, Indels from each sample were merged together by tissue type. Indel signatures were generated using MutationalPatterns. **b**, Age correlation of clonal indels per genome (corrected for callable genome) for the colon (top

panel) and testes (bottom panel). The whiskers in panel **b** extend to the largest/lowest value within the $1.5 \times \text{IQR}$ from Q3/Q1 of the data, respectively. The shaded region around the regression lines represents 95% CI.

[Extended Data Fig. 4 Summary of different SV types per tissue per genome.](#)

The number of different types of SVs identified, coded by colour, and the number of patches used to identify SV events per tissue per individual. Overall, colonic crypts across all three donors have the highest number of SV events. In particular, high numbers of retrotransposition events were identified in colonic crypts of the 78-year-old man (donor PD28690).

[Extended Data Fig. 5 Chromosome arm or focal losses, encompassing either NOTCH1 or TP53 in the oesophagus.](#)

Raw ASCAT profile containing allele-specific copy number for all loci. The *x* axis depicts the genomic location and the *y* axis shows the DNA copy number. The purple and blue indicate the copy number of the minor allele and the estimated overall copy number, respectively. **a**, PD43851k_P52_OSPHG_H12: *NOTCH1* missense mutation (Chr9: Pos139417476:G>T) and subclonal loss 9qter. **b**, PD43851k_P53_OSPHG_B2: *TP53* and loss of single copy 17p. **c**, PD43851k_P53_OSPHG_E2: *NOTCH1* missense mutation (Chr9: Pos139412332:C>T) and copy number neutral LOH of 9q. **d**, PD43851k_P53_OSPHG_G2: *NOTCH1* missense mutation (Chr9: Pos139412332:C>T) and *TP53* missense mutation (Chr17: Pos7579358:C>A) combined with copy number neutral LOH of 9qter (approximately 4.8 Mb).

[Extended Data Fig. 6 Telomere length comparison between the testes and colon.](#)

a, Absolute telomere length in seminiferous tubules (purple) and colonic crypts (orange) ($n = 6$ individuals). The centre dot represents the median,

with 25% and 75% percentiles indicated as point range. **b**, Regression lines from the linear models comparing the effect of age on telomere length between colonic crypts (red) and seminiferous tubules (blue). The shaded region around the regression lines represents 95% CI. **c**, Correlation between absolute SBS burden and telomere length in the microbiopsies of the colonic crypts. **d**, Correlation between absolute SBS burden and telomere length in the microbiopsies of the seminiferous tubules. **e**, Correlation between absolute SBS1 burden and telomere length in the microbiopsies of the colonic crypts. **f**, Correlation between absolute SBS1 burden and telomere length in the microbiopsies of the seminiferous tubule. **g**, Correlation between absolute SBS5 burden and telomere length in the microbiopsies of the colonic crypts. **h**, Correlation between absolute SBS5 burden and telomere length in the microbiopsies of the seminiferous tubules. Correlation was tested using Spearman's rank test and the respective coefficient (rho), and *P* values are stated on the plots in panels **c–h**. The samples sequenced on NovaSeq were excluded from the analyses. SBS1 and SBS5 contributions estimated by SigProfiler were used to estimate the mutation burden associated with the respective signatures.

Extended Data Fig. 7 Comparison of mutational biases in the oesophagus between individuals.

Mutations in the oesophagus were compared between two individuals. **a**, The \log_2 ratio of SBSs on the transcribed to non-transcribed strands for the six mutation classes. The asterisks indicate significant transcriptional strand biases after accounting for multiple tests ($P < 0.05$, two-sided Poisson test). **b–d**, Observed/expected mutation burden for intergenic, intronic and exonic regions (**b**), transcripts across four oesophagus-specific GTEx³⁵ gene expression level bins (**c**), and early, intermediate and late replicating regions of the genome (**d**). The expected burden for a bin is calculated based on the trinucleotide counts of regions in that bin and the average trinucleotide mutation rates in that tissue. The error bars indicate the 95% CI. PD28690 (a 78-year-old man), with SBS16, shows outlier patterns.

Extended Data Fig. 8 Effect of gene expression and transcription strand bias on germline mutation rate.

a, Mutation burden in germline datasets across spermatogonia expression groups. Observed/expected mutation burden for deCODE trio DNMs, gnomAD population variants and seminiferous tubules ($n = 13$ individuals) in transcripts across eight expression groups of increasing expression level identified from single-cell sequencing of spermatogonia³⁷. The expected burden for a bin is calculated based on the trinucleotide counts of regions in that bin and the average trinucleotide mutation rates in that dataset. The error bars indicate the 95% CI. **b**, Correlation between transcription strand bias and gene expression. Two SBS germline variant datasets were compared with 11 somatic tissues. The relative mutation rate of mutation classes on the transcribed and untranscribed strands across tissue-specific expression level bins. The relative mutation rate was calculated for each tissue bin as the mutation rate per base pair for each class divided by the total mutations per base pair.

Extended Data Fig. 9 Mutational signature contribution to mutational biases between the germline and the soma.

a–c, Mutational signature contribution to observed/expected mutation burden for intergenic, intronic and exonic regions (**a**), transcripts across four tissue-specific GTEx³⁵ gene expression level bins, and early, intermediate and late replicating regions of the genome. The expected burden for each bin is calculated based on the trinucleotide counts of regions in that bin and the average trinucleotide mutation rates in that tissue. The mutational signature breakdown is calculated using the probability of each variant belonging to each signature based on the fraction of signature in that tissue and the frequency of the mutation type with that signature.

Supplementary information

Supplementary Information

This file contains supplementary discussion, supplementary methods and supplementary figures 1 – 9.

Reporting Summary

Peer Review File

Supplementary Tables

This file contains Supplementary Tables 1–4 and 7–10.

Supplementary Table 1 | Information about the individuals recruited for this study

Supplementary Table 2 | Details of anatomical structures were sampled for this study

Supplementary Table 3 | Structural Variations identified per individual per cell type

Supplementary Table 4 | Sample Information

Supplementary Table 7 | List of known or suspected cancer drivers identified

Supplementary Table 8 | Mutational Signatures detected across individuals and tissues

Supplementary Table 9 | Pairing of PanBody and GTEx tissues

Supplementary Table 10 | Comparison of HDP signature extraction with the reference signatures.

Supplementary Table 5

Whole-genome SBS across all samples.

Supplementary Table 6

Whole-genome INDELs across all samples

Rights and permissions

[Reprints and Permissions](#)

About this article

Cite this article

Moore, L., Cagan, A., Coorens, T.H.H. *et al.* The mutational landscape of human somatic and germline cells. *Nature* **597**, 381–386 (2021).
<https://doi.org/10.1038/s41586-021-03822-7>

- Received: 23 November 2020
- Accepted: 13 July 2021
- Published: 25 August 2021
- Issue Date: 16 September 2021
- DOI: <https://doi.org/10.1038/s41586-021-03822-7>

Share this article

Anyone you share the following link with will be able to read this content:

[Get shareable link](#)

Sorry, a shareable link is not currently available for this article.

[Copy to clipboard](#)

Provided by the Springer Nature SharedIt content-sharing initiative

Further reading

- Clonal dynamics in early human embryogenesis inferred from somatic mutation

- Seongyeol Park
- , Nanda Maya Mali
- , Ryul Kim
- , Jeong-Woo Choi
- , Junehawk Lee
- , Joonoh Lim
- , Jung Min Park
- , Jung Woo Park
- , Donghyun Kim
- , Taewoo Kim
- , Kijong Yi
- , June Hyug Choi
- , Seong Gyu Kwon
- , Joo Hee Hong
- , Jeonghwan Youk
- , Yohan An
- , Su Yeon Kim
- , Soo A Oh
- , Youngoh Kwon
- , Dongwan Hong
- , Moonkyu Kim
- , Dong Sun Kim
- , Ji Young Park
- , Ji Won Oh
- & Young Seok Ju

Nature (2021)

- Extensive phylogenies of human development inferred from somatic mutations

- Tim H. H. Coorens
- , Luiza Moore
- , Philip S. Robinson

- , Rashesh Sanghvi
- , Joseph Christopher
- , James Hewinson
- , Moritz J. Przybilla
- , Andrew R. J. Lawson
- , Michael Spencer Chapman
- , Alex Cagan
- , Thomas R. W. Oliver
- , Matthew D. C. Neville
- , Yvette Hooks
- , Ayesha Noorani
- , Thomas J. Mitchell
- , Rebecca C. Fitzgerald
- , Peter J. Campbell
- , Iñigo Martincorena
- , Raheleh Rahbari
- & Michael R. Stratton

Nature (2021)

Mutation fingerprints encode cellular histories

- Kamila Naxerova

News & Views 25 Aug 2021

A body-wide view of somatic mutations

- Darren J. Burgess

Research Highlight 14 Sept 2021

This article was downloaded by **calibre** from <https://www.nature.com/articles/s41586-021-03822-7>

- Article
- [Published: 25 August 2021](#)

Extensive phylogenies of human development inferred from somatic mutations

- [Tim H. H. Coorens](#) [ORCID: orcid.org/0000-0002-5826-3554](#)^{1 na1},
- [Luiza Moore](#) [ORCID: orcid.org/0000-0001-5315-516X](#)^{1,2 na1},
- [Philip S. Robinson](#) [ORCID: orcid.org/0000-0002-6237-7159](#)^{1,3},
- [Rashesh Sanghvi](#) [ORCID: orcid.org/0000-0002-7703-9216](#)¹,
- [Joseph Christopher](#) [ORCID: orcid.org/0000-0002-2059-0154](#)^{1,3,4},
- [James Hewinson](#)¹,
- [Moritz J. Przybilla](#) [ORCID: orcid.org/0000-0001-5645-9492](#)¹,
- [Andrew R. J. Lawson](#) [ORCID: orcid.org/0000-0003-3592-1005](#)¹,
- [Michael Spencer Chapman](#) [ORCID: orcid.org/0000-0002-5320-8193](#)^{1,5,6},
- [Alex Cagan](#) [ORCID: orcid.org/0000-0002-7857-4771](#)¹,
- [Thomas R. W. Oliver](#) [ORCID: orcid.org/0000-0003-4306-0102](#)^{1,4},
- [Matthew D. C. Neville](#) [ORCID: orcid.org/0000-0001-5816-7936](#)¹,
- [Yvette Hooks](#)¹,
- [Ayesha Noorani](#)¹,
- [Thomas J. Mitchell](#) [ORCID: orcid.org/0000-0003-0761-9503](#)^{1,4,7},
- [Rebecca C. Fitzgerald](#) [ORCID: orcid.org/0000-0002-3434-3568](#)⁸,
- [Peter J. Campbell](#) [ORCID: orcid.org/0000-0002-3921-0510](#)¹,
- [Iñigo Martincorena](#) [ORCID: orcid.org/0000-0003-1122-4416](#)¹,
- [Raheleh Rahbari](#) [ORCID: orcid.org/0000-0002-1839-7785](#)¹ &
- [Michael R. Stratton](#) [ORCID: orcid.org/0000-0001-6035-153X](#)¹

[Nature](#) volume **597**, pages 387–392 (2021)

- 10k Accesses
- 282 Altmetric
- [Metrics details](#)

Subjects

- [Cell lineage](#)
- [Development](#)
- [Phylogenomics](#)

Abstract

Starting from the zygote, all cells in the human body continuously acquire mutations. Mutations shared between different cells imply a common progenitor and are thus naturally occurring markers for lineage tracing^{1,2}. Here we reconstruct extensive phylogenies of normal tissues from three adult individuals using whole-genome sequencing of 511 laser capture microdissections. Reconstructed embryonic progenitors in the same generation of a phylogeny often contribute to different extents to the adult body. The degree of this asymmetry varies between individuals, with ratios between the two reconstructed daughter cells of the zygote ranging from 60:40 to 93:7. Asymmetries pervade subsequent generations and can differ between tissues in the same individual. The phylogenies resolve the spatial embryonic patterning of tissues, revealing contiguous patches of, on average, 301 crypts in the adult colonic epithelium derived from a most recent embryonic cell and also a spatial effect in brain development. Using data from ten additional men, we investigated the developmental split between soma and germline, with results suggesting an extraembryonic contribution to primordial germ cells. This research demonstrates that, despite reaching the same ultimate tissue patterns, early bottlenecks and lineage commitments lead to substantial variation in embryonic patterns both within and between individuals.

Access options

[Subscribe to Journal](#)

Get full journal access for 1 year

\$199.00

only \$3.90 per issue

[Subscribe](#)

All prices are NET prices.

VAT will be added later in the checkout.

Tax calculation will be finalised during checkout.

Rent or Buy article

Get time limited or full article access on ReadCube.

from \$8.99

[Rent or Buy](#)

All prices are NET prices.

Additional access options:

- [Log in](#)
- [Access through your institution](#)
- [Learn about institutional subscriptions](#)

Fig. 1: Phylogenies of clonal populations.

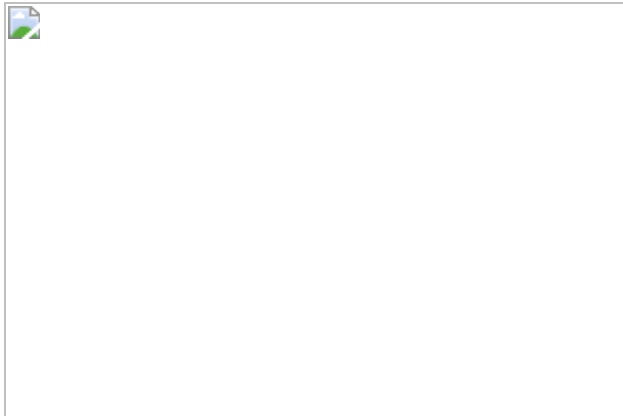


Fig. 2: Developmental phylogenies and embryonic asymmetries.

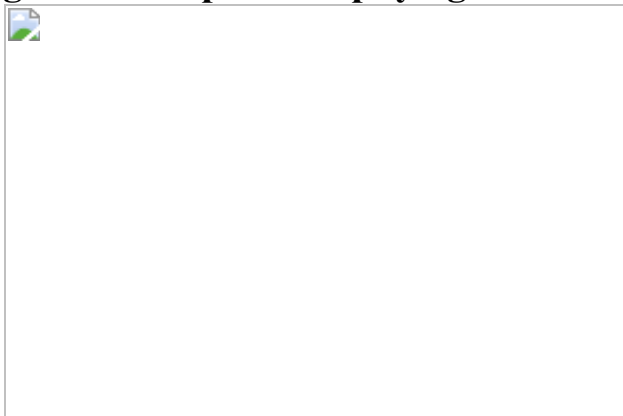


Fig. 3: Embryonic mosaicism in tissues and organs.

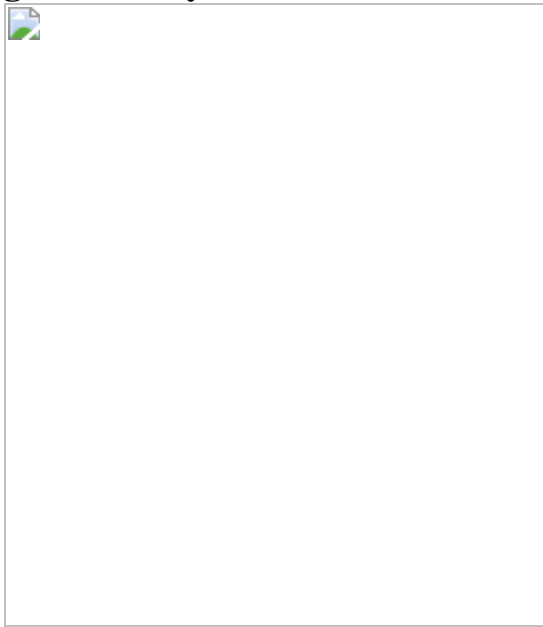
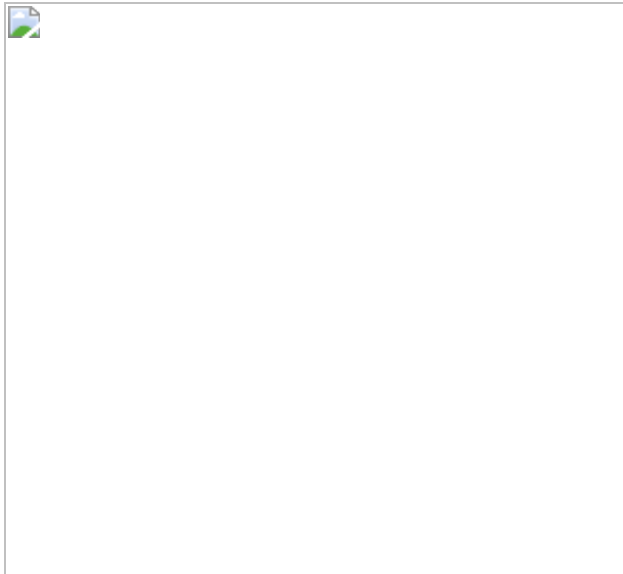


Fig. 4: Patterns of mutations in early embryogenesis.



Data availability

The DNA sequencing data are deposited in the European Genome-Phenome Archive (EGA) with the accession codes [EGAD00001006641](#) (whole-genome sequencing) and [EGAD00001006643](#) (targeted sequencing).

Code availability

The bespoke R scripts used for analysis and visualization in this study are available online from GitHub (https://github.com/TimCoorens/PanBody_Phylogenies).

References

1. 1.

Behjati, S. et al. Genome sequencing of normal cells reveals developmental lineages and mutational processes. *Nature* **513**, 422–425 (2014).

2. 2.

Ju, Y. S. et al. Somatic mutations reveal asymmetric cellular dynamics in the early human embryo. *Nature* **543**, 714–718 (2017).

3. 3.

Sulston, J. E. & Horvitz, H. R. Post-embryonic cell lineages of the nematode, *Caenorhabditis elegans*. *Dev. Biol.* **56**, 110–156 (1977).

4. 4.

Keller, P. J., Schmidt, A. D., Wittbrodt, J. & Stelzer, E. H. Reconstruction of zebrafish early embryonic development by scanned light sheet microscopy. *Science* **322**, 1065–1069 (2008).

5. 5.

Strnad, P. et al. Inverted light-sheet microscope for imaging mouse pre-implantation development. *Nat. Methods* **13**, 139–142 (2016).

6. 6.

McKenna, A. et al. Whole-organism lineage tracing by combinatorial and cumulative genome editing. *Science* **353**, aaf7907 (2016).

7. 7.

Alemany, A., Florescu, M., Baron, C. S., Peterson-Maduro, J. & van Oudenaarden, A. Whole-organism clone tracing using single-cell sequencing. *Nature* **556**, 108–112 (2018).

8. 8.

Stratton, M. R., Campbell, P. J. & Futreal, P. A. The cancer genome. *Nature* **458**, 719–724 (2009).

9. 9.

Coorens, T. H. H. et al. Embryonal precursors of Wilms tumor. *Science* **366**, 1247–1251 (2019).

10. 10.

Lee-Six, H. et al. Population dynamics of normal human blood inferred from somatic mutations. *Nature* **561**, 473–478 (2018).

11. 11.

Coorens, T. H. H. et al. Lineage-independent tumors in bilateral neuroblastoma. *N. Engl. J. Med.* **383**, 1860–1865 (2020).

12. 12.

Park, S. et al. Clonal dynamics in early human embryogenesis inferred from somatic mutation. *Nature* <https://doi.org/10.1038/s41586-021-03786-8> (2021).

13. 13.

Coorens, T. H. H. et al. Inherent mosaicism and extensive mutation of human placentas. *Nature* **592**, 80–85 (2021).

14. 14.

Lodato, M. A. et al. Somatic mutation in single human neurons tracks developmental and transcriptional history. *Science* **350**, 94–98 (2015).

15. 15.

Lodato, M. A. et al. Aging and neurodegeneration are associated with increased mutations in single human neurons. *Science* **359**, 555–559 (2018).

16. 16.

Lee-Six, H. et al. The landscape of somatic mutation in normal colorectal epithelial cells. *Nature* **574**, 532–537 (2019).

17. 17.

Moore, L. et al. The mutational landscape of human somatic and germline cells. *Nature* <https://doi.org/10.1038/s41586-021-03822-7> (2021).

18. 18.

Ye, A. Y. et al. A model for postzygotic mosaicism quantifies the allele fraction drift, mutation rate, and contribution to de novo mutations. *Genome Res.* **28**, 943–951 (2018).

19. 19.

Spencer Chapman, M. et al. Lineage tracing of human development through somatic mutations. *Nature* **595**, 85–90 (2021).

20. 20.

Kuijk, E. et al. Early divergence of mutational processes in human fetal tissues. *Sci. Adv.* **5**, eaaw1271 (2019).

21. 21.

Kobayashi, T. & Surani, M. A. On the origin of the human germline. *Development* **145**, dev150433 (2018).

22. 22.

Aitken, S. J. et al. Pervasive lesion segregation shapes cancer genome evolution. *Nature* **583**, 265–270 (2020).

23. 23.

Priestley, P. et al. Pan-cancer whole-genome analyses of metastatic solid tumours. *Nature* **575**, 210–216 (2019).

24. 24.

Forsberg, L. A. et al. Mosaic loss of chromosome Y in peripheral blood is associated with shorter survival and higher risk of cancer. *Nat.*

Genet. **46**, 624–628 (2014).

25. 25.

Loftfield, E. et al. Predictors of mosaic chromosome Y loss and associations with mortality in the UK Biobank. *Sci. Rep.* **8**, 12316 (2018).

26. 26.

Voet, T., Vanneste, E. & Vermeesch, J. R. The human cleavage stage embryo is a cradle of chromosomal rearrangements. *Cytogenet. Genome Res.* **133**, 160–168 (2011).

27. 27.

Shahbazi, M. N. et al. Developmental potential of aneuploid human embryos cultured beyond implantation. *Nat. Commun.* **11**, 3987 (2020).

28. 28.

Sancho, M. et al. Competitive interactions eliminate unfit embryonic stem cells at the onset of differentiation. *Dev. Cell* **26**, 19–30 (2013).

29. 29.

Moore, L. et al. The mutational landscape of normal human endometrial epithelium. *Nature* **580**, 640–646 (2020).

30. 30.

Olafsson, S. et al. Somatic evolution in non-neoplastic IBD-affected colon. *Cell* **182**, 672–684.e11 (2020).

31. 31.

Robinson, P. S. et al. Elevated somatic mutation burdens in normal human cells due to defective DNA polymerases. Preprint at

<https://doi.org/10.1101/2020.06.23.167668> (2020).

32. 32.

Ellis, P. et al. Reliable detection of somatic mutations in solid tissues by laser-capture microdissection and low-input DNA sequencing. *Nat. Protoc.* **16**, 841–871 (2020).

33. 33.

Lawson, A. R. J. et al. Extensive heterogeneity in somatic mutation and selection in the human bladder. *Science* **370**, 75–82 (2020)

34. 34.

Li, H. & Durbin, R., Fast and accurate short read alignment with Burrows–Wheeler transform. *Bioinformatics* **25**, 1754–1760 (2009).

35. 35.

Jones, D. et al. cgpCaVEManWrapper: simple execution of CaVEMan in order to detect somatic single nucleotide variants in NGS data. *Curr. Protoc. Bioinformatics* **56**, 15.10.1–15.10.18 (2016).

36. 36.

Ye, K., Schulz, M. H., Long, Q., Apweiler, R. & Ning, Z. Pindel: a pattern growth approach to detect break points of large deletions and medium sized insertions from paired-end short reads. *Bioinformatics* **25**, 2865–2871 (2009).

37. 37.

Van Loo, P., et al. Allele-specific copy number analysis of tumors. *Proc. Natl Acad. Sci. USA* **107**, 16910–16915 (2010).

38. 38.

Nik-Zainal, S. et al. The life history of 21 breast cancers. *Cell* **149**, 994–1007 (2012).

39. 39.

Benjamini, Y. & Hochberg, Y. Controlling the false discovery rate: a practical and powerful approach to multiple testing. *J. R. Stat. Soc. B* 289–300 (1995).

40. 40.

Yoshida, K. et al. Tobacco smoking and somatic mutations in human bronchial epithelium. *Nature* **578**, 266–272 (2020).

41. 41.

Gerstung, M., Papaemmanuil, E. & Campbell, P. J. Subclonal variant calling with multiple samples and prior knowledge. *Bioinformatics* **30**, 1198–1204 (2014).

42. 42.

Hoang, H. T. et al. MPBoot: fast phylogenetic maximum parsimony tree inference and bootstrap approximation. *BMC Evol. Biol.* **18**, 11 (2018).

43. 43.

Nguyen, L.-T. et al. IQ-TREE: a fast and effective stochastic algorithm for estimating maximum-likelihood phylogenies. *Mol. Biol. Evol.* **32**, 268–274 (2014).

44. 44.

Novelli, M. et al. X-inactivation patch size in human female tissue confounds the assessment of tumor clonality. *Proc. Natl Acad. Sci. USA* **100**, 3311–3314 (2003)

45. 45.

Gori, K. & Baez-Ortega, A. sigfit: flexible Bayesian inference of mutational signatures. Preprint at <https://doi.org/10.1101/372896> (2018).

46. 46.

Coorens, T. H. H. et al. Clonal hematopoiesis and therapy-related myeloid neoplasms following neuroblastoma treatment. *Blood* **137**, 2992–2997 (2021).

Acknowledgements

We thank the staff of the Wellcome Sanger Institute Sample Logistics, Genotyping, Pulldown, Sequencing and Informatics facilities for their contribution, especially L. O'Neill, C. Latimer and K. Roberts for their support with sample management and laboratory work; and S. Behjati, Y. S. Ju, S. Park, F. Abascal, J. Ijaz, P. Nicola and G. Collord for helpful discussions or critical review of the manuscript. This experiment was primarily funded by Wellcome (core funding to the Wellcome Sanger Institute and PhD studentship to T.H.H.C.; 203943/Z/16/Z). L.M. is a recipient of a Cancer Research UK (CRUK) Clinical PhD fellowship (C20/A20917) and the Jean Shank/Pathological Society of Great Britain and Ireland Intermediate Research Fellowship (grant reference no. 1175). T.J.M. is supported by CRUK and the Royal College of Surgeons (C63474/A27176). I.M. is funded by CRUK (C57387/A21777) and the Wellcome Trust. R.R. is funded by CRUK (C66259/A27114).

Author information

Author notes

1. These authors contributed equally: Tim H. H. Coorens, Luiza Moore

Affiliations

1. Wellcome Sanger Institute, Hinxton, UK

Tim H. H. Coorens, Luiza Moore, Philip S. Robinson, Rashesh Sanghvi, Joseph Christopher, James Hewinson, Moritz J. Przybilla, Andrew R. J. Lawson, Michael Spencer Chapman, Alex Cagan, Thomas R. W. Oliver, Matthew D. C. Neville, Yvette Hooks, Ayesha Noorani, Thomas J. Mitchell, Peter J. Campbell, Iñigo Martincorena, Raheleh Rahbari & Michael R. Stratton

2. Department of Pathology, University of Cambridge, Cambridge, UK

Luiza Moore

3. Department of Paediatrics, University of Cambridge, Cambridge, UK

Philip S. Robinson & Joseph Christopher

4. Cambridge University Hospitals NHS Foundation Trust, Cambridge, UK

Joseph Christopher, Thomas R. W. Oliver & Thomas J. Mitchell

5. Department of Haematology, Hammersmith Hospital, Imperial College Healthcare NHS Trust, London, UK

Michael Spencer Chapman

6. Department of Haematology, University of Cambridge, Cambridge, UK

Michael Spencer Chapman

7. Department of Surgery, University of Cambridge, Cambridge, UK

Thomas J. Mitchell

8. MRC Cancer Unit, University of Cambridge, Biomedical Campus, Cambridge, UK

Rebecca C. Fitzgerald

Contributions

T.H.H.C., L.M., R.R. and M.R.S. conceived the study design. T.H.H.C. wrote the scripts and performed the analyses with help or input from R.S., J.C., M.D.C.N., M.S.C. and I.M. L.M., P.S.R., A.C. and T.R.W.O. performed the microdissections with support from Y.H. M.J.P. and A.R.J.L. called and analysed mitochondrial variants. T.J.M., A.N. and R.C.F. aided in sample procurement. M.R.S. oversaw the study. T.H.H.C. and M.R.S. wrote the manuscript with input from all other authors.

Corresponding author

Correspondence to Michael R. Stratton.

Ethics declarations

Competing interests

The authors declare no competing interests.

Additional information

Peer review information *Nature* thanks Nuria Lopez-Bigas, Aaron Mckenna, David Posada and the other, anonymous, reviewer(s) for their contribution to the peer review of this work. Peer reviewer reports are available.

Extended data figures and tables

[Extended Data Fig. 1 VAF distributions reflect clonality of LCM sample.](#)

a, Schematic of three different progenitor or stem cell contributions to the eventual sample. Monoclonal samples consist of the progeny of one cell, while oligoclonal and polyclonal are derived from a few and many

progenitors, respectively. **b–d**, VAF histograms and binomial decompositions for a monoclonal (**b**), oligoclonal (**c**) and polyclonal (**d**) sample. The red and blue dashed lines indicate clonal decomposition through a binomial mixture model, with the estimated peak VAF of clones indicated in the legend. The number indicated in the title of each histogram is the SNV burden.

Extended Data Fig. 2 Model of early embryogenesis and ABC.

a, Heat maps showing the results of estimates of the early embryonic bottleneck obtained through approximate Bayesian computation, with and without cell death rate as a parameter ([Methods](#)). The darkness of the colour indicates the frequency of the observed bottleneck in the accepted simulations. **b**, Estimates of the mutation rate per cell per division before and after zygotic genome activation (ZGA); the dot indicates the mean of the 20,000 accepted simulations and the line spans the 95% confidence interval.

Extended Data Fig. 3 The most recent common ancestors of tissues and completeness of early lineages.

a–d, Phylogenetic trees with unit branch lengths for PD28690, showing the coalescence (red) of all samples from four tissues types: thyroid follicles (**a**), seminiferous tubules (**b**), small bowel crypts (**c**) and bronchial epithelium (**d**). The most recent common ancestor for all these tissues is the root of the tree. **e**, Sum of mean VAFs of branches of the same generation per bulk sample in PD28690 ($n = 33$), PD43850 ($n = 1$) and PD43851 ($n = 2$). The solid black line indicates the mean value across tissue samples. A total sum of mean VAFs approximating 0.5 indicates that all cells belong to one of the lineages of that generation and are accounted for, that is, no lineages are missing from the phylogeny. This is mostly the case for generations 1 and 2, but the total VAF of generation 3 indicates missing lineages.

Extended Data Fig. 4 Embryonic patch size in the colon.

a, Kernel smoothed 2D histogram of the linear distance (in number of crypts) and the number of shared SNVs between any two crypts from the same biopsy. The red line is shown at a shared SNV burden of 15, above which crypts were taken to be from the same embryonic patch. **b**, Histogram of the number of SNVs shared between all pairs of crypts showing a bimodal distribution on either side of an SNV burden of 15 (red line). **c**, Density plot of the prior distribution of the embryonic patch size radius. **d**, Plot of the radius versus the Euclidean distance in summary statistics between the simulations and our observed data. The red dots indicate those within the 5% closest simulations and are accepted. **e**, Density plot of the prior distribution (dashed line), the posterior distribution from the rejection method (black line) and the posterior distribution from the neural network regression (red line) of the embryonic patch size radius. **f**, A QQ-plot of the residuals of the neural network regression.

Extended Data Fig. 5 Clonal expansions later in life.

a, Phylogenetic tree for appendiceal crypts in PD28690, with annotated cancer driver mutations. An asterisk indicates that the two neighbouring crypts were taken as biological replicates of one another. Within the clade of crypts that acquired the *BRAF* mutation, the mutation burdens are Poisson distributed, consistent with a molecular clock ($P = 0.99$, dispersion test). Accordingly, we can estimate that the *BRAF* mutation was acquired before 23 years of age. **b**, **c**, Phylogeny (**b**) and sampling overview (**c**) for prostatic acini in PD28690, showing widespread benign prostatic hyperplasia in one biopsy. **d**, Histology and sampling overview alongside the phylogeny for a microscopic polyp in the colon of PD28690. **e**, Phylogeny of seminiferous tubules from PD42034, where a frameshift deletion in *MEIOB* was acquired after only six post-zygotic SNVs. Parts of the figure are composed of pictures from Servier Medical Art (<https://smart.servier.com/>). Servier Medical Art by Servier is licensed under a Creative Commons Attribution 3.0 Unported License (<https://creativecommons.org/licenses/by/3.0/>).

Extended Data Fig. 6 Decomposition of polyclonal samples.

Phylogenetic trees with unit branch lengths for four polyclonal samples of the epidermis from PD28690, showing the contribution (blue) of early embryonic progenitors in the phylogeny to the sample. These samples were not used for the reconstruction of the phylogeny because of their lack of a dominant clone, but can still be decomposed into the contributing embryonic lineages that give rise to these polyclonal aggregates. For example, ‘SKN2_D2’, while somatically polyclonal, seems to be derived from a single early lineage.

Extended Data Fig. 7 Targeted resequencing in PD28690.

Cladogram of PD28690 with contribution to 84 bulk samples (none derived from testes) as assessed through targeted resequencing of embryonic and spermatogonia-specific variants. The colour of the branch indicates the mean VAF of substitutions on that branch across all bulk samples. Nodes that gave rise to only seminiferous tubules are annotated with an asterisk. Branches coming from those nodes do not contribute to the bulk samples, confirming that the segregation of primordial germ cell lineages coincides with the observed branching point on the phylogenies.

Extended Data Fig. 8 Early embryogenesis and bottlenecks.

a, Overview of lineage commitments in the early human embryo, up until gastrulation and early organogenesis. The blue arrows indicate the putative contribution of extraembryonic cells to embryonic lineages (for yolk sac haematopoiesis and intercalation of the endoderm) or lineages with an unknown origin (primordial germ cells). **b**, Schematic of the possible influence of multiple, successive bottlenecks on the eradication of a specific lineage in a certain population of cells. The two daughter lineages of the zygote are coloured in red and blue. Note that this is a toy example merely for illustration and the relative cell numbers or size of the bottlenecks need not represent reality.

Extended Data Fig. 9 Patterns of mitochondrial and nuclear SNVs.

a–d, Phylogenies of nuclear SNVs with the VAF of mitochondrial mutations overlaid on them, showing a late shared SNV (**a**), an SNV that was heteroplasmic in the zygote (**b**), an SNV that is consistent with a shared subclone or stromal contamination (**c**) and an SNV recurrently acquired in samples from different tissues (**d**). **e**, Mutational spectrum and decomposition of early embryonic nuclear SNVs.

Extended Data Fig. 10 Loss of the Y chromosome.

a, b, Scatterplots showing the ratio between the mean Y-chromosomal coverage and autosomal coverage against the mean autosomal coverage for all samples from PD28690 (**a**) and PD43851 (**b**). The dashed red lines indicate the 95% confidence interval around an expected ratio of 0.5. The red dots indicate samples with significant evidence of loss of the Y chromosome. **c**, Phylogeny of PD28690 with samples exhibiting loss of the Y chromosome marked in red, indicating that all loss of the Y chromosome events are acquired independently.

Supplementary information

Supplementary Methods

This Supplementary Methods file includes Supplementary Tables 7–10 and Supplementary Fig. 1, and has the following sections: Proportion of SNVs filtered at each stage; Validation of phylogenies; Validation of non-monophyly of tissues; Recurrent SNVs and the infinite sites model; and Mutation rate in early embryogenesis.

Reporting Summary

Peer Review File

Supplementary Tables

Rights and permissions

[Reprints and Permissions](#)

About this article

Cite this article

Coorens, T.H.H., Moore, L., Robinson, P.S. *et al.* Extensive phylogenies of human development inferred from somatic mutations. *Nature* **597**, 387–392 (2021). <https://doi.org/10.1038/s41586-021-03790-y>

- Received: 25 November 2020
- Accepted: 01 July 2021
- Published: 25 August 2021
- Issue Date: 16 September 2021
- DOI: <https://doi.org/10.1038/s41586-021-03790-y>

Share this article

Anyone you share the following link with will be able to read this content:

[Get shareable link](#)

Sorry, a shareable link is not currently available for this article.

[Copy to clipboard](#)

Provided by the Springer Nature SharedIt content-sharing initiative

[Mutation fingerprints encode cellular histories](#)

- Kamila Naxerova

News & Views 25 Aug 2021

A body-wide view of somatic mutations

- Darren J. Burgess

Research Highlight 14 Sept 2021

This article was downloaded by **calibre** from <https://www.nature.com/articles/s41586-021-03790-y>.

| [Section menu](#) | [Main menu](#) |

- Article
- [Published: 25 August 2021](#)

Clonal dynamics in early human embryogenesis inferred from somatic mutation

- [Seongyeol Park](#) ORCID: [orcid.org/0000-0002-9236-5853^{1,2 na1}](https://orcid.org/0000-0002-9236-5853),
- [Nanda Maya Mali^{3 na1}](#),
- [Ryul Kim^{1 na1}](#),
- [Jeong-Woo Choi^{3,4}](#),
- [Junehawk Lee⁵](#),
- [Joonoh Lim¹](#),
- [Jung Min Park^{3,4}](#),
- [Jung Woo Park⁵](#),
- [Donghyun Kim^{3,4}](#),
- [Taewoo Kim¹](#),
- [Kijong Yi](#) ORCID: [orcid.org/0000-0003-1656-1243¹](https://orcid.org/0000-0003-1656-1243),
- [June Hyug Choi³](#),
- [Seong Gyu Kwon³](#),
- [Joo Hee Hong³](#),
- [Jeonghwan Youk](#) ORCID: [orcid.org/0000-0002-6761-3958¹](https://orcid.org/0000-0002-6761-3958),
- [Yohan An](#) ORCID: [orcid.org/0000-0001-7560-769X¹](https://orcid.org/0000-0001-7560-769X),
- [Su Yeon Kim¹](#),
- [Soo A Oh¹](#),
- [Youngoh Kwon²](#),
- [Dongwan Hong](#) ORCID: [orcid.org/0000-0002-7816-1299⁶](https://orcid.org/0000-0002-7816-1299),
- [Moonkyu Kim⁷](#),
- [Dong Sun Kim³](#),
- [Ji Young Park](#) ORCID: [orcid.org/0000-0002-7571-1064⁸](https://orcid.org/0000-0002-7571-1064),

- [Ji Won Oh](#) ORCID: [orcid.org/0000-0001-5742-5120^{3,4,9 na2}](https://orcid.org/0000-0001-5742-5120) &
- [Young Seok Ju](#) ORCID: [orcid.org/0000-0002-5514-4189^{1,2 na2}](https://orcid.org/0000-0002-5514-4189)

Nature volume **597**, pages 393–397 (2021)

- 9289 Accesses
- 1 Citations
- 176 Altmetric
- [Metrics details](#)

Subjects

- [Bioinformatics](#)
- [Development](#)
- [Embryogenesis](#)
- [Genome informatics](#)
- [Phylogeny](#)

Abstract

Cellular dynamics and fate decision in early human embryogenesis remain largely unknown owing to the challenges of performing studies in human embryos¹. Here, we explored whole-genomes of 334 single-cell colonies and targeted deep sequences of 379 bulk tissues obtained from various anatomical locations of seven recently deceased adult human donors. Using somatic mutations as an intrinsic barcode, we reconstructed early cellular phylogenies that demonstrate (1) an endogenous mutational rate that is higher in the first cell division but decreases to approximately one per cell per cell division later in life; (2) universal unequal contribution of early cells to embryo proper, resulting from early cellular bottlenecks that stochastically set aside epiblast cells within the embryo; (3) examples of varying degrees of early clonal imbalances between tissues on the left and right sides of the body, different germ layers and specific anatomical parts and organs; (4) emergence of a few ancestral cells that will substantially

contribute to adult cell pools in blood and liver; and (5) presence of mitochondrial DNA heteroplasmy in the fertilized egg. Our approach also provides insights into the age-related mutational processes and loss of sex chromosomes in normal somatic cells. In sum, this study provides a foundation for future studies to complete cellular phylogenies in human embryogenesis.

Access options

Subscribe to Journal

Get full journal access for 1 year

\$199.00

only \$3.90 per issue

[Subscribe](#)

All prices are NET prices.

VAT will be added later in the checkout.

Tax calculation will be finalised during checkout.

Rent or Buy article

Get time limited or full article access on ReadCube.

from \$8.99

[Rent or Buy](#)

All prices are NET prices.

Additional access options:

- [Log in](#)
- [Access through your institution](#)
- [Learn about institutional subscriptions](#)

Fig. 1: Tracing early cellular phylogenies using somatic mutations.



Fig. 2: Unequal contribution of early lineages to human bodies and early mutation rate.

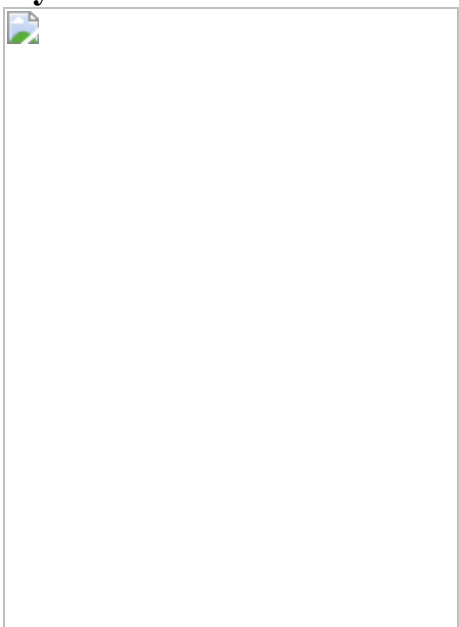


Fig. 3: Timing of fate determination of early cells.

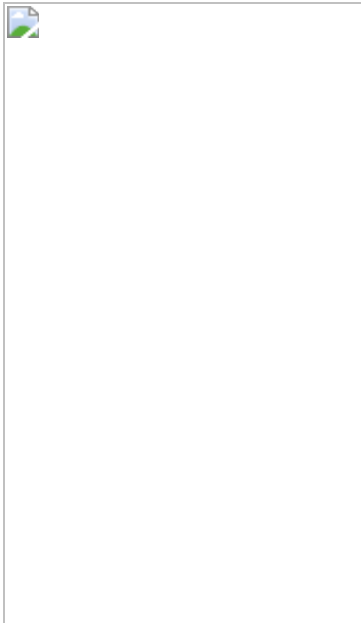
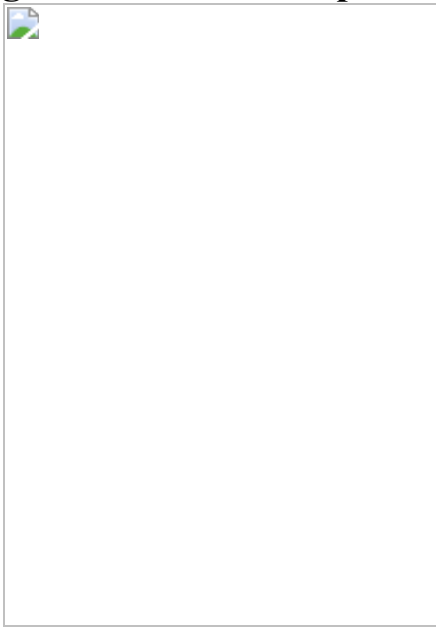


Fig. 4: mtDNA heteroplasmy in fertilized egg and late-stage mutations.



Data availability

Whole-genome and targeted sequencing data are deposited in the European Genome-phenome Archive (EGA) with accession EGAS00001004824 and are available for general research use.

Code availability

The information of sequenced clones and tissues, detected early mutations, and their anatomical tracking can be browsed through Somatic Clone Viewer (<https://julab.kaist.ac.kr/somatic-clone-viewer>). In-house scripts for genomic analyses and simulation studies are available on GitHub (https://github.com/seongyeol-park/Human_Lineage_Tracing and https://github.com/chrono0707/Human_Lineage_Tracing).

References

1. 1.
Wamaitha, S. E. & Niakan, K. K. Human pre-gastrulation development. *Curr Top Dev Biol* **128**, 295–338 (2018).
2. 2.
Sender, R., Fuchs, S. & Milo, R. Revised estimates for the number of human and bacteria cells in the body. *PLoS Biol.* **14**, e1002533 (2016).
3. 3.
Gasser, R. F., Cork, R. J., Stillwell, B. J. & McWilliams, D. T. Rebirth of human embryology. *Dev. Dyn.* **243**, 621–628 (2014).
4. 4.
Nakamura, T. et al. A developmental coordinate of pluripotency among mice, monkeys and humans. *Nature* **537**, 57–62 (2016).
5. 5.
Rossant, J. Mouse and human blastocyst-derived stem cells: vive les differences. *Development* **142**, 9–12 (2015).
6. 6.
Xiang, L. et al. A developmental landscape of 3D-cultured human pre-gastrulation embryos. *Nature* **577**, 537–542 (2020).

7. 7.

Shahbazi, M. N. & Zernicka-Goetz, M. Deconstructing and reconstructing the mouse and human early embryo. *Nat. Cell Biol.* **20**, 878–887 (2018).

8. 8.

Samuels, M. E. & Friedman, J. M. Genetic mosaics and the germ line lineage. *Genes (Basel)* **6**, 216–237 (2015).

9. 9.

Stratton, M. R., Campbell, P. J. & Futreal, P. A. The cancer genome. *Nature* **458**, 719–724 (2009).

10. 10.

Ju, Y. S. et al. Somatic mutations reveal asymmetric cellular dynamics in the early human embryo. *Nature* **543**, 714–718 (2017).

11. 11.

Behjati, S. et al. Genome sequencing of normal cells reveals developmental lineages and mutational processes. *Nature* **513**, 422–425 (2014).

12. 12.

Gerlinger, M. et al. Intratumor heterogeneity and branched evolution revealed by multiregion sequencing. *N. Engl. J. Med.* **366**, 883–892 (2012).

13. 13.

Lee-Six, H. et al. Population dynamics of normal human blood inferred from somatic mutations. *Nature* **561**, 473–478 (2018).

14. 14.

Lodato, M. A. et al. Somatic mutation in single human neurons tracks developmental and transcriptional history. *Science* **350**, 94–98 (2015).

15. 15.

Alexandrov, L. B. et al. The repertoire of mutational signatures in human cancer. *Nature* **578**, 94–101 (2020).

16. 16.

Coorens, T. H. H. et al. Extensive phylogenies of human development reveal variable embryonic patterns. *Nature* <https://doi.org/10.1038/s41586-021-0379-y> (2021).

17. 17.

Sulston, J. E., Schierenberg, E., White, J. G. & Thomson, J. N. The embryonic cell lineage of the nematode *Caenorhabditis elegans*. *Dev. Biol.* **100**, 64–119 (1983).

18. 18.

Hardy, K., Handyside, A. H. & Winston, R. M. The human blastocyst: cell number, death and allocation during late preimplantation development in vitro. *Development* **107**, 597–604 (1989).

19. 19.

Sancho, M. et al. Competitive interactions eliminate unfit embryonic stem cells at the onset of differentiation. *Dev. Cell* **26**, 19–30 (2013).

20. 20.

Biggins, J. S., Royer, C., Watanabe, T. & Srinivas, S. Towards understanding the roles of position and geometry on cell fate decisions during preimplantation development. *Semin. Cell Dev. Biol.* **47-48**, 74–79 (2015).

21. 21.

Spencer Chapman, M. et al. Lineage tracing of human development through somatic mutations. *Nature* **595**, 85–90 (2021).

22. 22.

Wennekamp, S., Mesecke, S., Nédélec, F. & Hiiragi, T. A self-organization framework for symmetry breaking in the mammalian embryo. *Nat. Rev. Mol. Cell Biol.* **14**, 452–459 (2013).

23. 23.

Blakeley, P. et al. Defining the three cell lineages of the human blastocyst by single-cell RNA-seq. *Development* **142**, 3151–3165 (2015).

24. 24.

Schulz, K. N. & Harrison, M. M. Mechanisms regulating zygotic genome activation. *Nat. Rev. Genet.* **20**, 221–234 (2019).

25. 25.

Gardner, R. L. Normal bias in the direction of fetal rotation depends on blastomere composition during early cleavage in the mouse. *PLoS ONE* **5**, e9610 (2010).

26. 26.

McKenna, A. et al. Whole-organism lineage tracing by combinatorial and cumulative genome editing. *Science* **353**, aaf7907 (2016).

27. 27.

Alemany, A., Florescu, M., Baron, C. S., Peterson-Maduro, J. & van Oudenaarden, A. Whole-organism clone tracing using single-cell sequencing. *Nature* **556**, 108–112 (2018).

28. 28.

Shluss, L. I. Age-related clonal hematopoiesis. *Blood* **131**, 496–504 (2018).

29. 29.

Wai, T., Teoli, D. & Shoubridge, E. A. The mitochondrial DNA genetic bottleneck results from replication of a subpopulation of genomes. *Nat. Genet.* **40**, 1484–1488 (2008).

30. 30.

Cummins, J. M. The role of maternal mitochondria during oogenesis, fertilization and embryogenesis. *Reprod. Biomed. Online* **4**, 176–182 (2002).

31. 31.

Floros, V. I. et al. Segregation of mitochondrial DNA heteroplasmy through a developmental genetic bottleneck in human embryos. *Nat. Cell Biol.* **20**, 144–151 (2018).

32. 32.

Coller, H. A. et al. High frequency of homoplasmic mitochondrial DNA mutations in human tumors can be explained without selection. *Nat. Genet.* **28**, 147–150 (2001).

33. 33.

Wonnapijij, P., Chinnery, P. F. & Samuels, D. C. The distribution of mitochondrial DNA heteroplasmy due to random genetic drift. *Am. J. Hum. Genet.* **83**, 582–593 (2008).

34. 34.

Sanders, M. A. et al. Life without mismatch repair. Preprint at <https://doi.org/10.1101/2021.04.14.437578> (2021).

35. 35.

Thompson, D. J. et al. Genetic predisposition to mosaic Y chromosome loss in blood. *Nature* **575**, 652–657 (2019).

36. 36.

Lee, J. J.-K. et al. Tracing oncogene rearrangements in the mutational history of lung adenocarcinoma. *Cell* **177**, 1842–1857.e21 (2019).

37. 37.

Lodato, M. A. et al. Aging and neurodegeneration are associated with increased mutations in single human neurons. *Science* **359**, 555–559 (2018).

38. 38.

Brunner, S. F. et al. Somatic mutations and clonal dynamics in healthy and cirrhotic human liver. *Nature* **574**, 538–542 (2019).

39. 39.

Lee-Six, H. et al. The landscape of somatic mutation in normal colorectal epithelial cells. *Nature* **574**, 532–537 (2019).

40. 40.

Moore, L. et al. The mutational landscape of normal human endometrial epithelium. *Nature* **580**, 640–646 (2020).

41. 41.

Moore, L. et al. The mutational landscape of human somatic and germline cells. *Nature* <https://doi.org/10.1038/s41586-021-03822-7> (2021).

42. 42.

Martincorena, I. et al. Somatic mutant clones colonize the human esophagus with age. *Science* **362**, 911–917 (2018).

43. 43.

Martincorena, I. et al. Tumor evolution. High burden and pervasive positive selection of somatic mutations in normal human skin. *Science* **348**, 880–886 (2015).

44. 44.

Yokoyama, A. et al. Age-related remodelling of oesophageal epithelia by mutated cancer drivers. *Nature* **565**, 312–317 (2019).

45. 45.

Zhu, M. et al. Somatic mutations increase hepatic clonal fitness and regeneration in chronic liver disease. *Cell* **177**, 608–621.e12 (2019).

46. 46.

Fasching et al. Early developmental asymmetries in cell lineage trees in living individuals? *Science* **371**, 1245–1248 (2021).

47. 47.

Jones, G. E. & Wise, C. J. Establishment, maintenance, and cloning of human dermal fibroblasts. *Methods Mol. Biol.* **75**, 13–21 (1997).

48. 48.

Rittié, L. & Fisher, G. J. Isolation and culture of skin fibroblasts. *Methods Mol. Med.* **117**, 83–98 (2005).

49. 49.

Vangipuram, M., Ting, D., Kim, S., Diaz, R. & Schüle, B. Skin punch biopsy explant culture for derivation of primary human fibroblasts. *J. Vis. Exp.* **(77)**, e3779 (2013). <https://doi.org/10.3791/3779>.

50. 50.

Spinazzola, J. M. & Gussoni, E. Isolation of primary human skeletal muscle cells. *Bio Protoc.* **7**, e2591 (2017).

51. 51.

Oh, J. W. et al. A guide to studying human hair follicle cycling in vivo. *J. Invest. Dermatol.* **136**, 34–44 (2016).

52. 52.

Li, H. & Durbin, R. Fast and accurate short read alignment with Burrows–Wheeler transform. *Bioinformatics* **25**, 1754–1760 (2009).

53. 53.

McKenna, A. et al. The Genome Analysis Toolkit: a MapReduce framework for analyzing next-generation DNA sequencing data. *Genome Res.* **20**, 1297–1303 (2010).

54. 54.

Van der Auwera, G. A. et al. From FastQ data to high confidence variant calls: the Genome Analysis Toolkit best practices pipeline. *Curr Protoc Bioinformatics* **11**, 11.10.1–11.10.33 (2013).

55. 55.

Koboldt, D. C. et al. VarScan 2: somatic mutation and copy number alteration discovery in cancer by exome sequencing. *Genome Res.* **22**, 568–576 (2012).

56. 56.

Robinson, J. T. et al. Integrative genomics viewer. *Nat. Biotechnol.* **29**, 24–26 (2011).

57. 57.

Nik-Zainal, S. et al. The life history of 21 breast cancers. *Cell* **149**, 994–1007 (2012).

58. 58.

Gusfield, D. Efficient algorithms for inferring evolutionary trees. *Networks* **21**, 19–28 (1991).

59. 59.

Yu, G., Smith, D. K., Zhu, H., Guan, Y. & Lam, T. T.-Y. GGTREE: An R package for visualization and annotation of phylogenetic trees with their covariates and other associated data. *Methods Ecol. Evol.* (2016).

60. 60.

Strnad, P. et al. Inverted light-sheet microscope for imaging mouse pre-implantation development. *Nat. Methods* **13**, 139–142 (2016).

61. 61.

Bertorelle, G., Benazzo, A. & Mona, S. ABC as a flexible framework to estimate demography over space and time: some cons, many pros. *Mol. Ecol.* **19**, 2609–2625 (2010).

62. 62.

Zernicka-Goetz, M., Morris, S. A. & Bruce, A. W. Making a firm decision: multifaceted regulation of cell fate in the early mouse embryo. *Nat. Rev. Genet.* **10**, 467–477 (2009).

63. 63.

Csilléry, K., François, O. & Blum, M. G. B. abc: an R package for approximate Bayesian computation (ABC). *Methods Ecol. Evol.* **3**, 475–479 (2012).

64. 64.

Krijthe, J. H. Rtsne: *t*-distributed stochastic neighbor embedding using a Barnes–Hut implementation (R package, 2015).

65. 65.

van den Ameele, J., Li, A. Y. Z., Ma, H. & Chinnery, P. F. Mitochondrial heteroplasmy beyond the oocyte bottleneck. *Semin. Cell Dev. Biol.* **97**, 156–166 (2020).

66. 66.

Taylor, R. W. & Turnbull, D. M. Mitochondrial DNA mutations in human disease. *Nat. Rev. Genet.* **6**, 389–402 (2005).

67. 67.

Hickerson, M. J., Stahl, E. & Takebayashi, N. msBayes: pipeline for testing comparative phylogeographic histories using hierarchical approximate Bayesian computation. *BMC Bioinformatics* **8**, 268 (2007).

68. 68.

Alexandrov, L. B. et al. Signatures of mutational processes in human cancer. *Nature* **500**, 415–421 (2013).

69. 69.

Borchers, H. W. pracma: practical numerical math functions (R package, 2019).

70. 70.

Favero, F. et al. Sequenza: allele-specific copy number and mutation profiles from tumor sequencing data. *Ann. Oncol.* **26**, 64–70 (2015).

71. 71.

Rausch, T. et al. DELLY: structural variant discovery by integrated paired-end and split-read analysis. *Bioinformatics* **28**, i333–i339 (2012).

Acknowledgements

We are deeply indebted to the individuals who donated their cells and tissues for this study. We thank M. R. Stratton, P. J. Campbell, T. H. H. Coorens, R. Rahbari, L. Moore, A. Cagan and M. V. Plikus for their fruitful comments and discussions. We thank J.-Y. Shin, M. S. Jun, H. Jung, J. H. Lee, H. S. Lee, J. Y. Jeon, J. H. Jeon, S. Cho and J. S. Lee, for their methodological advice and technical assistance. This work was supported by the Korea Health Technology R&D Project through the Korea Health Industry Development Institute funded by the Ministry of Health and Welfare of Korea (HI17C1836 to Y.S.J.), the Suh Kyungbae Foundation (SUHF-18010082 to Y.S.J.), a National Research Foundation (NRF) of Korea funded by the Korean Government (NRF-2020R1A3B2078973 to Y.S.J.; NRF-2019R1I1A3A01060675, NRF-2020R1A5A2017323 and NRF-2021R1C1C1014425 to J.W.O.; NRF-2020R1A6A3A01100621 to S.P.; and NRF-2019H1D3A2A02061168 to S.Y.K.).

Author information

Author notes

1. These authors contributed equally: Seongyeol Park, Nanda Maya Mali, Ryul Kim
2. These authors jointly supervised: Ji Won Oh, Young Seok Ju

Affiliations

1. Graduate School of Medical Science and Engineering (GSMSE), Korea Advanced Institute of Science and Technology (KAIST), Daejeon, Republic of Korea

Seongyeol Park, Ryul Kim, Joonoh Lim, Taewoo Kim, Kijong Yi, Jeonghwan Youk, Yohan An, Su Yeon Kim, Soo A Oh & Young Seok Ju

2. GENOME INSIGHT Inc, Daejeon, Republic of Korea

Seongyeol Park, Youngoh Kwon & Young Seok Ju

3. Department of Anatomy, School of Medicine, Kyungpook National University, Daegu, Republic of Korea

Nanda Maya Mali, Jeong-Woo Choi, Jung Min Park, Donghyun Kim, June Hyug Choi, Seong Gyu Kwon, Joo Hee Hong, Dong Sun Kim & Ji Won Oh

4. Immune Square Inc, Daegu, Republic of Korea

Jeong-Woo Choi, Jung Min Park, Donghyun Kim & Ji Won Oh

5. Korea Institute of Science and Technology Information (KISTI), Daejeon, Republic of Korea

Junehawk Lee & Jung Woo Park

6. Department of Medical Informatics, College of Medicine, Catholic University of Korea, Seoul, Republic of Korea

Dongwan Hong

7. Department of Immunology, School of Medicine, Kyungpook National University, Daegu, Republic of Korea

Moonkyu Kim

8. Department of Pathology, Kyungpook National University Chilgok Hospital, School of Medicine, Kyungpook National University, Daegu, Republic of Korea

Ji Young Park

9. Biomedical Research Institute, Kyungpook National University Hospital, Daegu, Republic of Korea

Ji Won Oh

Contributions

Y.S.J., J.W.O. and S.P. conceived the study; N.M.M. designed the warm autopsies and developed the entire protocol of the clonal expansion and bulk tissue preparation with help from J.W.O.; J.W.O., N.M.M., J.-W.C, J.M.P., D.K., J.H.C., S.G.K., J.H.H., M.K., D.S.K., J.Y.P., K.Y., T.K., J.Y., and Y.A. conducted autopsies, tissue sampling and clonal expansions. S.A.O. conducted DNA work. S.P. and R.K. conducted most of the genome and statistical analyses with a contribution from S.Y.K. and Y.S.J.; J. Lee and J.W.P. contributed to large-scale genome data management. J. Lim conducted mutational signature analysis. Y.K. and D.H. constructed the web tool (SCV). Y.S.J., S.P., R.K., N.M.M and J.W.O. wrote the manuscript with contributions from all the authors. Y.S.J. and J.W.O. supervised the study.

Corresponding authors

Correspondence to Ji Won Oh or Young Seok Ju.

Ethics declarations

Competing interests

Y.S.J. is a founder and chief executive officer of GENOME INSIGHT Inc. J.W.O. is a founder and chief executive officer of Immune Square Inc.

Additional information

Peer review information *Nature* thanks Chloé Baron, Aaron Mckenna and the other, anonymous, reviewer(s) for their contribution to the peer review of this work.

Publisher's note Springer Nature remains neutral with regard to jurisdictional claims in published maps and institutional affiliations.

Extended data figures and tables

Extended Data Fig. 1 Sample collection and phylogeny reconstruction.

a, A summary of the seven warm autopsies, in which clones (dots) and bulk tissues were collected. Internal organs contributing to bulk tissues are annotated (black line). The information can also be browsed in the Somatic Clone Viewer (<https://julab.kaist.ac.kr/somatic-clone-viewer>). The detailed information for each sample is shown in Supplementary Discussion 1, Supplementary Tables 2 and 3, for clones and bulk-tissues, respectively. **b**, A scatter plot showing peak VAF and mean coverage of the WGS of all the clones established in this study. Excluded clones, due to their multiclonal origins and/or atypical VAF peaks, are coloured in red. Finally, 334 clones are included for the downstream analyses. **c**, A schematic illustration demonstrating our approach reconstructing a developmental phylogenetic tree. Let $S = [s_1, s_2, \dots, s_5]$ be the set of 5 clones, and $G = [g_1, g_2, \dots, g_{23}]$ be the union set of mutations detected in one or more clones from the same individual. We then build a matrix M with rows labeled g_1, g_2, \dots, g_{23} , and columns labeled s_1, s_2, \dots, s_5 . If the VAF of somatic mutation g_i in clone s_j is determined to be true, M_{ij} was assigned to 1 (blue-coloured tile), while others to 0 (white-coloured tile). After removing germline variants (G_0), we grouped all mutations with the same profile into a mutation group according to the sharing pattern between clones. Over 8 distinct mutation groups in this example, mutation matrix $M_{8 \times 5}$ is defined such that each column represents a clone and each row represents a mutation group. From the mutation matrix $M_{8 \times 5}$, we reconstructed a phylogenetic tree. **d**, Mutation matrices constructed from all clones and all the detected embryonic mutations of the five individuals.

Extended Data Fig. 2 Detecting EEMs.

a, Examples of embryonic mutations found in DB3. A heatmap in the upper panel shows the VAFs of the early mutations detected in the capture phase. Integrative Genomics Viewer screenshots for two early mutations in WGS of four clones and a polyclonal blood are also shown in the lower panel. **b**, The aggregated VAFs for L1 and L2 mutation sets in bulk tissues (dot). Median and interquartile ranges (IQRs) are shown in boxplots with whiskers (1.5*IQRs). **c**, A scatter plot showing the number of clones established and the number of discovered early mutations. The number of base substitutions (triangle) and indels (circle) are shown separately. Red lines and shaded areas represent fitted lines from linear regression and 95% confidence intervals.

Extended Data Fig. 3 Features of EEMs.

a, The correlation between the number of early base substitutions and indels. A red line and shaded area represent fitted line from linear regression and 95% confidence intervals. **b**, An example of microsatellite length-changing mutation identified in the L1 branch of DB3. In this study, microsatellite regions were defined as 5 or more repeat of 1-6 nucleotides in the reference genome. **c**, Mutational spectrums of early and late mutations found in the study. The signatures of the early base substitutions ($n=488$) and indels ($n=49$) are delineated by version 3 COSMIC signatures (top). For late mutations, we categorized clones into two groups by the amount of ultraviolet (UV) light mediated mutations, (1) clones with prevalent UV-mediated mutations and (2) clones with lack of UV-mediated mutations, using the 5% cutoff for the proportion of the SBS7 mutations. The middle panel displays the mutational spectrums of base substitutions ($n=74,824$) and indels ($n=3,404$) in clones with $SBS7 \leq 5\%$ (without UV exposure), while the bottom panel displays the spectrums of substitutions ($n=1,457,489$) and indels ($n=31,805$) in clones with $SBS7 > 5\%$ (with UV exposure).

Extended Data Fig. 4 Lineage relationship among physically adjacent clones.

a, Lineages of physically adjacent clones established from $<1\text{cm}$ of the distance are shown with early phylogenies. Clone pairs from the same late

lineage are coloured in red. **b**, The distribution of distance scores between clones from same anatomical region. Distance score was calculated by $1/(\text{No. of shared mutations} + 1)$. The random distributions (density plots) were generated by randomly assigning clones to lineages on the established phylogenies. A red line represents the actual mean distance score the clones. Empirical p-values from simulation ($n=1,000$) are shown.

Extended Data Fig. 5 The patterns of early phylogenies.

a, Annotated phylogenetic trees of DB3, DB6, DB8, DB9, and DB10. Dichotomy (bifurcation) and polytomy (multifurcation) nodes are indicated by black-filled and hollow circles, respectively. At bifurcation nodes, two daughter lineages are then coloured in red (major) or blue (minor), according to their relative contribution in phylogenies. **b**, A schematic illustration demonstrating informative and uninformative cell divisions. In contrast to a cell division accompanying spontaneous mutations (informative division, left of dashed line), a cell division without intrinsic mutation cannot be reflected in our phylogenetic tree (uninformative division, right of dashed line) due to a lack of ‘cellular barcodes’. **c**, A schematic illustration showing the effect of initial mutation rate on the pattern of the trees. **d**, The unequal contribution of the two earliest branches (L1 and L2) consistently found in phylogenies and bulk tissues. Pie graphs represent the proportion of each lineage counted in the phylogenetic trees. Horizontal bar graphs show the VAFs of the lineage-specific mutations in targeted sequencing of bulk tissues. Expected VAFs from the phylogenies are shown by red dashed lines. **e**, A correlation between VAFs of the early mutations expected in the phylogenies (*x*-axis) and observed in bulk tissues (*y*-axis). Median and interquartile ranges (IQRs) are shown in boxplots with whiskers ($1.5 \times \text{IQRs}$). A red line drawing shows $y=x$ for comparison. **f**, The imbalance ratio at bifurcating nodes, which is the ratio between the numbers of the clones of major and minor lineages. The late-branched clones from the same lineage were counted as a single clone.

Extended Data Fig. 6 Cellular bottleneck and phylogenetic tree.

a, A developmental model showing the lineage imbalance in epiblast as an origin of global unequal L1 and L2 contribution. This model assumes the

number of cells (n) is selected for epiblast at s-cell stage. We presume two different mutation rates ($R_{\leq 2}$ and $R_{>2}$) in early embryogenesis. $R_{\leq 2}$, $R_{>2}$ are mutation rates until and after 2-cell stage, respectively. **b**, A cellular genealogy scenario that can explain the features of early phylogenetic trees. Assuming that the mutation rate is constant, a longer branch results from the lineage that contribute less to the embryo. **c**, Impact of stochastic cellular segregation during embryogenesis on early developmental phylogeny. This illustration shows the consequence of biased selection on cellular phylogeny. In a case that all of the epiblast cells are derived from one cell in two-cell stage, mutations accumulated at first division are shared among all embryonic cells. High initial mutation rate could be masked in this situation.

Extended Data Fig. 7 Imbalanced distribution of early embryonic cells in adult body axes.

a, The phylogenetic trees of five individuals coloured by the significance levels of imbalances between the left and right tissues. Mutations with higher VAF in left tissues are coloured in red, while with higher VAF in right tissues are coloured in blue. The left-right clonal imbalances are frequently seen from very early lineages (<10 early mutations) in all the individuals. **b**, t-SNE clustering of bulk tissues using the VAFs of the embryonic mutations for the four individuals (DB6 is available in Fig. 3b). The separation of left and right tissues is shown in top panels. Other information, such as anatomical regions and organs, is shown in bottom panels. **c**, A schematic illustration showing the emergence of primitive streak and formation of left-right axis in early embryogenesis. **d**, Box plots illustrating the median VAFs and interquartile ranges (IQRs) with whiskers (1.5*IQRs) of L1 and L2 mutations in cranial or caudal tissues. There was no significant VAF difference between cranial- and caudal-side tissues (two-sided Wilcoxon test). NS, not significant.

Extended Data Fig. 8 Imbalanced distribution of early embryonic cells in adult anatomical regions.

a, Median VAFs of the early mutations in the bulk tissues according to their dominant germ layers. The horizontal axis shows early mutations sorted by the averaged VAFs in bulk tissues in descending order, approximately from earlier to later mutations. Tissues with mixed germ layers are excluded in this figure. The lines are fitted curves by locally estimated scatterplot smoothing (LOESS) methods. **b**, The phylogenetic trees coloured by the significance of imbalances between ectoderm and meso-endodermal tissues. DB3 was not suitable for the analysis due to a lack of ectodermal tissues sequenced. Comparisons were performed by two-sided Wilcoxon tests. Red asterisks indicate the estimated point of the branching of the ectoderm-dominant lineage. **c**, the phylogenetic trees of four individuals (DBs 3, 6, 8, and 10) coloured by the VAF in blood tissues. An equivalent figure for DB9 is shown in Fig. 3d. Red asterisks indicate the estimated point of the branching of the blood-enriched lineages. Blue asterisk in DB10 indicate the major lineage of contaminated tumour cells in blood. **d**, Ratios of VAF for embryonic mutations between observed in blood tissues and expected from phylogenetic trees. The molecular time of the embryogenesis is shown on the x -axis by the number of mutations. Dots in the direct lineages are linked by lines. **e**, Histograms for showing the number of the blood-specific mutations (absent in phylogenetic trees). Blood-specific mutation was not found in DB3 ($n=0$). DB10 is excluded due to tumour contamination in the blood. **f**, The phylogenetic tree of DB10 coloured by VAF in cancer tissue with the branching point of the ancestral cell of breast cancer (shown by a red asterisk). **g**, Schematic representation demonstrating the clonal imbalance and their timing in early embryogenesis.

Extended Data Fig. 9 Heteroplasmic mtDNA variants in fertilized eggs.

a, VAFs of MT:16,256 C>T substitution (frequently found in DB10 clones) in WGS of 279 clones explored in the study. Applying a VAF cutoff of 0.5%, the variant was detected only in the 14 clones all established from DB10. **b**, a developmental model for inferring the heteroplasmic level of a mitochondrial variant in a fertilized egg. We assumed that $f\%$ of mtDNA in a fertilized egg has a functionally neutral mtDNA variant (mutant-mtDNA), which randomly segregates to daughter cells in successive cell divisions. Two summary statistics were drawn from this model: 1) the proportion of

samples harbouring mutant-mtDNA (p), and 2) the median heteroplasmic level of mutant-mtDNA (h). We compared the summary statistics (p, h) of each simulation to the observed summary statistics, and constructed the posterior distribution of f using the neural network regression algorithm of an approximate Bayesian computation. For detail, see the Methods section. **c**, a histogram of the null distribution of the statistic for the goodness of fit test assuming our model. **d**, Cross-validation to access the accuracy of parameter inference. **e**, a possible scenario underlying the recurrent mtDNA mutation. Mitochondrial bottleneck during the cleavage and random segregation of mtDNA during mitosis may underlie the early mtDNA variant. **f**, mtDNA variants and their heteroplasmic levels with 95% confidence intervals estimated by simulation ($n=500,000$) to be harboured in fertilized egg.

Extended Data Fig. 10 Features of late mutations.

a, Scatter plot showing the correlation between the number of total mutations and recurrent mutations. **b**, Total number and signature of somatic mutations in each of the 334 clones. Horizontal axis represents each clone in decreasing order of total mutation numbers. **c**, Linear correlation between the numbers of SBS7 (UV-mediated) and SBS5 (an endogenous, clock-like) mutations in skin fibroblast clones. Approximately one additional SBS5 mutation is acquired per ten SBS7 mutations. A red line represents the result of linear regression. **d**, The mutational spectrum of late recurrent base substitutions ($n=619$). **e**, A massive heterogeneity of UV-mediated mutational burden among clones established in the close anatomical location (inter-clonal distance $<\sim 1\text{ cm}$; top). The number of clones in each location is illustrated at the bottom. **f**, The rate of purely endogenous mutations in skin fibroblasts showing a linear correlation with age (24.3 substitutions per year). A red line represents the result of linear regression. The median number of endogenous substitutions with interquartile ranges (IQRs) from clones are drawn by boxplots (whiskers= $1.5 \times \text{IQRs}$) and scatter plots.

Extended Data Fig. 11 Somatic copy-number changes in normal cells.

a, Bar plot showing the frequency of large-scale copy-number alterations (> 10 Mb) per segment type detected in clones. **b**, Bar plot showing the counts of whole-chromosomal copy-number changes per chromosome. **c**, Timing estimation of the copy-number gains (> 50 Mb) observed in the clones. Ages at death are shown in red dashed lines. fb., fibroblast.

Supplementary information

Supplementary Information

This file contains Supplementary Discussion 1-9, including Supplementary Figures 1-6, and additional references.

Reporting Summary

Peer Review File

Supplementary Table 1

Demographic features, clone number, and mutation rate of the participants.

Supplementary Table 2

Cell types, tissue locations, and mutational features of 334 single-cell clones.

Supplementary Table 3

Tissue type, location, and *t*-SNE information of 379 bulk tissues recapturing early mutations via targeted deep sequencing.

Supplementary Table 4

Information on whole-genome sequences for bulk tissues.

Supplementary Table 5

No. of somatic variants and phylogenetic structure of cellular lineages.

Supplementary Table 6

List of early embryonic mutations detected in this study.

Supplementary Table 7

Number of variants in each filtering steps.

Rights and permissions

Reprints and Permissions

About this article

Cite this article

Park, S., Mali, N.M., Kim, R. *et al.* Clonal dynamics in early human embryogenesis inferred from somatic mutation. *Nature* **597**, 393–397 (2021). <https://doi.org/10.1038/s41586-021-03786-8>

- Received: 22 November 2020
- Accepted: 29 June 2021
- Published: 25 August 2021
- Issue Date: 16 September 2021
- DOI: <https://doi.org/10.1038/s41586-021-03786-8>

Share this article

Anyone you share the following link with will be able to read this content:

[Get shareable link](#)

Sorry, a shareable link is not currently available for this article.

[Copy to clipboard](#)

Provided by the Springer Nature SharedIt content-sharing initiative

Further reading

- [Extensive phylogenies of human development inferred from somatic mutations](#)
 - Tim H. H. Coorens
 - , Luiza Moore
 - , Philip S. Robinson
 - , Rashesh Sanghvi
 - , Joseph Christopher
 - , James Hewinson
 - , Moritz J. Przybilla
 - , Andrew R. J. Lawson
 - , Michael Spencer Chapman
 - , Alex Cagan
 - , Thomas R. W. Oliver
 - , Matthew D. C. Neville
 - , Yvette Hooks
 - , Ayesha Noorani
 - , Thomas J. Mitchell
 - , Rebecca C. Fitzgerald
 - , Peter J. Campbell
 - , Iñigo Martincorena
 - , Raheleh Rahbari
 - & Michael R. Stratton

Nature (2021)

Mutation fingerprints encode cellular histories

- Kamila Naxerova

News & Views 25 Aug 2021

A body-wide view of somatic mutations

- Darren J. Burgess

Research Highlight 14 Sept 2021

This article was downloaded by **calibre** from <https://www.nature.com/articles/s41586-021-03786-8>

| [Section menu](#) | [Main menu](#) |

- Article
- [Published: 25 August 2021](#)

A body map of somatic mutagenesis in morphologically normal human tissues

- [Ruoyan Li^{1,2} na1](#),
- [Lin Di^{1,2} na1](#),
- [Jie Li^{3,4} na1](#),
- [Wenyi Fan⁵ na1](#),
- [Yachen Liu⁵](#),
- [Wenjia Guo⁵](#),
- [Weiling Liu⁵](#),
- [Lu Liu^{1,2}](#),
- [Qiong Li^{3,4}](#),
- [Liping Chen⁵](#),
- [Yamei Chen ORCID: orcid.org/0000-0002-9072-5157⁵](#),
- [Chuanwang Miao⁵](#),
- [Hongjin Liu⁵](#),
- [Yuqian Wang⁵](#),
- [Yuling Ma⁵](#),
- [Deshu Xu^{1,2}](#),
- [Dongxin Lin ORCID: orcid.org/0000-0002-8723-8868^{5,6,7,8 na2}](#),
- [Yanyi Huang ORCID: orcid.org/0000-0002-7297-1266^{1,2,9,10,11 na2}](#),
- [Jianbin Wang ORCID: orcid.org/0000-0001-6725-7925^{3,4 na2}](#),
- [Fan Bai ORCID: orcid.org/0000-0001-6119-8936^{1,2,12 na2}](#) &
- [Chen Wu ORCID: orcid.org/0000-0003-4954-1011^{5,6,8,13 na2}](#)

[Nature](#) volume 597, pages 398–403 (2021)

- 9134 Accesses
- 114 Altmetric
- [Metrics details](#)

Subjects

- [Cancer genomics](#)
- [Genetic variation](#)
- [Mutation](#)
- [Phylogenetics](#)

Abstract

Somatic mutations that accumulate in normal tissues are associated with ageing and disease^{1,2}. Here we performed a comprehensive genomic analysis of 1,737 morphologically normal tissue biopsies of 9 organs from 5 donors. We found that somatic mutation accumulations and clonal expansions were widespread, although to variable extents, in morphologically normal human tissues. Somatic copy number alterations were rarely detected, except for in tissues from the oesophagus and cardia. Endogenous mutational processes with the SBS1 and SBS5 mutational signatures are ubiquitous among normal tissues, although they exhibit different relative activities. Exogenous mutational processes operate in multiple tissues from the same donor. We reconstructed the spatial somatic clonal architecture with sub-millimetre resolution. In the oesophagus and cardia, macroscopic somatic clones that expanded to hundreds of micrometres were frequently seen, whereas in tissues such as the colon, rectum and duodenum, somatic clones were microscopic in size and evolved independently, possibly restricted by local tissue microstructures. Our study depicts a body map of somatic mutations and clonal expansions from the same individual.

Access options

[Subscribe to Journal](#)

Get full journal access for 1 year

\$199.00

only \$3.90 per issue

[Subscribe](#)

All prices are NET prices.

VAT will be added later in the checkout.

Tax calculation will be finalised during checkout.

Rent or Buy article

Get time limited or full article access on ReadCube.

from \$8.99

[Rent or Buy](#)

All prices are NET prices.

Additional access options:

- [Log in](#)
- [Access through your institution](#)
- [Learn about institutional subscriptions](#)

Fig. 1: Research strategy and summary of genomic alterations detected in normal tissues from five donors.

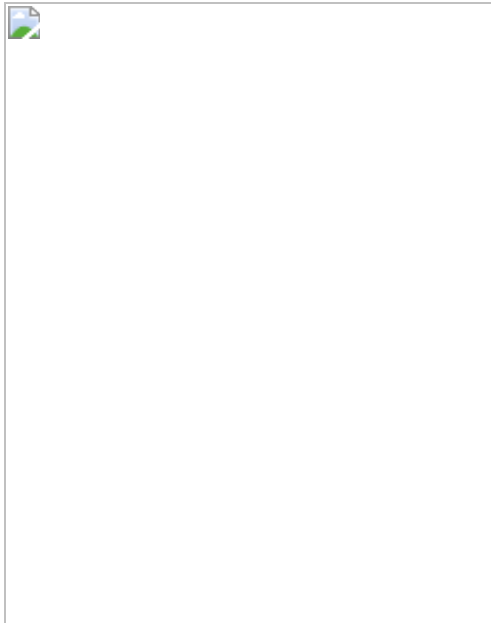


Fig. 2: Mutational signatures in normal tissues from five donors.

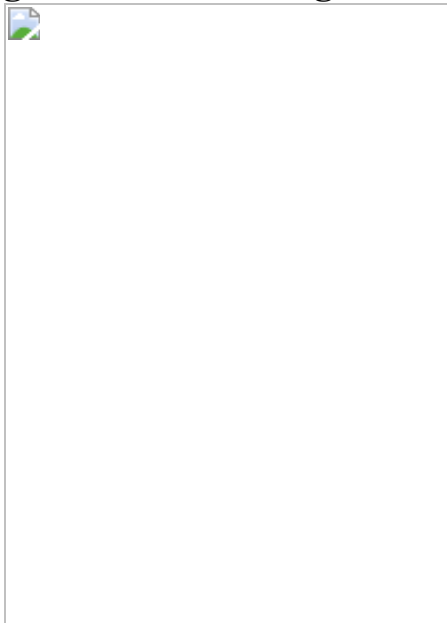


Fig. 3: Mutational landscape of driver genes across organs.

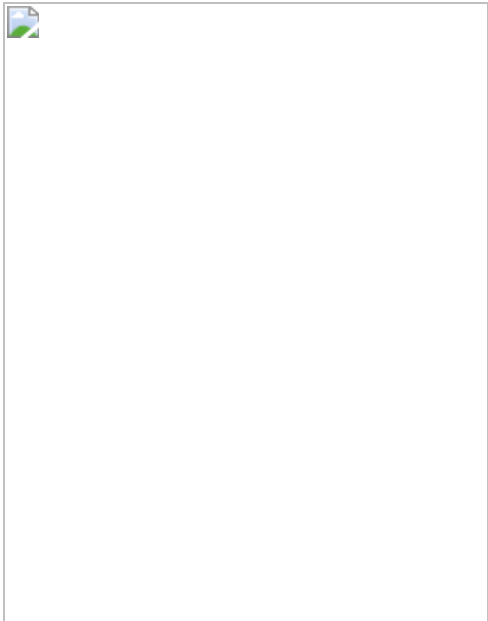


Fig. 4: Estimation of somatic mutant clonal sizes and construction of spatial clonal expansion maps.



Data availability

The raw WES and WGS data generated in this study have been deposited in the European Genome-phenome Archive (EGA) (<https://ega-archive.org>) with accession number EGAD00001007859 and the Genome Sequence Archive (GSA) of the Beijing Institute of Genomics with accession number HRA000356 (<https://ngdc.cncb.ac.cn/gsa-human>). To gain access to the raw sequencing data, please submit requests to the Pan-body Mutagenesis Data Access Committee (EGA accession number EGAC00001002218) or through the GSA online page of this study (<https://ngdc.cncb.ac.cn/gsa-human/browse/HRA000356>). All somatic mutations detected from WES with functional annotations and allele count information can be found in Supplementary Table 3. RefSeq database: <https://www.ncbi.nlm.nih.gov/refseq>. NHLBI Exome Sequencing Project: <http://evs.gs.washington.edu/EVS>. dbSNP database: <https://www.ncbi.nlm.nih.gov/snp>. COSMIC database:

<https://cancer.sanger.ac.uk/cosmic>. The GTEx project:
<https://gtexportal.org/home>.

Code availability

Mutational signature analysis was performed using the HDP R package v.0.1.5 (<https://github.com/nicolaroberts/hdp>). Code for mutational signature analysis was adapted from https://github.com/HLee-Six/colon_microbiopsies. Code for the Bayesian Dirichlet process clustering of MCFs was adapted from <https://github.com/sfbrunner/liver-pub-repo>. Adapted code is available at Zenodo (<https://doi.org/10.5281/zenodo.5012918>). Driver gene analysis was performed using the dNdScv v0.01 (<https://github.com/im3sanger/dndscv>).

References

1. 1.
Martincorena, I. & Campbell, P. J. Somatic mutation in cancer and normal cells. *Science* **349**, 1483–1489 (2015).
2. 2.
Risques, R. A. & Kennedy, S. R. Aging and the rise of somatic cancer-associated mutations in normal tissues. *PLoS Genet.* **14**, e1007108 (2018).
3. 3.
Martincorena, I. *et al.* Tumor evolution. High burden and pervasive positive selection of somatic mutations in normal human skin. *Science* **348**, 880–886 (2015).
4. 4.
Tang, J. et al. The genomic landscapes of individual melanocytes from human skin. *Nature* **586**, 600–605 (2020).

5. 5.

Martincorena, I. et al. Somatic mutant clones colonize the human esophagus with age. *Science* **362**, 911–917 (2018).

6. 6.

Yokoyama, A. et al. Age-related remodelling of oesophageal epithelia by mutated cancer drivers. *Nature* **565**, 312–317 (2019).

7. 7.

Lee-Six, H. et al. The landscape of somatic mutation in normal colorectal epithelial cells. *Nature* **574**, 532–537 (2019).

8. 8.

Brunner, S. F. et al. Somatic mutations and clonal dynamics in healthy and cirrhotic human liver. *Nature* **574**, 538–542 (2019).

9. 9.

Moore, L. et al. The mutational landscape of normal human endometrial epithelium. *Nature* **580**, 640–646 (2020).

10. 10.

Yoshida, K. et al. Tobacco smoking and somatic mutations in human bronchial epithelium. *Nature* **578**, 266–272 (2020).

11. 11.

Lodato, M. A. et al. Aging and neurodegeneration are associated with increased mutations in single human neurons. *Science* **359**, 555–559 (2018).

12. 12.

Bae, T. et al. Different mutational rates and mechanisms in human cells at pregastrulation and neurogenesis. *Science* **359**, 550–555 (2018).

13. 13.

Ju, Y. S. et al. Somatic mutations reveal asymmetric cellular dynamics in the early human embryo. *Nature* **543**, 714–718 (2017).

14. 14.

Lawson, A. R. J. et al. Extensive heterogeneity in somatic mutation and selection in the human bladder. *Science* **370**, 75–82 (2020).

15. 15.

Li, R. et al. Macroscopic somatic clonal expansion in morphologically normal human urothelium. *Science* **370**, 82–89 (2020).

16. 16.

Lee-Six, H. et al. Population dynamics of normal human blood inferred from somatic mutations. *Nature* **561**, 473–478 (2018).

17. 17.

Watson, C. J. et al. The evolutionary dynamics and fitness landscape of clonal hematopoiesis. *Science* **367**, 1449–1454 (2020).

18. 18.

Yizhak, K. et al. RNA sequence analysis reveals macroscopic somatic clonal expansion across normal tissues. *Science* **364**, eaaw0726 (2019).

19. 19.

Garcia-Nieto, P. E., Morrison, A. J. & Fraser, H. B. The somatic mutation landscape of the human body. *Genome Biol.* **20**, 298 (2019).

20. 20.

Alexandrov, L. B. et al. Signatures of mutational processes in human cancer. *Nature* **500**, 415–421 (2013).

21. 21.

Alexandrov, L. B. et al. The repertoire of mutational signatures in human cancer. *Nature* **578**, 94–101 (2020).

22. 22.

Alexandrov, L. B. et al. Clock-like mutational processes in human somatic cells. *Nat. Genet.* **47**, 1402–1407 (2015).

23. 23.

Nik-Zainal, S. et al. Mutational processes molding the genomes of 21 breast cancers. *Cell* **149**, 979–993 (2012).

24. 24.

Poon, S. L. et al. Mutation signatures implicate aristolochic acid in bladder cancer development. *Genome Med.* **7**, 38 (2015).

25. 25.

Ng, A. W. T. et al. Aristolochic acids and their derivatives are widely implicated in liver cancers in Taiwan and throughout Asia. *Sci. Transl. Med.* **9**, eaan6446 (2017).

26. 26.

Du, Y. et al. Mutagenic factors and complex clonal relationship of multifocal urothelial cell carcinoma. *Eur. Urol.* **71**, 841–843 (2017).

27. 27.

Chen, C. H. et al. Aristolochic acid-induced upper tract urothelial carcinoma in Taiwan: clinical characteristics and outcomes. *Int. J. Cancer* **133**, 14–20 (2013).

28. 28.

Martincorena, I. et al. Universal patterns of selection in cancer and somatic tissues. *Cell* **171**, 1029–1041 (2017).

29. 29.

The Cancer Genome Atlas Research Network. Comprehensive molecular characterization of gastric adenocarcinoma. *Nature* **513**, 202–209 (2014).

30. 30.

Bailey, M. H. et al. Comprehensive characterization of cancer driver genes and mutations. *Cell* **174**, 1034–1035 (2018).

31. 31.

Moore, L. et al. The mutational landscape of human somatic and germline cells. *Nature*, <https://doi.org/10.1038/s41586-021-03822-7> (2021).

32. 32.

Blokzijl, F. et al. Tissue-specific mutation accumulation in human adult stem cells during life. *Nature* **538**, 260–264 (2016).

33. 33.

Abascal, F. et al. Somatic mutation landscapes at single-molecule resolution. *Nature* **593**, 405–410 (2021).

34. 34.

Martin, M. Cutadapt removes adapter sequences from high-throughput sequencing reads. *EMBnet. J.* **17**, 10–12 (2011).

35. 35.

Langmead, B. & Salzberg, S. L. Fast gapped-read alignment with Bowtie 2. *Nat. Methods* **9**, 357–359 (2012).

36. 36.

Li, H. & Durbin, R. Fast and accurate short read alignment with Burrows–Wheeler transform. *Bioinformatics* **25**, 1754–1760 (2009).

37. 37.

Li, H. et al. The Sequence Alignment/Map format and SAMtools. *Bioinformatics* **25**, 2078–2079 (2009).

38. 38.

McKenna, A. et al. The Genome Analysis Toolkit: a MapReduce framework for analyzing next-generation DNA sequencing data. *Genome Res.* **20**, 1297–1303 (2010).

39. 39.

Cibulskis, K. et al. Sensitive detection of somatic point mutations in impure and heterogeneous cancer samples. *Nat. Biotechnol.* **31**, 213–219 (2013).

40. 40.

Cingolani, P. et al. A program for annotating and predicting the effects of single nucleotide polymorphisms, SnpEff. *Fly* **6**, 80–92 (2012).

41. 41.

Coorens, T. H. H. et al. Inherent mosaicism and extensive mutation of human placentas. *Nature* **592**, 80–85 (2021).

42. 42.

Olafsson, S. et al. Somatic evolution in non-neoplastic IBD-affected colon. *Cell* **182**, 672–684 (2020).

43. 43.

The GTEx Consortium. The GTEx Consortium atlas of genetic regulatory effects across human tissues. *Science* **369**, 1318–1330 (2020).

44. 44.

Roberts, N. D. *Patterns of Somatic Genome Rearrangement In Human Cancer*. PhD thesis, Univ. Cambridge (2018).

45. 45.

Rosenthal, R., McGranahan, N., Herrero, J., Taylor, B. S. & Swanton, C. DeconstructSigs: delineating mutational processes in single tumors distinguishes DNA repair deficiencies and patterns of carcinoma evolution. *Genome Biol.* **17**, 31 (2016).

46. 46.

O’Leary, N. A. et al. Reference sequence (RefSeq) database at NCBI: current status, taxonomic expansion, and functional annotation. *Nucleic Acids Res.* **44**, D733–745 (2016).

47. 47.

Cancer Genome Atlas Research, N. Comprehensive molecular profiling of lung adenocarcinoma. *Nature* **511**, 543–550 (2014).

48. 48.

The Cancer Genome Atlas Research Network. Integrated genomic characterization of oesophageal carcinoma. *Nature* **541**, 169–175 (2017).

49. 49.

The Cancer Genome Atlas Research Network. Comprehensive molecular characterization of human colon and rectal cancer. *Nature* **487**, 330–337 (2012).

50. 50.

The Cancer Genome Atlas Research Network. Comprehensive and integrative genomic characterization of hepatocellular carcinoma. *Cell* **169**, 1327–1341 (2017).

51. 51.

Wu, G., Feng, X. & Stein, L. A human functional protein interaction network and its application to cancer data analysis. *Genome Biol.* **11**, R53 (2010).

52. 52.

Papastamoulis, P. *label.switching: an R package for dealing with the label switching problem in MCMC outputs. J. Stat. Softw.* **69**, Code Snippet 1 (2016).

53. 53.

Kumar, S., Stecher, G., Li, M., Knyaz, C. & Tamura, K. MEGA X: molecular evolutionary genetics analysis across computing platforms. *Mol. Biol. Evol.* **35**, 1547–1549 (2018).

Acknowledgements

We thank all the donors and their families for their consent and participation in this study. This project was jointly supported by the National Natural Science Foundation of China (81725015 to C.W., 81988101 to D.L. and C.W., 22050004 to J.W. and 22050002 to Y.H.); Beijing Outstanding Young Scientist Program (BJWZYJH01201910023027 to C.W.); the Medical and Health Technology Innovation Project of the Chinese Academy of Medical

Sciences (2019-I2M-2-001 to D.L. and C.W.); the National Key R&D Program of China (2019YFC1315702, 2018ZX10302205 to F.B. and 2018YFA0108100 to Y.H.); Guangdong Province Key Research and Development Program (2019B020226002 to F.B.); Beijing Municipal Science and Technology Commission (Z201100005320016 to Y.H.); Beijing Advanced Innovation Center for Genomics; and Shenzhen Bay Laboratory.

Author information

Author notes

1. These authors contributed equally: Ruoyan Li, Lin Di, Jie Li, Wenyi Fan
2. These authors jointly supervised this work: Dongxin Lin, Yanyi Huang, Jianbin Wang, Fan Bai, Chen Wu

Affiliations

1. Biomedical Pioneering Innovation Center (BIOPIC), School of Life Sciences, Peking University (PKU), Beijing, China
Ruoyan Li, Lin Di, Lu Liu, Deshu Xu, Yanyi Huang & Fan Bai
2. Beijing Advanced Innovation Center for Genomics (ICG), Peking University, Beijing, China
Ruoyan Li, Lin Di, Lu Liu, Deshu Xu, Yanyi Huang & Fan Bai
3. School of Life Sciences, Tsinghua-Peking Center for Life Sciences, Tsinghua University, Beijing, China
Jie Li, Qiong Li & Jianbin Wang
4. Beijing Advanced Innovation Center for Structural Biology (ICSB), Tsinghua University, Beijing, China

Jie Li, Qiong Li & Jianbin Wang

5. Department of Etiology and Carcinogenesis, National Cancer Center/Cancer Hospital, Chinese Academy of Medical Sciences (CAMS) and Peking Union Medical College (PUMC), Beijing, China

Wenyi Fan, Yachen Liu, Wenjia Guo, Weiling Liu, Liping Chen, Yamei Chen, Chuanwang Miao, Hongjin Liu, Yuqian Wang, Yuling Ma, Dongxin Lin & Chen Wu

6. Collaborative Innovation Center for Cancer Personalized Medicine, Nanjing Medical University, Nanjing, China

Dongxin Lin & Chen Wu

7. Sun Yat-sen University Cancer Center, State Key Laboratory of Oncology in South China, Guangzhou, China

Dongxin Lin

8. CAMS Key Laboratory of Cancer Genomic Biology, Chinese Academy of Medical Sciences and Peking Union Medical College, Beijing, China

Dongxin Lin & Chen Wu

9. College of Chemistry and Molecular Engineering, Beijing National Laboratory for Molecular Sciences, Peking University, Beijing, China

Yanyi Huang

10. Peking-Tsinghua Center for Life Sciences, Peking University, Beijing, China

Yanyi Huang

11. Institute for Cell Analysis, Shenzhen Bay Laboratory, Guangdong, China

Yanyi Huang

12. Center for Translational Cancer Research, Peking University First Hospital, Beijing, China

Fan Bai

13. CAMS Oxford Institute (COI), CAMS, Beijing, China

Chen Wu

Contributions

F.B., C.W., Y.H., J.W., D.L. and R.L. conceived the study. R.L., L.D. and W.F. performed data analyses with assistance from L.L., D.X. and Y.W. W.F. performed sample collection, tissue sectioning and LCM with assistance from Y.L., W.G., W.L., L.C., Y.C., C.M., H.L. and Y.M. L.D. performed DNA extraction and library preparation. J.L. performed exome capture with assistance from Q.L. R.L., F.B., W.F., L.D. and J.L. wrote the manuscript with input from D.L., Y.H., J.W. and C.W. D.L., Y.H., J.W., F.B. and C.W. supervised all aspects of this study.

Corresponding authors

Correspondence to Dongxin Lin or Yanyi Huang or Jianbin Wang or Fan Bai or Chen Wu.

Ethics declarations

Competing interests

The authors declare no competing interests.

Additional information

Peer review information *Nature* thanks Ziyue Gao and the other, anonymous, reviewer(s) for their contribution to the peer review of this work.

Publisher's note Springer Nature remains neutral with regard to jurisdictional claims in published maps and institutional affiliations.

Extended data figures and tables

Extended Data Fig. 1 Normal tissue histology.

Representative H&E-stained samples showing the histological features of normal tissues sampled from nine organs from the five donors. Blanks in the figure represent samples that are not available in corresponding organs and donors. Scale bars, 100 μ m.

Extended Data Fig. 2 Detection of somatic mutations.

a, Bar plot showing the overlap of mutations detected from WES and WGS of 43 samples. **b**, Adjusted numbers of somatic mutations detected in the coding regions in tissue biopsies from the organs of five donors. Red vertical bars represent median mutation numbers and grey horizontal bars represent standard deviations. **c**, The mutation burdens (after the sensitivity correction) in samples with median VAFs between 0.08 and 0.14. Top, box plots showing the mutation burdens in organs from different donors. The lower edge, upper edge and centre of the box represent the 25th (Q1) percentile, 75th (Q3) percentile and the median, respectively. IQR = Q3 – Q1. Outliers are values beyond the whiskers (upper, $Q3 + 1.5 \times IQR$; lower, $Q1 - 1.5 \times IQR$). Detailed information about the box plots can be found in Supplementary Table 3. Bottom, dot plots showing the adjusted mutation burdens in different organs. Red bars represent the medians. **d**, Scatter plots showing the VAFs of somatic mutations detected in the normal tissues from the nine organs of the five donors. Dots are coloured by mutation type.

Extended Data Fig. 3 Correlations and interdependence between VAF distributions and mutation numbers.

In each tissue, we calculated the first quantile (Q1) and third quantile (Q3) of the VAF and mutation burden distribution. We defined $IQR = Q3 - Q1$ and considered samples with a median VAF or mutation burden greater than $Q3 + 1.5 \times IQR$ or less than $Q1 - 1.5 \times IQR$ as outliers. We excluded these outliers in this analysis. Corr., correlation. The error bands represent the 95% confidence intervals. *P* values are from two-sided correlation tests based on the Pearson correlation coefficient.

Extended Data Fig. 4 Mutation numbers and somatic CNAs.

a, Bar plots showing the number of mutations among the four intervals. Genes are divided into four intervals according to the tissue-specific gene expression levels. **b**, Heat maps showing somatic CNAs detected in the normal tissues from the nine organs of the five donors. Sex chromosomes were excluded.

Extended Data Fig. 5 Mutational spectra and signature analysis.

a, *t*-stochastic neighbour embedding (t-SNE) plots of the trinucleotide mutational spectra of biopsy samples from each donor, broken down by organ and donor. Only biopsy samples with more than 30 SNVs were included. **b**, Heat map showing the clustering of cosine similarities of the trinucleotide mutational context in different samples. Colour bars above indicate information of donors and tissue types. **c**, Trinucleotide mutational spectra for the unassigned signature and the seven signatures extracted using a Bayesian hierarchical Dirichlet process. The bars represent means (95% credible intervals) of the 96 trinucleotide contexts. **d**, Heat map depicting the cosine similarities between extracted mutational signatures and mutational signatures from COSMIC and PCAWG catalogues. Cosine similarities between the seven extracted mutational signatures and their most similar comparators are highlighted. **e**, Stacked bar plots showing the number of mutations that are caused by different mutational signatures.

Extended Data Fig. 6 Mutational signature analysis.

a, Transcriptional strand asymmetries across 96 mutation contexts for SBS4 and SBS22. Bar plots show the sum of assignment probabilities across trinucleotide contexts, split by whether the pyrimidine is on the template or coding strand. **b**, Transcriptional strand asymmetries across 96 mutation contexts for SBS4 and SBS22. Only mutations with an assignment probability greater than 0.5 are included. **c**, Trinucleotide mutational spectra of liver, oesophagus, duodenum and colon from donor PN1. Purple dots represent data points of the five tissue layers. Data are mean + s.d. Typical aristolochic-acid -associated mutational features are shaded in blue.

Extended Data Fig. 7 Intra-donor comparisons of mutational signatures.

a, The 96 mutation context profiles in two oesophagus samples from donor PN7 (top) and two liver samples from donor PN9 (bottom) based on somatic mutations detected from WGS. **b**, Trinucleotide mutational spectra of two dissected duodenum layers from donor PN7. Typical aristolochic-acid -associated mutational features are shaded in blue. **c**, H&E stained liver tissue (PN9 layer 2 to 4) with superimposed donut charts showing the proportional contributions of mutational signatures, as estimated by deconstructSigs. Scale bars, 200 μ m.

Extended Data Fig. 8 Landscape of driver mutations.

a, Mutational landscape of the 32 putative driver genes across different organs from the 5 donors. **b**, The functional interaction (network of the 32 driver genes. Driver genes are in blue nodes and linker genes (those not significantly mutated but highly connected to driver genes in the network) are in pink nodes. **c**, Significantly enriched pathways of the 32 driver genes. The vertical red line marks a false discovery rate (FDR) of 0.01. **d**, Bar plot showing the numbers of total mutations and cancer hotspot mutations in driver genes. The percentages of hotspot mutations are labelled on the top of the bar plot. **e**, Fraction of driver mutations that are private or shared by more than one biopsy sample. **f**, Heat maps showing the ratio of the numbers of observed to expected (O/E) driver mutations across different organs (left) and the *P* values for the enrichment (right). *P* values from one-sided hypergeometric tests. **g**, Bar plots comparing the number of mutations

in gastric cancer top-10 most frequently mutated driver genes in TCGA with normal stomach and cardia samples in this study. Adjustment for multiple comparisons was performed. Adjusted *P* values (*q*-value) are labelled.

Extended Data Fig. 9 Relationships between mutational burdens and average mutant MCFs.

Bubble plots show the correlations between average MCFs and mutational burdens in biopsy samples across different organs in donors PN1, PN2, PN7, PN8 and PN9.

Extended Data Fig. 10 Mutant clonal expansion in oesophageal epithelium.

a, Phylogenetic tree depicting the clonal relationships of the biopsy samples of the oesophagus of donor PN9. **b**, Heat maps show mutation clustering, spatial clonal architecture and potential driver mutations or CNAs in samples from the oesophagus. Scale bars, 800 µm. **c**, Heat maps showing potential driver mutations and CNAs in oesophagus samples from donor PN9.

Extended Data Fig. 11 Representative examples of large scale mutant clonal expansion.

a, Heat map showing the mutation clustering in liver samples from donor PN9. **b**, Spatial clonal architecture of liver tissue from donor PN9. The numbers in each layer represent the positions of LCM biopsy samples. The overlaid colours correspond to **a** and indicate the ranges of clonal expansions. **c**, Heat maps show mutation clustering in samples from the representative organs. Each cluster contains mutations with similar MCFs.

Extended Data Fig. 12 Representative examples of independent clonal evolution.

a, Phylogenetic tree depicting the clonal relationships of colon biopsy samples from donor PN9. **b**, Heat maps showing clustered mutations in samples from representative organs. Each cluster contains mutations with similar MCFs.

Supplementary information

Supplementary Information

This file contains the Supplementary Discussion, including additional discussions about the sampling strategy, mutation burden, clonal expansion patterns, mutational signatures, and copy number alterations in the current study.

Reporting Summary

Supplementary Table 1

Clinical information for the five donors in the current study.

Supplementary Table 2

Whole-exome sequencing information. Nomenclature of sample IDs: for example, ‘PN1E-1-2’ represents the number 2 oesophagus sample dissected from tissue layer 1 from donor PN1.

Supplementary Table 3

Somatic mutations with functional annotations and allele count information detected from whole-exome sequencing. Detailed information for box plots in Fig. 1c and Extended Data Fig. 2c.

Supplementary Table 4

Low-depth and high-depth whole-genome sequencing information and copy number analysis.

Supplementary Table 5

Input matrix for mutational signature analysis using HDP. SNVs detected in both coding and non-coding regions from the whole-exome sequencing data are included. Mutations detected from normal biopsy samples from each dissected layer are merged.

Supplementary Table 6

Extracted mutational signatures and their cosine similarities to the known signatures.

Supplementary Table 7

Relative activates of extracted mutational signatures.

Supplementary Table 8

Driver gene candidates from previous studies (126 gene list).

Supplementary Table 9

Cancer hotspot mutations detected in normal tissues in the current study.

Supplementary Table 10

P values for driver gene enrichment in different tissues. *P* values were calculated from one-sided hypergeometric tests.

Rights and permissions

Reprints and Permissions

About this article

Cite this article

Li, R., Di, L., Li, J. *et al.* A body map of somatic mutagenesis in morphologically normal human tissues. *Nature* **597**, 398–403 (2021). <https://doi.org/10.1038/s41586-021-03836-1>

- Received: 29 November 2020
- Accepted: 20 July 2021
- Published: 25 August 2021
- Issue Date: 16 September 2021
- DOI: <https://doi.org/10.1038/s41586-021-03836-1>

Share this article

Anyone you share the following link with will be able to read this content:

[Get shareable link](#)

Sorry, a shareable link is not currently available for this article.

[Copy to clipboard](#)

Provided by the Springer Nature SharedIt content-sharing initiative

[Mutation fingerprints encode cellular histories](#)

- Kamila Naxerova

News & Views 25 Aug 2021

[A body-wide view of somatic mutations](#)

- Darren J. Burgess

Research Highlight 14 Sept 2021

This article was downloaded by **calibre** from <https://www.nature.com/articles/s41586-021-03836-1>

| [Section menu](#) | [Main menu](#) |

- Article
- Open Access
- [Published: 02 August 2021](#)

Behavioural nudges increase COVID-19 vaccinations

- [Hengchen Dai](#) [ORCID: orcid.org/0000-0001-7640-6558¹](#),
[Silvia Saccardo²](#),
- [Maria A. Han³](#),
- [Lily Roh⁴](#),
- [Naveen Raja⁴](#),
- [Sitaram Vangala⁵](#),
- [Hardikkumar Modi⁶](#),
- [Shital Pandya⁶](#),
- [Michael Sloyan⁷](#) &
- [Daniel M. Croymans](#) [ORCID: orcid.org/0000-0001-9805-8048³](#)

[Nature](#) volume 597, pages 404–409 (2021)

- 20k Accesses
- 2 Citations
- 582 Altmetric
- [Metrics details](#)

Subjects

- [Decision making](#)
- [Human behaviour](#)

Abstract

Enhancing vaccine uptake is a critical public health challenge¹. Overcoming vaccine hesitancy^{2,3} and failure to follow through on vaccination intentions³ requires effective

communication strategies^{3,4}. Here we present two sequential randomized controlled trials to test the effect of behavioural interventions on the uptake of COVID-19 vaccines. We designed text-based reminders that make vaccination salient and easy, and delivered them to participants drawn from a healthcare system one day (first randomized controlled trial) ($n = 93,354$ participants; clinicaltrials number NCT04800965) and eight days (second randomized controlled trial) ($n = 67,092$ individuals; clinicaltrials number NCT04801524) after they received a notification of vaccine eligibility. The first reminder boosted appointment and vaccination rates within the healthcare system by 6.07 (84%) and 3.57 (26%) percentage points, respectively; the second reminder increased those outcomes by 1.65 and 1.06 percentage points, respectively. The first reminder had a greater effect when it was designed to make participants feel ownership of the vaccine dose. However, we found no evidence that combining the first reminder with a video-based information intervention designed to address vaccine hesitancy heightened its effect. We performed online studies ($n = 3,181$ participants) to examine vaccination intentions, which revealed patterns that diverged from those of the first randomized controlled trial; this underscores the importance of pilot-testing interventions in the field. Our findings inform the design of behavioural nudges for promoting health decisions⁵, and highlight the value of making vaccination easy and inducing feelings of ownership over vaccines.

[Download PDF](#)

Main

Vaccines have been crucial for eradicating or controlling several deadly infectious diseases¹. However, mobilizing people to get vaccines remains a challenge. Low or delayed vaccination uptake continues to threaten global health, and can lead to outbreaks of vaccine-preventable diseases⁶. Developing evidence-based communication strategies to enhance voluntary vaccine uptake is therefore critical⁴. Previous work suggests two major approaches to increasing vaccinations³. The first aims to boost vaccine uptake intentions among those who are uncertain about vaccination. Given that changing intentions is insufficient⁷, the second approach involves helping people to follow through on their vaccination intentions and overcome sources of friction, such as forgetfulness⁸, hassle costs⁹ and procrastination^{10,11}.

These approaches could help to increase vaccination rates in the context of the current COVID-19 pandemic¹², which has had unprecedented costs¹³. Despite the growing availability of COVID-19 vaccines, 30% of US adults were still either unwilling or uncertain about getting the COVID-19 vaccine in late June 2021, and the hesitancy

rate was similarly high in several other countries that had vaccines available¹⁴. Barriers to action may further lower vaccination rates among those who intend to get inoculated.

Nudges, defined as interventions that alter ‘people’s behavior in a predictable way without forbidding any options or significantly changing economic incentives’¹⁵, could improve the uptake of COVID-19 vaccines¹⁶. Low-cost behavioural interventions such as these have been effectively applied to other health-related decisions⁵, such as healthy eating¹⁷, exercising¹⁸ and influenza vaccinations^{19,20,21}. To maximize vaccine uptake, it is critical to understand how to best design behavioural interventions to boost intentions to get vaccinated, remove barriers to following through on good intentions or both³.

Here we report data from two sequential large-scale randomized controlled trials (RCTs) that investigate whether nudging people to get vaccinated, using reminders that are carefully designed to reduce barriers to following through, can improve the uptake of COVID-19 vaccines. Reminders are a popular nudge²² and have proven effective across policy-relevant domains^{8,20,23,24}. We further examine the benefits of combining our reminders with additional interventions, including (1) behaviourally informed messaging designed to amplify individuals’ desire to get vaccinated and (2) a traditional information-provision intervention aimed at correcting the misconceptions that drive vaccine hesitancy^{25,26}. Testing the effects of interventions on actual uptake of COVID-19 vaccines extends previous work that has studied hypothetical interventions^{27,28}.

Promoting vaccine uptake

We conducted two preregistered RCTs at University of California, Los Angeles (UCLA) Health (‘Data availability’ in Methods). Participants in these RCTs were drawn from the UCLA Health primary and speciality care attributed patient list. Starting from 29 January 2021, once patients became eligible for the COVID-19 vaccine, UCLA Health sent them an initial invitation to schedule their vaccination appointment. On the first weekday after the initial invitation (hereafter, the ‘first reminder date’), we enrolled eligible patients (hereafter, ‘participants’) in the first RCT. On the first weekday after the eighth day following the initial invitation (hereafter, the ‘second reminder date’), we enrolled participants eligible for the second RCT into it. The timeline and eligibility criteria are provided in ‘Enrolment and eligibility for RCTs’ in Methods; Fig. 1 shows the timeline, eligibility and randomization of the two RCTs.

Fig. 1: Timeline, assessment for eligibility and randomization of two sequential RCTs.

 figure1

Timeline, eligibility for enrolment, the total number of participants excluded from the analysis, the total number of participants included in the analysis, and the number of participants who were randomized into each condition and included in the analysis are displayed here for the first and second RCTs. t is the date on which participants received the initial invitation to take up a COVID-19 vaccine from UCLA Health. The first reminder date fell on the first weekday after the initial invitation was sent, and the second reminder date fell on the first weekday after the eighth day following the initial invitation. Exceptions were that participants who received the initial invitation during 19–29 January 2021 were enrolled in the first RCT on 1 February 2021 and the second RCT on 9 February 2021, owing to the delay in setting up the infrastructure needed to run the RCTs. In the first RCT, 38,983 participants were sequentially excluded from the analysis, including (1) 33,533 individuals who obtained the first dose before the first reminder date according to the vaccination records UCLA Health could access on 25 May 2021; (2) 5,392 individuals who made the first-dose appointment at UCLA Health before 15:00 h on the first reminder date; and (3) 58 individuals who were under 18 years old. In the second RCT, 35,583 participants were sequentially excluded from the analysis, including (1) 35,127 individuals who obtained the first dose before the second reminder date according to the vaccination records UCLA Health could access on 25 May 2021; (2) 408 individuals who made the first-dose appointment at

UCLA Health before 15:00 h on the second reminder date; and (3) 48 individuals who were under 18 years old.

In both RCTs, we randomized whether participants received text-message-based reminders or not. All reminders shared two elements that were intended to address two barriers to action. First, all reminders made vaccination top of mind to curb forgetfulness and prompt people to adopt the target behaviour^{8, 22}. Second, all reminders sought to reduce inconvenience as a potential source of friction²² by including a link to the appointment-scheduling website and allowing participants to easily book their appointment immediately.

Our primary outcome was whether participants scheduled their first-dose appointment at UCLA Health within six days of receiving a text reminder. Our secondary outcome was whether participants obtained the first dose at UCLA Health within four weeks of the reminder; the reasoning behind these time windows is given in ‘Outcome measures for RCTs’ in Methods.

We focus our data reporting on participants who were enrolled in the RCTs by 23 February 2021, as specified in our preregistration. All exclusion criteria and analyses were preregistered (‘Enrolment and eligibility for RCTs’ in Methods, Supplementary Information sections [1.1 and 1.3](#)).

First-reminder RCT

On the first reminder date, we randomly assigned participants enrolled in the first RCT at a 4:1 ratio to the ‘follow-through reminder’ arm, in which they received a text reminder at 15:00 h that encouraged them to schedule a vaccination appointment, or to the ‘holdout’ arm, in which they did not get a reminder.

We nested a 2×2 factorial design within the follow-through reminder arm to test whether reminders become more effective when combined with another behaviourally informed intervention to motivate action and/or with an information intervention that aims at shifting vaccination intentions.

The first factor varied whether the reminder attempted to further amplify people’s desire to act by inducing feelings of psychological ownership over the vaccine^{29,30}. Reminders containing the ownership intervention (designated ‘ownership reminder’ and ‘ownership reminder with video’) indicated the vaccine had ‘just been made available for you’ and encouraged participants to ‘claim your dose’. We used online experiments to confirm that such language would make participants feel more strongly that the vaccine was already theirs (ordinary least squares (OLS) regressions, $B = 0.376$, s.e. = 0.084, $P < 0.001$, $n = 1,987$; $B = 0.389$, s.e. = 0.116, $P < 0.001$, $n = 1,168$) (Supplementary Tables [26, 36](#)). Previous research has shown that similar

language—such as ‘the flu vaccine is reserved for you’—increased uptake of influenza vaccinations²⁰; psychological ownership could be one of the mechanisms at play.

The second factor manipulated whether the reminder contained a link to a 2-min video that provided information on COVID-19 and vaccine effectiveness, with the goal of correcting common misconceptions and boosting vaccination intentions. The video intervention was used in the ‘basic reminder with video’ and ‘ownership reminder with video’ sub-arms. We based the video on a literature review of vaccine hesitancy^{3,31,32} and our January 2021 survey of residents of California (USA) ($n = 515$) (‘Vaccination intention survey’ in Methods), which allowed us to identify common misconceptions about COVID-19 and authorized vaccines. A similar video intervention was used in previous work to increase influenza vaccinations²⁰.

Our analysis includes 93,354 participants (43.3% male, 53.5% white (excluding Hispanic or Latino) (all racial demographic data use self-reported terms), average age = 72.8, s.d. = 10.3). Study arms were well-balanced on demographic characteristics (Extended Data Table 1). All reported effect sizes come from OLS regressions (or, precisely, a linear probability model³³, given our binary outcome measures) with heteroscedasticity-robust standard errors that control for participant gender, age, race, ethnicity, preferred language, social vulnerability index, COVID-19 risk score and fixed effects of initial invitation dates. The results are robust to removing control variables, using logistic regressions and conducting intent-to-treat analyses with all participants enrolled in our RCTs by 23 February 2021 (Supplementary Information section 1.5).

In the holdout arm, 7.20% of participants made the first-dose appointment within six days of the first reminder date, and 13.89% received the first dose at UCLA Health within four weeks (Fig. 2). Our OLS regressions estimate that receiving a text reminder boosted appointment rates within six days by 6.07 percentage points and vaccination rates within four weeks by 3.57 percentage points (Extended Data Table 2), amounting to a relative increase of 84.33% and 25.71%, respectively. All reminder types outperformed the holdout arm (Extended Data Table 2). The top-performing reminder type contained the ownership language, and boosted appointment and vaccination rates at UCLA Health by 6.83 (94.84%) and 4.12 (29.63%) percentage points, respectively, relative to the holdout arm.

Fig. 2: Appointment and vaccination rates at UCLA Health by condition for the first RCT.

 **figure2**

a, b, Proportion of participants in each condition who scheduled an appointment for the first dose of the COVID-19 vaccine at UCLA Health between 15:00 h on the first reminder date and 23:59 h on the fifth day following the first reminder date (**a**) and the proportion of participants in each condition who obtained the first dose of the COVID-19 vaccine at UCLA Health within four weeks of the first reminder date (**b**). Error bars represent ± 1 s.e.m. The number of participants in each condition (from left to right in each panel) is 18,629, 18,592, 18,757, 18,627 and 18,749.

The gap between the follow-through reminder and holdout arms in vaccinations at UCLA Health persisted for eight weeks (Fig. 3), which suggests that reminders increased the number of vaccinated participants for as long as we observed (rather than only accelerating vaccinations). Notably, even if the holdout arm eventually caught up after the two months we observed, accelerating vaccination still benefits society³⁴.

Fig. 3: Kaplan–Meier curves reflecting the proportion of participants who had obtained the first dose at UCLA Health by a given day after the first reminder date in the first RCT.

 **figure3**

Kaplan–Meier curves tracking the percentage of participants in the holdout arm (blue) ($n = 18,749$) versus the follow-through reminder arm (red) ($n = 74,605$) of the first RCT who had obtained the first dose of COVID-19 vaccine at UCLA Health by a given day from the first reminder date (0 on the x axis) onward. All participants were right-censored at 55 days after the first reminder date. The solid horizontal line indicates that 18.38% of participants in the holdout arm had obtained the first dose at UCLA Health by the end of 55 days after the first reminder date.

Within the follow-through reminder arm, adding the ownership language to the reminder further increased appointment and vaccination rates at UCLA Health by 1.51 and 1.09 percentage points, respectively (Extended Data Table 2), compared to the 12.58% appointment rates and 17.01% vaccination rates among people who received a reminder without such language. By contrast, we found no evidence that inviting participants to watch the video improved either outcome variable, relative to reminders without a video (Extended Data Table 2).

The average effect of a reminder held for both participants who received the influenza shot in either of the two recent seasons ($n = 46,757$) and those who did not ($n = 46,597$) (Fig. 4) but was larger among the former than the latter group, by 4.4 percentage points for appointments (OLS regression, $B = 0.044$, s.e. = 0.004,

$P < 0.001$ for the interaction) and 2.3 percentage points for vaccinations at UCLA Health (OLS regression, $B = 0.023$, s.e. = 0.006, $P < 0.001$ for the interaction) (Supplementary Table 6).

Fig. 4: Regression-estimated increase in appointments and vaccinations induced by reminders.



a, b, Regression-estimated increase in appointment rates at UCLA Health within six days of the first reminder date (left panel in **a, b**) and vaccination rates at UCLA Health within four weeks of the first reminder date (right panel in **a, b**), induced by receiving a reminder (versus holdout) (**a**) and by receiving a reminder with ownership language (versus one without) (**b**) across participant subgroups in the first RCT. The full sample referred to 93,354 participants included in the analysis of the first RCT. ‘White’, subsample including 49,909 participants who identified as white (excluding Hispanic or Latino individuals); ‘minority’, subsample includes 29,784 participants who identified as Asian, Black, American Indian or Alaska Native, Native Hawaiian or Pacific Islander, other race (excluding participants whose race was unknown), and/or Hispanic or Latino. The ‘ ≥ 65 years old’ subgroup includes 84,075 participants who were at least 65 years old; the ‘ < 65 years old’ subgroup includes 9,279 participants under 65 years old. The ‘influenza vaccine’ subgroup includes 46,757 participants who received the influenza vaccine in either of two recent influenza seasons; the ‘no influenza vaccine’ subgroup includes 46,597 participants who did not receive an influenza vaccine in two recent influenza seasons. Extended Data Table 2, Supplementary Tables 3, 5, 6, 10, 11, 13 provide complete OLS regression results graphed here and the corresponding sample sizes. Error bars represent 95% confidence intervals of estimated increases.

Because our sample consists of predominantly elderly and white participants, we confirmed (Fig. 4) that the effects of follow-through reminders and ownership language largely held for racial and ethnic minorities as defined in Fig. 4 ($n = 29,784$) and participants under 65 years old ($n = 9,279$). Notably, the average effects of follow-through reminders on both appointments and vaccinations were comparable across white ($n = 49,909$), Hispanic ($n = 10,624$), Black ($n = 5,109$) and Asian ($n = 7,553$)

participants (Extended Data Table 2). Identifying solutions to improving vaccine uptake among racial and ethnic minority groups is critical, as these groups have been disproportionately hurt by the COVID-19 pandemic³⁵ and tend to experience increased vaccine hesitancy³⁶.

Second-reminder RCT

Participants who did not schedule their vaccine appointment a few days after the first reminder may have forgotten about it, been procrastinating or been more hesitant than those who got vaccinated. We conducted the second RCT to study the effect of sending these participants a second text reminder. On the second reminder date, we randomized eligible participants at a 6:1 ratio to receive another text message at 15:00 h that reminded them of vaccine availability and providing easy access to the scheduling website (the follow-through reminder arm) or to not receive the text message (the holdout arm).

To harness other psychological principles to motivate people to act, we randomized participants within the follow-through reminder arm to receive one of six messages that leveraged additional behavioural insights ('Design of the second-reminder RCT' in Methods). Following the preregistration, we present only the average effect of all text reminders combined relative to the holdout arm.

Our analysis includes 67,092 participants (43.5% male, 52.6% white (excluding Hispanic or Latino), average age = 73.7, s.d. = 10.0). Study arms were well-balanced on demographic characteristics (Extended Data Table 3).

Getting a second reminder increased participants' likelihood of scheduling the first-dose appointment within six days by 1.65 percentage points (53.36%) and obtaining the first dose at UCLA Health within four weeks by 1.06 percentage points (17.23%), relative to the 3.10% appointment rates and 6.16% vaccination rates in the holdout arm (Extended Data Table 4). All reminder types boosted appointments and vaccinations (Extended Data Table 4). Although small, these effects are noteworthy, as they are documented within a more hesitant population (as participants in the second RCT had not scheduled an appointment after two notifications and had been eligible for COVID-19 vaccines in California for some time).

Effect on vaccination anywhere

Because the text reminders made eligibility at UCLA Health salient and reduced barriers to appointment scheduling at UCLA Health, we have focused on appointments and vaccinations at UCLA Health as our outcome measures. We also investigated the effect of receiving a text reminder on whether participants received the first dose

inside or outside UCLA Health (hereafter, ‘anywhere’) within four weeks of getting a reminder (Supplementary Information section [1.5](#)).

For the first RCT, we find that reminders increased vaccinations anywhere by 2.1 percentage points, relative to a baseline of 31.85% in the holdout arm (OLS regression, $B = 0.021$, s.e. = 0.004, $P < 0.001$, $n = 93,354$) (Supplementary Table [22](#)). In addition, adding (versus not) the ownership language increased vaccinations anywhere by an additional 0.9 percentage points (OLS regression, $B = 0.009$, s.e. = 0.003, $P = 0.010$ without multiple comparison adjustment and $P = 0.020$ with a Holm–Bonferroni correction^{[37](#)}, $n = 74,605$) (Supplementary Table [22](#)). The fact that the effect of receiving one reminder on vaccinations at any location could last one month is notable, considering that participants may have been exposed to numerous sources of communication about the vaccine during this period.

Receiving a second reminder increased vaccination rates anywhere by 1.0 percentage points two weeks after the second reminder date (OLS regression, $B = 0.010$, s.e. = 0.004, $P = 0.008$, $n = 67,092$) (Supplementary Table [24](#)), relative to a baseline of 12.04% in the holdout arm. Although this effect was not statistically significant at four weeks (OLS regression, $B = 0.007$, s.e. = 0.004, $P = 0.127$, $n = 67,092$) (Supplementary Table [23](#)), sending a second text reminder can still contribute to accelerating vaccinations and avoiding unnecessary infections. It is also worth noting that, had we designed the reminders to remove barriers to getting vaccinated at a broad set of locations (rather than focusing on UCLA Health), our reminders might have exhibited larger effects on vaccination anywhere.

Vaccination intentions versus actual uptake

To inform policy, researchers often use surveys of intentions to evaluate the effectiveness of interventions aimed at encouraging vaccine uptake^{[3,27,28](#)}. Given that intentions do not always reflect real behaviours^{[7](#)}, we tested how the interventions deployed in our first RCT affected vaccination intentions and explored whether hypothetical responses would match actual behavioural responses.

We ran three preregistered experiments on Amazon’s Mechanical Turk and Prolific Academic: two concurrently to the first RCT in February 2021 and one as a replication in April 2021 (total $n = 3,181$). We randomized participants to receive one of the four reminders from the first RCT, asking about their intentions to get vaccinated using different questions on a seven-point scale (‘Procedures for online experiments’ in Methods). In contrast to the patterns observed in the first RCT, the video intervention resulted in a small—but statistically significant—increase in people’s self-reported interest in getting the vaccine; however, we found no evidence that adding ownership language increased vaccination intentions (Extended Data Table [5](#)).

The discrepancy between laboratory and field data (Extended Data Table 6) is unlikely to be driven by differences in political attitudes between samples³⁸, as the aforementioned findings about video and ownership interventions generally held both for those who self-identified as ‘Democrat’ and as ‘Republican’ online (Extended Data Table 5). One potential explanation for these discrepant findings is that, although we could require all online participants to watch the video, less than 21% of the participants in the first RCT opted to watch it (Supplementary Information section 1.3.4), possibly because of being too busy or active avoidance of information³⁹. Another possibility is that COVID-19 vaccine intentions were harder to change outside of a controlled online experiment, where various sources of information compete for people’s attention. As for the lack of evidence that ownership language affected vaccination intentions, it could be that individuals did not anticipate the motivating power of such language in hypothetical settings. Whereas the differences in sample characteristics and measurement (Extended Data Table 6) do not allow us to pinpoint the drivers of the discrepancy between our online studies and the first RCT, these results suggest that hypothetical responses to behavioural nudges should be taken with caution.

Discussion

Our research highlights that behavioural science insights can increase and speed up COVID-19 vaccinations at close-to-zero marginal cost. Text-based reminders designed to overcome barriers to scheduling can effectively encourage vaccinations across different demographic groups, with effects persisting for at least eight weeks. These effects are heightened when follow-through reminders leverage psychological ownership, making people feel that a dose of the vaccine belongs to them. However, we find no evidence that combining reminders with a video-based information intervention further increases vaccination, which suggests that more work is needed to uncover when information interventions can help to overcome vaccine hesitancy. Additional analyses of our RCT sample reveal that only about 10% of participants did not keep or show up for their first-dose appointment, and approximately 90% of participants who received the first dose at UCLA Health scheduled their second dose (Supplementary Information section 1.6). Thus, the biggest barrier to increasing COVID-19 vaccinations is getting participants to schedule the first-dose appointment.

Our research has implications for enhancing the uptake of life-saving vaccines in general, as it highlights the power of making vaccination easy and eliciting feelings of ownership over the vaccine. Although promoting vaccinations at scale requires a multifaceted approach, our findings suggest that behavioural nudges could be an important strategy to consider. If sent to all 263 million adults in the USA⁴⁰, and assuming the same absolute effect size observed in our first RCT would hold for the 60% of US adults who did not immediately obtain the vaccine⁴¹, our follow-through

reminders could result in 3.31–5.68 million extra people getting vaccinated within a month of the reminder. This estimated range is based on the average effect of receiving the first reminder on vaccination rates anywhere (that is, $60\% \times 263 \text{ million} \times 2.1$ percentage points) versus at UCLA Health ($60\% \times 263 \text{ million} \times 3.6$ percentage points). Similarly, reminders with the ownership framing would motivate 1.42–1.74 million extra people to get vaccinated than reminders without such framing (that is, $60\% \times 263 \text{ million} \times 0.9$ percentage points– $60\% \times 263 \text{ million} \times 1.1$ percentage points).

The insights from this work could inform strategies to motivate health-related behaviours more broadly, such as scheduling preventive care tests or participating in health-related programs. To that end, the discrepancy observed between our RCTs and online studies highlights the value of pilot-testing interventions in the field before deploying them at scale. As policymakers, public health experts and organizations strive to develop communication strategies to promote health-related behaviours, we hope that the effective interventions documented in our research—and behavioural science more generally—can become part of their toolbox.

Methods

For RCTs, we predetermined the end date of enrolment for analyses reported herein, but we could not predetermine sample size by the enrolment deadline owing to uncertainty about how many UCLA Health participants would satisfy inclusion and exclusion criteria. We preregistered data-analysis plans contingent on the actual sample size on the basis of power analysis. We used power analysis to predetermine sample sizes for online experiments. RCTs and online experiments were randomized, and investigators were blinded to allocation during experiments.

Ethics approval

This research was deemed to comply with all relevant ethical regulations. The Institutional Review Board at the UCLA approved the protocols of our randomized controlled trials (reference number 21-000268) and determined that a waiver of informed consent was appropriate. All online experiments and the vaccination intention survey were conducted under approval of the Institutional Review Board at Carnegie Mellon University (reference number IRBSTUDY2015_00000482), and informed consent was obtained from all online study participants as part of the enrolment process.

Setting for the RCTs

We conducted the RCTs in partnership with UCLA Health, a large integrated academic health system in California. Extended Data Table 7 provides a comparison of demographic characteristics and vaccination rates between our RCT sample, UCLA Health primary and specialty care attributed patient population, Los Angeles County and California.

Enrolment and eligibility for RCTs

Starting from 19 January 2021, UCLA Health invited primary and specialty care attributed patients who were eligible for the COVID-19 vaccine at the time to get vaccinated. UCLA Health followed the national Advisory Committee on Immunization Practices as well as state and county guidelines to determine patient COVID-19 vaccine eligibility phasing. Considering the large volumes of eligible patients in each phase, UCLA Health developed a risk model that incorporates clinical and social risk to subprioritize within each phase. According to this model, UCLA Health sent invitations to eligible patients in batches over time to guarantee enough vaccine supply for invited patients. The size of the batch was decided daily on the basis of (1) available doses, (2) available appointment slots and (3) expected appointment rate. If UCLA Health identified a patient as having already obtained the vaccine inside or outside UCLA Health when it was their turn to be invited, the health system did not send the invitation to that patient.

On the first reminder date, patients were automatically enrolled into the first RCT and became participants if they (1) had a SMS-capable telephone number, (2) had not scheduled the first-dose COVID-19 vaccination appointment at UCLA Health and (3) had not obtained the first dose anywhere by the end of the day before the first reminder date, according to the latest California Immunization Registry (CAIR) records UCLA Health could access as well as UCLA Health's internal records. The earliest first reminder date was 1 February 2021.

On the second reminder date, patients were automatically enrolled in the second RCT and became participants if they (1) had a SMS-capable telephone number, (2) had not scheduled the first-dose COVID-19 vaccination appointment at UCLA Health and (3) had not obtained the first dose anywhere by the end of the day before the second reminder date. The earliest second reminder date was 9 February 2021.

Figure 1 shows the timeline, eligibility and randomization of the two RCTs. For both RCTs, participants within each batch were randomized at the individual level to treatments according to the design detailed in 'Design of the first-reminder RCT' and 'Design of the second-reminder RCT'. Enrolment was conducted by the UCLA Health Office of Population Health and Accountable Care. Random assignment to interventions was performed by UCLA Health statisticians blind to the hypotheses and interventions using a computerized random number generator.

Design of the first-reminder RCT

We randomly assigned participants following simple randomized procedures at a 4:1 ratio to either the follow-through reminder arm, in which they received a reminder at 15:00 h on the first reminder date, or the holdout arm, in which they received no reminders. All reminders were designed to nudge individuals to schedule their vaccination appointments by (1) making vaccination top of mind to curb forgetfulness, and (2) providing the direct link to the scheduling website to reduce friction and increase convenience. The basic reminder read ‘UCLA Health: [participant’s first name], you can get the COVID-19 vaccine at UCLA Health. Make a vaccination appointment here: uclahealth.org/schedule.’

We nested a 2×2 factorial design within the follow-through reminder arm. The first factor was whether or not the reminder sought to enhance participants’ feelings of psychological ownership over the vaccine to amplify their desire to obtain their vaccine (ownership intervention). The ownership intervention added language to the reminder to make participants feel as if the vaccine was already theirs. The ownership reminder read ‘UCLA Health: [participant’s first name], a COVID-19 vaccine has just been made available to you at UCLA Health. Claim your dose today by making a vaccination appointment here: uclahealth.org/schedule.’

The second factor was whether or not the reminder linked to a video that was designed to shift vaccination intentions by providing information about COVID-19 and the authorized vaccines (video intervention). The video intervention was based on a survey of the vaccine hesitancy literature^{3,31,32,36} as well as a survey that we conducted in January 2021 with California residents (as described in ‘Vaccination intention survey’). The video (Supplementary Video 1) first highlighted the pandemic as a challenge, providing statistics on infections and ease of transmission. It then proposed the vaccine as an easy and safe solution, providing information about its effectiveness. The basic reminder with video read ‘UCLA Health: [participant’s first name], you can get the COVID-19 vaccine at UCLA Health. Please watch this important 2 min video: [link]. Make a vaccination appointment here: uclahealth.org/schedule.’

In the ownership reminder with video sub-arm, the reminder contained both the ownership and video interventions and read: ‘UCLA Health: [participant’s first name], a COVID-19 vaccine has just been made available to you at UCLA Health. Please take 2 simple steps: 1. Watch this important 2 min video: [link]. 2. Claim your dose today by making a vaccination appointment here: uclahealth.org/schedule.’

In all sub-arms, participants whose preferred language was Spanish received the text reminder (and the video (Supplementary Video 2), in the relevant cases) in Spanish. Participants within the follow-through reminder arm were randomly assigned

following simple randomization procedures to one of these four sub-arms with an equal probability.

Design of the second-reminder RCT

Eight days after the initial notification, eligible participants were enrolled in the second RCT. They were randomized following simple randomization procedures at a 6:1 ratio to the follow-through reminder arm, in which another text reminder was sent at 15:00 h on the second reminder date, or the holdout arm with no reminders.

Randomization was independent between the first and second RCTs (Supplementary Information section [1.1](#)). Similar to the first RCT, all text reminders in the second RCT heightened the salience of vaccine availability (so as to combat forgetfulness) and provided the direct link to the appointment scheduling website (so as to increase convenience).

We nested a 2×3 factorial design within the follow-through reminder arm, in which we leveraged behavioural insights to motivate people to schedule a vaccination appointment via different messaging. The first factor varied whether the reminder emphasized prosocial (versus personal) benefits of getting vaccinated^{[42,43](#)}. The second factor manipulated whether the reminder highlighted the exclusivity of having early access to the vaccine (early access framing), whether it framed the act of obtaining the vaccine as an opportunity to chart a new path forward (fresh start framing) or neither. The early access framing sought to leverage the principle of scarcity to increase vaccine demand^{[44,45](#)}, as vaccination was still exclusive at the early stage of distribution (January–February 2021). The fresh start framing was inspired by previous work showing that people are motivated to take actions at new beginnings^{[46,47](#)}. Here, we tested whether framing getting the vaccine as an opportunity to chart a new path forward for participants themselves or society could mobilize participants to get inoculated.

Specifically, the basic self/prosocial reminders read ‘UCLA Health: [participant’s name], to protect (yourself/your family, friends, and community), make your COVID-19 vaccine appointment here today: uclahealth.org/schedule.’’ The early access self/prosocial reminders read ‘UCLA Health: [participant’s name], you are one of few Americans who have early access to the COVID-19 vaccine based on national guidelines. Take this opportunity to protect (yourself/your family, friends, and community who may not have this access yet). Make your vaccine appointment here today: uclahealth.org/schedule.’’ The fresh start self/prosocial reminder read ‘UCLA Health: [participant’s name], (the past year has been tough/the past year has been tough for many). Now, the COVID-19 vaccine can offer the promise of a fresh start. Take this opportunity to protect (yourself/your family, friends, and community) and (chart a new path forward/help our nation chart a new path forward). Make your

vaccine appointment here today: uclahealth.org/schedule.’ The content in parentheses differed between the personal and prosocial messaging conditions. Participants within the follow-through reminder arm were randomly assigned following simple randomization procedures to one of these six sub-arms with an equal probability.

Analyses and exclusion criteria of RCTs

All analyses and exclusion criteria follow the preregistrations. We focus on participants enrolled in either RCT by 23 February 2021. This sample consists of participants eligible to get vaccinated at UCLA Health from 19 January to 22 February 2021, including participants at or above 65 years old, participants with any transplant and high-risk participants with qualifying pre-existing conditions. We report results using data extracted on 25 May 2021. We excluded participants who were enrolled in the first (second) RCT but either scheduled a vaccination appointment at UCLA Health by 15:00 h on their corresponding first (second) reminder date or obtained a COVID-19 vaccine somewhere before their corresponding first (second) reminder date according to the latest appointment and vaccination records UCLA Health could access on 25 May 2021. These participants could not have been motivated to schedule or obtain the first dose by our text reminders; thus, excluding them allows us to more accurately estimate the effect of our interventions on participants who could benefit from receiving our interventions. We additionally excluded participants under 18 years old as we only applied for the permission of the Institutional Review Board to analyse data about adult participants. The proportion of participants who were excluded in the analysis stage did not statistically significantly differ across conditions (Supplementary Table 1), and our results are robust if we conduct intent-to-treat analyses involving all participants who were enrolled in the RCTs by 23 February 2021 (Supplementary Information section 1.5).

For the first RCT, our preregistered analysis about participants enrolled by 23 February 2021 aimed to investigate (1) the average effect of sending a follow-through reminder; (2) whether all reminder types would outperform the holdout arm; (3) the effect of adding the video intervention to the reminder; (4) the effect of adding the ownership intervention; and (5) whether the aforementioned effects would differ between participants who received versus did not receive the influenza vaccine in either of two recent influenza seasons.

For the second RCT, our preregistered analysis about participants enrolled by 23 February 2021 aimed to investigate (1) the average effect of sending a second follow-through reminder and (2) whether all reminder types outperformed the holdout arm. Because we were uncertain about how many people would be enrolled in the second RCT by 23 February 2021, we preregistered to not compare sub-arms to each other with this data. Supplementary Information sections 1.3 and 1.4 describe for the scope

of analyses we plan to conduct once the full data collection has been completed about all participants ever enrolled in our RCTs from the beginning of the trials until UCLA Health stops sending out COVID-19 vaccine invitations.

Outcome measures for RCTs

Our preregistered primary outcome measure indicates whether participants scheduled a vaccination appointment for the first dose of COVID-19 vaccine at UCLA Health within six days of the first (second) reminder date (specifically, from 15:00 h on the first (second) reminder date to 23:59 h on the fifth day following the first (second) reminder date.). We preregistered this time window because UCLA Health targeted additional outreach efforts to participants who had not scheduled their vaccination appointment six days after the second reminder date and we wanted to use a consistent time window for the two RCTs. The results are robust to extending the time window to one month (Supplementary Tables 22 and [23](#)). Our secondary outcome measure in this Article is whether participants obtained the first dose of COVID-19 vaccine at UCLA Health within four weeks of the first (second) reminder date. We chose this window because UCLA Health generally only allowed participants to schedule an appointment for less than four weeks ahead. Consistent with this practice, 96.25% of the first-dose appointments made by participants in the analysis sample of the first RCT occurred within four weeks from the day they were scheduled. In the preregistrations, we listed additional secondary outcome variables; we explain why we did not focus on these in this Article in Supplementary Information section [1.2](#).

Procedures for online experiments

We ran two preregistered online experiments in February 2021, concurrently with the randomized controlled trials. In addition, we ran a preregistered replication experiment online in April 2021, when all US adults had become eligible to receive the vaccine.

In the February 2021 experiments, we instructed participants to imagine becoming eligible for the COVID-19 vaccine and receiving a text message from their healthcare provider encouraging them to get vaccinated. We randomly assigned participants to read one of the four reminders from the first RCT. Participants in the ‘video’ conditions were also instructed to watch the video. After reading the message, participants indicated their likelihood of scheduling a vaccination appointment: ‘How likely would you be to schedule a vaccination appointment after receiving this message from your healthcare provider?’ (1, not at all likely, to 7, very likely). They also rated the persuasiveness of the text message (1, not at all persuasive, to 7, very persuasive). To check whether the messages containing ownership language increased feelings of psychological ownership over the vaccine as we intended, we asked participants, ‘To what extent does the text message make you feel that the COVID-19

vaccine is already yours?’ (1, not at all, to 7, very much)³⁰. To understand how the video may have changed viewers’ perceptions and beliefs, we measured participants’ beliefs about the prevalence of COVID-19, worry about spreading the virus, perceived vaccine effectiveness, anticipated regret for not getting the vaccine and trust in the vaccine (Supplementary Information section [2](#) for questions and results).

The April 2021 experiment used identical procedures but adopted additional measures of vaccination intentions to test whether findings in our February 2021 studies are robust to different ways of soliciting intentions. For this purpose, we randomized whether participants answered questions in the same hypothetical manner as in the February studies, or responded to questions with a less hypothetical framing.

Participants randomized to answer the hypothetical version were asked ‘How likely would you be to schedule a vaccination appointment after receiving this message from your healthcare provider?’ (1, not at all likely, to 7, very likely) and ‘How much would you want the vaccine after receiving this message from your healthcare provider?’ (1, not at all, to 7, very much). These two questions were highly correlated ($r = 0.94$, $P < 0.001$) and aggregated into a composite. Participants randomized to answer the less hypothetical version of the intention questions were asked ‘How likely are you to schedule a vaccination appointment today after receiving this message from your healthcare provider?’ (1, not at all likely, to 7, very likely) and ‘How much do you want the vaccine now, after receiving this message from your healthcare provider?’ (1, not at all, to 7, very much). These two measures were highly correlated ($r = 0.93$, $P < 0.001$) and averaged into a composite. All participants also rated the persuasiveness of the message they read, using the same measure used in the February studies (Supplementary Information section [3](#)).

Sample for online experiments

We recruited participants from Amazon’s Mechanical Turk (MTurk) and Prolific Academic (Prolific) who had not received a COVID-19 vaccine or scheduled a first-dose vaccination appointment at the time of the study. To be assigned to treatment, participants had to first pass a Captcha and an attention check question. To be included in the analysis, participants had to complete our preregistered dependent variables and not report having technical problems with the video. Considering these criteria, our first February 2021 online experiment consists of 1,163 participants. Our second February 2021 online experiment consists of 840 participants recruited from Prolific who satisfied similar criteria as those in the first online experiment, except that we additionally required that they did not report having taken a similar survey on MTurk. In both experiments, we attempted to recruit a balanced sample of individuals who self-reported as Democrat or Republican to test the generalizability of our findings (Supplementary Information section [2.1](#) for recruitment detail). Participants received US\$0.90 on MTurk and US\$1.10 on Prolific for completing our 6-min survey. Across

the two February online experiments, our sample consists of 2,003 participants (47.1% male, 71.8% white (excluding Hispanic or Latino), 51.8% Democrat, average age = 37.9, s.d. = 13.4).

For our April 2021 online experiment, we recruited participants on MTurk and Prolific using the same eligibility criteria as the second online experiment. Participants on MTurk received US\$0.90 or US\$1.00 (we boosted the pay to US\$1.00 on the third day of data collection to attract more respondents) and those on Prolific received US\$1.10 for completing our 6-min survey. Our sample consists of 1,178 participants (44.9% male, 71.6% white (excluding Hispanic or Latino), 40.8% Democrat, average age = 36.7, s.d. = 12.0).

Vaccination intention survey

To design the video used in our first RCT, we ran a survey in January 2021 involving 515 residents of California recruited on MTurk and Prolific (49.3% male, 42.9% white (excluding Hispanic or Latino), 70.9% Democrat, average age = 33.9, s.d. = 12.7). Participants received US\$1.00 on MTurk or US\$1.20 on Prolific for completing our 9-min survey. We asked participants to consider the authorized vaccines (Pfizer and Moderna) when taking the survey. We elicited their vaccination intentions by asking ‘If one of the COVID-19 vaccines were available to you today, would you get the vaccine?’⁴¹. Participants chose one from four options: ‘Definitely would get the vaccine’, ‘Probably would get the vaccine’, ‘Probably would not get the vaccine’ and ‘Definitely would not get the vaccine’. We then elicited participants’ beliefs and perceptions about COVID-19 and the vaccines. Specifically, we measured beliefs about infection likelihood with and without the vaccine and the severity of COVID-19. We collected feelings of vulnerability to COVID-19, fear of infection, worry of transmitting COVID-19 to others, anticipated regret for not getting the vaccine and trust in the vaccine. We compared answers to these questions among people who reported that they definitely would get the vaccine versus those feeling more uncertain. Supplementary Information section 5 describes all variables and results.

Methods of investigating intentions versus actual uptake

In Extended Data Table 6, we report statistics about the estimated effects of adding ownership language and a video-based information intervention to a reminder on vaccination intentions (based on online experiments) versus actual vaccine uptake (based on the first RCT). The statistics we report include the 95% confidence interval, the absolute value of Cohen’s d or h , and η_p^2 of each estimated effect. To calculate Cohen’s h for the binary outcomes measured in the first RCT, we use $2 \times \text{arcsine } \sqrt{P_{\text{with an intervention}}} - 2 \times \text{arcsine } \sqrt{P_{\text{without an intervention}}}$ ⁴⁸ in which $\sqrt{P_{\text{with an intervention}}}$ represents the percentage of participants who scheduled an appointment for (or

obtained) the first dose at UCLA Health within six days (or within four weeks) of the first reminder date among those who received a text reminder containing a given intervention and $\sqrt{P_{\text{without an intervention}}}$ represents the percentage among participants who received a text reminder without that intervention. To calculate η_p^2 for the online experiments and the first RCT, we use $\eta_p^2 = F \times df_{\text{numerator}} / (F \times df_{\text{numerator}} + df_{\text{denominator}})$ ⁴⁹ in which the F value and numerator and denominator degrees of freedom came from the OLS regressions reported in Supplementary Tables 5, 39.

Reporting summary

Further information on research design is available in the [Nature Research Reporting Summary](#) linked to this paper.

Data availability

The two RCTs were pre-registered at clinicaltrials.gov (first-reminder RCT, <https://clinicaltrials.gov/ct2/show/NCT04800965>; second-reminder RCT, <https://clinicaltrials.gov/ct2/show/NCT04801524>). The three online experiments were preregistered at aspredicted.org (online experiment 1, <https://aspredicted.org/blind.php?x=u2ng5c>; online experiment 2, <https://aspredicted.org/blind.php?x=ae3ci5>; and online experiment 3, <https://aspredicted.org/blind.php?x=7wf9er> and <https://aspredicted.org/blind.php?x=u82hy5>). The data analysed in this Article about randomized controlled trials were provided by UCLA Health and contain protected health information. To protect participant privacy, we cannot publicly post individual-level data. Qualified researchers with a valuable research question and relevant approvals including ethical approval can request access to the de-identified data about these trials from the corresponding author. A formal contract will be signed and an independent data protection agency should oversee the sharing process to ensure the safety of the data. Data about our online experiments and vaccination intention survey are available at: https://osf.io/qn8hr/?view_only=cf7b2bc590054aee8c4a2bae99ef20c5.

Code availability

The code to replicate the analyses and figures in the Article and its [Supplementary Information](#) is available at https://osf.io/qn8hr/?view_only=cf7b2bc590054aee8c4a2bae99ef20c5.

References

1. 1.
Greenwood, B. The contribution of vaccination to global health: past, present and future. *Phil. Trans. R. Soc. Lond. B* **369**, 20130433 (2014).
2. 2.
MacDonald, N. E. & the SAGE Working Group on Vaccine Hesitancy. Vaccine hesitancy: definition, scope and determinants. *Vaccine* **33**, 4161–4164 (2015).
3. 3.
Brewer, N. T., Chapman, G. B., Rothman, A. J., Leask, J. & Kempe, A. Increasing vaccination: putting psychological science into action. *Psychol. Sci. Public Interest* **18**, 149–207 (2017).
4. 4.
Jarrett, C., Wilson, R., O’Leary, M., Eckersberger, E. & Larson, H. J. Strategies for addressing vaccine hesitancy – a systematic review. *Vaccine* **33**, 4180–4190 (2015).
5. 5.
Patel, M. S., Volpp, K. G. & Asch, D. A. Nudge units to improve the delivery of health care. *N. Engl. J. Med.* **378**, 214–216 (2018).
6. 6.
Jansen, V. A. A. et al. Measles outbreaks in a population with declining vaccine uptake. *Science* **301**, 804 (2003).
7. 7.
Sheeran, P. Intention–behavior relations: a conceptual and empirical review. *Eur. Rev. Soc. Psychol.* **12**, 1–36 (2002).
8. 8.
Karlan, D., McConnell, M., Mullainathan, S. & Zinman, J. Getting to the top of mind: how reminders increase saving. *Manage. Sci.* **62**, 3393–3411 (2016).
9. 9.

Bhargava, S. & Manoli, D. Psychological frictions and the incomplete take-up of social benefits: evidence from an IRS field experiment. *Am. Econ. Rev.* **105**, 3489–3529 (2015).

10. 10.

Shu, S. B. & Gneezy, A. Procrastination of enjoyable experiences. *J. Mark. Res.* **47**, 933–944 (2010).

11. 11.

Rogers, T., Milkman, K. L., John, L. K. & Norton, M. I. Beyond good intentions: prompting people to make plans improves follow-through on important tasks. *Behav. Sci.* **1**, 33–41 (2015).

12. 12.

Wood, S. & Schulman, K. Beyond politics—promoting COVID-19 vaccination in the United States. *N. Engl. J. Med.* **384**, e23 (2021).

13. 13.

Cutler, D. M. & Summers, L. H. The COVID-19 pandemic and the \$16 trillion virus. *J. Am. Med. Assoc.* **324**, 1495–1496 (2020).

14. 14.

Shelburne, P. U.S. lags behind global counterparts in driving down vaccine hesitancy, <https://morningconsult.com/global-vaccine-tracking> (accessed on 3 July 2021).

15. 15.

Thaler, R. H. & Sunstein, C. *NUUDGE: Improving Decisions About Health, Wealth, and Happiness*, vol. 47 (Penguin, 2009).

16. 16.

Volpp, K. G., Loewenstein, G. & Buttenheim, A. M. Behaviorally informed strategies for a national COVID-19 vaccine promotion program. *J. Am. Med. Assoc.* **325**, 125–126 (2021).

17. 17.

Wisdom, J., Downs, J. S. & Loewenstein, G. Promoting healthy choices: information versus convenience. *Am. Econ. J. Appl. Econ.* **2**, 164–178 (2010).

18. 18.

Milkman, K. L. et al. Megastudies improve the impact of applied behavioral science. *Nature* (in the press).

19. 19.

Chapman, G. B., Li, M., Colby, H. & Yoon, H. Opting in vs opting out of influenza vaccination. *J. Am. Med. Assoc.* **304**, 43–44 (2010).

20. 20.

Milkman, K. L. et al. A megastudy of text-based nudges encouraging patients to get vaccinated at an upcoming doctor's appointment. *Proc. Natl Acad. Sci. USA* **118**, e2101165118 (2021).

21. 21.

Milkman, K. L., Beshears, J., Choi, J. J., Laibson, D. & Madrian, B. C. Using implementation intentions prompts to enhance influenza vaccination rates. *Proc. Natl Acad. Sci. USA* **108**, 10415–10420 (2011).

22. 22.

Sunstein, C. R. in *The Handbook of Privacy Studies* (eds Sloot, B. & Groot, A.) 173–180 (Amsterdam Univ. Press, 2018).

23. 23.

Fishbane, A., Ouss, A. & Shah, A. K. Behavioral nudges reduce failure to appear for court. *Science* **370**, eabb6591 (2020).

24. 24.

Dale, A. & Strauss, A. Don't forget to vote: text message reminders as a mobilization tool. *Am. J. Pol. Sci.* **53**, 787–804 (2009).

25. 25.

Benartzi, S. et al. Should governments invest more in nudging? *Psychol. Sci.* **28**, 1041–1055 (2017).

26. 26.

Loewenstein, G. & Chater, N. Putting nudges in perspective. *Behav. Public Policy* **1**, 26–53 (2017).

27. 27.

Pink, S. L., Chu, J., Druckman, J., Rand, D. G. & Willer, R. Elite party cues increase vaccination intentions among Republicans. *Proc. Natl Acad. Sci. USA* **118**, e2106559118 (2021).

28. 28.

Serra-Garcia, M. & Szech, N. Choice architecture and incentives increase COVID-19 vaccine intentions and test demand. *SSRN Electron J. CESifo Working Paper No. 9003*, <https://ssrn.com/abstract=3827616> (2021).

29. 29.

Pierce, J. L., Kostova, T. & Dirks, K. T. Toward a theory of psychological ownership in organizations. *Acad. Manage. Rev.* **26**, 298–310 (2001).

30. 30.

Shu, S. B. & Peck, J. Psychological ownership and affective reaction: emotional attachment process variables and the endowment effect. *J. Consum. Psychol.* **21**, 439–452 (2011).

31. 31.

Kreps, S. et al. Factors associated with US adults' likelihood of accepting COVID-19 vaccination. *JAMA Netw. Open* **3**, e2025594 (2020).

32. 32.

Lazarus, J. V. et al. A global survey of potential acceptance of a COVID-19 vaccine. *Nat. Med.* **27**, 225–228 (2021).

33. 33.

Gomila, R. Logistic or linear? Estimating causal effects of experimental treatments on binary outcomes using regression analysis. *J. Exp. Psychol. Gen.* **150**, 700–709 (2021).

34. 34.

Castillo, J. C. et al. Market design to accelerate COVID-19 vaccine supply. *Science* **371**, 1107–1109 (2021).

35. 35.

Price-Haywood, E. G., Burton, J., Fort, D. & Seoane, L. Hospitalization and mortality among black patients and white patients with COVID-19. *N. Engl. J. Med.* **382**, 2534–2543 (2020).

36. 36.

Ruiz, J. B. & Bell, R. A. Predictors of intention to vaccinate against COVID-19: Results of a nationwide survey. *Vaccine* **39**, 1080–1086 (2021).

37. 37.

Holm, S. A simple sequentially rejective multiple test procedure. *Scand. Stat. Theory Appl.* **6**, 65–70 (1979).

38. 38.

Fridman, A., Gershon, R. & Gneezy, A. COVID-19 and vaccine hesitancy: a longitudinal study. *PLoS ONE* <https://doi.org/10.1371/journal.pone.0250123> (2021).

39. 39.

Golman, R., Hagmann, D. & Loewenstein, G. Information avoidance. *J. Econ. Lit.* **55**, 96–135 (2017).

40. 40.

US Census Bureau. American Community Survey (ACS), <https://www.census.gov/programs-surveys/acs> (accessed on 25 May 2021) (2020).

41. 41.

Funk, C. & Tyson, A. Intent to get a COVID-19 vaccine rises to 60% as confidence in research and development process increases. [https://www.pewresearch.org/science/2020/12/03/intent-to-get-a-covid-19-](https://www.pewresearch.org/science/2020/12/03/intent-to-get-a-covid-19-vaccine/)

[vaccine-rises-to-60-as-confidence-in-research-and-development-process-increases/](#) (2020).

42. 42.

Li, M., Taylor, E. G., Atkins, K. E., Chapman, G. B. & Galvani, A. P. Stimulating influenza vaccination via prosocial motives. *PLoS ONE* **11**, e0159780 (2016).

43. 43.

Grant, A. M. & Hofmann, D. A. It's not all about me: motivating hand hygiene among health care professionals by focusing on patients. *Psychol. Sci.* **22**, 1494–1499 (2011).

44. 44.

Goldstein, N. J., Martin, S. J. & Cialdini, R. B. *Yes!: 50 Scientifically Proven Ways to Be Persuasive* (Free, 2008).

45. 45.

Imas, A. & Madarasz, K. Mimetic dominance and the economics of exclusion: private goods in public context. *SSRN Electron J.*
<https://doi.org/10.2139/ssrn.3630697> (2020).

46. 46.

Dai, H., Milkman, K. L. & Riis, J. The fresh start effect: temporal landmarks motivate aspirational behavior. *Manage. Sci.* **60**, 2563–2582 (2014).

47. 47.

Dai, H., Milkman, K. L. & Riis, J. Put your imperfections behind you: temporal landmarks spur goal initiation when they signal new beginnings. *Psychol. Sci.* **26**, 1927–1936 (2015).

48. 48.

Cohen, J. *Statistical Power Analysis for the Behavioral Sciences* (2nd ed.) (Lawrence Erlbaum Associates, 1988).

49. 49.

Ben-Shachar, M., Lüdecke, D. & Makowski, D. Effect size: estimation of effect size indices and standardized parameters. *J. Open Source Softw.* **5**, 2815 (2020).

Acknowledgements

Funding support for this research was provided by UCLA Health, Anderson School of Management, Anderson Behavioral Lab and Carnegie Mellon University. We thank UCLA Health, particularly L. Ho, J. Ileto, A. Machalinski, and T. Tieu, for making this research possible; S. Bhargava, K. Brabaw, G. Chapman, N. Goldstein, K. Haggag, I. Hurst, C. Nyungen, K. Milkman, M. Serra-Garcia and K. Shonk for feedback on the paper; and J. Cervantez, M. Lanyon and S. Permut for assistance with this research.

Author information

Author notes

1. These authors contributed equally: Hengchen Dai, Silvia Saccardo

Affiliations

1. Anderson School of Management, University of California, Los Angeles, Los Angeles, CA, USA

Hengchen Dai

2. Department of Social and Decision Sciences, Carnegie Mellon University, Pittsburgh, PA, USA

Silvia Saccardo

3. Department of Medicine, David Geffen School of Medicine, University of California, Los Angeles, Los Angeles, CA, USA

Maria A. Han & Daniel M. Croymans

4. Office of Population Health and Accountable Care, University of California, Los Angeles, Los Angeles, CA, USA

Lily Roh & Naveen Raja

5. Department of Medicine Statistics Core, David Geffen School of Medicine,
University of California, Los Angeles, Los Angeles, CA, USA

Sitaram Vangala

6. Office of Health Informatics and Analytics, University of California, Los
Angeles, Los Angeles, CA, USA

Hardikkumar Modi & Shital Pandya

7. Department of Information Services and Solutions, UCLA Health System, Los
Angeles, CA, USA

Michael Sloyan

Contributions

D.M.C., H.D. and S.S. conceptualized the project; H.D., H.M., S.P., M.S. and S.S. curated the data; H.D., S.S. and S.V. undertook formal analyses; D.M.C. and M.A.H. acquired funding; D.M.C., H.D., S.S., M.A.H., N.R., and L.R. performed the investigations; D.M.C., H.D., S.S. and M.A.H. designed the methodology; D.M.C., H.D. and S.S. administrated the project; D.M.C., H.D. and S.S. supervised the work; H.D., S.S. and S.V. validated the findings; H.D. and S.S. visualized the data; H.D. and S.S. wrote the original draft, and D.M.C., H.D., S.S., M.A.H., H.M., S.P., M.S., L.R., N.R., and S.V. contributed to the review and editing of the paper.

Corresponding author

Correspondence to Daniel M. Croymans.

Ethics declarations

Competing interests

The authors declare no competing interests. The authors did not receive financial or non-financial benefits from UCLA Health or speaking/consulting fees related to any of the interventions presented here.

Additional information

Peer review information *Nature* thanks the anonymous reviewers for their contribution to the peer review of this work.

Publisher's note Springer Nature remains neutral with regard to jurisdictional claims in published maps and institutional affiliations.

Extended data figures and tables

Extended Data Table 1 Randomization check of the first RCT

Extended Data Table 2 Regression-estimated effects of text reminders on appointments and vaccinations at UCLA Health in the first RCT

Extended Data Table 3 Randomization check of the second RCT

Extended Data Table 4 Regression-estimated effects of text reminders on appointments and vaccinations at UCLA Health in the second RCT

Extended Data Table 5 Regression-estimated effects of ownership framing and video-based information intervention in online experiments

Extended Data Table 6 Comparison between the first RCT and online experiments

Extended Data Table 7 Comparison between UCLA Health participants, California residents and Los Angeles County residents

Supplementary information

Supplementary Information

This file contains Supplementary text, Supplementary Methods, Supplementary Figures 1 - 5, Supplementary Tables 1 – 41 and Supplementary References.

Reporting Summary

Video Addressing Vaccine Hesitancy (English Version)

Supplementary Video 1 . This is the English version of the video we developed to address COVID-19 vaccine hesitancy. It was used in the first RCT (presented to patients who did not indicate a preference for Spanish) and online experiments. We based this video on a literature review of vaccine hesitancy and our January 2021 survey of California residents ($N=515$; 'Vaccination Intention Survey' in Methods), which allowed us to identify common misconceptions about COVID-19 and authorized vaccines.

Video Addressing Vaccine Hesitancy (Spanish Version)

Supplementary Video 2 . This is the Spanish version of the video we developed to address COVID-19 vaccine hesitancy. It was used in the first RCT (presented to

patients who indicated a preference for Spanish). We based this video on a literature review of vaccine hesitancy and our January 2021 survey of California residents ($N=515$; 'Vaccination Intention Survey' in Methods), which allowed us to identify common misconceptions about COVID-19 and authorized vaccines. This video is identical to Supplementary Video 1 except that the voice and text here are in Spanish.

Rights and permissions

Open Access This article is licensed under a Creative Commons Attribution 4.0 International License, which permits use, sharing, adaptation, distribution and reproduction in any medium or format, as long as you give appropriate credit to the original author(s) and the source, provide a link to the Creative Commons license, and indicate if changes were made. The images or other third party material in this article are included in the article's Creative Commons license, unless indicated otherwise in a credit line to the material. If material is not included in the article's Creative Commons license and your intended use is not permitted by statutory regulation or exceeds the permitted use, you will need to obtain permission directly from the copyright holder. To view a copy of this license, visit <http://creativecommons.org/licenses/by/4.0/>.

Reprints and Permissions

About this article

Cite this article

Dai, H., Saccardo, S., Han, M.A. *et al.* Behavioural nudges increase COVID-19 vaccinations. *Nature* **597**, 404–409 (2021). <https://doi.org/10.1038/s41586-021-03843-2>

- Received: 01 April 2021
- Accepted: 21 July 2021
- Published: 02 August 2021
- Issue Date: 16 September 2021
- DOI: <https://doi.org/10.1038/s41586-021-03843-2>

Share this article

Anyone you share the following link with will be able to read this content:

[Get shareable link](#)

Sorry, a shareable link is not currently available for this article.

[Copy to clipboard](#)

Provided by the Springer Nature SharedIt content-sharing initiative

Further reading

- [**Text-message nudges encourage COVID vaccination**](#)

- Mitesh S. Patel

Nature (2021)

- [**A simple text has the power to increase COVID vaccinations**](#)

- Max Kozlov

Nature (2021)

[**A simple text has the power to increase COVID vaccinations**](#)

- Max Kozlov

News 02 Aug 2021

[**Text-message nudges encourage COVID vaccination**](#)

- Mitesh S. Patel

News & Views 02 Aug 2021

This article was downloaded by **calibre** from <https://www.nature.com/articles/s41586-021-03843-2>

- Article
- [Published: 18 August 2021](#)

Neuro-mesenchymal units control ILC2 and obesity via a brain–adipose circuit

- [Filipa Cardoso^{1,2}](#),
- [Roel G. J. Klein Wolterink¹](#),
- [Cristina Godinho-Silva¹](#),
- [Rita G. Domingues¹](#) nAffs,
- [Hélder Ribeiro](#) ORCID: orcid.org/0000-0002-7090-9274¹,
- [Joaquim Alves da Silva](#) ORCID: orcid.org/0000-0002-3967-3603¹,
- [Inês Mahú](#) ORCID: orcid.org/0000-0001-9215-7598³,
- [Ana I. Domingos⁴](#) &
- [Henrique Veiga-Fernandes](#) ORCID: orcid.org/0000-0001-6216-1836¹

Nature volume **597**, pages 410–414 (2021)

- 10k Accesses
- 228 Altmetric
- [Metrics details](#)

Subjects

- [Innate lymphoid cells](#)
- [Neuroimmunology](#)

Abstract

Signals from sympathetic neurons and immune cells regulate adipocytes and thereby contribute to fat tissue biology. Interactions between the nervous and immune systems have recently emerged as important regulators of host defence and inflammation^{1,2,3,4}. Nevertheless, it is unclear whether neuronal and immune cells co-operate in brain–body axes to orchestrate metabolism and obesity. Here we describe a neuro-mesenchymal unit that controls group 2 innate lymphoid cells (ILC2s), adipose tissue physiology, metabolism and obesity via a brain–adipose circuit. We found that sympathetic nerve terminals act on neighbouring adipose mesenchymal cells via the β 2-adrenergic receptor to control the expression of glial-derived neurotrophic factor (GDNF) and the activity of ILC2s in gonadal fat. Accordingly, ILC2-autonomous manipulation of the GDNF receptor machinery led to alterations in ILC2 function, energy expenditure, insulin resistance and propensity to obesity. Retrograde tracing and chemical, surgical and chemogenetic manipulations identified a sympathetic aorticorenal circuit that modulates ILC2s in gonadal fat and connects to higher-order brain areas, including the paraventricular nucleus of the hypothalamus. Our results identify a neuro-mesenchymal unit that translates cues from long-range neuronal circuitry into adipose-resident ILC2 function, thereby shaping host metabolism and obesity.

Access options

Subscribe to Journal

Get full journal access for 1 year

\$199.00

only \$3.90 per issue

[Subscribe](#)

All prices are NET prices.
VAT will be added later in the checkout.

Tax calculation will be finalised during checkout.

Rent or Buy article

Get time limited or full article access on ReadCube.

from \$8.99

[Rent or Buy](#)

All prices are NET prices.

Additional access options:

- [Log in](#)
- [Access through your institution](#)
- [Learn about institutional subscriptions](#)

Fig. 1: Sympathetic–mesenchyme interactions control ILC2s in the GAT.

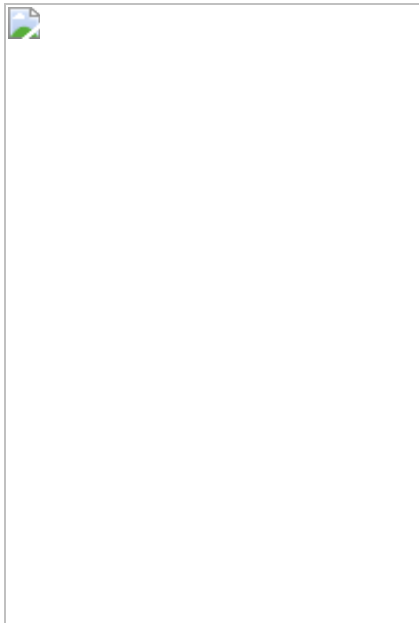


Fig. 2: Sympathetic cues orchestrate mesenchyme-derived GDNF and innate type 2 cytokines.

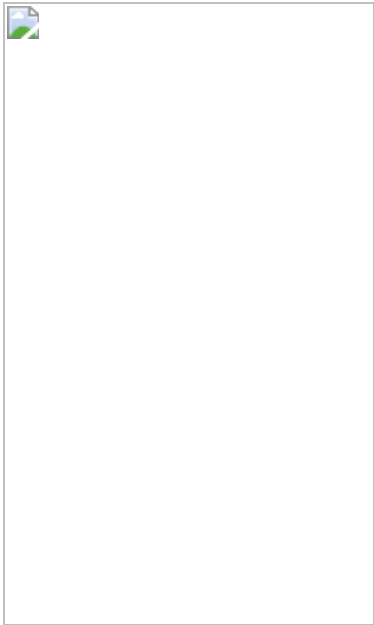


Fig. 3: ILC2-intrinsic RET cues control adipose tissue physiology and obesity.

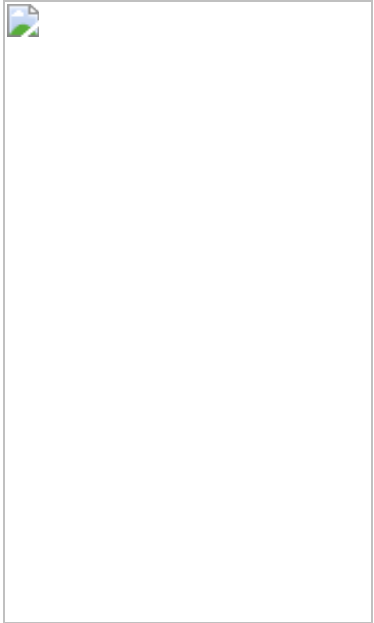
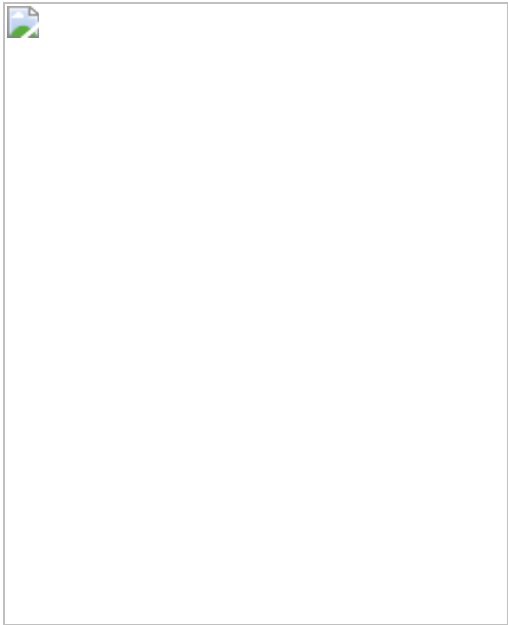


Fig. 4: An aorticorenal–adipose circuit connects to the brain and regulates ILC2.



Data availability

Source data for quantifications shown in all graphs plotted in figures and extended data figures are available in the online version of the paper. The datasets generated in this study are also available from the corresponding author upon reasonable request. The RNA-seq datasets analysed are publicly available in the Gene Expression Omnibus repository with the accession numbers [GSE179546](#) and [GSE179551](#) for MSCs and ILC2s, respectively. [Source data](#) are provided with this paper.

References

1. 1.

Godinho-Silva, C., Cardoso, F. & Veiga-Fernandes, H. Neuro-immune cell units: a new paradigm in physiology. *Annu. Rev. Immunol.* **37**, 19–46 (2019).

2. 2.

Huh, J. R. & Veiga-Fernandes, H. Neuroimmune circuits in inter-organ communication. *Nat. Rev. Immunol.* **20**, 217–228 (2020).

3. 3.

Veiga-Fernandes, H. & Artis, D. Neuronal-immune system cross-talk in homeostasis. *Science* **359**, 1465–1466 (2018).

4. 4.

Chu, C., Artis, D. & Chiu, I. M. Neuro-immune interactions in the tissues. *Immunity* **52**, 464–474 (2020).

5. 5.

Bartness, T. J., Vaughan, C. H. & Song, C. K. Sympathetic and sensory innervation of brown adipose tissue. *Int. J. Obes.* **34** (Suppl. 1), S36–S42 (2010).

6. 6.

Morrison, S. F. Central neural control of thermoregulation and brown adipose tissue. *Auton. Neurosci.* **196**, 14–24 (2016).

7. 7.

Zeng, W. et al. Sympathetic neuro-adipose connections mediate leptin-driven lipolysis. *Cell* **163**, 84–94 (2015).

8. 8.

Moro, K. et al. Innate production of T_H2 cytokines by adipose tissue-associated c-Kit⁺Sca-1⁺ lymphoid cells. *Nature* **463**, 540–544 (2010).

9. 9.

Brestoff, J. R. et al. Group 2 innate lymphoid cells promote browning of white adipose tissue and limit obesity. *Nature* **519**, 242–246 (2015).

10. 10.

Hams, E. et al. The helminth T2 RNase ω 1 promotes metabolic homeostasis in an IL-33- and group 2 innate lymphoid cell-dependent mechanism. *FASEB J.* **30**, 824–835 (2016).

11. 11.

Lee, M. W. et al. Activated type 2 innate lymphoid cells regulate beige fat biogenesis. *Cell* **160**, 74–87 (2015).

12. 12.

Molofsky, A. B. et al. Innate lymphoid type 2 cells sustain visceral adipose tissue eosinophils and alternatively activated macrophages. *J. Exp. Med.* **210**, 535–549 (2013).

13. 13.

Vivier, E. et al. Innate lymphoid cells: 10 years on. *Cell* **174**, 1054–1066 (2018).

14. 14.

Arighi, E., Borrello, M. G. & Sariola, H. RET tyrosine kinase signaling in development and cancer. *Cytokine Growth Factor Rev.* **16**, 441–467 (2005).

15. 15.

Mulligan, L. M. RET revisited: expanding the oncogenic portfolio. *Nat. Rev. Cancer* **14**, 173–186 (2014).

16. 16.

Fonseca-Pereira, D. et al. The neurotrophic factor receptor RET drives haematopoietic stem cell survival and function. *Nature* **514**, 98–101 (2014).

17. 17.

Ibiza, S. et al. Glial-cell-derived neuroregulators control type 3 innate lymphoid cells and gut defence. *Nature* **535**, 440–443 (2016).

18. 18.

Patel, A. et al. Differential RET signaling pathways drive development of the enteric lymphoid and nervous systems. *Sci. Signal.* **5**, ra55 (2012).

19. 19.

Veiga-Fernandes, H. et al. Tyrosine kinase receptor RET is a key regulator of Peyer's patch organogenesis. *Nature* **446**, 547–551 (2007).

20. 20.

Kahn, B. B. & Flier, J. S. Obesity and insulin resistance. *J. Clin. Invest.* **106**, 473–481 (2000).

21. 21.

Qiu, Y. et al. Eosinophils and type 2 cytokine signaling in macrophages orchestrate development of functional beige fat. *Cell* **157**, 1292–1308 (2014).

22. 22.

Morrison, S. F., Madden, C. J. & Tupone, D. Central neural regulation of brown adipose tissue thermogenesis and energy expenditure. *Cell Metab.* **19**, 741–756 (2014).

23. 23.

Sutton, A. K., Myers, M. G., Jr & Olson, D. P. The role of PVH circuits in leptin action and energy balance. *Annu. Rev. Physiol.* **78**, 207–221 (2016).

24. 24.

Mahlakõiv, T. et al. Stromal cells maintain immune cell homeostasis in adipose tissue via production of interleukin-33. *Sci. Immunol.* **4**, eaax0416 (2019).

25. 25.

Rana, B. M. J. et al. A stromal cell niche sustains ILC2-mediated type-2 conditioning in adipose tissue. *J. Exp. Med.* **216**, 1999–2009 (2019).

26. 26.

Spallanzani, R. G. et al. Distinct immunocyte-promoting and adipocyte-generating stromal components coordinate adipose tissue immune and metabolic tenors. *Sci. Immunol.* **4**, eaaw3658 (2019).

27. 27.

Ding, X. et al. IL-33-driven ILC2/eosinophil axis in fat is induced by sympathetic tone and suppressed by obesity. *J. Endocrinol.* **231**, 35–48 (2016).

28. 28.

Moriyama, S. et al. β_2 -adrenergic receptor-mediated negative regulation of group 2 innate lymphoid cell responses. *Science* **359**, 1056–1061 (2018).

29. 29.

Andersen, C. J., Murphy, K. E. & Fernandez, M. L. Impact of obesity and metabolic syndrome on immunity. *Adv. Nutr.* **7**, 66–75 (2016).

30. 30.

Guilherme, A., Henriques, F., Bedard, A. H. & Czech, M. P. Molecular pathways linking adipose innervation to insulin action in obesity and diabetes mellitus. *Nat. Rev. Endocrinol.* **15**, 207–225 (2019).

31. 31.

Zhuo, L. et al. hGFAP-cre transgenic mice for manipulation of glial and neuronal function in vivo. *Genesis* **31**, 85–94 (2001).

32. 32.

Roesch, K. et al. The transcriptome of retinal Müller glial cells. *J. Comp. Neurol.* **509**, 225–238 (2008).

33. 33.

de Boer, J. et al. Transgenic mice with hematopoietic and lymphoid specific expression of Cre. *Eur. J. Immunol.* **33**, 314–325 (2003).

34. 34.

Schlenger, S. M. et al. Fate mapping reveals separate origins of T cells and myeloid lineages in the thymus. *Immunity* **32**, 426–436 (2010).

35. 35.

Nussbaum, J. C. et al. Type 2 innate lymphoid cells control eosinophil homeostasis. *Nature* **502**, 245–248 (2013).

36. 36.

Savitt, J. M., Jang, S. S., Mu, W., Dawson, V. L. & Dawson, T. M. Bcl-x is required for proper development of the mouse substantia nigra. *J. Neurosci.* **25**, 6721–6728 (2005).

37. 37.

Hinoi, E. et al. The sympathetic tone mediates leptin's inhibition of insulin secretion by modulating osteocalcin bioactivity. *J. Cell Biol.* **183**, 1235–1242 (2008).

38. 38.

Mombaerts, P. et al. RAG-1-deficient mice have no mature B and T lymphocytes. *Cell* **68**, 869–877 (1992).

39. 39.

Cao, X. et al. Defective lymphoid development in mice lacking expression of the common cytokine receptor gamma chain. *Immunity* **2**, 223–238 (1995).

40. 40.

Smith-Hicks, C. L., Sizer, K. C., Powers, J. F., Tischler, A. S. & Costantini, F. C-cell hyperplasia, pheochromocytoma and sympathoadrenal malformation in a mouse model of multiple endocrine neoplasia type 2B. *EMBO J.* **19**, 612–622 (2000).

41. 41.

Madisen, L. et al. A robust and high-throughput Cre reporting and characterization system for the whole mouse brain. *Nat. Neurosci.* **13**, 133–140 (2010).

42. 42.

Sciolino, N. R. et al. Recombinase-dependent mouse lines for chemogenetic activation of genetically defined cell types. *Cell Rep.* **15**, 2563–2573 (2016).

43. 43.

Buch, T. et al. A Cre-inducible diphtheria toxin receptor mediates cell lineage ablation after toxin administration. *Nat. Methods* **2**, 419–426 (2005).

44. 44.

Almeida, A. R. et al. RET/GFR α signals are dispensable for thymic T cell development in vivo. *PLoS One* **7**, e52949 (2012).

45. 45.

Enomoto, H. et al. GFR alpha1-deficient mice have deficits in the enteric nervous system and kidneys. *Neuron* **21**, 317–324 (1998).

46. 46.

Rossi, J. et al. Retarded growth and deficits in the enteric and parasympathetic nervous system in mice lacking GFR alpha2, a functional neurturin receptor. *Neuron* **22**, 243–252 (1999).

47. 47.

Nishino, J. et al. GFR alpha3, a component of the artemin receptor, is required for migration and survival of the superior cervical ganglion. *Neuron* **23**, 725–736 (1999).

48. 48.

Godinho-Silva, C. et al. Light-entrained and brain-tuned circadian circuits regulate ILC3s and gut homeostasis. *Nature* **574**, 254–258 (2019).

49. 49.

Botta, P. et al. An amygdala circuit mediates experience-dependent momentary arrests during exploration. *Cell* **183**, 605–619.e22 (2020).

50. 50.

Pereira, M. M. et al. A brain-sparing diphtheria toxin for chemical genetic ablation of peripheral cell lineages. *Nat. Commun.* **8**, 14967 (2017).

51. 51.

Zhu, H. & Roth, B. L. Silencing synapses with DREADDs. *Neuron* **82**, 723–725 (2014).

52. 52.

Leggett, R. M., Ramirez-Gonzalez, R. H., Clavijo, B. J., Waite, D. & Davey, R. P. Sequencing quality assessment tools to enable data-driven informatics for high throughput genomics. *Front. Genet.* **4**, 288 (2013).

53. 53.

Bolger, A. M., Lohse, M. & Usadel, B. Trimmomatic: a flexible trimmer for Illumina sequence data. *Bioinformatics* **30**, 2114–2120 (2014).

54. 54.

Dobin, A. et al. STAR: ultrafast universal RNA-seq aligner. *Bioinformatics* **29**, 15–21 (2013).

55. 55.

McCarthy, D. J., Chen, Y. & Smyth, G. K. Differential expression analysis of multifactor RNA-seq experiments with respect to biological variation. *Nucleic Acids Res.* **40**, 4288–4297 (2012).

56. 56.

Love, M. I., Huber, W. & Anders, S. Moderated estimation of fold change and dispersion for RNA-seq data with DESeq2. *Genome Biol.* **15**, 550 (2014).

57. 57.

Ebihara, T. & Taniuchi, I. Transcription factors in the development and function of group 2 innate lymphoid cells. *Int. J. Mol. Sci.* **20**, 1377 (2019).

58. 58.

Grieger, J. C., Choi, V. W. & Samulski, R. J. Production and characterization of adeno-associated viral vectors. *Nat. Protocols* **1**, 1412–1428 (2006).

59. 59.

Huang, X. et al. AAV2 production with optimized N/P ratio and PEI-mediated transfection results in low toxicity and high titer for in vitro and in vivo applications. *J. Virol. Methods* **193**, 270–277 (2013).

60. 60.

Paxinos, G. & Franklin, K. B. J. *The Mouse Brain in Stereotaxic Coordinates* 2nd edition (Academic, 2001).

61. 61.

Huang, J. et al. A cationic near infrared fluorescent agent and ethyl-cinnamate tissue clearing protocol for vascular staining and imaging. *Sci. Rep.* **9**, 521 (2019).

Acknowledgements

We thank the Vivarium, Flow Cytometry, Histopathology, Molecular Biology and Hardware platforms at the Champalimaud Centre for the Unknown. We thank Congento LISBOA-01-0145-FEDER-022170, co-financed by FCT (Portugal) and Lisboa2020, under the PORTUGAL2020 agreement (European Regional Development Fund). pAAV-Ef1a-mCherry-IRES-Cre was a gift from K. Deisseroth. PRV-614 (PRV-Bartha) was a gift from L. Enquist and E. Engel. F.C., C.G.-S., and R.G.D. were supported by Fundação para a Ciência e Tecnologia (FCT), Portugal. R.G.J.K.W. is supported by a Marie Skłodowska-Curie Individual fellowship (European Commission, 799810-TOPNIN), a Cancer Research Institute/Irvington Postdoctoral Fellowship and a Postdoctoral Junior Leader fellowship from la Caixa Foundation, ID100010434; LCF/BQ/PR20/11770004. H.V.-F. is supported by ERC (647274), EU, The Paul G. Allen Frontiers Group, US, and FCT, Portugal.

Author information

Author notes

1. Rita G. Domingues

Present address: Lydia Becker Institute of Immunology and Inflammation, Manchester Collaborative Centre for Inflammation Research (MCCIR), Division of Infection, Immunity and Respiratory Medicine, Faculty of Biology, Medicine and Health, University of Manchester, Manchester, UK

Affiliations

1. Champalimaud Research, Champalimaud Centre for the Unknown, Lisbon, Portugal

Filipa Cardoso, Roel G. J. Klein Wolterink, Cristina Godinho-Silva, Rita G. Domingues, Hélder Ribeiro, Joaquim Alves da Silva & Henrique Veiga-Fernandes

2. Faculdade de Medicina, Universidade de Lisboa, Lisboa, Portugal

Filipa Cardoso

3. Max Planck Institute for Metabolism Research, Köln, Germany

Inês Mahú

4. Department of Physiology, Anatomy & Genetics, Oxford University, Oxford, UK

Ana I. Domingos

Contributions

F.C. designed, performed and analysed the experiments shown in Fig. 1–4 and Extended Data Fig. 1–9. R.G.J.K.W. performed the clearing and imaging in Fig. 1a, and the viral tracing and manipulation experiments in Fig. 4 and Extended Data Fig. 8. C.G.-S. and R.G.D. performed the electroablation surgeries in Extended Data Fig. 8. H.R. provided assistance for the experiments shown in Figs. 1–4. A.I.D. and I. M. provided technical

help for the experiment shown in Fig. [1c](#). J.A.d.S. provided help for the experiment in Extended Data Fig. [2d](#), [e](#). H.V.-F. supervised the work, planned the experiments and wrote the manuscript.

Corresponding author

Correspondence to Henrique Veiga-Fernandes.

Ethics declarations

Competing interests

The authors declare no competing interests.

Additional information

Peer review information *Nature* thanks John Horn and the other, anonymous, reviewer(s) for their contribution to the peer review of this work.

Publisher's note Springer Nature remains neutral with regard to jurisdictional claims in published maps and institutional affiliations.

Extended data figures and tables

[Extended Data Fig. 1 Gating strategy for ILC2s and MSCs.](#)

a, ILC2s were defined as: live CD45⁺Lin⁻Thy1.2⁺Sca-1⁺KLRG1⁺ (lineage comprised CD3ε, CD8α, TCRβ, TCRγδ, CD19, GR1, CD11c, CD11b and TER119). **b**, Stroma cells were defined as: live PDGFRA⁺ MSCs (CD45⁻CD31⁻PDGFRA⁺gp38⁺SCa-1⁺), PDGFRA⁻ MSCs (CD45⁻CD31⁻PDGFRA⁻gp38⁺), and endothelial cells (CD45⁻CD31⁺).

[Extended Data Fig. 2 Sympathetic nervous system in the GAT and ILC2 function.](#)

a, GAT. Red, sympathetic nerve fibres (TH); Green, endothelial cells (CD31). Scale bar, 300 μ m. **b**, GAT ILC2-derived Met-enk after 6-OHDA administration. $n = 5$. **c**, CD4 T cells and TH⁺ CD4 T cells after 6-OHDA administration. $n = 4$. **d, e**, Distance covered by mice in the open field test. $n = 3$. Scale bar, 10 cm. **f**, GAT ILC2-derived Met-enk after clenbuterol administration. $n = 5$. **g**, Heatmap of *Adrb1*, *Adrb2*, and *Adrb3* expression (read counts (fragments per kilobase of transcript per million mapped reads; FPKM) on ILC2s, $n = 4$). **h**, GAT ILC2s after CNO administration. *R26/3D^{fl}* $n = 4$, *R26Th* $n = 4$, and *R26/3DTh* $n = 5$. **i**, Heatmap of *Adrb1*, *Adrb2*, and *Adrb3* expression (read counts (transcripts per million; TPM) on MSCs, $n = 4$). **j**, *Gdnf* expression after in vitro stimulation of MSCs, $n = 3$. Data are representative of three independent experiments. n represents biologically independent animals. Data are presented as mean \pm s.e.m. Two-tailed unpaired Welch's *t*-test. * $P < 0.05$; *** $P < 0.005$; ns, not significant

[Source data](#).

Extended Data Fig. 3 Sympathetic regulation of GAT MSCs.

a, Heatmap of genes upregulated in MSCs upon 6-OHDA administration. Vehicle $n = 4$, 6-OHDA $n = 5$. **b**, GAT *Il33* expression after 6-OHDA treatment. $n = 5$. **c**, GAT *Il33* expression after clenbuterol administration. $n = 5$. **d**, MSC-derived *Il33* after 6-OHDA and clenbuterol administration. $n = 6$. **e**, MSC-derived *Il25* after 6-OHDA and clenbuterol administration. $n = 6$. **f**, GDNF on MSCs. *Adrb2^{fl}* $n = 6$, *Adrb2^{ΔPdgfra}* $n = 4$. Data are representative of three independent experiments. n represents biologically independent animals. Data are presented as mean \pm s.e.m. Two-tailed unpaired Welch's *t*-test. ns, not significant

[Source data](#).

Extended Data Fig. 4 RET signals do not affect ILC2 differentiation and activation genes.

a, b, Heatmaps showing log(raw counts) of ILC2-related genes in ILC2s from *Ret^{fl}* ($n = 4$) and *Ret^{ΔVav1}* ($n = 5$) mice (**a**) and *Rag1^{-/-}Ret^{WT}* ($n = 3$)

and $Rag1^{-/-}Ret^{MEN2B}$ ($n = 3$) mice (b)

[Source data](#).

Extended Data Fig. 5 ILC2-autonomous RET signals control type 2 innate cytokines in the GAT.

a–c, GAT ILC2 function. **a**, $Gfra1^{-/-}$ fetal liver chimeras. $n = 5$. **b**, $Gfra2^{+/+}$, $n = 10$; $Gfra2^{-/-}$, $n = 5$. **c**, $Gfra^{+/+}$, $n = 8$; $Gfra3^{-/-}$, $n = 8$. **d**, Ret^{AVav1} mixed BM chimeras scheme. **e**, GAT ILC2 from Ret^{AVav1} mixed BM chimeras. Ret^{fl} $n = 6$; Ret^{AVav1} $n = 7$. **f**, ILC2s from $Rag1^{-/-}Ret^{WT}$ ($n = 6$) and $Rag1^{-/-}Ret^{All5}$ ($n = 6$) mice. **g**, ILC2s from Ret^{WT} ($n = 10$) and Ret^{All5} ($n = 8$) mice. **h**, Ret^{All5} mixed bone marrow (BM) chimeras scheme. **i**, GAT ILC2 from Ret^{All5} mixed BM chimeras. Ret^{WT} $n = 4$, Ret^{All5} $n = 4$. **j**, GAT ILC2s in $Rag1^{-/-}Ret^{MEN2B}$ BM chimeras. $Rag1^{-/-}Ret^{WT}$ $n = 5$, $Rag1^{-/-}Ret^{MEN2B}$ $n = 6$. **k**, Ret^{MEN2B} mixed BM chimeras scheme. **l**, Mixed BM chimeras. $Rag1^{-/-}Ret^{WT}$ $n = 6$, $Rag1^{-/-}Ret^{MEN2B}$ $n = 7$. Data are representative of three independent experiments. n represents biologically independent animals. Data are presented as mean \pm s.e.m. Two-tailed unpaired Welch's *t*-test. * $P < 0.05$; ** $P < 0.01$; *** $P < 0.005$; ns, not significant

[Source data](#).

Extended Data Fig. 6 ILC2-intrinsic RET signalling is sufficient to control adipocyte physiology and obesity.

a, GAT ILC2s after 6-OHDA administration. Ret^{WT} $n = 8$ and Ret^{All5} $n = 7$. **b**, Weight gain during 16 weeks of HFD regimen. $Rag1^{-/-}Ret^{WT}$ $n = 4$, $Rag1^{-/-}Ret^{All5}$ $n = 5$. **c**, Intestinal lamina propria ILC3s. $Rag1^{-/-}Ret^{WT}$ $n = 5$, $Rag1^{-/-}Ret^{All5}$ $n = 5$. **d**, Weight gain during 16 weeks of HFD regimen. Ret^{WT} $n = 5$, Ret^{All5} $n = 5$. **e**, Frequency of ILC2 and ILC3 in Thy $^+$ Lin $^-$ lymphocytes from ILC2-chimeric mice after HFD. Each bar represents one mouse. $n = 4$. **f**, Total GAT RNA expression of *Ucp1*, *Cox8b* and *Cidea*. $n = 5$. Data are presented as mean \pm s.e.m. Two-tailed unpaired

Welch's *t*-test (**a, c, e**); repeated measures ANOVA corrected for multiple comparisons with the Benjamini, Krieger and Yekutieli procedure (**b, d**); and Mann–Whitney test (**f**). **P* < 0.05; ***P* < 0.01; ns, not significant

[Source data](#).

[Extended Data Fig. 7 RET signals control adipose tissue energy expenditure.](#)

Total RNA expression of adipose tissue-related genes in GAT. **a**, *Ret*^{fl} *n* = 4; *Ret*^{AVav1} *n* = 6. **b**, *Rag1*^{−/−}*Ret*^{WT} *n* = 4; *Rag1*^{−/−}*Ret*^{MEN2B} *n* = 5. **c**, GAT co-cultures scheme. **d**, GAT co-cultures with ILC2 and GDNF. Data are presented as mean ± s.e.m. Two-sided Mann–Whitney test. **P* < 0.05; ns, not significant

[Source data](#).

[Extended Data Fig. 8 An aorticorenal–adipose circuit connects to the brain.](#)

a, DRG at thoracic 13 (T13) level. Green, viral tracing (VT); red, TH. Scale bar, 100 μm. **b**, Left, brain atlas schemes of coronal sections. Right, polysynaptic tracing from the GAT corresponding to the highlighted areas on the left. **c**, Left, brain atlas schemes of coronal section. Right, polysynaptic tracing from the ARG corresponding to the highlighted areas on the left. **b, c**, Central amygdala (CA), zona incerta (ZI), periaqueductal grey (PAG), subcoeruleus nucleus (SubCD). Scale bars, 200 μm. **d**, Electrolytic lesion of the PVH. Scale bar, 500 μm. **e**, GAT ILC2s in PVH-ablated mice. Sham *n* = 5; PVH-ablated *n* = 6. **f**, GAT *Il33* expression in AAV(4D) mice compared to contralateral controls after CNO administration. *n* = 5. **g**, GAT *Il33* expression in AAV(3D) mice compared to contralateral control after CNO administration. *n* = 4. **h**, Scheme of combinatorial viral approach. The ARG was injected with an AAV carrying a Cre construct (AAV-Cre). Next, the GAT was injected with a Cre-inducible AAV(3D^{fl}). AAV(Cre) *n* = 7 and AAV(Cre)+AAV(3D^{fl}) *n* = 6. Data are representative of three independent experiments. *n* represents

biologically independent animals. Data are presented as mean \pm s.e.m. Two-tailed unpaired *t*-test (**e**); two-tailed Mann–Whitney test (**f, g**); two-tailed unpaired Welch’s *t*-test (**h**). * $P < 0.05$; ** $P < 0.01$; ns, not significant

[Source data](#).

Extended Data Fig. 9 A sympathetic aorticorenal–adipose circuit connects to the brain and regulates ILC2s.

GAT neuro-mesenchymal units translate sympathetic cues into neurotrophic factor expression. In turn, neurotrophic factors control adipose ILC2 function via the neuroregulatory receptor RET, shaping the host metabolism, energy expenditure and obesity. SNS, sympathetic nervous system.

Supplementary information

[**Reporting Summary**](#)

Source data

[**Source Data Fig. 1**](#)

[**Source Data Fig. 2**](#)

[**Source Data Fig. 3**](#)

[**Source Data Fig. 4**](#)

[**Source Data Extended Data Fig. 2**](#)

[**Source Data Extended Data Fig. 3**](#)

[**Source Data Extended Data Fig. 4**](#)

[**Source Data Extended Data Fig. 5**](#)

[**Source Data Extended Data Fig. 6**](#)

[**Source Data Extended Data Fig. 7**](#)

[**Source Data Extended Data Fig. 8**](#)

Rights and permissions

[Reprints and Permissions](#)

About this article

Cite this article

Cardoso, F., Klein Wolterink, R.G.J., Godinho-Silva, C. *et al.* Neuro-mesenchymal units control ILC2 and obesity via a brain–adipose circuit. *Nature* **597**, 410–414 (2021). <https://doi.org/10.1038/s41586-021-03830-7>

- Received: 05 November 2020
- Accepted: 16 July 2021
- Published: 18 August 2021
- Issue Date: 16 September 2021
- DOI: <https://doi.org/10.1038/s41586-021-03830-7>

Share this article

Anyone you share the following link with will be able to read this content:

[Get shareable link](#)

Sorry, a shareable link is not currently available for this article.

[Copy to clipboard](#)

Provided by the Springer Nature SharedIt content-sharing initiative

This article was downloaded by **calibre** from <https://www.nature.com/articles/s41586-021-03830-7>

| [Section menu](#) | [Main menu](#) |

- Article
- [Published: 01 September 2021](#)

AIM2 forms a complex with pyrin and ZBP1 to drive PANoptosis and host defence

- [SangJoon Lee¹](#),
- [Rajendra Karki](#) ORCID: [orcid.org/0000-0003-4436-9128¹](https://orcid.org/0000-0003-4436-9128),
- [Yaqiu Wang¹](#),
- [Lam Nhat Nguyen¹](#),
- [Ravi C. Kalathur](#) ORCID: [orcid.org/0000-0002-4889-8003²](https://orcid.org/0000-0002-4889-8003) &
- [Thirumala-Devi Kanneganti](#) ORCID: [orcid.org/0000-0002-6395-6443¹](https://orcid.org/0000-0002-6395-6443)

[Nature](#) volume 597, pages 415–419 (2021)

- 7607 Accesses
- 86 Altmetric
- [Metrics details](#)

Subjects

- [Infection](#)
- [Innate immunity](#)

Abstract

Inflammasomes are important sentinels of innate immune defence, sensing pathogens and inducing cell death in infected cells¹. There are several inflammasome sensors that each detect and respond to a specific pathogen- or damage-associated molecular pattern (PAMP or DAMP, respectively)¹. During infection, live pathogens can induce the release of multiple PAMPs and DAMPs, which can simultaneously engage multiple inflammasome sensors^{2,3,4,5}. Here we found that AIM2 regulates the innate immune sensors pyrin and ZBP1 to drive inflammatory signalling and a form of inflammatory cell death known as PANoptosis, and provide host protection during infections with herpes simplex virus 1 and *Francisella novicida*. We also observed that AIM2, pyrin and ZBP1 were members of a large multi-protein complex along with ASC, caspase-1, caspase-8, RIPK3, RIPK1 and FADD, that drove inflammatory cell death (PANoptosis). Collectively, our findings define a previously unknown regulatory and molecular interaction between AIM2, pyrin and ZBP1 that drives assembly of an AIM2-mediated multi-protein complex that we term the AIM2 PANoptosome and comprising multiple inflammasome sensors and cell death regulators. These results advance the understanding of the functions of these molecules in innate immunity and inflammatory cell death, suggesting new therapeutic targets for AIM2-, ZBP1- and pyrin-mediated diseases.

Access options

Subscribe to Journal

Get full journal access for 1 year

\$199.00

only \$3.90 per issue

[Subscribe](#)

All prices are NET prices.

VAT will be added later in the checkout.

Tax calculation will be finalised during checkout.

Rent or Buy article

Get time limited or full article access on ReadCube.

from \$8.99

[Rent or Buy](#)

All prices are NET prices.

Additional access options:

- [Log in](#)
- [Access through your institution](#)
- [Learn about institutional subscriptions](#)

Fig. 1: HSV1 induces AIM2-, pyrin- and ZBP1-mediated caspase-1 activation, cytokine release and cell death.

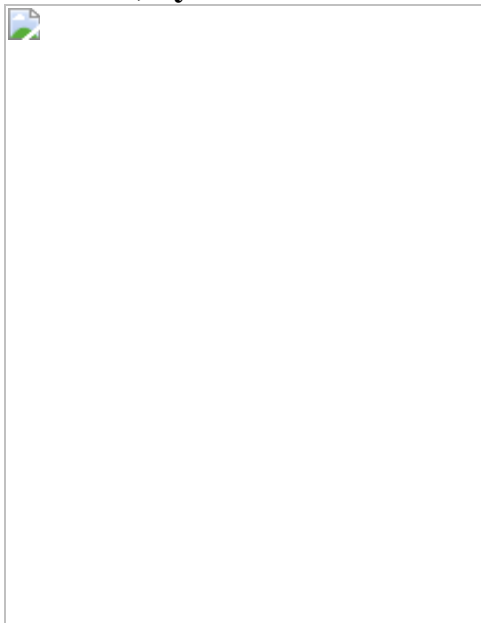


Fig. 2: ZBP1 cooperates with pyrin to drive AIM2-mediated caspase-1 activation, cytokine release and cell death.

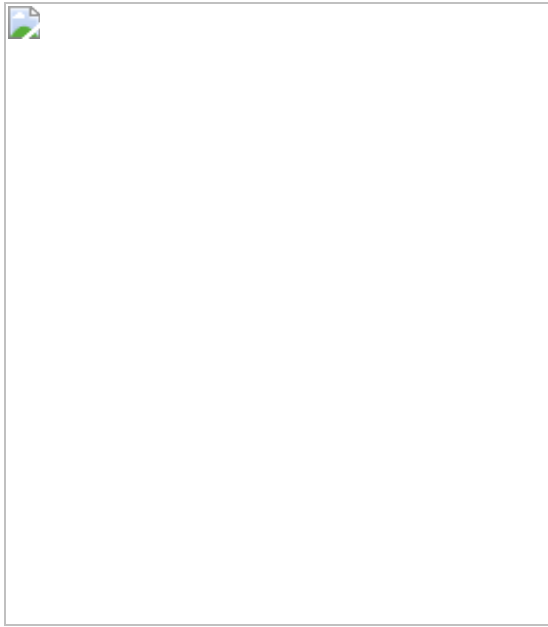


Fig. 3: AIM2, pyrin and ZBP1 promote inflammatory cell death in response to HSV1 and *F. novicida* infections.

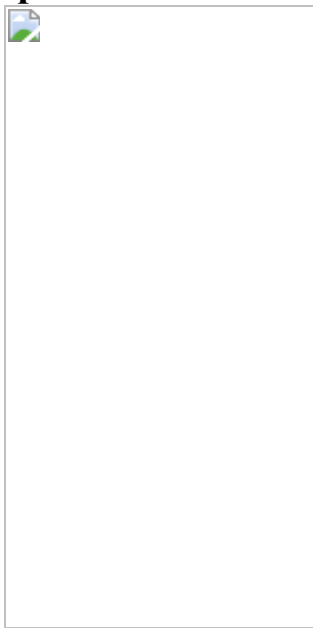


Fig. 4: AIM2-mediated signalling acts as an upstream regulator of pyrin and ZBP1, which are required to form the AIM2 PANoptosome.



Data availability

The datasets generated and analysed during the current study are contained within the manuscript and the accompanying extended data figures. [Source data](#) are provided with this paper.

References

1. 1.

Man, S. M., Karki, R. & Kanneganti, T. D. Molecular mechanisms and functions of pyroptosis, inflammatory caspases and inflammasomes in infectious diseases. *Immunol. Rev.* **277**, 61–75 (2017).

2. 2.

Karki, R. et al. Concerted activation of the AIM2 and NLRP3 inflammasomes orchestrates host protection against *Aspergillus* infection. *Cell Host Microbe* **17**, 357–368 (2015).

3. 3.

Broz, P. et al. Redundant roles for inflammasome receptors NLRP3 and NLRC4 in host defense against *Salmonella*. *J. Exp. Med.* **207**, 1745–1755 (2010).

4. 4.

Man, S. M. et al. Inflammasome activation causes dual recruitment of NLRC4 and NLRP3 to the same macromolecular complex. *Proc. Natl Acad. Sci. USA* **111**, 7403–7408 (2014).

5. 5.

Kalantari, P. et al. Dual engagement of the NLRP3 and AIM2 inflammasomes by plasmodium-derived hemozoin and DNA during malaria. *Cell Rep.* **6**, 196–210 (2014).

6. 6.

Man, S. M. et al. The transcription factor IRF1 and guanylate-binding proteins target activation of the AIM2 inflammasome by *Francisella* infection. *Nat. Immunol.* **16**, 467–475 (2015).

7. 7.

Sharma, B. R., Karki, R. & Kanneganti, T. D. Role of AIM2 inflammasome in inflammatory diseases, cancer and infection. *Eur. J. Immunol.* **49**, 1998–2011 (2019).

8. 8.

Lammert, C. R. et al. AIM2 inflammasome surveillance of DNA damage shapes neurodevelopment. *Nature* **580**, 647–652 (2020).

9. 9.

Hornung, V. et al. AIM2 recognizes cytosolic dsDNA and forms a caspase-1-activating inflammasome with ASC. *Nature* **458**, 514–518 (2009).

10. 10.

Rathinam, V. A. et al. The AIM2 inflammasome is essential for host defense against cytosolic bacteria and DNA viruses. *Nat. Immunol.* **11**, 395–402 (2010).

11. 11.

Fernandes-Alnemri, T. et al. The AIM2 inflammasome is critical for innate immunity to *Francisella tularensis*. *Nat. Immunol.* **11**, 385–393 (2010).

12. 12.

Zhu, Q., Man, S. M., Karki, R., Malireddi, R. K. S. & Kanneganti, T. D. Detrimental type i interferon signaling dominates protective AIM2 inflammasome responses during *Francisella novicida* infection. *Cell Rep.* **22**, 3168–3174 (2018).

13. 13.

Maruzuru, Y. et al. Herpes simplex virus 1 VP22 inhibits AIM2-dependent inflammasome activation to enable efficient viral replication. *Cell Host Microbe* **23**, 254–265.e257 (2018).

14. 14.

Kuriakose, T. et al. ZBP1/DAI is an innate sensor of influenza virus triggering the NLRP3 inflammasome and programmed cell death pathways. *Sci. Immunol.* **1**, aag2045 (2016).

15. 15.

Kesavardhana, S. et al. The Z α 2 domain of ZBP1 is a molecular switch regulating influenza-induced PANoptosis and perinatal lethality during development. *J. Biol. Chem.* **295**, 8325–8330 (2020).

16. 16.

Newton, K. et al. RIPK1 inhibits ZBP1-driven necroptosis during development. *Nature* **540**, 129–133 (2016).

17. 17.

Park, Y. H., Wood, G., Kastner, D. L. & Chae, J. J. Pyrin inflammasome activation and RhoA signaling in the autoinflammatory diseases FMF and HIDS. *Nat. Immunol.* **17**, 914–921 (2016).

18. 18.

Gao, W., Yang, J., Liu, W., Wang, Y. & Shao, F. Site-specific phosphorylation and microtubule dynamics control Pyrin inflammasome activation. *Proc. Natl Acad. Sci. USA* **113**, E4857–E4866 (2016).

19. 19.

Xu, H. et al. Innate immune sensing of bacterial modifications of Rho GTPases by the Pyrin inflammasome. *Nature* **513**, 237–241 (2014).

20. 20.

Masters, S. L. et al. Familial autoinflammation with neutrophilic dermatosis reveals a regulatory mechanism of pyrin activation. *Sci. Transl. Med.* **8**, 332ra345 (2016).

21. 21.

Van Gorp, H. et al. Familial Mediterranean fever mutations lift the obligatory requirement for microtubules in Pyrin inflammasome activation. *Proc. Natl Acad. Sci. USA* **113**, 14384–14389 (2016).

22. 22.

Kesavardhana, S. et al. ZBP1/DAI ubiquitination and sensing of influenza vRNPs activate programmed cell death. *J. Exp. Med.* **214**, 2217–2229 (2017).

23. 23.

Place, D. E., Lee, S. & Kanneganti, T. D. PANoptosis in microbial infection. *Curr. Opin. Microbiol.* **59**, 42–49 (2021).

24. 24.

Malireddi, R. K., Ippagunta, S., Lamkanfi, M. & Kanneganti, T. D. Cutting edge: proteolytic inactivation of poly(ADP-ribose) polymerase 1 by the Nlrp3 and Nlrc4 inflammasomes. *J. Immunol.* **185**, 3127–3130 (2010).

25. 25.

Lamkanfi, M. et al. Targeted peptidecentric proteomics reveals caspase-7 as a substrate of the caspase-1 inflammasomes. *Mol. Cell Proteomics* **7**, 2350–2363 (2008).

26. 26.

Lukens, J. R. et al. Dietary modulation of the microbiome affects autoinflammatory disease. *Nature* **516**, 246–249 (2014).

27. 27.

Gurung, P. et al. FADD and caspase-8 mediate priming and activation of the canonical and noncanonical Nlrp3 inflammasomes. *J. Immunol.* **192**, 1835–1846 (2014).

28. 28.

Karki, R. et al. Synergism of TNF- α and IFN- γ triggers inflammatory cell death, tissue damage, and mortality in SARS-CoV-2 infection and cytokine shock syndromes. *Cell* **184**, 149–168.e117 (2021).

29. 29.

Malireddi, R. K. S. et al. Innate immune priming in the absence of TAK1 drives RIPK1 kinase activity-independent pyroptosis, apoptosis,

necroptosis, and inflammatory disease. *J. Exp. Med.* **217**, e20191644 (2020).

30. 30.

Malireddi, R. K. S. et al. TAK1 restricts spontaneous NLRP3 activation and cell death to control myeloid proliferation. *J. Exp. Med.* **215**, 1023–1034 (2018).

31. 31.

Zheng, M., Karki, R., Vogel, P. & Kanneganti, T. D. Caspase-6 is a key regulator of innate immunity, inflammasome activation, and host defense. *Cell* **181**, 674–687.e613 (2020).

32. 32.

Banerjee, I. et al. Gasdermin D restrains type I interferon response to cytosolic DNA by disrupting ionic homeostasis. *Immunity* **49**, 413–426 e415 (2018).

33. 33.

Christgen, S. et al. Identification of the PANoptosome: a molecular platform triggering pyroptosis, apoptosis, and necroptosis (PANoptosis). *Front. Cell Infect. Microbiol.* **10**, 237 (2020).

34. 34.

Sharma, D., Malik, A., Guy, C., Vogel, P. & Kanneganti, T. D. TNF/TNFR axis promotes pyrin inflammasome activation and distinctly modulates pyrin inflammasomopathy. *J. Clin. Invest.* **129**, 150–162 (2019).

35. 35.

Jones, J. W. et al. Absent in melanoma 2 is required for innate immune recognition of *Francisella tularensis*. *Proc. Natl Acad. Sci. USA* **107**, 9771–9776 (2010).

36. 36.

Henry, T., Brotcke, A., Weiss, D. S., Thompson, L. J. & Monack, D. M. Type I interferon signaling is required for activation of the inflammasome during *Francisella* infection. *J. Exp. Med.* **204**, 987–994 (2007).

37. 37.

Kanneganti, T. D. et al. Bacterial RNA and small antiviral compounds activate caspase-1 through cryopyrin/Nalp3. *Nature* **440**, 233–236 (2006).

38. 38.

Mariathasan, S. et al. Differential activation of the inflammasome by caspase-1 adaptors ASC and Ipaf. *Nature* **430**, 213–218 (2004).

39. 39.

Ishii, K. J. et al. TANK-binding kinase-1 delineates innate and adaptive immune responses to DNA vaccines. *Nature* **451**, 725–729 (2008).

40. 40.

Alexopoulou, L., Holt, A. C., Medzhitov, R. & Flavell, R. A. Recognition of double-stranded RNA and activation of NF-κB by Toll-like receptor 3. *Nature* **413**, 732–738 (2001).

41. 41.

Yamamoto, M. et al. Role of adaptor TRIF in the MyD88-independent toll-like receptor signaling pathway. *Science* **301**, 640–643 (2003).

42. 42.

Gitlin, L. et al. Essential role of mda-5 in type I IFN responses to polyriboinosinic:polyribocytidyllic acid and encephalomyocarditis

picornavirus. *Proc. Natl Acad. Sci. USA* **103**, 8459–8464 (2006).

43. 43.

Kumar, H. et al. Essential role of IPS-1 in innate immune responses against RNA viruses. *J. Exp. Med.* **203**, 1795–1803 (2006).

44. 44.

Chen, G. Y., Liu, M., Wang, F., Bertin, J. & Núñez, G. A functional role for Nlrp6 in intestinal inflammation and tumorigenesis. *J. Immunol.* **186**, 7187–7194 (2011).

45. 45.

Zaki, M. H. et al. The NOD-like receptor NLRP12 attenuates colon inflammation and tumorigenesis. *Cancer Cell* **20**, 649–660 (2011).

46. 46.

Ozören, N. et al. Distinct roles of TLR2 and the adaptor ASC in IL-1 β /IL-18 secretion in response to *Listeria monocytogenes*. *J. Immunol.* **176**, 4337–4342 (2006).

47. 47.

Man, S. M. et al. IRGB10 liberates bacterial ligands for sensing by the AIM2 and Caspase-11-NLRP3 inflammasomes. *Cell* **167**, 382–396.e317 (2016).

48. 48.

Van Opdenbosch, N. et al. Caspase-1 engagement and TLR-induced c-FLIP expression suppress ASC/Caspase-8-dependent apoptosis by inflammasome sensors NLRP1b and NLRC4. *Cell Rep.* **21**, 3427–3444 (2017).

49. 49.

Karki, R. et al. IRF8 regulates transcription of *Naips* for NLRC4 inflammasome activation. *Cell* **173**, 920–933.e913 (2018).

50. 50.

Tummers, B. et al. Caspase-8-dependent inflammatory responses are controlled by its adaptor, FADD, and necroptosis. *Immunity* **52**, 994–1006.e1008 (2020).

51. 51.

Lakhani, S. A. et al. Caspases 3 and 7: key mediators of mitochondrial events of apoptosis. *Science* **311**, 847–851 (2006).

52. 52.

Zheng, T. S. et al. Deficiency in caspase-9 or caspase-3 induces compensatory caspase activation. *Nat. Med.* **6**, 1241–1247 (2000).

53. 53.

Newton, K., Sun, X. & Dixit, V. M. Kinase RIP3 is dispensable for normal NF-κBs, signaling by the B-cell and T-cell receptors, tumor necrosis factor receptor 1, and Toll-like receptors 2 and 4. *Mol. Cell. Biol.* **24**, 1464–1469 (2004).

54. 54.

Oberst, A. et al. Catalytic activity of the caspase-8FLIP_L complex inhibits RIPK3-dependent necrosis. *Nature* **471**, 363–367 (2011).

55. 55.

Dillon, C. P. et al. Survival function of the FADD–CASPASE-8–cFLIP_L complex. *Cell Rep.* **1**, 401–407 (2012).

56. 56.

Kuehne, S. A. et al. Importance of toxin A, toxin B, and CDT in virulence of an epidemic *Clostridium difficile* strain. *J. Infect. Dis.* **209**, 83–86 (2014).

57. 57.

Tweedell, R. E., Malireddi, R. K. S. & Kanneganti, T. D. A comprehensive guide to studying inflammasome activation and cell death. *Nat. Protoc.* **15**, 3284–33339 (2020).

58. 58.

Lee, S. et al. Influenza restriction factor MxA functions as inflammasome sensor in the respiratory epithelium. *Sci. Immunol.* **4**, eaau4643 (2019).

59. 59.

Lee, S., Hirohama, M., Noguchi, M., Nagata, K. & Kawaguchi, A. Influenza A virus infection triggers pyroptosis and apoptosis of respiratory epithelial cells through the type I interferon signaling pathway in a mutually exclusive manner. *J. Virol.* **92**, e00396–18 (2018).

Acknowledgements

We thank members of the Kanneganti laboratory for their comments and suggestions and R. Tweedell for scientific editing and writing support. *Mavs*^{-/-} mutant mice were kindly provided by M. Gale. We thank M. Yamamoto for the *Trif*^{-/-} mutant mouse strain. T.-D.K. is supported by NIH grants AI101935, AI124346, AI160179, AR056296 and CA253095 and by the American Lebanese Syrian Associated Charities. The content is solely the responsibility of the authors and does not necessarily represent the official views of the National Institutes of Health.

Author information

Affiliations

1. Department of Immunology, St Jude Children's Research Hospital, Memphis, TN, USA

SangJoon Lee, Rajendra Karki, Yaqiu Wang, Lam Nhat Nguyen & Thirumala-Devi Kanneganti

2. Department of Structural Biology, St Jude Children's Research Hospital, Memphis, TN, USA

Ravi C. Kalathur

Contributions

S.L., R.K. and T.-D.K. conceptualized the study; S.L. and R.K. designed the methodology; S.L., R.K., Y.W., L.N.N. and R.C.K. performed the experiments; S.L., R.K., Y.W. and L.N.N. conducted the analysis; S.L., R.K. and T.-D.K. wrote the manuscript. T.-D.K. acquired the funding and provided overall supervision.

Corresponding author

Correspondence to Thirumala-Devi Kanneganti.

Ethics declarations

Competing interests

The authors declare no competing interests.

Additional information

Peer review information *Nature* thanks the anonymous reviewer(s) for their contribution to the peer review of this work.

Publisher's note Springer Nature remains neutral with regard to jurisdictional claims in published maps and institutional affiliations.

Extended data figures and tables

Extended Data Fig. 1 *F. novicida* induces AIM2-, Pyrin-, ZBP1-mediated caspase-1 activation, cytokine release and cell death.

a, Immunoblot analysis of pro-caspase-1 (CASP1; P45) and cleaved CASP1 (P20) in *F. novicida*-infected or poly(dA:dT)-transfected wild type (WT) or *Aim2*^{-/-} bone marrow-derived macrophages (BMDMs). **b**, Cell death in BMDMs after *F. novicida* infection for 16 h. Red indicates dead cells. **c**, Quantification of the cell death in (b). **d–f**, Immunoblot analysis of CASP1 (**d**), cell death images at 16 h post-infection (**e**), and cell death quantification (**f**) from WT or *Nlrp3*^{-/-} BMDMs after *F. novicida* infection or LPS plus nigericin (LPS + Ni) treatment. **g–i**, Immunoblot analysis of CASP1 (**g**), cell death images at 16 h post-infection (**h**), and cell death quantification (**i**) from WT or *Nlrc4*^{-/-} BMDMs after *F. novicida* or *Salmonella* Typhimurium infection. **j–l**, Immunoblot analysis of CASP1 (**j**), cell death images at 16 h post-infection (**k**), and cell death quantification (**l**) from WT or *Mefv*^{-/-} BMDMs after *F. novicida* infection or *C. difficile* Toxin AB⁺ supernatant treatment. **m–o**, Immunoblot analysis of CASP1 (**m**), cell death images at 16 h post-infection (**n**), and cell death quantification (**o**) from WT or *Zbp1*^{-/-} BMDMs after *F. novicida* or influenza A virus (IAV) infection. **a, d, g, j, m**, Data are representative of at least three independent experiments. **b, e, h, k, n**, Images are representative of at least three independent experiments. Scale bar, 50 μm. **c, f, i, l, o**, Data are mean ± s.e.m. ns, not significant; *****P* < 0.0001 (two-tailed t-test; *n* = 8 from 4 biologically independent samples). Exact *P* values are presented in Supplementary Table 1. For gel source data, see Supplementary Figure 1.

[Source data](#)

Extended Data Fig. 2 Innate immune sensors TLR3, MDA5, NLRP6 and NLRP12 and adaptors Trif and MAVS are not

required for caspase-1 activation and cell death after HSV1 and *F. novicida* infections.

a, Immunoblot analysis of pro-caspase-1 (CASP1; P45) and cleaved CASP1 (P20) in HSV1-infected wild type (WT), *Tlr3*^{-/-}, *Trif*^{-/-} or *Asc*^{-/-} bone marrow-derived macrophages (BMDMs). **b**, Cell death in BMDMs after HSV1 infection for 16 h. Red indicates dead cells. **c**, Quantification of the cell death in **(b)**. **d–f**, Immunoblot analysis of CASP1 **(d)**, cell death images at 16 h post-infection **(e)**, and cell death quantification **(f)** from WT, *Mda5*^{-/-} or *Mavs*^{-/-} BMDMs after HSV1 infection. **g–i**, Immunoblot analysis of CASP1 **(g)**, cell death images at 16 h post-infection **(h)**, and cell death quantification **(i)** from WT, *Nlrp6*^{-/-} or *Nlrp12*^{-/-} BMDMs after HSV1 infection. **j–l**, Immunoblot analysis of CASP1 **(j)**, cell death images at 16 h post-infection **(k)**, and cell death quantification **(l)** from WT, *Tlr3*^{-/-} or *Trif*^{-/-} BMDMs after *F. novicida* infection. **m–o**, Immunoblot analysis of CASP1 **(m)**, cell death images **(n)**, and cell death quantification **(o)** from WT, *Mda5*^{-/-} or *Mavs*^{-/-} BMDMs after *F. novicida* infection. **p–r**, Immunoblot analysis of CASP1 **(p)**, cell death images at 16 h post-infection **(q)**, and cell death quantification **(r)** from WT, *Nlrp6*^{-/-} or *Nlrp12*^{-/-} BMDMs after *F. novicida* infection. **a, d, g, j, m, p**, Data are representative of at least three independent experiments. **b, e, h, k, n, q**, Images are representative of at least three independent experiments. Scale bar, 50 µm. **c, f, i, l, o, r**, Data are mean ± s.e.m. ns, not significant (one-way ANOVA with Dunnett's multiple comparisons test; *n* = 8 from 4 biologically independent samples). Exact *P* values are presented in Supplementary Table 1. For gel source data, see Supplementary Figure 1.

[Source data](#)

Extended Data Fig. 3 ZBP1 cooperates with Pyrin to drive AIM2-mediated cell death and cytokine release.

a, Cell death in bone marrow-derived macrophages (BMDMs) after HSV1 infection with or without colchicine (Col). Red indicates dead cells. Data are representative of at least three independent experiments. Scale bar, 50 µm. **b**, Quantification of the cell death from **(a)**. Data are mean ± s.e.m. ns,

not significant; $****P < 0.0001$ (one-way ANOVA with Dunnett's multiple comparisons test; $n = 12$ from 3 biologically independent samples). **c**, Cell death in BMDMs after *F. novicida* infection with or without Col. Red indicates dead cells. Data are representative of at least three independent experiments. Scale bar, 50 μm . **d**, Quantification of the cell death from (c). Data are mean \pm s.e.m. ns, not significant; $****P < 0.0001$ (one-way ANOVA with Dunnett's multiple comparisons test; $n = 9$ from 3 biologically independent samples). **e–h**, Release of IL-1 β (**e**, **g**) or IL-18 (**f**, **h**) following HSV1 (**e**, **f**) or *F. novicida* (**g**, **h**) infections with or without Col. Data are mean \pm s.e.m. ns, not significant; $****P < 0.0001$ (one-way ANOVA with Dunnett's multiple comparisons test; $n = 6$ from 3 biologically independent samples). Exact P values are presented in Supplementary Table 1.

Source data

Extended Data Fig. 4 Pyrin and ZBP1 are required for AIM2-mediated cell death following HSV1 infection, but not in response to poly(dA:dT).

a, b, Quantification of cell death in wild type (WT), *Aim2*^{-/-}, *Mefv*^{-/-}, *Zbp1*^{-/-} or *Mefv*^{-/-}*Zbp1*^{-/-} bone marrow-derived macrophages (BMDMs) over time during HSV1 (**a**) and *F. novicida* (**b**) infections. Data are mean \pm s.e.m. * $P < 0.05$; ** $P < 0.01$; *** $P < 0.001$; **** $P < 0.0001$ (one-way ANOVA with Dunnett's multiple comparisons test; $n = 4$). Data are representative of at least three independent experiments. **c**, Cell death in THP-1 macrophages treated with control siRNA (Control) or siRNA targeted to *AIM2* (*AIM2* KD), *MEFV* (*MEFV* KD) and/or *ZBP1* (*ZBP1* KD) after HSV1 infection. Red indicates dead cells. Images are representative of at least three independent experiments. Scale bar, 50 μm . **d**, Quantification of the cell death from (c). Data are mean \pm s.e.m. **** $P < 0.0001$ (one-way ANOVA with Dunnett's multiple comparisons test; $n = 4$). Data are representative of at least three independent experiments. **e**, Immunoblot analysis of caspase-1 (CASP1) activation and AIM2, Pyrin and ZBP1 expression in the indicated THP-1 cells. Data are representative of two independent experiments. **f**, Cell death in WT, *Aim2*^{-/-}, *Mefv*^{-/-}, *Zbp1*^{-/-} or *Mefv*^{-/-}*Zbp1*^{-/-} BMDMs

after poly(dA:dT) transfection. Red indicates dead cells. Images are representative of at least three independent experiments. Scale bar, 50 μ m. **g**, Quantification of the cell death from (f). Data are mean \pm s.e.m. ns, not significant; *** P < 0.0001 (one-way ANOVA with Dunnett's multiple comparisons test; n = 9 from 3 biologically independent samples). Exact P values are presented in Supplementary Table 1. **h**, Immunoblot analysis of CASP1 in the indicated BMDMs after poly(dA:dT) transfection. Data are representative of at least three independent experiments. For gel source data, see Supplementary Figure 1.

Source data

Extended Data Fig. 5 AIM2 acts as an upstream regulator of RhoA modifications, and the ZBP1 Za2 domain is required for cell death.

a, RhoA-GTP activity in wild type (WT), *Aim2*^{-/-}, *Mefv*^{-/-} or *Zbp1*^{-/-} bone marrow-derived macrophages (BMDMs) infected with HSV1 or treated with TcdB for 12 h. Activity was normalized to total RhoA levels. Data are mean \pm s.e.m. from three independent experiments. ns, not significant; *** P < 0.001; *** P < 0.0001 (one-way ANOVA with Dunnett's multiple comparisons test; n = 3, 6, 7 or 9). **b**, **c**, Activated RhoA (RhoA-GTP) assessed using a pull-down assay with Rhotekin-RBD beads from WT, *Aim2*^{-/-}, *Asc*^{-/-} or *Casp1*^{-/-} BMDMs infected with HSV1 (**b**) or *F. novicida* (**c**). Data are representative of at least three independent experiments. **d**, RhoA-GTP activity in WT BMDMs infected with HSV1 or transfected with poly(dA:dT) for 12 h. Data are mean \pm s.e.m. from three independent experiments. ns, not significant; ** P < 0.01 (one-way ANOVA with Dunnett's multiple comparisons test; n = 3). **e**, Activated RhoA (RhoA-GTP) assessed using a pull-down assay with Rhotekin-RBD beads from WT, *Aim2*^{-/-}, *Asc*^{-/-} or *Casp1*^{-/-} BMDMs transfected with poly(dA:dT). Data are representative of at least three independent experiments. **f**, **g** Cell death in WT, *Zbp1*^{-/-}, *Zbp1* ^{Δ Za2/ Δ Za2} or *Ripk3*^{-/-} BMDMs after HSV1 (**f**) or *F. novicida* (**g**) infections. Red indicates dead cells. Images are representative of at least three independent experiments. Scale bar, 50 μ m. **h**, **i**, Quantification of the cell death from **f** (**h**) or **g** (**i**).

Data are mean \pm s.e.m. $****P < 0.0001$ (one-way ANOVA with Dunnett's multiple comparisons test; $n = 9$ from 3 biologically independent samples). Exact P values are presented in Supplementary Table 1. For gel source data, see Supplementary Figure 1.

Source data

Extended Data Fig. 6 The expression of Pyrin and ZBP1 is not regulated by GSDMD or caspase-8, -7, -3 or -6 during HSV1 or F. novicida infections.

a, Immunoblot analysis of caspase-1 (CASP1) activation and ZBP1 and Pyrin expression in wild type (WT) or *Gsdmd*^{-/-} bone marrow-derived macrophages (BMDMs) after HSV1 or *F. novicida* infection. Data are representative of at least three independent experiments. **b, c**, Immunoblot analysis of ZBP1, Pyrin and AIM2 expression in the indicated BMDMs after HSV1 (**b**) or *F. novicida* (**c**) infections. Data are representative of at least three independent experiments. **d**, Immunoblot analysis of ZBP1, Pyrin and AIM2 expression in the indicated BMDMs after influenza A virus (IAV) infection. Data are representative of at least three independent experiments. For gel source data, see Supplementary Figure 1.

Extended Data Fig. 7 The expression of Pyrin and ZBP1 is regulated by AIM2 during HSV1 and F. novicida infections.

a–d, Relative expression of *Zbp1* (**a, b**) and *Mefv* (**c, d**) in wild type (WT), *Aim2*^{-/-}, *Asc*^{-/-} or *Casp1*^{-/-} bone marrow-derived macrophages (BMDMs) after HSV1 (**a, c**) or *F. novicida* (**b, d**) infections. Expression presented relative to that of the control gene *Gapdh*. Data are mean \pm s.e.m. from three independent experiments. $****P < 0.0001$ (one-way ANOVA with Dunnett's multiple comparisons test, $n = 6$). **e, f**, Release of IFN- β following HSV1 (**e**) or *F. novicida* (**f**) infections. Data are mean \pm s.e.m. $****P < 0.0001$ (one-way ANOVA with Dunnett's multiple comparisons test; $n = 6$ from 3 biologically independent samples). Exact P values are presented in Supplementary Table 1. **g, h**, Immunoblot analysis of ZBP1 and Pyrin expression in the indicated BMDMs after HSV1 (**g**) or *F. novicida* (**h**)

infections with or without IFN- β treatment. Data are representative of at least three independent experiments. For gel source data, see Supplementary Figure 1.

[Source data](#)

Extended Data Fig. 8 Loss of AIM2 or combined loss of Pyrin and ZBP1 prevents the formation of the AIM2 complex during HSV1 and *F. novicida* infections.

a, b, Immunoprecipitation (IP) in wild type (WT), *Aim2*^{-/-}, *Mefv*^{-/-}, *Zbp1*^{-/-} or *Mefv*^{-/-}*Zbp1*^{-/-} bone marrow-derived macrophages (BMDMs) with either IgG control antibodies or anti-ASC antibodies after HSV1 (**a**) or *F. novicida* (**b**) infection. Data are representative of three independent experiments. **c, d**, IP in WT, *Ripk3*^{-/-}, *Ripk3*^{-/-}*Casp8*^{-/-} or *Ripk3*^{-/-}*Fadd*^{-/-} BMDMs with either IgG control antibodies or anti-ASC antibodies after HSV1 (**c**) or *F. novicida* (**d**) infection. Data are representative of three independent experiments. For gel source data, see Supplementary Figure 1.

Extended Data Fig. 9 ASC speck colocalizes with AIM2, Pyrin and ZBP1, caspase-8 and RIPK3 in the same cell during HSV1 and *F. novicida* infections, and formation of this complex drives cell death.

a, Immunofluorescence images of wild type (WT) bone marrow-derived macrophages (BMDMs) at 12 h after *F. novicida* infection. Scale bars, 5 μ m. Arrowheads indicate the ASC speck. Images are representative of three independent experiments. **b**, Quantification of the percentage of cells with ASC⁺AIM2⁺Pyrin⁺ZBP1⁺specks among the ASC speck⁺ cells. Data are mean \pm s.e.m. **** $P < 0.0001$ (one-way ANOVA with Dunnett's multiple comparisons test; $n = 6$ from 3 biologically independent samples). **c**, Immunofluorescence images of WT BMDMs at 12 h after HSV1 infection. Scale bars, 5 μ m. Arrowheads indicate the ASC speck. Images are representative of three independent experiments. **d**, Quantification of the percentage of cells with ASC⁺RIPK3⁺CASP8⁺ specks among the ASC

speck⁺ cells. Data are mean ± s.e.m. ***P < 0.0001 (one-way ANOVA with Dunnett's multiple comparisons test; n = 6 from 3 biologically independent samples). e, Immunofluorescence images of WT BMDMs at 12 h after *F. novicida* infection. Scale bars, 5 μm. Arrowheads indicate the ASC speck. Images are representative of three independent experiments. f, Quantification of the percentage of cells with ASC⁺RIPK3⁺CASP8⁺ specks among the ASC speck⁺ cells. Data are mean ± s.e.m. ***P < 0.0001 (one-way ANOVA with Dunnett's multiple comparisons test; n = 6 from 3 biologically independent samples). g, Cell death in WT, *Ripk3*^{-/-}*Casp8*^{-/-} or *Ripk3*^{-/-}*Fadd*^{-/-} BMDMs at 16 h post-infection with HSV1 or *F. novicida*. Red indicates dead cells. Data are representative of at least three independent experiments. Scale bar, 50 μm. h, Quantification of the cell death from (g). Data are mean ± s.e.m. ***P < 0.0001 (one-way ANOVA with Dunnett's multiple comparisons test; n = 9 from 3 biologically independent samples). Exact P values are presented in Supplementary Table 1.

Source data

Extended Data Fig. 10 AIM2 regulates Pyrin and ZBP1 expression in vivo, and AIM2 provides host protection against HSV1 and *F. novicida*.

a, b, Immunoblot analysis of pro- (P45) and activated (P20) caspase-1 (CASP1), pro- (P53) and activated (P30) gasdermin D (GSDMD), pro- (P55) and cleaved (P18) caspase-8 (CASP8), pro- (P35) and cleaved (P17/P19) caspase-3 (CASP3), pro- (P35) and cleaved (P20) caspase-7 (CASP7), phosphorylated MLKL (pMLKL), total MLKL (tMLKL), ZBP1, Pyrin and AIM2 in lung from uninfected animals (PBS) or wild type (WT) or *Aim2*^{-/-} mice 3 days after HSV1 (a) or *F. novicida* (b) infection. Each lane indicates independent biological replicates. c, Viral quantification in WT, *Aim2*^{-/-}, *Mefv*^{-/-}, *Zbp1*^{-/-} or *Mefv*^{-/-}*Zbp1*^{-/-} BMDMs at 16 h post-infection with HSV1. Data are mean ± s.e.m. ***P < 0.0001 (one-way ANOVA with Dunnett's multiple comparisons test; n = 6 from 3 biologically independent samples). d, Bacterial quantification in WT, *Aim2*^{-/-}, *Mefv*^{-/-}, *Zbp1*^{-/-} or *Mefv*^{-/-}*Zbp1*^{-/-} BMDMs after *F. novicida*

infection. Data are mean \pm s.e.m. * $P < 0.05$ and *** $P < 0.0001$ (one-way ANOVA with Dunnett's multiple comparisons test; $n = 3$ from 3 biologically independent samples). **e**, In vivo bacterial quantification in lung, liver or spleen from WT or *Aim2*^{-/-} mice 2 days after *F. novicida* infection ($n = 5$). Each symbol represents one mouse. Data are pooled from two independent experiments. Data are mean \pm s.e.m. ** $P < 0.01$ and *** $P < 0.001$ (two-tailed t-test). **f**, Survival of WT, *Aim2*^{-/-}, *Mefv*^{-/-} and *Zbp1*^{-/-} mice infected subcutaneously with 5×10^5 CFU of *F. novicida* in 200 μ l PBS. Survival data are pooled from three independent experiments. ** $P < 0.01$; *** $P < 0.0001$ (log-rank (Mantel-Cox) test). Exact P values are presented in Supplementary Table 1. For gel source data, see Supplementary Figure 1.

[Source data](#)

Supplementary information

[Supplementary Information](#)

This file contains uncropped blots with molecular weight and size markers and an indication of how the images were cropped.

[Reporting Summary](#)

[Supplementary Table 1](#)

Exact P values for Figs. 1–4 and Extended Data Figs. 1–10.

Source data

[Source Data Fig. 1](#)

[Source Data Fig. 2](#)

[Source Data Fig. 4](#)

[Extended Data Source Data Fig. 1](#)

[Extended Data Source Data Fig. 2](#)

[Extended Data Source Data Fig. 3](#)

[Extended Data Source Data Fig. 4](#)

[Extended Data Source Data Fig. 5](#)

[Extended Data Source Data Fig. 7](#)

[Extended Data Source Data Fig. 9](#)

[Extended Data Source Data Fig. 10](#)

Rights and permissions

[Reprints and Permissions](#)

About this article

Cite this article

Lee, S., Karki, R., Wang, Y. *et al.* AIM2 forms a complex with pyrin and ZBP1 to drive PANoptosis and host defence. *Nature* **597**, 415–419 (2021). <https://doi.org/10.1038/s41586-021-03875-8>

- Received: 17 March 2021
- Accepted: 04 August 2021
- Published: 01 September 2021
- Issue Date: 16 September 2021

- DOI: <https://doi.org/10.1038/s41586-021-03875-8>

Share this article

Anyone you share the following link with will be able to read this content:

[Get shareable link](#)

Sorry, a shareable link is not currently available for this article.

[Copy to clipboard](#)

Provided by the Springer Nature SharedIt content-sharing initiative

This article was downloaded by **calibre** from <https://www.nature.com/articles/s41586-021-03875-8>

| [Section menu](#) | [Main menu](#) |

- Article
- [Published: 01 September 2021](#)

The polar oxy-metabolome reveals the 4-hydroxymandelate CoQ10 synthesis pathway

- [Robert S. Banh](#)^{1,3},
- [Esther S. Kim](#)^{1,3},
- [Quentin Spillier](#)^{1,3},
- [Douglas E. Biancur](#)^{1,3},
- [Keisuke Yamamoto](#) [ORCID: orcid.org/0000-0002-6323-9540](#)^{1,3},
- [Albert S. W. Sohn](#)^{1,3},
- [Guangbin Shi](#)^{1,3},
- [Drew R. Jones](#)²,
- [Alec C. Kimmelman](#)^{1,3} &
- [Michael E. Pacold](#) [ORCID: orcid.org/0000-0003-3688-2378](#)^{1,3}

Nature volume **597**, pages 420–425 (2021)

- 2676 Accesses
- 48 Altmetric
- [Metrics details](#)

Subjects

- [Metabolic pathways](#)
- [Metabolomics](#)
- [Oxidoreductases](#)

Abstract

Oxygen is critical for a multitude of metabolic processes that are essential for human life. Biological processes can be identified by treating cells with $^{18}\text{O}_2$ or other isotopically labelled gases and systematically identifying biomolecules incorporating labeled atoms. Here we labelled cell lines of distinct tissue origins with $^{18}\text{O}_2$ to identify the polar oxy-metabolome, defined as polar metabolites labelled with ^{18}O under different physiological O_2 tensions. The most highly ^{18}O -labelled feature was 4-hydroxymandelate (4-HMA). We demonstrate that 4-HMA is produced by hydroxyphenylpyruvate dioxygenase-like (HPDL), a protein of previously unknown function in human cells. We identify 4-HMA as an intermediate involved in the biosynthesis of the coenzyme Q10 (CoQ10) headgroup in human cells. The connection of HPDL to CoQ10 biosynthesis provides crucial insights into the mechanisms underlying recently described neurological diseases related to HPDL deficiencies^{1,2,3,4} and cancers with HPDL overexpression⁵.

Access options

Subscribe to Journal

Get full journal access for 1 year

\$199.00

only \$3.90 per issue

[Subscribe](#)

All prices are NET prices.

VAT will be added later in the checkout.

Tax calculation will be finalised during checkout.

Rent or Buy article

Get time limited or full article access on ReadCube.

from \$8.99

[Rent or Buy](#)

All prices are NET prices.

Additional access options:

- [Log in](#)
- [Access through your institution](#)
- [Learn about institutional subscriptions](#)

Fig. 1: Analysis of the oxy-metabolome identifies 4-HMA as a highly ^{18}O -labelled metabolite in human cells.

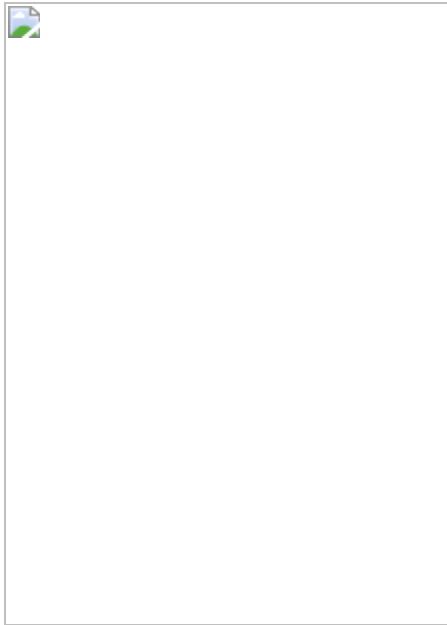


Fig. 2: 4-HMA is derived from tyrosine and synthesized by HPDL (4-hydroxyphenylpyruvate dioxygenase-like) in human cells.

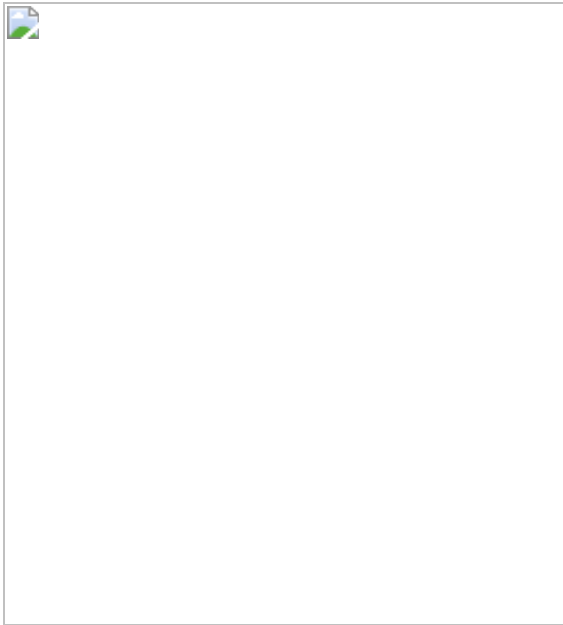


Fig. 3: HPDL and 4-HMA participate in the human CoQ10 headgroup biosynthesis pathway.



Data availability

TLCV2-sgHPDL and coHPDL expression plasmids are available from Addgene (IDs 174128, 174129, 174130, 174131, 174165 and 174166). All other data supporting the findings of this study are available from the

corresponding author upon reasonable request. [Source data](#) are provided with this paper.

References

1. 1.

Morgan, N. V. et al. Evidence that autosomal recessive spastic cerebral palsy-1 (CPSQ1) is caused by a missense variant in HPDL. *Brain Commun.* **3**, fcab002 (2021).

2. 2.

Husain, R. A. et al. Bi-allelic HPDL variants cause a neurodegenerative disease ranging from neonatal encephalopathy to adolescent-onset spastic paraplegia. *Am. J. Hum. Genet.* **107**, 364–373 (2020).

3. 3.

Ghosh, S. G. et al. Biallelic variants in HPDL, encoding 4-hydroxyphenylpyruvate dioxygenase-like protein, lead to an infantile neurodegenerative condition. *Genet. Med.* **23**, 524–533 (2021).

4. 4.

Wiessner, M. et al. Biallelic variants in HPDL cause pure and complicated hereditary spastic paraplegia. *Brain* **144**, 1422–1434 (2021).

5. 5.

Ye, X. et al. 4-hydroxyphenylpyruvate dioxygenase-like protein promotes pancreatic cancer cell progression and is associated with glutamine-mediated redox balance. *Front. Oncol.* **10**, 3074 (2021).

6. 6.

Tang, D., Kang, R., Berghe, T. V., Vandenabeele, P. & Kroemer, G. The molecular machinery of regulated cell death. *Cell Res.* **29**, 347–364 (2019).

7. 7.

Hirsila, M., Koivunen, P., Gunzler, V., Kivirikko, K. I. & Myllyharju, J. Characterization of the human prolyl 4-hydroxylases that modify the hypoxia-inducible factor. *J. Biol. Chem.* **278**, 30772–30780 (2003).

8. 8.

Masson, N. et al. Conserved N-terminal cysteine dioxygenases transduce responses to hypoxia in animals and plants. *Science* **365**, 65–69 (2019).

9. 9.

Laukka, T. et al. Fumarate and succinate regulate expression of hypoxia-inducible genes via TET enzymes. *J. Biol. Chem.* **291**, 4256–4265 (2016).

10. 10.

Moran, G. R. 4-Hydroxyphenylpyruvate dioxygenase. *Arch. Biochem. Biophys.* **433**, 117–128 (2005).

11. 11.

Ast, T. & Mootha, V. K. Oxygen and mammalian cell culture: are we repeating the experiment of Dr. Ox? *Nature Metabolism* **1**, 858–860 (2019).

12. 12.

Deshpande, A. R., Wagenpfeil, K., Pochapsky, T. C., Petsko, G. A. & Ringe, D. Metal-dependent function of a mammalian acireductone dioxygenase. *Biochemistry* **55**, 1398–1407 (2016).

13. 13.

Drazic, A. & Winter, J. The physiological role of reversible methionine oxidation. *Biochim. Biophys. Acta* **1844**, 1367–1382 (2014).

14. 14.

Choroba, O. W., Williams, D. H. & Spencer, J. B. Biosynthesis of the vancomycin group of antibiotics: involvement of an unusual dioxygenase in the pathway to (*S*)-4-hydroxyphenylglycine. *JACS* **122**, 5389–5390 (2000).

15. 15.

Hubbard, B. K., Thomas, M. G. & Walsh, C. T. Biosynthesis of l-*p*-hydroxyphenylglycine, a non-proteinogenic amino acid constituent of peptide antibiotics. *Chem. Biol.* **7**, 931–942 (2000).

16. 16.

Lemberger, L., Klutch, A. & Kuntzman, R. The metabolism of tyramine in rabbits. *J. Pharmacol. Exp. Ther.* **153**, 183 (1966).

17. 17.

Lichter-Konecki, U., Hipke, C. M. & Konecki, D. S. Human phenylalanine hydroxylase gene expression in kidney and other nonhepatic tissues. *Mol. Genet. Metab.* **67**, 308–316 (1999).

18. 18.

Gunsior, M., Ravel, J., Challis, G. L. & Townsend, C. A. Engineering *p*-hydroxyphenylpyruvate dioxygenase to a *p*-hydroxymandelate synthase and evidence for the proposed benzene oxide intermediate in homogentisate formation. *Biochemistry* **43**, 663–674 (2004).

19. 19.

O'Hare, H. M., Huang, F., Holding, A., Choroba, O. W. & Spencer, J. B. Conversion of hydroxyphenylpyruvate dioxygenases into hydroxymandelate synthases by directed evolution. *FEBS Lett.* **580**, 3445–3450 (2006).

20. 20.

Gunsior, M. et al. The biosynthetic gene cluster for a monocyclic β -lactam antibiotic, nocardicin A. *Chem. Biol.* **11**, 927–938 (2004).

21. 21.

Bhat, S. G. & Vaidyanathan, C. S. Involvement of 4-hydroxymandelic acid in the degradation of mandelic acid by *Pseudomonas convexa*. *J. Bacteriol.* **127**, 1108–1118 (1976).

22. 22.

Stefely, J. A. & Pagliarini, D. J. Biochemistry of mitochondrial coenzyme Q biosynthesis. *Trends Biochem. Sci.* **42**, 824–843 (2017).

23. 23.

Lu, T.-T., Lee, S. J., Apfel, U.-P. & Lippard, S. J. Aging-associated enzyme human clock-1: substrate-mediated reduction of the diiron center for 5-demethoxyubiquinone hydroxylation. *Biochemistry* **52**, 2236–2244 (2013).

24. 24.

Wang, Y. et al. The anti-neurodegeneration drug clioquinol inhibits the aging-associated protein CLK-1. *J. Biol. Chem.* **284**, 314–323 (2009).

25. 25.

Payet, L.-A. et al. Mechanistic details of early steps in coenzyme Q biosynthesis pathway in yeast. *Cell Chem. Biol.* **23**, 1241–1250 (2016).

26. 26.

Stefely, J. A. et al. Mitochondrial protein functions elucidated by multi-omic mass spectrometry profiling. *Nat. Biotechnol.* **34**, 1191–1197 (2016).

27. 27.

Valera, M. J. et al. The mandelate pathway, an alternative to the phenylalanine ammonia lyase pathway for the synthesis of benzenoids in ascomycete yeasts. *Appl. Environ. Microbiol.* **86**, e00701–20 (2020).

28. 28.

Kaymak, I. et al. Mevalonate pathway provides ubiquinone to maintain pyrimidine synthesis and survival in p53-deficient cancer cells exposed to metabolic stress. *Cancer Res.* **80**, 189–203 (2020).

29. 29.

Kapalczynska, M. et al. 2D and 3D cell cultures - a comparison of different types of cancer cell cultures. *Arch. Med. Sci.* **14**, 910–919 (2018).

30. 30.

Doimo, M. et al. Genetics of coenzyme q10 deficiency. *Mol. Syndromol.* **5**, 156–162 (2014).

31. 31.

Martínez-Reyes, I. et al. Mitochondrial ubiquinol oxidation is necessary for tumour growth. *Nature* **585**, 288–292 (2020).

32. 32.

Xie, L. X. et al. Resveratrol and para-coumarate serve as ring precursors for coenzyme Q biosynthesis. *J. Lipid Res.* **56**, 909–919 (2015).

33. 33.

Fernández-del-Río, L. et al. Kaempferol increases levels of coenzyme Q in kidney cells and serves as a biosynthetic ring precursor. *Free Radical Biol. Med.* **110**, 176–187 (2017).

34. 34.

Booth, A. N. et al. Urinary phenolic acid metabolites of tyrosine. *J. Biol. Chem.* **235**, 2649–2652 (1960).

35. 35.

Hartl, J., Kiefer, P., Meyer, F. & Vorholt, J. A. Longevity of major coenzymes allows minimal de novo synthesis in microorganisms. *Nat Microbiol* **2**, 17073 (2017).

36. 36.

Meyers, R. M. et al. Computational correction of copy number effect improves specificity of CRISPRCas9 essentiality screens in cancer cells. *Nat. Genet.* **49**, 1779–1784 (2017).

37. 37.

Uphoff, C. C. & Drexler, H. G. Detecting mycoplasma contamination in cell cultures by polymerase chain reaction. *Methods Mol. Biol.* **731**, 93–103 (2011).

38. 38.

Parker, S. J. et al. LKB1 promotes metabolic flexibility in response to energy stress. *Metab. Eng.* **43**, 208–217 (2017).

39. 39.

Wenig, P. & Odermatt, J. OpenChrom: a cross-platform open source software for the mass spectrometric analysis of chromatographic data. *BMC Bioinf.* **11**, 405 (2010).

40. 40.

Fernandez, C. A., Des Rosiers, C., Previs, S. F., David, F. & Brunengraber, H. Correction of ^{13}C mass isotopomer distributions for natural stable isotope abundance. *J. Mass Spectrom.* **31**, 255–262 (1996).

41. 41.

Gao, J. et al. Integrative analysis of complex cancer genomics and clinical profiles using the cBioPortal. *Sci Signal.* **6**, pl1 (2013).

42. 42.

Cerami, E. et al. The cBio cancer genomics portal: an open platform for exploring multidimensional cancer genomics data. *Cancer Discov.* **2**, 401–404 (2012).

Acknowledgements

We thank D. M. Sabatini for advice and for critical reading of the manuscript; R. L. Possemato and his laboratory for use of an incubator with physiologic oxygen (3% O₂); B. G. Neel for support at the inception of this project; and members of the Kimmelman and Pacold laboratories for their help and suggestions. We acknowledge the NYU Langone Health Experimental Pathology Research Laboratory, Microscopy Laboratory and Metabolomics Core Resource Laboratory for their help in acquiring the data presented. These shared resources are partially supported by the Cancer Center Support Grant P30CA016087 at the Laura and Isaac Perlmutter Cancer Center. R.S.B. is a Merck Fellow of the Damon Runyon Cancer Research Foundation (DRG-2348-18). Q.S. was supported by the Wallonie-Bruxelles International (WBI) fellowship. D.E.B. is supported by a Ruth L. Kirschstein Institutional National Research Service Award, T32 CA009161 (Levy), and the NCI F99/K00 award (F99 CA245822). K.Y. was supported by an Uehara Memorial Foundation Research Fellowship. A.C.K. is supported by National Cancer Institute Grants R01CA157490, R01CA188048, P01CA117969, R35CA232124; ACS Research Scholar Grant RSG-13-298-01-TBG; NIH grant R01GM095567; the Lustgarten Foundation, and Stand Up to Cancer (SU2C), a division of the

Entertainment Industry Foundation. SU2C is administered by the AACR. M.E.P. is a Damon Runyon-Rachleff Innovation Awardee supported in part by the Damon Runyon Cancer Research Foundation (DRR 63-20), and is supported by a Mary Kay Foundation Cancer Research Grant (017-32), the Shifrin-Myers Breast Cancer Discovery Fund at NYU, a V Foundation V Scholar Grant funded by the Hearst Foundation (V2017-004), an NCI K22 Career Transition Award (K22CA212059), the Tara Miller Melanoma Foundation – MRA Young Investigator Award (668365), the Harry J. Lloyd Trust, and laboratory-directed research funding from Max Raskin.

Author information

Affiliations

1. Department of Radiation Oncology, New York University Langone Health, New York, NY, USA

Robert S. Banh, Esther S. Kim, Quentin Spillier, Douglas E. Biancur, Keisuke Yamamoto, Albert S. W. Sohn, Guangbin Shi, Alec C. Kimmelman & Michael E. Pacold

2. Metabolomics Core Resource Laboratory, New York University Langone Health, New York, NY, USA

Drew R. Jones

3. Perlmutter Cancer Center, New York University Langone Health, New York, NY, USA

Robert S. Banh, Esther S. Kim, Quentin Spillier, Douglas E. Biancur, Keisuke Yamamoto, Albert S. W. Sohn, Guangbin Shi, Alec C. Kimmelman & Michael E. Pacold

Contributions

R.S.B. conceived, planned and guided the research, designed and performed all the experiments with assistance as described, analysed and interpreted

the data, and wrote the manuscript. E.S.K. contributed to, and analysed the data for, the labelling experiments, in vitro growth measurements and in vivo tumour studies. Q.S. provided biochemistry and chemistry expertise, and contributed to in vivo tumour studies. D.E.B., K.Y., A.S.W.S., G.S. and Q.S. performed mouse surgeries for orthotopic xenografts in the pancreas, and G.S. obtained tumour-response data. D.R.J. provided expertise on mass spectrometry and fragmentation. A.C.K. provided conceptual advice for the project. M.E.P. carried out gaseous labelling experiments, provided expertise on mass spectrometry, interpreted the data, supervised the project and wrote the manuscript. All authors critically analysed data, and edited and approved the manuscript.

Corresponding author

Correspondence to Michael E. Pacold.

Ethics declarations

Competing interests

A.C.K. has financial interests in Vescor Therapeutics, LLC. A.C.K. is an inventor on patents pertaining to KRAS-regulated metabolic pathways, redox control pathways in pancreatic cancer, targeting GOT1 as a therapeutic approach, and the autophagic control of iron metabolism. A.C.K is on the SAB of Rafael/Cornerstone Pharmaceuticals. A.C.K has been a consultant for Diciphera Pharmaceuticals. M.E.P. has options in Raze Therapeutics, is the recipient of travel funds from Thermo Fisher Scientific and consulted for aMoon Ventures. R.S.B., Q.S., and M.E.P. are co-inventors on a patent filing on aspects of CoQ10 metabolism. The other authors declare no competing interests.

Additional information

Peer review information *Nature* thanks Costas Lyssiotis, Joshua Rabinowitz, Jared Rutter and the other, anonymous, reviewer(s) for their contribution to the peer review of this work.

Publisher's note Springer Nature remains neutral with regard to jurisdictional claims in published maps and institutional affiliations.

Extended data figures and tables

Extended Data Fig. 1 A robust method for $^{18}\text{O}_2$ labelling of human cells.

a, Schematic of $^{18}\text{O}_2$ labelling. A closed system chamber is flushed multiple times with N_2 to remove $^{16}\text{O}_2$. A gas mixture containing $^{18}\text{O}_2$ and CO_2 is pulsed into the closed chamber to reach the desired oxygen concentration. At the assay endpoint, the chamber is opened, cells are extracted, and metabolites separated and identified by liquid chromatography-tandem mass spectrometry (LC-MS/MS). **b**, Oxygen measurements after N_2 flush, followed with or without pulses of $\text{O}_2:\text{CO}_2$ gas mixture in the closed chamber containing tissue culture plates and media ($n = 3$ technical replicates each). **c–e**, Oxygen percentage of O_2 -labelling experiments performed at 3% (c), 1% (d), and 0.2% (e) $^{16}\text{O}_2$ or $^{18}\text{O}_2$. ($n = 2$ technical replicates each). **f**, Cells were treated with several concentrations of MG132, DFO (an iron chelator), IOX1 (a dioxygenase inhibitor), or in combination at 5% O_2 for 24 h. Immunoblots of HIF1 α with ERK2 as a loading control. **g**, Immunoprecipitation of HIF1 α to determine its hydroxylation (P564-OH) levels by the indicated inhibitors. Immunoblots of HIF1 α and HIF1 α P564-OH are shown, with ERK2 serving as a loading control. Experiments were performed once for optimization of drug concentrations (f, g). Graphs represent mean \pm s.d. (c–e).

Source data

Extended Data Fig. 2 $^{18}\text{O}_2$ labelling of human cells reveals the oxy-metabolome.

a, Schematic of the approach used to identify ^{18}O -labelled features and metabolites that were labelled by ^{18}O . n represents the number of features or metabolites identified in MIAPACA2 cells grown at 3% $^{18}\text{O}_2$. See **b** for details. **b**, Summary of total and percentage of identified ^{18}O -labelled features for each cell line and oxygen tension as described in **a**. **c**, Venn diagram demonstrating the overlap of unique ^{18}O -labelled metabolite and features identified for each oxygen condition per cell line. **d**, Total number of unique dioxygenase-dependent, ^{18}O -labelled metabolites and features identified in each cell line and condition. Features were categorized into predicted or not predicted/unknown ^{18}O -labelled metabolites, based on known oxygen-dependent metabolic pathways, and sensitivity or insensitivity to IOX1 (dioxygenase inhibitor) treatment. **e**, Number of ^{18}O -labelled metabolites detected in cells grown in 3%, 1%, and 0.2% $^{18}\text{O}_2$ for 24 h in two sets of experiments. The overlap of the total number of detected ^{18}O -labelled metabolites and features in both experimental sets are shown. **f**, Venn diagram representing the distribution of common and unique ^{18}O -labelled metabolites identified in each cell line. **g**, List of the 46 unique ^{18}O -labelled metabolites that were identified in **f** and categorized into known oxygen-dependent metabolic pathways. ** represents metabolites that have matching MS2 spectra, but need to be validated due to multiple metabolite isomers.

[Source data](#)

[Extended Data Fig. 3 Fractional \$^{18}\text{O}\$ labelling of metabolites and features identified in human cells by \$^{18}\text{O}_2\$ labelling.](#)

a, Heatmap representing the median fractional ^{18}O labelling of the 46 metabolites and features in the indicated cell lines and oxygen tensions. “**” represents metabolites that have matching MS2 spectra, but need to be validated due to multiple metabolite isomers. The red arrow indicates a highly labelled unknown metabolite. **b**, Correlation matrixes demonstrating the Spearman rs value based on the fractional ^{18}O labelling of the 46 metabolites and features across the indicated cell lines and oxygen tensions.

c, Fractional ^{18}O labelling of unknown feature (167.0339 in negative ion mode, elution time of 8.2 min) in MIAPACA2, A498, and SKNDZ cells grown in 3%, 1%, and 0.2% $^{18}\text{O}_2$, and treated with vehicle or IOX1 (dioxygenase inhibitor) for 24 h ($n = 3$). **d–i**, Fractional ^{18}O labelling of metabolites and features by $^{18}\text{O}_2$ across multiple cell lines in response to different oxygen tensions, treated with or without IOX1 (dioxygenase inhibitor) for 24 h. ^{18}O labelling of predicted (**d**, **e**), not predicted (**f–h**), and unknown (**i**) metabolites or features are shown for the indicated cell line. ** represents metabolites that have matching MS2 spectra, but need to be validated due to multiple metabolite isomers. $n = 3$ biologically independent samples for each group and condition in all experiments. Graphs represent mean \pm s.e.m. and were compared using one- (**b–d**) or two-way ANOVA (**a**, **e**, **f**), followed by Tukey post hoc test (* $P < 0.05$, $^{\wedge}P < 0.01$, $^{\%}P < 0.005$, $^{\#}P < 0.0001$).

[Source data](#)

Extended Data Fig. 4 Total levels of unlabelled and ^{18}O -labelled metabolites identified in human cells.

a, Schematic of the carnitine biosynthesis pathway. Dioxygenases, TMLH (Trimethyllysine hydroxylase) and BBOX (butyrobetaine, 2-oxoglutarate dioxygenase), are shown in orange boxes, and ^{18}O labelling is indicated in blue by arrows. **b–d**, Total intracellular levels of unlabelled and ^{18}O -labelled γ -butyrobetaine from cells grown in 3%, 1%, and 0.2% $^{18}\text{O}_2$ with the indicated reagents for 24 h ($n = 3$). **e**, Schematic of the methionine salvage pathway. ADI1 (Acireductone dioxygenase 1), a dioxygenase, is shown in orange, and ^{18}O labelling is indicated in blue with arrows. **f–h**, Total intracellular levels of unlabelled and ^{18}O -labelled methionine from cells grown in 3%, 1%, and 0.2% $^{18}\text{O}_2$ with the indicated reagents for 24 h ($n = 3$). **i**, Schematic of methionine oxidation by ^{18}O -labelled reactive oxygen species indicated by arrows. **j–m**, Total intracellular levels of unlabelled and ^{18}O -labelled methionine sulfoxide from cells grown in 3%, 1%, and 0.2% $^{18}\text{O}_2$ with the indicated reagents for 24 h ($n = 3$). n represents

the number of biologically independent experiments for each group and condition. Graphs (mean \pm s.e.m.) were compared using two-tailed Student t-test (**c–d**, **g–h**, **k–m**) or one-way (**b**, **f**, **j**) ANOVA, followed by Tukey post hoc test (* $P < 0.05$, $^{\wedge}P < 0.01$, $^{ \% }P < 0.005$, $^{ \# }P < 0.0001$).

[Source data](#)

[Extended Data Fig. 5 Identification of \$^{18}\text{O}\$ -labelled 4-HMA in human cells.](#)

a, Tandem mass spectra (MS2) of homogentisate (HGA) standard, 4-hydroxymandelate (4-HMA) standard, unlabelled (167.0344 m/z) feature precursors, and the respective product fragments. Mass differences between the precursor and product ions reflect loss of one CO_2 . The red line indicates fragmentation of the precursor ion into the two product ions. The structure of the precursor and product ions are depicted on the left. **b**, MS2 of unlabelled (167.0344 m/z), +one ^{18}O (169.0387 m/z), and +two ^{18}O (171.0428 m/z) labelled 4-HMA precursors, and the respective product fragments. Mass differences between precursor and product ions reflects loss of unlabelled and +one ^{18}O -labelled CO_2 . The red line indicates precursor ion fragmentation into two product ions. The structure and position of ^{18}O -labelled (blue and arrow) 4-HMA are depicted on the left. **c, d**, Total levels of unlabelled and ^{18}O -labelled 4-HMA levels in A498 (**c**) and SKNDZ (**d**) cells grown in 3%, 1%, and 0.2% $^{18}\text{O}_2$, and treated with or without IOX1 (dioxygenase inhibitor) for 24 h. $n = 3$ in biologically independent replicates for each group and condition. Graphs represent mean \pm s.e.m. and were compared by two-way ANOVA (**c, d**), followed by Bonferroni post hoc test (* $P < 0.05$, $^{\wedge}P < 0.01$, $^{ \% }P < 0.005$, $^{ \# }P < 0.0001$).

[Source data](#)

[Extended Data Fig. 6 4-HMA is a tyrosine-derived metabolite synthesized from tyrosine in human cells.](#)

a, Schematic of known and proposed pathways involved in 4-HMA biosynthesis found in the literature. *A. orientalis* biosynthesizes 4-HMA from 4-hydroxyphenylpyruvate (4-HPPA), via hydroxymandelate synthase (HmaS), an Fe-dioxygenase. 4-HMA also has been proposed to be made from tyramine in rabbits by radioactive tracing studies. However, the proposed pathway was never formally demonstrated, as indicated by the dotted lines and box. **b**, Fractional labelling of Phe, Tyr, 4-HPPA, 4-HPLA, and 4-HMA from cells grown at 3% O₂ with or without ¹³C₉-Tyr or ¹³C₆-Phe for 24 h (*n* = 5 for each group). **c**, Total intracellular levels of unlabelled and ¹³C-labelled Tyr, 4-HPPA, 4-HPLA, and 4-HMA from cells grown at 3%, 1%, and 0.2% O₂ with ¹³C-Tyr for 24 h (*n* = 5 for each group). **d**, Total intracellular levels of unlabelled and ¹³C-labelled Tyr, 4-HPPA, 4-HPLA, and 4-HMA from cells grown in ¹³C-Tyr at 3% O₂ with the indicated reagents for 24 h (*n* = 5 for each group). *n* represents the number of biologically independent replicates for each group and condition. Graphs represent mean ± s.e.m. and were compared by two-way ANOVA (**b–d**), followed by Tukey post hoc test (**P* < 0.05, ^*P* < 0.01, %*P* < 0.005, #*P* < 0.0001).

[Source data](#)

Extended Data Fig. 7 Human HPDL is an ortholog of *A. orientalis* HmaS.

a, b, Phylogenetic tree of HPD, HPDL, and HmaS cDNA (**a**) and protein (**b**) sequences across several model organisms. **c**, Protein sequence alignment of HPD, HPDL and HmaS. Catalytic histidines involved in coordinating the iron ion needed for activity are highlighted in red. Specific residues in *Steptomyces avermitilis* and *Pseudomonas fluorescens* HPD have been mutated in other studies, and the human equivalent mutations are as indicated; hydrophobic (blue), polar (green) amino acids and proline (yellow). The HPD P239T mutant decreases HGA production and generates oxopinone. The N241I/L mutation abolishes HGA production by HPD. The HPD S226A mutations blocks HGA production. However, the mutation in the equivalent site in HMS (S201A) does not affect the generation of 4-HMA. The F337V/L mutation in HPD decreases HGA synthesis and allows

slight production of 4-HMA. **d**, Growth curve of MIAPACA2 cells with sgRNAs at 21% O₂. ($n = 3$ technical replicates for each cell line, performed at least twice). **e**, Unlabelled and ¹³C₈-labelled 4-HMA from PATU-8902 cells grown in ¹³C₉-Tyr at 21% ¹⁶O₂ for 24 h. ($n = 3$). Immunoblots of HPDL levels from PATU-8902 cells expressing control and HPDL sgRNAs. ERK2 serves as a loading control. **f**, Unlabelled and ¹³C-labelled Tyr, 4-HPPA, 4-HPLA from MIAPACA2 cells were grown in ¹³C₉-Tyr at 21% ¹⁶O₂ for 24 h (from Fig. 2a). ($n = 5$). **g**, Unlabelled and ¹³C-labelled Tyr, 4-HPPA, 4-HPLA from MIAPACA2 sgHPDL #3 cells were grown in ¹³C₉-Tyr at 21% ¹⁶O₂ for 24 h (from Fig. 2b). ($n = 5$). n represents the number of biologically independent replicates for each group and condition, unless indicated (**d**). Graphs are represented as mean \pm s.d. (**d**) or s.e.m. (**e–g**) and were compared by two-tailed Student t-test (**e**), or two-way ANOVA (**d, f, g**), followed by Tukey post hoc test (* $P < 0.05$, ^ $P < 0.01$, % $P < 0.005$, # $P < 0.0001$).

[Source data](#)

[Extended Data Figure 8 Expression of HPDL affects ¹³C₉-Tyr labelling of CoQ10.](#)

a, Schematic of known and unknown components of the CoQ10 biosynthesis pathway in humans. R¹ reflects the polyprenyl tail that is attached to 4-HB. **b**, Fractional labelling and total levels of CoQ10 from MIAPACA2 grown in unlabelled, ¹³C₉-Tyr-, and ¹³C₆-Phe-labelled media for 24 h at 3% ¹⁶O₂. ($n = 5$). **c**, Fractional labelling and total levels of CoQ10 from MIAPACA2 cells grown in ¹³C₉-Tyr at 21%, 3% and 0.1% ¹⁶O₂ for 24 h ($n = 5$). **d**, Fractional labelling and total levels of CoQ10 from MIAPACA2 cells grown in ¹³C₉-Tyr containing media, with the indicated compounds at 3% ¹⁶O₂ for 24 h ($n = 5$). **e**, Fractional labelling and total intracellular levels of unlabelled and ¹³C₆-labelled CoQ10 from the indicated MIAPACA2 cells. Cells were grown in ¹³C₉-Tyr at 21% ¹⁶O₂ for

24 h ($n = 5$). **f**, Fractional labelling of CoQ10 from indicated MIAPACA2 cells. Cells were grown in $^{13}\text{C}_9\text{-Tyr}$ at 21% $^{16}\text{O}_2$ for 24 h. ($n = 5$). **g**, Unlabelled and $^{13}\text{C}_6$ -labelled CoQ10 levels from PATU-8902 cells grown in $^{13}\text{C}_9\text{-Tyr}$ media ($n = 3$). **h**, Extracellular concentrations of $^{13}\text{C}_8$ -labelled 4-HMA released from MIAPACA2 cells expressing control and HPDL sgRNAs. Cells were grown in $^{13}\text{C}_9\text{-Tyr}$ at 21% $^{16}\text{O}_2$ for 24 h at low (LD) and high (HD) cell densities ($n = 3$). Representative images of LD and HD cells are shown. **i**, The effect of cell density on total intracellular levels of unlabelled and $^{13}\text{C}_6$ -labelled CoQ10 from the indicated MIAPACA2 cells. Cells were grown in $^{13}\text{C}_9\text{-Tyr}$ at 21% $^{16}\text{O}_2$ for 24 h at LD and HD ($n = 3$ for each group). “ n ” represents the number of biologically independent experiments for each group and condition. Graphs represent mean \pm s.e.m. and were compared using two-tailed Student t-test (**g**), one- (**d–f, h, i**) or two- (**b, c**) way ANOVA, followed by Tukey post hoc test (* $P < 0.05$, ^ $P < 0.01$, % $P < 0.005$, # $P < 0.0001$).

Source data

Extended Data Figure 9 CoQ10 synthesis is important for growth in 3D, but not 2D, conditions.

a, Schematic of pulse-chase study using tyrosine-derived intermediates shown in **c**. Cells were labelled with $^{13}\text{C}_9\text{-Tyr}$ for two weeks before being grown in $^{12}\text{C}_9\text{-Tyr}$ or $^{13}\text{C}_9\text{-Tyr}$ with or without unlabelled 4-HPPA, 4-HPLA, 4-HMA, and 4-HB for 24 h at 21% O_2 . **b**, Growth curve of MIAPACA2 cells with the indicated intermediates and times at 21% O_2 . ($n = 3$ technical replicates for each cell line, performed at least twice). **c**, Total levels and fractional labelling of unlabelled and ^{13}C -labelled metabolites in the CoQ10 headgroup biosynthesis pathway in humans, as described in **a** ($n = 4$). Endogenous 4-HB is below the limit of detection. **d**, Schematic of known and potential enzymes and intermediates in the CoQ10 headgroup biosynthesis pathway in humans and yeast. Dotted lines reflect potential pathways and enzymes. **e**, Immunoblot of the indicated MIAPACA2 cells. ERK2 is the loading control. Experiment was performed twice to check for

knockout efficiency. **f**, Growth in 2D culture of MIAPACA2 cells ($n = 4$). **g, h**, Total levels (**g**) and fractional labelling (**h**) of CoQ10 in MIAPACA2 cells. Cells were grown in $^{13}\text{C}_9\text{-Tyr}$ at 21% $^{16}\text{O}_2$ for 24 h ($n = 5$). **i**, Growth in 3D culture of MIAPACA2 cells ($n = 4$) after three days. **j**, Representative confocal fluorescent images of the indicated MIAPACA2 cells. Images are representative of three independent experiments. **k**, Fractional labelling of intracellular and mitochondrial CoQ10 from $^{13}\text{C}_9\text{-Tyr}$ in the indicated MIAPACA2 cells ($n = 4$). **l**, Immunoblot of total, cytosolic, and mitochondrial fractions from **k**. Subcellular fractionation was performed twice to determine the localization of HPDL. n represents the number of biologically independent experiments for each group and condition, unless indicated (**b**). Graphs (mean \pm s.e.m.) were compared by two-way ANOVA (**b, c, f–i, k**), followed by Tukey (**b, c, f–h, k**) or Dunnett's (**i**) post hoc test (* $P < 0.05$, ^ $P < 0.01$, % $P < 0.005$, # $P < 0.0001$).

[Source data](#)

[Extended Data Figure 10 HPDL is important for a subset of PDAC tumours.](#)

a, Orthotopic pancreatic tumour weight from the indicated MIAPACA2 xenografts. **b, c**, Tumour images (**b**) and weights (**c**) from a second experiment of orthotopic pancreatic tumour xenografts from MIAPACA2 cells expressing control or HPDL sgRNA with coHPDL WT or catalytically inactive mutant after 6 weeks post-injection. The first experiment set is found in **a**. **d–g**, Tumour images (**d, –f**) and weight (**e, g**) of orthotopic (**d, e**) or subcutaneous (**f, g**) pancreatic tumour xenograft of PATU-8902 cells expressing control or HPDL sgRNA after 5 weeks post-injection. **h, i**, Representative (**h**) and quantification (**i**) of H&E and immunohistochemistry for cleaved caspase 3 (CC3), phospho-histone H3 (p-HH3), and the death to proliferation ratio (CC3:p-HH3) from MIAPACA2 tumours from **a**. **j**, Overall and progression-free survival of HPDL high ($n = 44$) and low ($n = 96$) expressing PDAC tumours from the TCGA dataset. “ n ,” and each point represents the number of biologically independent experiments for each group and condition. Survival curve (**j**) was compared using the two-sided Log-rank (Mantel-Cox) test. Graphs

(median \pm max/min (**a**, **c**, **e**, **g**, **i**) were compared by two-tailed Mann Whitney test (**e**, **g**), one-way ANOVA (**a**, **c**, **i**), followed by Holm-Sidak post hoc test (* $P < 0.05$, $^{\wedge}P < 0.01$, $^{ \% }P < 0.005$, $^{ \# }P < 0.0001$).

Source data

Extended Data Figure 11 HPDL-dependent CoQ10 biosynthesis pathway.

The canonical tyrosine catabolism, HPDL-dependent (red), and HPDL-independent (purple) CoQ10 biosynthetic pathways are shown as indicated. The HPDL-independent pathway was proposed from earlier studies in rats³⁴. Dotted lines represent unknown pathway or transport steps. Potential intermediates and enzymes are proposed within the 4-HMA, HPDL-dependent and HPDL-independent pathways.

Extended Data Figure 12 Applications of gaseous labelling.

Our system for gaseous labelling can label cells with a wide range of isotopically labelled gases to study their incorporation into metabolites, lipids, nucleotides, proteins, and other cellular components to understand the mechanisms of the biological effects of these gases.

Supplementary information

Supplementary Information

This file contains raw western blot data for Fig. 2a–d, and Extended Data Figs. 1f, g, 7e, 9e, i.

Reporting Summary

Supplementary Table 1

List of ^{18}O -labelled metabolites.

Supplementary Table 2

Blastp HPDL alignment descriptions.

Supplementary Table 3

Reagents.

Source data

Source Data Fig. 1

Source Data Fig. 2

Source Data Fig. 3

Source Data Extended Data Fig. 1

Source Data Extended Data Fig. 2

Source Data Extended Data Fig. 3

Source Data Extended Data Fig. 4

Source Data Extended Data Fig. 5

Source Data Extended Data Fig. 6

Source Data Extended Data Fig. 7

Source Data Extended Data Fig. 8

Source Data Extended Data Fig. 9

Source Data Extended Data Fig. 10

Rights and permissions

Reprints and Permissions

About this article

Cite this article

Banh, R.S., Kim, E.S., Spillier, Q. *et al.* The polar oxy-metabolome reveals the 4-hydroxymandelate CoQ10 synthesis pathway. *Nature* **597**, 420–425 (2021). <https://doi.org/10.1038/s41586-021-03865-w>

- Received: 02 June 2020
- Accepted: 29 July 2021
- Published: 01 September 2021
- Issue Date: 16 September 2021
- DOI: <https://doi.org/10.1038/s41586-021-03865-w>

Share this article

Anyone you share the following link with will be able to read this content:

[Get shareable link](#)

Sorry, a shareable link is not currently available for this article.

[Copy to clipboard](#)

Provided by the Springer Nature SharedIt content-sharing initiative

This article was downloaded by **calibre** from <https://www.nature.com/articles/s41586-021-03865-w>

| [Section menu](#) | [Main menu](#) |

- Article
- Open Access
- [Published: 01 September 2021](#)

RecA finds homologous DNA by reduced dimensionality search

- [Jakub Wiktor¹](#)[✉],
[Arvid H. Gynnå](#) [ORCID: orcid.org/0000-0001-8087-7715](#)¹[✉],
- [Prune Leroy¹](#),
- [Jimmy Larsson¹](#),
- [Giovanna Coceano²](#),
- [Ilaria Testa](#) [ORCID: orcid.org/0000-0003-4005-4997](#)² &
- [Johan Elf](#) [ORCID: orcid.org/0000-0001-5522-1810](#)¹

Nature volume 597, pages 426–429 (2021)

- 13k Accesses
- 286 Altmetric
- [Metrics details](#)

Subjects

- [DNA recombination](#)
- [Homologous recombination](#)
- [Super-resolution microscopy](#)

Abstract

Homologous recombination is essential for the accurate repair of double-stranded DNA breaks (DSBs)¹. Initially, the RecBCD complex² resects the ends of the DSB into 3' single-stranded DNA on which a RecA filament assembles³. Next, the filament locates the homologous repair template on the sister chromosome⁴. Here we directly visualize the repair of DSBs in single cells, using high-throughput microfluidics and fluorescence microscopy. We find that, in *Escherichia coli*, repair of DSBs between

segregated sister loci is completed in 15 ± 5 min (mean \pm s.d.) with minimal fitness loss. We further show that the search takes less than 9 ± 3 min (mean \pm s.d) and is mediated by a thin, highly dynamic RecA filament that stretches throughout the cell. We propose that the architecture of the RecA filament effectively reduces search dimensionality. This model predicts a search time that is consistent with our measurement and is corroborated by the observation that the search time does not depend on the length of the cell or the amount of DNA. Given the abundance of RecA homologues⁵, we believe this model to be widely conserved across living organisms.

[Download PDF](#)

Main

To study the mechanism of homologous recombination in living bacteria, we created an inducible DSB system consisting of (1) an inducible Cas9 nuclease to create DSBs at a specific chromosomal location (the ‘cut site’), (2) a fluorescent *parS*/mCherry–ParB system (hereafter referred to as ParB) to visualize the chromosomal location of the break, and (3) an SOS-response⁶ reporter to select the cells undergoing DSB repair (Fig. 1a, Extended Data Fig 1a). We used a variant of the microfluidic mother machine⁷ that allows for brief induction of the Cas9 nuclease (Fig. 1a, Extended Data Fig. 1b).

Fig. 1: High-throughput imaging of DSB repair.

 **figure1**

a, Left, cartoon showing a mother machine device used to grow cells. Right, montage of a single growth channel showing SOS activation after induction of DSBs. **b**, Cartoon showing formation, processing and repair of a DSB. Cas9 binds to the cut site and creates a DSB. Next, RecBCD binds to DNA ends at the DSB site and begins end

processing, ejecting ParB proteins and generating a 3' ssDNA tail to which RecA binds and induces the SOS response. The RecA–ssDNA filament searches for homology, and after homology is located the DSB is repaired. **c**, A cell undergoing DSB repair. Loss and recovery of ParB focus are annotated. Cell outlines are displayed with white lines. **d**, The time of SOS induction in individual cells, defined as the time from the start of the Cas9 induction to the time at which the CFP signal from the SOS reporter reached half of the maximum signal. Only cells that increased CFP signal by more than fourfold were plotted. Data were aggregated from four (top) or three (middle, bottom) experiments. **e**, Localization of ParB foci along the cell length during DSB repair. Cells were oriented so that the remaining ParB focus was positioned on top. Time was aligned by ParB focus loss, as annotated in **c**. Insert shows a ParB channel of a single cell overlaid with outline and backbone (top), and mapping of the foci position along the cell's backbone (bottom), $n = 717$ cells from 4 experiments. **f**, Generation time (top left), size at the division (top right) and growth rates (bottom) of cells undergoing repair of a single DSB and their descendants. The reference (no DSB) sample consists of the cells without a DSB that were born during the time window of maximal DSB induction. The line represents the median and error bars show the first and the third quartile, $n = 60,405$ cells from 4 experiments. **g**, DSB repair times, with gamma distribution fitted to the data, $n = 765$ cells from 4 experiments.

[Source data](#).

DSB repair is fast and accurate

Formation of a DSB is followed by end processing by RecBCD, which removes ParB markers close to the break⁸, and by activation of the SOS-response reporter (Fig. [1b](#)). A pulse of Cas9 induces specific DSBs in cells with the chromosomal cut site, which is accompanied by an increase in the fraction of SOS-activated cells shortly after the induction (Fig. [1c,d](#), Extended Data Fig. [2a](#)). Expression of Cas9 in cells without the cut site or expression of catalytically dead Cas9 (dCas9) did not induce an SOS response (Fig. [1d](#), Extended Data Fig. [2b](#)). Activation of the SOS response depended on homologous recombination and was absent in cells lacking *recA* or *recB* genes (Extended Data Fig. [2b](#)). The ParB foci lost owing to DSBs were recovered and segregated in wild-type cells, but not in cells lacking critical components of recombination (Extended Data Fig. [2c,f](#)). These results show that the induced DSBs were repaired by homologous recombination. The repair is notably robust: 95.5% (447 out of 468) of cells that retained an uncleaved template repaired the DSB and subsequently divided. Repair was impaired in cells without a repair template, as none of the cells that cleaved all copies of the cut site divided during 4-h experiments ($n = 27$ cells, 3 experiments).

Next, we focused on the dynamics of the cut site loci during repair. Typically, after a DSB, the uncut locus first translocated to the middle of the cell and then split into two foci that subsequently segregated (Fig. 1c). This pattern was visible when we plotted the positions of the ParB foci along the cell length against the time relative to the DSB event (Fig. 1e). We then measured repair times in individual cells, that is, the time between the loss and reappearance of the ParB focus (Fig. 1c). We limited the analysis to cells that had two separated ParB foci before the DSB. We found that a DSB is repaired in 15.2 ± 5.0 min (Fig. 1g). These results were consistent between replicates (Extended Data Fig. 2d), and notably, when I-SceI was used instead of Cas9 to induce breaks (Extended Data Fig. 2e), or when the ParB marker was replaced by a *malO* array bound by Mali–Venus proteins (referred to as ‘Mali’) (Extended Data Fig. 3a). When the DSB was flanked by ParB on one side and Mali on the other, both ends were processed simultaneously and followed the same dynamics (Extended Data Fig. 3b). Given that the repair time is just a fraction of the generation time (here 35 ± 10 min), we tested whether it has negative effects on fitness. A single DSB delayed the division to 55 ± 10 min; however, this delay was compensated by faster divisions in the following generations (Fig. 1f). The growth rate was temporarily reduced by 4% in cells undergoing DSB repair (Fig. 1f).

Pairing between distant homologies

The loss of ParB foci prevented observation of the cleaved cut site locus. Therefore, to visualize the dynamics of the break site, we used a set of Mali markers integrated at distances that are not processed by RecBCD^{8,9} (-25 kb or $+170$ kb from the cut site) (Fig. 2b). Imaging either of the two Mali markers showed that after a DSB, both sister loci moved to the middle of the cell, where they colocalized (Fig. 2a,c, Extended Data Fig. 4a,c). The movement of the sister Mali markers was symmetric, unlike previously reported dynamics in which the cleaved sister locus moved much further after a DSB^{10,11}. To test whether the colocalization of sister loci is specific or caused by a global alignment of the chromosomes, we used a distant Mali marker integrated on the opposite arm of the chromosome (*ygaY*). The distant *ygaY* marker maintained its typical position during repair (Fig. 2d, Extended Data Fig. 4b), excluding a model in which homologous recombination repair induces pairing of entire chromosomes. Instead, it appears colocalization is specific for the cleaved cut site and its homology. As the sister locus is no different from any other chromosomal locus until it has been located through search, we concluded that the colocalization of sister loci implies completed homology search (Extended Data Fig. 4e). The -25 -kb markers colocalized 9.1 ± 3.3 min (Fig. 2e) after the DSB, and thus the homology search is faster than this.

Fig. 2: Pairing between segregated sisters.

 **figure2**

- a**, Cell with -25-kb MalI marker undergoing DSB repair. ParB focus loss and colocalization of MalI foci are annotated. Cell outlines are displayed with a white line.
- b**, Top, cartoon showing the circular *E. coli* chromosome with the locations of inserted cut site and *malO*/MalI markers. Bottom, cartoon showing the processing of a DSB in

presence of the *malO* array protected by *chi* sites. The *chi* sites prevent RecBCD from degrading the DNA before reaching *malO* sites. **c**, Localization of ~25-kb *Mall* foci in cells undergoing DSB. For each cell, the time was aligned by ParB focus loss. $n = 654$ cells from 3 experiments. **d**, As **c**, but for the *ygaY* *Mall* marker, on the opposite chromosomal arm to the cut site. $n = 753$ cells from 2 experiments. **e**, Distribution of *Mall* foci colocalization times for ~25 kb *Mall* marker during DSB repair. The solid line shows the gamma fit to the data. $n = 508$ cells from 3 experiments.

[Source data](#).

RecA filaments are thin and dynamic

The homology search is mediated by a RecA filament assembled on single-stranded DNA (ssDNA)³ and structures made by fluorescent RecA fusions have previously been imaged^{10,11,12,13,14}. We visualized RecA activity during DSB repair using a RecA–yellow fluorescent protein (YFP) fusion integrated in tandem with wild-type *recA*, a construct found to be fully active (Fig. 3c, Extended Data Fig. 5b,g). A similar construct has previously been shown to be fully functional¹⁴ but has not been used to characterize distant repair events.

Fig. 3: Thin RecA filaments mediate search for homology.

 figure3

a, RecA–YFP (green) and ParB (magenta) during DSB repair. Cell outlines are shown with a white line. **b**, Fast time-lapse of RecA–YFP during DSB repair. **c**, RecA–RecA–YFP tandem construct inserted into the *recA* locus. **d**, Lifetimes of RecA structures. The solid line shows the gamma fit to the data. $n = 3$ experiments, numbers of analysed cells are shown. **e**, RecA–ALFA construct inserted in the *recA* locus. **f**, Cell with an extended RecA–ALFA structure imaged in confocal and STED microscopy. Intensity profile between white markers is shown in Extended Data Fig. 6e. **g**, Distribution of thickness of RecA–ssDNA filaments measured as indicated in

Extended Data Fig. 6e. $n = 74$ from 2 experiments. **h**, STED images of cells with RecA–ALFA structures. White lines indicate cell outlines. **i**, Three-dimensional STED image of RecA–ALFA overlaid with confocal image of DNA stained by Pico488. Only the middle 400-nm section is shown (inset). **j**, Top, 3D STED image of RecA–ALFA overlaid with cell membrane stained with Nile red. Bottom, cross-sections at highlighted locations.

[Source data](#).

Induction of DSBs led to the *recB*-dependent formation of RecA structures at the DSB sites (Fig. 3a, Extended Data Fig. 5a,f). These structures appeared 35 ± 98 s (Extended Data Fig. 5h) before the loss of the ParB focus, and disassembled 6.6 ± 5.2 min (Extended Data Fig. 5i) before repair was complete, as defined by segregation of the ParB foci. The SOS response is activated by RecA filament assembled on ssDNA³. We predicted that if the structures are RecA–ssDNA filaments, their lifetime would correlate with the strength of the SOS response. As this was indeed the case (Pearson's $r = 0.36$, $P = 3 \times 10^{-12}$) (Extended Data Fig. 5d,e), we are confident that the structures are RecA–ssDNA filaments.

The RecA structures were highly dynamic on a timescale of tens of seconds (Fig. 3b). Their average lifetime was 8.8 ± 3.0 min (Fig. 3d), and during that time they displayed two forms: the initial spot at the DSB (existing for 2.6 ± 1.4 min) that increased in intensity (Extended Data Fig. 5a), suggesting RecA loading on ssDNA; and a filament extruding from the initial spot and extending throughout the cell (existing for 6.2 ± 2.8 min).

It has been reported that RecA forms bundle-like structures during bacterial DSB repair¹⁰. To test whether we could observe such structures, we used stimulated emission depletion super-resolution microscopy (STED) to image RecA tagged with the ALFA epitope¹⁵. RecA–ALFA alone was fully functional in DSB repair (Extended Data Fig. 5b,g). Immunostaining of cells undergoing DSB repair revealed that RecA forms thin, filamentous structures (Fig. 3f,h, Extended Data Fig. 6a) that were not associated with the membrane—rather, they appeared in the central region of the cell (Fig. 3i,j, Extended Data Fig. 6b-d, Supplementary Video 1). Deconvolution of the observed 60 ± 13 nm full width at half maximum (FWHM) with the point spread function (PFS) of the imaging system showed that the filament width is 37.5 ± 23.5 nm (Fig. 3g, Extended Data Fig. 6e,f). As expected, given the high mobility of the RecA–YFP structures in living cells, fixed cells exhibited a large variety of conformations, including complex, tangled threads or single, winding filaments spanning the length of the cell (Fig. 3h). Notably, we observed the same type of structures when immunostaining RecA–YFP in the tandem construct (Extended Data Fig. 6g), or the

RecA–ALFA, RecA–YFP tandem construct (Extended Data Fig. 6*h–k*). These results show that the homology search is performed by thin and flexible RecA filaments.

RecA reduces dimensionality of search

The fast target search by RecA compared with other systems that also rely on homology-directed search¹⁶ requires a different quantitative model. Owing to the slow diffusion rates of both the large RecA–ssDNA complex and the chromosomal loci¹⁷, the search cannot be explained by bi-molecular reaction–diffusion in three dimensions¹⁸. We propose that the RecA homology search is facilitated by a ‘reduced dimensionality’ mechanism that accelerates the process in two ways. First, ATP hydrolysis enables mechanical extension of the RecA–ssDNA filament across the cell in less than a minute, rapidly covering most of the distance between the broken ends and the search target as shown in Fig. 3*a*. Second, the extended filament interacts with many different sequences in parallel. Such simultaneous probing has previously been suggested on the basis of single-molecule experiments¹⁹ and cryo-electron microscopy structures²⁰. Our addition to the model is the realization that at any *z* coordinate (that is, along the long axis of the cell) there is always at least one segment of the stretched RecA–ssDNA filament that is homologous to a double-stranded DNA (dsDNA) segment at the same *z* position (Fig. 4*a*). This makes the search problem independent of the *z* coordinate and reduces the complexity from three to two dimensions. That is, the time of homology pairing is equal to the time it takes for a segment of chromosomal dsDNA to diffuse radially to the RecA–ssDNA filament, and not the time it takes for two segments to find each other by 3D diffusion in the whole cell. In this case, 2D search is approximately 100 times faster than 3D search²¹ (for a detailed description, see [Methods](#)).

Fig. 4: Reduction of dimensionality explains fast search times.

 **figure4**

a, The RecA–ssDNA filament and the repair template share one homologous segment (coloured bars) at each z coordinate along the length of a cell. As the repair template moves along the cell, only the segment at the current z coordinate is relevant. The search by the relevant segment thus occurs in 2D. **b**, Repair times as a function of cell length at the time of the break. The times were measured based on ParB foci splitting (left), RecA filament lifetime (middle) and Mali colocalization (right). Red lines display linear fit to the data. Numbers of analysed cells are displayed, $n = 4$ (ParB) or 3 (RecA, Mali) experiments.

[Source data](#).

In the Supplementary Information, we derive an expression for the expected time for the homologous sequences to encounter each other. Our model predicts that the search will be completed within 5 min on the basis of the rate of diffusion of the target DNA at the length scale of the radius of the nucleoid¹⁷. Of note, the model also predicts that the search time should be invariant with respect to the cell length, as only the radial distance is relevant. This distinguishes our model from previous models, such as the one presented in ref. ²². Experimental data confirm that the length of a cell has a minuscule effect on the search time estimated by either ParB foci splitting, RecA structure lifetimes or Mali foci colocalization in the mid-cell (Fig. 4b), despite larger cells having more DNA to explore (Extended Data Fig. 8).

Discussion

We propose that the stretched RecA–ssDNA filament—in a simple and elegant way—positions at least one ssDNA segment in the proximity of its homologous sister, such that the homologous dsDNA segment can find the ssDNA segment using a fast, short-range search. RecA is a prototypic member of the strand-exchange protein family, which is found in all forms of life and shares a common mechanism^{3,5}. A reduced-dimensionality mechanism may be a conserved property of these proteins. The advantage of the stretched filament is obvious in elongated cells, and long RecA structures have indeed been observed in *Caulobacter crescentus*¹¹ and *Bacillus subtilis*¹³. When DSB repair occurs at the replication fork, where the sister template is nearby, fluorescent RecA forms only a transient focus at the site of the break¹⁴, suggesting that the search may finish before the RecA filament is fully extended. Previous work has suggested that the repair of DSBs induced by I-SceI is carried out by ‘bundles’, which are complex structures formed by RecA¹⁰. These bundles are characterized by a thick central body, low mobility, tens-of-minutes lifetime, and are positioned between the nucleoid and the inner membrane. We have found that the RecA filaments involved in DSB repair are markedly different from these bundles: they are thin, dynamic, last only for minutes, and are present within the nucleoid (Fig. 3*h, i*). Notably, according to the reduced-dimensionality model, the search time is not affected by an increase in the amount of DNA, as long as the length of the filament scales with the amount of DNA. The mechanism therefore enables search in organisms with genomes larger than those of bacteria.

Methods

Strain construction

Strains used in this work are derivatives of *E. coli* TB28²³ in which we restored the *rph-1* mutation to wild type and deleted the *mall* gene and *malO* operator. Genetic integrations were done using lambda red integration²⁴, resistance cassettes were removed using the pCP20 plasmid²⁴, and markers were combined using P1 phage transduction.

The labels mCherry-ParBMt1²⁵ and Mall-Venus were expressed by constitutive promoters integrated into the *gtrA* locus. The *malO*/Mall marker consists of an array of 12 maltose operators, which are the binding sites for Mall-Venus.

The DSB cassette consists of the I-SceI recognition site flanked by two *lac* operators, a *parSMt1* site and three *chi* sites positioned outside the *parSMt1* and I-SceI recognition sequence (Extended Data Fig. 1). The Cas9 target site was chosen

about 100 bp away from the *parSMt1* site. Notably, the construct is designed in a way that there are no *chi* sites between the DSB site and *parSMt1* site. The DSB cassette was integrated into *codA* locus.

The RecA–YFP fusion was expressed directly downstream from the endogenous *recA* gene, and made by replacing mCherry with SYFP2 in the construct by ref. [14](#). The RecA–ALFA fusions were made by introducing ALFA C-terminal to *recA* in either the wild-type *recA* locus or into the tandem construct mentioned above.

List of the strains used in this study can be found in Extended Data Table [1](#).

Plasmid construction

p15a-SceIdeg-amp was cloned using HiFi DNA Assembly (NEB) by fusing two PCR fragments: (1) pSC101SceI_deg_amp⁸ fragment amplified with Jwu035 and Jwu036, and (2) p15aSceI_deg_Kan⁸ fragment amplified with Jwu037 and Jwu038. p15a-dSceIdeg-amp was cloned with Gibson assembly from two PCR fragments amplified from p15a-SceIdeg-amp template with two primer pairs: (1) Jwu088 and Jwu090, and (2) Jwu085 and Jwu091. p15a-Cas9deg-amp was cloned using Gibson assembly from two fragments: (1) p15a-SceIdeg-amp fragment amplified with Jwu273 and Jwu274, and (2) pCRED (gift from Daniel Camsund) fragment amplified with Jwu263 and Jwu264. Plasmid p15a-SceIdeg-amp-SOS was cloned using Gibson assembly protocol with: (1) p15a-SceIdeg-amp fragment amplified with primers Jwu330 and Jwu331, (2) fragment amplified form *E. coli* genome (from the strain EL1171) with primers Jwu332 and Jwu333. p15a-Cas9deg-amp-SOS plasmid was cloned using Gibson assembly with (1) p15a-wtCas9deg-amp fragment amplified with primers Jwu263 and Jwu272 and (2) p15a-SceIdeg-smp-SOS fragment amplified with primers Jwu273 and Jwu274. p15a-dCas9deg-amp-SOS was cloned using Gibson assembly protocol using (1) fragment amplified from p15a-SceIdeg-amp-SOS using primers Jwu273 and Jwu274 and (2) fragment amplified from *E. coli* genome (from the strain EL1605) using primers Jwu264 and Jwu272. pKD13-recA::ALFA-recAsh-SYFP2-frt-kan-frt was cloned using golden gate protocol with BbsI restriction enzyme from (1) fragment amplified from *E. coli* genome (from the strain EL2515) with primers Jwu485 and Jwu486, (2) fragment amplified from *E. coli* genome (from the strain EL2699) using primers Jwu487 and Jwu488, and (3) fragment amplified from pKD13-P58-SYFP2-frt-kan-frt with primers Jwu489 and Jwu490.

psgRNA-CS1 was cloned in *E. coli* Top10 by blunt-end ligation of a fragment generated with a PCR with Jwu267 and Jwu184 and psgRNA²⁶ plasmid as a template (psgRNA was a gift from D. Bikard; Addgene plasmid no. 114005), the guide RNA (gRNA) sequence is ACTGGCTAATGCACCCAGTA.

A list of primers used in this study can be found in Extended Data Table [2](#).

High-throughput DSB imaging

Growth conditions

For the microfluidic experiments cells were grown at 37 °C in M9 medium supplemented with 0.4% glucose, 0.08% RPMI 1640 amino acids (Sigma-Aldrich R7131), surfactant Pluronic F-109 (Sigma-Aldrich 542342, 21 µg ml⁻¹), and when relevant carbenicillin (40 µg ml⁻¹) or kanamycin (20 µg ml⁻¹). Cells from -80 °C freezer stock were used to inoculate LB medium supplemented with adequate antibiotics and grown overnight at 37 °C. On the next day, the cells were diluted 1/250 in M9 0.4% glucose 0.08% RPMI medium and grown for 2 h, then cells were loaded onto the microfluidic chip. Cells were grown in the microfluidic chip for at least 2 h before the start of the experiments. Induction of Cas9 and dCas9 was done with a 5-min (or 6-min for spot counting experiments in Extended Data Fig. [2c](#)) pulse of aTc (20 pg ml⁻¹).

Microscopy

Microscopy experiments were performed using a Ti2-E (Nikon) inverted microscope equipped with CFI Plan Apochromat DM Lambda 100× objective (Nikon), Sona 4.2B-11 sCMOS camera (Andor), and Spectra III (Lumencor) fluorescent light source. The microscope was controlled by Micro-Manager^{[27](#)} running in-house build plugins. Fluorescence light source was triggered by the camera with the TTL connection. Custom fluorescent cubes were used: CFP excitation filter: BrightLine FF02-438/24 (Semrock), emission filter: BrightLine FF01-494/41 (Semrock), dichroic mirror: Di02-R442 (Semrock); YFP excitation filter: FF01-514/3-25 (Semrock), emission filter: ET550/50M 200362 (Chroma), dichroic mirror: Di02-R514 (Semrock); mCherry excitation filter: FF01-559/34 (Semrock), emission filter: T590LP 262848 (Chroma), dichroic mirror: T585lpxr (Chroma). Imaging was done with a 1.5× intermediate magnification lens. Phase-contrast images were taken with the CFP cube inserted. Typically, a phase-contrast image was acquired every minute with 80 ms exposure, CFP channel every third minute with fluorescence light intensity set at 5% and exposure of 40 ms, mCherry channel was acquired every minute with fluorescent light intensity set at 20% and exposure of 80 ms, YFP channel was acquired every minute (for imaging RecA), or every second minute (for Mall experiments) with fluorescence light intensity set at 40% and exposure of 100 ms. For spot counting experiments in Extended Data Fig. [2c](#) the mCherry channel was imaged every third minute, and 3 z slices separated by 300 nm were taken at every time point and fluorescent images were reconstructed using maximum intensity projection.

Microfluidic experiments

Microfluidics experiments were performed using PDMS mother machine microfluidic chips developed previously⁷. This chip design allows for loading of two different strains and for automated switching of the medium. Medium pressure was controlled using an OB1 MK3+ microfluidic flow controller (Elveflow). The aTc was pulsed at the beginning of the for 3-h experiments, or 20 min after the start of image acquisition for 4-h experiments.

Chromosome staining with DAPI

Strains EL2504 and EL1743 (with *dnaC2*²⁸) were grown overnight in LB medium. The next day, cell cultures were diluted in 5 ml of M9 with 0.4% glucose and 0.08% RPMI 1640 amino acids (Sigma-Aldrich R7131), and incubated at 37 °C (strain EL2504). The EL1734 strain was grown at 30 °C for 2 h before imaging one aliquot of the culture was grown at 42 °C to induce replication arrest. DAPI was added to a final concentration of 1 µg ml⁻¹, and cells with DAPI were incubated for 30 min at the growth temperatures. Then 1 ml of cells was centrifuged at 4 °C, 7,000 rpm (5424 R, Eppendorf) for 3 min and resuspended in 50 µl of cold ITDE (Integrated DNA Technologies) buffer supplemented with 10 mM MgCl₂. Two µl of concentrated cells were mounted on an agarose pad for imaging. Imaging was done with a 445-nm laser at the power 12 mW cm⁻² and exposure time of 220 ms. Phase-contrast images were segmented using Nested-Unet neural network²⁹, trained in-house. DAPI images were corrected for background by subtracting the mean pixel intensity of the area outside of the cell.

Image analysis

Data analysis was done in MATLAB (Mathworks), with the exception of the cell segmentation, which was done in Python. Microscopy data were processed using an automated analysis pipeline developed previously³⁰, with several modifications. First, segmentation of phase-contrast images was done using Nested-Unet neural network²⁹ trained in-house, specifically for our microscopy setup. Pytorch 1.7.1 was used for the neural networks. We trained two networks, one to segment cells, and another to detect microfluidic growth channels on the phase-contrast images (Extended Data Fig. 1c). Transformation matrices between images acquired with different filter cubes were measured and fluorescent images were transformed to correct for the pixel shifts between fluorescence and phase-contrast images. Gramm³¹ toolbox was used to generate some of the plots in Matlab.

Selection and analysis of cells undergoing DSB

Cells undergoing a DSB repair were selected on the basis of an increase of at least fourfold in CFP signal from plasmid-borne SOS reporter. First, the CFP image was background corrected by subtracting an image filtered with a Gaussian filter with the kernel size of 20 pixels (using the Matlab function `imgaussfilt`) from the original CFP image. We limited the analysis to the cells that had no major errors in segmentation, lived for at least 9 min, and divided during the experiment. Manual repair dynamics annotation was done only on cells that contained two ParB foci prior to the DSB, and divided after the repair. Cells that had >2 ParB foci, or that induced a DSB more than once, were excluded from the analysis. In the experiment in Extended Data Fig. 2c ParB foci were detected automatically using a radial symmetry-based method. Spot positions were mapped on the cell length using a custom written Matlab code. All images showing example cells come from the experiments that were repeated at least twice, with exception of costaining of RecA–YFP and RecA–ALFA, which was done once (Extended Data Fig. 6 h–k).

Super-resolution STED microscopy

Sample preparation

Cells expressing RecA–ALFA, RecA–YFP, or both were grown for 3 h at 37 °C in M9 medium with glucose (0.4%), RPMI 1640 amino acids (0.08%), carbenicillin (20 µg ml⁻¹) and kanamycin (10 µg ml⁻¹). Cas9 was induced for 40 min with aTc (0.8 pg ml⁻¹), after which the cells were fixed with formaldehyde (3.5%) for 10 min. Fixing was quenched with 100 mM glycine and the cells were washed in PBS before permeabilization in 70% ethanol for 1 h. For staining, the cells were blocked in PBS with BSA (1%) for 30 min and then incubated with antibodies at 1:200 dilution for at least 1 h. We used camelid single domain antibodies conjugated to either Star635P or Star580, for RecA–ALFA FluoTag-X2 anti-ALFA (N1502-Ab635P) and for RecA–YFP FluoTag-X4 anti-GFP (N0304-Ab635P and N0304-Ab580, NanoTag Biotechnologies). In the absence of epitopes, no antibody binding was detected (Extended Data Fig. 7). To visualize the nucleoid and membranes, the cells were stained with Pico488 (1:400 dilution, Lumiprobe) and Nile red (5 µM), respectively. After three washes in PBS, the cells were mounted on an agarose pad for microscopy.

2D and 3D STED microscopy

Super-resolution imaging was performed with a custom-built STED setup³². Excitation of the dyes was done with pulsed diode lasers; at 561 nm (PDL561, Abberior Instruments), 640 nm (LDH-D-C-640, PicoQuant) and 510 nm (LDF-D-C-

510, PicoQuant). A laser at 775 nm (KATANA 08 HP, OneFive) was used as the depletion beam, which was split into two orthogonally polarized beams that were separately shaped to a donut and a top-hat respectively in the focal plane using a spatial light modulator (LCOS-SLM X10468-02, Hamamatsu Photonics), enabling both 2D- and 3D-STED imaging. The laser beams were focused onto the sample using a HC PL APO 100 \times /1.40 Oil STED White objective (15506378, Leica Microsystems), through which the fluorescence signal was also collected. The imaging was done with a 561-nm excitation laser power of 8–20 μ W, a 640 nm excitation laser power of 4–10 μ W and a 775 nm depletion laser power of 128 mW, measured at the first conjugate back focal plane of the objective.

Two-color STED imaging of RecA–YFP together with RecA–ALFA was done in a line-by-line scanning modality, averaging over 4 or 8 lines; while ParB and RecA–ALFA was recorded frame by frame, with the first channel in confocal and the second channel in STED. The pixel size for all 2D images was set to 20 nm with a pixel dwell time of 50 μ s.

Volumetric two-color 3D-STED imaging of RecA-ALFA together with Nile red was recorded in a line-by-line scanning modality, while a single confocal frame of Pico488 was recorded at the middle of the bacterial cell afterwards. The voxel size for *xyz* volumes was set to $25 \times 25 \times 80$ nm³. The pixel dwell time was set at either 30 or 50 μ s.

Raw images were processed and visualized using the ImSpector software (Max-Planck Innovation) and ImageJ^{33,34}. Brightness and contrast were linearly adjusted for the entire images. The size of the RecA filaments and RecA bundles were calculated tracing line profiles perpendicular to the structure orientation and averaged on two pixels on the raw images. The data were then fitted with a Gaussian function with the software OriginPro2020, from which the full width half maximum was extracted. For *xz* representation, images were deconvolved using the Richardson Lucy deconvolution algorithm implemented in ImSpector. 3D volumetric rendering was done with Huygens deconvolution in Imaris 9.1 (Bitplane).

The resolution of the microscope was measured on a calibration sample, made of sparse antibodies attached to the glass, coupled with the Star635P dye. The line profiles were extracted and fitted with a Lorentzian function³⁵, from which the width (*W*) was extracted as the dot size.

We estimated the diameter of the filaments to be 37.5 ± 23.5 nm as a deconvolution of observed 60 ± 13 nm FWHM width (Fig. 3g) with the 35 ± 11 nm (FWHM) Lorentzian PFS of the imaging system (Extended Data Fig. 6f) assuming that filament is a cylinder with a 3 nm layer of fluorophores at the surface.

I-SceI experiments

For experiments with the I-SceI meganuclease, cells with the p15a-I-SceI plasmid were cultured in M9 minimal medium, loaded in a microfluidic chip and then incubated at 37 °C in M9 medium with glucose (0.4%), RPMI 1640 amino acid supplement (Sigma-Aldrich R7131, 0.05%), carbenicillin ($20 \mu\text{g ml}^{-1}$) and Pluronic F-108 ($21 \mu\text{g ml}^{-1}$). DSBs were induced by switching for 3 min to medium also containing aTc (20 ng ml^{-1}) and IPTG (1 mM), and then for three min to medium with only IPTG. The cells were then imaged while repairing and recovering in the initial medium.

Serial-dilution plating assay

Bacteria cultures were streaked on LA plates from freezer stock and grown overnight at 37 °C. The following day, 5 ml of LB medium was inoculated with a single colony from the overnight plate and cultured for 6 h at 37 °C. Next, tenfold serial dilutions were made in LB and 4 μl of each dilution was plated on a LA plate, or LA plate containing $1 \mu\text{g ml}^{-1}$ of nalidixic acid. Plates were incubated overnight at 37 °C.

Search model by extended RecA filament

Homology search will be treated as a diffusion-limited reaction with a transport time for the homologous sequences to reach a reaction radius and a probing time once the sequences have met. The probing time for the correct sequence will be negligible compared to the time for getting the homologous sequences in contact, but the overall reaction will be slowed down by the overwhelming number of incorrect sentences that will need to be probed.

To quantify the situations we start with few approximations. Assume that the RecA–ssDNA filament is a thin rod in the centre of the cylindrical nucleoid reaching from pole to pole in the z direction, whereas the homologous dsDNA sequence is coiled up at a random position in the nucleoid. The relevant time for the homologous sequences to find each other is the time for a segment in the coiled up dsDNA to diffuse radially into the rod in the centre of the cell. The central realization in our model is that it does not matter at which z -coordinate it reaches the rod. This transforms the search problem from 3D to 2D, since we can describe the search process from the perspective of the dsDNA fragment that is homologous to the ssDNA sequence that happens to be at the z -position at which the rod is reached first.

An equivalent way to think about the situation is to consider that the first binding event for many independent searchers (that is, the chromosomal dsDNA segments), that each can bind to one out of many targets (that is, the RecA-bound ssDNA

segments), has the same rate as one searcher that can bind all targets. The total rate of binding is $\langle r = \sum_i \{r\}_i \rangle$, in which r_i is the rate for template segment $\langle i \rangle$ to find its homologous ssDNA segment. If we write out the dependence of at which z -coordinate, $\langle z_j \rangle$, the filament is reached, the total rate can be expressed as $\langle r = \sum_j \{r\}_j \sum_i \{r\}_i \langle z_j \rangle p(\langle z_j \rangle) \rangle$, in which $p(\langle z_j \rangle)$ is the probability to reach the filament at position $\langle z_j \rangle$ and $\langle \{r\}_i (\langle z_j \rangle) \rangle$ is the conditional rate for segment $\langle i \rangle$ of binding given that the filament is reached at $\langle z_j \rangle$. Here, the rate of binding is zero unless the template segment matches the ssDNA that is at the specific z -position, that is, $\langle \{r\}_i (\langle z_j \rangle \neq i) \rangle = 0$ which means that $\langle r = \sum_i \{r\}_i \langle z_i \rangle \rangle / p(\langle z_i \rangle)$, that is, the total binding rate is the same as the binding rate for a single dsDNA segment that can bind at any position at the filament, irrespective of z position, and for which each position is homologous.

Search time prediction for *E. coli*

In a first-order approximation of how long it takes for a chromosomal dsDNA segment to diffuse from a random radial position in the nucleoid to the filament in its centre, we can use the diffusion limited rate for reaching a rod in the centre of a cylinder²¹ of length $2L$, that is, $k = 2\pi(2L)D/\ln(R/r)$, in which r is the reaction radius of the rod, which is assumed to be in the order of a nucleotide (1 nm), and R is the nucleoid radius. The concentration of the searching dsDNA fragment is $c = 1/V = 1/(2L\pi R^2)$, in which V is the nucleoid volume. The average time to reach the rod is therefore $T = V/k = R^2 \ln(R/r)/2D$. The nucleoid radius $R \approx 200$ nm and the reaction radius is in the order of $r \approx 1$ nm, although the exact value is inconsequential as only its logarithm enters into the time. The complicated parameter is the diffusion rate constant D , as DNA loci movement is subdiffusive and D is therefore lower at a long length scale than a short. The process will however be limited by the long distance movement corresponding to R . At the length scale¹⁷ of $R = 200$ nm, $D_R \approx 0.0007 \text{ } \mu\text{m}^2 \text{ s}^{-1}$. The association step of the search process is thus $T \approx (0.2 \text{ } \mu\text{m})^2 \times \ln(200 \text{ nm}/1 \text{ nm})/0.0007 \text{ } \mu\text{m}^2 \text{ s}^{-1} = 300 \text{ s} = 5 \text{ min}$. If we consider that also the RecA filament is moving on the minute timescale this will only speed up search further.

Time for probing

The RecA filament will, however, not be accessible for binding all the time since it also needs to probe all other dsDNA segments. If only half of the measured search time (about 10 min) is needed for homologous sequences to meet, 5 min is still available for probing other sequences. Is this sufficient to probe all sequences? If the dsDNA is probed in n -bp-long segments, each of the equally long segments of the 2-kb-long ssDNA in the RecA filament will have to interrogate, on average, every

$2,000/n$ segments of the chromosome. There are 9.6 Mb (4.8 Mb per genome \times approximately 2 genomes per cell) of dsDNA in the cell, which corresponds to $9.6 \times 10^6/n$ probing segments. This, in turn, means that each ssDNA segment in the RecA filament needs to test $(9.6 \times 10^6/n)/(2,000/n) = 4,800$ dsDNA segments. The average time for each test cannot be longer than $300 \text{ s}/4,800 \approx 63 \text{ ms}$, which should be plenty of time, considering that Cas9–sgRNA takes on average 30 ms to perform a similar task¹⁶.

ATP binding and hydrolysis

ATP-RecA has high affinity towards ssDNA¹⁵ and upon binding results in a stretched and rigid filament with persistence length¹⁶ of about 900 nm. ATP hydrolysis lowers the affinity of RecA to ssDNA and is needed for rapidly discarding mismatched sequences^{17,36,37}. ATP turnover is therefore needed to stretch the filament in the intracellular environment where it otherwise would get stuck at partial homologies.

Alternative models

Alternative models for how to get sequences sufficiently close to probe for homology can come in many other flavours.

The most naive comparison is considering the diffusion limited bi-molecular reaction of a particle with diffusion rate corresponding to the dsDNA segment and a non-diffusive segment of the filament with a reaction radius corresponding to r (about 1 nm) anywhere in nucleiod. Here, the rate of the diffusion limited reaction is $k = 4\pi r D_L$, in which D_L is the diffusion^{38,39} rate at the length scale of the cell, whereas the concentration of the segment is the same as above ($c = 1/V = 1/(2L\pi R^2)$). This results in $T = V/k = LR^2/2rD_L$. This should be compared to $R^2\ln(R/r)/2D_R$ in the 2D situation. Importantly, the diffusion rate at the length scale of the nucleoid radius, D_R , is one order of magnitude¹⁷ faster than D_L . The ratio is $(L/rD_L)/(\ln(R/r)/D_R) \approx 1,750$, considering $L = 1 \mu\text{m}$, $R = 300 \text{ nm}$, $r = 1 \text{ nm}$ and $D_R/D_L \approx 10$. The actual value for r is more important in this case, because the number of rebinding events is more important than in the 2D case.

An intermediate step towards the 2D model is to parallelize the naive model and think of the homologous dsDNA as divided in segments that can search in parallel and independently for their respective homology in the RecA filament. For example, if we divide a 1,750-bases-long filament into segments of 10, the speed would increase by 175 times and the remaining difference compared to the 2D model would be $(D_R/D_L) - \text{fold difference of short- and long-range diffusion}$.

A final model is to consider the homologous DNA as static and that only the RecA filament moves similarly to a knitting needle in a ball of yarn. This situation is not as straightforward to quantify, since we do not know how rigid the RecA filament is on different length scales in the cell. It appears to be flexible on the 100-nm length scale, but the probing interactions will have to occur on the 1-nm scale and we therefore have no knowledge of how fast the filament would explore the genome. It can clearly probe many DNA segments simultaneously¹⁹ but it causes complex constraints to probe sequences with one part of the filament at the same time as the filament should move to explore the rest of the genome. Detailed simulations may be needed to predict the expected search times for this type of model.

Reporting summary

Further information on research design is available in the [Nature Research Reporting Summary](#) linked to this paper.

Data availability

Raw microscopy data are available at

<https://doi.org/10.17044/scilifelab.14815802>. Source data are provided with this paper.

Code availability

The computational code used for analysis and plotting is available at

<https://doi.org/10.17044/scilifelab.14815802>.

References

1. 1.

Kowalczykowski, S. C. An overview of the molecular mechanisms of recombinational DNA repair. *Cold Spring Harb. Perspect. Biol.* **7**, a016410 (2015).

2. 2.

Dillingham, M. S. & Kowalczykowski, S. C. RecBCD enzyme and the repair of double-stranded DNA breaks. *Microbiol. Mol. Biol. Rev.* **72**, 642–671 (2008).

3. 3.

Bell, J. C. & Kowalczykowski, S. C. RecA: regulation and mechanism of a molecular search engine. *Trends Biochem. Sci.* **41**, 491–507 (2016).

4. 4.

Renkawitz, J., Lademann, C. A. & Jentsch, S. Mechanisms and principles of homology search during recombination. *Nat. Rev. Mol. Cell Biol.* **15**, 369–383 (2014).

5. 5.

Bianco, P. R., Tracy, R. B. & Kowalczykowski, S. C. DNA strand exchange proteins: a biochemical and physical comparison. *Front. Biosci.* **3**, D570–D603 (1998).

6. 6.

Radman, M. SOS repair hypothesis: phenomenology of an inducible DNA repair which is accompanied by mutagenesis. *Basic Life Sci.* **5A**, 355–367 (1975).

7. 7.

Baltekin, Ö., Boucharin, A., Tano, E., Andersson, D. I. & Elf, J. Antibiotic susceptibility testing in less than 30 min using direct single-cell imaging. *Proc. Natl Acad. Sci. USA* **114**, 9170–9175 (2017).

8. 8.

Wiktor, J., van der Does, M., Büller, L., Sherratt, D. J. & Dekker, C. Direct observation of end resection by RecBCD during double-stranded DNA break repair in vivo. *Nucleic Acids Res.* **46**, 1821–1833 (2018).

9. 9.

Cockram, C. A., Filatenkova, M., Danos, V., El Karoui, M. & Leach, D. R. F. Quantitative genomic analysis of RecA protein binding during DNA double-strand break repair reveals RecBCD action in vivo. *Proc. Natl Acad. Sci. USA* **112**, E4735–E4742 (2015).

10. 10.

Lesterlin, C., Ball, G., Schermelleh, L. & Sherratt, D. J. RecA bundles mediate homology pairing between distant sisters during DNA break repair. *Nature* **506**, 249–253 (2014).

11. 11.
Badrinarayanan, A., Le, T. B. K. & Laub, M. T. Rapid pairing and resegregation of distant homologous loci enables double-strand break repair in bacteria. *J. Cell Biol.* **210**, 385–400 (2015).
12. 12.
Renzette, N. *et al.* Localization of RecA in *Escherichia coli* K-12 using RecA-GFP. *Mol. Microbiol.* **57**, 1074–1085 (2005).
13. 13.
Kidane, D. & Graumann, P. L. Dynamic formation of RecA filaments at DNA double strand break repair centers in live cells. *J. Cell Biol.* **170**, 357–366 (2005).
14. 14.
Amarh, V., White, M. A. & Leach, D. R. F. Dynamics of RecA-mediated repair of replication-dependent DNA breaks. *J. Cell Biol.* **217**, 2299–2307 (2018).
15. 15.
Götzke, H. *et al.* The ALFA-tag is a highly versatile tool for nanobody-based bioscience applications. *Nat. Commun.* **10**, 4403 (2019).
16. 16.
Jones, D. L. *et al.* Kinetics of dCas9 target search in *Escherichia coli*. *Science* **357**, 1420–1424 (2017).
17. 17.
Weber, S. C., Spakowitz, A. J. & Theriot, J. A. Nonthermal ATP-dependent fluctuations contribute to the in vivo motion of chromosomal loci. *Proc. Natl Acad. Sci. USA* **109**, 7338–7343 (2012).
18. 18.
Collins, F. C. & Kimball, G. E. Diffusion-controlled reaction rates. *J. Colloid Sci.* **4**, 425–437 (1949).
19. 19.

Forget, A. L. & Kowalczykowski, S. C. Single-molecule imaging of DNA pairing by RecA reveals a three-dimensional homology search. *Nature* **482**, 423–427 (2012).

20. 20.

Yang, H., Zhou, C., Dhar, A. & Pavletich, N. P. Mechanism of strand exchange from RecA–DNA synaptic and D-loop structures. *Nature* **586**, 801–806 (2020).

21. 21.

Berg, O. G. & Blomberg, C. Association kinetics with coupled diffusional flows. *Biophys. Chem.* **4**, 367–381 (1976).

22. 22.

Kochugaeva, M. P., Shvets, A. A. & Kolomeisky, A. B. On the mechanism of homology search by RecA protein filaments. *Biophys. J.* **112**, 859–867 (2017).

23. 23.

Bernhardt, T. G. & de Boer, P. A. J. The *Escherichia coli* amidase AmiC is a periplasmic septal ring component exported via the twin-arginine transport pathway. *Mol. Microbiol.* **48**, 1171–1182 (2003).

24. 24.

Datsenko, K. A. & Wanner, B. L. One-step inactivation of chromosomal genes in *Escherichia coli* K-12 using PCR products. *Proc. Natl Acad. Sci. USA* **97**, 6640–6645 (2000).

25. 25.

Nielsen, H. J., Ottesen, J. R., Youngren, B., Austin, S. J. & Hansen, F. G. The *Escherichia coli* chromosome is organized with the left and right chromosome arms in separate cell halves. *Mol. Microbiol.* **62**, 331–338 (2006).

26. 26.

Cui, L. *et al.* A CRISPRi screen in *E. coli* reveals sequence-specific toxicity of dCas9. *Nat. Commun.* **9**, 1912 (2018).

27. 27.

Edelstein, A. D. *et al.* Advanced methods of microscope control using µManager software. *J. Biol. Methods* Ch.14, Unit14.20 (2010).

28. 28.

Withers, H. L. & Bernander, R. Characterization of *dnaC2* and *dnaC28* mutants by flow cytometry. *J. Bacteriol.* **180**, 1624–1631 (1998).

29. 29.

Zhou, Z., Siddiquee, M. M. R., Tajbakhsh, N. & Liang, J. UNet++: redesigning skip connections to exploit multiscale features in image segmentation. *IEEE Trans. Med. Imaging* **39**, 1856–1867 (2020).

30. 30.

Camsund, D. *et al.* Time-resolved imaging-based CRISPRi screening. *Nat. Methods* **17**, 86–92 (2020).

31. 31.

Pierre, M. Gramm: grammar of graphics plotting in Matlab. *J. Open Source Software* **3**, 568 (2018).

32. 32.

Alvelid, J. & Testa, I. Stable stimulated emission depletion imaging of extended sample regions. *J. Phys. D* **53**, 024001 (2019).

33. 33.

Schindelin, J. *et al.* Fiji: an open-source platform for biological-image analysis. *Nat. Methods* **9**, 676–682 (2012).

34. 34.

Rueden, C. T. *et al.* ImageJ2: ImageJ for the next generation of scientific image data. *BMC Bioinf.* **18**, 529 (2017).

35. 35.

Vicidomini, G. *et al.* STED nanoscopy with time-gated detection: theoretical and experimental aspects. *PLoS ONE* **8**, e54421 (2013).

36. 36.

Lee, J. Y., Qi, Z. & Greene, E. C. ATP hydrolysis Promotes Duplex DNA Release by the RecA Presynaptic Complex. *J. Biol. Chem.* **291**, 22218–22230 (2016).

37. 37.

Danilowicz, C., Hermans, L., Coljee, V., Prévost, C. & Prentiss, M. ATP hydrolysis provides functions that promote rejection of pairings between different copies of long repeated sequences. *Nucleic Acids Res.* **45**, 8448–8462 (2017).

38. 38.

Berg, O. G. On diffusion-controlled dissociation. *Chem. Phys.* **31**, 47–57 (1978).

39. 39.

Baba, T. et al. Construction of *Escherichia coli* K-12 in-frame, single-gene knockout mutants: the Keio collection. *Mol. Syst. Biol.* **2**, 2006.0008 (2006).

Acknowledgements

We thank D. Fange, I. Barkefors and D. Jones for helpful input on the manuscript, D. Camsund for the pCRED plasmid, S. Zirkin and P. Karempudi for help with the image analysis. J.W. is an EMBO non-stipendiary fellow (EMBO ALTF 1029-2018). This work was funded by the H2020 Marie Curie Individual Fellowship grant (RecPAIR:842047) to J.W., European Research Council (BIGGER:885360), the Swedish Research Council (2016.06213 and 2018.03958), the Knut and Alice Wallenberg Foundation (2016.0077, 2017.0291 and 2019.0439) and the eSENSE e-science initiative to J.E., and SSF (FFL15-0031) to I.T.

Author information

Author notes

1. These authors contributed equally: Jakub Wiktor, Arvid H. Gynnå

Affiliations

1. Department of Cell and Molecular Biology, Science for Life Laboratory, Uppsala University, Uppsala, Sweden

Jakub Wiktor, Arvid H. Gynnå, Prune Leroy, Jimmy Larsson & Johan Elf

2. Department of Applied Physics, Science for Life Laboratory, KTH Royal Institute of Technology, Stockholm, Sweden

Giovanna Coceano & Ilaria Testa

Contributions

J.E., J.W. and A.H.G. conceived the study and interpreted results. A.H.G., J.W. and J.L. conducted the experiments. J.W. and J.L. performed imaging with Cas9-induced breaks; A.H.G. performed imaging with SceI-induced breaks and STED sample preparation. J.W. and A.H.G. wrote analysis code and analysed data, A.H.G., J.W. and P.L. constructed the strains, P.L. made and tested the new RecA fusion, J.E. derived equations and G.C. and I.T. contributed the STED imaging. J.E., A.H.G. and J.W. wrote the manuscript with the input of all authors.

Corresponding author

Correspondence to Johan Elf.

Ethics declarations

Competing interests

The authors declare no competing interests.

Additional information

Peer review information *Nature* thanks Anatoly Kolomeisky, David Leach and Stephan Uphoff for their contribution to the peer review of this work. Peer reviewer reports are available.

Publisher's note Springer Nature remains neutral with regard to jurisdictional claims in published maps and institutional affiliations.

Extended data figures and tables

[Extended Data Figure 1 DSB induction system and image processing.](#)

a, Genetic constructs used in the DSB reporter system. Cas9 and SOS-reporter are encoded on a single plasmid and sgRNA is on a separate plasmid. A map of the circular *E. coli* chromosome with the site at which the cut site was integrated is shown. Bottom cartoon shows a magnified view of the cut site cassette integrated into *codA* locus on the chromosome. The histogram shows the distribution of the number of cut site copies in the cells measured as the number of ParB foci. $n = 9,263$ cells from 3 experiments. **b**, Top, cartoon showing a simplified schematic of a microfluidic chip. Bottom: cartoons showing a medium input junction and flow of the medium during growth (left) and induction (right) phases of the experiment. The rightmost cartoon shows an arrangement of the growth channels on the chip. Typically strains transformed with an active Cas9 and dCas9 were loaded on separate sides of the chip, to serve as a control for induction strength. **c**, Left: Steps in the image analysis pipeline. Right: *Top* image shows a full field of view (FOV) of a single position of the microfluidic chip. Typically 16 positions were imaged during an experiment. *Middle* image shows an enlarged section of the FOV with an overlaid mask of segmented channels. *Bottom* image shows the same section of FOV as in the middle, but overlaid are segmented cells

[Source data.](#)

[Extended Data Figure 2 Specificity of the DSB induction.](#)

a, Top: Cells during a DSB experiment showing SOS reporter channel, cells that activated SOS response are outlined and displayed on the bottom. The arrow points at ParB focus that is lost in the next frame. Scale bar is 2 μm . **b**, Fractions of cells that activated SOS response in different strains and for active, or dead Cas9 variants. Cut-site- strain lacks chromosomal *cut-site*. Bars represent the mean, points represent a mean for each of the biological replicates of the experiments. **c**, Mean ParB foci number per cell after induction of Cas9 or dCas9 (induction was at $t = 20$ min). Solid line shows mean, light colored area shows 95% confidence interval measured by bootstrap. Wt: $n = 3$ experiments, $\Delta recA$: $n = 2$ experiments, $\Delta recB$: $n = 2$ experiments. **d**, Repair times measured by ParB focus loss to recovery in each of 4 experimental replicates. Centre line represents the median, box boundaries show 25th and 75th percentiles, whiskers show the most extreme values, or 1.5-fold of upper and lower interquartile range (IQR) if the most extreme values are beyond that cutoff, the solid dots represent the data points beyond the cutoff. N (for each experiment): rep. 1 - 250 cells, rep. 2 - 150 cells, rep. 3 - 174 cells, rep. 4 - 171 cells. **e**, Repair times measured by ParB focus loss to recovery of DSBs caused by either Cas9 (Cas9 data is the same in Fig. 1g) or I-SceI enzyme. Box plots as in d. I-SceI: $n = 73$ cells, 8 experiments, Cas9: $n = 765$ cells, 4 experiments. **f**, $\Delta ruvC \Delta recG$ cells after a DSB. Scale bar is 2 μm

[Source data](#).

Extended Data Figure 3 DSB repair dynamics in presence of different markers.

a, Two example cells undergoing DSB repair. Events of MalI focus loss and recovery are annotated, as well as the repair time. Cell outlines are displayed with a solid gray line. Scale bar is 2 μ m. Cartoon shows a cut-site construct with *malO*/MalI marker, the distance between the markers and cut-site is indicated. The box plots display the repair time measurements for the strain with MalI markers compared to the strain with ParB markers (ParB data is the same in Fig. 1g). Centre line represents the median, box boundaries show 25th and 75th percentiles, whiskers show the most extreme values, or 1.5-fold of upper and lower interquartile range (IQR) if the most extreme values are beyond that cutoff, the solid dots represent the data points beyond the cutoff. ParB: n = 765 cells from 4 experiments, MalI: n = 221 cells from 2 experiments. **b**, Two example cells undergoing DSB repair. Repair time is annotated with a solid white line. Cell outlines are displayed with a gray solid line. Scale bar is 2 μ m. Cartoon shows a cut-site flanked by *malO*/MalI and *parS*/ParB markers, distance between the markers and the cut-site is indicated

[Source data](#).

Extended Data Figure 4 Paring of the distant homologues.

a, Cell with +170kb MalI markers undergoing DSB repair. ParB focus loss and recovery events are shown. **b**, As in **a**, but for a cell with *ygaY* MalI marker. Event of MalI markers pairing is shown. **c**, Spatial localization of +170kb MalI foci in time in cells undergoing DSB. For each cell, the time was aligned based on the time of ParB focus loss. Color bar displays density of counts, n = 337 cells from 2 experiments. **d**, Time of ParB focus splitting after pairing of the -25 kb MalI foci, n = 507 cells from 3 experiments. **e**, Cartoon showing events leading to the colocalization of MalI foci in the centre of the cell. 1. DSB induced by Cas9. 2. ParB focus at the site of the DSB is lost due to end resection. 3. Repair template is identified and the homologous loci move and colocalize at the centre of the cell. 4. DSB is repaired, ParB focus is restored, and the homologous loci segregate

[Source data](#).

Extended Data Figure 5 RecA structures are specific.

a, Cells with ParB and RecA labels undergoing DSB repair. **b**, Growth of strains with different RecA variants without, or in presence of DNA damage induced by nalidixic

acid. **c**, Correlation between the time of activation of SOS response measured by fluorescence from plasmid SOS reporter and from RecA expression. SOS activation was measured by the time at which fluorescent signals reached half maximum value. Analysis was restricted only to cells that activated SOS response. Red line shows linear fit to the data (black), dashed lines show 95% confidence interval. Right-hand plot shows SOS (blue) and RecA (green) intensity traces for a single cell. Time of half-maximum signal for each channel is shown. Correlations are Pearson's r , $n = 255$ cells, from 1 experiment. P values are from F-test. **d**, Correlation between the lifetime of RecA structure and increase of SOS signal intensity for cells undergoing DSB repair. The solid red line shows linear fit, dashed red lines show confidence bounds, correlation is Pearson's r , $n = 358$ cells from 3 experiments. P values are from F-test. **e**, Same as in **d** but for a correlation between RecA structure lifetime and increase in expression of the RecA-YFP, correlation is Pearson's r , $n = 358$ cells from 3 experiments. P values are from F-test. **f**, Fraction of cells with RecA structure after the induction of DSB (at time=0), $n = 2$ experiments. **g**, Repair times measured by ParB focus loss to recovery of DSBs for different RecA variants (wild-type data is the same in Fig. 1g). Centre line represents the median, box boundaries show 25th and 75th percentiles, whiskers show the most extreme values, or 1.5-fold of upper and lower interquartile range (IQR) if the most extreme values are beyond that cutoff, the solid dots represent the data points beyond the cutoff, RecA-YFP: $n = 371$ cells from 4 experiments, wt: $n = 765$ cells from 4 experiments, RecA-ALFA: 361 cells from 2 experiments. **h**, Times between appearance of RecA structure to loss of ParB focus, $n = 358$ cells from 3 experiments. **i**, Times between the disassembly of RecA structure to splitting of ParB focus, $n = 358$ cells from 3 experiments

Source data.

Extended Data Figure 6 STED microscopy of RecA filaments.

a, Cells with Cas9-induced DSBs, expressing RecA-ALFA and labeled by anti-ALFA-Star635P antibodies. Star635P was imaged in STED and ParB in confocal microscopy. Cell outlines are indicated by dashed lines. The indicated cell is shown in Fig. 3f. **b**, Volumetric three dimensional view of cells (also presented in Fig. 3i) with extended RecA-ALFA structures, imaged by 3D STED. **c**, Top: 3D STED cross-sections of cells with RecA-ALFA and Nile red membrane stain as indicated in Fig. 3j. Bottom: Line profiles of RecA and membrane intensities as indicated above. Peak-to-peak distances between RecA and membrane are indicated. **d**, Left: Average distribution of membrane dye and RecA in the cross-section of cell segments with extended RecA structures. Right: Radial density of membrane and RecA in the cross-sections to the left, $n = 17$ cells from 2 experiments. **e**, Line profiles between markers in Fig. 3f, in confocal and STED microscopy. Solid line indicates Gaussian fit of the STED profile. Filament width is measured as the FWHM of the Gaussian fit. **f**, Measurement of

STED resolution using Star635P-conjugated antibodies. Left: Profile over single antibody as indicated in the insert, and Lorenzian fit of this profile. Right: Distribution of FWHM of Lorenzian fitted line profiles of antibodies, representing the resolution of the STED microscope, $n = 50$ from one experiment. **g**, STED image of cells with extended structures and RecA-RecA-YFP construct, labeled by anti-GFP antibody. **h**, Genetic construct expressing both RecA-ALFA and RecA-YFP, inserted in the native *recA* locus. **i**, STED images of cell with extended RecA filament, stained with anti-GFP-Star580 and anti-ALFA-Star635P antibodies. **j**, Fluorescence intensity profile as indicated in **i**, showing overlap between the two antibodies. **k**, Further STED image with immunolabeled cells as in **i**

[Source data](#).

Extended Data Figure 7 Validation of antibodies.

Specificity of intracellular antibody labeling, indicated by binding of Star635P-conjugated antibodies specific to ALFA and GFP-derivatives, in strains with or without epitopes, and with and without DNA damage induction.

Extended Data Figure 8 DNA amount scales with the cell size.

Scatter plot showing DNA content (DAPI) as a function of cell size, $n = 9065$ cells from 1 experiment

[Source data](#).

Extended Data Table 1 List of strains used in the study

Extended Data Table 2 List of primers used in the study

Supplementary information

Video 1 Subcellular localization of RecA filament

3D STED reconstruction of cells with Cas9-induced DSBs, expressing RecA-ALFA and labeled by anti-ALFA Star635P antibodies (green), and cell membrane stained by Nile red (magenta).

Reporting Summary

Peer Review File

Source data

[Source Data Fig. 1](#)

[Source Data Fig. 2](#)

[Source Data Fig. 3](#)

[Source Data Fig. 4](#)

[Source Data Extended Data Fig. 1](#)

[Source Data Extended Data Fig. 2](#)

[Source Data Extended Data Fig. 3](#)

[Source Data Extended Data Fig. 4](#)

[Source Data Extended Data Fig. 5](#)

[Source Data Extended Data Fig. 6](#)

[Source Data Extended Data Fig. 8](#)

Rights and permissions

Open Access This article is licensed under a Creative Commons Attribution 4.0 International License, which permits use, sharing, adaptation, distribution and reproduction in any medium or format, as long as you give appropriate credit to the original author(s) and the source, provide a link to the Creative Commons license, and indicate if changes were made. The images or other third party material in this article are included in the article's Creative Commons license, unless indicated otherwise in a credit line to the material. If material is not included in the article's Creative Commons license and your intended use is not permitted by statutory regulation or exceeds the permitted use, you will need to obtain permission directly from the copyright holder. To view a copy of this license, visit <http://creativecommons.org/licenses/by/4.0/>.

[Reprints and Permissions](#)

About this article

Cite this article

Wiktor, J., Gynnå, A.H., Leroy, P. *et al.* RecA finds homologous DNA by reduced dimensionality search. *Nature* **597**, 426–429 (2021). <https://doi.org/10.1038/s41586-021-03877-6>

- Received: 19 February 2021
- Accepted: 04 August 2021
- Published: 01 September 2021
- Issue Date: 16 September 2021
- DOI: <https://doi.org/10.1038/s41586-021-03877-6>

Share this article

Anyone you share the following link with will be able to read this content:

[Get shareable link](#)

Sorry, a shareable link is not currently available for this article.

[Copy to clipboard](#)

Provided by the Springer Nature SharedIt content-sharing initiative

This article was downloaded by **calibre** from <https://www.nature.com/articles/s41586-021-03877-6>

- Article
- [Published: 01 September 2021](#)

Structure of *Geobacter* pili reveals secretory rather than nanowire behaviour

- [Yangqi Gu](#) ORCID: [orcid.org/0000-0002-8206-8804^{1,2 na1}](https://orcid.org/0000-0002-8206-8804),
- [Vishok Srikanth](#) ORCID: [orcid.org/0000-0003-2498-4641^{1,3 na1}](https://orcid.org/0000-0003-2498-4641),
- [Aldo I. Salazar-Morales](#) ORCID: [orcid.org/0000-0002-8126-9460^{1,3}](https://orcid.org/0000-0002-8126-9460),
- [Ruchi Jain^{1,3}](#),
- [J. Patrick O'Brien^{1,3}](#),
- [Sophia M. Yi](#) ORCID: [orcid.org/0000-0001-9219-9536^{1,3}](https://orcid.org/0000-0001-9219-9536),
- [Rajesh Kumar Soni⁴](#),
- [Fadel A. Samatey^{1,3}](#),
- [Sibel Ebru Yalcin](#) ORCID: [orcid.org/0000-0002-6041-5297^{1,3}](https://orcid.org/0000-0002-6041-5297) &
- [Nikhil S. Malvankar](#) ORCID: [orcid.org/0000-0001-5611-6633^{1,3}](https://orcid.org/0000-0001-5611-6633)

[Nature](#) volume **597**, pages 430–434 (2021)

- 4444 Accesses
- 144 Altmetric
- [Metrics details](#)

Subjects

- [Cryoelectron microscopy](#)
- [Element cycles](#)
- [Molecular evolution](#)

- [Nanoscale biophysics](#)
- [Soil microbiology](#)

Abstract

Extracellular electron transfer by *Geobacter* species through surface appendages known as microbial nanowires¹ is important in a range of globally important environmental phenomena², as well as for applications in bio-remediation, bioenergy, biofuels and bioelectronics. Since 2005, these nanowires have been thought to be type 4 pili composed solely of the PilA-N protein¹. However, previous structural analyses have demonstrated that, during extracellular electron transfer, cells do not produce pili but rather nanowires made up of the cytochromes OmcS^{2,3} and OmcZ⁴. Here we show that *Geobacter sulfurreducens* binds PilA-N to PilA-C to assemble heterodimeric pili, which remain periplasmic under nanowire-producing conditions that require extracellular electron transfer⁵. Cryo-electron microscopy revealed that C-terminal residues of PilA-N stabilize its copolymerization with PilA-C (to form PilA-N–C) through electrostatic and hydrophobic interactions that position PilA-C along the outer surface of the filament. PilA-N–C filaments lack π -stacking of aromatic side chains and show a conductivity that is 20,000-fold lower than that of OmcZ nanowires. In contrast with surface-displayed type 4 pili, PilA-N–C filaments show structure, function and localization akin to those of type 2 secretion pseudopili⁶. The secretion of OmcS and OmcZ nanowires is lost when *pilA-N* is deleted and restored when PilA-N–C filaments are reconstituted. The substitution of *pilA-N* with the type 4 pili of other microorganisms also causes a loss of secretion of OmcZ nanowires. As all major phyla of prokaryotes use systems similar to type 4 pili, this nanowire translocation machinery may have a widespread effect in identifying the evolution and prevalence of diverse electron-transferring microorganisms and in determining nanowire assembly architecture for designing synthetic protein nanowires.

Access options

Subscribe to Journal

Get full journal access for 1 year

\$199.00

only \$3.90 per issue

[Subscribe](#)

All prices are NET prices.

VAT will be added later in the checkout.

Tax calculation will be finalised during checkout.

Rent or Buy article

Get time limited or full article access on ReadCube.

from \$8.99

[Rent or Buy](#)

All prices are NET prices.

Additional access options:

- [Log in](#)
- [Access through your institution](#)
- [Learn about institutional subscriptions](#)

Fig. 1: Discovery and identification of *G. sulfurreducens* pili.

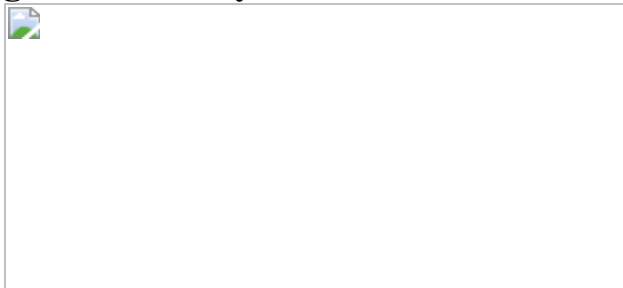


Fig. 2: PilA-N recruits PilA-C to form a heterodimer that polymerizes into a filament.

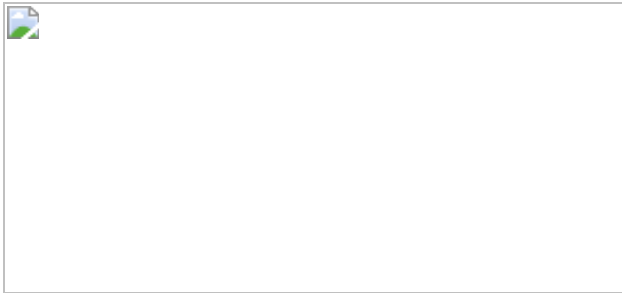
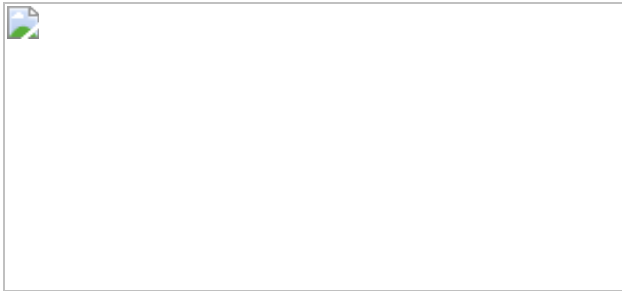


Fig. 3: *Geobacter sulfurreducens* PilA-N-C pili are involved in the translocation of OmcS and OmcZ nanowires.



Data availability

The key relevant datasets generated during and/or analysed during the current study are publicly available. Cryo-EM data have been deposited with the Electron Microscopy Data Bank (accession code [EMD-21225](#)) and with the Protein Data Bank (PDB) (accession code [6VK9](#)). All other relevant data are included in the [Supplementary Information](#). An interactive 3D visualization is available at <http://Proteopedia.org/w/Malvankar/3>. Source data are provided with this paper.

Code availability

No special software code was used to collect data.

References

1. 1.

Reguera, G. et al. Extracellular electron transfer via microbial nanowires. *Nature* **435**, 1098–1101 (2005).

2. 2.

Wang, F. et al. Structure of microbial nanowires reveals stacked hemes that transport electrons over micrometers. *Cell* **177**, 361–369 (2019).

3. 3.

Filman, D. J. et al. Cryo-EM reveals the structural basis of long-range electron transport in a cytochrome-based bacterial nanowire. *Commun. Biol.* **2**, 219 (2019).

4. 4.

Yalcin, S. E. et al. Electric field stimulates production of highly conductive microbial OmcZ nanowires. *Nat. Chem. Biol.* **16**, 1136–1142 (2020).

5. 5.

Malvankar, N. S. et al. Tunable metallic-like conductivity in microbial nanowire networks. *Nat. Nanotechnol.* **6**, 573–579 (2011).

6. 6.

Michel, G. P. & Voulhoux, R. in *Bacterial Secreted Proteins: Secretory Mechanisms and Role in Pathogenesis* (ed. Wooldridge, K.) 67–92 (Caister Academic, 2009).

7. 7.

Yalcin, S. E. & Malvankar, N. S. The blind men and the filament: understanding structures and functions of microbial nanowires. *Curr. Opin. Chem. Biol.* **59**, 193–201 (2020).

8. 8.

Liu, X., Zhuo, S., Rensing, C. & Zhou, S. Syntrophic growth with direct interspecies electron transfer between pili-free *Geobacter* species. *ISME J.* **12**, 2142–2151 (2018).

9. 9.

Richter, L. V., Sandler, S. J. & Weis, R. M. Two isoforms of *Geobacter sulfurreducens* PilA have distinct roles in pilus biogenesis, cytochrome localization, extracellular electron transfer, and biofilm formation. *J. Bacteriol.* **194**, 2551–2563 (2012).

10. 10.

Shu, C., Xiao, K., Yan, Q. & Sun, X. Comparative analysis of type IV pilin in *Desulfuromonadales*. *Front. Microbiol.* **7**, 2080 (2016).

11. 11.

O'Brien, J. P. & Malvankar, N. S. A simple and low-cost procedure for growing *Geobacter sulfurreducens* cell cultures and biofilms in bioelectrochemical systems. *Current Protoc. Microbiology* **43**, A.4K.1–A.4K.27 (2017).

12. 12.

Liu, X., Zhan, J., Jing, X., Zhou, S. & Lovley, D. R. A pilin chaperone required for the expression of electrically conductive *Geobacter sulfurreducens* pili. *Environ. Microbiol.* **21**, 2511–2522 (2019).

13. 13.

Vignon, G. et al. Type IV-like pili formed by the type II secreton: specificity, composition, bundling, polar localization, and surface presentation of peptides. *J. Bacteriol.* **185**, 3416–3428 (2003).

14. 14.

Durand, E. et al. XcpX controls biogenesis of the *Pseudomonas aeruginosa* XcpT-containing pseudopilus. *J. Biol. Chem.* **280**, 31378–

31389 (2005).

15. 15.

Wang, F. et al. Cryoelectron microscopy reconstructions of the *Pseudomonas aeruginosa* and *Neisseria gonorrhoeae* type IV pili at sub-nanometer resolution. *Structure* **25**, 1423–1435 (2017).

16. 16.

Richter, L. V., Franks, A. E., Weis, R. M. & Sandler, S. J. Significance of a posttranslational modification of the PilA protein of *Geobacter sulfurreducens* for surface attachment, biofilm formation, and growth on insoluble extracellular electron acceptors. *J. Bacteriol.* **199**, e00716-16 (2017).

17. 17.

Parge, H. E. et al. Structure of the fibre-forming protein pilin at 2.6 Å resolution. *Nature* **378**, 32–38 (1995).

18. 18.

Harvey, H. et al. *Pseudomonas aeruginosa* defends against phages through type IV pilus glycosylation. *Nat. Microbiol.* **3**, 47–52 (2018).

19. 19.

Vik, Å. et al. Insights into type IV pilus biogenesis and dynamics from genetic analysis of a C-terminally tagged pilin: a role for O-linked glycosylation. *Mol. Microbiol.* **85**, 1166–1178 (2012).

20. 20.

Craig, L., Pique, M. E. & Tainer, J. A. Type IV pilus structure and bacterial pathogenicity. *Nat. Rev. Microbiol.* **2**, 363–378 (2004).

21. 21.

López-Castilla, A. et al. Structure of the calcium-dependent type 2 secretion pseudopilus. *Nat. Microbiol.* **2**, 1686–1695 (2017).

22. 22.

Li, J., Egelman, E. H. & Craig, L. Structure of the *Vibrio cholerae* type IVb Pilus and stability comparison with the *Neisseria gonorrhoeae* type IVa pilus. *J. Mol. Biol.* **418**, 47–64 (2012).

23. 23.

Liu, X. et al. A *Geobacter sulfurreducens* strain expressing *pseudomonas aeruginosa* type IV pili localizes OmcS on pili but is deficient in Fe(III) oxide reduction and current production *Appl. Environ. Microbiol.* **80**, 1219–1224 (2014).

24. 24.

Xiao, K. et al. Low energy atomic models suggesting a pilus structure that could account for electrical conductivity of *Geobacter sulfurreducens* pili. *Sci. Rep.* **6**, 23385 (2016).

25. 25.

Shipps, C. et al. Intrinsic electronic conductivity of individual atomically resolved amyloid crystals reveals micrometer-long hole hopping via tyrosines. *Proc. Natl Acad. Sci. USA* **118**, e2014139118 (2021).

26. 26.

Mehta, T., Childers, S. E., Glaven, R., Lovley, D. R. & Mester, T. A putative multicopper protein secreted by an atypical type II secretion system involved in the reduction of insoluble electron acceptors in *Geobacter sulfurreducens*. *Microbiology* **152**, 2257–2264 (2006).

27. 27.

Shi, L. et al. Direct involvement of type II secretion system in extracellular translocation of *Shewanella oneidensis* outer membrane cytochromes MtrC and OmcA. *J. Bacteriol.* **190**, 5512–5516 (2008).

28. 28.

Bouhenni, R. A. et al. The role of *Shewanella oneidensis* MR-1 outer surface structures in extracellular electron transfer. *Electroanalysis* **22**, 856–864 (2010).

29. 29.

Liu, X., Ye, Y., Xiao, K., Rensing, C. & Zhou, S. Molecular evidence for the adaptive evolution of *Geobacter sulfurreducens* to perform dissimilatory iron reduction in natural environments. *Mol. Microbiol.* **113**, 783–793 (2020).

30. 30.

Craig, L., Forest, K. T. & Maier, B. Type IV pili: dynamics, biophysics and functional consequences. *Nat. Rev. Microbiol.* **17**, 429–440 (2019).

31. 31.

Coppi, M. V., Leang, C., Sandler, S. J. & Lovley, D. R. Development of a genetic system for *Geobacter sulfurreducens*. *Appl. Environ. Microbiol.* **67**, 3180–3187 (2001).

32. 32.

Mehta, T., Coppi, M. V., Childers, S. E. & Lovley, D. R. Outer membrane c-type cytochromes required for Fe(III) and Mn(IV) oxide reduction in *Geobacter sulfurreducens*. *Appl. Environ. Microbiol.* **71**, 8634–8641 (2005).

33. 33.

Nevin, K. P. et al. Anode biofilm transcriptomics reveals outer surface components essential for high density current production in *Geobacter*

sulfurreducens fuel cells. *PLoS ONE* **4**, e5628 (2009).

34. 34.

Chan, C. H., Levar, C. E., Zacharoff, L., Badalamenti, J. P. & Bond, D. R. Scarless genome editing and stable inducible expression vectors for *Geobacter sulfurreducens*. *Appl. Environ. Microbiol.* **81**, 7178–7186 (2015).

35. 35.

Lefort, V., Longueville, J.-E. & Gascuel, O. SMS: smart model selection in PhyML. *Mol. Biol. Evol.* **34**, 2422–2424 (2017).

36. 36.

Yu, G., Smith, D. K., Zhu, H., Guan, Y. & Lam, T. T. Y. ggtree: an R package for visualization and annotation of phylogenetic trees with their covariates and other associated data. *Methods Ecol. Evol.* **8**, 28–36 (2017).

37. 37.

R Core Team. R: a language and environment for statistical computing (R Foundation for Statistical Computing, 2013).

38. 38.

Shevchenko, A., Tomas, H., Havlis, J., Olsen, J. V. & Mann, M. In-gel digestion for mass spectrometric characterization of proteins and proteomes. *Nat. Protocols* **1**, 2856–2860 (2006).

39. 39.

Cox, J. & Mann, M. MaxQuant enables high peptide identification rates, individualized p.p.b.-range mass accuracies and proteome-wide protein quantification. *Nat. Biotechnol.* **26**, 1367–1372 (2008).

40. 40.

Zivanov, J. et al. New tools for automated high-resolution cryo-EM structure determination in RELION-3. *eLife* **7**, e42166 (2018).

41. 41.

Zhang, K. Gctf: real-time CTF determination and correction. *J. Struct. Biol.* **193**, 1–12 (2016).

42. 42.

Desfosses, A., Ciuffa, R., Gutsche, I. & Sachse, C. SPRING – an image processing package for single-particle based helical reconstruction from electron cryomicrographs. *J. Struct. Biol.* **185**, 15–26 (2014).

43. 43.

He, S. & Scheres, S. H. W. Helical reconstruction in RELION. *J. Struct. Biol.* **198**, 163–176 (2017).

44. 44.

Egelman, E. H. The iterative helical real space reconstruction method: surmounting the problems posed by real polymers. *J. Struct. Biol.* **157**, 83–94 (2007).

45. 45.

Zivanov, J., Nakane, T. & Scheres, S. H. W. A Bayesian approach to beam-induced motion correction in cryo-EM single-particle analysis. *IUCrJ* **6**, 5–17 (2019).

46. 46.

Pettersen, E. F. et al. UCSF Chimera—a visualization system for exploratory research and analysis. *J. Comput. Chem.* **25**, 1605–1612 (2004).

47. 47.

Emsley, P. & Cowtan, K. Coot: model-building tools for molecular graphics. *Acta Crystallogr. D* **60**, 2126–2132 (2004).

48. 48.

Afonine, P. V. et al. Real-space refinement in PHENIX for cryo-EM and crystallography. *Acta Crystallogr. D* **74**, 531–544 (2018).

49. 49.

Nečas, D. & Klapetek, P. Gwyddion: an open-source software for SPM data analysis. *Open Phys.* **10**, 181–188 (2012).

Acknowledgements

We thank L. Craig, S. Lory and Y. Xiong for discussions; E. Martz for calling our attention to the flaps in PilA-N-C, for the Supplementary Videos and for the interactive 3D visualizations; D. Lovley, K. Inoue and B. Kazmierczak for providing strains; S. Wu and M. Llaguno for help with cryo-EM; T. Lam and J. Kanyo for help with mass spectrometry analysis; Yale West Campus Imaging and Material Characterization Core; and T. Croll for help with ISOLDE. This research was supported by a Career Award at the Scientific Interfaces from Burroughs Wellcome Fund (to N.S.M.), the National Institutes of Health Director’s New Innovator award (1DP2AI138259-01 to N.S.M.) and an NSF CAREER award no. 1749662 (to N.S.M.). Research was sponsored by the Defence Advanced Research Project Agency (DARPA) Army Research Office (ARO) and was accomplished under Cooperative Agreement Number W911NF-18-2-0100 (with N.S.M.). This research was supported by NSF Graduate Research Fellowship award 2017224445 (to J.P.O.) and NIH Training Grant T32 GM007223, which supported V.S. Research in the laboratory of N.S.M. was also supported by the Charles H. Hood Foundation Child Health Research Award, and The Hartwell Foundation Individual Biomedical Research Award.

Author information

Author notes

1. These authors contributed equally: Yangqi Gu, Vishok Srikanth

Affiliations

1. Microbial Sciences Institute Yale University, West Haven, CT, USA

Yangqi Gu, Vishok Srikanth, Aldo I. Salazar-Morales, Ruchi Jain, J. Patrick O'Brien, Sophia M. Yi, Fadel A. Samatey, Sibel Ebru Yalcin & Nikhil S. Malvankar

2. Department of Molecular, Cellular and Developmental Biology, Yale University, New Haven, CT, USA

Yangqi Gu

3. Department of Molecular Biophysics and Biochemistry, Yale University, New Haven, CT, USA

Vishok Srikanth, Aldo I. Salazar-Morales, Ruchi Jain, J. Patrick O'Brien, Sophia M. Yi, Fadel A. Samatey, Sibel Ebru Yalcin & Nikhil S. Malvankar

4. Proteomics and Macromolecular Crystallography Shared Resource, Herbert Irving Comprehensive Cancer Center, Columbia University Irving Medical Center, New York, NY, USA

Rajesh Kumar Soni

Contributions

Y.G. prepared and optimized cryo-EM grids, collected data used to build the atomic model, performed the image analysis, reconstructed the pili filament structure, generated and refined the filament model with help from F.A.S. and V.S., biochemically analysed filaments, performed AFM, circular dichroism, conductivity measurements, electrode fabrication and negative-staining TEM images. V.S. identified and purified pili filaments. A.I.S.-M.

performed adhesion and twitching motility assays. A.I.S.-M. and R.J. carried out biochemical analyses and genetic experiments. J.P.O. grew biofilms on electrodes in microbial fuel cell. Y.G., S.M.Y. and R.K.S. carried out mass-spectrometric analyses. S.E.Y. performed AFM imaging of cell-attached filaments. N.S.M. conceived, designed and supervised the project. Y.G., V.S. and N.S.M. wrote the manuscript with input from all authors.

Corresponding author

Correspondence to Nikhil S. Malvankar.

Ethics declarations

Competing interests

The authors declare no competing interests.

Additional information

Peer review information *Nature* thanks Andreas Schramm and the other, anonymous, reviewer(s) for their contribution to the peer review of this work. Peer reviewer reports are available.

Publisher's note Springer Nature remains neutral with regard to jurisdictional claims in published maps and institutional affiliations.

Extended data figures and tables

[Extended Data Fig. 1 Discovery and identification of PilA-N and PilA-C in pili.](#)

a, b, Immunoblot of filament preparation and whole cells lysate for PilA-N (**a**) and PilA-C (**b**). M, marker. For gel source data, see Supplementary Fig. [14](#) and Supplementary Fig. [5](#) for PilA-N and PilA-C, respectively. **c, d**,

TEM image (**c**) and SDS-PAGE (**d**) gel of PilA-NC filaments purified from *ΔomcS* cells. M, marker. Scale bar, 200 nm (**a**). For gel source data, see Supplementary Fig. [6](#). **e, f**, Immunoblot and corresponding mass spectrometry analysis for PilA-C (**e**) and PilA-N (**f**) containing band. For gel source data, see Supplementary Fig. [7](#).

Extended Data Fig. 2 Overexpressing PilA-N and PilA-C in wild-type *G. sulfurreducens* yielded pili-like filaments on the bacterial surface.

a, Immunoblot of whole-cell lysate showing overexpression of PilA-N and PilA-C under induced conditions. For gel source data, see Supplementary Fig. [8](#). **b, c**, Negative-stain TEM images of wild-type cells under uninduced (**b**) and induced (**c**) conditions. **d**, Zoomed image of pili-like filament shown in **c**. Scale bars, 200 nm (**b, c**), 50 nm (**d**).

Extended Data Fig. 3 De novo atomic model of PilA-N–C filament fit into the cryo-EM map.

a, PilA-N and PilA-C sequences. **b–f**, Zoomed view of the regions indicated in **a** for PilA-N (**b**) and PilA-C (**c–f**). **g, h**, Zoomed view of electron microscopy density and aromatic amino acids in PilA-N–C filament.

Extended Data Fig. 4 Contacts between PilA-N (orange) and PilA-C (cyan).

a, Pilus model. **b**, PilA-C translucent, showing protrusions of PilA-N. **c**, Heterodimer showing C-terminal residues 57–61 of PilA-N protruding to the right into PilA-C. **d**, Flaps of PilA-C (thick coils) enclosing protrusion of PilA-N. Four glycines (red balls) could provide hinges that may enable flaps to open. Animations are presented in Supplementary Videos [1–3](#).

Extended Data Fig. 5 Comparison between *K. oxytoca* pseudopili (PDB code 5WDA), *P. aeruginosa* T4P (PDB code

5XVY), *G. sulfurreducens* PilA-N–C filament and *G. sulfurreducens* PilA-N-alone filament model.

a, Helical arrangement with P and P + 4 subunits shown in the same colour. **b**, Hydrophobicity surface coloured from yellow (hydrophobic) to blue (hydrophilic). **c**, Interactions between PilA-N determines the structure as 1-start, 3-start and 4-start helix. **d**, Interactions between PilA-N and PilA-C, which is consistent with the studies on monomers that mutating E39 or E60 could disrupt the interactions while mutating E48 showed no disruption.

Extended Data Fig. 6 Post-translational modifications in PilA-N–C filament.

a, Lack of PTM in Y32 of PilA-N. Mass spectra of PilA-N did not show any modified peptide in AYNSAASSDLR with expected mass of 1.154 kDa. Inset, MS/MS spectra showed no modification on Y32 in PilA-N. **b**, Mass spectra showed methylated peptide FTLIELLVVAIIGILAAIAIPQQFSAYR with mass 3.044 kDa. Inset, MS/MS spectra showed N-terminal methylation. **c**, Cryo-EM map for PilA-C showing an extra density on Ser94, suggesting a post-translational modification. **d**, Gel of purified filaments showing glycosylated PilA-C (left lane) and positive control using horseradish peroxidase (right lane).

Extended Data Fig. 7 *Geobacter sulfurreducens* PilA-N–C pilus is structurally similar to a T2SS pseudopilus and does not show structure or functions of T4aP.

a, The globular domain of the PilA-N–C pilin protomer lacks hallmarks of T4P (PDB code 5XVY): disulfide bridge (green), four β -strands motif (blue) and D-region (magenta), consistent with pseudopili (PDB code 5O2Y). **b**, Hydrophobic interactions are the main interactions between PilA-N chains, similar to pseudopili, whereas T4P are additionally stabilized via intersubunit electrostatic interactions between F1 and E5. **c, d**, Comparison of bacterial adhesion to glass (**c**) and twitching motility (**d**). Error bars, s.d. ($n = 3$). **e, f**, Core aromatic residues in the theoretical model of PilA-N filament²⁴ (**e**) and cryo-EM structure of PilA-N–C filament (**f**). **g**,

AFM image of a PilA-N–C filament (red) bridging gold electrodes and corresponding height profile at location shown by a black line. Scale bar, 200 nm. **h, i**, Current–voltage curve (**h**) and corresponding conductivity comparison (**i**) for individual PilA-N–C filament versus OmcS nanowire³. Error bars, s.d. ($n = 4$ biological replicates).

[Source data](#).

Extended Data Fig. 8 Thermal stability comparison between filaments of *G. sulfurreducens* PilA-N–C with *P. aeruginosa* T4P.

a, b, Circular dichroism spectra for *P. aeruginosa* T4P (**a**) and *G. sulfurreducens* PilA-N–C filaments (**b**) showing thermal denaturation. **c, d**, TEM images of *P. aeruginosa* T4P (**c**) and *G. sulfurreducens* PilA-N–C filaments (**d**) treated at the temperatures indicated for 5 min. Scale bars, 200 nm.

Extended Data Fig. 9 Cryo-EM reconstruction suggests that the previously claimed ‘PilA-N-alone’ filament could be DNA.

a, Cryo-EM image of filaments claimed to be PilA-N alone³. **b**, Cryo-EM images showed similar filaments in our OmcS filament preparations. Scale bars, 20 nm (**a, b**). Black arrows represent OmcS filaments in **a, b**. **c**, Two-dimensional average showed no helical features consistent with T4P. Scale bar, 5 nm. **d, e**, Cryo-EM density map (**d**) and docking with DNA molecule (**e**) (PDB code 1BNA), suggested the identity of the filaments to be DNA.

Extended Data Fig. 10 Expression of PilA-N–C filaments restores the secretion of OmcS and OmcZ nanowires in Δ pilA-N cells.

a, AFM images of Δ pilA-N/pilA-N-C cell showed pili on the surface of the cell. **b**, Zoomed-in image of Δ pilA-N/pilA-N-C cell. **c**, Height analysis of the pili consistent with PilA-N–C filament. **d, e**, Δ pilA-N/pilA-N-C cell showed the secretion of OmcS (**d**) and OmcZ (**d**) nanowires. Scale bars, 1

μm (**a**), 300 nm (**b**), 100 nm (**d, e**). **f**, Height analysis of filaments at locations shown in **e** showed the diameter consistent with OmcS and OmcZ filaments. **g**, Immunoblotting with OmcS antibody showing the restoration of secretion defect in OmcS nanowires in $\Delta pila-N/pila-N-C$ cells. FP, filament preparation; PP, periplasmic fraction; M, marker. For gel source data, see Supplementary Fig. 16. **h, i**, TEM image of filament preparation from $\Delta pila-N$ showing no filament (**h**) and OmcS filaments from $\Delta pila-N/pila-N-C$ (**i**). Scale bars, 200 nm (**h, i**). $\Delta pila-N/pila-N-C$: in-trans expression of an episomal copy of wild-type *pila-N* and *pila-C* in $\Delta pila-N$.

Supplementary information

Supplementary Information

This file contains Supplementary Figures 1-16 and Supplementary Tables 1-4.

Reporting Summary

Peer Review File

Video 1

Heterodimeric assembly of *Geobacter* pilin subunit. PilA-N (gold) and PilA-C (cyan) form a heterodimeric pilin in contrast to the model proposed since 2005 that *Geobacter* type 4 pili composed solely of PilA-N protein. Cryo-EM structure reveals that the C-terminal residues of PilA-N stabilize its copolymerization with PilA-C via electrostatic and hydrophobic interactions that position PilA-C along the outer surface of the filament. PilA-N is composed of two α -helices, linked by a short coil (Fig. 2d). A staggered helical array of PilA-N subunits forms the core of the PilA-N-C filament (Fig. 2e). PilA-C consists of four anti-parallel β -strands surrounded by a web of loops (Fig. 2d).

41586_2021_3857_MOESM5_ESM.mp4

Video 2 *Geobacter* PilA-N binds to PilA-C to form heterodimers. PilA-N's C terminus (gold) protrudes into a socket in PilA-C (cyan). PilA-C binds PilA-N via electrostatic and hydrophobic interactions that stabilizes the PilA-N/PilA-C heterodimer. In addition, the C-terminal 5-residues of PilA-N protrude and are held between two "flaps" of PilA-C (Extended Data Fig. 4). The N-terminus of PilA-C (Ala1) interacts with the C-terminus of PilA-N (Ser61) via hydrogen bonding or possibly a salt bridge (Fig. 2f). As the N-terminal of PilA-N is primarily hydrophobic, binding to PilA-C prevents the exposure of the hydrophobic side chains to the aqueous environment that could increase filament stability (Fig. 2e, Extended Data Fig. 5b).

Video 3

Assembly of *Geobacter* pseudopilus filament. A heterodimer of PilA-N (gold) and PilA-C (cyan) polymerizes into a filament. The overall structural features of the filament are similar to T4P, with a helical core and globular head domain arranged within a right-handed helix (Fig. 2b). The electrostatic and hydrophobic interactions (Fig. 2g) appear critical for filament stability. The filament is mainly organized via the interactions between adjacent PilA-N subunits (Extended Data Fig. 5a,c), with little direct interaction between PilA-C within the filament. The filament shows N-terminal methylation of PilA-N (Extended Data Fig. 6) and extra density around S94 for PilA-C for an O-linked glycosylation (Extended Data Fig. 6b-d).

Source data

Source Data Fig. 1

Source Data Extended Data Fig. 7

Rights and permissions

Reprints and Permissions

About this article

Cite this article

Gu, Y., Srikanth, V., Salazar-Morales, A.I. *et al.* Structure of *Geobacter* pili reveals secretory rather than nanowire behaviour. *Nature* **597**, 430–434 (2021). <https://doi.org/10.1038/s41586-021-03857-w>

- Received: 28 February 2020
- Accepted: 28 July 2021
- Published: 01 September 2021
- Issue Date: 16 September 2021
- DOI: <https://doi.org/10.1038/s41586-021-03857-w>

Share this article

Anyone you share the following link with will be able to read this content:

[Get shareable link](#)

Sorry, a shareable link is not currently available for this article.

[Copy to clipboard](#)

Provided by the Springer Nature SharedIt content-sharing initiative

This article was downloaded by **calibre** from <https://www.nature.com/articles/s41586-021-03857-w>